Faculty of Science
Department of Biology

Faculty of Bioscience Engineering
Department of Animal Sciences and
Aquatic Ecology

Elucidating the Biological Reactivity of (Aged) Micro- and Nanoplastic Particles in Marine Invertebrates: From Cellular to Organismal Responses

---

Het Ophelderen van de Biologische Reactiviteit van (Verouderde) Micro- en Nanoplasticdeeltjes in Mariene Ongewervelden: Van Cellulaire tot Organismale Reacties

A dissertation submitted to obtain the degree of
Doctor of Science: Biology at the University of Antwerp and
Doctor of Bioscience Engineering at Ghent University
to be defended by

Jenevieve Hara

Supervisors:

Prof. dr. Raewyn M. Town
Prof. dr. Ronny Blust
Prof. dr. Jana Asselman
Prof. dr. Colin R. Janssen

Antwerp, 2026

ISBN: 9789463579995

Cover images:

"Underwater and Lights", photo by Cristian Palmer, used under the Unsplash License.
"Mussels", photo by Moses Ndugwa, used with permission.

Disclaimer:

The author allows to consult and copy parts of this work for personal use. Further reproduction or transmission in any form or by any means, without the prior permission of the author is strictly forbidden.

The PhD researcher and supervisors declare that the PhD research was conducted according to the principles of scientific integrity, as mentioned in the General PhD Regulations and Charter for PhD Researchers of UAntwerp and the Integrity Charter for PhD Researchers and Supervisors affiliated with the University of Antwerp.

Members of the Doctoral Committee

Chairperson:

Prof. dr. Lieven Bervoets (University of Antwerp, Belgium)

Members:

Prof. dr. Jérôme F.L. Duval (University of Lorraine-CNRS, France)

Prof. dr. Karen Smeets (Hasselt University, Belgium)

Prof. dr. Caroline De Tender (Ghent University, Belgium)

Prof. dr. Jonas Schoelynck (University of Antwerp, Belgium)

Promoters:

Prof. dr. Raewyn M. Town (University of Antwerp, Belgium)

Prof. dr. Jana Asselman (Ghent University, Belgium)

Prof. dr. Ronny Blust (University of Antwerp, Belgium)

Prof. dr. Colin R. Janssen (Ghent University, Belgium)

Deans:

Prof. dr. Sabine Van Doorslaer (University of Antwerp, Faculty of Science)

Prof. dr. Els Van Damme (Ghent University, Faculty of Bioscience Engineering)

Rectors:

Prof. dr. Herwig Leirs (University of Antwerp)

Prof. dr. Petra De Sutter (Ghent University)

This work was supported by the RESPONSE project, funded under the Joint Action Ecological Aspects of Microplastics of JPI Oceans (B2/20E/P1/ RESPONSE “Toward a risk-based assessment of microplastic pollution in marine ecosystems”) and Research Foundation – Flanders (FWO) (G053320N “Towards ecological risk assessment of nanoplastics: dynamic considerations).

Acknowledgements

My PhD journey has been marked by growth, resilience, and the pursuit of new knowledge. Starting this chapter of my life in the midst of a global pandemic, during a time of uncertainty, and far from home, tested my courage and perseverance in ways I could never have imagined. Looking back, I am deeply grateful to everyone who stood beside me and helped make this journey not only possible, but truly meaningful.

First and foremost, I am grateful to my supervisors for entrusting me with the opportunity to pursue this PhD. I am especially grateful to Prof. Raewyn and Prof. Jana for their continuous support, invaluable scientific insight, practical advice, and constant encouragement throughout this experience. Your guidance has shaped my development as a researcher and strengthened my confidence in navigating scientific challenges.

My sincere appreciation also goes to the professors who guided me in the early stages of my learning journey, Profs. Roger, Jhonamie, Róisín, and João, as well as to my former supervisor, Sir Jong, all of whom were among the first to believe in my potential and support my doctoral applications. Your encouragement and trust gave me the courage to pursue this path.

I am likewise grateful to the members of my doctoral committee, Profs. Karen, Caroline, Jérôme, Jonas, and Lieven, for dedicating the time and effort to thoroughly review my thesis, engaging in thoughtful discussions, and providing constructive feedback, which have significantly improved the quality of this work.

A special thank you goes to Maaike, my postdoctoral mentor, for her guidance, support, and generosity in sharing her knowledge. Your patience, willingness to help, and encouraging words, especially during challenging moments, made a lasting difference throughout this journey. I also thank Sébastjen for sharing his passion for advanced microscopy and introducing me to ImageJ during the early stages of this project. Through training workshops, hands-on practice, and the analysis of hundreds of images, I gradually developed both confidence and genuine interest in the research application of this technique.

I am thankful for the opportunity to mentor and work alongside MSc students Gethrie and Philippe, whose curiosity and dedication made the experience truly rewarding.

My appreciation further extends to Prof. Jérôme and the entire LIEC team for giving me the opportunity to collaborate, access to advanced imaging equipment, and the technical support that enabled me to explore my research questions in greater depth.

I also extend my appreciation to the ECOSPHERE staff, especially Valentine, Steven, Nemo, and Bieke, for their patience, technical guidance, and help, from training on equipment and mussel dissection to setting up experimental tanks and assisting with administrative matters. Your support made the daily challenges of research much lighter.

For creating a warm and supportive working environment, I am grateful to my ECOSPHERE and BGRL colleagues and friends. The shared experiences and laughter, both in and outside the lab, made this journey far more memorable. I am especially grateful to Allen and Harvey for their constant presence, kindness, and encouragement. Their support extended far beyond the workplace, always ready to offer a helping hand, from assisting me find accommodation during the pandemic and navigating life abroad, to sharing the joys and challenges of sporting pursuits, whether completing 10-mile runs together or taking on the new experience of learning tennis. I am also thankful to Moses, Gunter, Jodie, and Cara for their positivity, collaborative spirit, encouragement, and support in the lab. It was also a pleasure to work alongside my fellow plastic researchers, Marie, Mathilde, and especially Miao.

Living in Europe was made especially meaningful by the Filipino families I had the privilege to meet, the Sajulga, Colminar, Maga-ao, and Maglinte-Papi families, who welcomed me so warmly and made me feel at home. Your kindness and generosity meant more than words can express. I am also grateful to my dear friends, especially Annie, Claire, Faith, Lyca, Che, Novy, Jelly, Dorothy, Jam, Kim, Gina, and Dada, for a friendship that knows no distance and for always being people I can count on.

I cannot thank my family enough, Papa, Mama, and my brothers Jai, John, Dale, and Nono, for their unconditional love, sacrifices, and unwavering support. You all have always been my greatest source of inspiration. To my father, Pang, as you often joke, you only had to tell me once to study well, and here I am today, having come this far. I can now truly say that all the nails you hammered and the fishing nets you cast to support my early education were worth every effort. To my niece Ellie, who has brought immense joy and inspiration into my life, I look forward to finally seeing and hugging you when I visit Palawan after completing this journey.

I am equally grateful to Mama Éva and Papa Attila for warmly embracing me as part of your family. Your constant prayers, encouragement, and assurance have been a great source of comfort and strength.

My deepest gratitude goes to Andris for his love, patience, steadfast support, and encouragement. Your dedication, perseverance, and passion for what you do have continually inspired me to go beyond my limits. You have also supported this work in countless practical ways, from helping with mussel collection in the field and fixing the flow cytometer, to contributing to the development of the image-processing pipeline and patiently helping me understand complex code. During challenging times, you gave me the gentle push I needed to keep moving forward.

I also wish to honor my grandfathers, who taught me to dream beyond the horizon. Though you are no longer here to witness this moment, your stories, your faith, and the quiet wonder you awakened in me have guided every step of this journey.

Above all, I thank God, who made all things possible and granted me the strength and wisdom to reach this milestone.

Contents

Members of the Doctoral Committee 4

Acknowledgements 5

List of Abbreviations 14

Summary 17

Dutch summary 20

Chapter 1: Plastic Pollution in the Marine Environment 23

1.1 Historical Perspective on Plastic Development 24

1.1.1 The innovation phase: early developments 24

1.1.2 The plastic revolution: mass production and public adoption 25

1.1.3 Growing awareness of plastic pollution and global responses 26

1.2 Global Plastic Production and Waste Generation 27

1.3 Major Sources of Plastic Pollution in the Marine Environment 29

1.3.1 Land-based sources 29

1.3.2 Marine-based sources 31

1.3.3 Atmospheric transport of plastic particles 33

1.4 Characterization of Plastic Particles 33

1.4.1 Physicochemical properties of plastic particles 33

1.4.2 Analytical techniques and challenges for particle characterization 36

1.5 Fate of Plastic Particles in the Marine Environment 41

1.5.1 Abundance and composition in water column and sediment 41

1.5.2 Transport mechanisms of MNPs 43

1.5.3 Weathering processes of plastic particles in the marine environment 45

1.6 Exposure Pathways and Biological Effects of MNPs in Marine Organisms 48

1.6.1 Exposure pathways 48

1.6.2 Biological effects of MNP exposure 52

1.7 Research Gaps 57

1.7.1 Lack of environmentally relevant exposure scenarios 57

1.7.2 High variability in experimental designs 58
1.7.3 Applicability for risk assessment 59
1.8 Research Aims and Thesis Outline 60
Chapter 2: Systematic Assessment of the Mechanisms and Risks of MNP Exposure in Marine Invertebrates 63
2.1 Introduction 65
2.2 Materials and Methods 66
2.2.1 Data source 66
2.2.2 Data structure 67
2.2.3 Data screening and quality criteria for the assessment of biological effects 67
2.2.4 Additional screening and quality criteria for risk assessment 68
2.2.5 SSD construction 69
2.3 Results and Discussion 70
2.3.1 Trends in experimental *in vivo* studies on the effects of MNPs in marine invertebrates 70
2.3.2 Distribution of chronic toxicity data 76
2.3.3 Species sensitivity distributions (SSD) 81
2.3.4 Derivation of preliminary safe standard (PSS) 83
2.4 Conclusions, Limitations and Future Directions 86
2.5 Acknowledgements 87
Chapter 3: Cellular and Tissue-Level Responses of Mussels to Aged PET MNPs 89
3.1 Introduction 91
3.2 Materials and Methods 93
3.2.1 Characterization of the aged PET micro- and nanoplastic particles 93
3.2.2 Test organisms 94
3.2.3 Experimental set-up 94
3.2.4 Sampling procedure 95
3.2.5 Assessment of cellular-level effect endpoints 95
3.2.6 Assessment of tissue-level effect endpoints 97
3.2.7 Statistical analysis 98
3.2.8 Quality assurance and control 98

3.3 Results 98
3.3.1 Cellular responses to aged PET MNP exposure 98
3.3.2 Histopathological responses to aged PET MNP exposure 99
3.3.3 Growth and survival of mussels exposed to aged PET MNPs 103
3.4 Discussion 107
3.4.1 Cellular responses to aged PET MNP exposure 107
3.4.2 Tissue alterations induced by aged PET MNP exposure 109
3.4.3 Implications for organismal health 111
3.5 Conclusions, Limitations, and Future Directions 113
3.6 Acknowledgements 114
Chapter 4: Differential Sensitivity of Hemocyte Subpopulations to Aged PET MNPs 115
4.1 Introduction 117
4.2 Materials and Methods 119
4.2.1 Characterization of the aged PET Micro- and nanoplastic particles 119
4.2.2 Maintenance of the mussel culture 120
4.2.3 Hemolymph extraction and cell culture preparation 120
4.2.4 *In vitro* exposure experiments 121
4.2.5 Assessment of cellular endpoints 121
4.2.6 Flow cytometry analysis 122
4.2.7 Statistical analysis 123
4.3 Results 123
4.3.1 Cellular morphology (size and complexity) 123
4.3.2 Lysosomal stability 123
4.3.3 Oxidative activity 126
4.3.4 Hemocyte mortality 126
4.4 Discussion 128
4.4.1 Morphological characterization of hemocyte subpopulations 128
4.4.2 Lysosomal destabilization in response to aged PET exposure 131
4.4.3 Oxidative stress induced by aged PET NPs 132
4.4.4 Mechanisms of hemocyte dysfunction induced by aged PET exposure 132
4.4.5 Influence of weathering on particle-induced cellular responses 133

4.5 Conclusions, Limitations, and Future Directions 134
4.6 Acknowledgements 135
Chapter 5: Characterization of NP-Induced Responses in Hemocytes Using 3D RI Mapping 137
5.1 Introduction 139
5.2 Materials and Methods 141
5.2.1 Characterization of the aged PET NPs 141
5.2.2 Maintenance of the mussel culture 142
5.2.3 Hemolymph extraction and cell culture preparation 143
5.2.4 *In vitro* exposure experiments 143
5.2.5 Label-free 3D live-cell imaging using holotomography 143
5.2.6 3D image processing to segment and identify the cellular structures and nanoplastics 144
5.3 Results and Discussion 156
5.3.1 3D holotomographic visualization of hemocyte subpopulations 156
5.3.2 Cellular internalization and localization of aged PET NPs 159
5.3.3 Characterization of the morphological changes in hemocytes 162
5.4 Conclusions and Future Directions 171
5.5 Acknowledgements 172
Chapter 6: General Discussion and Future Perspectives 173
6.1 Integrative Synthesis of Key Findings and Contributions 174
6.1.1 Estimation of community-level hazard thresholds 174
6.1.2 Effect assessment under environmentally relevant exposure scenarios 175
6.1.3 Intracellular internalization and localization of aged PET NPs in hemocytes 177
6.2 Critical Reflections and Limitations 178
6.2.1 Use of a single polymer type 178
6.2.2 Reliance on a single model species 179
6.2.3 Application of mechanically and chemically aged test particles 179
6.2.4 Lack of non-plastic particle control 180
6.2.5 Scaling and extrapolation challenges 180
6.3 Future Research Directions 181

6.3.1 Elucidation of molecular pathways and signaling cascades involved in immune dysregulation 181
6.3.2 Examination of multi-stressor interactions 183
6.3.3 Chronic and multigenerational effect assessment 183
6.3.4 Methodological standardization 184
6.4 Final Remarks 185
Bibliography 187
Supplementary Information 221
Supplementary Information: Chapter 2 222
Selection process for the systematic review 222
Quality scores of MNP toxicity studies in ToMEx 2.0 database 223
Trends in experimental studies 227
Distributions of toxicity data 229
Species sensitivity distributions 234
MNP abundance and characteristics in marine environmental matrices 242
Supplementary Information: Chapter 3 244
Characterization of the aged micro-and-nanoplastic particles (MNPs) 244
Experimental set-up and handling procedure 245
Quality assurance and control 247
Growth parameters 249
Summary of recently published *in vivo* studies on MNP toxicity 250
Supplementary Information: Chapter 4 253
Characterization of the aged micro-and-nanoplastic particles (MNPs) 253
Validation of the cellular assays 257
Overview of cellular responses to aged PET micro- and nanoplastic exposure 259
Summary of recently published studies on MNP toxicity 260
Supplementary Information: Chapter 5 262
Characterization of the aged PET NPs 262
Annotation of the cellular structures 266
Refractive index distributions of the cellular structures 267
Image processing workflow 270

Image processing validation 288
Reference hemocyte images 291
Curriculum Vitae 292

List of Abbreviations

Abbreviation	Meaning
AF	Assessment Factors
AIC	Akaike Information Criterion
ALDFG	Abandoned, Lost, or Discarded Fishing Gear
ANOVA	Analysis of Variance
AOP	Adverse Outcome Pathway
ASW	Artificial Seawater
At	Atrophied Tubules
AZ	Abfrontal Zone
BME	Basal Medium Eagle
CAT	Catalase
CM	Culture Media
DEB-IBM	Dynamic Energy Budget with Individual-based modelling
DLS	Dynamic Light Scattering
DMD	Digital Micromirror Device
DT	Digestive Tubules
ECV	Enlargement of the Central Vessel
ECx	Effect Concentration
ERMs	Ecologically Relevant Metrics
ESEM	Environmental Scanning Electron Microscopy
FSC	Forward Scatter
FTIR	Fourier Transform Infrared Spectroscopy
FZ	Frontal Zone
GPx	Glutathione Peroxidase
GSH	Glutathione
H&E	Hematoxylin and Eosin
HC5	Hazardous Concentration for 5% of Species
HDPE	High-Density Polyethylene
Hi	Hemocyte Infiltrations
HONEC	Highest Observed No-Effect Concentration
HS	Hemolymph Serum
HV	Hemolymphatic Vessel
IZ	Intermediate Zone
JRC	Joint Research Centre
LCx	Lethal Concentration
LDPE	Low-Density Polyethylene
LF	Lamellar Fusion
LIS	Live-Cell Imaging Solution
LLDPE	Linear Low-Density Polyethylene

LMS	Lysosomal Membrane Stability
LOEC	Lowest Observed Effect Concentrations
LZ	Lateral Zone
MAPK	Mitogen-Activated Protein Kinase
MNPs	Micro- and Nanoplastic Particles
MPs	Microplastic Particles
NC	Negative Control
NOEC	No-Observed-Effect Concentration
NPs	Nanoplastic Particles
NRRT	Neutral Red Retention Time
NTA	Nanoparticle Tracking Analysis
OM	Optical Microscopy
PA	Polyamide
PAH	Polycyclic Aromatic Hydrocarbon
PBS	Phosphate-Buffered Saline
PC	Positive Control
PDI	Polydispersity Index
PE	Polyethylene
PET	Polyethylene Terephthalate
PEVA	Polyethylene Vinyl Acetate
PHA	Polyhydroxyalkanoates
PI	Propidium Iodide
PIM	Polymer Identification Model
PLA	Polylactic Acid
PMMA	Polymethylmethacrylate
POPs	Persistent Organic Pollutants
PP	Polypropylene
PRISMA	Preferred Reporting Items for Systematic Reviews and Meta-Analyses
PS	Polystyrene
PSS	Preliminary Safe Standards
PTFE	Polytetrafluoroethylene
PUR	Polyurethane
PVC	Polyvinyl chloride
Py-GC-MS	Pyrolysis-Gas Chromatography-Mass Spectrometry
QA/QC	Quality Assurance and Quality Control
RI	Refractive Index
ROI	Regions of Interest
ROS	Reactive Oxygen Species
SEM	Scanning Electron Microscopy
SI	Supplementary Information
SLS	Static Light Scattering
SOD	Superoxide Dismutase
SPES	Single Particle Extinction and Scattering
SSC	Side Scatter

SSD	Species Sensitivity Distributions
TEM	Transmission Electron Microscopy
ToMEx	Toxicity of Microplastic Explorer for Aquatic Organisms
TWRPs	Tire and Road Wear Particles
UV	Ultraviolet
UW	Ultrapure Water
WWTPs	Wastewater Treatment Plants
2D	Two-Dimensional
3D	Three-Dimensional

Summary

The ubiquitous presence of micro- and nanoplastics (MNPs) in the marine environment constitutes a critical environmental challenge due to the heterogeneity of their physicochemical properties, their persistence and associated risks. Once released into the environment, plastics undergo continuous fragmentation and aging processes, generating particles across a broad size spectrum with altered physicochemical properties as compared to the original pristine materials. Such changes directly influence the way in which MNPs interact with biota. Despite growing recognition of their potential ecological impacts, mechanistic understanding of how environmentally relevant MNPs interact with biological systems remains limited. More in-depth understanding is needed to support robust ecological risk assessment frameworks.

This thesis addresses these current research gaps through an integrated, multi-tiered investigation of MNP toxicity across successive levels of biological organization. The **main objective** is to elucidate the biological reactivity of aged MNPs, with a particular focus on mechanistic assessment of cellular, tissue, and organismal responses under environmentally relevant exposure scenarios in marine invertebrates. **Chapter 1** sets the stage and summarizes the state-of-the-art and research challenges. Then, through four complementary research chapters, this thesis presents the results of a multi-level investigation that spans from community-specific hazard thresholds assessments to the intricate (sub)cellular mechanisms underlying particle-induced toxicity, as outlined below.

Chapter 2 provides a systematic evaluation of MNP toxicity across diverse marine invertebrate taxa. Using curated exposure data from the Toxicity of Microplastic Explorer (ToMEx) database for Aquatic Organisms (version 2.0), chronic no-observed-effect concentration (NOEC) values derived from mortality, fitness, and functional-related endpoints were analyzed as a function of particle characteristics (e.g., polymer type, size and shape). To translate reported biological effects into ecologically relevant risk estimates, species sensitivity distributions (SSDs) were constructed using chronic fitness-related endpoints, accounting for two distinct exposure mechanisms: food dilution via ingestion and tissue translocation. Preliminary Safe Standards (PSS), calculated using SSD-derived HC_5 values, offer provisional thresholds for protecting marine invertebrate communities. These findings provide critical insights into MNP toxicity, identify sensitive taxa and endpoints, and highlight key knowledge gaps to advance risk assessment frameworks for MNPs in marine ecosystems.

Chapter 3 transitions from interspecies comparisons to an in-depth, *in vivo* investigation of cellular and tissue-level responses to environmentally relevant concentrations of aged polyethylene terephthalate (PET) MNPs with diameters ranging from 600 nm to 3.1 µm

(mean: 1.9 µm) in a sentinel bivalve species, namely the mussel *Mytilus edulis*. In contrast to prior studies that have mainly relied on pristine, spherical particles, this research employed test plastic particles with heterogeneous shapes and sizes, reflecting modifications characteristic of naturally aged particles. The biological responses were analyzed across multiple effect endpoints during both the exposure (days 1, 3, 7, and 14) and the subsequent recovery periods (3 and 10 days post-exposure), via flow cytometry and histopathology. The results revealed the sensitivity of hemocyte subpopulations, including granulocytes and hyalinocytes, to aged PET MNPs. Concentration- and time-dependent changes in lysosomal stability, oxidative activity, and hemocyte mortality were observed, demonstrating both immediate cellular perturbations and recovery potential to alleviate particle-induced effects. Histopathological analysis of key tissues exhibited significant alterations, particularly in the gill, suggesting potential impairment of essential physiological functions. No mussel mortality or significant changes in growth metrics were observed under the tested experimental conditions.

Chapter 4 builds upon the cellular focus of the previous chapter by assessing the differential sensitivity of hemocyte subpopulations, granulocytes and hyalinocytes, to aged PET MPs and NPs with mean diameters of 1.9 µm and 0.68 µm, respectively, under controlled *in vitro* conditions. Using flow cytometry and a panel of functional biomarkers, this chapter provides mechanistic insights into the differential sensitivities of granulocytes and hyalinocytes to aged PET. Specifically, aged PET MPs and NPs induce distinct size and concentration-dependent patterns of lysosomal destabilization, coinciding with the loss of functional integrity. Elevated reactive oxygen species (ROS) levels were observed only in granulocytes and hyalinocytes exposed to high concentrations of aged PET NPs, underscoring the effects on oxidative stress. Both aged PET MPs and NPs induce significant increases in cellular mortality, particularly after 24 h of exposure at high concentrations. These findings highlight the complex cellular mechanisms underlying hemocyte functional impairment following exposure to aged PET particles under environmentally and biologically relevant conditions.

Chapter 5 advances the investigation of the interactions of aged PET NPs with hemocyte subpopulations using label-free three-dimensional live-cell imaging by holotomography. This chapter characterizes particle internalization and localization patterns, as well as the associated morphological alterations across hemocyte subpopulations. Representative refractive index (RI) tomograms revealed clear visualization of internalized PET nanoplastics with defining high-RI signals distinguishable from intrinsic cellular structure contributions, across different exposure conditions. Hemocytes exhibited morphological alterations, including extensive cytoplasmic vacuolation, granulation, and signs of membrane damage following exposure to aged PET NPs. These findings demonstrate the unique capability of holotomography to resolve unlabeled nanoplastics within living hemocytes and track their intracellular localization, offering mechanistic insight into uptake pathways and immunotoxicological responses.

An integrated discussion of the overall findings is provided in **Chapter 6**. Overall, this thesis provides a comprehensive, multi-level investigation into the biological reactivity of MNPs. These findings show that, even in the absence of lethal effects, aged MNP exposure induces measurable sublethal effects across multiple levels of biological organization, potentially compromising individual fitness and survival under chronic or combined stressors. Using aged test particles enhances the environmental relevance of the findings, but certain limitations were identified and are considered in the general discussion. Additionally, building on these insights, future research directions are outlined to advance effect assessments and integrate mechanistic understanding into risk characterization frameworks.

Dutch summary

De alomtegenwoordigheid van micro- en nanoplastics (MNPs) in het mariene milieu vormt een kritieke milieu-uitdaging omwille van de heterogeniteit van hun fysisch-chemische eigenschappen, hun persistentie en de daarmee samenhangende risico's. Eenmaal in het milieu terechtgekomen, ondergaan plastics continue fragmentatie- en verouderingsprocessen, waardoor deeltjes ontstaan met een brede diversiteit aan groottes en gewijzigde fysisch-chemische eigenschappen in vergelijking met het oorspronkelijke, onveranderde materiaal. Dergelijke veranderingen beïnvloeden de manier waarop deze MNP's interageren met organismen. Ondanks de groeiende erkenning van hun potentiële ecologische impact, blijft de mechanistische kennis over hoe zulke milieurelevante MNP's interageren met biologische systemen beperkt. Een diepgaander begrip is nodig om robuuste ecologische risicoschatting te ondersteunen.

Deze thesis pakt de huidige lacunes in het onderzoek aan door middel van een geïntegreerd, meerlagig onderzoek naar de toxiciteit van MNPs op opeenvolgende niveaus van biologische organisatie. Het **hoofddoel** is het ophelderen van de biologische reactiviteit van verouderde MNPs, met een bijzondere focus op de mechanistische beoordeling van cellulaire, weefsel- en organismale reacties onder milieurelevante blootstellingsscenario's bij mariene ongewervelden. **Hoofdstuk 1** schetst de huidige onderzoekscontext en vat de stand van zaken en de onderzoeksuitdagingen samen. Vervolgens presenteert deze thesis, via vier complementaire onderzoekshoofdstukken, de resultaten van een meerlagig onderzoek dat zich uitstrekt van beoordelingen van gemeenschapsspecifieke gevarendrempels tot de complexe (sub)cellulaire mechanismen die ten grondslag liggen aan de door deeltjes geïnduceerde toxiciteit, zoals hieronder beschreven.

Hoofdstuk 2 biedt een systematische evaluatie van de toxiciteit van micro- en nanoplasticdeeltjes (MNPs) voor diverse mariene ongewervelde taxa. Aan de hand van gecureerde blootstellingsgegevens uit de Toxicity of Microplastic Explorer (ToMEx)-databank voor waterorganismen (versie 2.0) werden chronische NOEC-waarden (no-observed-effect concentration) geanalyseerd, afgeleid van mortaliteit, fitheid en functionele eindpunten, alsook de functie van de deeltjeskenmerken (bijv. polymeertype, grootte en vorm). Om gerapporteerde biologische effecten te vertalen naar ecologisch relevante risicoschattingen, werden soortgevoeligheidsverdelingen (SSD's) geconstrueerd met behulp van chronische fitheidsgerelateerde eindpunten. Hierbij werd rekening gehouden met twee verschillende blootstellingsmechanismen: verdunning via voedselopname en weefseltranslocatie. Voorlopige veilige normen (Preliminary Safe Standards, PSS), berekend met behulp van SSD-afgeleide HC_5-waarden, bieden voorlopige drempelwaarden voor de bescherming van mariene ongewervelde gemeenschappen. Deze bevindingen bieden cruciale inzichten in de toxiciteit van MNPs, de identificatie van

gevoelige taxa en eindpunten en benadrukken belangrijke kennislacunes om risicobeoordelingen voor MNP's in mariene ecosystemen te verbeteren.

Hoofdstuk 3 gaat van vergelijkingen tussen soorten over naar een diepgaand *in vivo* onderzoek naar de reacties op cellulair en weefselniveau op milieurelevante concentraties van verouderde polyethyleentereftalaat (PET) MNPs met diameters variërend van 600 nm tot 3,1 µm (gemiddeld: 1,9 µm) in een sentinel-schelpdiersoort, namelijk de mossel *Mytilus edulis*. In tegenstelling tot eerdere studies die voornamelijk gebruik maakten van zuivere, bolvormige deeltjes, werden in dit onderzoek plastic deeltjes met heterogene vormen en groottes gebruikt, die de modificaties weerspiegelen die kenmerkend zijn voor natuurlijk verouderde deeltjes. De biologische reacties werden geanalyseerd aan de hand van meerdere effect-eindpunten tijdens zowel de blootstelling (dag 1, 3, 7 en 14) als de daaropvolgende herstelperioden (3 en 10 dagen na blootstelling), met behulp van flowcytometrie en histopathologie. De resultaten toonden de gevoeligheid aan van hemocyten-subpopulaties, waaronder granulocyten en hyalinocyten, voor verouderde PET-MNPs. Concentratie- en tijdsafhankelijke veranderingen in lysosomale stabiliteit, oxidatieve activiteit en hemocytensterfte werden waargenomen. Dit toont zowel onmiddellijke cellulaire verstoringen als herstelpotentieel aan om de door de deeltjes veroorzaakte effecten te verminderen. Histopathologisch onderzoek van belangrijke weefsels vertoonde significante veranderingen, met name in de kieuwen, wat wijst op een mogelijke aantasting van essentiële fysiologische functies. Onder de geteste experimentele omstandigheden werd geen sterfte van mosselen of significante veranderingen in groeiparameters waargenomen.

Hoofdstuk 4 bouwt voort op de cellulaire focus van het vorige hoofdstuk door de differentiële gevoeligheid van hemocyten-subpopulaties, granulocyten en hyalinocyten, voor verouderde PET-microdeeltjes (MPs) en -nanodeeltjes (NPs) met respectievelijk gemiddelde diameters van 1,9 µm en 0,68 µm te beoordelen onder gecontroleerde *in vitro*-omstandigheden. Met behulp van flowcytometrie en een reeks functionele biomarkers biedt dit hoofdstuk mechanistische inzichten in de differentiële gevoeligheid van granulocyten en hyalinocyten voor verouderd PET. Specifiek induceren verouderde PET-microdeeltjes en -NP's verschillende grootte- en concentratieafhankelijke patronen van lysosomale destabilisatie, die samenvallen met het verlies van functionele integriteit. Verhoogde niveaus van reactieve zuurstofsoorten (ROS) werden alleen waargenomen in granulocyten en hyalinocyten die werden blootgesteld aan hoge concentraties verouderde PET-NPs, wat de effecten op oxidatieve stress onderstreept. Zowel verouderde PET-microdeeltjes als -nanodeeltjes veroorzaken een significante toename van de celdood, met name na 24 uur blootstelling aan hoge concentraties. De bevindingen benadrukken de complexe cellulaire mechanismen die aan de basis liggen van de functionele aantasting van hemocyten na blootstelling aan verouderde PET-deeltjes onder milieu- en biologisch relevante omstandigheden.

Hoofdstuk 5 bouwt voort op het onderzoek naar de interacties van verouderde PET-nanodeeltjes met hemocytenpopulaties met behulp van labelvrije driedimensionale live-cell imaging door middel van holotomografie. Dit hoofdstuk beschrijft de internalisatie- en lokalisatiepatronen van de deeltjes, evenals de bijbehorende morfologische veranderingen in de verschillende hemocytenpopulaties. Representatieve refractie-index (RI)-tomogrammen lieten een duidelijke visualisatie zien van geïnternaliseerde PET-nanodeeltjes met duidelijke hoge RI-signalen die te onderscheiden waren van bijdragen van de intrinsieke celstructuur, onder verschillende blootstellingsomstandigheden. Hemocyten vertoonden morfologische veranderingen, waaronder uitgebreide cytoplasmatische vacuolisatie, granulatie en tekenen van membraanschade na blootstelling aan verouderde PET-nanodeeltjes. Deze bevindingen tonen de unieke mogelijkheid van holotomografie aan om ongelabelde nanodeeltjes in levende hemocyten te visualiseren en hun intracellulaire lokalisatie te volgen, wat mechanistisch inzicht biedt in opnameroutes en immunotoxicologische reacties.

Een geïntegreerde bespreking van de algemene bevindingen is te vinden in **hoofdstuk 6.** Deze thesis biedt dus een uitgebreid onderzoek op meerdere niveaus naar de biologische reactiviteit van MNPs. De bevindingen tonen aan dat blootstelling aan MNPs, zelfs zonder dodelijke gevolgen, meetbare subletale effecten teweegbrengt op meerdere niveaus van biologische organisatie. Dit kan de individuele fitheid en overleving onder chronische of gecombineerde stressfactoren in gevaar brengen**.** Het gebruik van verouderde testdeeltjes vergroot de relevantie van de bevindingen voor het milieu, maar er zijn bepaalde beperkingen vastgesteld die in de algemene discussie worden besproken. Daarnaast worden, voortbouwend op deze inzichten, toekomstige onderzoeksrichtingen geschetst om effectbeoordelingen te verbeteren en mechanistisch inzicht te integreren in risicokarakteriseringsmodellen.

Chapter 1

Plastic Pollution in the Marine Environment

1.1 Historical Perspective on Plastic Development

The history of plastic materials encompasses three key stages: the innovation phase, the plastic revolution marked by mass production and public adoption, and the rise of global awareness and responses to plastic pollution. Each stage has shaped the role of plastics in society, from their emergence as revolutionary materials to their current status as a global environmental challenge.

1.1.1 The innovation phase: early developments

The origins of plastics can be traced back to the mid-19th century, when the first synthetic polymeric materials were developed (Figure 1.1). One of the earliest examples was Parkesine, invented by Alexander Parkes in 1862, which is derived from a combination of cellulose and nitric acid (Gilbert, 2016). The next significant milestone was the invention of Bakelite by a Belgian chemist Leo Baekeland, in 1907, which earned him the title "Father of the Plastics Industry". Bakelite was the first fully synthetic polymer, made from a reaction between phenol and formaldehyde. Its durability, non-conductivity, and heat resistance properties enabled a wide range of applications. This innovation laid the foundation for the development of more different types of synthetic polymers in the following decades (Kaufmann, 2011).

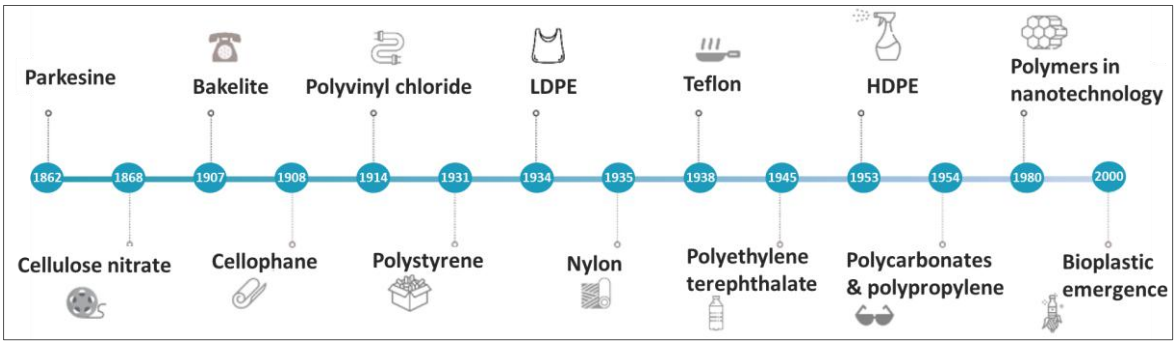

Figure 1.1. *Historical timeline showcasing key milestones in the development of synthetic plastic polymers and their applications. Adapted from: Melchor-Martínez et al., 2022.*

The discovery and development of thermoplastics such as polyvinyl chloride (PVC), polystyrene (PS), and polyethylene (PE) marked a major turning point in polymer science. These materials exhibited distinct properties such as enhanced stiffness, higher softening point, and higher density as compared to previously synthesized polymers (Shashoua, 2008; Stanley et al., 2025). The polymer PVC, synthesized through free radical polymerization of vinyl chloride monomers, is characterized by notable chemical resistance and thermal stability. Its versatility enables various applications, from high-volume construction materials to electrical insulation and protective coatings (McKeen, 2012). On the other hand, PS, produced through the polymerization of styrene, is available in various grades that exhibit differing mechanical properties. It is particularly valued for its excellent

insulating properties and diverse packaging applications (Satterthwaite, 2017). Low-Density Polyethylene (LDPE), first synthesized accidentally in 1932, is known for its unique molecular structure and versatile applications, including films, coatings, and insulation materials (Shashoua, 2008).

1.1.2 The plastic revolution: mass production and public adoption

The World War II era marked the beginning of the "Plastic Revolution." The war had increased demand and driven the development of new polymers, particularly for military and electronic applications, such as gas masks, helmets, electrical insulation, and radio components. A deeper understanding of polymer chemistry also emerged, enabling the development and production of high-performance materials. Among these innovations were polytetrafluoroethylene (PTFE, commonly known as Teflon), valued for its exceptional thermal stability (effective from –270°C to 250°C), as well as its non-stick and corrosion-resistant properties. Other developments during this time included water-repellent silicones, heat-resistant paints and epoxy resins, polymethylmethacrylate (PMMA), and polyamide (nylon) (Melchor-Martínez et al., 2022; Shashoua, 2008).

The post-war economic boom further increased consumer plastic production, with widespread adoption of materials such as PVC, PE, PS, PP, and polyethylene terephthalate (PET), which are lightweight, durable, and inexpensive to produce (Gilbert, 2016). Among these, PET emerged as a particularly versatile material, extensively used in both packaging and textile industries. Patented in 1941, PET is a thermoplastic polymer synthesized through esterification reaction of ethylene glycol and terephthalic acid with the exclusion of water molecules during polymerization. Owing to its ability to be processed into films, molded components, and fibers, PET has become integral to various material applications (Shashoua, 2008). Initially developed for fiber production in the early 1940s and subsequently for film applications, PET was not prominently used as beverage packaging bottles until 1973 (Gilbert, 2016). In the early 1950s, high-density polyethylene (HDPE) and polypropylene (PP) were also developed. Compared to LDPE, HDPE offers greater chemical resistance, hardness, stiffness, and tensile strength. These materials are widely used today in packaging materials, automotive parts, textiles, reusable containers, electrical, and biomedical applications (Lambert & Wagner, 2018; Shashoua, 2008). Various copolymers and blends emerged between 1960 and 2000, expanding the functional scope of the plastic industry (Melchor-Martínez et al., 2022).

More recently, the development of bioplastics has emerged as a sustainable alternative to the environmental drawbacks of conventional petroleum-based plastics. This diverse class of materials is defined by their renewable biological origin, designed biodegradability, or a combination of both. The term biobased refers to plastics derived from plant sources (e.g., corn, sugarcane, or cellulose). In contrast, biodegradable plastics are defined by their capacity to decompose into natural substances without the need for artificial additives (Stanley et al., 2025). Examples include polylactic acid (PLA) and polyhydroxyalkanoates

(PHA), which are both biobased and biodegradable. Partially biobased but non-biodegradable plastics, such as bio-PE, bio-PET, and bio-PP, have been developed and produced at a commercial scale due to their functionality and substantial potential in packaging applications. While bioplastics offer a more sustainable option, they are not without their challenges. Large scale production from agroindustrial wastes is constrained by logistics, high costs, and the need for optimized microbial fermentation processes. Consumer applications, particularly in food packaging, are limited by poor barrier performance, opacity, low tensile strength, and susceptibility to UV degradation. Moreover, biodegradable plastics are prone to hydrolysis, exhibit reduced molecular weight upon degradation, and generally possess low recycling quality (Melchor-Martínez et al., 2022; Nandakumar et al., 2021; Rahman & Bhoi, 2021; Thakur et al., 2018).

1.1.3 Growing awareness of plastic pollution and global responses

Plastics have become an indispensable material in society due to their versatility and low cost, yet their environmental consequences are now recognized as a global concern (Stanley et al., 2025).

Plastic pollution in the marine environment has emerged as a particularly pressing issue. Researchers began observing plastic debris in oceans by the 1970s. One early study documented plastic particles in the Sargasso Sea surface of up to 3,500 pieces per square kilometer (Carpenter & Smith, 1972). In 1997, the Great Pacific Garbage Patch was discovered, which was recently estimated to contain at least 79,000 tons of floating plastics within an area of approximately 1.6 million km² (Z. Huang et al., 2023; L. Lebreton et al., 2018). In 2004, the term *microplastic* was first used to describe plastic debris as small as ~20 µm in diameter, marking a turning point in scientific and public awareness of the pervasive and microscopic nature of plastic pollution (Thompson et al., 2004).

Awareness of plastic pollution has further evolved, with growing recognition that its impacts extend beyond ecological concerns, posing risks to human health and causing socio-economic harm to key sectors such as fisheries, agriculture, and tourism (Udhayakumar et al., 2025). In response, global initiatives have intensified, ranging from policy interventions and scientific innovations to widespread public education campaigns (Rangel-Buitrago et al., 2023). Regulatory measures now range from bans on single-use plastics to the promotion of sustainable alternatives. For instance, the European Union's Single-Use Plastics Directive (EU Directive 2019/904) particularly targets mitigation of the environmental impact of plastic items such as bags, straws, cutlery, food and beverage containers, etc.

Nonetheless, managing plastic pollution remains inherently complex, requiring a multifaceted approach that integrates innovative strategies, multidisciplinary collaboration, and adaptive policy frameworks (Rangel-Buitrago et al., 2023). After two

decades of research into microplastic pollution, significant advancements have been made in understanding its sources, distribution, and impacts. However, critical knowledge gaps remain, particularly in assessing the risks associated with widespread environmental accumulation, which limit the development of effective mitigation strategies and policy actions (Thompson et al., 2024).

1.2 Global Plastic Production and Waste Generation

Global plastic production has increased at an exponential rate since 1950. From an annual output of 2 million metric tons (Mt), plastic production has recently reached approximately 460 Mt (OECD, 2022). China remains the leading producer of plastics, contributing 33.3% of total global production. This is followed by other Asian countries (excluding China and Japan), which collectively contribute 19.7%, Europe at 17.1%, and North America at 12.3% (Plastics Europe, 2024).

The most commonly produced polymers globally are PP (15.9%), HDPE (12.1%), and low-density/linear low-density polyethylene (LDPE/LLDPE, 11.8%) (Figure 1.2). Other major contributors include PVC (11.1%), PET (5.46%), and PS (4.59%). Collectively, these six polymer types represent over 60% of total global plastic production.

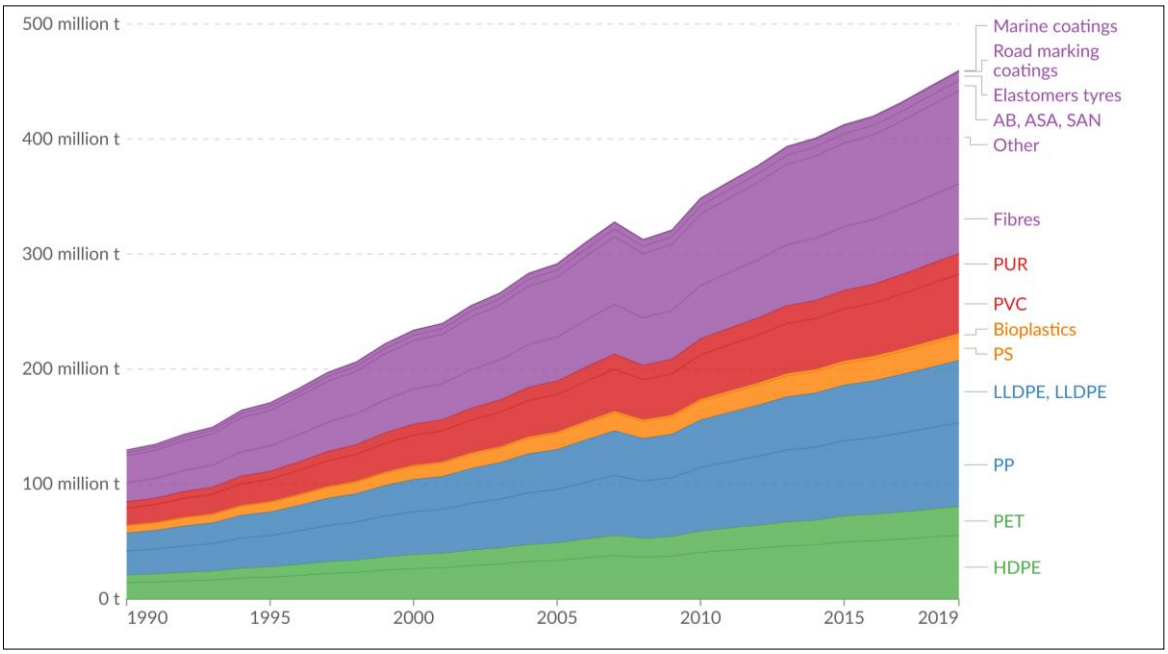

Figure 1.2. *Global primary plastic production by polymer, 1990 to 2019. Polymers are color-coded according to recyclability: green (widely recycled), blue (moderately recycled), orange (limited recyclability), red (usually non-recycled), and violet (unknown recyclability). Source: OECD (2022) – processed by Our World in Data.*

The plastic demand is primarily driven by six major industrial sectors (Figure 1.3). Packaging remains the largest end-use category, accounting for approximately 31.0% of total plastic consumption. The construction industry comprises about 16.7% of plastic usage, employing materials such as PVC and polyurethane (PUR) in pipes, window frames, insulation, and cladding. The automotive and transportation sectors account for 13.5% of global plastic demand, while the textile industry, electronics, and consumer and institutional products collectively contribute an additional 23.5% (OECD, 2022).

The waste footprint resulting from this global plastic consumption is substantial (Figure 1.4). By 2015, an estimated 6,300 Mt of plastic waste, encompassing both primary and recycled plastics, had been generated. Of this, only 9% were effectively recycled, while 12% were incinerated. The remaining ~79% was either disposed of in landfills or the environment. If current trends in plastic production and waste management persist, the cumulative volume of plastic waste accumulating in landfills or the environment is projected to reach approximately 12,000 Mt by 2050 (Geyer et al., 2017a).

The composition of plastic waste is largely determined by the intended application and lifespan of plastic products. Short-lived items, such as packaging, consumer goods, and textiles, contribute significantly to the volume of accumulated waste, predominantly composed of PP, LDPE, HDPE, PET, and PS. In contrast, materials like PVC and PUR, which are primarily used in long-lasting applications, contribute to waste generation only after extended periods and constitute a large share of the in-use plastic stock within the economy (OECD, 2022).

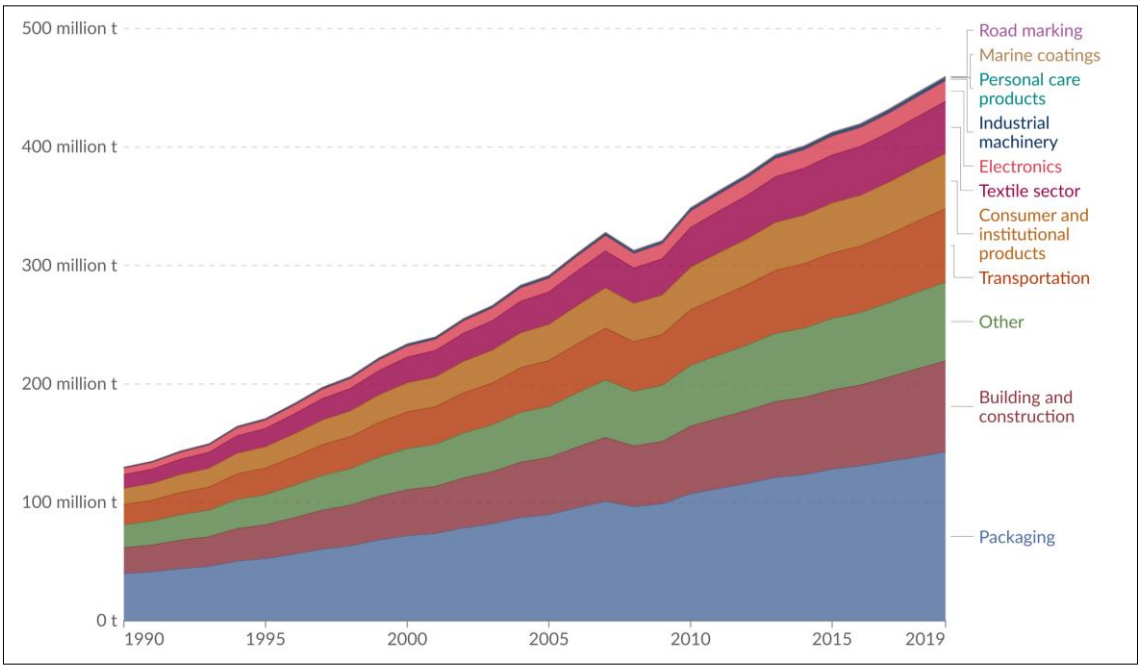

Figure 1.3. *Global primary plastic production by industrial sector, 1990 to 2019. Source: OECD (2022) – processed by Our World in Data.*

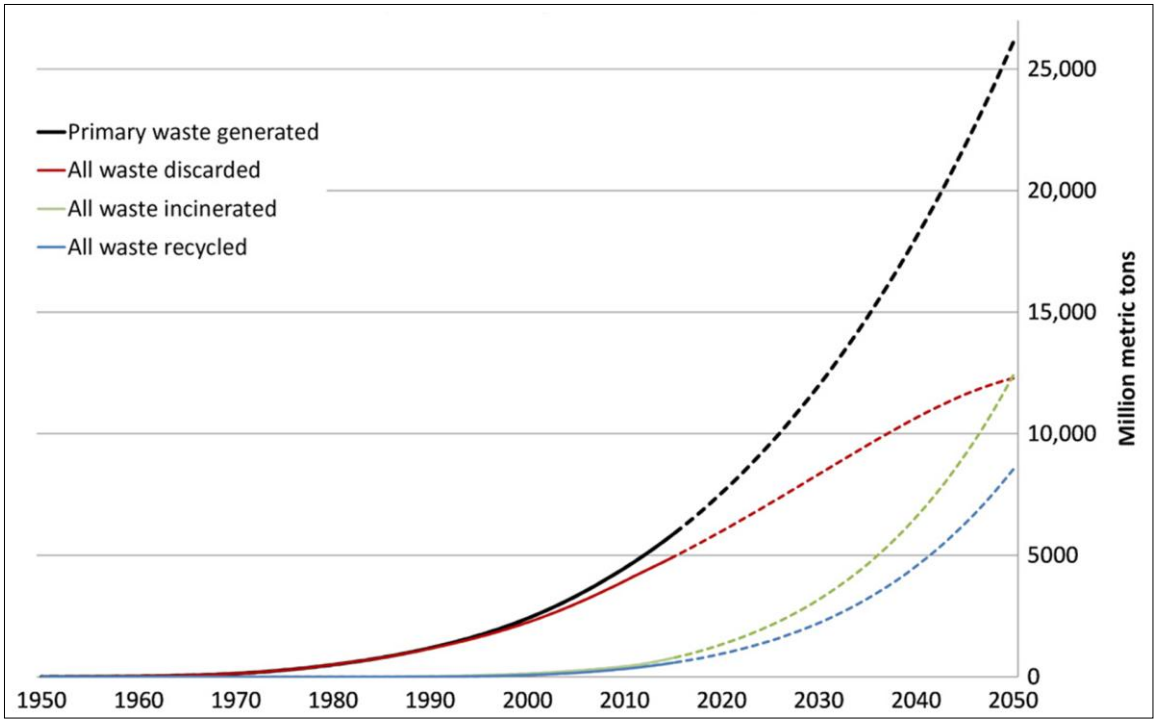

Figure 1.4. *Cumulative global plastic waste generation and disposal (in million metric tons; adapted from Geyer et al., 2017). The solid lines represent historical data from 1950 to 2015, while the dashed lines indicate projected trends extending to 2050.*

1.3 Major Sources of Plastic Pollution in the Marine Environment

The major sources of plastic pollution in the marine environment encompass a wide array of human activities on land, at sea, and in the atmosphere (Figure 1.5). Land-based sources remain the predominant contributor to plastic pollution, but marine-based and atmospheric sources introduce complexities in distribution, monitoring, and mitigation.

1.3.1 Land-based sources

Land-based sources are widely recognized as the predominant contributor, accounting for an estimated 80% of the plastic debris found in marine environments (Osman et al., 2023). These sources are diverse and include both point and diffuse pollution pathways.

1.3.1.1 Improper waste management

Solid waste mismanagement is a major driver of plastic leakage into the environment. Both legal and illegal waste handling practices, including landfills and open dumps with inadequate infrastructure, and improper disposal in unauthorized locations, represent significant point sources for the release of plastic debris. These practices enable plastics to escape into waterways and ultimately reach the marine environment (Sheavly & Register, 2007). Projections indicate that approximately 9% of solid waste is discarded near coastal areas, while the vast majority (91%) originates inland and is transported via large riverine

systems (>100 km²), highlighting rivers as key pathways for land-based plastic waste entering the ocean (L. Lebreton & Andrady, 2019).

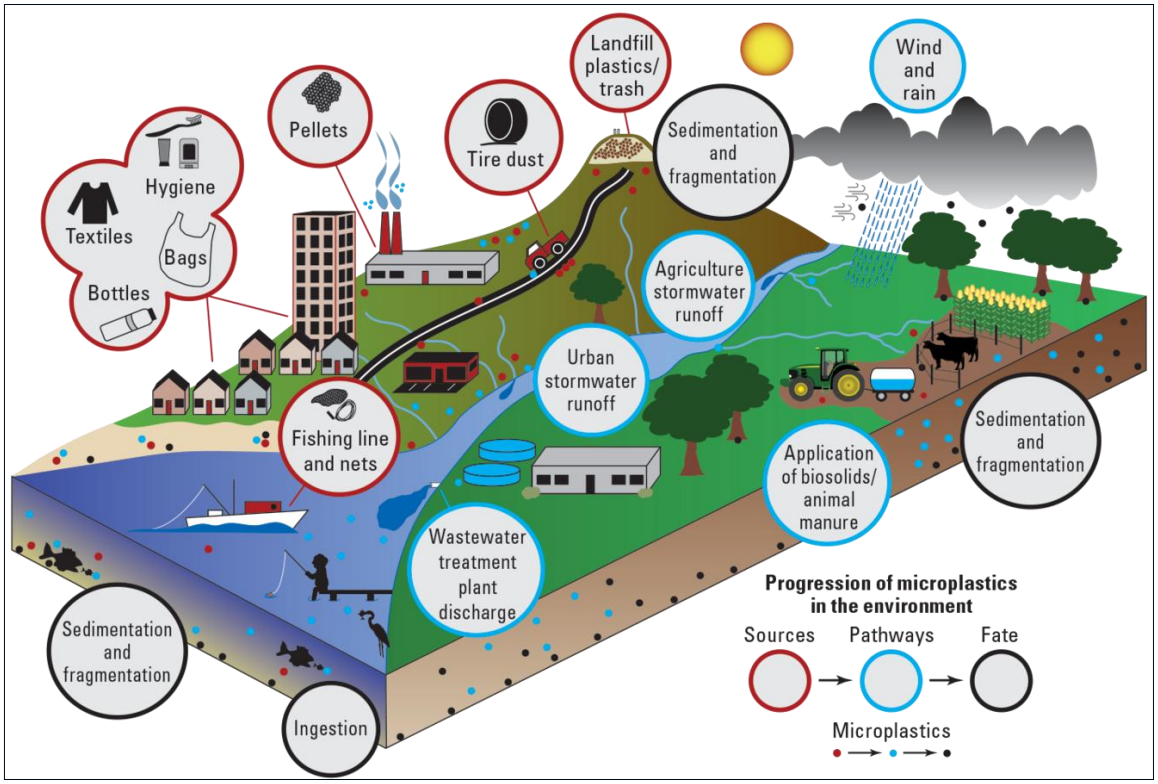

Figure 1.5. *A conceptual diagram illustrating the major sources, environmental pathways, and fate of plastic particles in the environment. Adapted from: Environmental Health Program of USGS (2023).*

Industrial processes also generate large volumes of plastic waste. In particular, pre-production plastic materials, such as pellets, flakes, and powder, represent another substantial source of pollution when spilled during manufacturing, transportation, or handling (Duis & Coors, 2016). The total annual release of pellets from the production site to the surrounding environment is estimated to range between 3 and 36 million annually (Karlsson et al., 2018).

1.3.1.2 Urban runoff and wastewater effluents

Urban stormwater runoff is another critical pathway for transporting fragmented plastic particles into aquatic environments. The extent is primarily influenced by various factors, including land use patterns, rainfall intensity, drainage infrastructure, and the physical characteristics of the plastics involved. Common plastic particle types in stormwater runoff include tire and road wear particles (TRWPs), fragments, foams, and films (Beheshtimaal et al., 2024; Shafi et al., 2024). The size and concentration of these particles vary considerably, with dominant fractions typically smaller than 1000 µm. Globally, reported concentrations range from as low as 1.2 particles/L to as high as 18,966 ± 191 particles/L (Hoang et al., 2025).

Similarly, plastic fiber discharge from textile industries, particularly from synthetic fabrics like polyester and nylon, can occur at rates up to thousands of times higher than those from domestic wastewater (Chan et al., 2023). Other industries such as cosmetics, paint, rubber manufacturing, and waste recycling facilities contribute additional plastic particles through the use of polymer-based ingredients and mechanical degradation of materials (Brown et al., 2023; Cubas et al., 2022; Gaylarde et al., 2021).

Wastewater treatment plants (WWTPs), though effective at removing a substantial proportion of plastic particles with reported removal efficiencies ranging from 16.5% to 98.4%, can still contribute to environmental pollution due to the large volumes of effluent discharged into receiving water bodies (Bodzek et al., 2024). Advanced final-stage treatment technologies, including disc filters, rapid sand filters, dissolved air flotation, and membrane bioreactors, have been reported to remove more than 95% of MPs larger than 20 µm (Talvitie et al., 2017). Household activities, particularly laundry washing and the typical daily use of personal care products, packaging, and containers, were identified as major contributors in WWTPs (Ma et al., 2024; A. Singh & Mishra, 2023). Globally, daily emissions from effluents have been estimated to range from approximately 0.46 million to 140 billion particles (Jose et al., 2024). Even at high removal rates, considerable quantities of plastic particles are released into the environment daily. For instance, in a reclaimed WWTP and a centralized sludge facility employing tertiary treatment processes, approximately 30 million plastic particles per day were released into the downstream river, while 51.8 billion were retained in sludge, posing further risks upon disposal (Y. Wang et al., 2024).

1.3.1.3 Agricultural practices

Agriculture practices, from crop cultivation to livestock farming, are increasingly dependent on plastic products such as mulch films, greenhouse covers, irrigation pipes, protective nets, and polymer-coated fertilizers (S. Singh et al., 2025). Among these materials, plastic mulch films represent one of the most significant sources of plastic input into agricultural soils. For example, the abundance of plastic particles in soil increases progressively with continued use of plastic mulching over time. In fields where plastic mulching was employed for 5, 15, and 24 years, plastic concentrations ranged from 80.3 to 1075.6 pieces per kilogram of soil (Y. Huang et al., 2020; Tian et al., 2022).

1.3.2 Marine-based sources

While land-based sources are predominant, marine-based sources also play a significant role in contributing to the persistence and complexity of plastic pollution in various marine environmental compartments. These sources are often associated with fishing, shipping, aquaculture, and tourism sectors, which introduce plastic debris directly into the ocean.

1.3.2.1 Fishing and aquaculture

Fishing activities are a major marine-based source of plastic pollution, largely due to abandoned, lost, or discarded fishing gear (ALDFG). It is estimated that ALDFG contributes approximately 640,000 tonnes of marine debris each year (Macfadyen et al., 2009; UNEP, 2016). More recent global assessments indicate that nearly 2% of all fishing gear deployed is lost to the marine environment annually. Specifically, this includes a substantial loss of purse seine nets (75,049 km^2), trawl nets (218 km^2), gillnets (2,963 km^2), longlines mainlines (739,583 km), and more than 25 million pots and traps (Richardson et al., 2022).

Aquaculture systems also contribute to the generation of plastic debris through both structural degradation and the intentional or accidental release of plastic materials (Lin et al., 2022). Commonly used equipment includes mesh bags, pipes, ropes, incubation and water tanks, floating cages, buoys, and rafts deployed at sea, all of which are susceptible to damage, loss, or wear in harsh marine environments. Pathways for plastic pollution from aquaculture often involve mechanical failure, weather-induced breakage, poor installation and maintenance, and improper waste handling practices (Skirtun et al., 2022). For instance, Norwegian aquaculture releases an average of 25,000 tons of plastic at sea annually, primarily from floating collars, pipes, nets, and ropes (Huntington, 2019). Pearl farming alone generates around 1,603 tons of plastic waste annually, of which 75% is mismanaged, with 46% of it at risk of entering the marine environment (Crusot et al., 2023).

1.3.2.2 Shipping and offshore operations

Commercial shipping and offshore operations contribute through direct discharges and indirect sources such as maintenance activities and accidental spills. Marine coatings, primarily polymers such as polyurethanes and epoxies, are released into the marine environment through weathering, abrasion, in-water cleaning, and paint removal during routine ship maintenance. In-water hull cleaning, either through manually or remotely operated tools, is estimated to release a total of 295–13,481 tons of coating particles from various ship types annually (Soon et al., 2024).

Other offshore industrial activities, including oil, gas, and wind energy operations, contribute to the localized accumulation of plastic particles in marine environments. Notably, offshore wind farms can release plastics through the erosion of turbine blades, with reported mass losses ranging from 80 to 1,000 g per blade per year, substantially higher than those observed in onshore installations (Mishnaevsky et al., 2024).

1.3.2.3 Tourism and coastal activities

Beaches and coastal zones heavily used for recreation are hotspots for plastic accumulation, especially during peak tourism seasons. Single-use plastics (e.g., bottles, straws, packaging items) dominate the debris found in these areas. The tourism industry, including hotels, resorts, restaurants, and vendors, significantly contributes to this problem through the extensive use of disposable plastic products. In addition to packaging waste,

cigarette butts, with plastic-based filters, are also a prevalent type of beach litter. Studies have shown a direct correlation between tourist presence and plastic load on coastal areas (Garcés-Ordóñez et al., 2020; Kataržytė et al., 2020; Şener & Yabanlı, 2023).

1.3.3 Atmospheric transport of plastic particles

Plastics particles are also transported through the atmosphere via various pathways, contributing to the widespread global distribution. Road traffic, particularly tire and brake wear, is recognized as a dominant contributor of atmospheric plastic particles, with an estimated ~100 kt per yr and ~40 kt per yr, respectively, ultimately deposited in the world's oceans (Evangeliou et al., 2020). Industrial activities, like manufacturing and recycling facilities, also discharge plastic fragments and powders into the air through fugitive emissions and handling losses. For example, mechanical shredding can emit submicron and micron-sized particles at concentrations 3 to 2,910 times higher than background levels (Swinnerton et al., 2024). Textile fibers released during garment production, clothing wear and laundering represent another critical source of airborne plastics (Mishra et al., 2019; Periyasamy & Tehrani-Bagha, 2022).

Removal of atmospheric plastic particles occurs through dry deposition by gravitational settling and wet deposition via in-cloud and below-cloud scavenging, both primarily influenced by meteorological conditions and particle properties (Y. Liu et al., 2025).

1.4 Characterization of Plastic Particles

As part of a structured approach to defining plastic debris (Figure 1.6), Hartmann et al. (2019) proposed a framework distinguishing between *defining criteria for* basic properties, such as chemical composition, solid state, and solubility (Criteria I–III), and *auxiliary criteria* for further categorization, such as size, shape and structure, color, and origin (Criteria IV–VII).

1.4.1 Physicochemical properties of plastic particles

1.4.1.1 Chemical composition

Chemical composition is among the most fundamental criterion for defining plastic particles, as it determines both material classification and environmental persistence. Materials composed of synthetic and semi-synthetic polymers, including heavily modified natural materials like rayon, are generally included in the definition, while slightly modified natural polymers are often excluded. Synthetic polymers are man-made materials derived from petroleum-based sources, whereas semi-synthetic polymers originate from natural substances but undergo partial chemical modification. Although around 60,000 plastic formulations have been developed, petroleum-based polymers such as PP, LDPE, HDPE, PVC, PUR, PS, and PET dominate global production. In contrast, bio-based alternatives like

PLA and PHA are gaining attention as more sustainable options. Importantly, the classification disregards consideration of additive contents, such as plasticizers, flame retardants, or stabilizers, as it is the polymer backbone that fundamentally defines the material. Copolymers and polymer composites, which include non-polymeric reinforcements or mixed monomers, also fall within the definition. Tire wear and surface coating particles also meet this criterion due to their substantial synthetic polymer content (Coleman, 2017; Hartmann et al., 2019; Ivar do Sul, 2021; Rani et al., 2015; Stanley et al., 2025; Wagner et al., 2018). The analytical techniques used to determine the chemical composition of the plastic particles are described in Section 1.4.2.2.

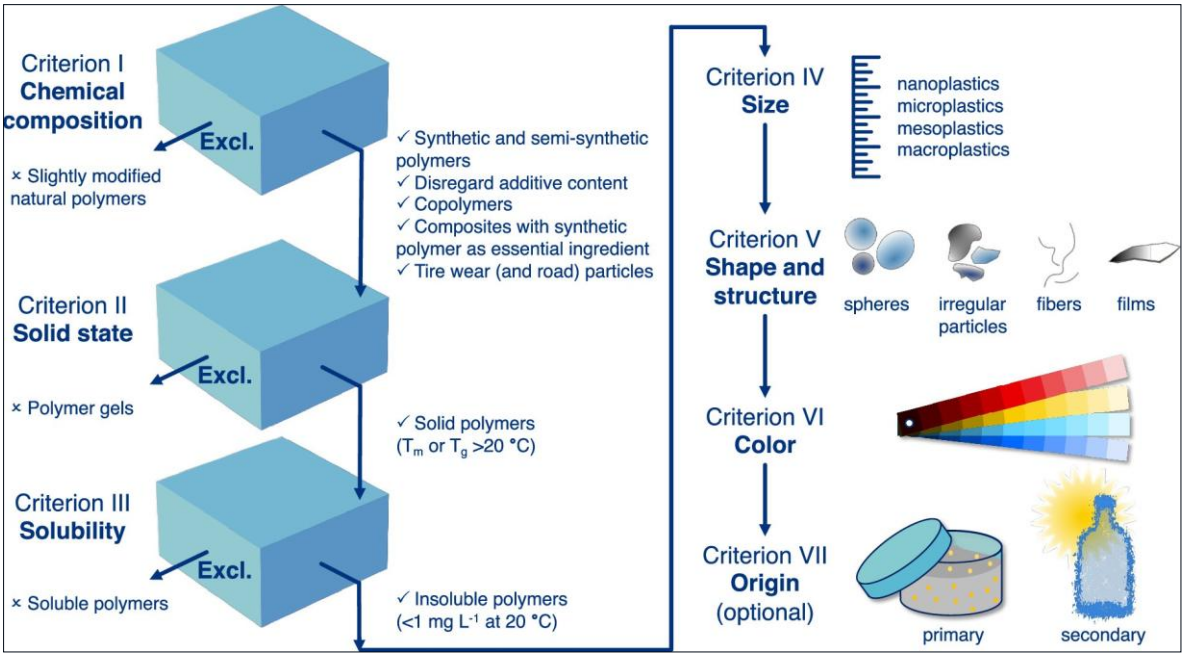

Figure 1.6. *Framework for the definition and categorization of plastic particles proposed by Hartmann et al. (2019), based on seven hierarchical criteria: chemical composition, solid state, insolubility, size, shape and structure, color, and (optionally) origin.*

1.4.1.2 Solid state and solubility

According to the framework proposed by Hartmann et al. (2019), only solid polymers are considered, explicitly excluding wax-like, semisolid and liquid-phase polymers. Polymer gels, although chemically classified as solids, become soft and viscous in water and are therefore excluded from this definition. Another criterion refines this by including only polymers considered poorly soluble, defined as having a water solubility of less than 1 mg/L at 20°C, in accordance with REACH guidance. Together, these criteria emphasize the inclusion of only physically stable, poorly soluble polymers, clearly distinguishing particulate plastic materials from dissolved or semi-solid polymer forms that behave differently in aquatic environments.

1.4.1.3 Size

Plastic debris is commonly classified by size, using the largest dimension as the defining criterion, into three main categories: macroplastics (>5 mm), microplastics (1 µm to 5000 µm), and nanoplastics (<1 µm) (Frias & Nash, 2019; Hartmann et al., 2019; Ramkumar et al., 2022; Thompson et al., 2024). Although this size-based classification is widely used, it remains a subject of ongoing discussion, particularly concerning the lack of standardized consensus on the lower and upper limits (Hartmann et al., 2019; X. Liu et al., 2024). For instance, there is no universally accepted cut-off for nanoplastics, with reported definitions ranging from <100 nm to <1 µm (X. Liu et al., 2024).

The 5 mm upper size bound for microplastics was initially established at a policy meeting hosted by the National Oceanic and Atmospheric Administration (NOAA), based on evidence indicating that particles within this range could be readily ingested by organisms and might pose different ecological risks than larger items (Arthur et al., 2009). Although the commonly used size limits for classifying microplastics do not strictly conform to the International System of Units (SI), they have been widely adopted to encompass particles ranging to millimeter scale. This approach, while inconsistent with the formal metric system, facilitates comparability across studies and aligns with the classification schemes used in the majority of the literature (Ramkumar et al., 2022).

For this thesis, microplastics are defined as particles ranging from 1 µm to 5000 µm in size, whereas nanoplastics are defined as particles smaller than 1 µm.

1.4.1.4 Shape and structure

Plastic particles exist in a wide array of distinct shapes and structural forms. This classification scheme evaluates particle dimensions at a scale where the entire object is viewed as a whole (Cowger et al., 2020). According to the classification adapted from Hartmann et al. (2019) plastic debris can be classified into six shape categories (Table 1.1), including sphere, spheroid, cylindrical pellet, fragment, film, and fiber.

Table 1.1. *Categories used when classifying plastic particles by shape. Adapted from: Hartmann et al. (2019).*

Category	***Description***
Sphere	Every surface point has the same distance from the center
Spheroid	Imperfect but approximate sphere
Cylindrical pellet	Rod-shaped, cylindrical object
Fragment	Particles with irregular shape
Film	Planar, considerably smaller in one than in the other dimensions
Fiber	Significantly longer in one than wide in two dimensions

In environmental samples, fibers and fragments are the most frequently encountered shapes, largely due to the prevalence of synthetic textiles and the breakdown of larger

consumer plastics, respectively. Spheres and pellets are less commonly found in environmental settings and are typically linked to industrial spillage in proximity to industrial sites, while their detection on urban beaches indicates potential for long-range marine transport (Cowger et al., 2020; Hidalgo-Ruz et al., 2012). Additionally, shape characteristics of particles can hint at their origin, for instance, microbeads from personal care products or pre-production pellets used in plastic manufacturing. Edge morphology offers clues to particle history: sharp edges indicate recent fragmentation, while smooth edges suggest prolonged environmental abrasion (Hartmann et al., 2019; Hidalgo-Ruz et al., 2012). Notably, the form of plastic particles is not merely descriptive; it may influence biological responses. There is growing evidence that the physical shape of polymers can modulate their adverse effects (Wright et al., 2013).

1.4.1.5 Color

Plastic particles are often categorized by color, typically including red, orange, yellow, green, blue, pink, brown, white, opaque, transparent, crystalline, clear, cream, and pigmented varieties (Hidalgo-Ruz et al., 2012). While this classification can offer insights into potential sources (Lim et al., 2024), the process is inherently subjective and vulnerable to human bias. Observer variability and methodological inconsistencies further limit the comparability and reliability of color-based data. For instance, particles with eye-catching colors are more likely to be isolated and identified, whereas dull-colored particles may be easily overlooked during visual inspection (Hidalgo-Ruz et al., 2012). To mitigate these issues, some researchers employ standardized tools, such as a reference palette of 120 Pantone colors, to enhance consistency in categorization (Martí et al., 2020). Color classification has also been used as a proxy for photodegradation, residence time at the sea surface, and weathering (Hidalgo-Ruz et al., 2012). It is also relevant for behavioral studies, as some aquatic organisms exhibit color preferences linked to prey resemblance (Wright et al., 2013).

1.4.1.6 Origin

Plastic debris in the environment is commonly classified into primary and secondary origins, particularly when referring to micro-sized particles. Primary plastic particles are intentionally manufactured at microscopic scales for specific industrial or consumer applications, such as microbeads in personal care products, pre-production resin pellets, and abrasives in industrial cleaning agents. In contrast, secondary microplastics are generated in the environment through the fragmentation of larger plastic items, including packaging materials, fishing gear, synthetic textiles, and automotive components (Hartmann et al., 2019).

1.4.2 Analytical techniques and challenges for particle characterization

Accurate characterization of MNPs requires rigorous sampling and pre-treatment protocols tailored to specific environmental matrices (Figure 1.7). The choice of methodology is

critical to minimize contamination, ensure representative recovery, and preserve particle integrity for downstream analysis.

1.4.2.1 Sample collection, separation, and purification from environmental samples

Sampling strategies vary depending on the environmental compartment. In aquatic environments, net sampling and bulk water collection are commonly employed. Mesh nets, bottles, or automated sampler systems are used to retrieve waterborne particles. While net sampling is effective for larger particles, it cannot capture nanosized particles due to mesh size limitations. In contrast, bulk sampling allows for the collection of all size fractions, including submicron particles, but is limited by small sample volumes, labor-intensive, and longer processing times (Luo et al., 2025; Prata et al., 2019). For sediments and soils, tools such as spatulas, shovels, corers, or bottom samplers like Van Veen or Ekman grab are used in combination with homogenization methods (e.g., drying, grinding, and sieving). Airborne particles are collected using passive (e.g., deposition plates, metallic funnel) and active techniques (e.g., high-flow atmospheric particulate samplers) (Zheng et al., 2024). Biological samples require sample acquisition of organisms using nets (e.g., nets, trawls, and traps), followed by dissection and tissue isolation under clean lab conditions (Löder & Gerdts, 2015; Luo et al., 2025).

Effective sample pre-treatment is essential for accurate analysis, involving both chemical and physical methods to remove matrix interferences while preserving particle integrity. Density separation using saturated salt solutions (e.g., sodium chloride (NaCl), zinc chloride ($ZnCl_2$), calcium chloride ($CaCl_2$), and sodium iodide (NaI)) enables the extraction of plastic particles based on the density differences between the polymers and the liquid medium. Organic matter is typically removed using oxidative, alkaline, acid, and enzymatic digestion using reagents such as hydrogen peroxide (H_2O_2), potassium hydroxide (KOH), or Fenton's reagent, sodium hypochlorite (NaClO), nitric or sulfuric acid, and Proteinase K. However, some chemicals can partially degrade or affect the physicochemical properties of MNPs, while incomplete digestion may leave residues that hinder accurate identification and quantification (Ershova & Frank, 2024; Luo et al., 2025; C. Sun, Gao, et al., 2024).

Following extraction, samples are further subjected to preconcentration and purification to enhance analytical resolution. Techniques such as ultrafiltration, ultracentrifugation, and cloud point extraction are effective in concentrating particles from treated samples (Luo et al., 2025). Membrane filtration with defined pore sizes (e.g., acetate, nitrate, or glass fiber membranes) enables size-based separation of plastic particles by passing the solution through a filter, typically aided by a vacuum pump (Hidalgo-Ruz et al., 2012). Ultracentrifugation is another enrichment method for concentrating particles while simultaneously removing solvent, but its small sample capacity (10–100 mL) limits its applicability for environmental water samples. Additionally, the high centrifugal forces and mechanical stress may induce aggregation or damage to plastic particles (Cai, Chen, et al.,

2021; Schwaferts et al., 2019). Cloud point extraction technique employs non-ionic surfactants like Triton X, heated above its cloud-point temperature, to partition particles into a surfactant-rich phase, particularly for smaller-sized plastics. Since the process involves thermal degradation of surfactants, it is primarily compatible with mass-based quantification methods such as pyrolysis-GC/MS (X. X. Zhou et al., 2019).

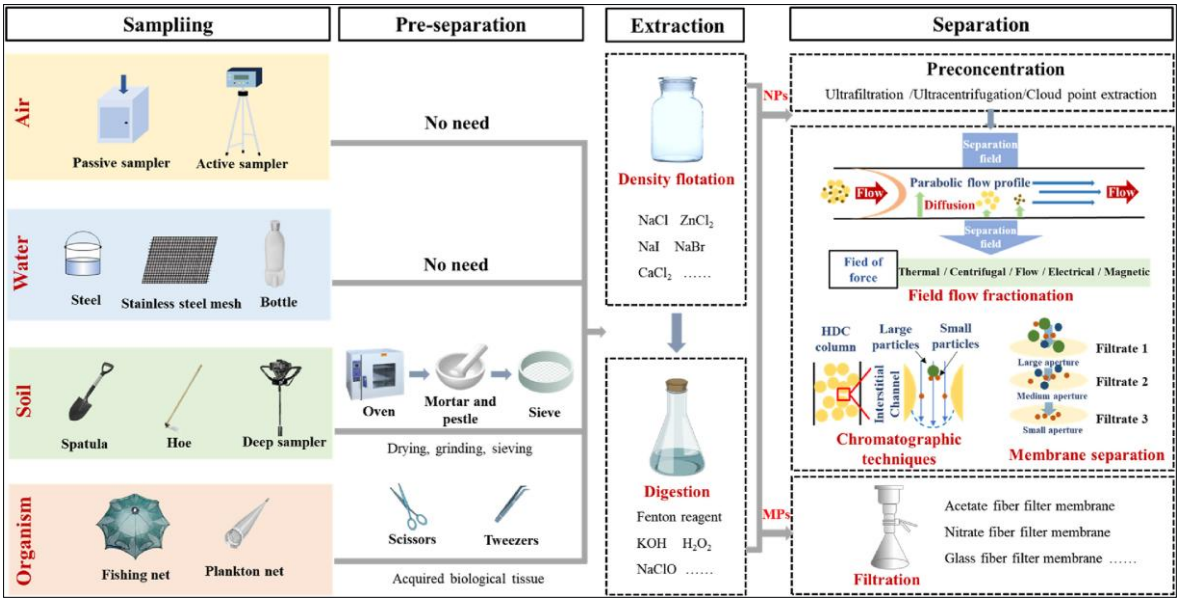

Figure 1.7. *Protocols for sampling, pre-separation, extraction, and separation of MNPs from environmental and biological matrices. Adapted from: Luo et al. (2025).*

1.4.2.2 Characterization and quantification

The characterization and quantification of plastic particles rely on a diverse suite of analytical methods designed to extract information about particle size, morphology, surface properties, and chemical identity. While methods are well-established for microplastics down to 1 µm, the analysis of particles within the nanosized range remain challenging (Figure 1.8), highlighting a significant methodological gap (Schwaferts et al., 2019).

1.4.2.2.1 Microscopy-based techniques

Microscopy-based techniques offer critical insights into particle morphology, yet each comes with inherent trade-offs in resolution, sample preparation, and applicability. Optical microscopy (OM) is a widely accessible and straightforward tool for the preliminary screening of particles based on morphology and surface features. However, its applicability is constrained by the optical diffraction limit. To address this limitation, transmission electron microscopy (TEM) and scanning electron microscopy (SEM) are often applied for detailed characterization of particle size, shape, and surface morphology in the submicron to nanometer range. When combined with energy-dispersive X-ray spectroscopy or electron energy loss spectroscopy, both techniques also enable elemental analysis. However, their application is constrained by extensive sample preparation and analytical

requirements (e.g., high-pressure conditions and use of conductive coatings), which may compromise particle integrity and limit their suitability for delicate environmental and biological samples (Schwaferts et al., 2019). Environmental SEM (ESEM) offers a valuable alternative by enabling nanoscale imaging of wet or insulating samples under low-pressure conditions, without the need for conductive coatings or high vacuum. Although this expands applicability to environmental samples, it comes with the drawbacks of reduced image resolution and contrast (Zhang et al., 2019).

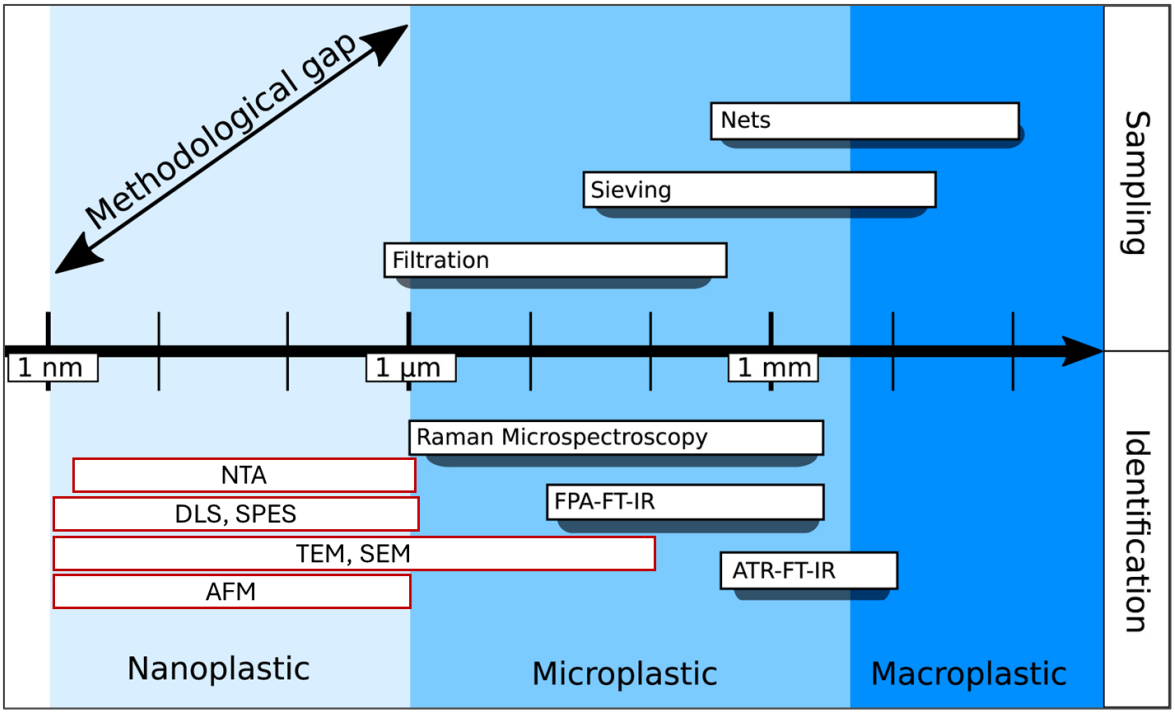

Figure 1.8. *Overview of current analytical methodologies for sampling and identifying plastic particles across size ranges, highlighting a critical methodological gap for nanoplastic particles (<1 µm). Techniques indicated in red boxes are mainly applicable in controlled or clean matrices and have limited applicability for complex biological or environmental samples. Abbreviations: NTA, nanoparticle tracking analysis; DLS, dynamic light scattering; SPES, single-particle extinction and scattering; TEM, transmission electron microscopy; SEM, scanning electron microscopy; AFM, atomic force microscopy; FPA-FT-IR, focal plane array Fourier-transform infrared spectroscopy; ATR-FT-IR, attenuated total reflectance Fourier-transform infrared spectroscopy. Adapted from: Schwaferts et al. (2019).*

Atomic force microscopy (AFM) offers high-resolution topographical mapping of plastic particles at the nanoscale, making it valuable for studying surface morphology, mechanical properties, and particle interactions with biological interfaces. However, its slow scanning process and need for accessible, clean surfaces limit its suitability for high-throughput analysis of complex environmental samples, where embedded contaminants and biofilms can obscure surface features and compromise data accuracy (Nene et al., 2025). Another widely applied technique for detecting MNPs is fluorescence microscopy, especially when combined with dyes like Nile Red, which facilitates rapid detection of plastic particles in complex matrices. Advanced variants, including confocal and super-resolution fluorescence

microscopy, enable nanoscale imaging beyond the diffraction limit of conventional light microscopy. However, fluorescence-based technique is limited by non-specific dye binding to hydrophobic materials (e.g., lipids), poor staining efficiency of functionalized particles, especially those with hydrophilic surface modification, and signal interference from organic matter aggregates, collectively compromising specificity and quantification accuracy (Bianco et al., 2023; De-la-Torre et al., 2025; Nene et al., 2025).

1.4.2.2.2 Spectroscopy-based techniques

Fourier Transform Infrared Spectroscopy (FTIR) is a widely used technique for identifying plastic polymers through their characteristic vibrational spectra (Renner et al., 2018). The technique involves irradiating samples with infrared light, which induces vibrational transitions that produce a unique absorbance spectrum, serving as chemical fingerprints. FTIR can operate in either transmission or reflectance modes. Attenuated Total Reflectance (ATR-FTIR) is commonly used for bulk surface analysis of larger particles (>500 µm). For smaller particles, micro-FTIR, often equipped with a focal plane array detector, enables spectral analysis of particles down to ~10 µm collected on filters. Complementing FTIR techniques, Raman spectroscopy offers higher spatial resolution for single particle analysis down to ~1 µm. However, limitations include fluorescence interference from the background organic matter, which can obscure characteristic peaks and reduce spectral clarity (Frère et al., 2016; Kusch, 2022; Schwaferts et al., 2019).

Pyrolysis-Gas Chromatography-Mass Spectrometry (Py-GC-MS) allows identification and mass-based quantification of plastic polymers based on their unique pyrolysis products. It is highly sensitive and well suited for complex matrices. However, Py-GC–MS is inherently destructive due to the thermal degradation process, and thus does not support measurement of particle number, size, or morphology (De-la-Torre et al., 2025; Schwaferts et al., 2019). Although this technique has been applied for the detection of MNPs in environmental samples (Fries et al., 2013; Ter Halle et al., 2017), it is best used in combination with non-destructive methods for comprehensive analysis.

1.4.2.2.3 Light scattering and particle tracking techniques

Dynamic Light Scattering (DLS) is a commonly employed technique for characterizing the hydrodynamic size of particles in suspension based on fluctuations in scattered light intensity. When coupled with Electrophoretic Light Scattering (ELS), it is particularly effective in assessing the colloidal stability of nanoparticle suspensions through zeta potential measurements, an important electrokinetic parameter. Despite its advantages, DLS has limitations, such as potential inaccuracies in size distribution analysis and sensitivity to sample polydispersity, which make it unsuitable for the characterization of environmental samples that typically contain broad and heterogeneous particle sizes (Schwaferts et al., 2019; Xu, 2015).

While conceptually similar to DLS, Static Light Scattering (SLS), also known as multi-angle light scattering (MALS), measures the angular distribution of scattered laser light to determine particle size. SLS exhibits poor sensitivity for particles below 200 nm, rendering it unsuitable for the detection of the smaller fraction of NPs (Caputo et al., 2021; Schwaferts et al., 2019). In combination with Asymmetric Flow Field-Flow Fractionation (AF4), this technique is effective for separating and measuring particle sizes in complex biological matrices, although its performance can be hindered by elevated background signals (Correia & Loeschner, 2018).

By tracking the Brownian motion of individual particles, Nanoparticle Tracking Analysis (NTA) provides quantitative measurements of particle concentration and size distributions. It is applicable to particles ranging from 30 to 1000 nm and allows the visualization of particles in suspension. Unlike DLS, NTA can resolve complex and heterogeneous samples, exhibiting accurate characterization of both monodisperse and polydisperse particle populations (Cai, Xu, et al., 2021; Filipe et al., 2010). For instance, NTA was applied to monitor nanoplastic formation during the degradation of a PS-based consumer product over time (Lambert & Wagner, 2016).

Single-Particle Extinction and Scattering (SPES) represents a more recent advancement, offering real-time, single-particle characterization by combining light extinction and scattering signals. This dual-modality approach enables simultaneous determination of particle size, refractive index, and dynamic behaviour in solution. Unlike conventional DLS technique, SPES enables quantitative measurement even in polydisperse systems and is sensitive to detect minute changes in physical properties of NPs in solution. Preliminary studies have demonstrated its robustness in polydisperse and dynamic systems, highlighting its potential for applications in environmental nanoplastics research. However, current implementations remain largely confined to controlled laboratory conditions, and its broader applicability in natural matrices is yet to be fully validated (Potenza, Sanvito, Argentiere, et al., 2015; Seghers et al., 2025).

1.5 Fate of Plastic Particles in the Marine Environment

1.5.1 Abundance and composition in water column and sediment

MNPs are globally distributed, with high concentrations accumulating in oceanic gyres due to surface currents and inputs from both land and marine-based sources (Figure 1.9). As of the early 2010s, approximately 5.25 trillion plastic particles, weighing around 268,940 metric tons, were estimated to be floating in the oceans, based on oceanographic modelling of data from 1,571 sampling locations across subtropical gyres, coastal regions, and enclosed seas. Of this, MPs in the 330–4,750 µm size range accounted for 92.4% of the global particle count (Eriksen et al., 2014). Recent models estimate MP concentrations to range from 10^{-4} to 10^{4} particles per cubic meter, with variability driven by proximity to

shore, water depth, and oceanographic conditions (S. Zhao et al., 2025). These estimates align with in situ observations worldwide, with mean MP abundances reported mainly from surface seawater, ranging from 4.8×10^{-6} particles/m³ to 1.6×10^{4} particles/m³ and peak levels reaching 1.03×10^{5} particles/m³, highlighting spatial variability and localized hotspots (Shim et al., 2018).

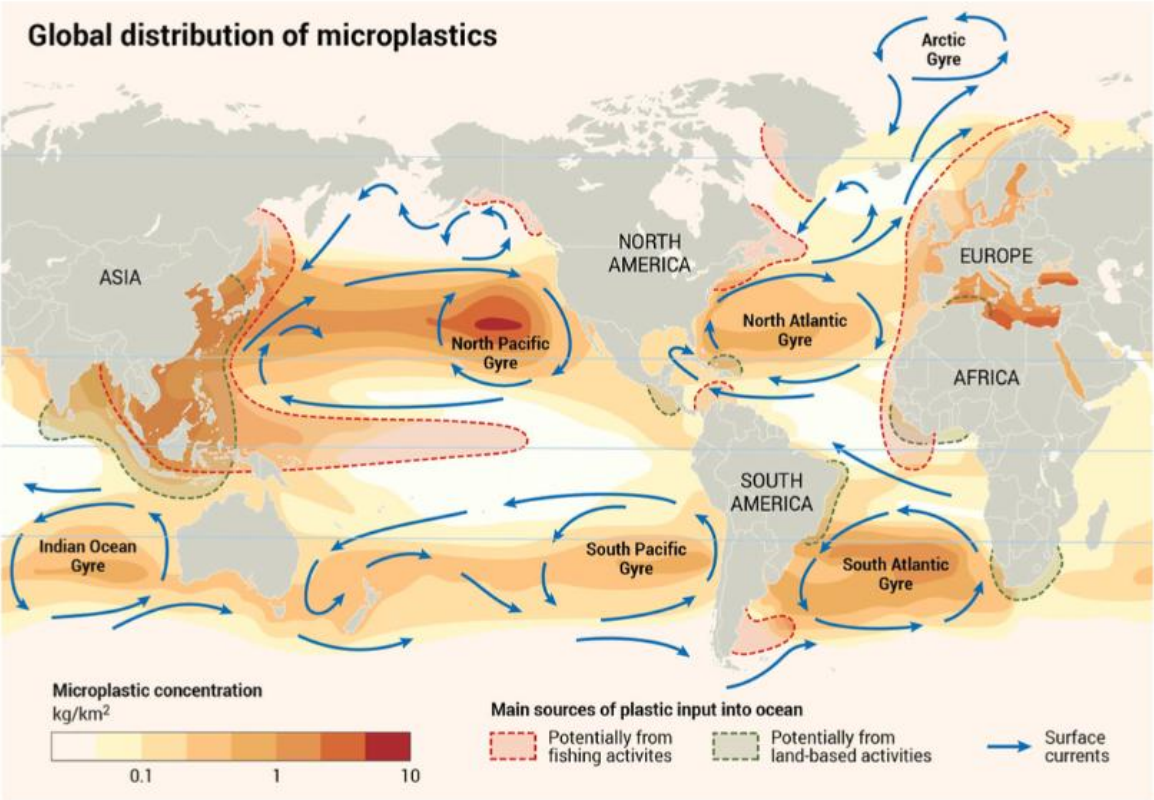

Figure 1.9. *Global distribution of microplastics in the world's oceans. Concentrations of floating microplastics (kg/km²) are shown overlaid with major surface currents (blue arrows), highlighting accumulation zones in the five subtropical gyres and elevated inputs near densely populated coastal regions. Dashed lines denote major sources of plastic input: red for fishing activity and green for land-based runoff. Adapted from GRID-Arendal Resources Library (www.grida.no.vag), based on data from Jambeck et al. (2015); L. C. M. Lebreton et al. (2017); Ritchie & Roser (2018); Van Sebille et al. (2015).*

In estuarine waters, a global median MP concentration of 1.97×10^{2} particles/m³ was reported across 126 estuaries, with values ranging from 7.0×10^{-3} to 7.92×10^{5} particles/m³. Majority of particles reported in estuarine waters were smaller than 500 µm, with higher concentrations observed in Asia and Oceania (Di et al., 2024). Notably, MP concentrations as high as 8.09×10^{5} particles/m³ have also been reported even within marine protected areas (Nunes et al., 2023). Most MP concentrations have been reported from surface waters (<5 m), while data from deeper layers remain scarce. Fragments and fibers are the most prevalent particle shapes, with PE and PP being the most identified polymers; however, the absence of detailed polymer characterization remains a major constraint for comprehensive assessments (Di et al., 2024; Nunes et al., 2023). NPs, due to their

nanoscale size, are more challenging to quantify in environmental samples, but emerging evidence suggests their presence across marine environments (J. Wang et al., 2021), including remote polar regions (Materić et al., 2022) and subtropical gyres (Ter Halle et al., 2017), particularly involving polymers such as PE, PP, PET, PS, and PVC.

Marine sediments act as major sinks for MPs, often exhibiting significantly higher concentrations than overlying water columns. Globally, MP concentrations in sediments vary widely, from undetectable to 6.28×10^4 particles/m² in beach sands and up to 1.86×10^4 particles/m³ in seabed sediments. The detected MPs are predominantly composed of PE, PS, PP, as well as nylon and polyester (L. Peng et al., 2020). Another study reported MP abundances of up to 4.79×10^4 particles/m² and 3.32×10^3 particles/kg in intertidal and subtidal sediments, respectively, indicating potential hotspots such as harbors (Shim et al., 2018). In vegetated coastal habitats, the global average concentration of MPs in sediment is $3.74\times10^3 \pm 2.02\times10^4$ items/kg, with regional hotspots observed in the Indian Ocean and South Atlantic and commonly consist of PE, PP, PS, PET, PA, PUR, and PVC (Hernán et al., 2024). The difference in units reflects the sampling method employed (quadrat or grab/core sampling) and the availability of sufficient information for conversion.

1.5.2 Transport mechanisms of MNPs

The distribution patterns of plastic particles in the marine environment are complex, driven by a combination of physical and biological processes, as well as physicochemical properties of the plastic materials (Mutuku et al., 2024; Shim et al., 2018).

The large-scale circulation, driven by surface winds and generating so-called Ekman drift, plays a dominant role in the horizontal distribution of plastic particles at the global scale. Buoyant plastic items can be transported across ocean basins by surface currents, leading to accumulation in convergence zones such as the five subtropical gyres (Van Sebille et al., 2020). These large-scale accumulation zones, colloquially referred to as ‘garbage patches,’ have been documented through in-situ observations at the centers of subtropical gyres in the North and South Pacific, North and South Atlantic, and the Indian Ocean (Cózar et al., 2014; Eriksen et al., 2013; Law et al., 2010, 2014). Beyond basin-scale gyre patterns, mesoscale and submesoscale oceanic processes significantly influence the redistribution of plastic particles. Mesoscale eddies (10–100 km), both cyclonic and anticyclonic, can trap and transport debris over long distances via radial surface flows. In contrast, submesoscale fronts and vortices (<10 km), though smaller and shorter-lived, are more effective at accumulating floating plastics at density fronts due to enhanced convergence and circulation (Van Sebille et al., 2020).

The vertical transport of plastic particles in the marine environment is primarily influenced by a combination of both physical processes, such as wind-induced mixing, and biological dynamics, including biofilm formation (Fischer et al., 2022). Field and modelling studies

have demonstrated that wind-driven mixing can vertically redistribute a substantial portion of buoyant plastic particles within the upper water column, highlighting underestimations of net-based surface measurements (Kukulka et al., 2012). Another important mechanism is through biofouling, whereby microbial colonization forms dense biofilms on plastic particle surfaces. This biological growth, collectively known as the "plastisphere," can increase the density of initially buoyant polymers, particularly when it incorporates calcareous or mineralizing organisms, ultimately leading to their sinking (Y. Du et al., 2022; Kooi et al., 2017). As reported, polymers with density below seawater depend on this biological overgrowth to achieve the composite density necessary for downward flux, whereas denser plastic types can sink unaided, with 10 µm solid particles reaching sinking velocities of up to 1,637 meters per day depending on polymer composition (Benner & Passow, 2024). Particularly in regions with high biological activity combined with strong near-surface mixing, positively buoyant particles in the 10–1000 µm size range can be transported far below the euphotic zone and mixed layer (Fischer et al., 2022).

Complementary findings from a study assessing the surface longevity of LDPE and HDPE fragments further demonstrated a direct relationship between particle size and buoyancy retention, as all samples eventually became sufficiently biofouled to sink, with smaller fragments losing buoyancy significantly faster than larger ones (Fazey & Ryan, 2016). Sinking velocity is further modulated by particle shape, surface texture, and biofilm coverage. In sheet-like materials, velocity increases with size up to a threshold, then decreases due to oscillatory motion and drag. Irregularity in biofilm formation can further reduce settling velocity by inducing motion instabilities, despite increasing particle density (Jalón-Rojas et al., 2022). An in-situ deployment across six sites in the Mediterranean and Atlantic Oceans revealed rapid colonization of LDPE, PP, and PLA within seven days, identifying a diverse assemblage comprised of 50 eukaryotic groups and 70 prokaryotic orders, with composition varying by season and location (Lacerda et al., 2025).

Additionally, plastics can aggregate with organic and inorganic matter to form marine snow, another key vector for their vertical transport to deeper ocean layers. Marine snow consists of heterogeneous aggregates typically >0.5 mm in diameter, composed of living and non-living organic matter, fecal pellets, planktonic detritus, marine gels, and mineral particles such as clay and calcite (Galloway & Porter, 2024). The vertical distribution of these aggregates is closely associated with density stratification in the water column, particularly at pycnoclines, where abrupt changes in salinity or temperature occur (MacIntyre et al., 1995). In situ observations have revealed elevated concentrations of microplastics within these pycnocline layers (Choy et al., 2019; Q. Zhou et al., 2021; Zobkov et al., 2019), suggesting that induced stratification may modulate their vertical retention. Notably, accumulation at the stratified layers primarily involves larger microplastic particles, while the abundance of smaller particles (<100 µm) gradually decreases with depth, reflecting a broader vertical distribution (Zhao et al., 2025). Laboratory studies showed that buoyant polymers such as PP fibers and PE beads, which would normally float

based on their density, became negatively buoyant upon incorporation into marine snow, with sinking velocities increasing from -82 and -0.19 m/day to 576 and 818 m/day, respectively (Porter et al., 2018).

Another biological process influencing plastic distribution is active transport by marine organisms. For instance, some zooplankton and fish that undergo diel vertical migration can ingest MNPs at the water surface and release them at depth through excretion or death. Larger animals, such as marine mammals and turtles can redistribute plastics horizontally and vertically during long-range movements or deep dives. Even sessile organisms like mussels and oysters contribute by filtering particles and depositing them as pseudofeces on the seafloor, thereby facilitating transfer to benthic sediments (Lusher, 2015; Meng et al., 2024).

1.5.3 Weathering processes of plastic particles in the marine environment

Plastic debris undergoes progressive alteration in marine environments through a combination of physical, chemical, and biological weathering processes (Figure 1.10). These interconnected pathways facilitate the breakdown of larger plastic fragments into secondary MNPs, altering the physicochemical properties of the particles over time (W. He et al., 2023). The dynamics of this aging process are influenced by both the intrinsic properties of the plastic and a complex interplay of external environmental factors (Z. Zhang et al., 2024).

1.5.3.1 Physical abrasion

Plastics are subjected to continuous mechanical stressors, including wind, tides, waves, and sand abrasion, that promote surface cracking and fragmentation. These forces, particularly intense in sediment-rich or coastal zones, drive the physical breakdown of plastics into progressively smaller particles (Z. Zhang et al., 2024). Under simulated riverine and coastal conditions, both pristine and decommissioned PP and HDPE fragments undergo significant erosion by water-borne sediments, resulting in substantial MP formation. PP showed the highest erosion rate (5160 µm/year), producing approximately 669 particles/mm² annually, while HDPE eroded at 3254 µm/year (187 particles/mm²/year). Decommissioned fragments produced smaller particles, averaging 60 µm for PP and 23 µm for HDPE, with erosion rates nearly double those of pristine counterparts (Al-Darraji et al., 2024). This enhanced susceptibility of decommissioned plastics likely reflects prior environmental exposure, where photo-oxidation and hydrolysis induce surface embrittlement and microcracks that exacerbate mechanical abrasion (Z. Zhang et al., 2024). Combined weathering experiments demonstrated that prolonged ultraviolet (UV) exposure significantly enhances the susceptibility of common polymers to mechanical abrasion, highlighting distinct polymer- and size-dependent fragmentation rates (Song et al., 2017).

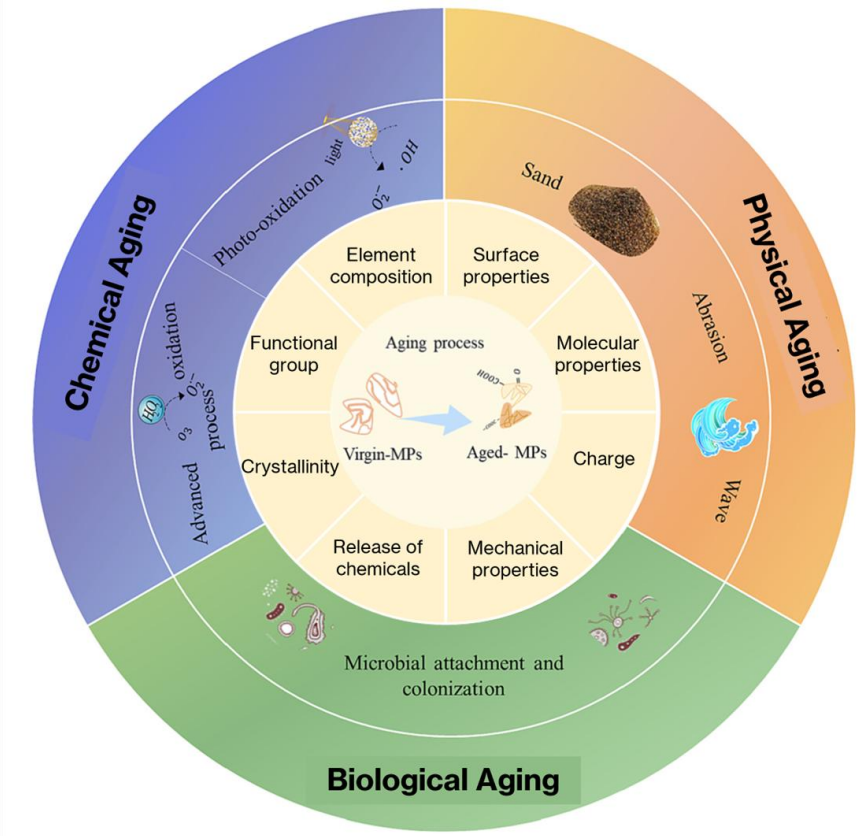

Figure 1.10. *Processes involved in the degradation of plastics through chemical, physical, and biological aging pathways. Adapted from: He et al., (2023).*

1.5.3.2 Chemical oxidation

Chemical weathering, primarily through photo-oxidation, is a critical abiotic pathway driving the molecular degradation of plastics in the environment. The photo-oxidative degradation of plastics proceeds via a free-radical chain reaction mechanism, encompassing initiation, propagation, and termination steps (W. He et al., 2023). UV-induced radical formation triggers a cascade of peroxy radical reactions, ultimately leading to polymer chain scission or crosslinking, oxidation, and the formation of low-molecular-weight fragments. In polymers with a carbon–carbon backbone, such as PE, PP, and PS, this process is initiated by the homolytic cleavage of C–H bonds upon UV energy absorption, resulting in the chain reactions of free radicals. In contrast, plastics containing heteroatoms in the main chain, such as PET, PUR, and PC, initially undergo hydrolysis. This leads to ester bond cleavage and the formation of carboxyl groups, which in turn render the polymer more susceptible to subsequent photo-oxidation (Gewert et al., 2015; Z. Zhang et al., 2024). UV irradiation, particularly in the wavelength range of 290–400 nm, initiates these reactions (Baby et al., 2024). Photodegradation rates measured under simulated marine conditions for various plastic types, including virgin PE, PP, PS, and PET, as well as environmentally recovered PE and PP fragments, revealed degradation rates of 1.78–2.31% per year, corresponding to estimated half-lives of ≤44.4 years (Delre et al., 2023). Another study investigated the generation of particles following a 112-day simulated aging protocol

under continuous exposure to visible and ultraviolet light (320–400 nm). The extent of particle formation in the 30 nm to 2 µm size range analyzed using NTA varied markedly among the polymers, with the highest concentrations observed for PS (6.4×10^8 particles/mL), followed by PLA (5.3×10^8), PE pellets (3.4×10^8), PP film (1.8×10^8), PET (1.7×10^8), PP pellets (1.7×10^8) and PP sheets (1.5×10^8), compared to the control (0.2×10^8) (Lambert & Wagner, 2016b). The rate and extent of photodegradation are governed by polymer composition, the presence of chromophoric additives or impurities, and environmental factors such as UV spectrum and intensity, temperature, and moisture (Nechifor, 2016).

1.5.3.3 Biological degradation

The biological degradation of plastics primarily involves a wide range of organisms. Microorganisms, particularly bacteria and fungi, utilize enzymatic mechanisms to break down plastic polymer chains into smaller molecules (Habib et al., 2024). Invertebrates such as worms also contribute to the fragmentation of larger plastic particles into MNPs. For example, earthworms such as *Eisenia andrei* have been shown to fragment plastic particles into MNPs, which are formed within the digestive tracts and subsequently introduced into soils through cast excretion (Kwak & An, 2021). Microorganisms, particularly bacteria and fungi, utilize enzymatic mechanisms to break down plastic polymer chains into smaller molecules (Habib et al., 2024). Plastic biodegradation by microorganisms proceeds through four successive stages: biodeterioration, depolymerization, assimilation, and mineralization. Biodeterioration involves the initial breakdown of polymer structures through combined microbial activity and abiotic factors. In depolymerization under aerobic or anaerobic conditions, microbial enzymes and free radicals cleave polymer chains into oligomers, dimers, and monomers. These smaller molecules are then taken up during assimilation, through metabolic processes to generate energy, biomass, and metabolites. The final stage, mineralization, converts the metabolic byproducts into carbon dioxide (CO_2) and methane (CH_4) depending on aerobic or anaerobic conditions (Heris, 2024).

Various microorganisms have demonstrated measurable capacities to degrade a wide range of plastic polymers, with degradation efficiencies highly dependent on the microbial species, polymer properties, and experimental conditions (S. S. Ali et al., 2021; W. He et al., 2023; Urbanek et al., 2018). For instance, a microbial consortium composed of multiple bacterial strains demonstrated the ability to utilize LDPE and HDPE as sole carbon sources, with weight loss ranging from 21.7% to 24.5% (Satlewal & Zaidi, 2008; Soni et al., 2009). *Zalerion maritimum*, a marine fungus present in Portuguese coastal waters, has been shown to biodegrade PE, inducing over 43% mass loss in plastic pellets after 28 days and a corresponding increase in band intensities of hydroxyl and carbonyl groups associated with oxidation (Paço et al., 2017). A comparative analysis of PET film degradation by marine-derived isolates showed that the bacterial strain *Vibrio* sp. degraded PET more efficiently, with 35% weight loss over six weeks, compared to 22% by the fungal strain *Aspergillus* sp. under identical conditions (Sarkhel et al., 2020). A novel bacterium, *Ideonella sakaiensis*

201-F6, isolated from a sediment sample, produces enzymes capable of hydrolyzing PET film, resulting in the formation of environmentally benign monomers (terephthalic acid and ethylene glycol). Although PET hydrolase (PETase) is heat-labile, it exhibits remarkable hydrolytic activity at moderate temperatures and is uniquely effective at degrading PET in its rigid, glassy state (Yoshida et al., 2016). Complementing this, the strain *Gordonia* sp. CN2K, induced approximately 40.4% biodegradation of PET sheets over 45 days. Metabolite analysis of the spent medium revealed key depolymerization intermediates, confirming enzymatic breakdown via a conserved degradation pathway (Chandramouli Swamy et al., 2024).

Despite reported degradation rates for various polymers, complete and rapid biodegradation under ambient environmental conditions remains unfeasible. Biodegradation of synthetic plastics is inherently complex and influenced by various factors. These include intrinsic material properties such as chemical structure, molecular weight and distribution, crystallinity, glass transition temperature, elasticity, polymer size, surface area, composition (e.g., blends or copolymers), additives, surface roughness, and hydrophilicity. Environmental conditions, like temperature, microbial abundance and activity, moisture availability, pH, oxygen concentration, enzymatic presence, and UV radiation, further modulate degradation dynamics. Additionally, external variables such as the residence time in the environment, its weathering state, and the ratio of plastic material to degrading medium significantly impact degradation outcomes (Afshar et al., 2024; Khoshtinat, 2023; Montazer et al., 2020).

1.6 Exposure Pathways and Biological Effects of MNPs in Marine Organisms

1.6.1 Exposure pathways

Marine organisms are exposed to MNPs through multiple exposure pathways. The primary route is ingestion, which occurs across trophic levels. Ingestion can be direct, either deliberate, when plastics are mistaken for prey items, or accidental, as in passive uptake by filter feeders and detritivores, or indirect, through trophic transfer via contaminated prey (Ryan, 2019). Feeding behavior plays a critical role in determining an organism's susceptibility to MNP exposure. Suspension feeders such as mussels, oysters, and clams exhibit particularly high vulnerability due to their highly efficient particle filtration systems, which enable them to process large volumes of seawater and inadvertently capture MNPs alongside food particles. Similarly, deposit feeders that consume organic-rich sediments are at risk of ingesting sediment-bound MNPs, particularly high-density particles that tend to accumulate in benthic environments (Baun et al., 2008; Pinheiro et al., 2020; Wright et al., 2013). Invertebrate species thus represent critical entry points for MNPs into the aquatic food web (Figure 1.11), thereby facilitating trophic transfer to higher organisms and ultimately humans (Baun et al., 2008). The relationship between feeding mode and

MNP ingestion was demonstrated in a mesocosm experiment involving invertebrates with diverse feeding strategies and habitats. Particle ingestion occurred across all assessed taxa, with uptake rates influenced by particle concentration, feeding behavior, and encounter rate within the patchy environment. Suspension-feeding bivalves exhibited the highest particle loads due to continuous filtration, while free-swimming crustaceans ingested more beads than sediment-surface feeders (Setälä et al., 2016).

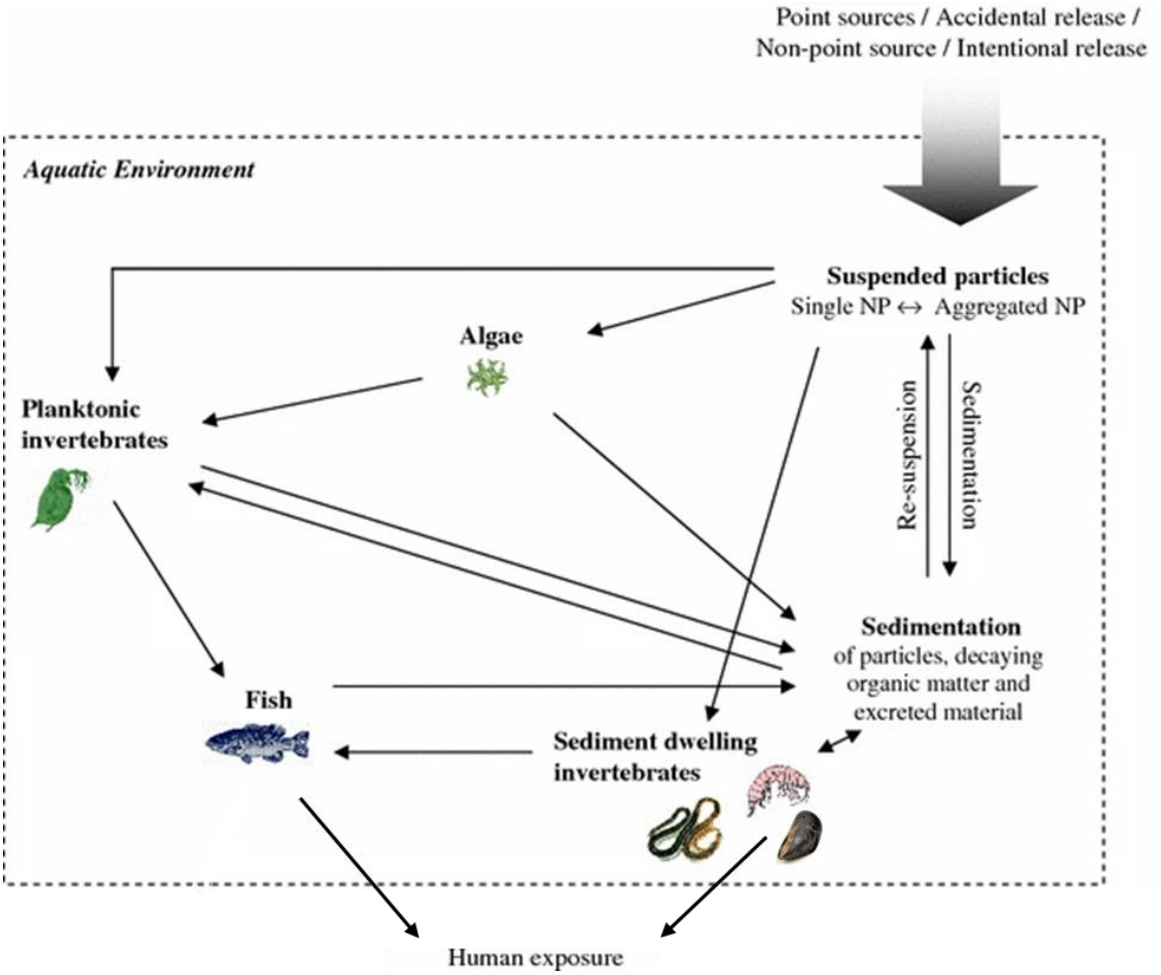

***Figure 1.11**. Routes of exposure and the significance of invertebrate species in the aquatic food web, highlighting their role in mediating MNP uptake and transfer. Adapted from: Baun et al. (2008).*

Beyond direct ingestion, MNPs can enter the main base of the marine food web through surface absorption (Al-Thawadi, 2020; Lusher, 2015). For instance, NPs have been shown to adhere to phytoplankton surfaces such as *Pseudokirchneriella subcapitata*, with neutral and positively charged plastic particles exhibiting stronger adsorption to the algal cell wall than their negatively charged counterparts (Nolte et al., 2017). This charge-dependent interaction was also observed in algal genera like *Chlorella* and *Scenedesmus*, where adsorption also varies with algal morphology and motility (Bhattacharya et al., 2010). Additionally, in the reef-building coral *Danafungia scruposa*, plastic particle retention occurs primarily through passive adhesion, while ingestion rates are relatively higher for

biofouled particles, suggesting a reduced ability to discriminate plastics from natural prey (Corona et al., 2020).

Several studies have demonstrated indirect ingestion through trophic transfer of MNPs across various marine food webs (Santos et al., 2021). For instance, in Baltic Sea littoral food chains, 10 µm fluorescent PS were tracked through a three-level system involving zooplankton, chameleon shrimp, and rockpool prawn, confirming MP ingestion and transfer up to the third trophic level via fluorescence microscopy (Kangas et al., 2023). Similarly, in another study involving microalgae, crustaceans, and fish, NPs adsorbed to algal cell surfaces were gradually transferred to higher trophic organisms. While transfer was confirmed, the particle uptake via trophic exposure was significantly lower than that observed in organisms subjected to direct exposure, highlighting differences in bioavailability and uptake efficiency between exposure pathways (L. Kim et al., 2022).

As of the most recent synthesis, 1,288 marine species have been reported to ingest plastics, underscoring the growing scale of the problem (Santos et al., 2021)**.** The prevalence of MP ingestion, measured in field studies as the percentage of individuals containing plastic, varies substantially among species, with reported values ranging from <1% to 100%. This variability reflects not only interspecific differences in habitat (e.g., pelagic vs. benthic zones), feeding strategy (e.g., filter feeding, deposit feeding, predation), and trophic level, but also spatial heterogeneity in environmental plastic contamination (Lusher, 2015).

The mechanisms of MNP uptake and internalization primarily depend on particle size and the physiology of the organism. Larger MPs typically remain within digestive compartments (stomach, gut) until egested, but smaller MNPs can cross biological barriers (Lusher, 2015). Translocation is particularly evident for particles with size range below 83 µm, exhibiting wider organ distributions and longer retention times as size decreases (Mehinto et al., 2022). Several studies indicated that MNPs can translocate to various tissues such as the digestive gland, liver, stomach, gills, mantle, muscle, brain, kidney, pancreas, gallbladder, and yolk sac, with the gastrointestinal tract and gill being frequent locations for plastic accumulation (Franzellitti et al., 2019; W. Liu et al., 2024). In bivalves, MNPs can translocate from the gastrointestinal tract into the circulatory system (hemolymph) during exposure and persist for extended periods, indicating systemic distribution and prolonged retention (Browne et al., 2008).

The extent and rate of uptake and accumulation of MNPs is influenced by both the organism's feeding strategy and egestion efficiency, as well as the particle properties such as size, composition, shape, surface chemistry, and concentration (Benson et al., 2022). Notably, some species exhibit the ability to discriminate between plastic particles and natural prey, and the excretion of particles during depuration has been documented across various taxa (W. Liu et al., 2024; Lusher, 2015). For example, sea urchin larvae (*Tripneustes gratilla*) demonstrated the ability to excrete the ingested MPs, with complete clearance

observed after 7 hours of depuration (Kaposi et al., 2014). Under laboratory conditions, zebrafish (*Danio rerio*) also exhibited indiscriminate feeding behavior as a mechanism to expel ingested but inedible microplastics (Y. Chen et al., 2022; S. W. Kim et al., 2019). Moreover, filter feeding bivalves also exhibit similar mechanisms of selection by producing pseudofeces to reject indigestible particles with low nutritional content before they pass the gut (Kaposi et al., 2014; Kooijman, 2006). Nevertheless, plastic particles are able to bypass such defences, especially in species without strong discriminatory feeding mechanism. Once ingested, retention times can be remarkably long; for instance, mussels have been shown to retain MPs, especially those smaller than 3 µm, for over 48 days (Browne et al., 2008). This prolonged retention facilitates the translocation and accumulation of plastic particles into vital organs, tissues, and cells (Sendra, Saco, et al., 2020).

At the cellular level, particle internalization primarily occurs via endocytosis, a well-characterized form of active transport. Endocytosis is broadly categorized into phagocytosis and pinocytosis, which differ in both mechanism and size range of the endocytotic vesicles. Phagocytosis ("cell eating") is carried out by specialized phagocytic cells, such as macrophages in vertebrates and hemocytes in invertebrates, and typically involves the uptake of larger particles (>0.5 µm), including apoptotic cells, microorganisms and foreign particles, such as MNPs. In contrast, pinocytosis ("cell drinking") is a non-discriminating process employed by nearly all cell types to internalize smaller particles, generally ranging from a few to several hundred nanometers. Pinocytosis can be further subdivided into clathrin-mediated endocytosis and caveolae-mediated endocytosis, each involving distinct vesicular pathways. The efficiency and route of endocytic uptake are influenced by several physicochemical properties of the particles, such as size, surface charge, shape, and surface chemistry, as well as species- and cell type-specific factors (Foroozandeh & Aziz, 2018b; Uribe-Querol & Rosales, 2020; F. Zhao et al., 2011). In mussel hemocytes, the uptake of virgin PS MNPs, up to six particles per cell, was confirmed via fluorescence microscopy by their presence in the cytoplasm and colocalization with lysosomal compartments. Notably, particle internalization by hemocytes was mediated by distinct endocytic pathways and exhibited a size-dependent pattern, with 50 nm PS NPs taken up most efficiently, followed by 100 nm and 1 µm particles (Katsumiti et al., 2021; Sendra, Saco, et al., 2020). Confocal microscopy images (Figure 1.12) revealed that exposure to fluorescently labelled PS NPs of different sizes (50 nm, 100 nm, and 1 µm) not only confirmed their internalization but also revealed associated alterations in actin cytoskeleton organization (Sendra, Saco, et al., 2020). However, it is important to note that most studies to date have employed virgin polymers, underscoring a research gap in understanding how aged or weathered particles are internalized and impact cellular processes (Revel et al., 2021). The cellular internalization of MNPs has critical implications for their fate and impact on biological systems. Internal exposure, resulting from the ingestion of MNPs, whether direct or indirect, is a critical driver of both lethal and sublethal toxicological effects (Benson et al., 2022; Panariti et al., 2012).

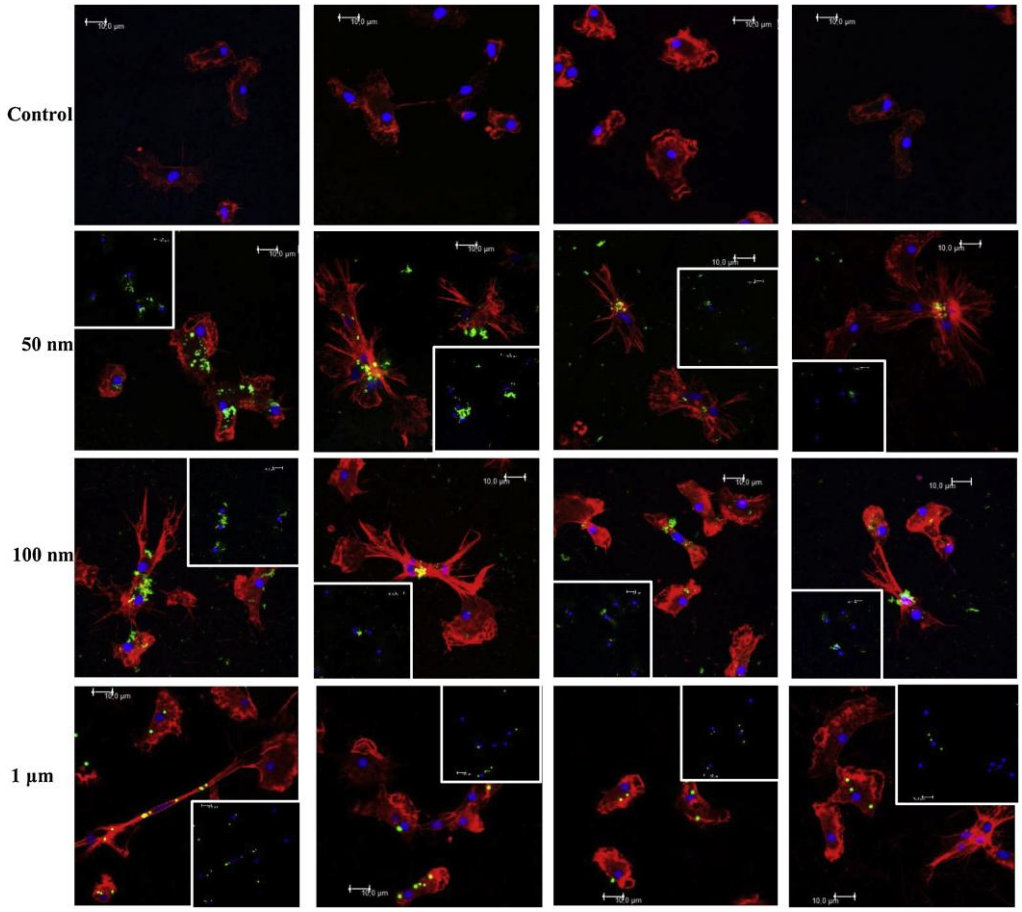

Figure 1.12. *Confocal microscopy images showing internalization of fluorescently labeled polystyrene NPs and associated changes in actin cytoskeleton conformation. The cell nuclei are stained with DAPI (blue), actin filaments are labelled with phalloidin (red), and PS NPs appear in green. Images illustrate cellular responses to exposures of 50 nm, 100 nm, and 1 µm PS NPs compared with control cells. Adapted from: Sendra et al. (2020).*

1.6.2 Biological effects of MNP exposure

The effects of MNP exposure in marine organisms are evident across all levels of biological organization (Figure 1.13), from subcellular changes to ecosystem-level effects (Galloway et al., 2017; Thompson et al., 2024).

At the cellular level, internalized MNPs can induce toxicity in marine organisms through multiple pathways, leading to profound physiological and biochemical alterations. Although cytotoxicity assessments of MNPs remain limited and primarily focus on virgin polymers, emerging evidence indicates that oxidative stress, lysosomal dysfunction, cellular membranes and organelles disruption, immune activation, and genotoxicity as key mechanisms underlying MNP toxicity (Feng et al., 2024; T. He et al., 2023; Prinz & Korez, 2020; Z. Yang et al., 2023). These MNP-induced mechanisms are primarily influenced by particle size, surface properties, polymer type, as well as cell type (Matthews et al., 2021).

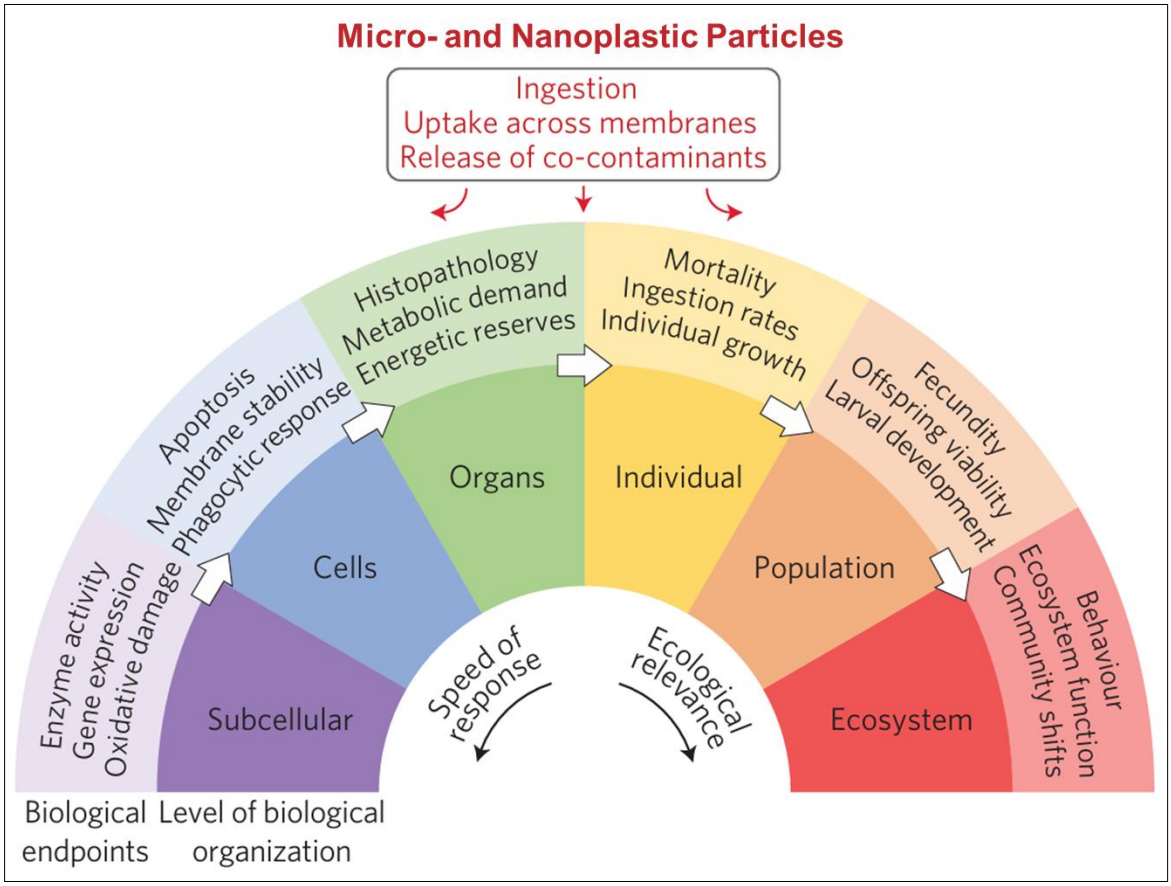

Figure 1.13. *Framework illustrating the potential biological impacts of micro- and nanoplastic particle exposure across different levels of biological organization, from subcellular responses to ecosystem-level effects. Adapted from: Galloway et al. (2017).*

Cells may initiate autophagy in response to exposure; however, particle-induced lysosomal dysfunction, characterized by pH disruption, membrane permeabilization, and rupture, can impair this process. Accumulation of amine-modified PS NPs (NH_2-PS) in lysosomes has been shown to block autophagic flux, ultimately leading to cell death (Feng et al., 2024; F. Wang et al., 2018). These lysosomal and autophagic processes are linked to oxidative stress induction in response to particle exposure (M. N. Moore et al., 2006). Oxidative stress occurs from an imbalance between reactive oxygen species (ROS) production and antioxidant defense capacity (Hu & Palić, 2020). Excessive ROS generation triggers a cascade of cellular disturbances, including endoplasmic reticulum (ER) stress, cytoskeletal dysfunction, protein oxidation, lipid peroxidation, and DNA damage. These events also activate redox-sensitive signaling pathways and pro-inflammatory transcription factors. Collectively, these interconnected intracellular events drive a vicious cycle of cellular injury and death and understanding how they converge within stress-response networks is critical for evaluating the fate and toxicity of MNPs (Simmons et al., 2009; Z. Yang et al., 2023). Several studies have reported size- and concentration-dependent changes in ROS levels in copepods, rotifers, medaka, zebrafish, and mussels exposed to virgin PS microbeads (Jeong et al., 2016, 2017; Kang et al., 2021; Lu et al., 2016; Sendra et al., 2020). Notably, surface

alterations induced by weathering processes, such as UV-driven oxidation, can enhance the intrinsic ROS-generation potential of MNPs compared to pristine ones, thereby influencing the overall ROS burden and redox balance in cellular environments (Jeon et al., 2021).

Histopathological alterations serve as sensitive biomarkers for detecting sublethal toxic effects in marine organisms. The targeted examination of organ-specific lesions enables identification of contaminant-induced physiological stress and provides insight into the cumulative impacts of exposure. Among the most responsive organs are the gills and digestive glands, which exhibit well-characterized histological changes in response to a wide array of pollutants, including MNPs (Au, 2004; Salamat & Zarie, 2016). Exposure to polyethylene (10.7–93.9 μM) at 10 μg L^{-1} (PEL) and 1000 μg L^{-1} (PEH), and PET (9.0–56.0 μM) at 10 μg L^{-1} (PETL) and 1000 μg L^{-1} (PETH), induced several histopathological alterations in both gill and digestive gland tissues. These include distinct histopathological signs as shown in Figure 1.14, such as hemocyte infiltration, enlargement of the central vessel of the gill filament, cilium shedding, epithelial cell coagulation, and necrosis (Teng, Zhu, et al., 2021)**.** As multifunctional organs essential for respiration, osmoregulation, and ion regulation, gills are particularly susceptible to waterborne contaminants. The gill filaments and lamellae present a large surface area that facilitates direct and continuous exposure to suspended particles (Au, 2004). For instance, histological lesions, such as alterations in lamellar structure and degree of hemocyte infiltration, are often associated with inflammatory responses in gill tissues (Bouallegui et al., 2017; Gornati et al., 2016). Similarly, the digestive tract is a primary site of MNP accumulation through ingestion. Its central role in digestion and nutrient assimilation makes it a critical target for assessing ingestion-related toxicity (Y. Lee et al., 2025; Lobo-da-Cunha, 2019; Salamat & Zarie, 2016). Particle exposure can induce a range of tubular and intertubular alterations, with atrophy, hemocyte infiltration, and lipofuscin accumulation commonly reported as outcomes (Bouallegui et al., 2018; González-Soto et al., 2019; Paul-Pont et al., 2016). These histopathological changes reflect disruptions in vital biological functions, impairing organ integrity and homeostasis, with potential downstream effects on organismal fitness and survival. Increasing evidence shows that MPs can affect multiple organ systems across diverse species, highlighting their systemic toxicity and the importance of integrative assessments in ecotoxicology (Y. Lee et al., 2025).

Effect assessments of MNP exposure in marine organisms have primarily focused on the individual organism-level endpoints, such as growth, reproduction and survival (Moyo, 2022). While these studies are essential for defining hazard thresholds, they often overlook sub-organismal responses such as cellular, molecular, and biochemical alterations that can act as early indicators of toxicity (Suman et al., 2021). When integrated with exposure assessments, effect thresholds (e.g., no observed effect concentrations, NOECs, or lowest observed effect concentrations, LOECs) provide the basis for characterizing risks to populations and ecosystems (Besseling et al., 2019).

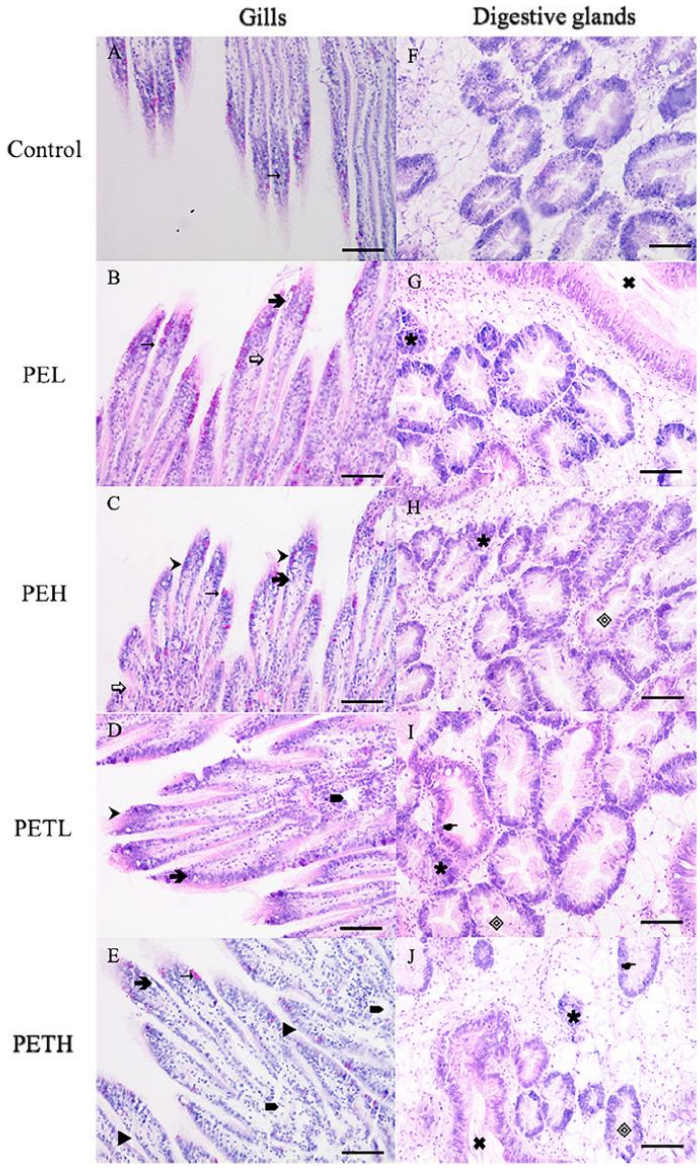

Figure 1.14. *Representative micrographs adapted from Teng et al. (2021), showing gill and digestive gland tissues of bivalves (Pacific oyster, Crassostrea gigas) exposed to PE (10.7–93.9 µM) and PET (9.0–56.0 µM) MPs for 21 days. Critical histopathological alteration reported includes: hemocyte infiltration (➞); gill flap enlargement (➡); digestive tract necrosis (☛); epithelial cell coagulation (✱); and cytoplasmic damage dispersion (◈).*

Although chronic exposure to plastic particles is rarely lethal, numerous studies have demonstrated a wide range of sublethal effects at the individual level, including impaired reproduction, reduced growth, and altered behavior across multiple taxa (Ferreira et al., 2019; Leistenschneider et al., 2023; Prinz & Korez, 2020). While lethality is typically observed at concentrations exceeding environmental relevance (Galloway et al., 2017), emerging evidence shows that even realistic exposure levels can impair growth and survival, particularly during sensitive developmental stages (Amran et al., 2022; de Souza Teodoro et al., 2024; Naidoo & Glassom, 2019).

The effect of MNP exposure at the individual level can scale up to affect entire populations. Declines in population size may directly result from adverse effects such as reduced growth, impaired reproductive output, and decreased offspring viability (Galloway & Lewisa, 2016). Although chronic exposure data remains limited, a consistent pattern emerging from plastic toxicity studies is the reallocation of internal energy reserves toward maintaining homeostasis in response to plastic-induced physiological stress. This energetic trade-off, often at the expense of growth, reproduction, and storage, compromises organismal fitness and may limit long-term population sustainability (Applebaum et al., 2014; Galloway & Lewisa, 2016; Smith, 2020). Supporting this, a recent modeling study integrating experimental data demonstrated that even moderate reductions in sublethal physiological endpoints, specifically clearance rate, can result in measurable declines in mussel growth (6–16%) and reproductive output 7–19%) (Hatzonikolakis et al., 2024). Exposure to PS MPs also induced physiological changes in oysters, leading to disrupted energy uptake and allocation, which played a major role in reproductive impairment (Sussarellu et al., 2016). Additionally, compromised individual performance, such as diminished ability to capture prey or evade predators, can further exacerbate mortality risks and reduce population resilience (Prinz & Korez, 2020).

Pollutant-induced changes in key species populations can ultimately trigger a cascading effect on communities and ecosystem-level dynamics (Galloway et al., 2017). For example, lugworms (*Arenicola marina*), key bioturbators in sandy sediments, exhibited reduced sediment-mixing activity as measured by the production of surface casts, when exposed to microplastic-contaminated substrates. As ecosystem engineers, such behavioral impairments can compromise critical biogeochemical processes, such as sediment oxygenation, nutrient cycling, and primary productivity in benthic habitats (Galloway et al., 2017; Green et al., 2016). Similarly, impairment in filtration capacity of bivalves due to plastic particle exposure can disrupt the ecological functioning of biogenic habitats by altering nutrient fluxes and reshaping benthic community structure (Green et al., 2017). Oysters, for example, play a crucial role in mitigating eutrophication by maintaining high filtration rates and reducing algal blooms driven by nitrogen loading. However, while moderate microplastic exposure may not immediately impair this ecosystem service, extreme concentrations can significantly reduce filtration efficiency, signaling the potential collapse of this ecosystem function under escalating pollution scenarios (Bricker et al., 2020; McAfee et al., 2023). Field evidence further highlights impact not only on biogeochemical processes but also on the restructuring of community assemblages. A nine-week experiment on an intertidal shore found that both conventional and biodegradable plastic items significantly affected the abundance and composition of infaunal invertebrate communities (Green et al., 2015).

While invertebrates, especially filter feeders and deposit feeders, are among the most vulnerable (Baun et al., 2008), the incorporation of MNPs into the marine food web indicates no trophic level is entirely spared (Leistenschneider et al., 2023; Lusher, 2015).

MNPs are thus recognized as a growing ecological threat, and ongoing research initiatives continue to refine our understanding of how these pollutants translate into biological risk. The evidence so far underscores that MNPs have the potential to impair marine organisms at multiple levels of biological organization, ultimately threatening the stability and functioning of marine ecosystems (Galloway et al., 2017; Thompson et al., 2024). The challenge ahead lies in determining environmentally realistic effect thresholds of MNP exposure.

1.7 Research Gaps

Despite significant progress in understanding the effects of MNPs, critical research gaps persist. Table 1.2 summarizes these gaps and provides recommendations to guide future research.

1.7.1 Lack of environmentally relevant exposure scenarios

A fundamental challenge in MNP toxicity research is the frequent use of exposure concentrations that are several orders of magnitude above those reported in marine environments. Such concentrations, though sometimes used for mechanistic insight and to simulate worst-case scenarios, can compromise environmental relevance. To enhance the translational value of laboratory findings, future studies must align exposure conditions with environmentally realistic concentrations derived from field data (e.g., seawater, sediments, and biota) (Lenz et al., 2016; Phuong et al., 2016).

Another limitation lies in the widespread use of commercially synthesized spherical plastic polymers, which do not reflect the physicochemical characteristics of environmental MNPs (W. Liu et al., 2024). Employing aged or weathered particles, whether produced through natural (Bhat et al., 2024) or artificial aging/weathering processes (Seghers et al., 2025), is crucial for enhancing environmental relevance in toxicity assessments. The use of aged or weathered plastic particles better reflects the transformations that occur in natural systems and may exhibit heightened toxicological profiles than pristine polymers (Völkl et al., 2022; von der Esch et al., 2020). It is necessary to investigate the effects of polymers with shapes, sizes, and concentrations representative of aquatic environments to ensure experimental outcomes reflect real-world exposure scenarios (Revel et al., 2021).

Moreover, most studies focus on acute or short-term exposures, failing to reflect the chronic nature of MNP exposure typical of marine environments. Incorporating chronic, long-term exposure studies, including multigenerational approaches where appropriate, is essential to capture the full scope of cumulative and latent effects, as well as the potential for recovery, following MNP exposure (Cunningham et al., 2023; Junaid et al., 2023). Research must also account for particle mixtures, additives, and co-occurring

environmental contaminants, since these factors may interact synergistically to exacerbate or mitigate adverse effects (Mkuye et al., 2022).

Table 1.2. *Summary of key research gaps and recommended research priorities identified based on a critical synthesis of the existing literature, including recent review studies.*

Research Gap	Recommended Actions
Lack of environmentally relevant exposure scenarios	
Use of unrealistic exposure concentrations.	Use environmentally relevant exposure concentrations based on field data (e.g., seawater, sediment, biota) (Lenz et al., 2016; Phuong et al., 2016).
Environmental relevance of test particles.	Employ naturally (Bhat et al., 2024) and/or artificially (Seghers et al., 2025) aged/weathered MNPs to improve environmental relevance.
Insufficient understanding of long-term effects.	Incorporate chronic exposure scenarios, including multigenerational assessments where applicable (Cunningham et al., 2023; Junaid et al., 2023).
High variability in experimental designs	
Underrepresentation of marine taxa.	Expand species selection to incorporate ecologically and commercially important marine organisms, particularly sentinel species (Biamis et al., 2021; V. V. Ribeiro et al., 2023).
Limited focus on sensitive sub-lethal functional endpoints.	Assess sensitive sub-lethal functional endpoints as early indicators of toxicity (Ferreira et al., 2019; Kataoka & Kashiwada, 2021).
Nanoplastics are underrepresented in toxicity studies.	Systematically investigate size-dependent toxicity across a wide range of particle sizes (Masseroni et al., 2022).
Incomplete characterization of MNPs.	Conduct thorough characterization of test particles using advanced, complementary techniques, particularly size distribution, morphology, chemical composition, surface properties, and behavior in exposure media (Gangadoo et al., 2020; Schwaferts et al., 2019).
Applicability for risk assessment	
Limited quality assurance and harmonization.	Implement rigorous QA/QC standards and harmonized reporting to enhance reliability and relevance for risk assessment (De Ruijter et al., 2020; Thornton Hampton et al., 2022).

1.7.2 High variability in experimental designs

Toxicity assessments of MNPs exhibit substantial variability in experimental designs, which hinders interstudy comparability and the development of overarching conclusions. Previous studies also focus on a limited number of conventional model organisms. This underrepresentation may obscure taxa-specific vulnerabilities. To address this, future studies should expand taxonomic breadth by incorporating both ecologically and

commercially important species, particularly sentinel organisms, e.g. mussels (Beyer et al., 2017; Biamis et al., 2021; V. V. Ribeiro et al., 2023).

Equally important is the need to identify and characterize targeted toxicity mechanisms, as these provide mechanistic insights that link sub-organismal responses to higher-level ecological effects (T. He et al., 2023; Matthews et al., 2021). Particular attention should be given to expanding data on sub-lethal functional endpoints, including metabolic, immune, and other systemic responses, which have shown heightened sensitivity but remain understudied. These endpoints can serve as early indicators of toxicity with cascading effects at higher levels of biological organization (Ferreira et al., 2019; Kataoka & Kashiwada, 2021; Sharifinia et al., 2020; Zaki & Aris, 2022).

In parallel, nanoplastics, despite their potentially enhanced biological interactions due to their high surface-to-volume ratio and ability to cross biological barriers (Rist & Hartmann, 2018), remain underexplored. This narrow focus limits insight into size-specific toxicodynamics. Future research should prioritize the systematic evaluation of size-dependent effects across a wide range of particle sizes and polymer types to better identify the most hazardous fractions and elucidate their mechanisms of action (Masseroni et al., 2022).

Compounding this issue is the insufficient characterization of test particles, making it difficult to attribute observed effects to particle-specific properties. Thorough characterization, including size distribution, morphology, chemical composition, behavior in exposure media, and the presence of any additives or surfactants, is essential for advancing mechanistic understanding (Gangadoo et al., 2020; Schwaferts et al., 2019).

1.7.3 Applicability for risk assessment

Finally, the broader applicability of MNP toxicity studies for environmental risk assessment is limited by the lack of harmonization in methodological standards. Inconsistencies in study design, reporting practices, and QA/QC procedures limit reproducibility and cross-study comparability. To improve the reliability and relevance of experimental findings, there is a pressing need to implement rigorous quality assurance and quality control protocols (De Ruijter et al., 2020; Thornton Hampton et al., 2022). Harmonized frameworks will not only enhance scientific rigor but also facilitate the integration of research outcomes into comprehensive risk assessment strategies.

1.8 Research Aims and Thesis Outline

The main objective of this thesis is to elucidate the biological reactivity of MNPs, with a particular focus on mechanistically assessing cellular, tissue, and organismal responses under environmentally relevant exposure scenarios. The thesis is organized into four interrelated research chapters, each contributing a distinct yet complementary perspective on responses across different levels of biological organization. Together, these chapters form a multi-tiered investigation that spans from community-specific hazard thresholds assessments to the intricate cellular mechanisms underlying particle-induced toxicity.

To fulfill the main objective, the following key research questions are addressed in separate chapters:

1. How do particle characteristics, particularly size, shape, and concentrations, influence the toxicity of MNPs across marine invertebrate taxa? Which species and biological endpoints are most sensitive to MNP exposure, and how can this information inform community-specific hazard thresholds?

2. Do aged PET MNPs induce persistent cellular- and tissue-level effects in *Mytilus edulis* under environmentally relevant exposure conditions?

3. How do different hemocyte subpopulations respond to aged PET particles *in vitro*, and what are the mechanistic underpinnings of observed immune responses?

4. How are internalized nanoparticles distributed and localized within cellular compartments, and what are the associated effects on hemocyte integrity?

The thesis begins with a comprehensive **introductory chapter (Chapter 1)** regarding *Plastic Pollution in the Marine Environment*, which provides essential background and scientific context for the subsequent research chapters. This chapter traces the historical development of plastics and the evolution of global plastic production and waste generation. It identifies the major sources of marine plastic pollution, and discusses the physicochemical characteristics of plastic particles, their environmental aging processes, and the challenges of their analytical characterization. It also addresses the environmental fate and transport mechanisms of MNPs in marine systems, and outlines known exposure pathways and biological effects to marine organisms. This chapter establishes the conceptual framework for focusing on environmentally relevant exposure scenarios and sets the stage for the targeted research questions addressed in the thesis.

Following this, **Chapter 2** establishes the mechanisms and risks of MNP exposure across marine invertebrate taxa through a systematic analysis of chronic exposure data. Drawing

from high-quality entries in the ToMEx v2.0 database, this chapter evaluates how particle-specific characteristics, such as size, shape, and concentrations, modulate biological effects across marine invertebrate species. Using species sensitivity distributions (SSDs), it provides community-specific hazard thresholds and identifies key sensitive species to plastic particle exposure. This foundational chapter provides critical insight into the mechanistic drivers of sensitivity and offers provisional thresholds for protecting marine invertebrate communities.

Chapter 3 transitions from interspecies comparisons to an in-depth, *in vivo* investigation of biological responses to environmentally relevant concentrations of aged PET MNPs in a sentinel bivalve species, *Mytilus edulis*. Through time-resolved analyses of hemocyte function and tissue histopathology, the chapter demonstrates how aged MNPs elicit concentration- and time-dependent immune perturbations and structural damage to key organs, particularly the gills. Importantly, the recovery phase assessments highlight the organism's physiological resilience following exposure, providing a nuanced view of both immediate cellular perturbations and recovery potential.

Chapter 4 builds upon the cellular focus of the previous chapter by assessing the differential sensitivity of hemocyte subpopulations, granulocytes and hyalinocytes, to aged PET MPs and NPs under controlled *in vitro* conditions. Using flow cytometry and a panel of functional biomarkers, this chapter reveals particle size- and concentration-dependent variations in lysosomal stability, oxidative stress, and hemocyte mortality. The findings highlight the complex cellular mechanisms underlying hemocyte functional impairment following exposure to aged PET particles.

Chapter 5 advances the investigation into the intracellular fate and associated effects of aged PET NPs in mussel hemocyte subpopulations. Using label-free three-dimensional live-cell imaging by holotomography, this chapter characterizes particle internalization and localization patterns, as well as the associated morphological alterations across hemocyte subpopulations. The findings demonstrate the utility of holotomography for resolving unlabeled aged PET NPs within living hemocytes, offering critical insight into the pathways driving hemocyte morphological and functional impairment under relevant exposure scenarios.

The final chapter, **Chapter 6**, presents the general conclusions of the thesis by synthesizing key findings across all research chapters. It critically highlights the scientific contributions, methodological limitations and future directions for assessing the impact of plastic pollution on marine organisms and ecosystem as a whole.

Chapter 2

Systematic Assessment of the Mechanisms and Risks of Micro- and Nanoplastic Particle Exposure in Marine Invertebrates

Published as:

Hara, J., Vercauteren, M., Janssen, C. R., Blust, R., Asselman, J., & Town, R. M. Systematic assessment of the mechanisms and risks of micro- and nanoplastic particle exposure in marine invertebrates. *Ecotoxicology and Environmental Safety, 311, 119877*. https://doi.org/10.1016/j.ecoenv.2026.119877.

Abstract

Marine invertebrates are among the most vulnerable organism groups to micro- and nanoplastic (MNP) exposure, yet understanding of their interspecies sensitivity and mechanistic responses remains limited. This study provides a systematic evaluation of MNP toxicity across diverse marine invertebrate taxa by (i) evaluating the effects of MNP exposure on key biological endpoints as a function of key particle characteristics, and (ii) constructing species sensitivity distributions (SSDs) to derive ecologically relevant hazard thresholds. Data were extracted from the Toxicity of Microplastic Explorer (ToMEx) for Aquatic Organisms database (version 2.0), with quality evaluated using the Technical and Risk Assessment "Red" Criteria framework to ensure the inclusion of essential experimental parameters. Chronic no-observed-effect concentration (NOEC) values, derived from mortality, fitness, and functional-related endpoints, were analyzed as a function of particle size (nanoplastics: <1 µm; microplastics: 1–5000 µm), shape (spherical vs. non-spherical), and exposure medium (water vs. sediment) to identify particle-specific toxicity trends. To translate reported biological effects into ecologically relevant risk estimates, SSDs were constructed using chronic fitness-related endpoints, accounting for two distinct exposure mechanisms: food dilution via ingestion and tissue translocation. *Psedechinus huttoni* (Echinoderm) emerged as the most sensitive, while *Paracentrotus lividus* (Echinoderm) were the least sensitive across both models. Preliminary Safe Standards (PSS), calculated using SSD-derived HC_5 values, offer provisional thresholds for protecting marine invertebrate communities. These findings provide insights into MNP toxicity and aid in identifying sensitive taxa and endpoints, while highlighting key knowledge gaps to advance risk assessment frameworks for MNPs in marine ecosystems.

Keywords: Micro- and Nanoplastics; Marine Invertebrates; Biological Effects; Species Sensitivity Distributions; Risk Assessment

2.1 Introduction

Plastic pollution is one of the most pressing environmental challenges (Veneral et al., 2023). Cumulative plastic waste generation reached approximately 6,300 million metric tons by 2015, with 79% accumulating in landfills or natural environments due to inadequate recycling and waste management. Without intervention, annual inputs could double by 2050 under a "business-as-usual" scenario (Geyer et al., 2017). A substantial portion of this plastic debris ends up in marine environments, where it undergoes fragmentation into secondary micro- and nanoplastic particles (MNPs) through physical abrasion, chemical oxidation, light irradiation, and biological degradation processes (W. He et al., 2023; L. Peng et al., 2020). MNPs have been detected in various compartments, from soils, fresh and marine surface waters and water columns to coastal and deep-sea sediments, and even remote polar regions (Pittura et al., 2023; Yeo et al., 2023). Owing to their ubiquity, persistence, and bioavailability these particles interact with marine organisms at all levels of biological organization, posing significant ecological risks (Galloway et al., 2017).

Marine invertebrates, which play crucial roles in ecosystem processes such as nutrient cycling, sediment stabilization, water filtration, and trophic energy transfer (Baun et al., 2008), are susceptible to MNP pollution due to their diverse habitats, comprising both pelagic and benthic compartments, and diverse feeding strategies (Canesi & Procházková, 2014). For instance, suspension-feeding bivalves such as mussels, oysters, and clams possess efficient particle uptake systems, filtering large volumes of seawater and incidentally capturing MNPs along with food particles. Deposit-feeding organisms, which ingest organic-rich sediments, are inherently exposed to sediment-bound particles, especially high-density MNPs that accumulate in benthic layers (Baun et al., 2008; Wright et al., 2013). Beyond direct ingestion, other marine invertebrate species such as corals interact with MNPs through passive surface adhesion (Corona et al., 2020). Due to their multiple exposure pathways, these organisms are particularly at high risk of MNP ingestion and retention, making them a critical group for assessing MNP-induced effects (Canesi & Procházková, 2014).

An increasing number of ecotoxicological studies have shown that MNP exposure adversely affects invertebrates across diverse taxa. Once ingested, MNPs can cross biological barriers, accumulate in tissues, and disrupt physiological processes (Gonçalves & Bebianno, 2021; Trestrail et al., 2020). *In vitro* and *in vivo* studies have demonstrated that MNP exposure affects multiple levels of biological organization, from molecular and cellular stress responses to organism-level alterations. Invertebrates across diverse taxa, including bivalves, polychaetes, decapod crustaceans, sea urchins, and corals, exhibit a broad range of adverse effects, such as physiological stress, immune dysregulation, alteration in gene expressions and proteomic profiles, as well as histopathological, behavioral, developmental, and growth impairments (D'Costa, 2022; W. Huang et al., 2021; Manzo & Schiavo, 2022; Pires et al., 2022; Sendra et al., 2021). In some cases, MNP exposure has led

to increased mortality in sensitive invertebrate species (Doyle et al., 2022; Foley et al., 2018). The severity and nature of these effects can vary across species and life stages, depending on key particle characteristics such as polymer type, particle size, shape, surface chemistry, exposure duration, and route (Kögel et al., 2020).

Given the multifaceted responses to MNP exposure, a systematic data synthesis is crucial for integrating findings across taxa and exposure conditions, including key particle characteristics of MNPs, while identifying overarching trends and effect magnitudes that are not evident from individual studies. Existing syntheses have primarily focused on individual-level endpoints relevant to fitness or organismal performance, such as growth, reproduction, and mortality (Doyle et al., 2022; Foley et al., 2018; Moyo, 2022). However, emerging evidence indicates that the effects of MNP exposure span multiple levels of biological organization (Galloway et al., 2017) and vary considerably across marine invertebrate taxonomic groups (Bhavika et al., 2025; Porter et al., 2023). A more comprehensive analysis extending beyond fitness indicators to encompass key biological functions and systems is important to assess the generality of these patterns, identify taxonomic differences, and reveal underlying mechanisms driving specific sensitivities to MNP exposure. Equally important, such an approach can identify gaps in existing research, pinpointing which invertebrate phyla, particle characteristics, or exposure scenarios are understudied and thus warrant further investigation.

As such, this study aims to (i) systematically evaluate the effects of MNP exposure on key biological endpoints across diverse marine invertebrate taxa, as a function of key particle characteristics (size, shape, and concentration), and (ii) quantitatively assess interspecies sensitivity using species sensitivity distributions (SSDs) to derive specific hazard thresholds for marine invertebrate communities. By synthesizing evidence from rigorously screened studies that meet technical and risk assessment quality criteria, this study identifies patterns of MNP toxicity, highlights critical knowledge gaps, and outlines future research priorities to advance the biological effect and risk assessment of MNP exposure.

2.2 Materials and Methods

2.2.1 Data source

The data used in this study were obtained from the latest version of the Toxicity of Microplastic Explorer (ToMEx) for Aquatic Organisms database (version 2.0) (Hampton et al., 2025), accessed on September 17, 2025 through the following link (https://microplastics.sccwrp.org/). The ToMEx is community-curated database compiling published toxicity studies on MNP effects in aquatic organisms. The studies included in the database were scored by two independent reviewers using modified technical and risk assessment “red” criteria originally proposed by De Ruijter et al. (2020). These criteria can

then be used by users to filter studies according to specific analytical needs (Thornton Hampton et al., 2022).

2.2.2 Data structure

The ToMEx dataset is organized into six broad categories as outlined by Thornton Hampton et al. (2022). These categories include: (1) Data types, encompassing particle-only exposures, chemical co-exposure, chemical transfer, and leachate studies; (2) Test organisms, covering details such as genus, species, taxa, environment, life stage, and sex; (3) Experimental parameters, which include exposure duration, exposure media (e.g., water, sediment, or food), the use of solvents alongside water (e.g., ethanol), sample size, dose, and treatment groups; (4) Biological effects, detailing broad and specific endpoint categories, biological levels of organization, and effect metrics or concentrations (e.g., No Observed Effect Concentration (NOEC), Lowest Observed Effect Concentration (LOEC), as Highest Observed No Effect Concentration (HONEC), Effect Concentration (ECx), and Lethal Concentration (LCx); (5) Particle characteristics, such as polymer type, size, morphology, density, charge, functionalization, and weathering state; and (6) Experimental verification, which involves particle characterization, background contamination, and verification of exposure concentrations.

2.2.3 Data screening and quality criteria for the assessment of biological effects

The systematic review process used herein adhered to the Preferred Reporting Items for Systematic Reviews and Meta-Analyses (PRISMA) guidelines (Page et al., 2021). The detailed selection process, including records identified, screened, excluded, and retained, was conducted following a structured workflow for the identification of studies via databases and registers and is summarized in the PRISMA flowchart (Supplementary Figure A2.1).

A total of 12,798 records related to aquatic organisms were extracted from the ToMEx 2.0 database (Hampton et al., 2025). A series of inclusion and exclusion criteria were applied during the screening process to focus exclusively on marine invertebrates. Records related to freshwater species, accounting for 6,757 entries, were excluded. Additionally, 2,263 records pertaining to non-invertebrates, such as fish, bacteria, dinoflagellates, and Ciliophora, were also excluded. In addition, 105 records from *in vitro* assessments were also excluded. Only records explicitly addressing *in vivo* effects in marine invertebrate species were retained for further evaluation.

The quality assessment of the retained records was then conducted using the Technical "Red" Criteria, which applied only to particle-only exposure data of ToMEx 2.0 dataset (Thornton Hampton et al., 2022). These criteria ensured the inclusion of studies reporting essential experimental parameters (Supplementary Figures A2.2 – A2.4), while recognizing

that they are not intended as a replacement for the full set of criteria previously defined (De Ruijter et al., 2020). As reported in earlier evaluations (De Ruijter et al., 2020; Thornton Hampton et al., 2022), the full criteria set is rarely met; and strict application would exclude most studies. The technical subset specifically encompassed key details, including particle characteristics (e.g., size, shape, polymer type, and source of test particles), exposure conditions (e.g., test medium vehicle, administration route, and exposure duration), and study design elements (e.g., test species, sample size, control group, and data reporting of both mass and number nominal concentrations (Thornton Hampton et al., 2022). A total of 901 records were excluded due to quality concerns, such as failure to meet the criteria and inapplicable scoring, as well as records with effects marked as not available (NA). Ultimately, 2,772 records extracted from 72 published *in vivo* studies on marine invertebrates that met the Technical "Red" Criteria, were included in the final review for chronic toxicity data analysis.

To enable cross-study comparisons, *in vivo* effect concentrations were standardized to chronic NOECs by applying assessment factors described by Wigger et al. (2020). For each species–endpoint–MNP property combination, only one effect metric was included. Other reported descriptors, such as HONEC, LOEC, ECx, and LCx, were only considered when NOEC was not available, following a structured prioritization scheme with the corresponding conversion rules and assessment factors (Supplementary Figure A2.5). In such cases, the descriptor higher in the decision hierarchy (e.g., LOEC rather than EC_{50}) was selected and converted to NOEC to ensure conservative and consistent estimates. An additional assessment factor of 10, as provided in the ToMEx database, was applied to convert acute to chronic values, specifically in cases where only acute data were available. This approach is consistent with the test-duration criteria as described by Wigger et al. (2020), where exposures shorter than the organism-specific thresholds (e.g., Mollusca <28 days; Crustacea <21 days) are classified as acute. The resulting dataset comprised a harmonized matrix of chronic NOEC values expressed as particle number (particles/mL) and mass concentrations (µg/mL) and was visualized using Plotly (a Python graphing library) to illustrate distributions by particle characteristics (size, shape, concentration), with data points color-coded by taxonomic group within each broad endpoint category.

2.2.4 Additional screening and quality criteria for risk assessment

To translate observed biological effects into ecologically relevant risk estimates, studies were further screened for quality, retaining only those that met both predefined Technical and Risk Assessment "Red" Criteria to ensure ecological relevance. Only studies meeting both sets of criteria were retained and used for species sensitivity distribution (SSD) development. The criteria for risk assessment encompassed eight experimental components: specific endpoints linked to threats at the individual and population levels; food availability; exposure duration; inclusion of environmentally relevant concentration range; application of multiple doses (at least six, including a treatment control), effect thresholds; microplastic diversity; and particle aging and biofouling. Among these,

endpoint relevance and the use of multiple doses were defined as the “Red” Criteria, representing the minimum requirements for inclusion in risk assessment. Although verification of exposure concentrations in both the test media and organisms contributes substantially to the reliability of toxicity data, these components were not included in the predefined minimum criteria for risk assessment. Additionally, this analysis focused exclusively on particle-only exposure data and did not include studies involving chemical co-exposure, contaminant transfer, or leachate effects. Supplementary Figures A2.2 and A2.4 illustrate the proportion of studies scoring as adequate (blue), adequate with restrictions (grey), or inadequate (red) across these domains. This refined subset was then processed using the ToMEx module (Thornton Hampton et al., 2022), which uses the *ssdtools* R package, to derive species sensitivity distributions (SSDs). An SSD is a probabilistic statistical tool that fits a distribution to toxicity data across multiple species, enabling estimation of a low percentile, typically the lower 5% of the distribution (HC_5), which represents a protective threshold in ecological risk assessments (Besseling et al., 2019; Fox et al., 2021; Posthuma et al., 2019).

2.2.5 SSD construction

2.2.5.1 Effect metrics and alignment

SSDs were developed using the latest version of the ToMEx toxicity database within the ToMEx SSD module (https://sccwrp.shinyapps.io/aq_mp_tox_shiny/; accessed September 17, 2025. All effect metrics were standardized using alignment procedures and assessment factors integrated within the ToMEx SSD module. The SSDs were constructed using chronic NOEC values derived from fitness-related endpoints, expressed in both particle number (particles/mL) and mass (µg/mL), with conversions provided in the database. For SSD derivation, the NOEC or EC_{10} value was preferentially used when available. If neither was reported for a species, the LOEC was divided by 2 to estimate a NOEC as the representative effect metric (Jung et al., 2021). In cases where only acute data were available, an assessment factor (AF = 10), as mentioned above, was applied to convert values to chronic equivalents (Wigger et al., 2020).

Toxicity data were used from studies reporting effects on fitness-related endpoints for different species, including growth, reproduction, body condition, development, and mortality, in accordance with the data requirements outlined in the EU technical guidance for deriving environmental quality standards (European Commission, 2018). Although the dataset does not include all taxonomic groups recommended, such as fish, algae, or higher plants, it encompasses a broad taxonomic range of marine invertebrates, with representatives from major phyla such as Crustacea, Echinodermata, Mollusca, and Rotifera.

Separate SSDs were developed to account for the two different exposure mechanisms of MNP: food dilution via ingestion and tissue translocation. For food dilution, species-specific

ingestible particle size limits, based on mouth opening dimensions, were applied to define the upper threshold within 1–5000 µm. For tissue translocation, a fixed upper default size limit of 83 µm was used to represent particles most likely to cross biological barriers, following the approach applied by Mehinto et al. (2022). Prior to incorporation into SSD, data were aligned to a default size range (e.g. 1–5,000 µm) and rescaled to ecologically relevant metrics (ERMs), such as particle volume for food dilution, and surface area for tissue translocation (Mehinto et al., 2022). This alignment involved two key corrections: (1) bioaccessibility filtering based on (a) species-specific ingestion limits and (b) fixed threshold for translocation; and (2) polydispersity correction, which rescaled monodisperse microplastic effect concentrations to environmentally representative particle size distributions, defined by power-law slopes specific to each ERM (Kooi et al., 2021), as specified in Supplementary Table A2.1.

2.2.5.2 Model selection and hazard concentration derivation

Several statistical distributions were fitted to the data, including log-logistic, log-normal, log-Gumbel, Weibull, and Gamma (Yanagihara et al., 2024). Model selection was based on the Akaike Information Criterion corrected for sample size (AICc), with the best-fitting model identified as the one with the lowest AICc value (Schwarz et al., 2019). Following established best practices, distributions with delta values < 2 were averaged based on the relative AICc weights to account for model uncertainty, thereby reducing bias associated with single-model reliance. To enhance the robustness of the threshold estimate, the SSD curve was generated using bootstrapping with 10, 100, and 1000 iterations, and the hazard concentration affecting 5% of species (HC_5) was calculated as the primary risk metric.

2.3 Results and Discussion

2.3.1 Trends in experimental *in vivo* studies on the effects of MNPs in marine invertebrates

2.3.1.1 Species selection and methodological design

The key trends in research on the systemic effects of MNPs on marine invertebrates are shown in Figure 2.1 (Panels A–D). The data showed that Mollusca emerged as the most extensively studied taxon, accounting for 43.6%, with a predominant focus on bivalves such as *Crassostrea gigas* and *Mytilus galloprovincialis* (Supplementary Table A2.2). Crustacea was the second most represented group, comprising 29.5%, with notable contributions from species such as *Tigriopus japonicus* and *Diaphanosoma celebensis*. Echinoderms accounted for 9.0%, with species such as *Apostichopus jap*onicus and *Paracentrotus lividus* receiving particular attention. Both Annelida and Cnidaria represented 7.7% and 6.4%, with *Hediste diversicolor* and *Tubastrea aurea* being the most frequently studied species, respectively. Rotifera was the least studied group, contributing only 3.8%, primarily represented by *Branchionus sp*.

Regarding the life stages examined, adults were the most frequently studied, constituting 53.5% of the research focus, followed by early-stage organisms at 30.2%. Juveniles were comparatively underrepresented (9.3%), while 7.0% of the studies did not report the life stage explicitly. Water was the primary medium of exposure (79.5%), with sediment and food exposure receiving comparatively limited focus accounting for 9.0% and 7.7%, respectively. Other exposure pathways, including combined water-food, parental transfer, and parental-water exposure, were minimally studied, each accounting for 1.3% of cases. Among the *in vivo* studies assessed, 77.3% addressed acute effects and 22.7% addressed chronic effects.

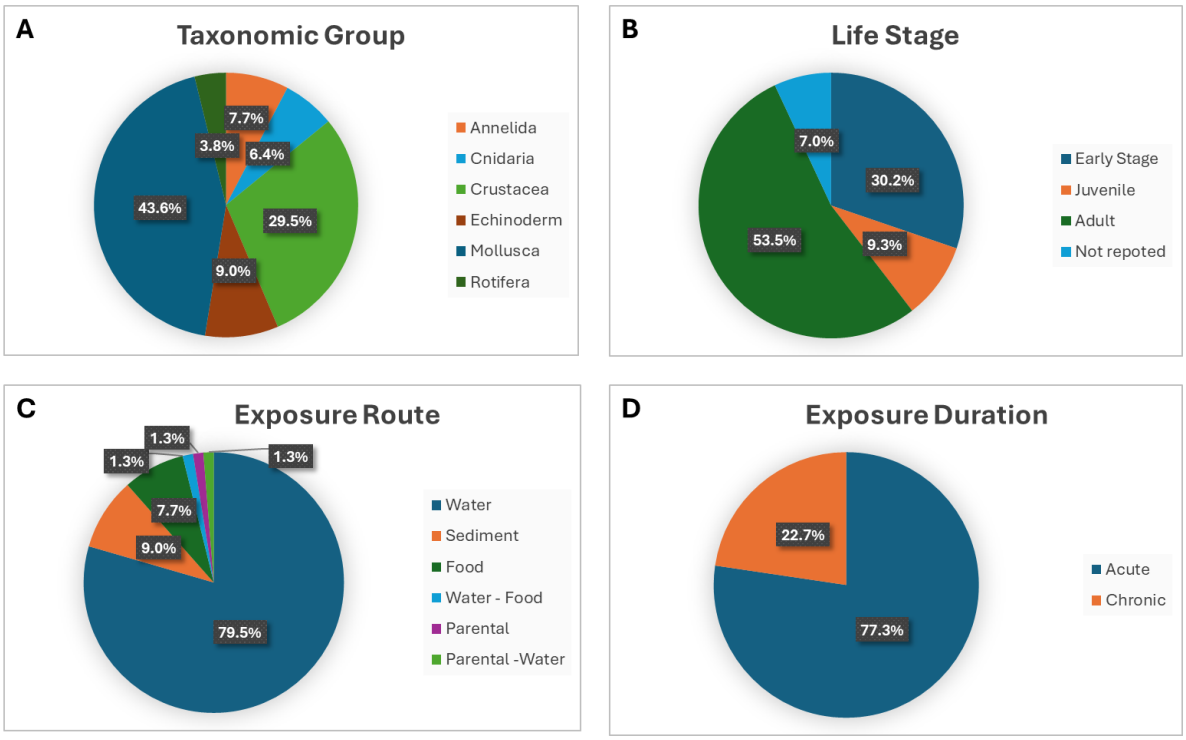

Figure 2.1. *Proportion of taxonomic groups (n = 78), life stage (n = 86), exposure route (n = 78), and exposure duration (n = 75) used in the in vivo toxicity assessment of micro- and nanoplastic particles in marine invertebrates. The pie charts have n > 72 as several studies used more than one test species, life stage, exposure route and/or experiment type.*

2.3.1.2 Particle characteristics of MNPs used in experimental studies

Figure 2.2 and Figure 2.3 (Panels A – D) illustrates the characteristics of the test particles used in *in vivo* toxicity assessments.

The majority of studies predominantly utilized pristine particles (87.8%), while weathered or biofouled particles accounted for only 12.2%. Spherical particles were the most frequently assessed shape (61.3%), followed by fragments (25.0%) and fibers (8.8%). Particle shape was not reported in 5.0% of cases. Regarding particle size, most assessments involved 1–100 µm range (51.1%), followed by 100 µm–1 mm (18.1%), 1–100 nm (16.0%)

and 100 nm–1 µm (11.7%). Larger particles (1–5 mm) were minimally represented (2.1%), while 1.1% of studies did not report particle size.

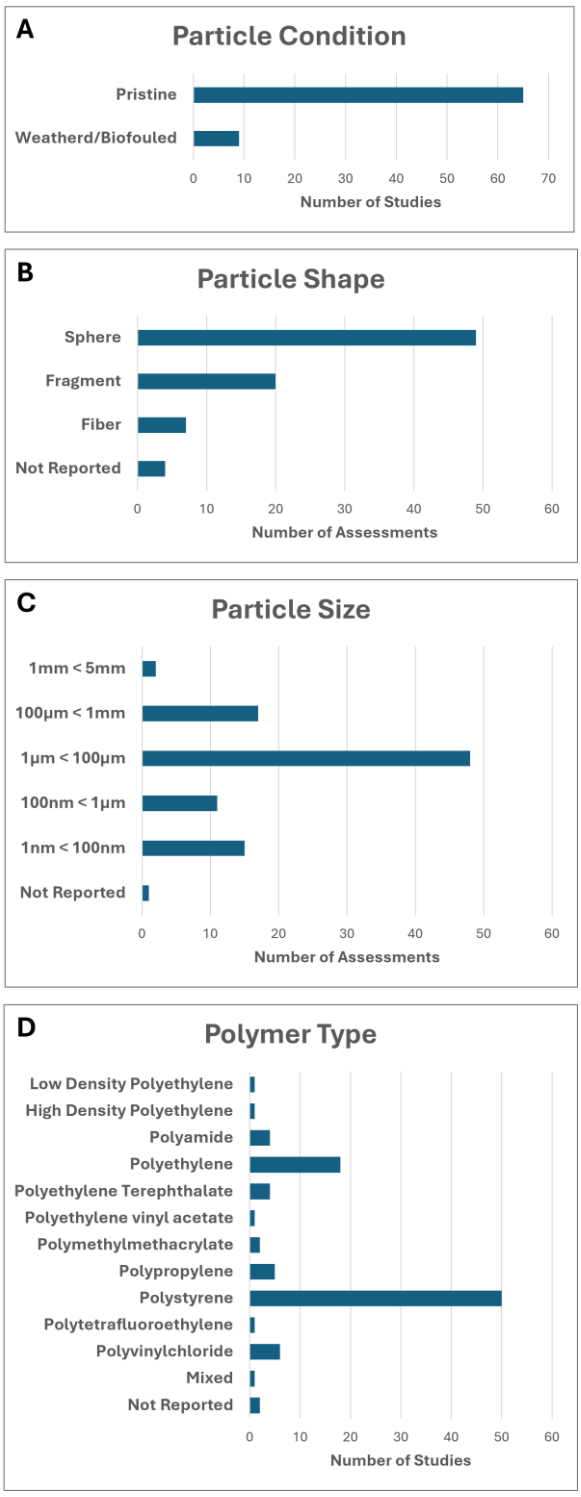

Figure 2.2. *Distribution of particle characteristics assessed in in vivo MNP toxicity studies (n = 72) on marine invertebrates: (A) particle condition, (B) particle shape, (C) particle size, and (D) polymer type. 'Not Reported' indicates the absence of explicitly reported particle properties in the reviewed studies.*

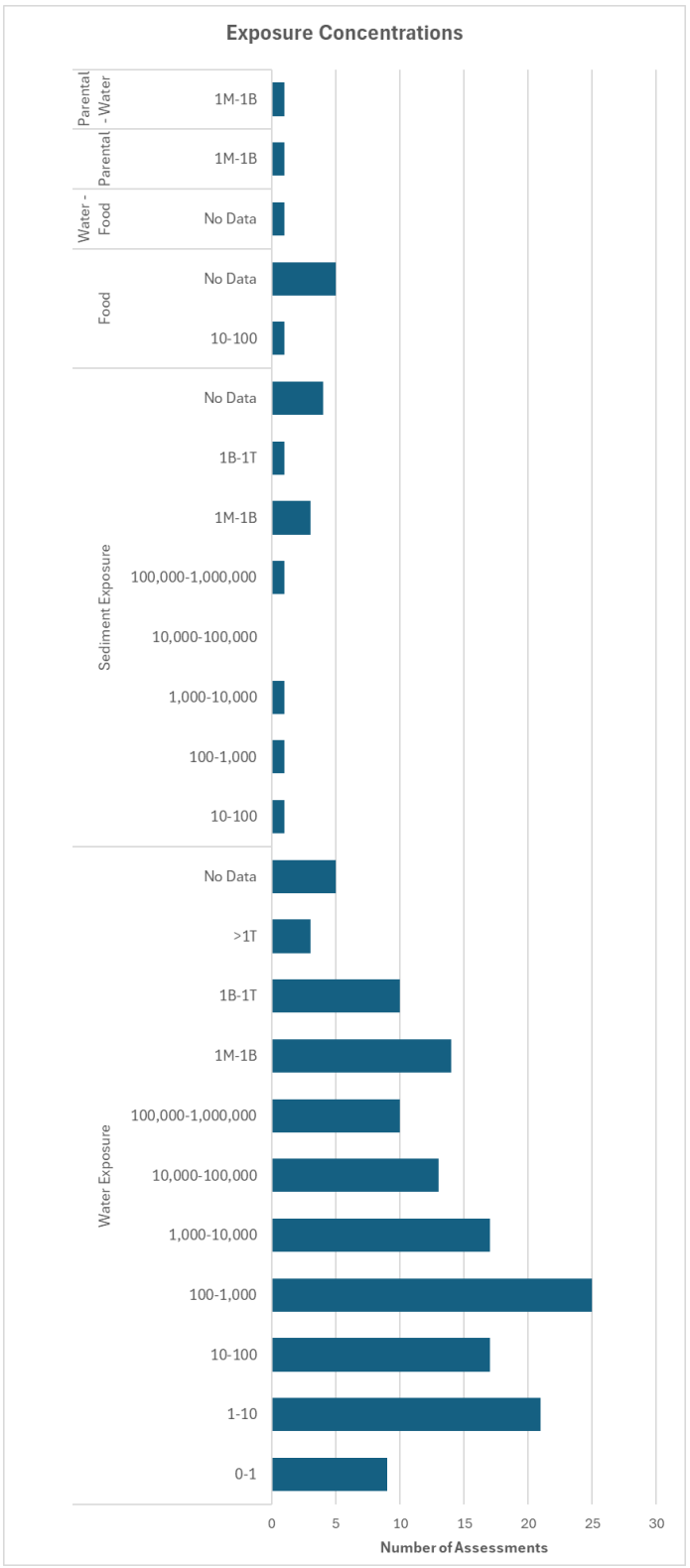

Figure 2.3. *Distribution of particle exposure concentrations assessed in in vivo MNP toxicity studies (n = 72) on marine invertebrates. Exposure routes include sediment (particles/kg dry weight) and water, along with other exposure pathways (particles/mL). 'No Data' indicates the absence of explicitly reported concentration values in the reviewed studies.*

Among the polymers assessed (Figure 2.2), polystyrene (PS) was the most frequently studied, comprising 52.1% of experiments, followed by polyethylene (PE) (18.8%). Other polymers, including polypropylene (PP), polyethylene terephthalate (PET), polyvinylchloride (PVC), polyamide (PA), polymethylmethacrylate (PMMA), low- and high-density polyethylene (LDPE, HDPE), polyethylene vinyl acetate (PEVA), and polytetrafluoroethylene (PTFE), were examined to a much lesser extent (1.0–6.3%). A small fraction of studies used mixed polymers (1.0%) or did not report polymer type (2.1%).

Waterborne exposures spanned a wide concentration range (Figure 2.3), most frequently at 100–1,000 particles/mL (17.4%), followed by 1–10 (14.6%), and 10–100 and 1,000–10,000 particles/mL (11.8% each). High concentrations were also tested, ranging from 10^4 to 10^{12} particles/mL, which together accounted for 32.6% of waterborne exposure assessments. A smaller fraction of studies employed even extreme concentrations above 10^{12} particles/mL (2.1%). However, approximately 3.5% of assessments did not specify concentration values.

Sediment exposure experiments primarily employed concentrations in the range of 10^6–10^{12} particles/kg dry weight, which together accounted for 41.7% of studies with limited exploration of low concentrations. A considerable proportion of studies (33.3%) did not explicitly report exposure concentrations.

Exposure experiments via contaminated food mainly lacked concentration data; when reported, values typically ranged from 10^1–10^2 particles/mL. In contrast, parental and parental–water exposures were conducted at higher concentrations (10^6–10^9 particles/mL).

2.3.1.3 Biological endpoints assessed in MNP exposure studies

The distribution of biological endpoints assessed across key biological functions and systems in MNP toxicity studies are shown in Figure 2.4.

As a fundamental aspect of organismal health, fitness indicators account for the largest proportion of endpoints assessed *in vivo* (41.2%), with mortality being the most frequently examined category, followed by body condition, growth, reproduction, and development.

Given its broad relevance across physiological processes, metabolism is the second most extensively studied category (28.8%). Of which, oxidative stress is the most frequently assessed, followed by detoxification, and general metabolism. Lipid metabolism, carbohydrate metabolism, lysosomal activity, and photosynthesis are among the less commonly examined endpoints. These assessments included whole-body homogenates, as well as specific tissues such as the intestine, gills, and soft tissue, depending on the endpoint.

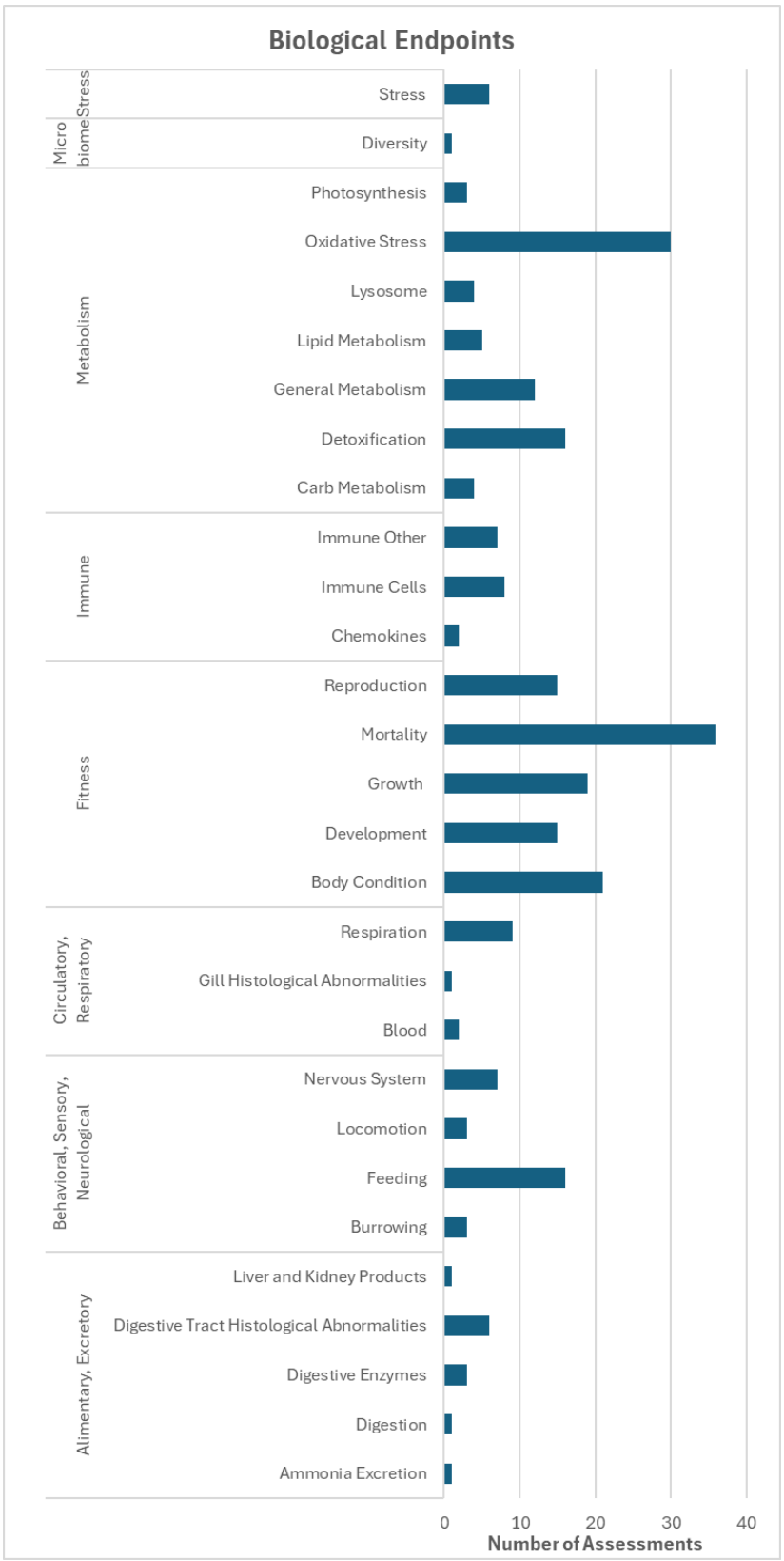

Figure 2.4. *Distribution of biological endpoints (n = 257) assessed in in vivo MNP toxicity studies (n = 72) on marine invertebrates.*

Endpoints related to behavioral, sensory, and neurological functions accounted for 11.3% of assessments. Feeding behavior, which reflects disruptions in algal consumption, capture, clearance, and ingestion rates, were the most frequently studied, followed by endpoints linked to the nervous system. Burrowing behavior in sediment-dwelling organisms and locomotion, measured through movement patterns, swim speed, and reaction time, parameters critical for predator avoidance, were less frequently assessed.

Despite the growing recognition of immunotoxicity in plastic research, immune system indicators remain underrepresented, accounting for only 6.6% of assessed endpoints. Among these, immune cell responses constitute the primary focus, followed by other immune indicators such as enzymatic activity and immune-related gene expression, and chemokine activity in various target cells and tissues.

Alimentary and excretory function endpoints accounted for 4.7% of cases. Digestive tract histology, providing direct evidence of tissue-level damage, was the most frequently assessed, followed by digestive enzyme activity. Less common measures included ammonia excretion, digestion efficiency, and liver and kidney products, providing insight into metabolic waste processing and organ function.

Circulatory and respiratory systems also accounted for 4.7% of assessments. Respiration was most frequently evaluated, followed by blood parameters, while gill histological abnormalities were least represented.

Stress-related endpoints accounted 2.3% of cases, representing key molecular and cellular markers linked to apoptosis, mitochondrial function, and stress-signaling pathways. Microbiome-related endpoints, particularly microbial diversity, were the least studied, accounting for only 0.4% of cases.

2.3.2 Distribution of chronic toxicity data

To provide insight into how particle characteristics influence toxicity across biological endpoints and taxa, chronic NOEC values were systematically analyzed as a function of key particle characteristics, including size (NPs: <1 µm and MPs: 1–5000 µm), shape (spherical and non-spherical), and depending on exposure route (water and sediment). Only studies that passed the technical red quality criteria and explicitly reported these particle characteristics, along with corresponding effect metrics, were included in the analysis. Given the limited availability of high-quality *in vitro* data, the analysis focused exclusively on *in vivo* studies. Moreover, due to the predominance of PS in the dataset and limited representation of other polymer types, trend analysis by polymer type was not feasible. Toxicity endpoints were consolidated into three main categories to facilitate interpretation: (1) mortality, representing lethal effects; (2) fitness-related endpoints, including reproduction, growth, development, and body condition; and (3) functional

endpoints, encompassing metabolism, immune system responses, alimentary and excretory functions, circulatory and respiratory functions, as well as behavioral, sensory, and neurological processes.

2.3.2.1 Mortality

A total of 58 chronic NOEC values derived from 15 studies for mortality were analyzed, revealing distinct toxicity patterns across particle characteristics (Figure 2.5, in particle number concentrations). The corresponding plot based on particle mass concentration is provided in Supplementary Figure A2.6.

Spherical MPs (1–5000 µm) in waterborne exposure exhibited the lowest median NOEC value of 1.0×10^{3} particles/mL, with observed values ranging from 30 to 1.4×10^{5} particles/mL. Non-spherical particles of the same size range displayed a higher median NOEC of 7.12×10^{4} particles/mL relative to their spherical counterparts, with a range of 397–7.96×10^{6} particles/mL. In contrast, spherical NPs (<1 µm) demonstrated the highest median NOEC among waterborne exposure, at 1.78×10^{8} particles/mL (range: 3.51×10^{5} to 4.47×10^{11} particles/mL, several orders of magnitude higher than the NOECs reported for both spherical and non-spherical MPs. Despite their hypothesized heightened toxicity due to increased surface area and biological membrane penetration potential, these results indicate that nanoscale particles require substantially higher exposure concentrations to elicit chronic mortality effects. This likely reflects differences in organismal uptake-clearance dynamics or particle aggregation behavior in the exposure medium, both of which can limit effective bioavailability (X. Li et al., 2024; W. Liu et al., 2024).

Similarly, non-spherical MPs in sediment exposure, where particle-organism interaction is highly influenced by environmental partitioning and selective ingestion behaviors, showed a median NOEC of 4.11×10^{8} particles/kg (range: 2.35×10^{3} to 5.90×10^{8} particles/kg).

2.3.2.2 Fitness-related endpoints

Chronic NOEC values (*n* = 112) derived from 22 studies for fitness-related endpoints, including reproduction, growth, development, and body condition, exhibited consistent patterns with those observed for mortality, with all particle categories showing values within the same order of magnitude (Figure 2.6). The corresponding plot based on particle mass concentration is provided in Supplementary Figure A2.7.

Spherical MPs had the lowest median NOEC at 1.0×10^{3} particles/mL (range: 10–5.58×10^{5}), aligning with mortality outcomes for the same particle characteristic. Similarly, non-spherical MPs had a higher median NOEC (7.12×10^{4} particles/mL), with a broader distribution, ranging from 11.2 to 7.96×10^{6} particles/mL. For spherical NPs in water exposure, the median NOEC was 1.06×10^{8} particles/mL (100 to 3.57×10^{10} particles/mL). This reinforces earlier observations that nanoscale particles require substantially higher concentrations to elicit chronic sublethal effects. Exposure to non-spherical MPs in

sediment yielded fitness-related NOEC values consistent with mortality findings, with a median of 4.11×10^{8} particles/kg (range: 2.35×10^{3}–5.90×10^{8} particles/kg).

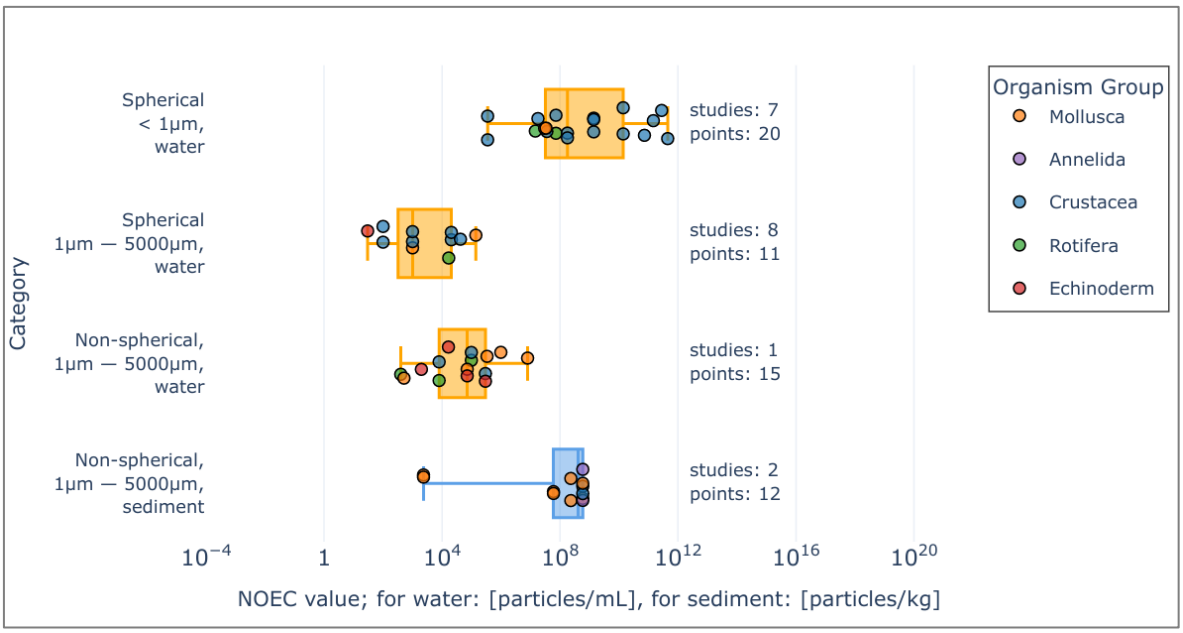

Figure 2.5. *Distribution of chronic NOEC values for mortality across particle characteristics. Data were categorized according to size class (<1 µm and 1–5000 µm), shape (spherical vs. non-spherical), and exposure route (water vs. sediment), with individual data points color-coded by organism group. An interactive version of this plot, developed using Plotly, is available at this link: jphara.github.io/EES2026PaperChronicToxicityData/Mortality.html. Users can open the link and hover over individual points to view detailed data, including species, specific endpoint, polymer type, original and converted effect metrics, and study reference.*

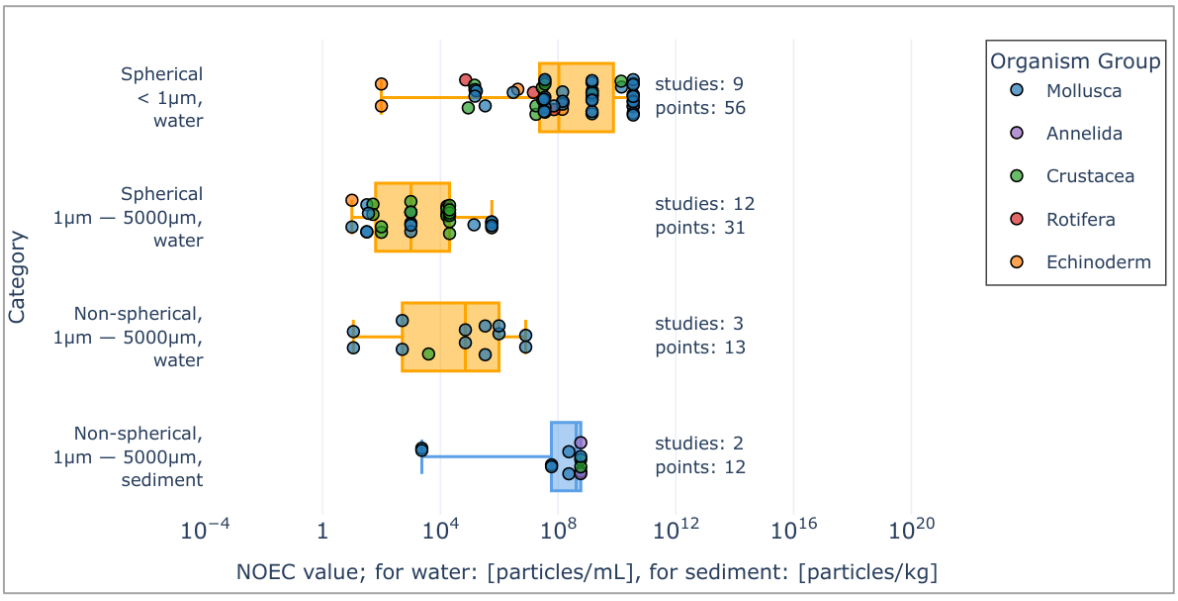

Figure 2.6. *Distribution of chronic NOEC values for fitness-related endpoints, including reproduction, growth, development, and body condition, across particle characteristics. Data were categorized according to size class (<1 µm and 1–5000 µm), shape (spherical vs. non-spherical), and exposure route (water vs. sediment),*

with individual data points color-coded by organism group. An interactive version of this plot, developed using Plotly, is available at this link: jphara.github.io/EES2026PaperChronicToxicityData/Fitness.html. Users can open the link and hover over individual points to view detailed data, including species, specific endpoint, polymer type, original and converted effect metrics, and study reference.

As reported by Jung et al. (2021), non-spherical MPs (≥20 µm) may pose greater lethal and sublethal toxicity to aquatic organisms on a number basis, as reflected by lower effect concentration values, compared to non-spherical MPs <20 µm and spherical MPs of both size categories. However, their analysis was limited to a binary size categorization of particles (>20 µm or <20 µm), whereas the present study incorporates a broader size range to better assess particle size and shape-dependent toxicity patterns.

2.3.2.3 Functional endpoints

Chronic NOEC values for functional endpoints (*n* = 167) derived from 13 studies were markedly lower than those for mortality and fitness-related endpoints, indicating higher sensitivity (Figure 2.7, see Supplementary Figure A2.8 for the corresponding mass-based plot).

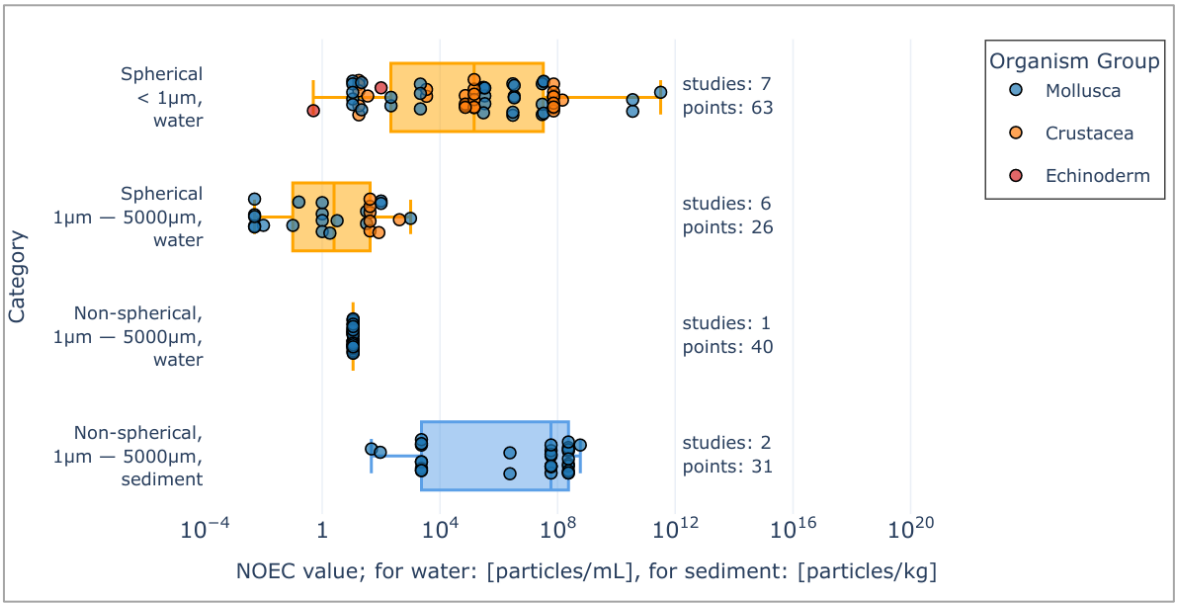

Figure 2.7. *Distribution of chronic NOEC values for functional endpoints across particle characteristics. Endpoints include metabolism, immune system responses, alimentary and excretory functions, circulatory and respiratory functions, as well as behavioral, sensory, and neurological processes. Data were categorized according to size class (<1 µm and 1–5000 µm), shape (spherical vs. non-spherical), and exposure route (water vs. sediment), with individual data points color-coded by organism group. An interactive version of this plot, developed using Plotly, is available at this link: jphara.github.io/EES2026PaperChronicToxicityData/FunctionalEndpoints.html. Users can open the link and hover over individual points to view detailed data, including species, specific endpoint, polymer type, original and converted effect metrics, and study reference.*

Spherical MPs exhibited the lowest median NOEC of all categories at 2.51 particle/mL, with concentrations ranging from 0.005 to 1.0×10^{3} particles/mL. This is approximately three orders of magnitude lower than corresponding values for mortality and fitness-related

endpoints (1.0×10^{3} particles/mL), suggesting that functional processes may be disrupted at much lower exposure levels. In contrast, non-spherical MPs exhibited a median NOEC of 11.2 particles/mL, approximately over three orders of magnitude lower than the corresponding mortality and fitness-related NOECs (7.12×10^{4} particles/mL) for the same particle category.

For spherical NPs in water, the median NOEC was 1.46×10^{5} particles/mL, also relatively lower than mortality (1.78×10^{8} particles/mL) and fitness-related endpoints (1.06×10^{8} particles/mL) thresholds, with a broad concentration range of 0.5 to 3.20×10^{11} particles/mL. Sediment exposure to non-spherical MPs resulted in a median of 6.00×10^{7} particles/kg (range: 47–5.90×10^{8}), relatively lower than mortality and fitness-related findings (4.11×10^{8} particles/kg).

The observed variability, particularly under water exposure conditions, further reflects the differential sensitivity across functional mechanisms to MNP toxicity, highlighting the systemic- and particle-specific nature of sub-lethal responses. To illustrate this in detail, separate graphs for each functional category are provided in the Supplementary Figures A2.9 – A2.13.

Among the assessed functional endpoints, immune processes, metabolism and behavioral, sensory and neurological parameters emerged as particularly sensitive endpoints. For spherical NPs (<1 µm), the most sensitive endpoints were behavioral, sensory and neurological and metabolic responses, with median NOEC values of 1771 particles/mL and 1.46×10^{5} particles/mL, respectively. In contrast, for spherical MPs (1–5000 µm), immune (0.005 particles/mL) and metabolic responses (1.82 particles/mL) represented the most sensitive endpoints. All assessed functional endpoints for non-spherical particles shared an identical median NOEC of 11.2 particles/mL. These exceptionally low thresholds suggest that fundamental physiological processes such as energy regulation, oxidative balance, detoxification, neurological and immune mechanisms may be among the earliest disrupted by chronic plastic particle exposure.

However, the interpretation of these trends is limited by the availability of data across particle types, endpoint categories, and taxonomic groups. While preliminary findings indicate endpoint- and particle-specific sensitivity, the uneven representation of particle morphologies, particularly non-spherical MNPs, and the relatively small number of studies across both water and sediment exposure routes limit statistical confidence and the robustness of conclusions. As such, these results should be interpreted as initial indications of potentially sensitive biological pathways and toxicity thresholds, rather than as definitive conclusions.

2.3.3 Species sensitivity distributions (SSD)

To evaluate the ecological risks associated with plastic particle exposure in marine invertebrates, SSDs were constructed using chronic effect concentrations derived from fitness-related endpoints across multiple taxa. The SSD curve provides a probabilistic estimate of the percentage of species affected at increasing MNP concentrations, expressed in both particle number (particles/mL) and mass (µg/mL). Two ERMs were considered in constructing the SSDs (Mehinto et al., 2022), each reflecting a different exposure mechanism of MNP toxicity: food dilution via ingestion (volume-based ERM, Figure 2.8) and tissue translocation (surface area-based ERM, Figure 2.9). The dataset used to construct the SSD (Supplementary Table A2.3 – Table A2.6), along with the modeled species sensitivity distributions and associated uncertainty estimates, are provided in Supplementary Table A2.7 – Table A2.10.

Among the candidate distributions, the log-normal and log-logistic models provided the best fits for SSDs for food dilution and translocation-based MNP toxicity mechanism, respectively, yielding the lowest AICc (Supplementary Figure A2.14 – Figure A2.17). In contrast, Gamma models exhibited higher AICc and delta (Δ) values >2, indicating relatively poorer fits (Schwarz et al., 2019). Based on model selection criteria, the top three distributions (log-logistic, log-normal, log-Gumbel) were included in a model-averaging approach (Δ < 2), weighted according to AIC-derived weights, to account for model uncertainty. Graphical inspection of the fitted curves further supported the suitability of these models, with the top-ranked distributions closely following the empirical cumulative data, as shown in Supplementary Figure A2.14 – Figure A2.17.

For SSDs constructed using volume-based ERM associated with food dilution as toxicity mechanism (Figure 2.8), the hazardous concentration affecting 5% of species (HC_5) was estimated at 6.74×10^{-4} particles/mL (equivalent to 0.674 particles/L) and 0.111 µg/mL (111 µg/L) for the particle number- and mass-based SSDs, respectively. In contrast, for the surface area–based ERM particularly relevant to translocation of particles ranging from 1–83 µm (Figure 2.9), HC_5 values were higher, at 1.37×10^{0} particles/mL (1,370 particles/L) and 2.25×10^{2} µg/mL (225,000 µg/L), respectively. These findings align with the tiered toxicity threshold framework proposed by Mehinto et al. (2022)**,** which defines concentration ranges for microplastic impacts based on two relevant toxicity mechanisms across four management levels, with markedly lower thresholds for food dilution compared to tissue translocation.

Across SSDs derived for both food dilution (Figure 2.8) and tissue translocation (Figure 2.9) mechanisms, *Psedechinus huttoni* (Echinoderm) was identified as the most sensitive species, occupying the lower tail of the distribution. In contrast, *Paracentrotus lividus* (Echinoderm) were the least sensitive species for both food dilution and translocation-based thresholds, showing adverse effects only at relatively high particle concentrations.

Taxonomic grouping revealed that crustaceans, echinoderms, and mollusks were distributed across a moderate sensitivity range, with some intra-group variability.

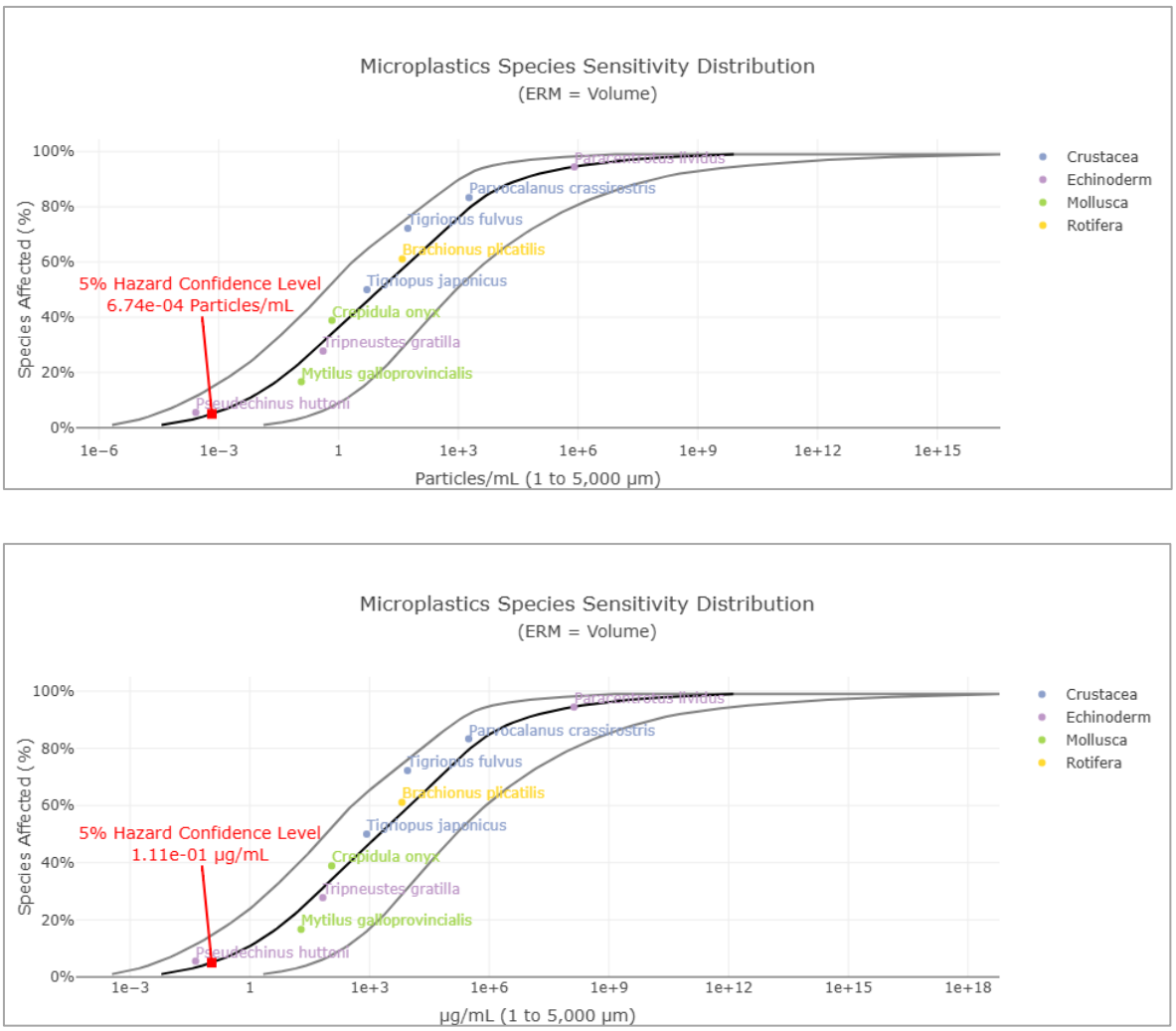

Figure 2.8. *Species sensitivity distributions (SSDs; black line) based on chronic NOECs with 95% confidence intervals (CI, gray line), derived for food dilution via ingestion as a mechanism of toxicity, particularly relevant for ingestible particles within 1–5000 µm size range. All effect concentrations, expressed in both particle number (upper panel, particles/mL) and mass (lower panel, µg/mL), were aligned to a common volume-based ecologically relevant metric (ERM) for food dilution, as applied by Mehinto et al. (2022). Endpoints included fitness-related parameters, including growth, reproduction, body condition, development, and mortality. SSD curves were fitted using multiple distributions (log-logistic, log-normal, log-Gumbel), with model averaging applied based on AICc values. Taxa are color-coded by phylum. Red arrows indicate the hazardous concentration affecting 5% of species (HC_5).*

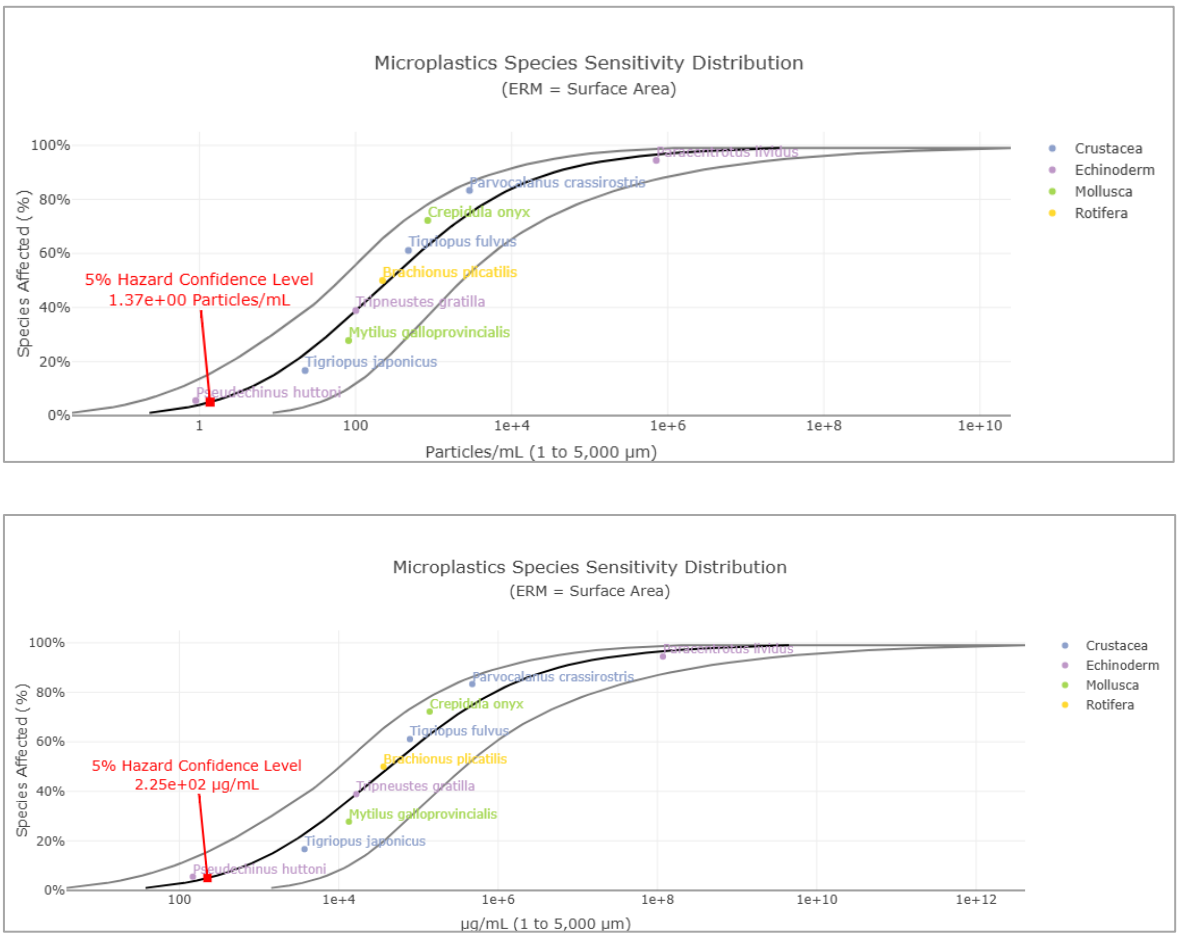

Figure 2.9. *Species sensitivity distributions (SSDs; black line) based on chronic NOECs with 95% confidence intervals (CI, gray line), derived for tissue translocation as a mechanism of toxicity, particularly relevant for particles of 1–83 µm size range. All effect concentrations, expressed in both particle number (upper panel, particles/mL) and mass (lower panel, µg/mL), were aligned to a common surface area-based ecologically relevant metric (ERM) for translocation mechanism, as applied by Mehinto et al. (2022). Endpoints included fitness-related parameters, including growth, reproduction, body condition, development, and mortality. SSD curves were fitted using multiple distributions (log-logistic, log-normal, log-Gumbel), with model averaging applied based on AICc values. Taxa are color-coded by phylum. Red arrows indicate the hazardous concentration affecting 5% of species (HC_5).*

2.3.4 Derivation of preliminary safe standard (PSS)

Using the SSD-derived HC_5, preliminary safe standard (PSS) values were calculated by applying an assessment factor (AF) of 5 (Table 2.1), consistent with the approach applied by Besseling et al. (2019) and Jung et al. (2021). For the volume-based ERM for food dilution, the resulting PSS values in particle number and mass concentrations of 0.135 particles/L and 22.2 µg/L, respectively. In contrast, the surface area-based ERM relevant for translocation yielded substantially higher PSS values of 274 particles/L and 45,000 µg/L for particle number and mass concentrations, respectively.

Table 2.1. *Preliminary safe standard (PSS) values for microplastic particle exposure in marine invertebrates, derived from HC_5 values of volume and surface area-based SSDs constructed using both particle number and mass-based concentration metrics. HC_5: hazardous concentration for 5% of the species, AF: assessment factor. Bootstrap iteration counts ≥10 yield convergent mean and median estimates, producing identical HC_5 values. The table presents HC_5 values together with their associated standard errors and confidence intervals generated using multiple bootstrap iteration settings (10, 100, and 1,000).*

Mechanism of Toxicity	Concentration Metric	HC_5	Iterations	Standard Error	Lower 95% Confidence Limit	Upper 95% Confidence Limit	AF	PSS
Food dilution (Volume-based ERM, 1–5000 µm)	Particle Number	6.74×10^{-4} particles/mL or 0.674 particles/L	10 iterations	9.97×10^{-2} particles/mL	2.76×10^{-5} particles/mL	2.55×10^{-1} particles/mL	5	0.135 particles/L
			100 iterations	6.42×10^{-1} particles/mL	1.81×10^{-5} particles/mL	4.96×10^{-1} particles/mL		
			1000 iterations	8.69×10^{-1} particles/mL	1.42×10^{-5} particles/mL	2.47×10^{-1} particles/mL		
	Particle Mass	1.11×10^{-1} µg/mL Or 111 µg/L	10 iterations	1.64×10^{1} µg/mL	4.54×10^{-3} µg/mL	4.20×10^{1} µg/mL	5	22.2 µg/L
			100 iterations	1.09×10^{2} µg/mL	2.61×10^{-3} µg/mL	7.84×10^{1} µg/mL		
			1000 iterations	1.43×10^{2} µg/mL	2.34×10^{-3} µg/mL	4.06×10^{1} µg/mL		
Translocation (Surface area-based ERM, 1–83 µm)	Particle Number	1.37×10^{0} particles/mL Or 1,370 particles/L	10 iterations	1.29×10^{1} particles/mL	1.55×10^{-1} particles/mL	3.54×10^{1} particles/mL	5	274 particles/L
			100 iterations	2.51×10^{1} particles/mL	1.69×10^{-1} particles/mL	5.12×10^{1} particles/mL		
			1000 iterations	1.90×10^{1} particles/mL	1.35×10^{-1} particles/mL	3.89×10^{1} particles/mL		
	Particle Mass	2.25×10^{2} µg/mL or 225,000 µg/L	10 iterations	2.13×10^{3} µg/mL	2.54×10^{1} µg/mL	5.81×10^{3} µg/mL	5	45,000 µg/L
			100 iterations	4.12×10^{3} µg/mL	2.78×10^{1} µg/mL	8.40×10^{3} µg/mL		
			1000 iterations	3.00×10^{3} µg/mL	2.15×10^{1} µg/mL	6.56×10^{3} µg/mL		

The marine invertebrate–specific thresholds derived in this study align closely with thresholds developed for all marine organisms (Hampton et al., 2025), which are calculated using organism- and population-level toxicity data from ToMEx 2.0 for both food dilution and tissue translocation mechanisms. Specifically, the derived values fall within the same order of magnitude as the management planning (Threshold 3) and source control (Threshold 4) benchmarks. This concordance suggests that thresholds based solely on marine invertebrates are sufficiently conservative, thereby supporting management and source control actions at the ecosystem level.

In comparison with other previously reported thresholds, Jung et al. (2021) reported an HC_5 of 59.8 particles/L and a PSS of 12.0 particles/L, derived from an SSD based on microplastic in the 20–300 µm size range. Additionally, Besseling et al. (2019) reported mass-based HC_5 and PSS values derived from SSDs constructed using a combination of taxa spanning both freshwater and marine ecosystems. For MPs, the reported HC_5 and PSS were 0.002 µg/L and 0.0004 µg/L, respectively, while for NPs, the corresponding values were 5.4 µg/L and 1.1 µg/L. Similarly, Thornton Hampton et al. (2022) indicated an HC_5 of 2.55×10^{-3} particles/mL (2.55 particles/L) and a PSS equivalent of 5.1×10^{-4} particles/mL (0.51 particles/L) for particles of the same size range, using a volume-based ERM consistent with the present study.

These discrepancies among reported SSD-derived thresholds likely reflect multiple interacting factors. In particular, trait-based differences among species, such as feeding strategy, trophic position, or life-history characteristics, can strongly influence sensitivity patterns, with certain trait groups more vulnerable to specific types of stressors than others (Belanger et al., 2017). Variation in particle characteristics, particularly size and shape, can markedly shift sensitivity distributions, underscoring the importance of incorporating these characteristics into SSD estimations for plastic particle exposure (Iwasaki et al., 2023). The application of ERM alignment and rescaling approaches is also critical in the derivation of hazard thresholds (Koelmans et al., 2020; Kooi et al., 2021), as they enable direct comparability across mono- and polydisperse datasets and correct for bioavailability, thereby resolving inconsistencies in toxicity data (Mehinto et al., 2022).

When compared to concentrations recorded in the marine environment, significant spatial discrepancies are evident (Supplementary Table A2.11). For instance, in the North Sea, reported concentrations in surface waters ranged from 0.1 to 254.4 particles/m³ (equivalent to 0.0001–0.2544 particles/L) for particles smaller than 100 µm (Lorenz et al., 2019) and 23 to 9,700 particles/m³ (0.023–9.7 particles/L) for particles ranging from 11 to 500 µm (Roscher et al., 2021). In highly urbanized and industrialized estuarine systems, considerably higher concentrations have been observed, ranging from 500 to 10,200 particles/m³ (equivalent to 0.5–10.2 particles/L) in the Yangtze Estuary, China (S. Zhao et al., 2014). Although these environmental concentrations remain well below the surface area-based PSS of 274 particles/L, in some cases they exceed the volume-based PSS

threshold of 0.135 particles/L. This disparity indicates that, depending on the toxicological mechanism (e.g., ingestion versus translocation), current environmental MNP burdens may already pose ecological risks to marine invertebrate communities.

Also, it is important to note that the SSDs developed in the present study are based exclusively on marine invertebrates, unlike those by Besseling et al. (2019) and Jung et al. (2021), which included primary producers (e.g., algae) and vertebrates (e.g., fish). While this narrows the taxonomic scope and may under- or overestimate sensitivity at other trophic levels, it is consistent with established practices in chemical risk assessment, such as those applied in pesticide regulation (D. Moore et al., 2021). Accordingly, the derived PSS values should be considered provisional, reflecting thresholds protective for marine invertebrate communities but not necessarily the entire marine ecosystem. Although these values do not currently meet the data requirements for regulatory use, they provide a valuable scientific basis for identifying sensitive taxa and community-specific toxicity thresholds. Further refinement is recommended as more robust ecotoxicological datasets become available.

2.4 Conclusions, Limitations and Future Directions

This study provides a systematic cross-taxa evaluation of MNP toxicity in marine invertebrates by integrating available toxicity data from the ToMEx database. Our findings demonstrate that functional processes, particularly immune, metabolic, behavioral, sensory, and neurological responses, are highly sensitive to MNP exposure, with chronic NOEC values several orders of magnitude lower than those for mortality or fitness. The construction of SSDs, accounting for distinct exposure mechanism of MNP toxicity, enabled the derivation of preliminary safe standards from HC_5 values. These findings highlight both the vulnerability of specific taxa and the utility of SSD-based approaches for establishing provisional thresholds to protect marine invertebrate communities.

Despite these insights, several constraints limit the broader applicability of the current findings. The dataset was dominated by pristine polystyrene particles, while other polymer types were underrepresented, preventing meaningful cross-polymer comparisons. The majority of studies focused on acute exposures, necessitating extrapolation to chronic scenarios and thereby limiting the ability to fully assess long-term biological risks. Furthermore, experimental conditions often lacked environmental realism, as exposures typically used pristine, spherical particles at concentrations not reflective of natural systems, with minimal attention to particle weathering, shape variability, or environmentally relevant concentrations.

To advance the ecological relevance and regulatory utility of MNP toxicity research, several priorities must be addressed. Chronic exposure studies that capture subtle yet ecologically meaningful disruptions to organismal function and population dynamics are urgently

needed. Experimental designs should incorporate artificially or environmentally aged particles with representative size distributions, morphologies, polymer types, and concentrations to better approximate field conditions. In parallel, mechanistic investigations, particularly into immunological, metabolic, and neurological processes, will provide critical insights into pathways of toxicity and their ecological consequences. Equally important is the adoption of harmonized methodological frameworks and rigorous QA/QC protocols to enhance reproducibility, enable robust analyses, and support integration of findings into environmental risk assessment. Establishing such standards will be critical for developing science-based, effective thresholds to safeguard marine ecosystems from MNP pollution.

2.5 Acknowledgements

We thank the coordinators of the ToMEx 2.0 database for providing access to the curated database and associated SSD tools. We also thank Dr. András Retzler (D2Lab, Ghent University) for assistance with coding and developing interactive visualizations using Plotly and Dr. Essie Rodgers (Murdoch University) for guidance in defining the screening criteria for the systematic review.

Chapter 3

Cellular and Tissue-Level Responses of Mussels (*Mytilus edulis*) to Aged Polyethylene Terephthalate (PET) Micro-and Nanoplastic Particles

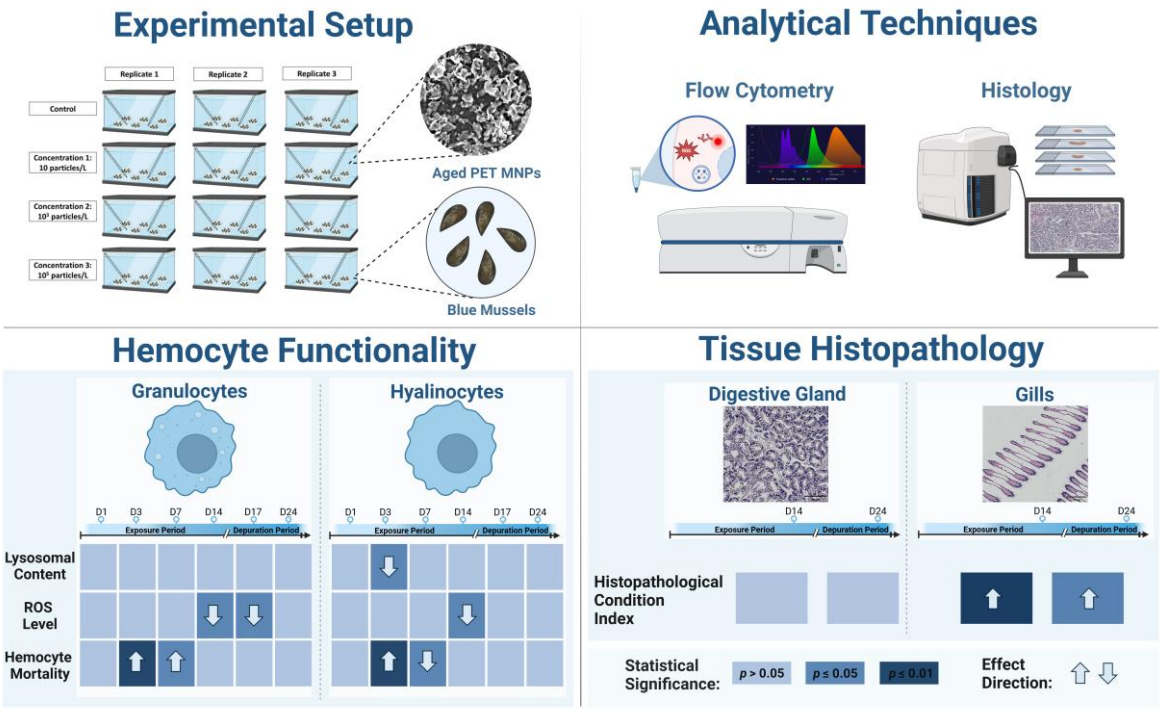

Published as:

Hara, J., Oraño, G. B., Vercauteren, M., Mubiana, K. V., Janssen, C. R., Blust, R., Asselman, J. & Town, R. M. (2025). Cellular and tissue-level responses of mussels (*Mytilus edulis*) to aged polyethylene terephthalate (PET) micro-and nanoplastic particles. *Aquatic Toxicology*, 283, 107369. https://doi.org/10.1016/j.aquatox.2025.107369.

Abstract

Micro- and nanoplastic particles (MNPs) are pollutants of global concern due to their persistence, ubiquity, and associated risks. Laboratory studies, however, have predominantly focused on pristine MNPs, which do not adequately reflect the characteristics of environmental plastic debris. To address this gap, this study investigated the cellular and tissue-level responses of mussels (*Mytilus edulis*) to aged polyethylene terephthalate (PET) MNPs (diameter 600 nm to 3.1 µm) at three environmentally relevant concentrations: 10, 10^3, and 10^5 particles/L. The particles' physicochemical characteristics and stability in exposure media were analyzed using a combination of advanced analytical techniques. The biological responses were analyzed across multiple effect endpoints during both the exposure (days 1, 3, 7, and 14) and the subsequent recovery periods (3 and 10 days post-exposure), via flow cytometry and histopathology. The results revealed the sensitivity of hemocyte subpopulations, including granulocytes and hyalinocytes, to aged PET MNPs. Concentration- and time-dependent changes in lysosomal stability, oxidative activity, and hemocyte mortality were observed, demonstrating both immediate cellular perturbations and recovery potential to alleviate particle-induced effects. Histopathological analysis of key tissues exhibited significant alterations, particularly in the gill, suggesting potential impairment of essential physiological functions. No mussel mortality or significant changes in growth metrics were observed under the tested experimental conditions. These findings underscore the systemic impacts across multiple tissues of aged MNP exposure and highlight the importance of adopting integrative, environmentally realistic approaches to assess the biological consequences in future research.

Keywords: Aged micro- and nanoplastics, Polyethylene terephthalate, Environmentally relevant concentrations, Histopathology, Immunotoxicity, Mussels

3.1 Introduction

The escalating production and improper disposal of plastic waste have led to the pervasive presence of micro- and nanoplastic particles (MNPs) in aquatic ecosystems. These plastic particles, with defined sizes smaller than 5 mm and 1000 nm, respectively, are now recognized as pollutants of global concern due to their persistence, ubiquity, and associated risks (Khanna et al., 2024). MNPs are introduced into the environment either through direct release or generated via the fragmentation of larger plastic debris. Their size, high surface area-to-volume ratio, and capacity to adsorb harmful chemicals can amplify their potential toxicity, underscoring the urgent need to elucidate the mechanisms underlying the biological effects (da Costa et al., 2019).

Polyethylene terephthalate (PET) is among the most prevalent polymers in marine environments, commonly found in water columns and sediment layers due to its widespread use in consumer products (Ashrafy et al., 2023). Once released into the environment, plastic particles undergo aging processes, including photodegradation, biodegradation, thermal oxidation, and mechanical abrasion. While PET is highly resistant to photodegradation, with photoaging degradation times exceeding 500 years, it can undergo surface modifications through other processes such as hydrolysis and microbial activity (Q. Lu et al., 2023). For instance, alkali-resistant bacteria have been shown to degrade PET microplastics, causing 11.04% weight loss and visible etching and fractures on the PET fiber surface within five days (X. Li et al., 2023). These processes not only modify the surface properties of particles but also influence their environmental behavior, including their tendency to aggregate, position within the water column, and accumulation in sedimentary environments (Galloway et al., 2017). Such changes increase the risks posed to benthic habitats and organisms, particularly filter feeders, which are directly exposed to these particles in both the water column and sediment layers.

Benthic organisms, such as mussels, are particularly susceptible to ingesting plastic particles (Canesi et al., 2012). Mussels are widely used as sentinel organisms for monitoring marine pollution due to their wide geographic distribution, ecological significance, and feeding behavior (Beyer et al., 2017). As filter feeders, mussels process large volumes of water, making them prone to ingesting suspended MNPs, which can subsequently accumulate in their tissues and translocate to the circulatory system (Canesi et al., 2012; F. Ribeiro et al., 2019). These traits, combined with their ease of cultivation for aquaculture, and their established role as bioindicators (Beyer et al., 2017), mark their significance as both a model organism and proxy for assessing the risks associated with MNP exposure.

Previous studies have extensively examined the effects of MNPs, documenting diverse biological responses, including oxidative stress, immune dysfunction, histopathological alterations, and other physiological changes (Barría et al., 2025). A meta-analysis focused on bivalves identified oxidative stress as a key mechanism of MNP toxicity, characterized

by a time-dependent induction that disrupts redox balance and leads to cellular damage (Z. Li et al., 2022). However, the environmental relevance of such studies remains limited, as they predominantly focus on pristine, commercially available particles, while aged plastics, which exhibit altered physicochemical properties, have received comparatively less attention (Cunningham et al., 2023). Accurately simulating environmentally realistic exposure scenarios requires test particles that mirror those found in natural environments, accounting for particle aging, polymer type, shape, concentration, and size ranges (Revel et al., 2021). Despite advances in understanding the toxicity of pristine MNPs, most laboratory studies employ concentrations orders of magnitude higher than those found in natural environments (Lenz et al., 2016). Additionally, PET, one of the most commonly detected MNP polymers in mussels, remains underrepresented in toxicity studies (Barría et al., 2025; Fraissinet et al., 2024). Particularly, particles in the nano-sized range pose heightened risks due to their ability to bioaccumulate, cross biological barriers, penetrate cells, and influence cellular and tissue systems (Browne et al., 2008; Fernández & Albentosa, 2019b, 2019a).

Assessing immunological and histopathological endpoints can provide critical insights into the cellular and tissue-level responses induced by aged particles. In mussels, hemocyte-mediated immune responses, including lysosomal stability, oxidative activity, and cellular mortality, serve as key indicators of particle-induced toxicity. Disruptions to these immune functions can compromise homeostasis and trigger systemic stress responses (Canesi & Procházková, 2014). Given the persistence and aging processes of MNPs in natural environments, their capacity to induce immune dysfunction may be exacerbated by co-occurring stressors, further compromising physiological and defense performance in mussels (X. Huang et al., 2022; Mkuye et al., 2022). Similarly, histopathological alterations in key tissues, such as the gills and digestive gland, offer valuable indicators of morphological and structural changes associated with physiological dysfunction. In the digestive gland, endpoints such as lipofuscin aggregation, hemocyte infiltration, atrophy, and necrosis, are indicative of inflammatory response and regressive and progressive changes in tissue structure (Bouallegui et al., 2018; Carella et al., 2015). Additionally, histopathological changes in the gills, particularly lamellar fusion, and the enlargement of the central vessel, can significantly impair essential functions, including filtration, respiration, osmoregulation, and particle transport (Leis et al., 2024). Integrating these multiple histopathological alterations into condition indices provides a robust framework for linking sensitivity to particle exposure effects with tissue integrity and organismal health (Costa et al., 2013). Collectively, these endpoints can reveal the systemic impacts of MNP exposure and offer an integrative approach to understanding their broader biological consequences.

In this study, we tested the hypothesis that aged PET MNPs, exhibiting environmentally relevant particle characteristics, elicit pronounced and potentially persistent adverse effects at both cellular and tissue levels. Specifically, we aimed to mechanistically evaluate

the immunological and histopathological responses of blue mussels (*Mytilus edulis*) following *in vivo* exposure to aged PET MNPs under environmentally relevant conditions. A suite of cellular and tissue-level endpoints was assessed at multiple timepoints during both the exposure (days 1, 3, 7, and 14) and recovery (3 and 10 days post-exposure) periods to capture the dynamics of biological responses.

3.2 Materials and Methods

3.2.1 Characterization of the aged PET micro- and nanoplastic particles

The stock suspension of chemically aged PET MNPs was prepared and provided by the European Commission Joint Research Centre (JRC in Geel, Belgium). The aging process involved mechanical cryomilling and chemical aging through treatment with potassium hydroxide solution (KOH) combined with sonication (Seghers et al., 2025). The particles were washed six times with ultrapure water to remove residual KOH and any potential by-products generated during the chemical treatment. This process induced the formation of polar COO^- groups, resulting in enhanced particle hydrophilicity (Seghers et al., 2025) and surface modifications comparable to those of naturally aged particles (von der Esch et al., 2020). However, it should be noted that this artificial aging approach only approximates the complexity of environmental aging processes. Aged PET particles were suspended in Milli-Q water without surfactant. The particles had an average dimension, *D*, of 1.9 µm, with size distribution values of D_{10} = 600 nm, D_{50} = 1.4 µm, and D_{90} = 3.1 µm (Supplementary Figure A3.1, Panel A), as analyzed using the Single Particle Extinction and Scattering (SPES) technique (ClassizerONE S1.4.34, EOS; JRC in Ispra, Italy). D_{10}, D_{50}, and D_{90} denote the particle sizes below which 10%, 50%, and 90% of the total population fall, respectively. This size range is ecologically relevant, as it encompasses the predominant plastic particle sizes accumulating in mussel hemolymph (Browne et al., 2008) and key tissues, including the digestive gland and gills (Fernández & Albentosa, 2019a). The primary stock solution used in this study contained 4.0×10^7 particles/mL.

The aged PET MNPs were verified with a 0.97 match score to the reference spectrum using Raman spectroscopy and Open Specy reference library. Complementary scanning electron microscopy (SEM, Phenom™ ProX) images confirmed the fragmented and irregular shapes of particles (Supplementary Figure A3.1, Panel B and C). To ensure particle stability under *in vivo* exposure conditions, the hydrodynamic size and electrophoretic mobility of aged PET MNPs in filtered artificial seawater (ASW; 100 nm membrane filters, Millipore) was measured at 1 h, 24 h, and 48 h using Dynamic Light Scattering (DLS, Zetasizer Nanoseries, Malvern Instruments) (Supplementary Figure A3.2). Prior to analysis, the surfactant-free stock suspension of aged PET MNPs was sonicated for 20 minutes, and a working solution (10^5 particles/mL) was prepared in sterile glass containers using filtered ASW. Reference standards (ZTS1240, Malvern Panalytical) were included for quality control, and three replicate measurements in folded capillary cell were performed per time point. Specifically,

the electrophoretic mobility was measured at a constant direct current electric field of 10 V/cm, and the corresponding zeta (ζ) potential was calculated by the instrument software using the Henry equation. The particles displayed relatively uniform dispersion over time, with hydrodynamic diameters ranging from 478 nm to 650 nm. Zeta potential measurements illustrated particle stability in ASW, with values remaining between -14.7 mV and -17.1 mV, aligning with electrophoretic mobility data (-1.04 to -1.21 µm·cm/V/s).

3.2.2 Test organisms

Approximately 400 adult blue mussels (*Mytilus edulis*) with a mean shell length of 43.4 ± 2.47 mm and wet weight of 15.2 ± 2.54 g were collected from Hoedekenskerke, The Netherlands. Mussels were kept in glass aquaria with artificial seawater prepared using purified water from double-pass reverse osmosis (RO) units (Eurowater) and high-quality sea salt (hw-Marinemix Professional). The tanks were equipped with portable aeration (Eheim Air Pump 400) and mechanical-biological filtration (Eheim Biopower 200) systems. The temperature was maintained at 15 ± 0.5°C with 12:12 h photoperiod. Mussels were fed every two days with microalgae suspension (*Tetraselmis suecica*, Tetraprime S Proviron), at a final concentration of 4×10^6–5×10^6 cells per mussel (equivalent to 4,000–5,000 cells/mL), supporting optimal filtration efficiency and growth (L. L. Li et al., 2020; Riisgard, 1991; Riisgard et al., 2011) and in line with feeding regimes used in other toxicity studies of comparable or extended duration (Bråte et al., 2018; Pinto et al., 2019; Santana et al., 2018). Water inflow was interrupted for 2 h during feeding. Water was renewed daily by 50%, and quality parameters in the experimental aquaria containing mussels (pH: 8.10 ± 0.04, salinity: 31.2 ± 0.4‰, dissolved oxygen: 8.15 ± 0.10 mg/L, ammonia: 0.25 mg/L, nitrite: <0.3 mg/L, and nitrate: 12.5 mg/L) were monitored using Hach HQ40D meters and Tetra test kits (Von Moos et al., 2012). No progressive increase in nutrient concentrations was observed during the experimental period, indicating stable conditions were maintained under the applied water renewal regime. Mussels were acclimated and depurated for at least three weeks, with no mortality observed during this period.

3.2.3 Experimental set-up

In total, 12 aquaria were set up for the *in vivo* experiment, each containing 30 individuals (1 L ASW per individual). A negative control (NC) group in triplicate was maintained in clean ASW throughout the experiment. Exposure treatments comprised three nominal concentrations of aged PET MNPs: 10 particles/L (C1), 10^3 particles/L (C2), and 10^5 particles/L (C3). These concentrations align with modeled scenarios for marine environments (Besseling et al., 2019; Lenz et al., 2016) and reflect the estimated exposure concentrations assuming the complete degradation of spherical PET particles (Sioen et al., 2024a).

Each experimental condition included three replicate aquaria, all maintained under the same controlled conditions as described above. Mussels were randomly placed in glass

petri dishes in groups of five, corresponding to the number of individuals collected at each timepoint. This setup facilitated byssal attachment and minimized handling stress during water renewal (as illustrated in Supplementary Figure A3.3). Exposure was conducted continuously for 14 days, during which mussels were fed every two days as previously described (Section 3.2.2). After each feeding, the water was completely renewed and replenished with the appropriate volume of aged PET MNPs from the working suspension (10^6 particles/mL) to maintain target exposure concentrations, based on water volume and mussel count (Supplementary Table A3.1). The particle stock suspension was sonicated for 20 minutes before use.

During the exposure period, five mussels (thus one glass petri dish) per tank were collected at four time points (D1, D3, D7, D14) for analysis. The 14-day exposure period was followed by a 10-day recovery period, chosen based on the observed timeline for plastic particle uptake and elimination (Fernández & Albentosa, 2019b). For this, the remaining mussels from aged PET MNP treatment tanks were rinsed with ASW and transferred to clean tanks for recovery. After 3 and 10 days post-exposure, samples were again collected. Throughout the experiment, each tank was aerated using two glass pipettes connected to a silicone hose for constant aeration and to promote uniform particle dispersion. Tanks were covered with aluminum foil to prevent contamination.

3.2.4 Sampling procedure

Mussel condition was assessed individually at baseline (day 0) and each timepoint by measuring shell length (mm) with a digital caliper (0.1 mm precision) and weight (g) with a scale (0.01 g precision). At each time point, five mussels (thus one glass petri dish) were collected from each replicate aquarium (15 individuals per experimental condition), and then anesthetized for 30 min in a filtered (100 nm, Millipore) and sterilized 0.3 M magnesium chloride ($MgCl_2$) solution. Hemolymph was extracted from the posterior adductor muscle using a sterile 2 mL syringe (Injekt) with a 23G needle (Terumo Neolus), pooled, and then filtered through a 70 µm cell strainer (Greiner) (Auguste et al., 2020; Canesi et al., 2015). Samples were maintained at 4°C in a final volume of 300 µL per assay to minimize hemocyte aggregation until further analysis (Chen & Bayne, 1995) (Section 3.2.5.1 – 3.2.5.3). For histopathological examination, the digestive gland and gill tissues were dissected from 2 mussels per replicate aquarium using a sterile kit. Tissues were fixed overnight in 4% paraformaldehyde (PFA, Invitrogen) at 4°C, and rinsed three times in phosphate-buffered saline (PBS, 0.01 M). Samples were stored at 4°C until analysis (Section 3.2.6.1). All procedures were conducted in a laminar flow cabinet (Spetec).

3.2.5 Assessment of cellular-level effect endpoints

The responses of hemocyte subpopulations to aged PET MNPs were analyzed by fluorescent labeling and flow cytometry with BD™ LSR II (BD Biosciences), as previously applied (Hara et al., 2024; Wang et al., 2019).

3.2.5.1 Lysosomal stability

Lysosomal stability was assessed using the LysoTracker™ Blue DND-22 (Invitrogen). Hemolymph samples (300 µl) were incubated with LysoTracker to a final concentration of 75 nM and incubated in the dark at 15°C for 1 h. Fluorescence was measured with excitation and emission wavelengths of 373 nm and 422 nm, respectively. Data were expressed as the mean geometric fluorescence in hemocyte subpopulations relative to the negative control (set to 100%).

3.2.5.2 Reactive oxygen species (ROS) production

The intracellular ROS levels were evaluated using the 5-(and-6)-chloromethyl-2',7'-dichlorodihydrofluorescein diacetate acetyl ester (CM-H_2DCFDA, Invitrogen), dissolved in dimethylsulfoxide (DMSO). To validate assay sensitivity, oxidative activity was induced with 100 µM H_2O_2 as a positive control (Hara et al., 2024; Sendra, Carrasco-Braganza, et al., 2020). Hemolymph samples (300 µl) were incubated with CM-H_2DCFDA to a final concentration of 10 µM and incubated in the dark at 15°C for 1 h. Fluorescence was measured with the FITC signal detector of the flow cytometer. Data were expressed as the mean geometric fluorescence in hemocyte subpopulations relative to the negative control (set to 100%).

3.2.5.3 Hemocyte mortality

Hemocyte mortality was assessed using Propidium Iodide (PI; Abcam), following the manufacturer's protocol with modification (Wang et al., 2019). As previously reported (Hara et al., 2024; Olabarrieta et al., 2001), cadmium chloride ($CdCl_2$, 800 µM) was used as a chemical control (PC CT), while 1-hour sonication served as a non-chemical control (PC ST) to induce cell death. Hemolymph samples (300 µl) were incubated with 5 µl of PI, and incubated in the dark at 15°C for 5–10 min. Fluorescence was measured with excitation and emission wavelengths of 535 nm and 617 nm, respectively. Data were expressed as the percentage (%) of cells with iodide fluorescence relative to the total number in each hemocyte subpopulation.

3.2.5.4 Flow cytometry analyses

All measurements were performed with BD LSR II flow cytometer (BD Biosciences) equipped with 488 nm (blue), 633 nm (red), 405 nm (violet), and 355 nm (UV) lasers. Hemocyte subpopulations were detected based on side scatter (SSC) and forward scatter (FSC) parameters, which reflect cell size and internal complexity, respectively. A gating technique using the SSC vs. FSC dot plots was then employed to distinguish the sub-population of interest, consistent with the flow cytometric characterization applied in the subsequent chapter (Supplementary Figure A4.5). A total of 10,000 cells were analyzed for each sample replicate. To ensure accurate parameter measurements throughout the experiment, regular calibration was conducted using calibration beads. Data were processed using FACSDiva™ Software (Version 5.0) and FlowJo (Version 10.9.0).

3.2.6 Assessment of tissue-level effect endpoints

The effect of aged PET MNP exposure on mussel physiology was assessed through histopathological examination of tissues.

3.2.6.1 Histopathological analysis

Digestive gland and gill tissues were collected from two mussels per replicate aquarium (six mussels in total) from the control and the highest-aged PET treatment (C3) groups at the end of the exposure (day 14) and recovery period (10 days post-exposure). Samples were processed for histopathological analysis at the Antwerp Centre for Advanced Microscopy (ACAM). Fixed tissues were dehydrated through a series of graded ethanol, cleared in xylene, and then embedded in paraffin. Tissue samples were sectioned at 5 µm using a microtome, then stained with hematoxylin and eosin (H&E) (Costa et al., 2013). The stained sections were fully scanned using a Zeiss Axioscan digital slide scanner. Six tissue sections of the digestive gland and gills, each with eight image annotations, were analyzed per treatment (48 in total) using QuPath software (Version 0.4.3).

3.2.6.2 Histopathological condition indices

The semi-quantitative histopathological condition index (I_h) was calculated for gills and digestive glands of mussels by following the method previously employed (Costa et al., 2013; Ertürk Gürkan & Gürkan, 2021; Pinto et al., 2019). The I_h was calculated based on the differential biological significance of each observed alteration (weight) and its degree of dissemination (score). The weights (w) assigned to each histopathological alteration (j), as described by Ertürk Gürkan & Gürkan (2021) were applied to assess changes in the digestive gland (lipofuscin aggregation, hemocyte infiltration, hyperplasia, atrophy, and necrosis) and gills (lipofuscin aggregation, hemocyte infiltration, enlarged central vessel, loss of cilia, and lamellar fusion). The weight ranged from 1 (indicating minimum severity) to 3 (maximum severity), and the score ranged from 0 (alteration not observed) to 6 (diffuse). I_h was calculated using the described formula:

$$I_h = \frac{\sum_l^j w_j a_{jh}}{\sum_l^j M_j},$$

where I_h is the histopathological condition index calculated per organ for each individual mussel h; w_j the weight of the jth histopathological alteration; a_{jh} the score attributed to the hth individual for the jth alteration; M_j is the maximum attributable value (weight × maximum score) for the jth alteration. The equation denominator normalizes I_h to a value between 0 and 1.

The I_h results were then categorized based on the prevalence of histopathological alterations as follows: low (0–0.25), moderate (0.25–0.50), high (0.50–0.75), or very high (0.75–1) (Costa et al., 2013).

3.2.7 Statistical analysis

The data were assessed for normality using Shapiro-Wilk test and homogeneity of variances was evaluated using the Brown–Forsythe test. Statistical analyses were then performed to assess the significant effects of exposure concentration and time using either one-way analysis of variance (ANOVA) or the non-parametric Kruskal-Wallis, followed by Tukey's HSD or Dunn's post-hoc test, respectively. The intensities of histopathological conditions (semi-quantitative data) were compared using the Mann-Whitney U-test to assess differences between control and exposed groups across exposure and depuration periods. Statistical significance was set at $p < 0.05$. All analyses were performed using GraphPad Prism (Version 10.1.2). The graphical abstract was created in BioRender (Hara, J. 2025): https://BioRender.com/lzxe4xy.

3.2.8 Quality assurance and control

This experiment achieved a score of 62.5% (25/40) on the proposed quality assurance and control (QA/QC) criteria, surpassing the reported average score of 44.6% (De Ruijter et al., 2020). Although using MNPs posed analytical challenges that hindered compliance with quality criteria 8, 9, and 11 for background contamination, exposure concentration, and organism exposure (e.g., MNP ingestion or accumulation), the overall score demonstrates strong quality performance. Detailed explanations for each criterion are provided in Supplementary Table A3.2.

3.3 Results

3.3.1 Cellular responses to aged PET MNP exposure

The responses of mussels to exposure with varying concentrations of aged PET MNPs (10 (C1), 10^3 (C2), and 10^5 (C3) particles/L) were assessed across multiple cellular effect endpoints during both the exposure (days 1, 3, 7, and 14) and recovery periods (days 17 and 24 or 3 and 10 days post-exposure), respectively.

3.3.1.1 Lysosomal content stability

Lysosomal content in granulocytes (Figure 3.1, panel A) showed relative fluctuations over time, although no statistically significant differences were observed across all tested aged PET concentrations and the negative control during both the exposure and recovery periods. In contrast, hyalinocytes (Figure 3.1, panel B) exhibited a significant decrease in lysosomal content only at the highest aged PET MNP concentration (C3) compared with the control after 3 days of exposure ($p = 0.016$). No significant changes, indicating lysosomal

content recovery, were observed by day 7 and maintained throughout the subsequent exposure and recovery periods.

3.3.1.2 Oxidative activity

In granulocytes (Figure 3.2, Panel A), exposure to the lowest concentration of aged PET (C1) did not induce significant changes in ROS levels throughout both the exposure and recovery periods. However, exposure to aged PET MNP C2 induced a significant decrease in ROS levels only on day 14 of the exposure period (p = 0.023), while C3 exhibited a significant decrease 3 days post-exposure compared to the control (p = 0.012) and lower concentrations (C1: p = 0.029 and C2: p = 0.003). Similarly, in hyalinocytes (Figure 3.2, Panel B), aged PET MNP C2 exposure led to a significant decrease in ROS levels only on day 14 compared to the control (p = 0.049). Although C3 resulted in the lowest ROS levels three days post-exposure, this difference was not significant from the concurrent control.

The observed changes in both granulocytes and hyalinocytes were transient, with no significant changes in ROS levels compared to the control by 10 days post-exposure, demonstrating reversibility.

3.3.1.3 Hemocyte mortality

As shown in Figure 3.3 (Panel A), exposure to aged PET C2 (p = 0.006) and C3 (p < 0.0001) significantly increased mortality in granulocytes only after 3 days of exposure while C1 (p = 0.021) induced an increase only after 7 days of exposure compared with the control. No significant increases in granulocyte mortality were observed by day 14 compared with the concurrent control and maintained throughout the subsequent recovery period.

In hyalinocytes (Figure 3.3, Panel B), only the aged PET C3 (p = 0.001) induced a significant increase in mortality compared with the control after 3 days of exposure. Subsequently, by day 7, the C2 treatment group displayed the lowest percentage of hemocyte mortality among all treatments (p < 0.05). Similar to granulocytes, no significant changes in hyalinocyte mortality were observed compared with the control by day 14 of the exposure period and throughout the recovery period.

3.3.2 Histopathological responses to aged PET MNP exposure

The histopathological responses and condition indices of the digestive gland and gills were assessed during both the exposure (day 14) and recovery periods (10 days post-exposure) (Figure 3.4 – Figure 3.6).

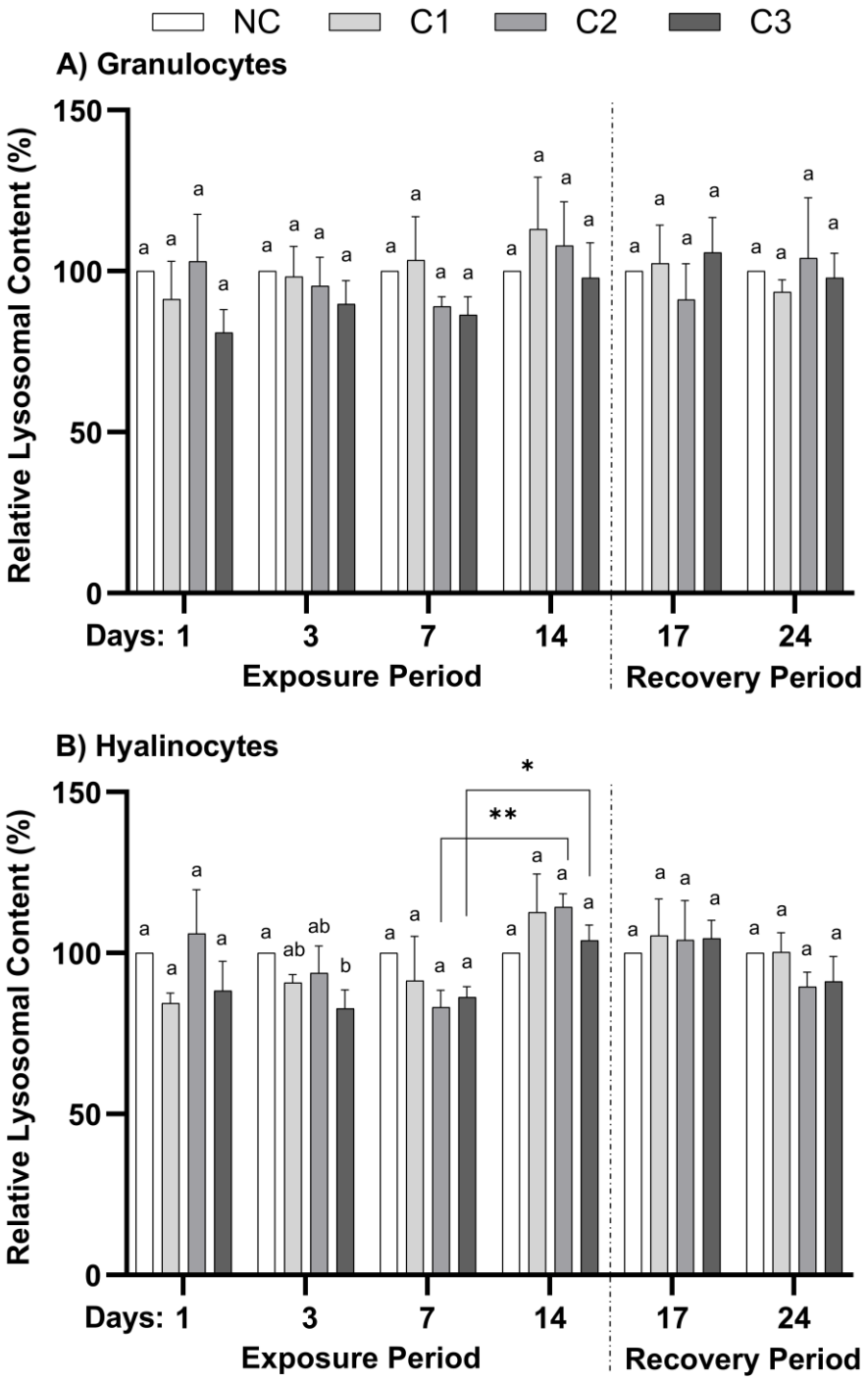

Figure 3.1. *Relative lysosomal content in (A) granulocytes and (B) hyalinocytes exposed to different concentrations of aged PET (10 (C1), 10^3 (C2), and 10^5 (C3) particles/L) over the exposure (Days 1, 3, 7, and 14) and depuration periods (3 and 10 days post-exposure). Data are expressed as mean ± SD (n = 3). Different lower-case letters denote significant differences among concentrations at each time point ($p < 0.05$), while asterisks indicate significant differences within each concentration over time (*$p < 0.05$; **$p \leq 0.01$; ***$p \leq 0.001$).*

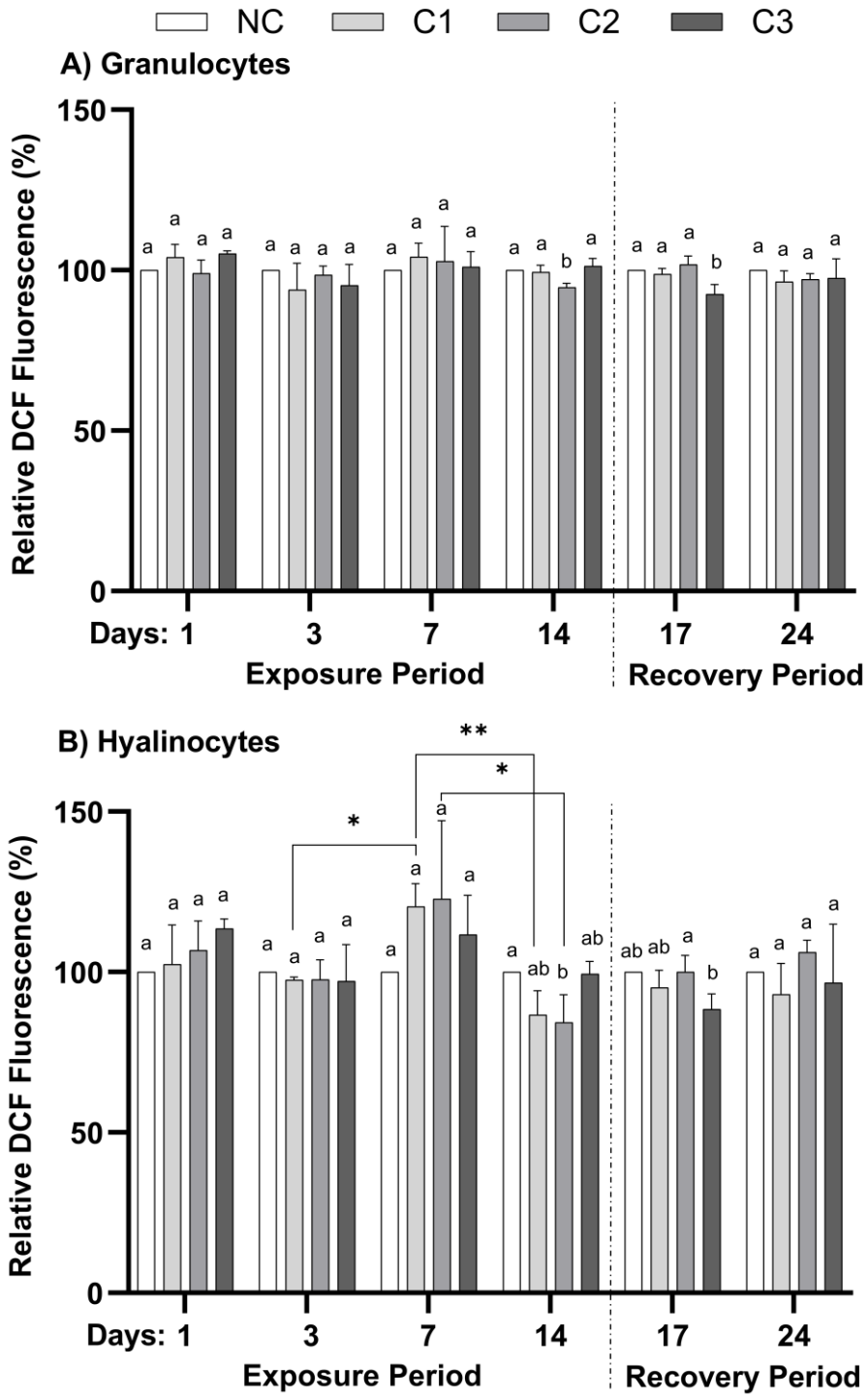

***Figure 3.2**. Relative reactive oxygen species (ROS) production in (A) granulocytes and (B) hyalinocytes exposed to different concentrations of aged PET (10 (C1), 10^3 (C2), and 10^5 (C3) particles/L) over the exposure (Days 1, 3, 7, and 14) and depuration periods (3 and 10 days post-exposure). Data are expressed as mean ± SD (n = 3). Different lower-case letters denote significant differences among concentrations at each time point ($p < 0.05$), while asterisks indicate significant differences within each concentration over time (*$p < 0.05$; **$p \leq 0.01$; ***$p \leq 0.001$).*

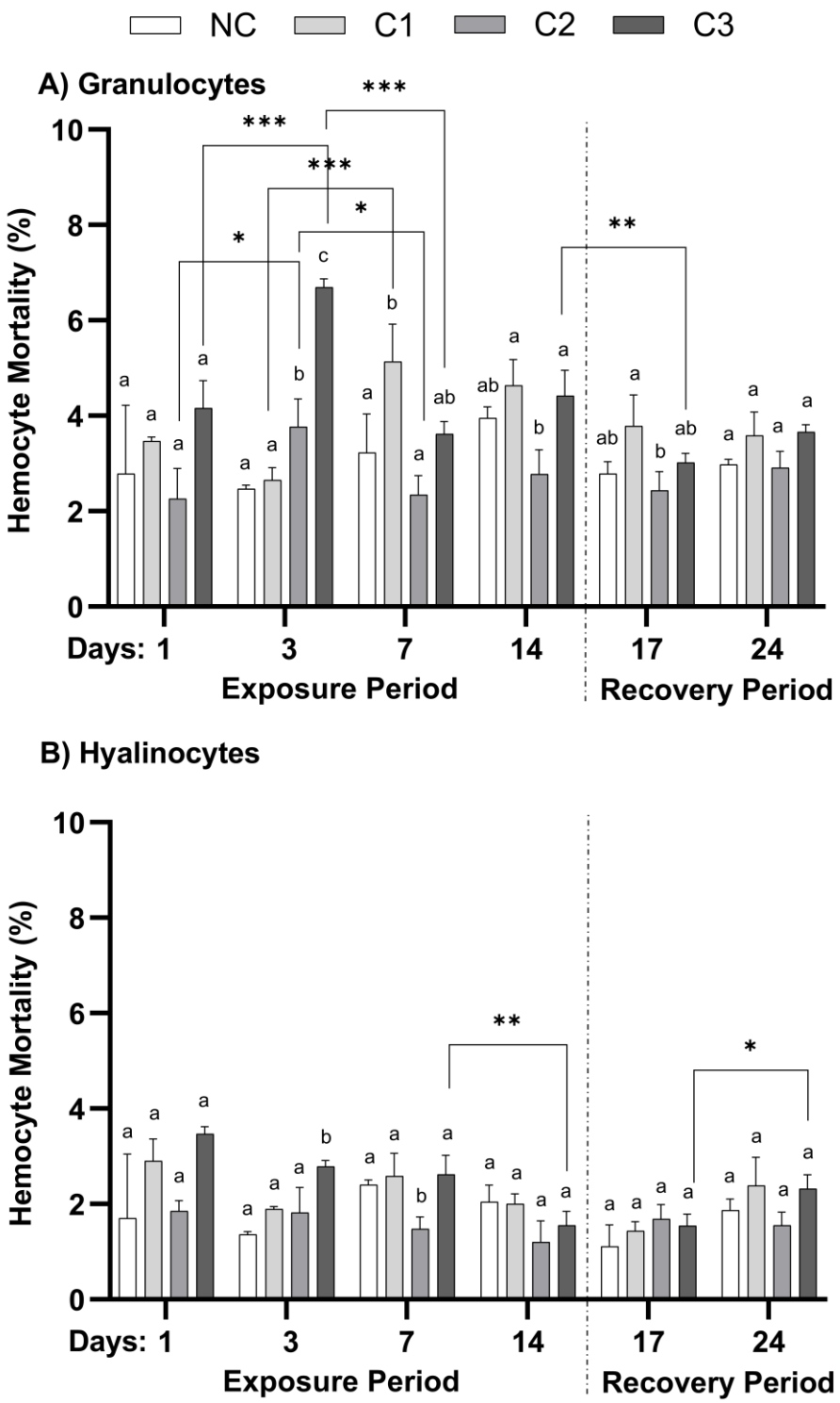

Figure 3.3. *Cellular mortality in (A) granulocytes and (B) hyalinocytes exposed to different concentrations of aged PET (10 (C1), 10^3 (C2), and 10^5 (C3) particles/L) over the exposure (Days 1, 3, 7, and 14) and depuration periods (3 and 10 days post-exposure). Data are expressed as mean ± SD (n = 3). Different lower-case letters denote significant differences among concentrations at each time point ($p < 0.05$), while asterisks indicate significant differences within each concentration over time (*$p < 0.05$; **$p \leq 0.01$; ***$p \leq 0.001$).*

3.3.2.1 Digestive gland

As shown in Figure 3.4, the digestive gland for control samples demonstrated normal structure, with digestive tubules characterized by a single layer of cells surrounding a narrow or occluded tubular lumen. In comparison with the control, the group exposed to the highest concentration of aged PET (C3) exhibited pronounced occurrences of atrophic and necrotic digestive tubules, particularly during the depuration period. The exposed groups also exhibited a higher extent of hemocyte infiltration and larger lipofuscin aggregation. Although the exposed group exhibited a relatively higher I_h (Figure 3.6, Panel A) compared to the control group during both the exposure (p = 0.316) and recovery periods (p = 0.080), these differences were not statistically significant. The I_h remained consistently within the low category (0–0.25), across both the control (NC) and exposed groups (C3).

3.3.2.2 Gills

The histopathological analysis of the gill filaments (Figure 3.5) in control samples demonstrated the typical structure, with well-defined lamellae formed by a single layer of epithelial cells, tightly structured central vessel, and minimal presence of lipofuscin aggregation and hemocyte infiltration. In contrast, exposure to the highest tested concentration of aged PET (C3) induced several lesions in the gill tissues. These changes included a progressive presence of lamellar fusion in the lateral and abfrontal zones coupled with the enlargement of the central vessels, particularly evident during the exposure period. A higher extent of hemocyte infiltrations and lipofuscin aggregations were observed in association with gill filaments showing regressive changes. The I_h for gills (Figure 3.6, Panel B) was significantly higher in the exposed group (aged PET C3) compared to the control during the exposure period (p = 0.004). By the recovery period, the I_h in the exposed group (C3) remained significantly elevated (p = 0.015), with an index value within the moderate category (0.25–0.50), compared to the control (low, 0–0.25).

3.3.3 Growth and survival of mussels exposed to aged PET MNPs

Exposure to aged PET MNPs did not result in mortality or significant alterations in growth parameters, including weight and shell length, in mussels (Supplementary Figure A3.4, Panels A and B). The mean shell length (41.7–46.3 mm) and mean weight (13.8–17.1 g) remained consistent across all groups during both the exposure period and recovery period. Statistical analysis of absolute changes, calculated as the difference between baseline (Day 0) and final values, confirmed no significant differences (p > 0.05) in these parameters across the negative control and treatment groups exposed to varying concentrations of aged PET MNPs.

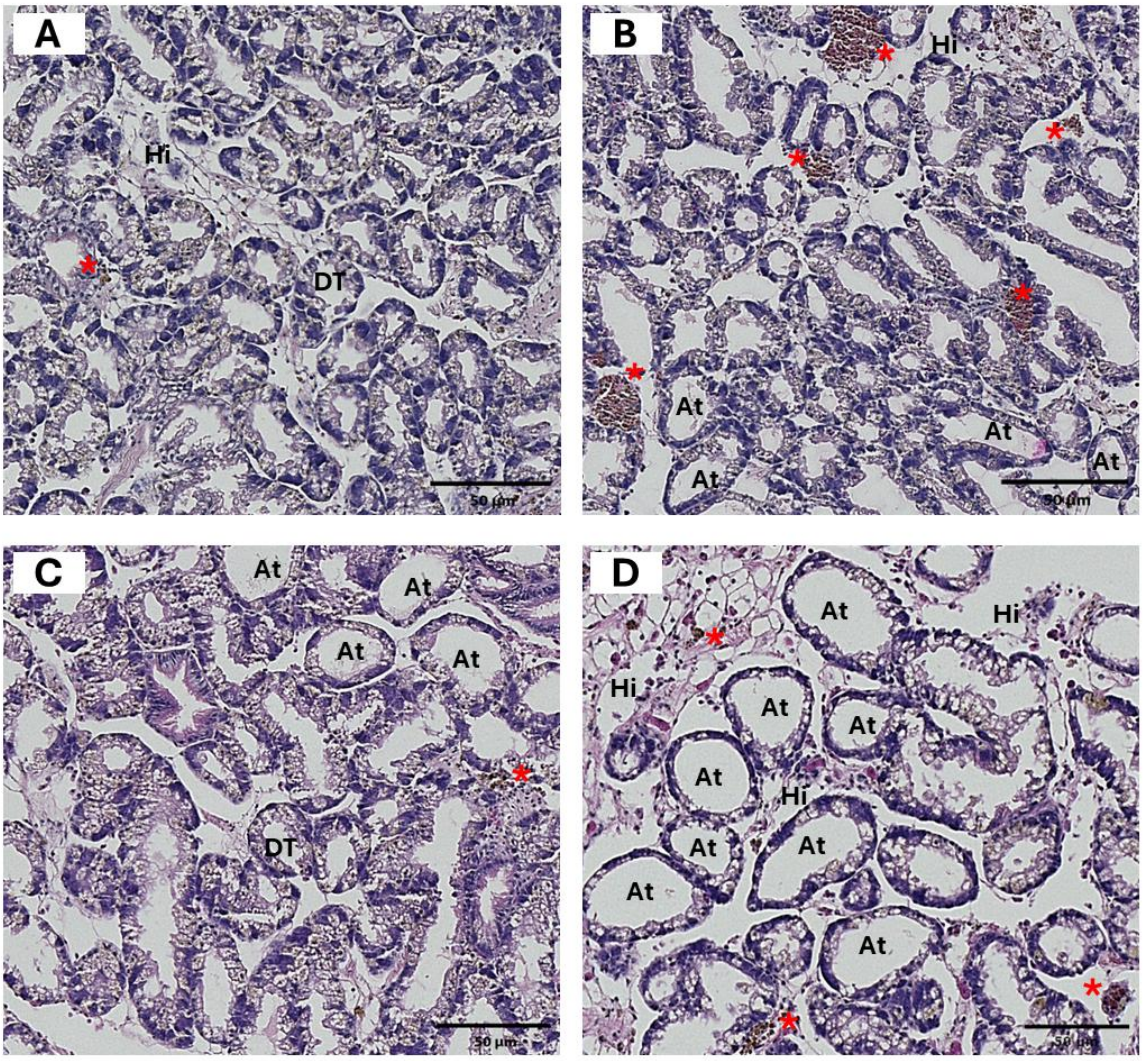

Figure 3.4. *Micrographs of the digestive gland of M. edulis in (A, C) control and (B, D) exposed groups following a 14-day exposure to aged PET (C3: 10^5 particles/L) and a subsequent 10-day recovery period, respectively.* ***A.*** *Digestive tubules in the control group showing normal structure (DT) constituted by a single layer of cells surrounding a narrow or occluded tubular lumen with minimal presence of hemocyte infiltration (Hi) and lipofuscin aggregation (red asterisks).* ***B.*** *Section of the digestive gland from the exposed group after a 14-day exposure period to aged PET (C3) displaying atrophied digestive tubules (At) with enlarged lumen, thinner epithelium, and pronounced lipofuscin aggregation (red asterisks) characterized by brown pigments.* ***C.*** *Section from the control group following the 10-day recovery period showing minimal occurrences of the atrophied tubules (At) and lipofuscin aggregations (red asterisks).* ***D.*** *The exposed group following the recovery period with more pronounced occurrences of atrophied digestive tubules (At), hemocyte infiltrations (Hi), and lipofuscin aggregations (red asterisks). Scale bar: 50 µm.*

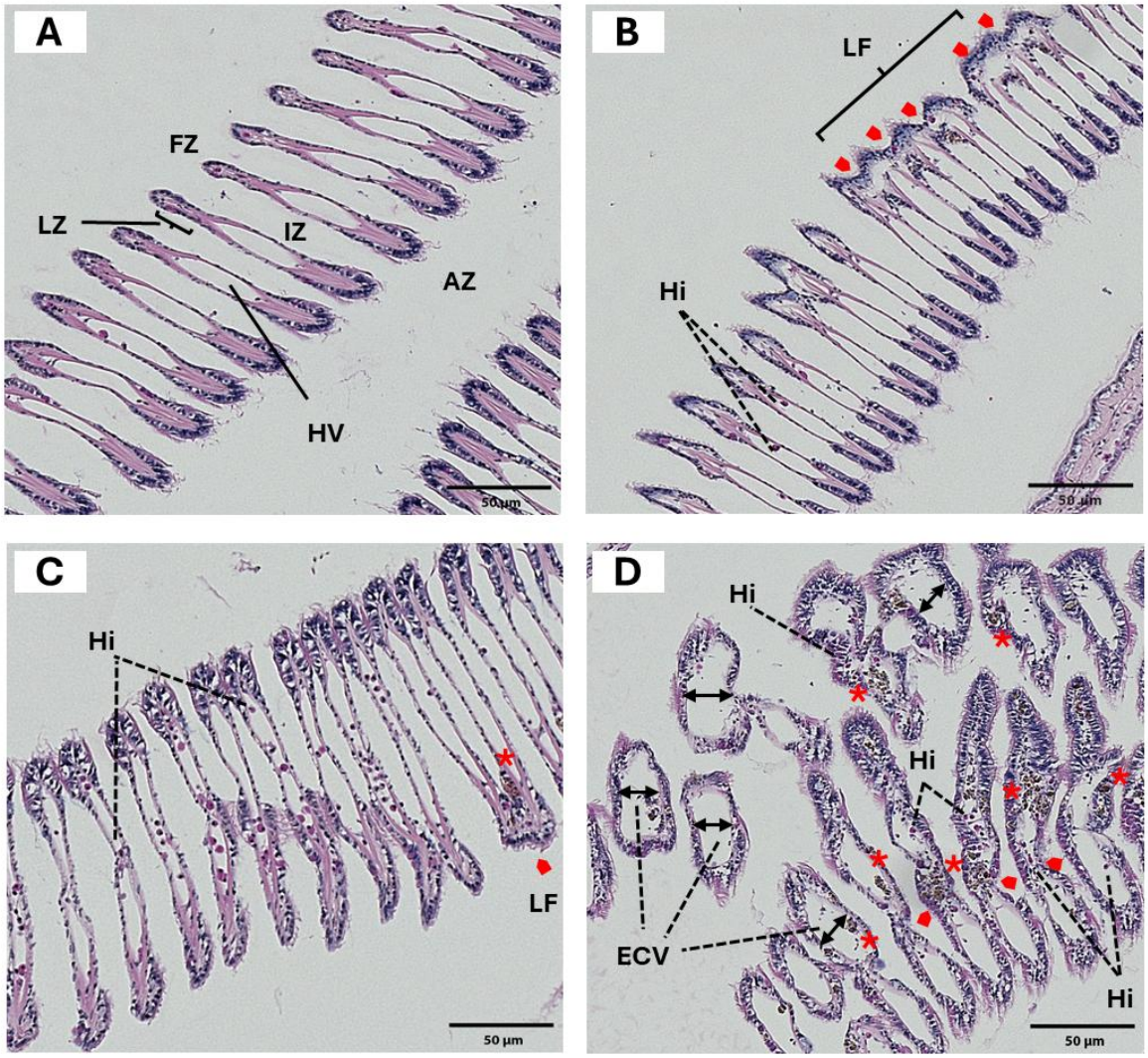

Figure 3.5. *Micrographs of the longitudinal section through the gill filaments of M. edulis in (A, C) control and (B, D) exposed groups following a 14-day exposure to aged PET (C3: 10^5 particles/L) and a subsequent 10-day recovery period, respectively.* ***A.*** *Gill filaments in the control group showing normal structure with indication of the frontal zone (FZ), lateral zone (LZ), abfrontal zone (AZ), intermediate zone (IZ), and hemolymphatic vessel (HV).* ***B.*** *Gill filaments in the exposed group following a 14-day exposure period to aged PET (C3) exhibiting lamellar fusion (LF, red arrowheads) in the lateral zone.* ***C.*** *Control group following the 10-day recovery period with indications of lipofuscin aggregations (red asterisks) and hemocyte infiltrations (HI).* ***D.*** *The exposed group following the recovery period with an evident enlargement of the central vessel (ECV, double-headed arrows), lamellar fusion in the abfrontal zone (LF, red arrowheads), including abundant lipofuscin aggregations (red asterisks) and hemocyte infiltrations (HI). Scale bar: 50 µm.*

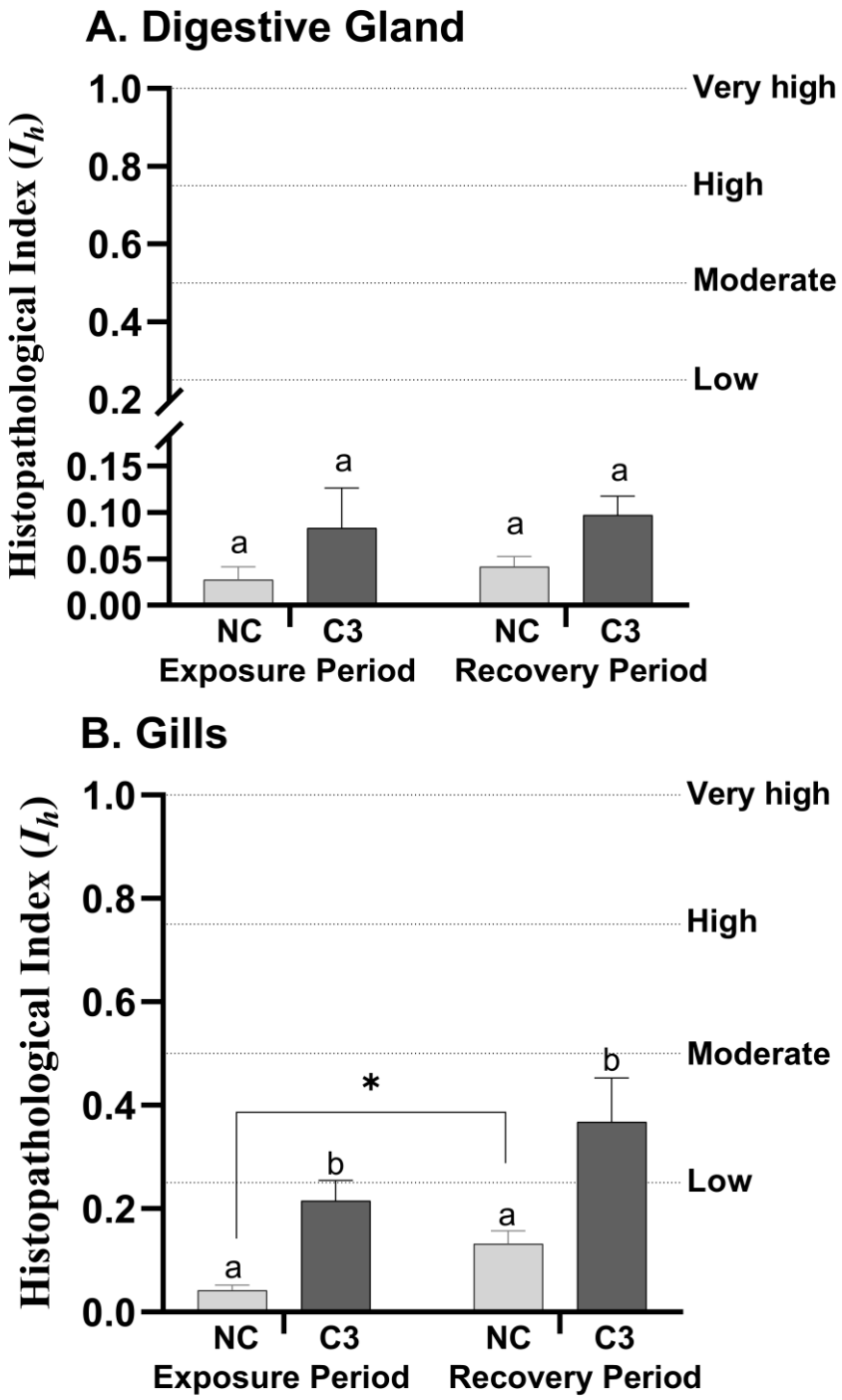

Figure 3.6. *Histopathological condition indices (Ih) in the (A) digestive gland and (B) gills of M. edulis for control (NC) and exposed groups (aged PET C3: 10^5 particles/L) after the exposure period (Day 14) and recovery period (Day 24; 10 days post-exposure). Data are expressed as mean ± SE (n = 6 tissue replicates per treatment). The I_h were categorized according to Costa et al. (2013) as low (0–0.25), moderate (0.25–0.50), high (0.50–0.75), or very high (0.75–1). Different lower-case letters denote significant differences between the groups within each period, while asterisks indicate significant differences within each group over time (Mann-Whitney U, $p < 0.05$).*

3.4 Discussion

This study provides an integrative analysis of cellular, tissue, and organismal-level responses of mussels exposed to environmentally relevant concentrations of aged PET MNPs. Current findings reveal concentration- and time-dependent effects, demonstrating both immediate cellular perturbations and recovery potential. Histopathological analysis revealed tissue-specific alterations. While no immediate effects on growth and mortality were observed in mussels, long-term implications for organismal health cannot be excluded nor potential mixture effects with other stressors.

3.4.1 Cellular responses to aged PET MNP exposure

In marine bivalves, hemocytes are multifunctional circulating cells essential for immune defense, nutrient transport, tissue repair, and maintaining homeostasis (de la Ballina et al., 2022). Understanding the responses of hemocyte subpopulations, such as granulocytes and hyalinocytes, to aged plastic particle exposure is crucial for assessing impacts on immune function and physiological resilience.

Cellular responses, such as perturbations in lysosomal integrity and stability, are regarded as sensitive indicators of cellular injury (M. N. Moore et al., 2006). In the current study, granulocytes demonstrated resilience to aged PET MNP exposure, maintaining lysosomal stability even at the highest tested concentration. In contrast, hyalinocytes exhibited significant lysosomal destabilization only at the highest concentration (C3) after 3 days of exposure. These results are in line with those obtained for undifferentiated mussel hemocytes (*Mytilus galloprovincialis)*, where a significant decrease in lysosomal membrane stability (LMS) was observed after 21 days of exposure to 50 nm PS-NPs (1.5–150 ng/L or 2.17×10^{5}–2.17×10^{7} particles/L) and 3 µm PS MPs (15–150 ng/L; 1,000–10,000 particles/L), as measured by the neutral red retention time (NRRT) assay (Capolupo et al., 2021). Another study performed at higher particle concentrations reported prominent lysosomal destabilization induced by amino polystyrene NPs (50 nm PS-NH_2, 10 µg/L or 1.46×10^{11} particles/L converted concentrations in Supplementary Table A3.3) after 24 hr of exposure, and, to a lesser extent upon repeated exposure following 3 days of depuration (Auguste et al., 2020). This transient destabilization contrasts with nano titanium dioxide (TiO_2, 25 and 100 nm at 0.1–10 mg/L or 2.89×10^{12}– 2.89×10^{14} and 4.52×10^{10}–4.52×10^{12} particles/L, respectively), which induced concentration- and size-dependent lysosomal destabilization in mussels that persists throughout both exposure and recovery periods (Wang et al., 2019).

ROS are naturally produced in all cells, including hemocytes, but overproduction can lead to oxidative damage and disrupt homeostasis (Z. Li et al., 2022). As observed, exposure to moderate (C2) and high (C3) concentrations of aged PET caused a significant but transient reduction in ROS levels in both hemocyte subpopulations. Similarly, a transient ROS

reduction in oyster hemocytes (*Crassostrea hongkongensis*) was observed after 7-day *in vivo* exposure to zinc (Zn, 300 µg/L, 4.6×10^{-6} M), primarily in granulocytes and to a lesser extent in hyalinocytes, with no significant changes at subsequent time points (Luo & Wang, 2022). These findings are notable because they diverge from the typically observed oxidative stress response, where MNP exposure has been linked to increased ROS production in various cell types (Hu & Palić, 2020). Recent findings suggest that physicochemical changes associated with plastic aging can modulate ROS dynamics. Specifically, Jeon et al. (2021) demonstrated that weathered plastic particles, despite higher intrinsic ROS potential, generated less ROS in biological media due to enhanced protein binding, leading to lower net ROS levels in cellular systems. Although our study did not directly assess antioxidant responses, the ROS reduction observed may also reflect a compensatory activation of endogenous antioxidant systems. Key enzymes such as catalase (CAT), superoxide dismutase (SOD), glutathione peroxidase (GPx), and glutathione (GSH) can be upregulated in response to particle-induced oxidative stimuli (Z. Li et al., 2022). For instance, mussel (*Mytilus spp*.) exposed to mixed PS MPs (2–6 µm, 32 µg/L or 2.0×10^{6} particles/L) combined with fluoranthene (30 µg/L or 1.5×10^{-7} M) efficiently neutralized ROS, linked to antioxidant activation and low lipid peroxidation (Paul-Pont et al., 2016). The transient nature of ROS reductions suggests that aged PET MNPs, like other chemicals, can temporarily alter cellular redox balance, potentially contributing to cumulative mixture effects.

Consequently, the current findings, in combination with *in vitro* studies on aged PET MNPs as described in Chapter 4 (Hara et al., 2024), reveal significant concentration- and time-dependent effects on hemocyte mortality. As observed, granulocytes showed early susceptibility, with increased mortality observed after 3 days of exposure to aged PET C2 and C3, while C1-induced effects were delayed until day 7. In contrast, hyalinocytes exhibited significant changes in mortality only when exposed to aged PET C3 after 3 days of exposure. Similarly, exposure to environmental PE NPs (1–1200 nm, 0.08 µg/L or 9.61×10^{4}–1.66×10^{14} particles/L) and MPs (1.2–300 µm, 0.08 and 10 µg/L, or within 6.15×10^{-3}–1.20×10^{7} particles/L, calculated based on the given mass concentration and the full range of particle sizes) induced concentration-dependent cytotoxicity, reducing cell viability within 24 hours (Roman et al., 2023). In comparison, metallic nanoparticles such as TiO_2 (25 and 100 nm at 0.1–10 mg/L or 2.89×10^{12}–2.89×10^{14} and 4.52×10^{10}–4.52×10^{12} particles/L, respectively) induce sustained hemocyte mortality even after 14 days post-exposure, which was attributed to the synergistic interplay of particle size and concentration (Wang et al., 2019).

The differential sensitivity of granulocytes and hyalinocytes to aged PET particles likely reflects their distinct immune functions. Granulocytes, characterized by high phagocytic activity, are more actively involved in internalizing foreign particles, which makes them prone to oxidative fluctuations and membrane destabilization, key mechanisms of particle-induced cytotoxicity. In contrast, hyalinocytes exhibit lower phagocytic capacity, reducing

their susceptibility to these cytotoxic mechanisms (Canesi et al., 2012; T. He et al., 2023; Le Foll et al., 2010). The absence of significant hemocyte mortality at later exposure time points and during the recovery period suggests the activation of cellular repair mechanisms. Recent studies suggested that bivalves can exhibit a shift in immune parameters and reestablish basal functions to restore immune homeostasis after repeated exposure to 50 nm PS-NH_2 (10 µg/L or 1.46×10^{11} particles/L) (Auguste et al., 2020). It is worth noting, however, that MNP-induced cytotoxicity in hemocytes may be exacerbated or mitigated when co-exposed with other associated contaminants, highlighting the complexity of these interactions in real-world conditions (Mkuye et al., 2022). Additionally, simultaneous exposure to global change-driven stressors, such as ocean warming, acidification, deoxygenation, and marine heat waves, can intensify stress responses (Catarino et al., 2022). Impairment in cellular immunity under these compounded stressors has significant consequences, such as increased susceptibility to pathogen infections. These cascading effects can extend beyond individual organisms, influencing populations, communities, and entire ecosystems (Kataoka & Kashiwada, 2021).

3.4.2 Tissue alterations induced by aged PET MNP exposure

Several studies have reported that MNPs, including HDPE (≤ 22 µm, mean 4–6 µm), PS (3 µm, 9.6 µm), PE (10.7–93.9 µm), and pristine PET (9.0–56.0 µm), exhibit efficient particle clearance and tissue accumulation dynamics in bivalves (see Supplementary Table A3.3 for exposure details) (Browne et al., 2008; Fernández & Albentosa, 2019a; Teng, Zhu, et al., 2021). Notably, mussels have been reported to exhibit size-dependent accumulation, with 0.07 µm PS particles demonstrating significantly higher retention in the digestive tract compared to larger particles (S. Wang et al., 2021). Despite partial elimination during depuration, smaller MNPs persist in critical organs, such as the digestive gland and gills of mussels (Browne et al., 2008; Fernández & Albentosa, 2019a, 2019b). Histopathological changes in these organs are widely recognized as sensitive biomarkers of environmental stress and pollution, offering insights into organismal health (Ertürk Gürkan & Gürkan, 2021). The current study builds on this knowledge, revealing the differential histopathological responses of these organs to aged PET MNP (C3) exposure.

While no significant increase was observed in the histopathological condition index, notable alterations were evident in the digestive glands of exposed mussels. Most prominently, an increased prevalence of atrophied tubules was observed, with thinner epithelium and an enlarged lumen (Cuevas et al., 2015). Mussels (*M. galloprovincialis)* exposed to virgin and weathered PE fragments (50–590 µm; 1,180 and 1,186 particles/L, 21 days) and PET microfibers (20–140 µm; 6.1×10^{5} particles/L and 6.1×10^{6} particles/L, 32 days) also exhibited digestive tubule atrophy (Bråte et al., 2018; J. S. Choi et al., 2022). Similarly, exposure to 200 nm PS NPs particularly at concentrations of 200 µg/L (4.55×10^{10} particles/L) and 2,000 µg/L (4.55×10^{11} particles/L) for 14 days induced thinner epithelia, barren digestive cells, wider lumens, and exfoliated cells. These changes in the digestive tubule morphology and planimetric parameters have been linked to severely disrupted

metabolic capability (Z. Lu et al., 2023). Such regressive changes occur in association with cellular degeneration and necrotic processes and can lead to impaired digestive function (Carella et al., 2015).

In the present work, exposure to the highest concentration of aged PET MNPs induced pronounced histopathological alterations in the gills, accompanied by significant increases in I_h values during both exposure and recovery periods. Key alterations, such as lamellar fusion and the enlargement of the central vessels, were prominently observed. Lamellar fusions were observed across the lateral and abfrontal zones of the gill filaments, which are critical for water pumping, lubrication, gill cleaning, gas exchange, and particle trapping (Leis et al., 2024). Similar severe alterations, including damaged inter-lamellar junctions, epithelial loss, and swollen lumens, were reported in gills of mussels (*Perna viridis*) exposed to weathered PE particles (15% <32 µm and 85% 32–43 µm, at 1,150–3,360 particles/m^3 or 1.15–3.36 particles/L) for 30 days. These structural alterations highlight the potential impairment of essential gill functions, including respiration, osmoregulation, and filtration efficiency (Hariharan et al., 2021). Inflammatory responses, evidenced by hemocyte infiltration in epithelial layer or hemolymph vessels, exacerbated the structural damage and correlated with diffuse gill inflammation. Exposure to 10–1000 µg/L of irregularly-shaped PE (10.7–93.9 µm, 4.19×10^2–4.19×10^4 particles/L) and PET (9.0–56.0 µm, 4.60×10^2–4.60×10^4 particles/L) induced severe hemocyte infiltration in the gills of oysters (*Crassostrea gigas*) (Teng, Zhu, et al., 2021). Extensive hemocyte infiltration alters lamellar structure through overcrowding and cause recurrent enlargement of the hemolymphatic vessels (Costa et al., 2013; Leis et al., 2024). Interestingly, gill filament deformation may also occur without hemocytic intrusion, likely representing an early-stage inflammatory response that precedes hemocyte invasion of the target site (Bouallegui et al., 2017).

Lipofuscin aggregates, particularly observed in digestive tubules and gill filaments exhibiting regressive changes, suggest a heightened oxidative imbalance (Leis et al., 2024). Formed through iron-catalyzed oxidative processes, lipofuscin is a non-degradable intralysosomal, polymeric substance composed of cross-linked protein and lipid residues. Its indigestible nature is associated with progressive lysosomal dysfunction, with cascading effects on various cellular activities. Its accumulation can interfere with autophagy by serving as a sink for newly produced lysosomal enzymes, which in turn hinders the recycling of cellular components. This disruption prevents effective cellular renewal, exacerbates the accumulation of damaged cellular constituents, and ultimately advances tissue degeneration (Brunk & Terman, 2002). The presence of these aggregates potentially indicates localized oxidative stress in tissues directly interacting with MNPs (Leis et al., 2024).

Varying degrees of histopathological alterations induced by MNPs have been documented in mussel tissues. For instance, *Mytilus coruscus* exposed to 20 mg/L PS MPs (1 µm, 3.64×10^{10} particles/L) exhibited less severe digestive tissue damage than PS NPs (100 nm,

3.64×10^{13} particles/L) (Qi et al., 2023). Similarly, 7-day exposure to PS (2–6 µm, 32 µg/L; 2.0×10^{6} particles/L) alone or combined with fluoranthene (30 µg/L, 1.5×10^{-7} M) significantly increased histopathological lesions, with persistent hemocyte infiltration and lipofuscin aggregation after the depuration period, especially in co-exposure group (Paul-Pont et al., 2016). Weathered PE particles (15% <32 µm and 85% 32–43 µm, at 1,150–3,360 particles/m^3 or 1.15–3.36 particles/L) also caused comparable lesions, with minimal recovery even after a 7-day depuration period (Hariharan et al., 2021). The persistence of these moderate lesions post-exposure underscores delayed or incomplete tissue repair within the tested experimental duration, potentially indicating a prolonged physiological burden from particle exposure. Consequently, the alterations observed in this study could be attributed to the physical properties of aged PET particles, particularly surface irregularities, which may induce mechanical abrasion. A recent study reported that PET induced a higher damage index than PE in both tissues, attributed to its more angular and rough edges (Teng, Zhu, et al., 2021).

To contextualize the histopathological effects of aged PET MNPs, comparisons with tissue-specific damage indices for other particulate toxicants in mussels are essential. For instance, exposure to gamma aluminum oxide (γ-Al_2O_3, 5 nm, 5–40 mg/L or 1.93×10^{16}–1.54×10^{17} particles/L) for 4 days caused severe damage in both organs, with mean I_h values within the high to very high category (Ertürk Gürkan & Gürkan, 2021). Exposure to lanthanum (La) in the form of dissolved ions for 28 days exhibit progressive, dose-dependent damage, with gill I_h values rising from moderate (0.1 mg/L or 7.2×10^{-7} M) to high (1.0–10.0 mg/L or 7.2×10^{-6} M–7.2×10^{-5} M) and digestive gland values progressing from low to moderate at the same concentrations (Pinto et al., 2019). Interestingly, exposure to 10 µg/L cadmium-based quantum dots (CdTe QDs, 6 nm, 1.43×10^{13} particles/L) and dissolved Cd (8.9×10^{-8} M) counterparts for 14 days significantly increased digestive gland I_h compared to controls, while remaining within the low category except for dissolved Cd (Rocha et al., 2016). These analyses provide insights into the severity and nature of tissue damage, influenced by particle properties, exposure conditions, and uptake routes, with critical implications for organismal health (Bouallegui et al., 2018).

3.4.3 Implications for organismal health

While cellular and tissue level analyses exhibited differential sensitivities, no significant effects on survival or growth metrics were observed following exposure to aged PET MNPs. Similarly, a 21-day exposure of mussels (*M. galloprovincialis*) to virgin and weathered PE (50–590 µm at 1,180 and 1,186 particles/L, respectively) caused no mortality or changes in condition index, despite evidence of histopathological alterations (Bråte et al., 2018). Exposure to 10 and 1000 µg/L of irregularly-shaped PE (10.7–93.9 µm, 4.19×10^{2}–4.19×10^{4} particles/L) and PET (9.0–56.0 µm, 4.60×10^{2}–4.60×10^{4} particles/L) for 21 days similarly showed no significant effects on the condition index in oysters (*C. gigas*) (Teng, Zhao, et al., 2021), though changes in histopathological parameters, lipid metabolism biomarkers, and cell membrane integrity, were observed (Teng, Zhu, et al., 2021). In contrast, exposure to

40–48 µm virgin PE at 100 µg/L (1.88–3.24×10^3 particles/L) and 1000 µg/L (1.88–3.24×10^4 particles/L) for 14 days caused significant weight loss and immune alterations without inducing mortality in other bivalve species (*Ruditapes decussatus*) (Abidli et al., 2023).

The variability in responses highlights the critical role of particle characteristics, such as size, shape, and weathering state, along with exposure duration and concentration, in determining the mode and extent of MNP-induced effects. Aging processes significantly alter the surface and physicochemical properties of plastic particles, influencing environmental behavior and interaction with organisms. These alterations, including fragmentation into smaller particles, discoloration, formation of oxygen-containing groups, and biofilm development, can modulate their biological impacts (P. Liu et al., 2020). For instance, plastic particles smaller than 4 µm have been reported to accumulate in the digestive gland of mussels, exhibiting longer retention times and higher translocation rates to the circulatory system compared to larger particles (Browne et al., 2008; Fernández & Albentosa, 2019a, 2019b). In mussels, two distinct pathways for plastic particle uptake have been reported. The first involves direct transport through gill surfaces, via microvilli-mediated endocytosis, primarily for smaller particles. The second pathway relies on ciliary movement to transfer particles through the digestive system, including the stomach, intestine, and ultimately the digestive gland ducts and tubules (Von Moos et al., 2012).

The histopathological alterations observed in gills and digestive gland align with previous findings, underscoring the susceptibility of these tissues to MNP exposure (Barría et al., 2025). While the observed recovery at the cellular level suggests that bivalves exhibit compensatory mechanisms to alleviate stress after an acute exposure event (Auguste et al., 2020). Moreover, differences in gene expression observed between single and repetitive exposures to HDPE (1–50 µm, 4.6×10^5 particles/L) highlight the development of stress memory. However, the increased energy demands associated with repeated high-concentration exposure raise concerns about the sustainability of these mechanisms. Chronic exposure to elevated MNP levels could overwhelm the organisms' physiological resilience, leading to impaired fitness, and potentially compromising long-term population viability (Détrée & Gallardo-Escárate, 2018).

Additionally, the interplay between MNPs and other environmental stressors, such as chemical pollutants, may exacerbate or mitigate their physiological impacts (Mkuye et al., 2022). MNPs' capability to impair essential biological functions, when combined with other stressors, could potentially propagate adverse effects beyond the organismal level. One potential major problem is the ability of MNPs to accumulate toxic compounds, either adsorbed from the environment or retained during manufacturing processes (Barría et al., 2025). Contaminated PE and PS have been reported to transfer polycyclic aromatic hydrocarbon (PAHs) to exposed mussels, increasing bioavailability post-ingestion and inducing toxicological effects at molecular and cellular levels (Avio et al., 2015). In some cases, MNPs may reduce the bioavailability of other organic compounds, depending on

inherent particle properties, and interactions within the exposure medium and the organism. This highlights the need for further research on MNP-contaminant interactions across diverse scenarios (Tang, 2021).

3.5 Conclusions, Limitations, and Future Directions

This study provides an integrative analysis of the cellular and tissue-level responses of the blue mussel (*M. edulis*) to aged PET MNP under environmentally relevant conditions, offering valuable insights into the underlying mechanisms of toxicity associated with aged particles. Current findings revealed the sensitivity of hemocyte subpopulations, including granulocytes and hyalinocytes, following exposure to aged PET MNPs. Concentration- and time-dependent changes in lysosomal stability, oxidative activity, and hemocyte mortality were observed, demonstrating both immediate cellular perturbations and recovery potential to alleviate particle-induced effects. Histopathological analysis indicated significant alterations, particularly in the gill tissues, suggesting potential impairment of essential physiological functions. No mortality or significant changes in growth metrics were observed in mussels following exposure to aged PET MNPs. Notably, the magnitude of these observed responses aligns with those reported for different types of MNPs and other materials, under similar exposure concentrations and durations.

While this study provides valuable insights into the physiological responses associated with aged MNP exposure, certain limitations must be acknowledged. The detection and quantification of aged MNPs in complex matrices remain a challenge due to analytical constraints (Cunningham et al., 2023; da Costa et al., 2019). Although techniques such as Nile red staining coupled with machine learning have shown potential for detecting MNPs in mussel tissues, the recently developed polymer identification model (PIM) exhibited lower predictive accuracy for PET particles compared to other polymers. PIM is a semi-automated technique designed to classify four polymer categories (PE/PP, PS, PET, and PVC) through fluorescent particle staining following tissue digestion and filtration (Meyers et al., 2024). Histopathological indices, while informative and effective, may not detect rare and early-stage precursor lesions linked to particle exposure. Long-term mechanistic studies are needed to assess a broader range of sub-lethal effects associated with aged MNPs, including immunotoxicity, reproductive and transgenerational toxicity, as well as to elucidate potential recovery processes following chronic exposure (T. He et al., 2023; Yi et al., 2024). Importantly, future research should incorporate environmentally relevant exposure scenarios, particularly co-exposure with other contaminants (e.g., persistent organic pollutants) (T. Wang et al., 2020) and global change-related stressors (e.g., ocean warming and acidification) (Catarino et al., 2022), to better capture potential synergistic or antagonistic interactions that may modulate toxicity outcomes. These efforts are essential for understanding the combined effects of these stressors and conducting robust risk assessments for aged MNP exposure (Cunningham et al., 2023).

3.6 Acknowledgements

Test particles and the primary characterization were supplied by the Joint Research Centre (JRC), with the support of John Seghers, Håkan Emteborg, and Claudia Cella. We thank the experts at the Antwerp Centre for Advanced Microscopy (Sofie Thys, Isabel Pintelon, and Prof. Jean-Pierre Timmermans) for their invaluable support with tissue processing and histopathological analysis. We also appreciate the help of András Retzler, Allen Jun Anies, and Moses Ndugwa with mussel sample collection.

Chapter 4

Differential Sensitivity of Hemocyte Subpopulations (*Mytilus edulis)* to Aged Polyethylene Terephthalate Micro- and Nanoplastic Particles

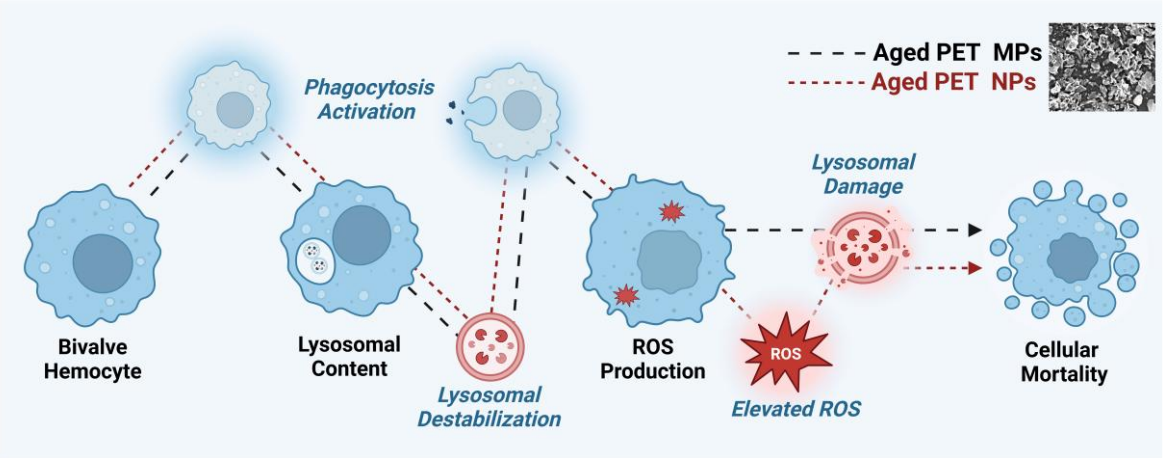

Published as:

Hara, J., Vercauteren, M., Schoenaers, S., Janssen, C. R., Blust, R., Asselman, J., & Town, R. M. (2024). Differential sensitivity of hemocyte subpopulations (*Mytilus edulis*) to aged polyethylene terephthalate micro-and nanoplastic particles. *Ecotoxicology and Environmental Safety*, 286, 117255. https://doi.org/10.1016/j.ecoenv.2024.117255.

Abstract

Bivalve hemocytes, particularly granulocytes and hyalinocytes, play a crucial role in cell-mediated immunity. However, their interactions with aged plastic particles, exhibiting altered properties that more closely resemble those in natural environments, remain largely underexplored. This study assesses the differential responses of hemocyte subpopulations *(Mytilus edulis)* to chemically aged polyethylene terephthalate (PET) microplastic (MPs) and nanoplastic (NPs) particles across multiple cellular effect endpoints. Particle characteristics were analyzed using Single Particle Extinction and Scattering, Raman Spectroscopy, Scanning Electron Microscopy, and Dynamic Light Scattering. *In vitro* experiments with aged PET MPs (1.9 µm) and NPs (0.68 µm) were conducted at three internally relevant concentrations: 10 (C1), 10^3 (C2), and 10^5 particles/mL (C3). Cellular responses were assessed by measuring lysosomal content stability, reactive oxygen species (ROS) production, cellular mortality, and morphological parameters using flow cytometry at 6, 12, 24, and 48 hours. Our findings provide mechanistic insights into the differential sensitivities of granulocytes and hyalinocytes to aged PET, influenced by particle size and concentration. Specifically, aged PET MPs and NPs induce distinct size and concentration-dependent patterns of lysosomal destabilization, coinciding with the loss of functional integrity. Elevated ROS levels were observed only in granulocytes and hyalinocytes exposed to high concentrations of aged PET NPs, underscoring the effects on oxidative stress. Both aged PET MPs and NPs induce significant increases in cellular mortality, particularly after 24 h of exposure at high concentrations. These findings reveal the complex cellular mechanisms underlying hemocyte functional impairment following exposure to aged PET particles under environmentally and biologically relevant conditions.

Keywords: Aged PET, Hemocytes, *In vitro*, Functional assays, Immunotoxicity

4.1 Introduction

Plastic pollution, particularly in the form of micro- and nanoplastic particles, is prevalent in the environment, raising concerns about its adverse effects on aquatic organisms (L. Liu et al., 2024). These particles mainly originate from two sources: the direct discharge of primary MPs into the environment and the degradation of larger plastic materials, resulting in the formation of secondary particles (N. Ali et al., 2024). While there is a growing body of research documenting various biological responses to plastic particle exposure, systematic analyses of effect endpoints at the cellular level remain limited (Prinz & Korez, 2020). Yet, this information is crucial for understanding the fundamental pathways and mechanisms of exposure and determining how MPs and NPs pose health risks (Sharifinia et al., 2020).

Innate immunity, the primary defense mechanism in invertebrates, is integral for overall functioning (Canesi & Procházková, 2014). It affects various biological aspects, including histopathology, bioenergetics, and susceptibility to infections, which can ultimately lead to mortality (Kataoka & Kashiwada, 2021). Invertebrate immune cells, particularly hemocytes of bivalve mollusks, play a crucial role in cell-mediated immunity and serve as valuable models for investigating particle-induced responses (Canesi & Procházková, 2014). Different subpopulations of hemocytes, such as granulocytes and hyalinocytes, exhibit distinct morphological and functional characteristics (Le Foll et al., 2010), including internal cell signaling pathways that regulate various cellular processes (Canesi et al., 2006). Granulocytes are the dominant cell type in the hemolymph of *Mytilus spp*., characterized by high phagocytic activity and oxyradical production, whereas hyalinocytes have lower phagocytic ability (Le Foll et al., 2010). Phagocytosis, one of the critical immune defense functions of these specialized cells, regulates the internalization of particles (>0.5 µm in diameter), such as pathogens, apoptotic bodies, and other foreign materials (Rosales & Uribe-Querol, 2017). Phagocytosis typically occurs concomitantly with autophagy, a lysosome-based degradative pathway essential for maintaining cellular homeostasis (Gustafson et al., 2015). However, dysregulation of autophagy can compromise lysosomal stability, disrupt homeostasis, and lead to oxidative stress, inflammation, and mitochondrial dysfunction. These cellular disturbances can ultimately trigger cell death pathways, potentially resulting in adverse effects at the organismal level (Stern et al., 2012). Extensive literature has documented the effects of various particles, including metallic, ceramic, and polymeric nanoparticles, on cellular systems. These studies revealed that micro and nanoparticles can induce a range of cellular responses, from uptake and processing to adverse toxicological outcomes (Stern et al., 2012). The interactions of particles with cells and the resulting biological effects are significantly influenced by physicochemical properties, including particle size, shape, surface charge, and composition (Foroozandeh & Aziz, 2018b). Despite the recognized capability of various particles, including plastic particles, to penetrate biological membranes and affect cellular

mechanisms, significant gaps remain in understanding systemic toxicity, particularly concerning the immune system (Sharifinia et al., 2020).

The intricate response pathways and regulatory networks governing cellular stress and death offer multiple targets for comprehensive toxicological studies (Simmons et al., 2009), taking into account various physicochemical properties. However, numerous studies have raised concerns regarding the environmental relevance of plastic particles employed in laboratory experiments (Karami, 2017). Previous studies investigating the effects of MPs and NPs have predominantly utilized PS spheres or beads and often involve unrealistic exposure conditions (Ferreira et al., 2019), including simplified particle sizes, shapes, and concentrations that do not reflect real-world scenarios. This narrow focus limits the understanding of the broader impact of plastic pollution, as it overlooks the environmental relevance and potential toxicity of other polymers, such as PET. For instance, PET is one of the most prevalent polymer types in the marine environment (Ashrafy et al., 2023) and is commonly ingested by filter-feeding organisms, particularly mussels (Pequeno et al., 2021; Qu et al., 2018). Studies have reported that ingested MPs accumulate in the hemolymph of mussels, with smaller particles (3.0 µm) being more abundant than larger ones (9.6 µm) and persisting in the circulatory system for over 48 days (Browne et al., 2008). Using concentrations that match those detected internally, such as in the hemolymph of mussels, is crucial for a more accurate assessment of biological responses.

Additionally, the aging and weathering of plastic particles introduce critical variables that significantly affect the interaction with biological systems (Q. Lu et al., 2023). Through processes such as photodegradation, physical abrasion, and chemical degradation, aged and weathered particles acquire altered surface and physicochemical properties (W. He et al., 2023). These changes can potentially lead to heightened toxicological profiles compared to their pristine counterparts (Völkl et al., 2022). Modifications induced by particle aging, particularly in size, shape, and surface properties, can enhance particle-cell interactions, thereby influencing cellular uptake mechanisms and toxicity profiles (Foroozandeh & Aziz, 2018b). Using aged particles is crucial to accurately reflect actual environmental conditions (Revel et al., 2021), where particles are rarely pristine and often undergo significant transformations before interacting with biological systems.

To address existing knowledge gaps, this study investigated the responses of hemocyte subpopulations to chemically aged polyethylene terephthalate micro- and nanoplastic particle exposure across multiple cellular effect endpoints. Specifically, hemocytes extracted from blue mussels (*Mytilus edulis*) were exposed to aged PET particles with two distinct size ranges and three concentrations, chosen to reflect both environmentally and biologically relevant conditions. Cellular responses (lysosomal content stability, ROS production, cellular mortality) and morphological parameters (cell size and complexity), were assessed using flow cytometry at various time points. By integrating responses related

to particle size, concentration, and exposure time, this study provided insights into the critical cellular mechanisms underlying the effects of exposure to aged plastic particles.

4.2 Materials and Methods

4.2.1 Characterization of the aged PET Micro- and nanoplastic particles

Aged PET MPs and NPs with irregular shapes and heterogeneous sizes were obtained through mechanical cryomilling and chemical aging through treatment with potassium hydroxide solution (KOH) combined with sonication. The procedures applied for the particle aging process are described in the previous chapter (Section 3.2.1), while more detailed methodological information is provided in Seghers et al. (2025). The primary stock suspensions with particles smaller than 5 µm were processed and provided by the Joint Research Centre (JRC) of the European Commission. To isolate the particles in the sub-micrometer range, the suspension was sonicated for 20 minutes, sedimented for 12 h, and filtered through a 1 µm membrane filter.

The polymer composition, size, shape, and concentration of the particles in the stock solution were confirmed using Raman spectroscopy (reference library Open Specy), scanning electron microscopy (SEM, Phenom™ ProX Desktop), and the single particle extinction and scattering (SPES, Classizer™ ONE) technique (Supplementary Figures A4.1 - A4.3). Two different size ranges of aged PET were utilized: MPs with an average diameter of 1.9 µm (D_{10} = 0.6 µm; D_{50} = 1.4 µm and D_{90} = 3.1 µm) and NPs with an average diameter of 0.68 µm (D_{10} = 0.39 µm; D_{50} = 0.57 µm; and D_{90} = 1.1 µm). D_{10}, D_{50}, and D_{90} represent percentile values from the cumulative particle size distribution analyzed using SPES, indicating the size below which 10%, 50%, and 90% of the particles are found (Supplementary Figure A4.1 (Panel A and B and Table A4.1). Stock solutions contained 4.0×10^7 and 1.66×10^7 particles per mL (denoted as P/mL), respectively. Aged PET particles were suspended in Milli-Q water without surfactant. The Raman spectroscopy results, verified using the Open Specy reference library, showed a high spectral match score of 0.97 for aged PET MPs and 0.94 for aged PET NPs with the reference spectrum (Supplementary Figure A4.2). Complementary SEM images confirmed the irregular shapes of particles, providing visual evidence of the particle morphology (Supplementary Figure A4.3).

Secondary characterization of the aged PET MPs and NPs was conducted using Dynamic Light Scattering (DLS, Zetasizer Nanoseries, Malvern Instruments) at various time points (1 h, 24 h, and 48 h) to ensure particle stability under conditions adopted for the *in vitro* exposure experiments (Supplementary Figure A4.4, Panel A–D). Surfactant-free stock suspensions were sonicated for 20 min before dilution to 10^5 P/mL in 10 mL sterile glass containers containing filtered (100 nm, Millipore) media: ultrapure water (UW), culture media (CM), or hemolymph serum (HS; 1:2, serum:CM). Following incubation at 15°C, the hydrodynamic size and electrophoretic mobility were measured at 1, 24, and 48 h in folded

capillary cells. Electrophoretic mobility was determined under a constant direct current electric field of 50 V/cm, and the corresponding zeta (ζ) potential was calculated by the instrument software using the Henry equation. Reference standards (ZTS1240, Malvern Panalytical) were included in the analytical process for quality control. Triplicate measurements were performed at each time point. Aged PET MPs and NPs showed mean Z-average (*d*, nm) of 536.3 nm and 294.3 nm in UW, respectively. In CM, aged PET MPs displayed higher size variability, whereas NPs remained relatively uniform. Both particle types exhibited consistently reduced sizes in hemolymph serum, indicating distinct interaction profiles with this medium (Supplementary Figure A4.4, Panel A). The average polydispersity index (PDI) values ranged from 0.27–0.76 (MPs) and 0.25–0.59 (NPs) (Panel B), reflecting moderate to high polydispersity consistent with broad particle size distributions observed. The ζ-potential values for both MPs and NPs were consistently negative across all conditions (Panel C–D), ranging from -30.2 to -35.0 mV in UW, -12.2 to -21.2 mV in CM, and -5.9 to -8.7 mV in HS, consistent with trends in electrophoretic mobility.

4.2.2 Maintenance of the mussel culture

Adult mussels (*Mytilus edulis)* were collected from the Scheldt Estuary in Hoedekenskerke, Netherlands. Mussels were kept in a glass aquarium with artificial seawater (hw-Marinemix Professional), equipped with portable aeration (Eheim Air Pump 400) and mechanical-biological filtration (Eheim Biopower 200) systems. The temperature was maintained at 15 ± 0.4°C with a photoperiod (12:12 h). The mussels were fed daily with microalgae suspension (*Tetraselmis suecica*, Tetraprime S Proviron), with the water inflow interrupted for 2 hours during feeding. Water was replaced by 50% daily, and quality parameters (pH (8.08 ± 0.05), salinity (30.9 ± 0.5‰), dissolved oxygen (8.12 ± 0.21 mg/L), ammonia (0.25 mg/L, nitrite (<0.3 mg/L), and nitrate (12.5 mg/L) were monitored using Hach HQ40D meters and Tetra test kits. Prior to experimental procedures, the mussels were acclimatized and depurated under laboratory conditions for a minimum period of three weeks. No mortality was observed under these conditions.

4.2.3 Hemolymph extraction and cell culture preparation

A total of 80–100 adult mussels, with shell lengths of 4–6 cm, were selected for hemolymph extraction and cell culture following established protocols (Katsumiti et al., 2017). Mussels were anesthetized for 30 minutes using a filtered (100 nm, Millipore) and sterilized 0.3 M magnesium chloride ($MgCl_2$) solution within a laminar airflow cabinet (Spetec). Hemolymph was extracted from the posterior abductor muscle using a sterile 2 mL syringe (Injekt) with a 23G needle (Terumo Neolus). The extracted hemolymph was pooled, filtered through a 70 µm cell strainer (Greiner) to eliminate impurities and aggregates, and then diluted at a 9:1 ratio in an anti-aggregation solution (171 mM NaCl; 0.2 M Tris; 0.15% v/v HCl 1N; 24 mM EDTA, with reported > 95% viability (Katsumiti et al., 2017)). The concentration and purity of the cell suspension were verified using a hemocytometer (MUHWA Scientific, Neubauer), microscope (Nikon, Eclipse LV100N POL),

and flow cytometer (BD Biosciences). Cell suspensions were then seeded into pre-labeled 24-well glass bottom microplates (Greiner Bio-one) and maintained in filtered (0.2µm; Millipore) culture media (Basal Medium Eagle (BME), Sigma Aldrich) supplemented with L-Glutamine and an antibacterial agent (0.001% Gentamicin). Strict aseptic techniques were maintained throughout the procedure to prevent contamination.

4.2.4 *In vitro* exposure experiments

The experiment employed a full factorial design, comprising two aged PET particle size ranges and three concentrations: 10 P/mL (C1); 10^3 P/mL (C2); and 10^5 P/mL (C3). These chosen particle properties align with the reported concentration ranges and represent the most abundant size classes of accumulated plastic particles in the hemolymph of mussels (Browne et al., 2008). Initially, working solutions (10^6 P/mL) of MPs and NPs were separately prepared in culture media and diluted to obtain the desired exposure concentrations. Suspensions were systematically sonicated for 20 minutes to ensure uniform particle dispersion before use.

The *in vitro* exposure experiment was carried out using pooled hemocytes suspended in culture media with a cell concentration of 1.0×10^6 cells/mL and incubated at 15°C. This selected cell concentration has been effectively applied in previous *in vitro* experiments with various test particles (Katsumiti et al., 2021), compounds (Bouki et al., 2013; Katsumiti et al., 2017), and microbial challenges (Tanguy et al., 2018). Each treatment was conducted in triplicate and cells were incubated under stable culture conditions for 6 h, 12 h, 24 h, and 48 h. Treatments included a pure culture medium as the negative control (NC) and a culture medium containing varying concentrations of aged PET MPs and NPs. Adequate positive control treatments were included for each measured parameter (see below). At each sample time, cells were collected from the culture wells and washed twice with phosphate-buffered saline (PBS) before analysis.

4.2.5 Assessment of cellular endpoints

Cellular endpoints were measured to assess the effect of aged PET MPs or NPs exposure on hemocyte subpopulations using fluorescent labeling and flow cytometry with BD™ LSR II (BD Biosciences).

4.2.5.1 Cellular morphology

Morphological changes in hemocytes were detected using the side scatter (SSC) and forward scatter (FSC) detectors of the flow cytometer, which are parameters based on cell size and internal complexity (Sendra, Carrasco-Braganza, et al., 2020). Data on morphological parameters are expressed in arbitrary units (A.U.).

4.2.5.2 Lysosomal stability

Lysosomal stability was assessed using the LysoTracker™ Blue DND-22 (Invitrogen), a cell-permeable dye applicable for labeling and tracing acidic organelles such as lysosomes (Wang et al., 2019). Hydrogen peroxide (H_2O_2, 100 µM) was used as a positive control to induce cellular stress conditions impacting lysosomal stability (Brunk et al., 1995). Cell samples were suspended in PBS with 75 nM LysoTracker™ and incubated in the dark at 15°C for 1 h. Fluorescence was measured with the flow cytometer at excitation and emission wavelengths of 373 nm and 422 nm, respectively. Intracellular lysosomal content is expressed as the mean geometric fluorescence in hemocyte subpopulations relative to the negative control (set to 100%).

4.2.5.3 Reactive oxygen species (ROS) production

Intracellular ROS production was assessed using the 5-(and-6)-chloromethyl-2',7'-dichlorodihydrofluorescein diacetate acetyl ester (CM-H_2DCFDA, Invitrogen), dissolved in dimethylsulfoxide (DMSO) (M. Yang & Wang, 2022). As a positive control, oxidative activity was induced using H_2O_2 at a sub-lethal concentration of 100 µM (Brunk et al., 1995; Sendra, Carrasco-Braganza, et al., 2020). Cell samples were suspended in PBS with 10 µM CM-H_2DCFDA and incubated in the dark at 15°C for 1 h. DCF green fluorescence was measured with the FITC signal detector (FL1) of the flow cytometer. ROS production is expressed as the mean geometric fluorescence in hemocyte subpopulations relative to the negative control (set to 100%).

4.2.5.4 Hemocyte mortality

Cellular mortality was assessed using Propidium Iodide (PI; Abcam), following the manufacturer's protocol with modifications (Wang et al., 2019). As positive controls, cells were incubated with Cadmium Chloride ($CdCl_2$, 800 µM) to induce cellular death (PC CT) (Olabarrieta et al., 2001). Additionally, sonication for 1 h was included as a second non-chemical positive control (PC ST). Cell samples were suspended in 500 µl of binding buffer with 5 µl of PI (50 µg/mL), and incubated in the dark at 15°C for 5–10 min. Fluorescence was measured with excitation and emission wavelengths of 535 nm and 617 nm, respectively. Data were expressed as the percentage (%) of non-viable cells relative to the total cell count per hemocyte subpopulation.

4.2.6 Flow cytometry analysis

Flow cytometry, a fluorescence-based technology, was used to identify and characterize hemocyte subpopulations, such as granulocytes and hyalinocytes. Analysis was performed using a BD™ LSR II flow cytometer (BD Biosciences) equipped with 488 nm (blue), 633 nm (red), 405 nm (violet), and 355 nm (UV) lasers. Hemocyte subpopulations were detected using SSC and FSC parameters, based on cell size and complexity. Initially, unexposed hemocytes served as a baseline to establish the normal SSC and FSC profiles, ensuring measurements were unaffected by potential interference from plastic particles. A gating

technique using the SSC vs. FSC dot plots was then employed to distinguish the sub-population of interest (Supplementary Figure A4.5). A total number of 10,000 cells was analyzed in each sample replicates. Regular calibration was performed using calibration beads to ensure accurate parameter measurement throughout the experiment. Data were processed using FACSDiva™ Software (Version 5.0) and FlowJo (Version 10.9.0).

4.2.7 Statistical analysis

The normal distribution of the data was assessed using the Shapiro-Wilk test and homogeneity of variances was evaluated using the Brown–Forsythe test. The effects of particle size and concentration of aged PET MPs and NPs were analyzed by two-way analysis of variance (ANOVA). If interactions between factors were identified, significant effects of particle size, concentration, and time were further examined either using a one-way ANOVA or the non-parametric Kruskal-Wallis test, based on normality assessment of the data. Pairwise comparisons were performed with Tukey's HSD post-hoc test (Wang et al., 2019). Differences were considered significant at $p < 0.05$. All analysis was conducted using GraphPad Prism (Version 10.1.2). The graphical abstract was created with BioRender.com.

4.3 Results

The responses of hemocyte subpopulations to various concentrations of aged PET MPs and NPs across multiple cellular effect endpoints are described in detail in the following sections and summarized in Supplementary Table A4.2.

4.3.1 Cellular morphology (size and complexity)

Granulocytes and hyalinocytes exposed to increasing concentrations of aged PET MPs and NPs showed no significant changes in cell size (Figure 4.1) and complexity (Figure 4.2) over 6, 12, 24, and 48 h.

4.3.2 Lysosomal stability

Analysis of lysosomal content in hemocytes after exposure to different concentrations of aged PET MPs and NPs revealed distinct size-specific and concentration-dependent patterns of destabilization (Figure 4.3).

Granulocytes exposed to aged PET MPs showed a size-specific increase in lysosomal content at 12 h and 48 h of exposure (Figure 4.3, panel A). Particularly, concentration-dependent increases of 43.2% and 45.5% at C2 ($p = 0.045$) and C3 ($p = 0.030$) compared with the control were observed after 48 h. Among the NP-treated groups, only the highest aged PET NP concentration (C3) induced a significant increase in lysosomal content at 24 h, by 78.7% and 76.5% compared to the control ($p = 0.020$) and C1 ($p = 0.024$).

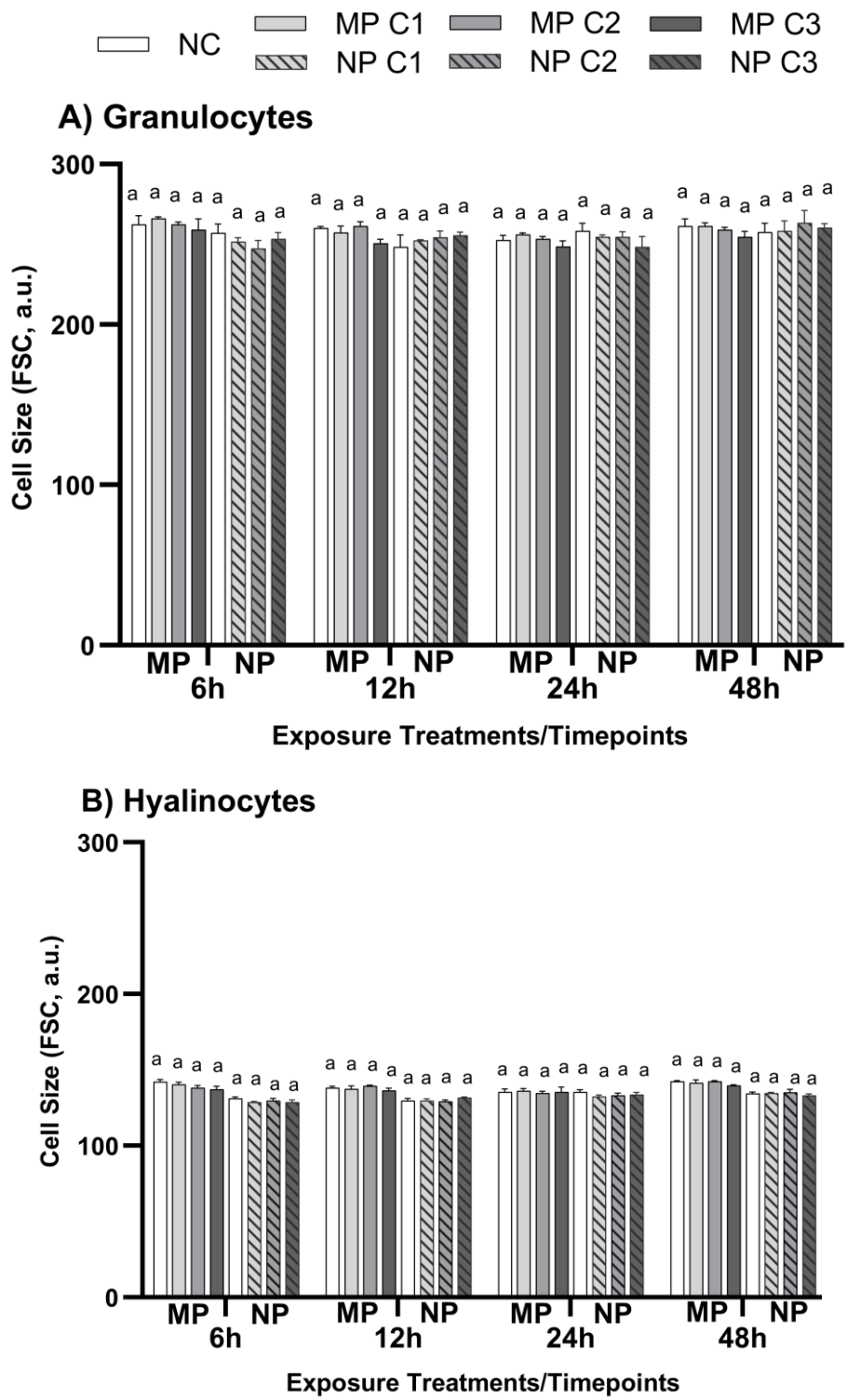

Figure 4.1. *Cell size (Forward Scatter, FSC, expressed in arbitrary units) in (A) granulocytes and (B) hyalinocytes exposed to different concentrations of aged PET microplastic (MP) and nanoplastic (NP) particles over 6, 12, 24, and 48 h. Data are expressed as mean ± SD (n = 3). Different lower-case letters at each fixed MP or NP treatment denote significant differences among concentrations at each time point ($p < 0.05$). Asterisks indicate significant differences between particle sizes at each concentration per time point (*$p < 0.05$; **$p \leq 0.01$; ***$p \leq 0.001$).*

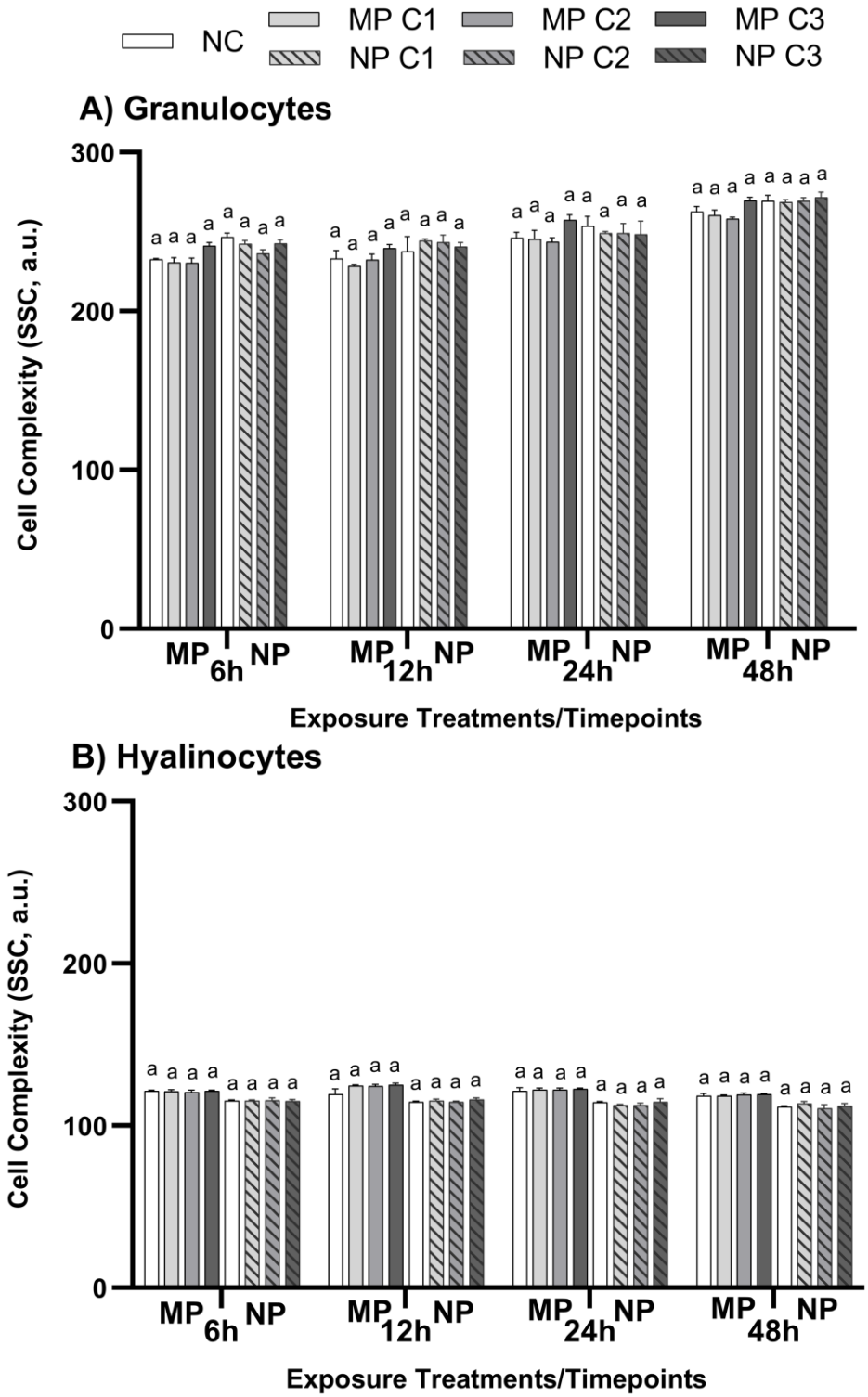

Figure 4.2. *Cell complexity (Side Scatter, SSC, expressed in arbitrary units) in (A) granulocytes and (B) hyalinocytes exposed to different concentrations of aged PET microplastic (MP) and nanoplastic (NP) particles over 6, 12, 24, and 48 h. Data are expressed as mean ± SD (n = 3). Different lower-case letters at each fixed MP or NP treatment denote significant differences among concentrations at each time point ($p < 0.05$). Asterisks indicate significant differences between particle sizes at each concentration per time point (*$p < 0.05$; **$p \leq 0.01$; ***$p \leq 0.001$).*

Interestingly, a relatively lower lysosomal content was observed in all NP-treated groups after 48 h, though not significantly different from the concurrent control. Hyalinocytes exhibited a variable lysosomal response to aged PET particle exposure (Figure 4.3, panel B). In MP-treated groups, a concentration-dependent elevation in lysosomal content was observed only at 48 hours, with MP C2 (p = 0.015) and C3 (p = 0.026) inducing increases of 54.3% and 50.9%. While in hyalinocytes exposed to NPs, no significant changes in lysosomal content were observed across all time points. Similar trends of relatively lower lysosomal content were evident after 48 h of NP exposure, though not statistically significant.

As the positive control, H_2O_2 induced an abrupt increase in lysosomal content in both hemocyte subpopulations ($p < 0.05$), followed by a stabilization over time (Supplementary Figure A4.6, Panel A and B).

4.3.3 Oxidative activity

ROS levels in granulocytes exposed to various aged PET MP concentrations did not show significant differences across all time points (Figure 4.4, panel A). In contrast, exposure to aged PET NPs resulted in a significant increase in ROS production only at the highest concentration (C3) at 24 h, with a 45.5% increase compared to the control (p = 0.047). Similarly, hyalinocytes exposed to various MP concentrations did not exhibit significant differences in ROS production compared to the control (Figure 4.4, panel B). However, exposure to NPs resulted in a significant increase in ROS production of 184% only at the highest concentration (C3) at 24 h (p = 0.009).

The positive control with H_2O_2 induced significant changes ($p < 0.05$) in ROS levels in granulocytes only at 6 h, while no significant changes were observed in hyalinocytes (Supplementary Figure A4.6, Panel C and D).

4.3.4 Hemocyte mortality

The results demonstrated a significant adverse effect of aged PET exposure on hemocyte mortality, with a concentration- and time-dependent increase in PI-positive cells (Figure 4.5). Specifically, aged PET MP concentrations C2 and C3 significantly increased granulocyte mortality to 15.9% (p = 0.021) and 16.5% (p = 0.007), respectively, compared with the control (11.6%). These correspond to percentage increases of approximately 37.8% and 42.9% after 24 h of exposure. No significant concentration-dependent changes in mortality were observed 48 h post-exposure to MPs, though C2 exhibited the highest rate among all tested concentrations (Figure 4.5, panel A). Among the NP-treated groups, only C3 induced a significant increase in granulocyte mortality to 17.6% (p = 0.016) compared with the control (13.0%) at 24 h, corresponding to a 35.0% increase. After 48 h exposure, NP C3 remained elevated although not statistically significant.

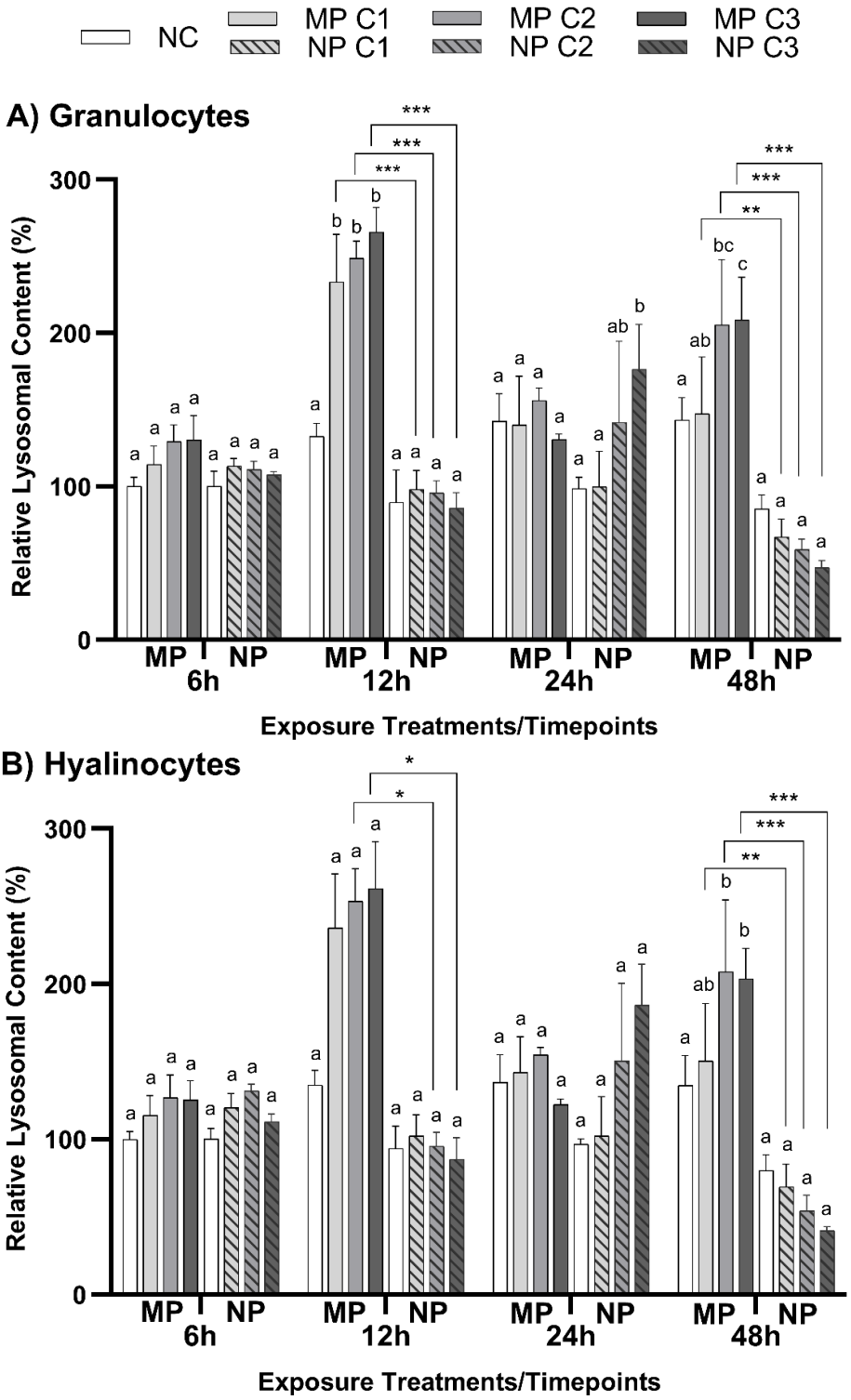

Figure 4.3. *Relative lysosomal content in (A) granulocytes and (B) hyalinocytes exposed to different concentrations of aged PET microplastic (MP) and nanoplastic (NP) particles (C1:10 P/mL; C2: 103 P/mL; C3: 105 P/mL) over 6, 12, 24, and 48 h. Data are expressed as mean ± SD (n = 3). Different lower-case letters at each fixed MP or NP treatment denote significant differences among concentrations at each time point (p < 0.05). Asterisks indicate significant differences between particle sizes at each concentration per time point (*p < 0.05; **p ≤ 0.01; ***p ≤ 0.001).*

In hyalinocytes (Figure 4.5, panel B), only the highest MP concentration (C3) significantly increased mortality to 13.0% compared with the control (8.42%) at 24 h (p = 0.039), corresponding to a 54.5% increase compared to the control cells. Although there were increments in mortality rates at higher concentrations after 48 h, no significant concentration-dependent differences between MPs and NPs were observed in hyalinocytes. The positive controls, PC ST (sonication treatment, $p < 0.0001$ in both hemocyte subpopulations) and PC CT (chemical treatment, $p < 0.0001$ in granulocytes and $p < 0.05$ in hyalinocytes), exhibited a high number of PI-positive cells, particularly after 24 h. This indicates high mortality rates and validates the sensitivity of the assay (Supplementary Figure A4.7, Panel A and B).

4.4 Discussion

Hemocytes serve as the first line of defense against contaminants in bivalves, making them a crucial model for evaluating the effects of MPs and NPs on immune functions (Canesi & Procházková, 2014). This study aimed to elucidate how these particles, particularly aged PET, affect hemocyte subpopulations through the analysis of multiple cellular effect endpoints. Key findings revealed differential sensitivities of hemocyte subpopulations, influenced by particle size, concentration, and exposure time.

4.4.1 Morphological characterization of hemocyte subpopulations

Flow cytometry enabled the morphological differentiation of hemocyte subpopulations and quantitative assessment of cellular markers (Bajgelman, 2019). This technique effectively distinguished two distinct hemocyte subpopulations: granulocytes, characterized by larger cell size and higher internal complexity, and hyalinocytes, with smaller size and lower complexity (Le Foll et al., 2010). Exposure to increasing concentrations of aged PET MPs and NPs did not induce significant changes in cell size or complexity for both subpopulations over time. In contrast, exposure of hemocytes to different concentrations of PS NPs (100 nm and 1 µm) resulted in significant changes in cell size, while no corresponding changes in cell complexity were observed (Sendra, Carrasco-Braganza, et al., 2020). In another cell type, exposure to 50 nm amine-modified polystyrene (NH_2-PS-NPs, 50 µg/mL or 7.28×10^{11} P/mL converted concentration in Supplementary Table A4.3) did not alter cell size but increased complexity over time, likely due to enhanced vacuolization (Wang et al., 2013).

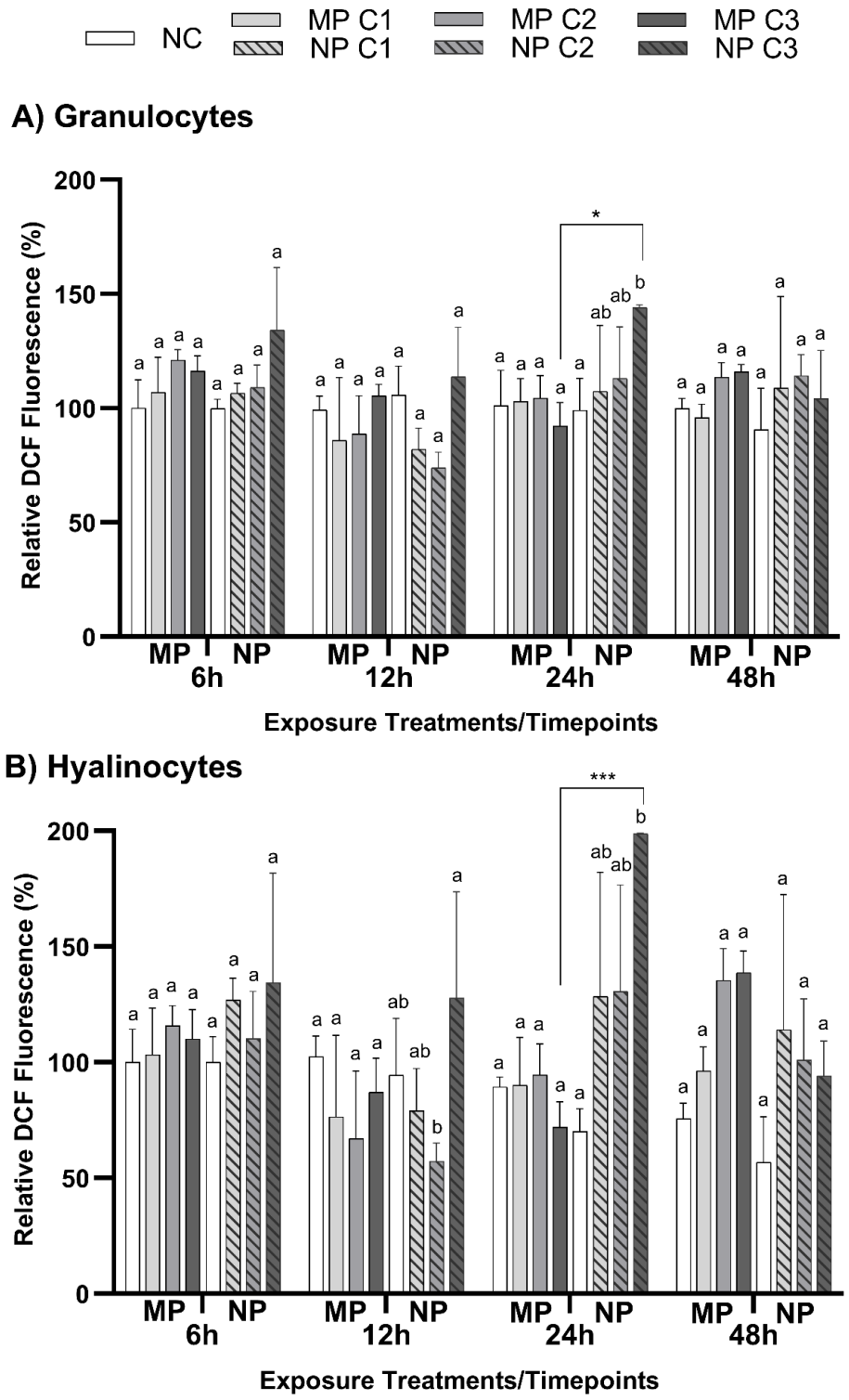

Figure 4.4. *Relative reactive oxygen species (ROS) production in (A) granulocytes and (B) hyalinocytes exposed to different concentrations of aged PET microplastic (MP) and nanoplastic (NP) particles (C1:10 P/mL; C2: 103 P/mL; C3: 105 P/mL) over 6, 12, 24, and 48 h. Data are expressed as mean ± SD (n=3). Different lower-case letters at each fixed MP or NP treatment denote significant differences among concentrations at each time point ($p < 0.05$). Asterisks indicate significant differences between particle sizes at each concentration per time point (*$p < 0.05$; **$p \leq 0.01$; ***$p \leq 0.001$).*

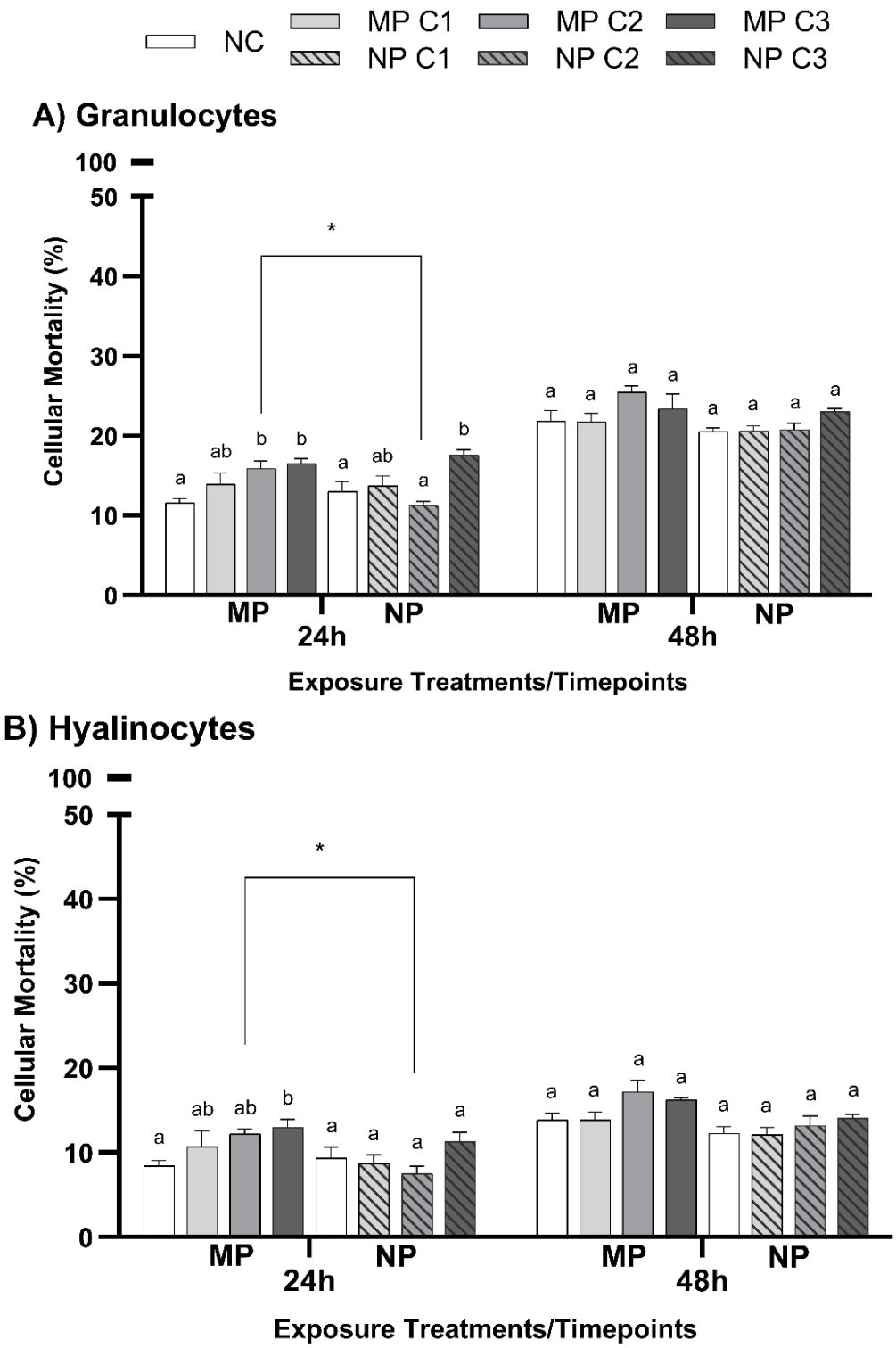

Figure 4.5. *Cellular mortality in (A) granulocytes and (B) hyalinocytes exposed to different concentrations of aged PET microplastic (MP) and nanoplastic (NP) particles (C1:10 P/mL; C2: 103 P/mL; C3: 105 P/mL) over 24 h and 48 h. Data are expressed as mean ± SD (n=3). Different lower-case letters at each fixed MP or NP treatment denote significant differences among concentrations at each time point ($p < 0.05$). Asterisks indicate significant differences between particle sizes at each concentration per time point (*$p < 0.05$; **$p \leq 0.01$; ***$p \leq 0.001$).*

4.4.2 Lysosomal destabilization in response to aged PET exposure

This study reveals distinct patterns of lysosomal destabilization influenced by particle size and concentration. As observed, exposure to aged PET MPs resulted in progressive fluctuations in lysosomal content across hemocyte subpopulations at higher concentrations. Aged NP exposure significantly increased lysosomal content in granulocytes at the highest tested concentration, followed by a subsequent reduction after prolonged NP exposure, suggesting potential alterations in lysosomal membrane integrity. For this analysis, the acidotropic dye LysoTracker was used to label acidic cellular compartments, primarily lysosomes. Fluctuations in LysoTracker fluorescence intensity indicate changes in lysosomal pH, membrane permeabilization, and overall functionality (Gaudioso et al., 2022; Oberle et al., 2010). Similar patterns were observed in embryonic zebrafish fibroblast cell lines exposed to different sizes of NH_2-PS-NPs beads. Larger-sized particles (1000 nm, 20 µg/mL or 3.64×10^7 P/mL) have been reported to induce acidification of the lysosomal compartment, whereas smaller-sized NPs (100 nm, 20 µg/mL or 3.64×10^{10} P/mL) exhibited a decrease in fluorescence within 3–9 h post-exposure, both coinciding with the loss of lysosomal integrity (M. Yang & Wang, 2022). This reduction can be attributed to the leakage of proteolytic lysosomal enzymes into the cytosol, causing alkalization and lysosomal dysfunction (Lunov et al., 2011).

Additionally, the observed changes in lysosomal stability suggest that hemocytes undergo activation of phagocytic machinery in response to particle exposure. The activation of phagocytic pathways refers to the cellular process where highly specialized phagocytes (Le Foll et al., 2010), such as granulocytes, recognize and internalize extracellular particles. Due to their active role in the intracellular digestion of foreign material, granulocytes have been reported to exhibit a substantially higher lysosomal content than hyalinocytes (Sendra, Carrasco-Braganza, et al., 2020). Engulfed particles are typically processed within the lysosomal compartment, where phagosomes fuse with lysosomes to form phagolysosomes for degradation (Rosales & Uribe-Querol, 2017). Several studies have confirmed particle localization within lysosomes. For instance, in mussel hemocytes exposed to 0.5 µm and 4.5 µm PS at 10^8 P/mL and 10^9 P/mL, particles were found inside membrane-bound phagolysosomal vesicles (Katsumiti et al., 2021). Similarly, in mouse macrophages, PET NPs (191.6 nm) were reported to exhibit higher uptake than other tested particles (160 nm and 1.30 µm LDPE, and 1.85 µm PET), accumulating in lysosomes and the cytosol but not in mitochondria or other organelles (Deng et al., 2022). This indicates a preferential uptake and irreversible accumulation of polymeric particles within lysosomal compartments, with no clear evidence of particle degradation or exit processes (Salvati et al., 2011). Another study demonstrated that PET NPs remain stable in a simulated lysosomal environment, even over extended periods of up to two months, highlighting their intracellular biopersistence and long-term stability (Magrì et al., 2018).

4.4.3 Oxidative stress induced by aged PET NPs

The marked increase in ROS production observed only with aged PET NPs, particularly at the highest concentration tested in this study, indicates a significant size-specific and concentration-dependent effect on oxidative stress. Oxidative stress occurs when ROS production exceeds the capacity of antioxidant defenses, including enzymes like glutathione peroxidase, catalase, and superoxide dismutase. This imbalance can abnormally activate cellular signaling pathways (Chaitanya et al., 2016). Previous studies have extensively reported heightened ROS production induced by various MPs and NPs as a key initiating event, potentially leading to irreparable oxidative damage. This size-dependent effect, particularly pronounced in aged PET NPs, is attributed to the increased surface-to-mass ratio, which enhances their ability to interact with and penetrate cellular components (Hu & Palić, 2020). Similarly, PP fragments aged through UV irradiation have been reported to induce nearly twice the ROS generation in hemocytes compared to pristine fragments, emphasizing the influence of particle aging on oxidative stress processes (Chelomin et al., 2024). Other carbon-based (C60 fullerenes), silicon-based (SiO_2), and metal oxide (TiO_2) NPs exhibited varying extents and time courses of ROS production in hemocytes, with SiO_2 reported to induce the highest concentration-dependent increase (Canesi et al., 2010). In RAW 264.7 macrophage cells, exposure to PET NPs (50–250 nm) with irregular shapes and sizes also led to a significant increase in intracellular ROS, but with no concentration-dependent correlation (Aguilar-Guzmán et al., 2022). These findings highlight that while particle size and concentration are crucial factors influencing ROS generation potential, their effects can vary across various cell types.

4.4.4 Mechanisms of hemocyte dysfunction induced by aged PET exposure

The significant increase in cellular mortality observed after 24 h of *in vitro* exposure highlights the concentration-dependent cytotoxicity of aged PET particles. The adverse effects were more pronounced at high concentrations, particularly in granulocytes, as shown by the increase in PI-positive cells. PI, which binds to DNA, only penetrates cells with compromised membranes, emitting red fluorescence that identifies dead cells regardless of the mechanism of cell death (Crowley et al., 2016). Similarly, a dose-dependent increase in hemocyte mortality was observed after 24 h of *in vitro* exposure to environmental NPs and MPs, mainly composed of PE with sizes ranging from 1 – 1.2 µm and 1.2 – 300 µm (Roman et al., 2023). Exposure to 50 nm PS-NH_2 significantly increased the percentage of hemocytes undergoing necrotic processes, detected after a shorter exposure duration of 45 min at the highest tested concentration (50 µg/mL or 7.28×10^{11} P/mL) (Canesi et al., 2015). In another study with virgin PS (1 µm), granulocytes were identified as the most affected hemocyte subpopulation, with a comparatively higher percentage of non-viable cells (36.3%) after 3 h of exposure (10 mg/L or 1.82×10^{7}) (Sendra, Carrasco-Braganza, et al., 2020). Exposure to environmental NPs and MPs (LDPE, PET, and PS) in mouse macrophages did not significantly induce cellular mortality, suggesting these cells can adapt to chronic exposure despite initial signs of dysfunction (Deng et al., 2022).

The findings of this study provide insights into the complex cellular mechanisms underlying hemocyte functional impairment following exposure to aged particles under environmentally and biologically relevant conditions. Initially, cellular defense mechanisms, involving lysosomal and phagocytic pathways, attempt to mitigate the cytotoxic effects, but these defenses become overwhelmed over time. This distinct induction of cellular dysfunction aligns with recent studies, such as those on embryonic zebrafish fibroblast cell lines, where NH_2-PS particles of different sizes induced varying lysosomal changes and ROS production, leading to different cell death mechanisms (M. Yang & Wang, 2022).

As a recognized mechanism of particle toxicity, lysosomal dysfunctions induced by particle exposure play a crucial role in modulating cellular death signaling pathways (Stern et al., 2012). Previous studies have highlighted the 'proton sponge' effect, where particles, especially those containing amine groups, absorb protons in the acidic lysosomal environment. This process leads to ion and water influx, causing lysosomal swelling and rupture and contributing to the induction of cytotoxicity (A. E. Nel et al., 2009). For instance, a time-resolved study demonstrated that the accumulation of NH_2-PS-NPs initiated these processes, ultimately inducing mitochondrial damage and apoptosis (Wang et al., 2013). Specifically, partial lysosomal membrane permeabilization (LMP) is linked to ROS induction and apoptosis, whereas massive LMP causes cytosolic acidification and necrosis (Stern et al., 2012). The effect on lysosomal functionality is not unique to polymeric particles, as negatively charged silica particles have also been linked to lysosomal injury and the release of lysosomal enzymes, which induce apoptosis in alveolar macrophages (Thibodeau et al., 2004). Thus, incorporating assays for lysosomal function into the biological screening system is essential for detecting pathological alterations associated with particle exposure (Xia et al., 2008).

4.4.5 Influence of weathering on particle-induced cellular responses

Moreover, the cellular effects of weathered particles can be linked to the accumulation of reactive groups and radicals on the surface. For instance, weathered polystyrene particles (2 µm at 150 µg/mL or 3.41×10^7 P/mL) have been observed to induce significantly higher ROS levels in murine macrophages compared to pristine counterparts (Völkl et al., 2022). Conversely, in THP-1 macrophages exposed to particles with size ranges of approximately 90 µm at 20,000 P/mL, pristine MPs induced higher cellular ROS levels compared to weathered polypropylene and polystyrene. As previously indicated, weathered particles have a higher binding affinity for serum proteins than pristine ones. These proteins act as ROS scavengers, neutralizing free radicals and thereby reducing the overall ROS generation potential of the weathered MPs (Jeon et al., 2021). Nevertheless, as another recognized mechanism of particle-induced systemic toxicity, the extent of ROS generation and its impact on cellular health are influenced by particle properties, cell types, and exposure conditions (Hu & Palić, 2020).

Previous studies indicated that the cytotoxic effects of plastic particle exposure could be partly attributed to leachable components, such as surfactants and residual monomers (Völkl et al., 2022). To minimize the compounding influence of leachable components, a surfactant-free particle stock suspension was used in this study. Although PET typically contains plasticizers such as di-n-propyl phthalate, diethyl phthalate (DEP), and di-n-butyl phthalate (DBP), it demonstrates enhanced stability compared to polymers with a carbon-only backbone (PP, PE, PS, and PVC) (Do et al., 2022). Extensive studies have shown that PET microplastics have slow rates of additive leaching and contain the lowest additive levels among tested polymers under environmental conditions (Bridson et al., 2023). Biological assessments in mussel hemocytes, particularly focusing on lysosomal membrane stability, revealed no significant impact from PET leachates. This suggests that the observed cytotoxicity is primarily driven by the particles themselves rather than by any leachate components (Capolupo et al., 2020).

4.5 Conclusions, Limitations, and Future Directions

This study provides mechanistic insights into how aged PET MPs and NPs affect both granulocytes and hyalinocytes by analyzing multiple cellular endpoints. Key findings reveal differential sensitivity among hemocyte subpopulations, influenced by particle size and concentration. Specifically, aged PET MPs and NPs induce distinct size-specific and concentration-dependent patterns of destabilization, both coinciding with the loss of functional integrity. Elevated ROS levels were observed only with aged PET NPs at high concentrations, underscoring effects on oxidative stress. Both aged PET MPs and NPs induce significant increases in cellular mortality, particularly after 24 hours of exposure at high concentrations. The findings underscore the complex cellular mechanisms that impact hemocyte functional integrity following exposure to aged PET particles under environmentally and biologically relevant conditions.

It is important to note that evaluating the potential exacerbation of cellular responses under chronic exposure conditions is constrained by the limited longevity of primary hemocyte cultures. No permanent cell line from marine invertebrates has been established yet, as these cells typically stop dividing and exhibit cellular quiescence within 24–72 hours post-isolation (Rinkevich, 2011). In studying contaminants such as nanomaterials, it has been noted that outcomes from short-term *in vitro* experiments with isolated cells may not reliably reflect the potential effects observed at the organism level *in vivo* (Canesi et al., 2012). This limitation underscores the necessity of employing relevant exposure conditions for *in vitro* testing, ensuring that particle concentrations align with those detected internally in organisms. Previous studies have demonstrated that cytotoxicity was induced in hemocytes following both *in vitro* and *in vivo* exposure (Luo & Wang, 2022; Roman et al., 2023). These findings suggest that when properly designed, *in vitro* approaches can serve as reliable predictors of *in vivo* outcomes (Barrick et al., 2018), given that primary cells offer relevant transcriptomic and proteomic profiles, as well as physiological functions and

responses (Gaudioso et al., 2022). Moreover, *in vitro* models are invaluable tools for generating extensive data and providing fast, reliable assessment of the ecotoxic properties of plastic particles (Revel et al., 2021). Given the morphological and functional similarity to mammalian immune cells, bivalve hemocytes can serve as a useful model for comparative regulatory studies (Canesi & Procházková, 2014).

While this study provides crucial mechanistic insights, the intrinsic toxicity mechanisms of a broader range of environmentally relevant plastic particle properties alongside the need for *in vivo* validation, highlight areas for future research. Subsequent studies should focus on elucidating the mechanisms of particle uptake and intracellular trafficking routes to better assess ensuing toxicity profiles (Foroozandeh & Aziz, 2018b). With the potential of hemocytes to exhibit heightened bioreactivity and intracellular accumulation, a thorough understanding of the impacts on cellular organelles and processes is imperative. Holotomography, as a cutting-edge imaging technique, provides high-resolution, label-free, and three-dimensional visualization capabilities for assessing both intracellular localization and dynamic cellular responses (Yoon et al., 2015). Such a holistic approach will provide a comprehensive understanding of the potential systemic effects of environmentally relevant MPs and NPs on both cellular and organismal health.

4.6 Acknowledgements

Test particles and the primary characterization were supplied by the Joint Research Centre (JRC), with the support of John Seghers, Håkan Emteborg, and Claudia Cella. We thank András Retzler, Mathilde Falcou Préfol, Allen Jun Anies and Moses Ndugwa for their help with mussel sample collection. We also appreciate the assistance of Gethrie Oraño with the *in vitro* experiment.

Chapter 5

Characterization of Nanoplastic-Induced Responses in *Mytilus edulis* Hemocytes Using 3D Label-Free Refractive Index Mapping by Holotomography

Adapted from:

Hara, J., Bihannic, I., Gley, R., Caillet, C., Vercauteren, M., Janssen, C.R. Blust, R., Asselman, J., Béguiristain, B., Cordier, H.L., Town, R.M., and Duval, J.F.L. Characterization of Nanoplastic-Induced Responses in *Mytilus edulis* Hemocytes Using 3D Label-Free Refractive Index Mapping by Holotomography. Manuscript in preparation.

Abstract

Micro- and nanoplastics (MNPs) represent a pervasive contaminant with the capacity to cross biological barriers and accumulate in tissues and cells, yet their intracellular fate and associated effects remain underexplored. Herein, we investigated the interactions of aged polyethylene terephthalate (PET) nanoplastics with hemocyte subpopulations of *Mytilus edulis* using label-free three-dimensional live-cell imaging by holotomography. Specifically, this study aims to (i) evaluate morphological changes in hemocytes following exposure to environmentally relevant concentrations of aged PET nanoplastics, and (ii) employ three-dimensional refractive index (RI) mapping to detect and localize internalized particles within subcellular compartments. Label- free, live-cell imaging by holotomography enabled the 3D characterization of distinct hemocyte subpopulations, including blast-like cells, hyalinocytes, granulocytes and granular asterocytes. Representative RI tomograms revealed clear visualization of internalized PET nanoplastics with defining high-RI signals distinguishable from intrinsic cellular structure contributions, across different exposure conditions. Following exposure to aged PET NPs hemocytes exhibited morphological alterations, including extensive cytoplasmic vacuolation, granulation, and signs of membrane damage. These findings demonstrate the unique capability of holotomography to resolve unlabeled nanoplastics within living hemocytes and track their intracellular localization, offering mechanistic insight into uptake pathways and immunotoxicological responses. Future directions will include refining image-processing pipelines to improve accuracy and reproducibility, and integrating quantitative dose-response analyses. Together, these advances will provide a robust framework for elucidating the (intra)cellular fate and toxicity of environmentally relevant nanoplastics.

Keywords: Aged PET, Nanoplastics, Hemocyte subpopulations, Holotomography, Cellular internalization.

5.1 Introduction

Micro- and nanoplastics (MNPs) are now pervasive in marine ecosystems and have been detected in a wide range of organisms, with demonstrated capacity to cross biological barriers and accumulate within cells and tissues (Mattsson et al., 2018; Patil et al., 2020; Sendra, Saco, et al., 2020; Thompson et al., 2024). Despite extensive research on organismal responses to plastic particle exposure, systematic analyses at the cellular level remain scarce, limiting mechanistic insight into MNP toxicity and thus our understanding of long-term effects.

Mussels (e.g., *Mytilus edulis*) are widely recognized as sentinel organisms in coastal biomonitoring and are routinely employed to evaluate the impacts of nanoparticle exposure (Canesi et al., 2012; Canesi & Procházková, 2014; Weng et al., 2022). Hemocytes, the principal effector cells of the bivalve innate immune system, comprise morphologically and functionally distinct subpopulations. These subpopulations regulate internal cell signaling pathways that control processes such as phagocytosis, oxidative balance, and immune homeostasis. Among these subpopulations, granulocytes are characterized by high phagocytic activity and oxyradical production, whereas hyalinocytes exhibit comparatively lower phagocytic ability (Canesi et al., 2006; de la Ballina et al., 2022; Le Foll et al., 2010). Differential sensitivity of these subpopulations to various toxicants, including plastic particles, mainly limited to pristine spherical polystyrene NPs, has been reported and underpins their diagnostic utility (Evariste et al., 2017; Sendra, Carrasco-Braganza, et al., 2020; T. Wang et al., 2019a).

As a critical component of innate immunity, phagocytosis, carried out particularly by these specialized cells, regulates the internalization and elimination of particles larger than 0.5 µm in diameter (Rosales & Uribe-Querol, 2017; Uribe-Querol & Rosales, 2020). This primary cellular defense mechanism involves several phases (phagosome formation, maturation, and resolution) and is orchestrated by specific receptors and signaling pathways, leading to cytoskeletal rearrangements and membrane remodeling (Levin et al., 2016; Rosales & Uribe-Querol, 2017; Uribe-Querol & Rosales, 2020). Phagocytosis, however, is not an isolated innate defense mechanism in response to nanoparticle exposure as it typically occurs with autophagy, a lysosome-based degradative pathway essential for maintaining cellular homeostasis (Gustafson et al., 2015). Nanoparticles have been shown to induce autophagy dysfunction by overloading or damaging the lysosomal compartment and altering the cell cytoskeleton, resulting in a blockade of the autophagy flux, and accumulation of cytoplasmic vacuoles (Stern et al., 2012). Vacuole accumulation represents an early initiating event that can trigger metabolic stress, autophagy-related cell death, and broader cytotoxic outcomes (Shubin et al., 2016). These include lysosomal destabilization, oxidative stress, inflammation, accumulation of ubiquitinated protein aggregates, mitochondrial dysfunction, and ultimately the activation of cell death pathways (Stern et al., 2012). Given these interconnected mechanisms, a detailed analysis of nanoparticle

uptake pathways, intracellular trafficking routes, and stress-response networks is critical for evaluating the fate and toxicity of nanoplastic particles (Foroozandeh & Aziz, 2018b; Gustafson et al., 2015; Simmons et al., 2009). Such integrative assessment highlights multiple targets that can reveal how particle internalization processes affect cellular health and integrity.

Currently, evidence for cellular uptake, localization, and associated effects of MNPs in mussel hemocytes is well established, though most work remains limited to pristine particles, particularly polystyrene (Chang & Wang, 2024; Katsumiti et al., 2021; Sendra, Saco, et al., 2020). In contrast, environmental aging and weathering processes, such as photodegradation, mechanical abrasion, and chemical oxidation, can modify particle surfaces and the physicochemical particle properties (Bihannic et al., 2024; W. He et al., 2023; Town et al., 2023). These modifications introduce critical variables that shape particle–cell interactions (Town et al., 2025) and often enhance toxicological outcomes compared with pristine counterparts (Völkl et al., 2022). As such, there is an urgent need to investigate environmentally realistic particle types, shapes, size distributions, and concentrations, as these factors fundamentally determine the mechanisms of cellular uptake and as a consequence, toxicity (Foroozandeh & Aziz, 2018b).

A variety of methods are available to investigate nanoparticle internalization and cellular toxicity, each with inherent advantages and limitations. Conventional approaches often rely on fluorescent labeling. However, fluorescence signals can change upon internalization, potentially altering uptake dynamics, inducing phototoxicity, and limiting sensitivity for detecting smaller particles (Gottstein et al., 2013; Wan et al., 2019). Recent technological advances, particularly holotomography, have transformed this field by enabling label-free, three-dimensional imaging of live cells (G. Kim et al., 2024). This approach allows simultaneous assessment of morphological and biophysical parameters, which are crucial for interpreting cellular responses to various stimuli, and it has been applied primarily in human cell lines (Buzalewicz et al., 2022; Sandoz et al., 2019; Yakimovich et al., 2018; Yamazaki et al., 2022; Yoon et al., 2015; Zadka et al., 2021). Additionally, it enables the measurement of cellular internalization and localization of nano- and microparticles, through 3D refractive index (RI)-based mapping. For instance, nanodiamonds of 4–5 nm with a crystalline diamond core and graphene-like shell structure have been detected in human pancreatic cancer cells (Panc-1) (Géloën et al., 2021), while Yoon et al. (2015) demonstrated RI-based tracking of relatively large (~1 µm) pristine polystyrene beads in macrophages of Balb/c mice. While these studies establish the feasibility of RI-based mapping for nanodiamonds and micrometre-scale beads, applying this approach to nanosized plastic particles is far more challenging due to their smaller dimensions, compositional heterogeneity and expected lower RI-contrast in cellular microenvironments. Importantly, such capabilities offer unique opportunities to establish dose–response profiles and mechanistic insights into nanoparticle-cell interactions and the time dependence thereof.

As such, this research investigates the interactions of aged PET nanoplastic particles with hemocyte subpopulations of *Mytilus edulis* using label-free 3D live-cell imaging by holotomography. A particular emphasis is placed on elucidating how internalized environmentally relevant nanoparticles are distributed and localized within the cellular compartments. Specifically, this study aims to: (1) evaluate morphological changes in hemocytes following their exposure to aged PET NP, integral to assessing potential effects on cellular integrity; and (2) employ 3D refractive index mapping to detect and characterize the intracellular distribution and localization patterns of internalized nanoplastic particles. This work provides critical insight into the cellular fate of environmentally relevant nanoplastics, with broader implications for understanding immunotoxicity.

5.2 Materials and Methods

5.2.1 Characterization of the aged PET NPs

Aged polyethylene terephthalate (PET) particles were produced by mechanical cryomilling followed by chemical aging, as previously described (Seghers et al., 2025), and the primary stock suspensions were supplied by the Joint Research Centre (JRC, European Commission). Chemical aging in potassium hydroxide (KOH) under ultrasonic treatment increased particle hydrophilicity (Seghers et al., 2025) and yielded surface modifications comparable to environmentally aged plastics (von der Esch et al., 2020).

The particle size distribution, concentration, polymer composition and shape of aged PET particles were characterized using a suite of analytical physicochemical techniques, including single particle extinction and scattering (SPES, Classizer™ ONE), Raman spectroscopy (reference library Open Specy), and scanning electron microscopy (SEM, Phenom™ ProX Desktop) (Supplementary Figures A5.1–A5.3). SEM imaging of the primary stock suspension of aged PET MNPs (<5 µm) confirmed the fragmented and irregular shapes of aged particles (Supplementary Figure A5.1). The refractive index of aged PET particles was first characterized by SPES analysis of the primary stock suspension of aged MNPs (<5 µm, Supplementary Figure A5.2) in Milli-Q water. This analysis yielded an RI value of 1.45 + 0.00*i* (where *i* denotes the imaginary unit of the complex RI, indicating negligible absorption at the measurement wavelength). The RI values obtained from SPES represent a distribution of individual particle-level RI measurements; therefore, the reported standard deviation (± 0.05); coefficient of variation (0.03) and skewness (0.41) describe the dispersion and asymmetry of this RI distribution. Subsequent SPES measurements of aged PET NPs isolated from this primary stock suspension revealed a heterogenous, number-based particle size distribution, with an average equivalent diameter of 0.68 µm and percentile diameter values of D_{10} = 0.39 µm, D_{50} = 0.57 µm, and D_{90} = 1.1 µm (Supplementary Figure A5.3, Panel A). Polymer composition of aged PET NPs was verified with a 0.94 match score to the reference spectrum using Raman spectroscopy and the Open Specy reference library (Supplementary Figure A5.3, Panel B). Stock solutions in Milli-

Q water without surfactants contain approximately 1.66×10^7 particles per mL (denoted as P/mL).

To characterize the aged PET NPs under conditions adapted for *in vitro* exposure, particle stability was assessed by Dynamic Light Scattering (DLS, Zetasizer Nanoseries, Malvern Instruments) (Supplementary Figure A5.4). The stock suspension was sonicated for 20 min and subsequently diluted to 10^5 P/mL in 10 mL sterile glass containers containing filtered (100 nm, Millipore) culture media (CM), live-cell imaging solution (LIS), and sodium chloride solutions with varying ionic strength (NaCl, 0.1–250 mM, pH 7). Following incubation at 15°C, the hydrodynamic size and electrophoretic mobility were measured at different timepoints (1 h and 24 h for CM and LIS; 24 h in NaCl solutions) using folded capillary cells. Electrophoretic mobility was determined under a constant direct current electric field of 50 V/cm, from which the zeta (ζ) potential was calculated by the instrument software using the Henry equation. Reference standards (ZTS1240, Malvern Panalytical) were included in the analytical process for quality control. Measurements were performed in triplicate at each time point, with 10 runs per replicate. Aged PET NPs were found to have a mean average diameter *d* of 314.0 nm (1 h) and 271.9 nm (24 h) in CM, and 322.1 nm (1 h) and 305.4 nm (24 h) in LIS (Supplementary Figure A5.4, Panel A). The ζ-potential values (Supplementary Figure A5.4, Panel B) were consistently negative across all conditions, ranging from -31.4 mV (1 h) and -33.5 mV (24 h) in CM, and -31.0 mV (1 h) and -33.4 mV (24 h) in LIS, consistent with trends in electrophoretic mobility (CM: -2.23–-2.38 µm·cm/V/s; LIS: -2.20–-2.37 µm·cm/V/s in Supplementary Figure A5.4, Panel C). The average polydispersity index (PDI) values ranged from 0.43–0.49 and 0.46–0.49 in CM and LIS, respectively. These measurements, obtained in both CM (14.5 mS/cm) and LIS (14.8 mS/cm), corresponded in terms of solution ionic strength to that of a 150 mM NaCl suspension (14.2 mS/cm), in which PET NPs exhibited a hydrodynamic size of 189.4 nm, a ζ-potential of -27.2 mV, and an electrophoretic mobility of -1.93 µm·cm/V/s. No aggregation was observed in any of the tested media, confirming suspension stability throughout the tested period.

5.2.2 Maintenance of the mussel culture

A total of 80–100 adult mussels (*Mytilus edulis*) with shell lengths ranging from 4 to 6 cm were selected as test organisms from the established mussel culture within the laboratory (University of Antwerp). Mussels were maintained in a glass aquarium containing artificial seawater (hw-Marinemix Professional), equipped with portable aeration (Eheim Air Pump 400) and mechanical-biological filtration (Eheim Biopower 200) systems. The water temperature was kept at 14–15°C, following ASTM E724-983 guidelines (ASTM International, 2012). The mussels were fed daily with an appropriate volume of suspension of the microalgae *Tetraselmis suecica* (Tetraprime S Proviron), and water was renewed after each feeding. Water quality parameters (pH, salinity, dissolved oxygen, ammonia, nitrite, and nitrate) were monitored using Hach HQ40D meters and Tetra test kits. Mussels

transported to the host laboratory (LIEC, CNRS, France) were acclimatized for at least three days prior to experiments. No mortality was observed under these conditions.

5.2.3 Hemolymph extraction and cell culture preparation

Adult mussels were anesthetized for approximately 30 min in filtered (100 nm, Millipore) and sterilized magnesium chloride solution (0.3 M, $MgCl_2$) within a laminar airflow cabinet (ESI FluFrance). Hemolymph was extracted from the posterior abductor muscle using a sterile 2 mL syringe (Injekt) fitted with a 23G needle (Terumo Neolus). Extracted hemolymph was filtered through 70 µm cell strainers (Greiner), pooled, and diluted 9:1 in anti-aggregation solution (171 mM NaCl; 0.2 M Tris; 0.15 % v/v HCl 1 N; 24 mM EDTA, with reported > 95 % viability (Katsumiti et al., 2017).

Cell concentration and purity was assessed with a hemocytometer (MUHWA Scientific, Neubauer) and microscope (Nikon Eclipse LV100N POL). Cell suspensions were then seeded into pre-labeled 24-well glass bottom microplates (Greiner Bio-one) and maintained in culture media (Basal Medium Eagle (BME), Sigma Aldrich) with essential supplements (L-Glutamine) and antibacterial agent (0.001 % Gentamicin). Culture media were freshly prepared and filtered through 0.2 µm syringe filters (Millipore) prior to use. All procedures were performed under strict aseptic conditions to prevent contamination.

5.2.4 *In vitro* exposure experiments

In vitro exposure experiments were carried out with a cell concentration of 1×10^6 cells/mL and incubated at 15°C. Treatments included incubation with the pure culture medium (BME) as the negative control (NC) and the culture medium containing varying concentrations of aged PET NPs: 10 P/mL (C1); 10^3 P/mL (C2); and 10^5 P/mL (C3). As positive control, cells were incubated in culture media containing Cadmium Chloride ($CdCl_2$) at specified concentrations reported to induce morphological changes (PC $CdCl_2$ C1: 100 µM) and cellular death (PC $CdCl_2$ C2: 800 µM) *in vitro* (Olabarrieta et al., 2001).

Samples were incubated under stable culture conditions for 24 h and 48 h. At each time point, cells were gently detached from the culture wells and then prepared for live-cell imaging. Live-cell imaging experiments, particularly for NC and aged PET NP treatments (C1–C3), were performed at least twice to ensure reproducibility.

5.2.5 Label-free 3D live-cell imaging using holotomography

The label-free 3D live cell imaging was performed using a holotomography system (HT-2H, Tomocube), equipped with a 60× water-immersion objective (numerical aperture 1.2). Holotomography is a 3D, label-free optical imaging technique that utilizes refractive index as an inherent quantitative contrast parameter. A series of 2D holograms is acquired under multiple illumination angles using a coherent laser beam modulated by a digital

micromirror device (DMD). Each hologram contains both amplitude and phase information generated by interference of light with the specimen. Reconstructing the recorded holograms through an inverse scattering algorithm yields a 3D RI map of the sample, enabling detailed visualization of cellular structures without the need for staining or labeling (G. Kim et al., 2024).

Following cell exposure up to the desired timepoint, 30 µL of cell suspension was transferred to a glass bottom imaging dish (TomoDish, diameter: 50 mm, observation area: 20 mm × 20 mm) and covered with a top coverslip, carefully avoiding air bubble formation. The imaging dish was then mounted and aligned on the microscope stage. The acquisition tab of TomoStudio (HT-2H 3.3.9) was configured in a consistent mode for the whole imaging process. To cover the entire sample, a total of 210 Z-planes was configured based on the thickness of the specimen and the optical resolution of the system. The HT system offers lateral and axial optical resolutions of 110 and 356 nm, respectively, with corresponding reconstructed voxel resolutions of 110 and 220 nm. A 532 nm, 0.05 mW class-1 laser served as the illumination source, with a maximum illumination angle of 63° in the sample plane. The acquired 3D image stacks were saved and backed up in MHD format. Every image stack consists of two files: a header file (.mhd extension) containing metadata like the image dimensions and element spacing, and the main data file (.raw extension), which contains the RI values corresponding to the 3D voxel grid, stored with 32-bit floating point data type. The typical range of RI values obtained in the image datasets of interest in this work was 1.328 to 1.47.

5.2.6 3D image processing to segment and identify the cellular structures and nanoplastics

The 3D image processing pipeline described here represents an exploratory framework developed to enable segmentation and visualization of (intra)cellular structures and nanoplastic particles.

A main principle underlying the algorithm is that each of the (intra)cellular structures have a specific RI value range, thus, range-based thresholding is incorporated as an important part of the method. To establish a robust and scientifically grounded basis for the estimation of these thresholds, the RI ranges of manually labelled target structures are evaluated in section 5.2.6.1. The subsequent section 5.2.6.2 describes the whole processing pipeline, along with the morphological filtering steps employed to reduce noise effects on the images. Finally, section 5.2.6.3 while presenting the preliminary validation procedures used to assess the robustness and reliability of the approach, also outlines some limitations associated with the image-processing strategy.

5.2.6.1 Image annotations to determine the threshold refractive index levels

Holotomography provides 3D refractive-index maps that reflect intrinsic biophysical properties of cells (P. Y. Liu et al., 2016). To ensure biologically relevant and reproducible segmentation of (intra)cellular structures of the different hemocyte subpopulations, RI thresholds were derived from a reference dataset by analyzing histograms of manually annotated regions. Representative tomograms (n = 50) were selected from negative controls (NC; n = 10), positive controls (PC: $CdCl_2$; C1: n = 10; C2: n = 10), and hemocyte exposed to aged PET NPs (C2: n = 10; and C3: n = 10) after 24 h and 48 h of exposure. For each representative image (n = 50) across all conditions and timepoints, annotation of the target structures was performed on three slices per tomogram (total number = 150 slices) to capture variations along the z-axis and ensure measurement reproducibility (Supplementary Figure A5.5). Representative regions of interest (ROIs) corresponding to the background (n = 450), cytoplasm (n = 840), granules (n = 741), and vacuoles (n = 657) were manually annotated. Background ROIs represented extracellular regions defining baseline RI parameters; cytoplasmic ROIs encompassed homogeneous cellular areas excluding organelles (granules and vacuoles); granule ROIs included dense, high-RI structures within the cytoplasm; and vacuole ROIs corresponded to low-RI compartments relative to the surrounding cytoplasm. For each ROI, quantitative morphological metrics (number, area, slice number, stack position), and RI distributions were extracted to assess optical characteristics of the annotated structures across conditions (Figure 5.1, and Supplementary Figures A5.6–A5.8). These distributions enabled the comparison of structure-specific RI ranges of the cytoplasm (double lines in Figure 5.1 and in Supplementary Figures A5.6–A5.8), granules (dotted lines), vacuoles (solid lines), and the background (dashed lines), serving as the empirical basis for threshold selection for the automated segmentation.

The RI threshold values based on Figure 5.1 and applied in the segmentation pipeline were: cytoplasm (1.335–1.351); granules and nucleus (>1.351–1.43); vacuoles (<1.331) and the nanoplastics (>1.43). Each threshold was chosen to minimize the overlap between the target and the neighboring structures, while accounting for potential biological shifts. In particular, the RI threshold applied for the detection of internalized NPs are consistent with the optical properties of aged PET derived from SPES measurement (RI = 1.45 + 0.00i).

Holotomography systems provide significant advantages in high-resolution imaging of cellular structures, but they can be limited by issues such as speckle noise and artefacts in reconstruction, causing partial overlap with the RI range of the cytoplasm. Such noise originates from the extended coherence length of laser illumination and the associated undesired diffraction effects, which typically require hardware-based solutions and countermeasures (G. Kim et al., 2024). Post-imaging computational approaches also exist for noise removal. For example, in Choi et al. (2019), an artificial intelligence-assisted noise removal technique is introduced. However, the framework is currently limited to 2D denoising and is not yet applicable to whole 3D tomograms.

Additionally, direct threshold-based segmentation of the full hemocyte presented a challenge due to substantial RI overlap between vacuoles and the extracellular background, which led to false positives during direct RI-based thresholding. To overcome these challenges, complementary pipeline with a multi-step 3D morphological processing operations was employed to minimize the noise and discriminate between true (intra)cellular structures and the background.

5.2.6.2 Image processing workflow

The image processing workflow (Figure 5.2) was carried out using ImageJ-Fiji (Version 1.54p) with customized macro scripts calling various functions, primarily from the MorphoLibJ and 3D Viewer plugins (Legland et al., 2016; Schmid et al., 2010). Representative examples of the image processing outputs are provided in the Supplementary Information, illustrating two selected situations: (i) hemocyte with internalized nanoplastic particles (Supplementary Figure A5.9), and (ii) hemocytes without nanoplastics (Supplementary Figure A5.10).

As a first step in the macro, the MHD image stack was imported into Fiji, and the voxel dimensions (approximately 0.095 µm × 0.095 µm × 0.189 µm in the *x*, *y*, and *z* directions), were set based on the ElementSpacing values extracted from the image metadata to ensure proper spatial calibration. The stack was then duplicated into multiple working copies, each assigned to a specific segmentation target to enable processing without overwriting original data. The overall image processing workflow comprised seven major stages, which are described in detail below.

Part I. Derivation of a Preliminary Mask for the Hemocyte.

A duplicate of the original stack (steps 1a and 1b in Supplementary Figures A5.9 and A5.10) was used for hemocyte segmentation. The preliminary hemocyte mask (excluding vacuoles, which exhibit a RI range similar to the background and are addressed in Parts II and III of the workflow) was determined using RI-based thresholding followed by 3D morphological post-processing. An RI threshold of 1.333 was chosen as a preliminary conservative cutoff to separate the cell region from the background (step 1c).

The thresholded volume was then subjected to opening (step 1d), a 3D morphological filtering operation (Legland et al., 2016), in which a small structuring element is scanning through the volume twice, first performing erosion and then dilation. The purpose of this step is to remove elongated or curved patches, originating from the speckle noise, that were still connected to the main hemocyte structure after applying the aforementioned threshold. One can find an example of such patches on the sampled image in step 1c.

Ideally, if these noise patches were not there, the main hemocyte structure could be selected by choosing the largest connected component in the volume. However, it can be

observed that these noise patches are often connected through only 1 or 2 voxels. The erosion stage of the opening operation breaks these minimal connections, and the subsequent dilation approximately restores the original size of the objects without redoing these undesired connections. The smallest spherical structuring element (ball, radius: 2 voxels) that effectively disconnects the unwanted patches on a selection of representative images was chosen.

Although the opening operation introduces minor edge distortions (Legland et al., 2016), the preliminary hemocyte mask is not intended for direct quantitative morphological analysis. Instead, it serves as a rough inclusion mask encompassing the target cellular regions. This rough mask is then intersected later on with other finer masks (e.g., those for the cytoplasm, granules or the NPs), ensuring that only those (intra)cellular objects are retained for downstream measurement and visualization.

As delineating the hemocyte boundary was the goal, 3D hole-filling was applied as the next logical step (step 1e), which filled the vacuoles and certain holes that appeared due to noise. However, some intracellular vacuoles that are clearly identifiable as physically intact still remained unfilled, as they appeared to have direct connections to the background along the Z axis. A special treatment for these cases is detailed in Part II and III.

The last step was performed to apply 3D connected components labeling (6-connectivity) to assign unique labels to a set of connected structures (step 1f), ensuring that only connected cell components were detected while excluding remaining noise and detached fragments such as apoptotic bodies or other disconnected cellular debris located in the frame. It is then followed by retention of the largest connected component using a “Keep Largest Label” operation, corresponding to the target hemocyte structure. Retaining the largest connected component for cell segmentation is a known technique, also appearing in studies by Raj et al. (2024). The resulting mask (step 1g), a binary image with values [0 = black, 1 = white], was then used as a preliminary hemocyte mask for subsequent subcellular segmentation.

Part II. Segmentation of Vacuoles.

For isolating vacuolar compartments from the background, a straightforward approach would be to label all the holes inside the opened hemocyte mask, as discussed in the previous step. However, this approach is not feasible, because some of the intact vacuoles appear connected to the extracellular region through a small cavity in the measured 3D volume. Vacuoles are membrane-bound organelle within a cytoplasm, often containing cell sap, which includes water, ions, and enzymes. As such, in holotomography images, the RI of intracellular vacuoles, being predominantly filled with water, closely matches that of the surrounding aqueous background medium. This RI similarity often results in weak or indistinguishable vacuole boundaries in the 3D RI map, causing physically enclosed

vacuoles to appear partially open or connected to the exterior. To reliably separate adjacent low-contrast compartments, a 3D distance transform watershed was applied in the subsequent segmentation step. This approach separates touching objects by calculating the distance transform of a binary image and applying watershed segmentation to delineate boundaries between adjacent objects (Legland et al., 2016).

Starting from a copy of the original image, thresholding was applied using a voxel intensity cutoff of values above 1.331 to generate a binary vacuole mask (step 2a in Part II-Supplementary Figures A5.9 and A5.10). Vacuoles effectively contain water, for which the tabulated RI value is 1.333. However, the measured RI values of vacuoles were around 1.330, which indicates a small offset. As the speckle noise also observed inside the vacuoles is relatively low, a threshold level of 1.331 was determined in line with the RI distribution displayed in Figure 5.1.

As a note, within the hemocyte segmentation step (Part I-Figures A5.9 and A5.10 in SI), we empirically chose to apply a slightly higher threshold level of 1.3330 because the background is the location of stronger speckle noise as compared to that in vacuoles, which is also reflected in its larger range of RI (Figure 5.1).

Similar to the hemocyte segmentation, a 3D morphological closing operation (step 2b) using the smallest effective structuring element (ball, radius = 2 voxels) was applied to reduce the noise. Closing was applied instead of opening, because the image is inverted compared to that in Part I, thus, by swapping the order of erosion and dilation, essentially the same effect is achieved. The purpose of this operation is to disconnect the elongated patches originating from the speckle noise, although the lower threshold level allows more patches to remain attached to the hemocyte structure. Despite this, the vacuolar compartments were followed more accurately by the mask.

To ensure that the watershed algorithm only operates on compartments connected to the hemocyte structure, the noisy background was removed as done in Part I, i.e., through 3D connected components labeling (step 2c), followed by retention of the largest connected region only (step 2d).

The subsequent main step involved the application of a 3D distance transform watershed to the inverted mask. While connected component labeling assigns a single label to each connected component, this watershed algorithm can separate a single connected component to multiple parts by creating a border (step 2e), practically labeling each semi-closed compartment separately. In contrast, structures that do not form distinct basins in the distance map remain connected to the background.

However, defining the border of a semi-closed compartment is an artificial choice, which may affect the measured vacuolar volume. For example, in Supplementary Figure A5.11, a

few options (shown in different colors) could be identified even by visual inspection. The fact that the borders in some cases are not clear along the Z axis makes it difficult even for an expert observer to determine with certainty where the vacuole ends and the background begins.

The choice that the compartment boundary was determined using the distance transform watershed algorithm provided satisfactory and consistent results across the representative images. As some of the clearly identifiable vacuoles exhibit a certain degree of partial opening or background connectivity, this approach represents a practical compromise achievable within the constraints of the imaging modality. The use of a 3D distance-transform watershed for automated vacuole segmentation, implemented through MorpholibJ, has been demonstrated in an earlier study using fluorescence images in combination with deep-learning based preprocessing (Egebjerg et al., 2024).

The resulting image (step 2e, Figures A5.9 and A5.10 in SI) shows that the watershed method labels not only the vacuoles but also splits the background into several regions, which could easily be discarded by removing all border-touching labels (step 2f). In some cases, there remained certain non-border-touching large background regions, which were subsequently removed through an additional size-based filtering. By retaining only objects smaller than 100,000 voxels in capacity (empirically established from the analysis of vacuole sizes in the representative hemocytes), only the target vacuoles remained. A visual inspection was essential at this stage to confirm the effectiveness of the size filtering, particularly in rare cases where extremely large vacuoles were also present.

The final output of this stage was a binary vacuole mask (step 2g, Figures A5.9 and A5.10 in SI) with values [0 = black, 1 = white] and a label image distinguishing individual vacuoles along with the corresponding actual RI values (step 2h) for further 3D analysis and visualization purposes.

Part III. Combination of Vacuoles and Hemocyte Masks.

To generate a full hemocyte mask that properly delineated the whole cell and included all internal vacuolar compartments, the vacuole mask (step 3a, Part III, Figure A5.9 and A5.10 in SI) was dilated using a spherical structuring element (ball, radius = 2 voxels). The dilated vacuole mask was then merged with the hemocyte mask using the union operation (Image Calculator “OR”), assigning a voxel value of 1 wherever one of the input masks has a voxel value of 1 (step 3b). The resulting image was a combined binary mask representing the full hemocyte (step 3c), which was subsequently used to restrict the detection of internalized nanoplastic particles to intracellular regions (as described below, in Part VI).

Thus, at this point, there were two hemocyte masks A and B defined as follows:

A. Preliminary hemocyte mask (step 1g): only the vacuoles that were fully enclosed (no connectivity to the background) were filled;
B. Full hemocyte mask (step 3c): vacuoles that were semi-open (with direct connectivity to the background through a small cavity) were also filled.

As discussed earlier, these masks are not intended for direct quantitative measurements, but were designed to easily remove the background in subsequent steps. Both masks A and B contain the cytoplasm and the granules, but mask A, as a tighter and morphologically less altered mask, was chosen for removing these target compartments from the background. Regarding NP detection, mask A would exclude some of the particles localized in semi-open vacuoles, and, accordingly, the full mask (B) that include these regions was used for NP-related processing.

Part IV. Segmentation of the Cytoplasm.

Cytoplasmic regions were identified by applying an RI range threshold between 1.335 to 1.351 to a duplicate of the original stack (step 4a, Part IV, Figures A5.9 and A5.10 in SI). The intersection of the thresholded image and the preliminary hemocyte mask A (step 1g) was calculated using the Image Calculator ("Multiply" function), which retains only the overlapping voxel regions common to both inputs. This step (4b) automatically excludes background regions as well as the irrelevant regions caused by speckle noise, thereby ensuring that only cytoplasmic voxels within the masked cellular boundary were retained for subsequent analysis. The final output of this stage was a binary cytoplasm mask (step 4c) with values [0 = black, 1 = white] and the corresponding segmented volume of the cytoplasm with actual RI values (step 4d), for further 3D analysis and visualization purpose.

To summarize, a rough but strongly denoised mask of the hemocyte was intersected with a fine mask corresponding to the strict RI region defining the cytoplasm, using the first to successfully remove the speckle noise from the second. A similar strategy was applied for granules, as described in the following part.

Part V. Segmentation of Granules.

Granules were segmented by applying an RI range threshold between 1.351 and 1.43 (step 5a, Figures A5.9 and A5.10 in SI). The intersection of the thresholded image and the preliminary hemocyte mask A (step 1g) was calculated using the Image Calculator ("Multiply" function). This step (5b) only retains regions corresponding to granules within the defined cellular boundary for subsequent analysis. The final output of this stage was a binary granule mask (step 5c) with values [0 = black, 1 = white] and the corresponding

segmented volume with actual RI values (step 5d). As granules tend to aggregate or coalesce, individual granules were not separated by means of different labels.

Part VI. Segmentation of Nanoplastics.

Nanoplastic particles were segmented by first applying an RI threshold range corresponding to values larger than 1.43 (step 6a, Part VI, Figure A5.9 in SI), in line with the optical properties of aged PET as derived from SPES measurement (RI: 1.45 + 0.00*i*). The thresholded volume was intersected with the full hemocyte mask B previously defined (step 3c) using the Image Calculator, thereby restricting detection to intracellular regions, including all detected vacuoles. This step ensured that only internalized aged PET NPs were detected within the cellular compartments, and that particles localized in vacuoles (defined by a RI value equivalent to that of the background) were properly detected.

Connected-component labelling (6-connectivity) was applied to distinguish and label individual nanoplastics for subsequent analysis. The final output of this stage was a binary nanoplastics mask with labels distinguishing individual particles (step 6c) and the corresponding segmented volume of internalized nanoplastic particles with actual RI values (step 6d).

Part VII. 3D Analysis of Segmented Structures, Visualization and File Saving.

Each segmented structure was then visualized separately using the ImageJ 3D Viewer. Distinct pseudo-colors were assigned to each compartment (e.g., white for cytoplasm (step 7b, part VII, Figures A5.9 and A5.10 in SI), cyan for vacuoles (step 7c), yellow for granules (7d), red for internalized NPs (step 7e)) and subsequently subjected into a single and merged 3D scene rendering (3D composite image). The displayed voxel color intensity was based on the actual RI values corresponding to the voxels selected by each mask. The cytoplasm (white) was rendered semi-transparent to enable visualization of internal structures in the merged 3D volume (step 7a). For visualization purpose, 360° rotation videos were generated directly from the 3D Viewer.

The custom macro-scripts also allowed quantitative morphometric and intensity analyses using the “MorpholibJ Intensity Measurements 2D/3D” and “Analyze Regions 3D” plugins in Fiji. For each labelled compartment, including the vacuoles (step 2h), cytoplasm (step 4d), granules (step 5d), and nanoplastics (step 6d), voxel intensity (or, equivalently RI) metrics (mean, median, maximum, minimum, standard deviation, skewness, and kurtosis) can be extracted from the original 3D volume (step 1a) within each segmented region. Morphometric features also include the amount of voxels, volume, surface area, mean breadth, sphericity, Euler number, bounding box dimensions, centroid coordinates, and equivalent ellipsoid parameters. All measurements were compiled into distinct result tables.

All outputs were automatically exported from Fiji/ImageJ into a specified directory named after the original MHD stack. The macro-script saved (i) all binary masks (TIFF format), (ii) segmented structures with actual RI values (TIFF), (iii) 360° 3D rotation animations (GIF), and (iv) quantitative measurement tables (CSV) containing morphometric and intensity measurements.

5.2.6.3 Image Processing Validation and Limitations

Although the threshold-based strategy combined with morphological filtering enabled biologically relevant discrimination of cellular features, some limitations remain. These include the possible dependence of the segmentation process on manually defined reference annotations for determining the RI threshold levels, and the persistent challenges to separate some structures from background noise and artifacts.

One way to evaluate the segmentation performance is by calculating the RI-distribution pertaining to the segmented structures, similar to what was done with the manually annotated regions. Ideally, the RI distribution for each of the classes will fall mainly within their corresponding threshold range. With respect to the manually annotated data, a few voxels appeared outside of the threshold ranges, partly due to a spatial overlap between structure classes and the inherent difficulty to manually annotate overlapping target regions with perfect accuracy. In turn, it is expected that, in some cases, the output of the automatic classifier will also contain a few of such voxels in the form of outliers.

The stack histogram profiles of the segmented structures containing the actual RI values, calculated from representative 3D images (total n = 28), are shown in Supplementary Figures A5.12–A5.15. The analyzed histogram data contained representatives of the different hemocyte subpopulations across all experimental conditions, including negative control, positive control, NP-treated hemocytes, and hemocytes where NPs were detected. For each structure, the voxels with RI values falling outside their specified threshold ranges derived from manual annotation (e.g. for the cytoplasm: <1.335 and >1.351) were still accounted in the distributions, and their proportion relative to the total voxel count was estimated, and results are discussed below. It is important to note that these counts falling outside the expected RI-threshold range are not a direct measure of the classifier quality, but they do capture the effect of the morphological filtering operations. While such operations are mandatory and unavoidable for suppressing noise, they may slightly alter predefined RI-region boundaries, as previously discussed.

For an ideal noise-free image, the whole pipeline could be implemented using direct thresholding alone, without any post-processing steps. However, as some images exhibit elevated noise levels, such an approach would cause substantial misclassification errors, even if all the voxels would remain within the predetermined RI-ranges. For this reason, the implementation of morphological operations within RI-based treatment is a required

compromise, thus underscoring the balance required between effective noise suppression and reliable intracellular structure detection capability.

Segmentation of the cytoplasm (Supplementary Figure A5.13), granules (Supplementary Figure A5.14), and nanoplastics (Supplementary Figure A5.15) lead to 0% of voxels with RI value falling below or above the lower and upper RI-thresholds of the structures they were part of. While this observation logically follows from the various steps of the RI-based treatment, it confirms that the morphological operations on the hemocyte mask did not cause major biases, as they did not generate voxels that were outside of the expected RI range defining the structure they belong to. In contrast, vacuole segmentation led to a small proportion of voxels outside the defined RI range (Supplementary Figure A5.12). Across all images analyzed and experimental conditions tested, an average of 2.35% of detected voxels were defined by RI values above 1.333 (overlap upper limit between vacuoles and the background). Of these, only 0.82% of the voxels exceeded 1.335, which thus reflects a minor spillover into the cytoplasmic RI range. These are potential residual noise or misclassifications pulled into the vacuole class by the morphological operations. Some of these could be the harmless byproduct of morphological operations, such as the closing and the distance transform watershed. Percentages were calculated per representative image; images without detectable vacuoles were assigned a value of 0%, as the absence of vacuolar voxels inherently resulted in zero out-of-range values and thus reflected proper segmentation behavior (e.g., no false positive vacuole detections).

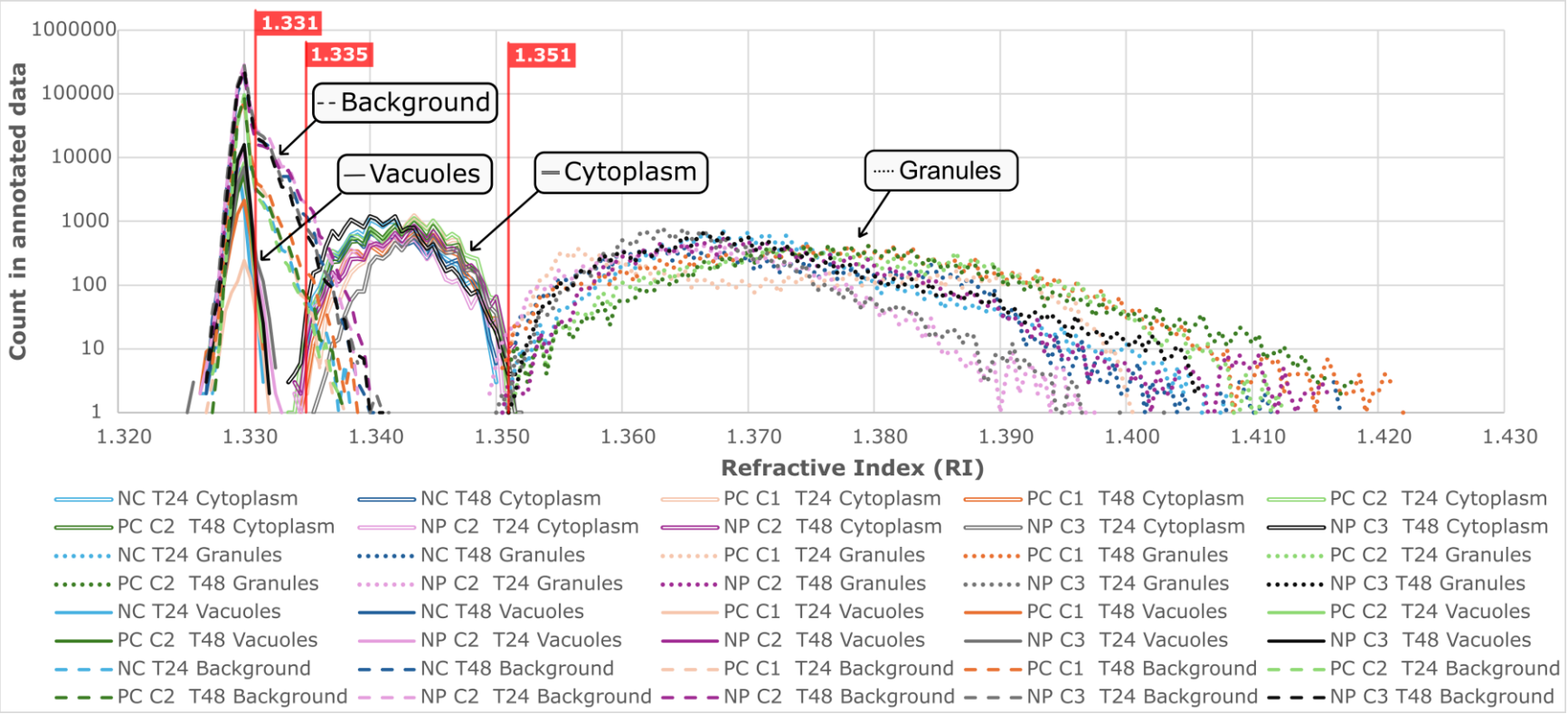

Figure 5.1. *Distribution of refractive index (RI) values across manually annotated structures, including cytoplasm (double lines), granules (dotted lines), vacuoles (single solid lines), and the background (dashed lines). RI histograms were generated from manually annotated regions in representative images of the negative control (NC), positive controls (PC C1 and C2), and hemocytes exposed to aged PET nanoparticles (NP C2 and C3) for 24 h and 48 h. For each condition tested, the same color shade was used for both time points, with the 48 h lines shown in a darker tone. These distributions served as the empirical basis for defining the lower and upper bounds used for RI-based thresholding in the image analysis pipeline. Note that the counts shown reflect the number of annotated voxels. As annotating was limited to a few representative samples, they do not reflect the total count of voxels of the given class in the whole 3D volume. Thus, the lines allow the assessment of the shape of the probability distributions from which descriptive characteristics like the spread and modality can be deducted, but the actual number of overlapping voxels between classes in the full image representatives is not possible to assess.*

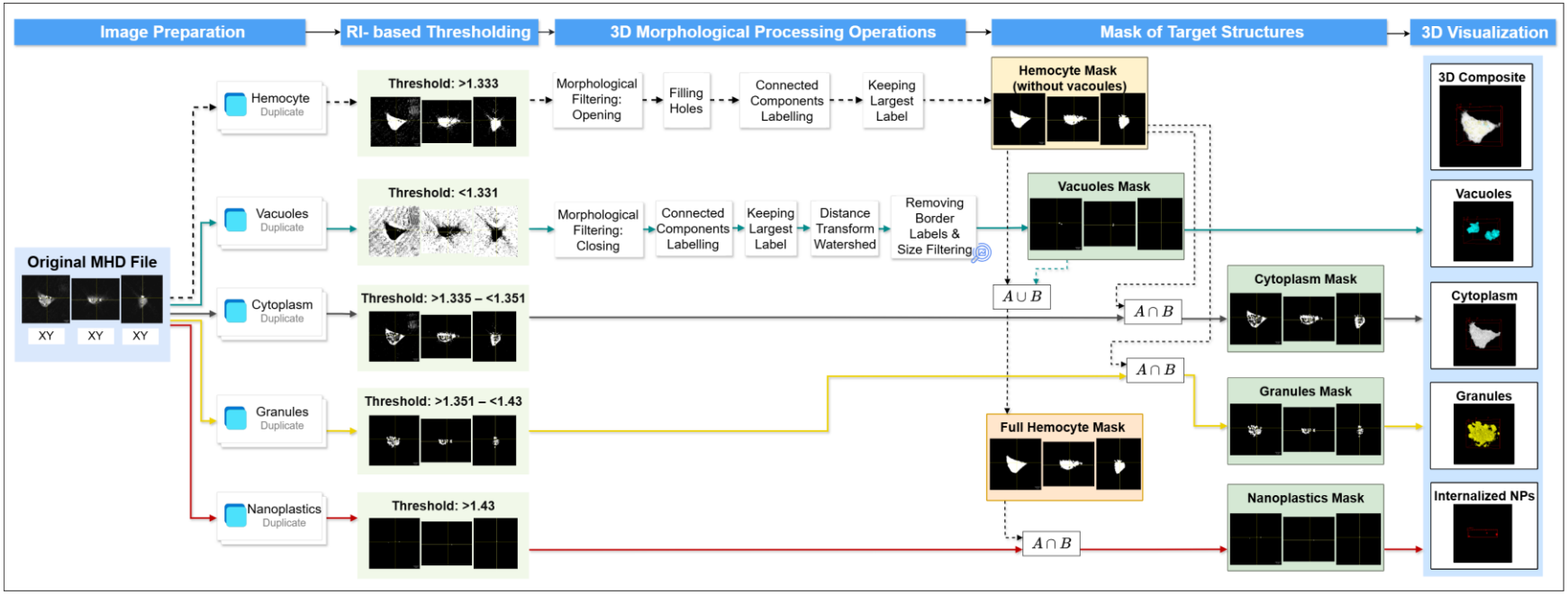

Figure 5.2. *Schematic overview of the image-processing pipelines applied to 3D refractive-index (RI) tomograms. The workflow was implemented in ImageJ-Fiji (Version 1.54p) using customized macro-scripts that called various functions, primarily from the MorphoLibJ and 3D Viewer plugins (cf. text for details). Key steps include spatial calibration, thresholding, 3D morphological processing, image calculator operations (union: ∪ and intersection: ∩) and 3D visualization and quantitative analyses of segmented cell structures. Supplementary Figures A5.9 and A5.10 provide representative examples of each step, illustrating encountered situations for hemocytes featuring or not internalized nanoplastic particles, respectively.*

5.3 Results and Discussion

5.3.1 3D holotomographic visualization of hemocyte subpopulations

High-resolution, label-free live-cell imaging using holotomography enabled the three-dimensional characterization of the different hemocyte subpopulations: blast-like cells, round hyalinocytes, round granulocytes, spindle granulocytes, and granular asterocytes (Figure 5.3A–E). Representative RI tomograms of the hemocyte subpopulations revealed distinct morphological characteristics (as shown in the reference images in Supplementary Figure A5.16), including differences in cell size, shape, and granularity, as well as intracellular RI distributions. In addition, 3D-rendered reconstructions provided detailed visualization of specific cellular structures, including the cytoplasm (white), nucleus and granules (yellow), and vacuoles (cyan) (Figure 5.4A–E).

Blast-like cells (Figures 5.3A and 5.4A), characterized by their small size, with a diameter of approximately 6–8 μm, high nucleus-to-cytoplasm ratio and low organelle content, are considered as hemocyte precursors or progenitors with no phagocytotic capability. Although their designation remains variable across studies, with alternative terms including small hyalinocytes, basophils, hemoblast-like cells or lymphoid hemocytes, these cells are consistently interpreted as immature precursor forms based on their morphometric features (de la Ballina et al., 2022; Evariste et al., 2016). Hyalinocytes (Figures 5.3B and 5.4B), which exhibit an agranular cytoplasm containing few or no granules, are generally associated with low phagocytic activity. In contrast, granulocyte morphotypes (round and spindle-shaped in Figures 5.3C–D and 5.4C–D) are characterized by abundant granules or vesicles in the cytosol and a low N/C ratio, features that underpin their high phagocytic capability and central role in cellular defense (de la Ballina et al., 2022; Evariste et al., 2016; Le Foll et al., 2010). Another granulocyte morphotype, the granular asterocyte (Figures 5.3E and 5.4E), is characterized by complex cytoskeletal structures that may facilitate intercellular interactions and signaling (Baldwin et al., 2024; Ray et al., 2013).

The visualization of specific intracellular structures was made possible by contrast variations that are directly correlated with differences in composition and density of cellular contents (Buzalewicz et al., 2022). Previous reports indicated that RI values for other cell types, at the whole-cell level, range from 1.346 for immortalized normal oral keratinocytes to 1.478 for epithelial cells. As indicated, whole cell RI values may vary even within the same cell type, depending on organelle presence and distribution, protein accumulation, and overall cell size and mass, underscoring the importance of (sub)population-level analyses when interpreting RI-based imaging data. Subcellular organelles of other human and murine cell types exhibit an even broader RI spectrum, ranging from ~1.34 for nuclei to ~1.70 for melanosomes, reflecting differences in size, molecular composition, and biogenesis of organelles (Gul et al., 2021).

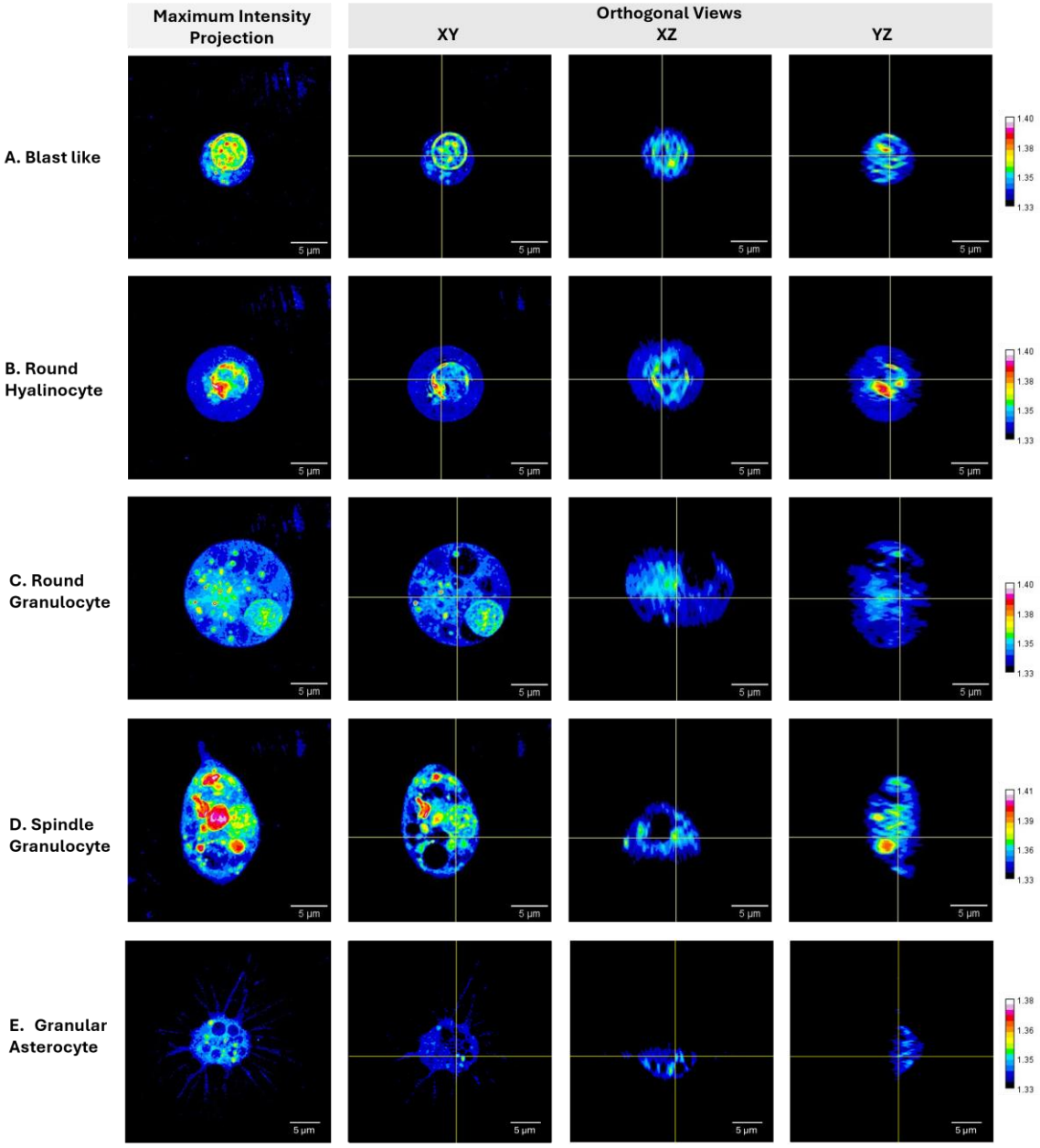

Figure 5.3. *Representative refractive index (RI) tomograms corresponding to negative control condition, enabling the visualization of hemocyte subpopulations: A) Blast-like, B) Round Hyalinocyte, C) Round Granulocyte, D) Spindle Granulocyte, and E) Granular Asterocyte (specified). Refractive index maps are shown as maximum intensity projections and orthogonal views in XY, XZ and YZ planes. A pseudo-color scale, based on the actual RI range, was applied to visualize refractive index variations. Scale bar: 5 µm. The color bar on the right indicates the scale for RI-values.*

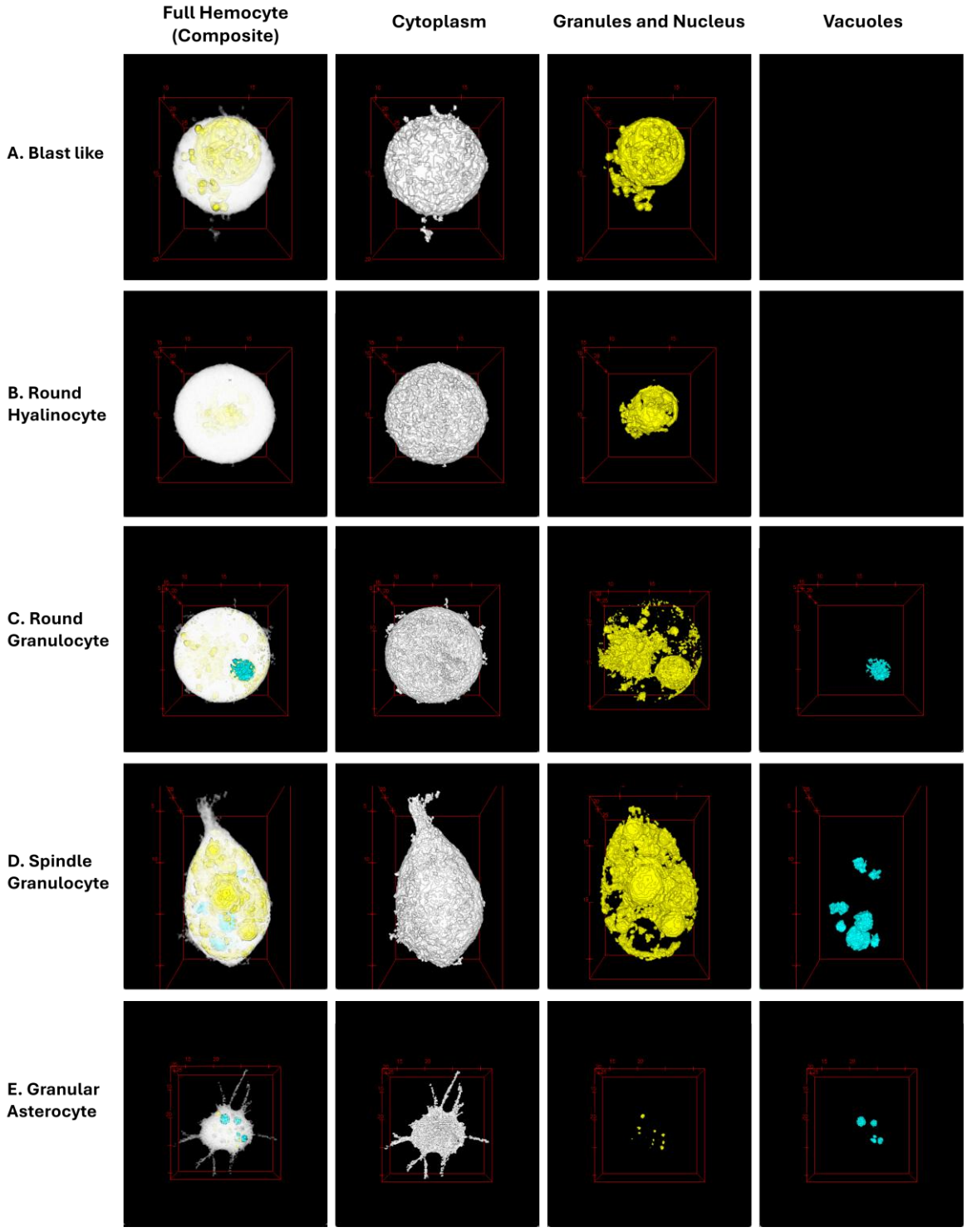

Figure 5.4. *Representative 3D refractive index (RI) tomographic renderings of hemocyte subpopulations corresponding to negative control condition: A) Blast-like, B) Round Hyalinocyte, C) Round Granulocyte, D) Spindle Granulocyte, and E) Granular Asterocyte (specified). Segmented structures were represented with distinct pseudo-colors: cytoplasm (white), granules (yellow), and vacuoles (cyan). Panels include the composite reconstruction of the hemocyte with cytoplasmic transparency adjusted so as to reveal internal structures. A 3D bounding box with scale markers (|—|, each representing a 5 µm increment) is included to indicate the physical dimensions along all three spatial axes. Black panels indicate the absence of detectable vacuoles. The full 3D volume of the hemocyte subpopulations recorded with 360° rotation can be viewed*

through this link (select Hemocyte Subpopulations): https://mysite.harajenevieve.workers.dev/hemocyte-a1793b4f897569cde9d0d70a1ccacf58ab1871/. Note: to view the 3D animations, use the tree view in the navigation panel to expand and select categories to display the content.

Accurate determination of RI values is influenced by both the heterogeneity of individual organelles and the sensitivity of the advanced 3D optical techniques employed (Gul et al., 2021; P. Y. Liu et al., 2016). The ability of holotomography to exploit these intrinsic optical properties allows an accurate and label-free discrimination of intracellular hemocyte structures, thereby supporting simultaneous morphological and biophysical analysis at the single-cell level. Such quantifiable parameters include volume, surface area, sphericity, and dry mass (Buzalewicz et al., 2022; Yoon et al., 2015).

5.3.2 Cellular internalization and localization of aged PET NPs

Representative 3D RI tomograms and renderings of hemocytes exposed to aged PET NPs at increasing concentrations (C1–C3) for 24 h and 48 h demonstrated internalization and intracellular localization of the particles. Internalized particles were distinguished from intrinsic subcellular structures because of the high refractive index compared to that of the relevant component cell structures. As shown in the RI tomograms (Figure 5.5A–D), the spatial positioning of aged PET NP within the cell was highlighted in the cross-sectional XY, XZ and YZ planes. Engulfed particles were identified by the RI value of the aged PET NPs of approximately ∼1.45 ± 0.01. This observation is consistent with previous studies demonstrating the phagocytosis and dynamic RI-based tracking of polystyrene microbeads in macrophages, where internalized particles exhibited RI values of ∼1.41 in the cytoplasm (Yoon et al., 2015). Another study evidenced that unlabelled nanodiamonds could be detected through RI measurements. Géloën et al. (2021) reported a distinct RI shift in Panc-1 cells exposed to 0.25–0.5 mg/mL nanodiamonds, occurring from 1.38 to 1.39, compared with control cells (1.365–1.395, maximum values centered at 1.3725), and that difference was attributed by the authors to the presence of internalized nanodiamonds. However, because the RI value defining the nanodiamonds falls within the range of RI pertaining to the cellular components, the optical contrast operative in the work by Géloën et al. (2021) is limited, underscoring the need for nanoparticles with RI values substantially higher than the cellular components to enhance detection sensitivity.

In this study, aged PET NPs were observed within the cytoplasmic boundaries of hemocytes, indicating efficient cellular internalization and distinct localization patterns mainly evident in granulocytes (Figure 5.6A-D). Granulocytes were the main hemocyte subpopulation observed to internalize aged PET NPs; however, not all granulocytes that were imaged exhibited particle internalization. When internalization was present, the pattern was consistently observed across all tested concentrations and exposure durations. This finding aligns with the recognized high phagocytic capability of granulocytes, which are primarily responsible for particle uptake and immune defense in bivalves (de la Ballina et al., 2022; Le Foll et al., 2010).

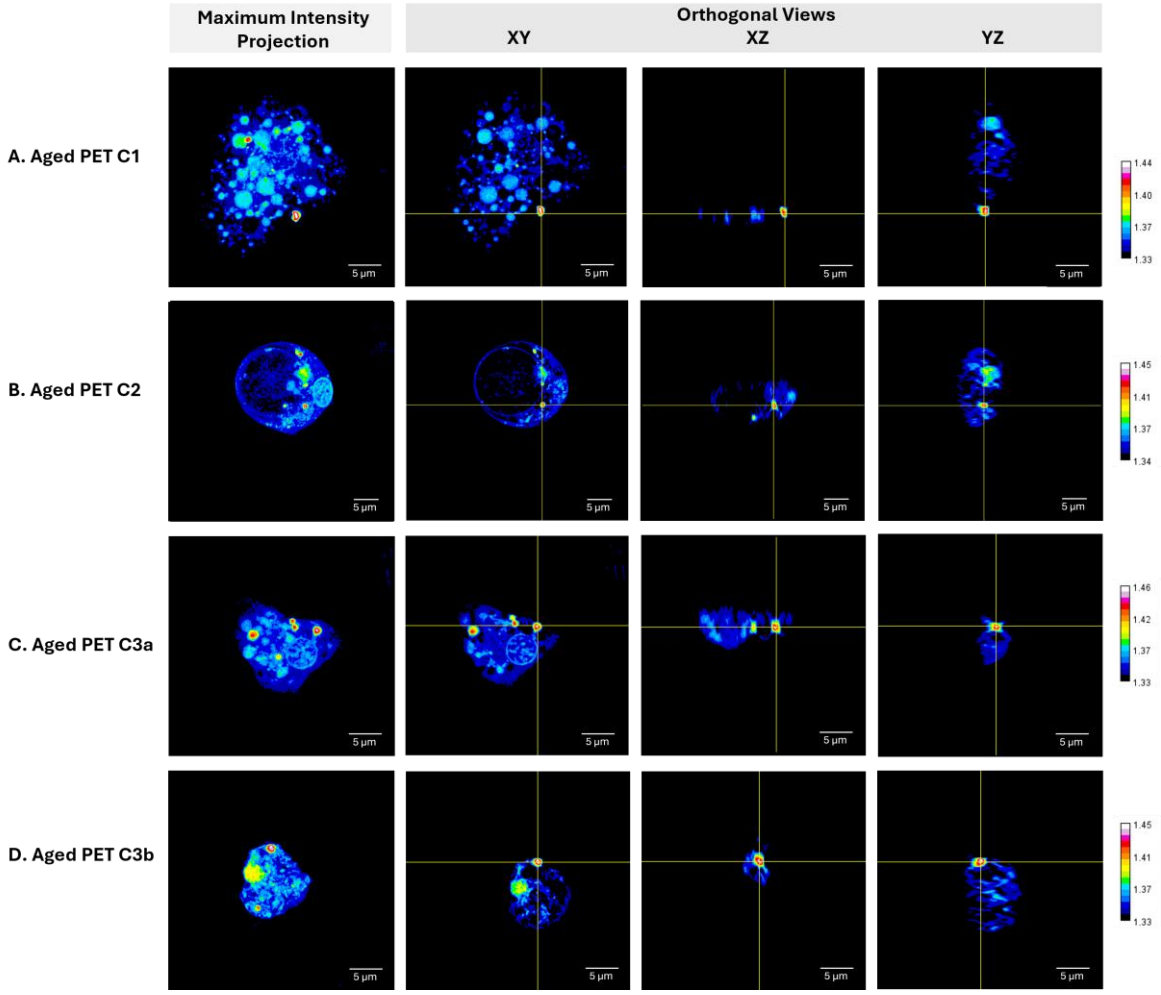

Figure 5.5. *Representative holotomography images of hemocytes, primarily* ***granulocytes****, showing internalized and localized aged PET nanoplastic particles following exposure to C1 (10 P/mL, 48 h, Panel A), C2 (10^3 P/mL, 48 h, Panel B), and C3 (10^5 P/mL, Panels C (24 h) and D (48 h)). Granulocytes were the main subpopulation observed with internalized particles, consistently across all tested concentrations. Engulfed PET NPs are identified by a refractive index (RI) of ~1.45. Refractive index maps are shown as maximum intensity projections and orthogonal views in XY, XZ and YZ planes. A pseudo-color scale, based on the actual RI range, was applied to visualize refractive index variations. The spatial positioning of aged PET NP within the cell is highlighted in the cross-sectional XY, XZ and YZ planes. Scale bar: 5 µm. The color bar on the right indicates the scale for RI-values.*

The representative images shown in Figure 5.6 also reflect the state of internalization and localization within granulocytes. In Panels B-D of Figure 5.6, particles were localized adjacent to or embedded within dense granular structures, whereas Panel A showed an aged PET NP that is enclosed within cell surface extensions, indicating an early stage of uptake. While representative images typically showed a single PET NP per hemocyte, multiple internalized particles (e.g., four NPs displayed in red in Figure 5.6C) were also observed. Prior studies have demonstrated that hemocytes are capable of internalizing multiple particles, in some cases up to six (Katsumiti et al., 2021). Previous *in vitro* observations indicated that hemocytes internalize MNPs primarily through endocytic routes. Uptake is size-dependent: smaller particles (≤0.5 µm) enter via clathrin- or

caveolae-mediated endocytosis and macropinocytosis, whereas larger particles (≥0.5 µm) are mainly taken up by phagocytosis (Katsumiti et al., 2021; Sendra, Saco, et al., 2020; Uribe-Querol & Rosales, 2020).

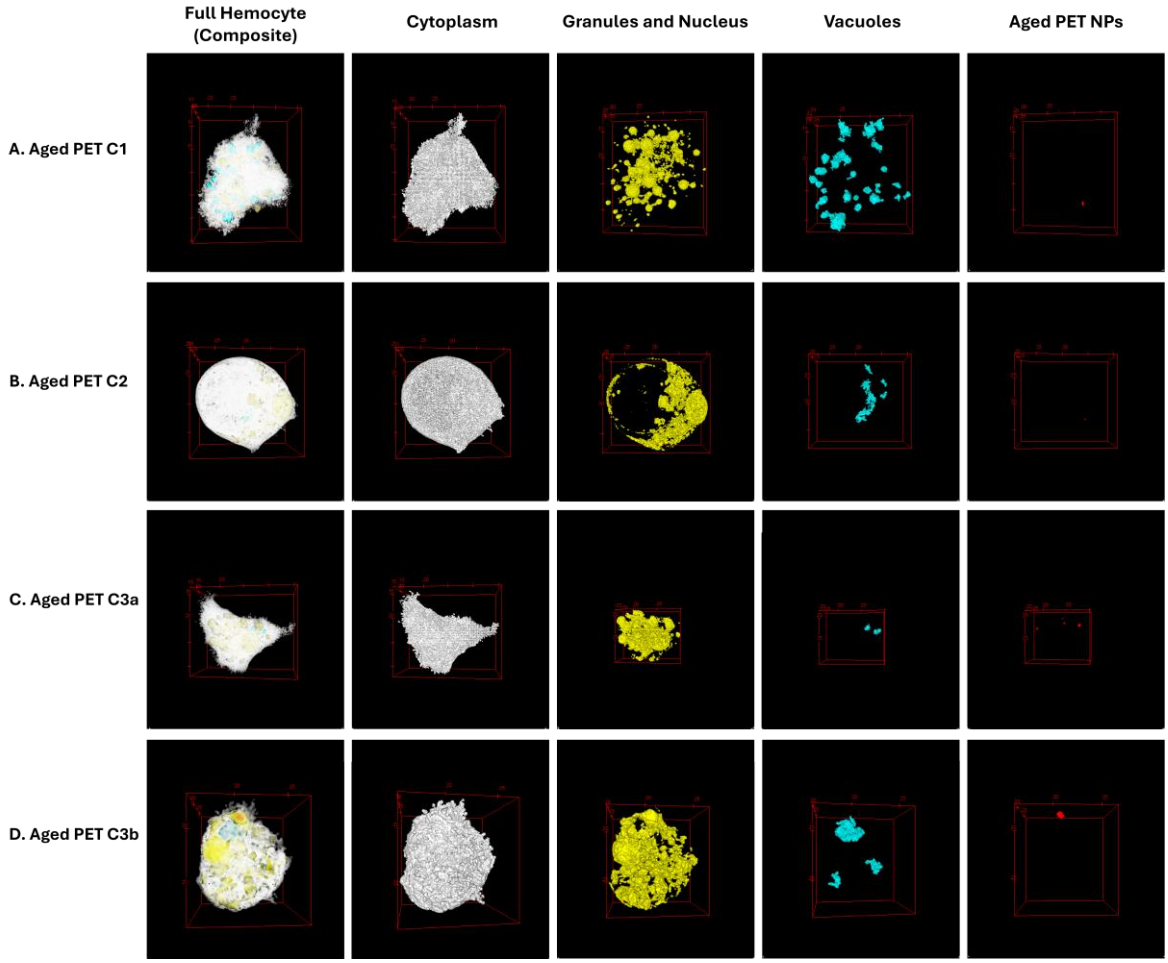

Figure 5.6. *Representative 3D refractive index (RI) tomographic renderings of* ***granulocytes****, showing internalized and localized aged PET nanoplastic particles following exposure to C1 (10 P/mL, 48 h, Panel A), C2 (10^3 P/mL, 48 h, Panel B), and C3 (10^5 P/mL, Panels C (24 h) and D (48 h)). Segmented structures were represented with distinct pseudo-colors: cytoplasm (white), granules (yellow), vacuoles (cyan), and internalized aged PET NPs (red). Panels include the composite reconstruction of the hemocyte with cytoplasmic transparency adjusted so as to reveal internal structures. A 3D bounding box with scale markers (|—|, each representing a 5 µm increment) is included to indicate the physical dimensions along all three spatial axes. The full 3D volume of granulocytes with internalized NPs recorded with 360° rotation can be viewed through this link (select Aged PET NP Internalization and Localization): https://mysite.harajenevieve.workers.dev/hemocyte-a1793b4f897569cde9d0d70a1ccacf58ab1871/. Note: to view the 3D animations, use the tree view in the navigation panel to expand and select categories to display the content.*

Once internalized, these particles are generally trafficked into lysosomal compartments, which act as the principal intracellular sink for particle accumulation and processing (Canesi et al., 2012; Stern et al., 2012). As observed in Figure 5.6B–D, internalized aged PET NPs were predominantly sequestered within dense cytoplasmic granules (displayed in yellow in the 3D rendering of Figure 5.6), which are typically a form of lysosomes

containing hydrolytic enzymes that degrade phagocytosed foreign particles (Chang & Wang, 2024; de la Ballina et al., 2022; Mao et al., 2020; Pipe, 1990). Another study demonstrated the uptake, intracellular trafficking, and ultimate colocalization of aggregation-induced emission nanoplastics (AIE-NPs, 50 nm and 200 nm) with lysosomes in hemocyte subpopulations through confocal imaging (Chang & Wang, 2024). Interestingly, NP uptake was reported to accelerate the differentiation of agranulocytes into granulocytes, enhancing their immunoreactivity. However, the limited clearance previously observed in both subpopulations indicates that persistent lysosomal accumulation could exacerbate cellular stress (Chang & Wang, 2024). Similar observations have been reported in corneal and skin keratocyte cells, for which holotomographic microscopy and fluorescence imaging capability revealed that 500–1000 nm polystyrene particles and 500 nm silica particles were efficiently internalized, with a fraction reaching lysosomal compartments within just 2 hours of exposure (Thiyagarajan et al., 2024). The consistent confinement of NPs within these compartments underscores lysosomes as both the primary site of nanoplastic sequestration and a critical hotspot of toxicity, given that lysosomal overload and destabilization are key mechanisms of particle-induced cytotoxicity (Stern et al., 2012).

5.3.3 Characterization of the morphological changes in hemocytes

Representative images illustrate the observable morphological changes across different hemocyte subpopulations, including the blast-like (Figure 5.7–Figure 5.8), hyalinocytes (Figure 5.9–Figure 5.10), granulocytes (Figure 5.11–Figure 5.12), and granular asterocyte (Figure 5.13–Figure 5.14), following 48 h exposure to aged PET NPs and to $CdCl_2$ as positive control for cytotoxicity. Hemocytes exposed to the selected concentrations of aged PET NPs exhibited distinct morphological changes, including extensive cytoplasmic vacuolation and cytoplasmic granulation, particularly in granulocytes (Figure 5.12A–C). In blast-like cells (Figure 5.8C) and hyalinocytes (Figure 5.10A–C), vacuole formation was also observed, particularly extensive at the highest tested concentration (C3) of aged PET NPs. Granular asterocytes exposed to aged PET NPs, particularly at the highest tested concentration (Figure 5.14C), were observed with increased branching structures, indicating a reactive asterocyte phenotype typically associated in response to various stimuli (Escartin et al., 2021; Falcone, 2022; H. G. Lee et al., 2022).

Similarly, cells exposure to $CdCl_2$ induced comparable morphological changes in the organization of cytoplasmic granules and vacuoles than an exposure to aged PET NPs. Signs of cellular blebbing were particularly observed in hyalinocytes (Figure 5.10D) and granulocytes (Figure 5.12D–E). The $CdCl_2$-treated hemocytes, especially those exposed to the highest tested concentration (C2, 800 µM, 48h) used as a positive control to induce cell death, exhibited obvious and clear membrane disruption (Figure 5.12F) compared to other treatment groups, consistent with its established role as a potent cytotoxicant. Following exposure to $CdCl_2$ at C2, no hyalinocytes and granular asterocytes could be identified.

While these observations provide qualitative evidence, quantitative analyses are necessary to validate the extent of the aforementioned morphological changes and to establish their concentration-dependent nature.

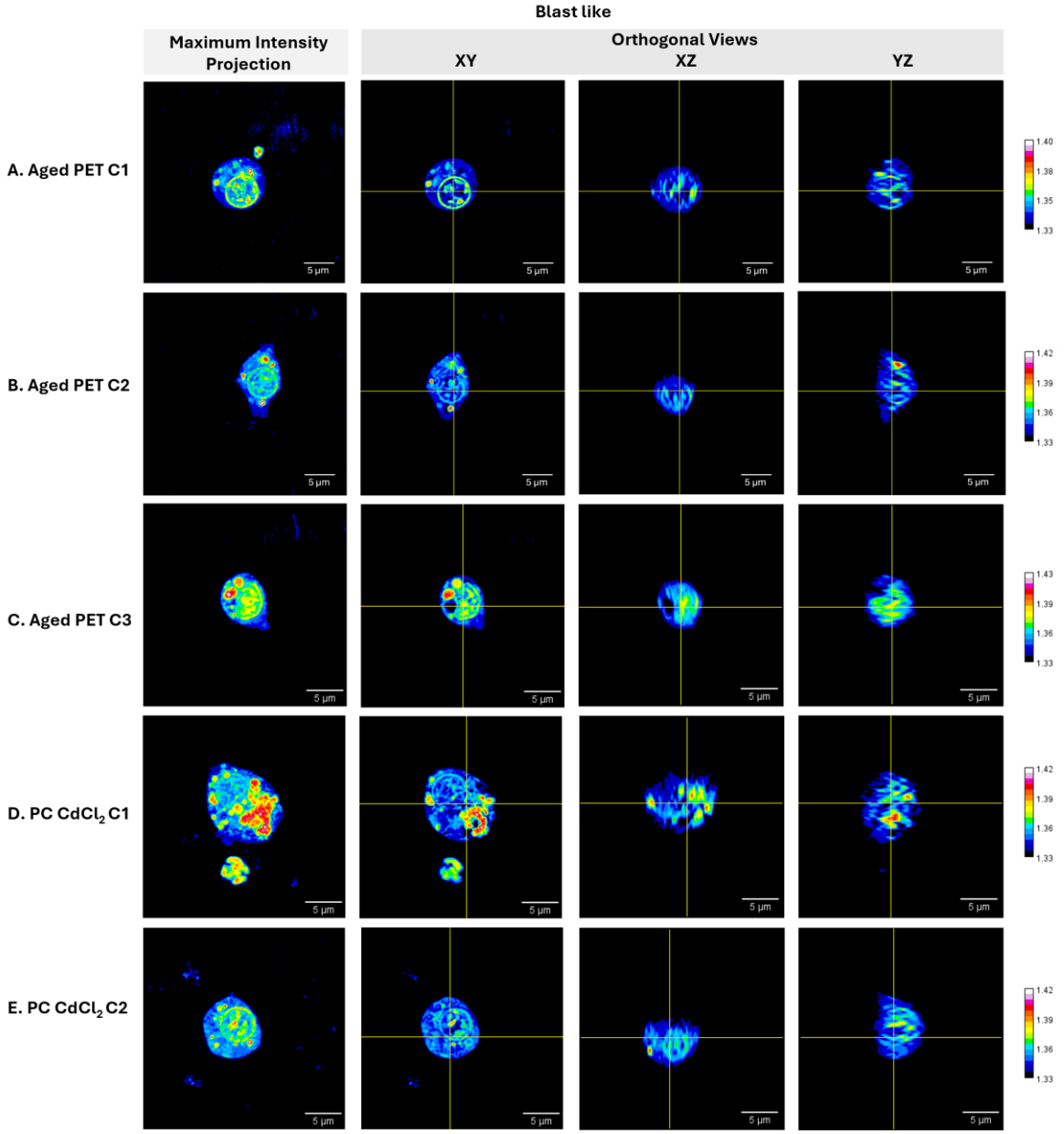

Figure 5.7. *Representative holotomography images of* ***blast-like cells*** *following 48 h exposure to aged PET nanoplastic particles (C1–C3; Panel A–C) and cadmium chloride ($CdCl_2$; Panel D–E) as positive control. Refractive index maps are shown as maximum intensity projections and orthogonal views in XY, XZ and YZ planes. A pseudo-color scale, based on the actual RI range, was applied to visualize refractive index variations. Scale bar: 5 µm. The color bar on the right indicates the scale for RI-values.*

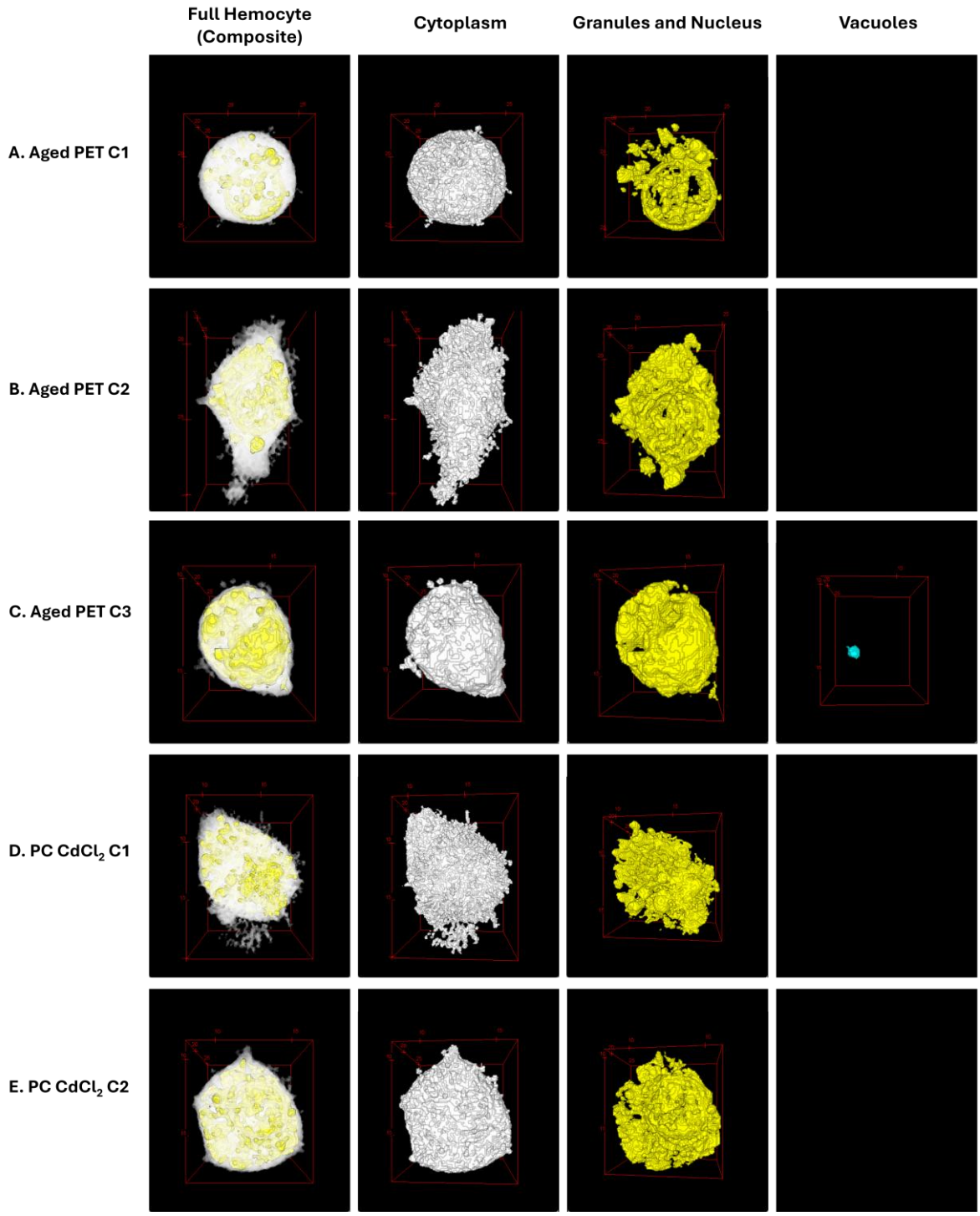

Figure 5.8. *Representative 3D refractive index (RI) tomographic renderings of* ***blast-like cells*** *following 48 h exposure to aged PET nanoplastic particles (C1–C3; Panel A–C) and cadmium chloride ($CdCl_2$; Panel D–E) as positive control. Segmented structures were represented with distinct pseudo-colors: cytoplasm (white), granules (yellow), and vacuoles (cyan). Panels include the composite reconstruction of the hemocyte with cytoplasmic transparency adjusted so as to reveal internal structures. A 3D bounding box with scale markers (|—|, each representing a 5 µm increment) is included to indicate the physical dimensions along all three spatial axes. Black panels indicate the absence of detectable vacuoles. The full 3D volume recorded with 360° rotation can be viewed through this link (select Morphological Observations: Blast- like): https://mysite*

.harajenevieve.workers.dev/hemocyte-a1793b4f897569cde9d0d70a1ccacf58ab1871/. Note: to view the 3D animations, use the tree view in the navigation panel to expand and select categories to display the content.

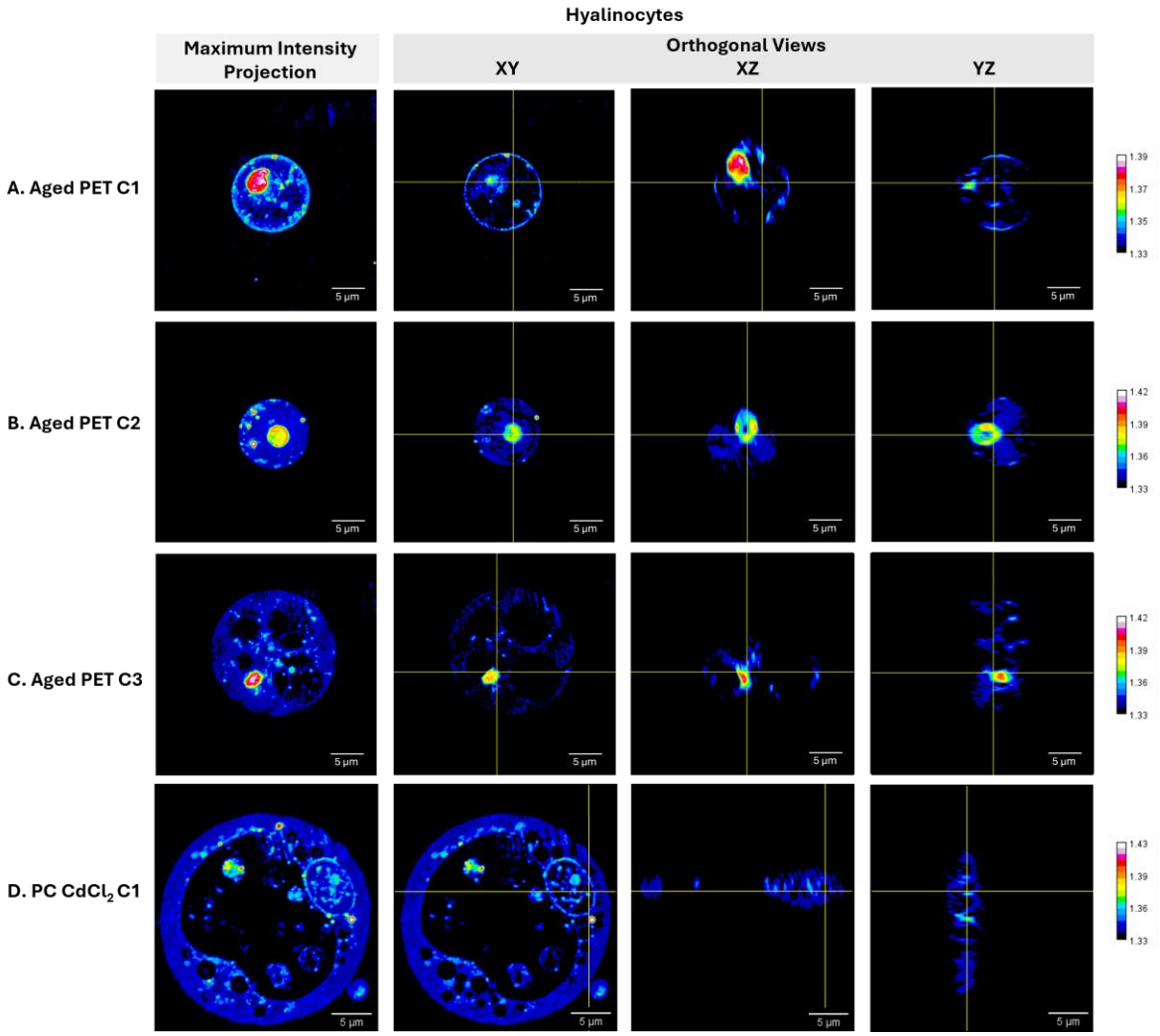

Figure 5.9. *Representative holotomography images of* ***hyalinocytes*** *following 48 h exposure to aged PET nanoplastic particles (C1–C3; Panel A–C) and cadmium chloride ($CdCl_2$ C1; Panel D) as positive control. Distinct cellular responses, including vacuolization in Panel C (aged PET NP C3) and cellular blebbing with detached cellular bodies in Panel D (PC $CdCl_2$ C1). Following exposure to $CdCl_2$ at C2, no hyalinocytes could be identified. Refractive index maps are shown as maximum intensity projections and orthogonal views in XY, XZ, and YZ planes. A pseudo-color scale, based on the actual RI range, was applied to visualize refractive index variations. Scale bar: 5 µm. The color bar on the right indicates the scale for RI-values.*

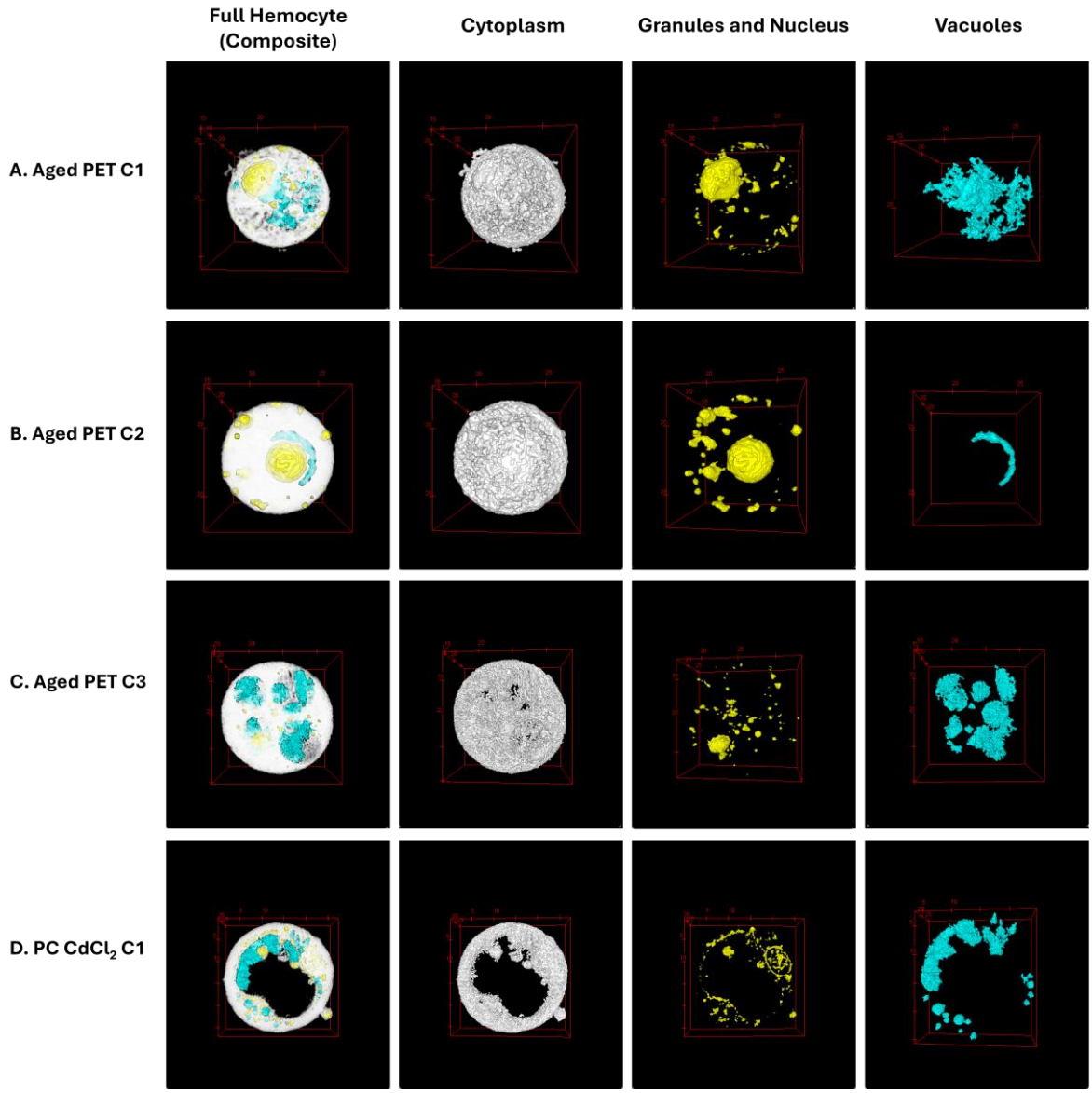

Figure 5.10. *Representative 3D refractive index (RI) tomographic renderings of* ***hyalinocytes*** *following 48 h exposure to aged PET nanoplastic particles (C1–C3; Panel A–C) and cadmium chloride ($CdCl_2$ C1; Panel D) as positive control. Distinct cellular responses, including vacuolization in Panel C (aged PET NP C3) and cellular blebbing with detached cellular bodies in Panel D (PC $CdCl_2$ C1). Segmented structures were represented with distinct pseudo-colors: cytoplasm (white), granules (yellow), and vacuoles (cyan). Panels include the composite reconstruction of the hemocyte with cytoplasmic transparency adjusted so as to reveal internal structures. A 3D bounding box with scale markers (|—|, each representing a 5 µm increment) is included to indicate the physical dimensions along all three spatial axes. The full 3D volume of hyalinocytes recorded with 360° rotation can be viewed through this link (select Morphological Observations: Hyalinocytes): https://mysite.harajenevieve.workers.dev/hemocyte-a1793b4f897569cde9d0d70a1ccacf58ab1871/. Note: to view the 3D animations, use the tree view in the navigation panel to expand and select categories to display the content.*

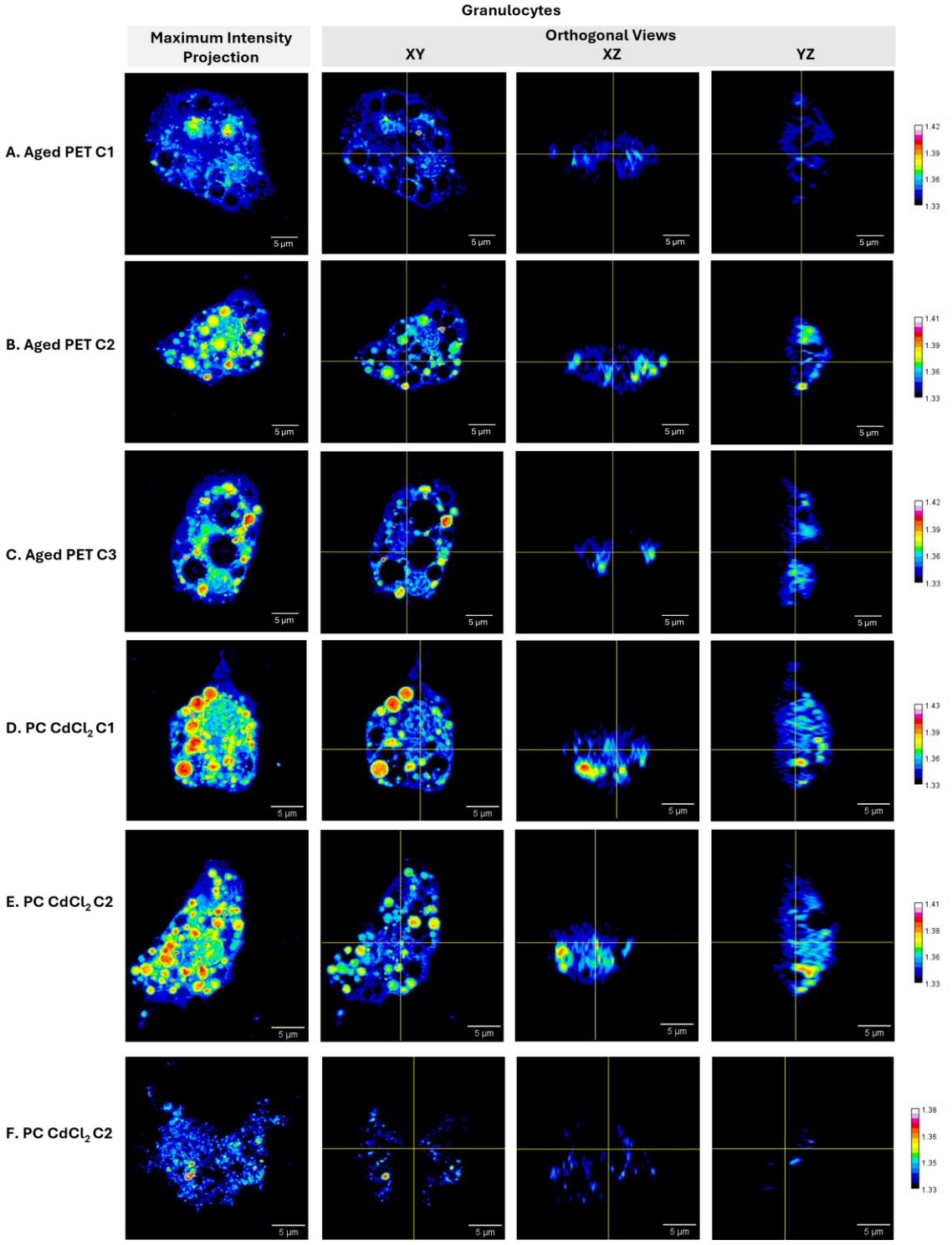

Figure 5.11. *Representative holotomography images of* ***granulocytes*** *following 48 h exposure to aged PET nanoplastic particles (C1–C3; Panel A–C) and cadmium chloride ($CdCl_2$; Panel D–F) as positive control. Distinct cellular responses included extensive vacuolization (Panels A–E) and increased cytoplasmic granulation (Panels B–E), while membrane disruption is evident in Panel F. Refractive index maps are shown as maximum intensity projections and orthogonal views in XY, XZ, and YZ planes. A pseudo-color scale, based on the actual RI range, was applied to visualize refractive index variations. Scale bar: 5 µm. The color bar on the right indicates the scale for RI-values.*

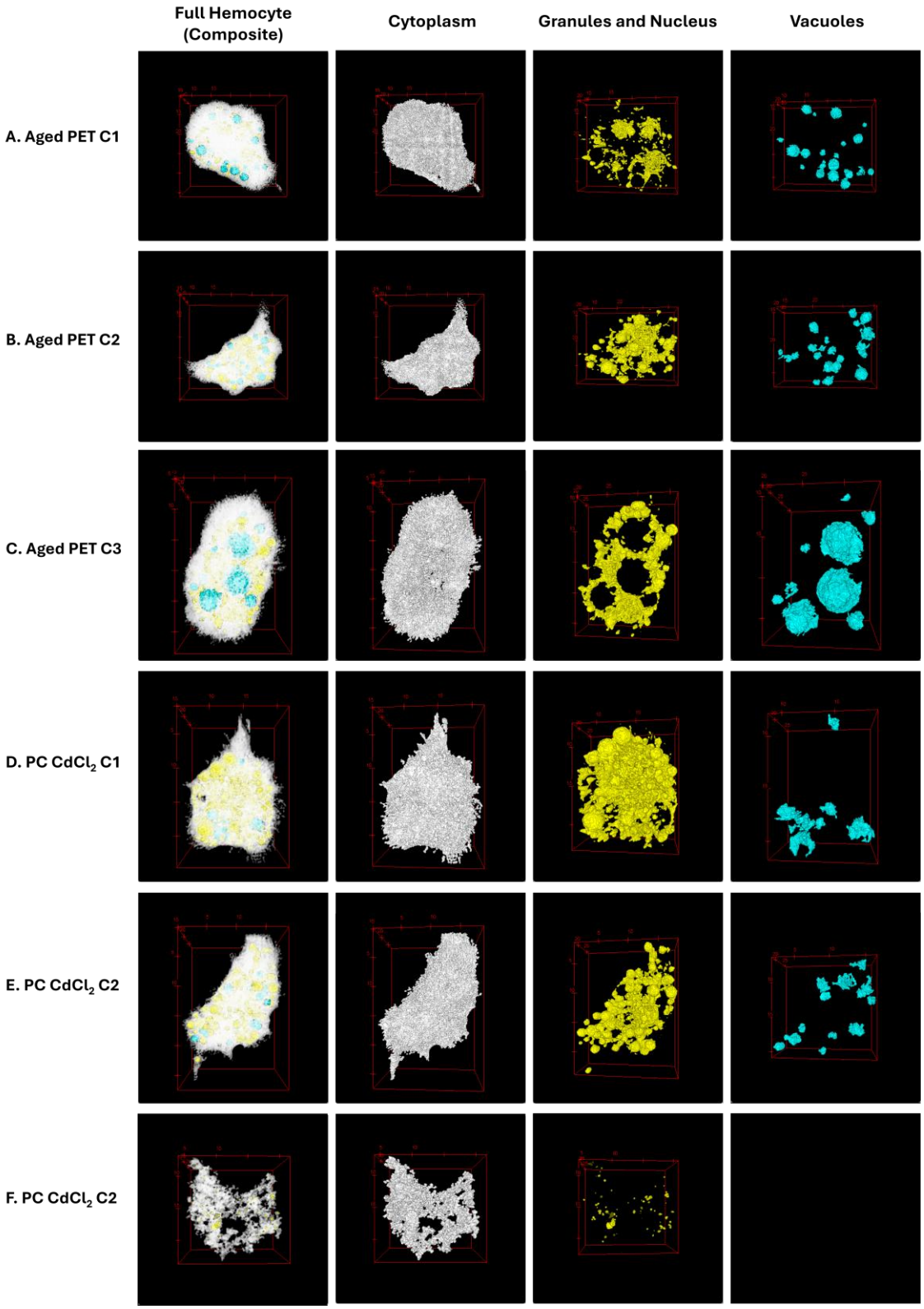

Figure 5.12. *Representative 3D refractive index (RI) tomographic renderings of* ***granulocytes*** *following 48 h exposure to aged PET nanoplastic particles (C1–C3; Panel A–C) and cadmium chloride ($CdCl_2$; Panel D–F) as positive control. Distinct cellular responses included extensive vacuolization (Panels A–E) and increased*

cytoplasmic granulation (Panels B–E), while membrane disruption is evident in Panel F. Segmented structures were represented with distinct pseudo-colors: cytoplasm (white), granules (yellow), and vacuoles (cyan). Panels include the composite reconstruction of the hemocyte with cytoplasmic transparency adjusted so as to reveal internal structures. A 3D bounding box with scale markers (|—|, each representing a 5 µm increment) is included to indicate the physical dimensions along all three spatial axes. The full 3D volume recorded with 360° rotation can be viewed through this link (select Morphological Observations: Granulocytes): https://mysite.harajenevieve.workers.dev/hemocyte-a1793b4f897569cde9d0d70a1ccacf58ab1871/. Note: to view the 3D animations, use the tree view in the navigation panel to expand and select categories to display the content.

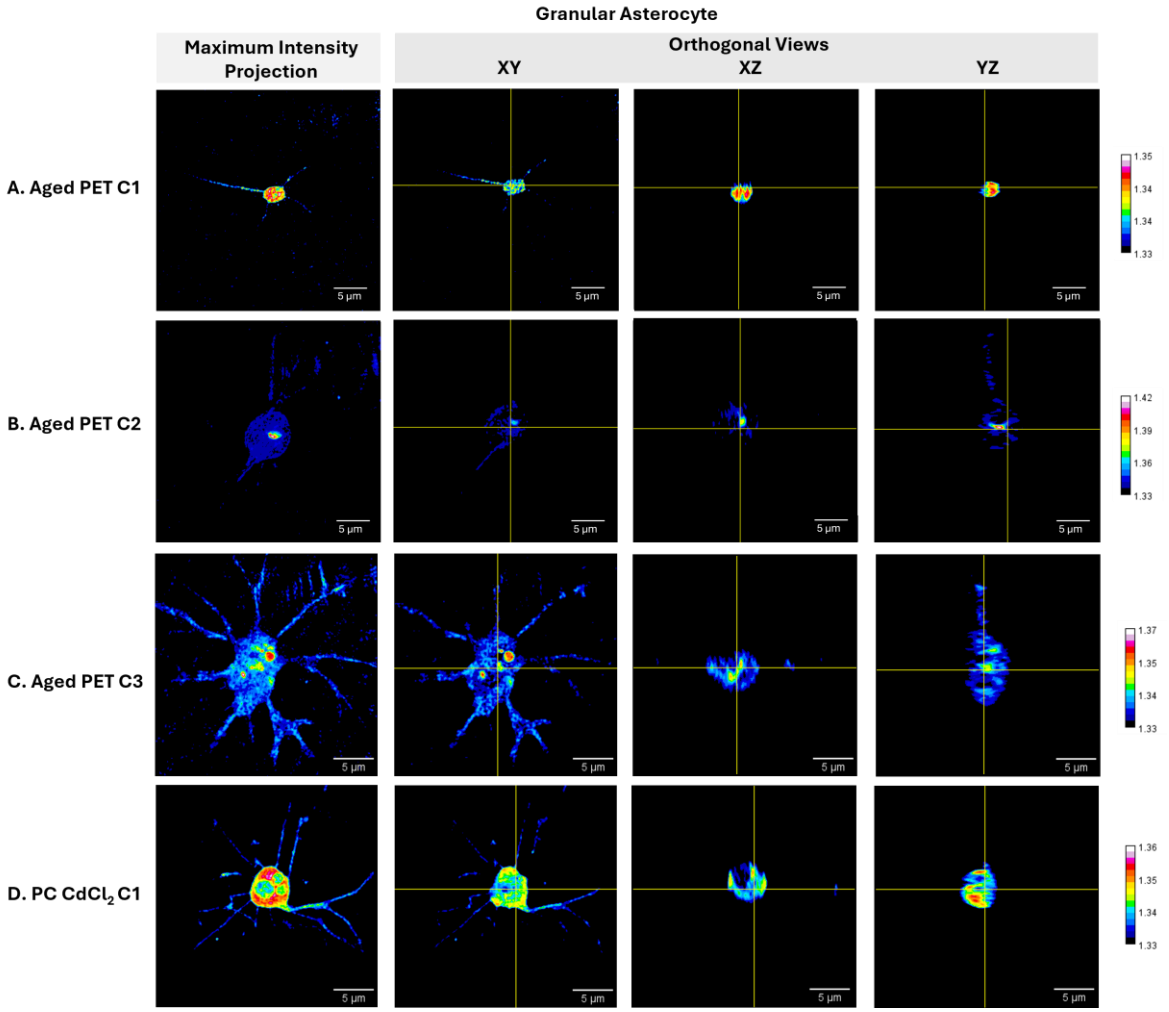

Figure 5.13. *Representative holotomography images of* ***granular asterocyte*** *following 48 h exposure to aged PET nanoplastic particles (C1–C3; Panel A–C) and cadmium chloride ($CdCl_2$ C1; Panel D) as positive control. Following exposure to $CdCl_2$ at C2, no granular asterocyte could be identified. Refractive index maps are shown as maximum intensity projections and orthogonal views in XY, XZ, and YZ planes. A pseudo-color scale, based on the actual RI range, was applied to visualize refractive index variations. Scale bar: 5 µm. The color bar on the right indicates the scale for RI-values.*

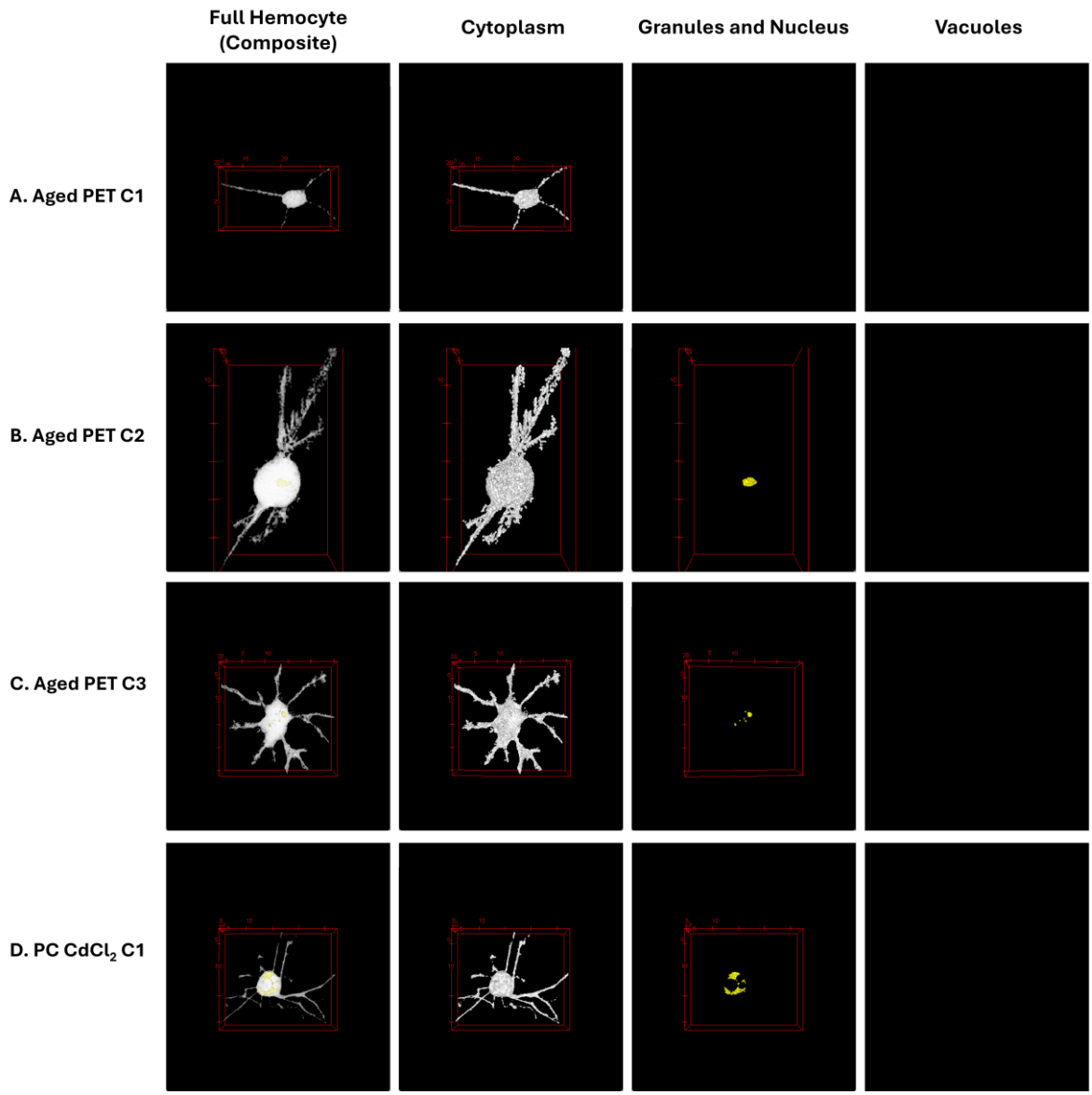

Figure 5.14. *Representative holotomography images of* ***granular asterocyte*** *following 48 h exposure to aged PET nanoplastic particles (C1–C3; Panel A–C) and cadmium chloride ($CdCl_2$ C1; Panel D) as positive control. Distinct cellular responses observed was an increase in branching structure, indicative of a reactive asterocyte phenotype (Panel C and D). Segmented structures were represented with distinct pseudo-colors: cytoplasm (white), granules (yellow), and vacuoles (cyan). Panels include the composite reconstruction of the hemocyte with cytoplasmic transparency adjusted so as to reveal internal structures. A 3D bounding box with scale markers (|—|, each representing a 5 µm increment) is included to indicate the physical dimensions along all three spatial axes. Black panels indicate the absence of detectable vacuoles or granules. The full 3D volume recorded with 360° rotation can be viewed through this link (select Morphological Observations: Granular Asterocytes): https://mysite.harajenevieve.workers.dev/hemocyte- a1793b4f897569cde9d0d70a1ccacf58ab1871/. Note: to view the 3D animations, use the tree view in the navigation panel to expand and select categories to display the content.*

As observed, hemocyte exposure to aged PET NPs and $CdCl_2$ induced enhanced cytoplasmic granulation. Cytoplasmic granules are enriched with hydrolytic enzymes such as proteinases, glycosidases, and sulphatases, acting as a form of lysosomes in hemocytes

(Pipe, 1990). The induction of granulation likely represents an adaptive activation of lysosomal systems to compartmentalize and attempt to degrade foreign materials (Stern et al., 2012). Interestingly, PET NPs have been reported to maintain a stable hydrodynamic size under chronic exposure of up to two months in a simulated lysosomal environment, underscoring their potential for intracellular bio-persistence and long-term stability (Magrì et al., 2018). Such persistence increases the risk of unmetabolized substrate accumulation and lysosomal overload, which can induce lysosomal dysfunction with adverse consequences including impaired intracellular trafficking and disrupted signaling (Stern et al., 2012). This dysfunction is characterized by disruption of the acidic microenvironment, rupture of the lysosomal membrane, and increased membrane permeabilization, processes that compromise cellular homeostasis and can trigger cell death pathways (Feng et al., 2024).

In addition to cytoplasmic granulation, hemocytes exposed to aged PET NPs also exhibited cytoplasmic vacuolation. Comparable vacuolation has been reported in hemocytes exposed to 50 nm amine-terminated polystyrene NPs (Canesi et al., 2016) and other classes of toxicants like pyrethroid pesticides (Ray et al., 2013). Such observations reinforce the finding that cytoplasmic vacuolation is not restricted to plastic exposure but that it is a conserved morpho-pathological response across diverse stressors. It is characterized by the formation of substantial vacuole-like structures from multiple cellular organelles, and is associated with cellular stress responses and, in severe cases, progression toward cell death (Shubin et al., 2016; Wen & Ma, 2025). In particular, the vacuolization of endosomal-lysosomal components is associated with disturbances in organellar ionic balance or sorting and fusion of the organelles (Shubin et al., 2016). Persistent or excessive vacuolation disrupts organelle integrity and homeostasis, and can act as a precursor to cell death pathways, particularly oncosis, which is characterized by swelling, vacuolation, membrane blebbing, and increased permeability as hallmarks of irreversible damage. Mechanistically, oncosis results from the failure of plasma membrane ion pumps, most often caused by toxic agents that impair adenosine triphosphate (ATP) production or increase membrane permeability. When unresolved, these alterations advance rapidly, typically within 24 hours, culminating in necrosis (Guo et al., 2024; Majno & Joris, 1995). As a potent cytotoxicant, $CdCl_2$ used as positive control is known to activate multiple death pathways in parallel, which collectively accelerate programmed necrosis (Messner et al., 2016). The major morphological features of necrosis have been illustrated using holographic microscopy (Balvan et al., 2015), which typically involves multiple cytoplasmic blebbing, cytoplasmic translucency, cell swelling leading to nuclear dilatation, and eventual plasma membrane disruption.

5.4 Conclusions and Future Directions

This work demonstrates the applicability of three-dimensional label-free live cell imaging using holotomography to characterize hemocyte responses to aged PET NPs. By employing

3D refractive index mapping, we qualitatively visualized intracellular distribution of internalized nanoplastics, providing insight into uptake mechanisms and localization patterns. The ability to resolve unlabeled particles within living hemocytes underscores the unique advantage of holotomography for evaluating nanoplastic–cell interactions and their implications for cellular integrity.

Future directions will include the integration of quantitative analyses to characterize hemocyte subpopulations and systematically evaluate their dose-response profiles to aged nanoplastic exposure. The quantitative capabilities are particularly valuable for tracking intracellular localization and assessing dynamic morphological and biophysical changes. Such approaches would significantly advance the mechanistic understanding of nanoplastic toxicity at the single-cell level.

Additionally, methodological refinement and validation of the image processing pipeline are critical next steps. Establishing robust ground truth comparisons, improving object detection accuracy (with comprehensive evaluation of true and false positives/negatives), and reducing sensitivity to imaging noise and artifacts will be essential for improving analysis reliability. A more rigorous approach is currently being developed to improve robustness, sensitivity, and quantitative accuracy.

With further development and refinement of quantitative metrics and advanced image analysis pipelines, this approach will provide high-resolution, label-free insights into the cellular and subcellular impacts of exposure to aged PET nanoplastics, thereby enabling more comprehensive and mechanistic evaluations of plastic particle toxicity.

5.5 Acknowledgements

This work was done with resources from the Pôle de compétences en physico-chimie de l'environnement, ANATELo, LIEC laboratory, UMR 7360 CNRS – Université de Lorraine. The authors specifically thank Mohamed Lo for his contribution during the experimentation. Special thanks are extended to András Retzler (Dynamic Design Lab, UGent) for his support and contribution to the development of the image processing pipeline. Test particles and the primary characterization were supplied by the Joint Research Centre (JRC), with the support of John Seghers, Håkan Emteborg, and Claudia Cella.

Chapter 6

General Discussion and Future Perspectives

6.1 Integrative Synthesis of Key Findings and Contributions

This thesis provides a comprehensive, multi-level investigation into the biological reactivity of MNPs, addressing the overarching aim of mechanistically assessing their effects at the cellular, tissue, and organismal levels under environmentally relevant exposure scenarios. By integrating four interrelated research chapters, this work provides a distinct and complementary perspective on responses across multiple levels of biological organization.

6.1.1 Estimation of community-level hazard thresholds

The systematic evaluation in **Chapter 2** demonstrated that marine invertebrates exhibit marked interspecies variability in sensitivity to MNP exposure. The effects of MNP exposure on biological endpoints, including mortality, fitness, and functional responses, were analyzed as a function of particle characteristics to identify the key determinants of toxicity. The construction of SSDs, considering the different exposure mechanisms of MP toxicity such as food dilution and tissue translocation (Mehinto et al., 2022), provided a quantitative framework for estimating community-level hazard thresholds. SSDs were constructed to derive hazardous concentration for 5% of species (HC_5) (Besseling et al., 2019), thereby enabling the derivation of preliminary safe standards for marine invertebrate communities. A similar approach has also been applied in previous studies (Jung et al., 2021), particularly for MPs in the 20–300 µm size range covering eight taxonomic classes. In addition, Besseling et al. (2019) constructed SSDs using a combination of taxa spanning freshwater, estuarine, and marine ecosystems. Specifically, the marine invertebrate–specific thresholds derived here are consistent with thresholds developed for all marine organisms (Hampton et al., 2025), which are based on organism- and population-level toxicity data from ToMEx 2.0 for both food dilution and tissue translocation mechanisms. This alignment with the management planning (Threshold 3) and source control (Threshold 4) benchmarks indicates that marine invertebrate-based thresholds are sufficiently conservative to support ecosystem-level management actions. This represents an attempt to translate existing experimental findings, primarily derived from pristine MPs, into relevant risk estimates grounded in ecologically relevant endpoints. However, despite the increasing number of plastic-toxicity studies, critical gaps remain in addressing key factors necessary for robust risk assessment of the nanosized-range particles, including their sources, fate and transport, exposure pathways, toxicity, and biological effects (Cunningham et al., 2023). Nanoplastics, despite their potentially enhanced biological interactions due to their high surface-to-volume ratio and ability to cross biological barriers, remain underrepresented in current research (Rist & Hartmann, 2018). Additionally, the reliance on pristine particles has long been recognized as a limitation in the field (W. Liu et al., 2024), as weathering processes fundamentally alter polymer properties, surface chemistry, and interactions with biological systems (Chelomin et al., 2024; W. He et al., 2023). Addressing the identified research gaps, **Chapters 3, 4, and 5** of this thesis advanced the use of aged PET MNPs as test particles under environmentally relevant exposure

conditions, enabling the multi-level assessment of biological effects with a focus on sensitive sub-lethal functional endpoints.

6.1.2 Effect assessment under environmentally relevant exposure scenarios

Unlike prior studies that mainly rely on pristine, spherical particles, this research employed aged test plastic particles with heterogeneous shapes and sizes, reflecting modifications characteristic of naturally aged particles (Seghers et al., 2025; von der Esch et al., 2020a). Prior to exposure experimentation, thorough physicochemical characterization of the test particles was conducted including assessment of size distribution, morphology, surface properties, and stability in exposure media. In addition, strict quality assurance and quality control procedures, following De Ruijter et al. (2020), were implemented throughout particle handling, exposure, and analysis to minimize contamination and ensure the reliability and reproducibility of the results.

In **Chapter 3,** the results demonstrated that *in vivo* exposure to environmentally relevant concentrations of aged PET MNPs elicited systemic cellular and tissue-level perturbations in mussels (*Mytilus edulis*), a widely used sentinel species (Beyer et al., 2017; V. V. Ribeiro et al., 2023). Hemocyte subpopulations, particularly granulocytes and hyalinocytes, exhibited concentration- and time-dependent changes, including lysosomal stability, oxidative activity, and mortality. These findings underscore the sensitivity of hemocytes as early indicators of MNP-induced immunotoxicity (Canesi et al., 2012). Similar immunological disturbances have been reported for a broad range of particles, including carbon-, silicon-, and metal-based particles, in addition to polymeric MNPs, with the magnitude of effects varying according to particle size and concentration (Canesi et al., 2010b; Impellitteri et al., 2022; Pikula et al., 2020; T. Wang et al., 2019b; Weng et al., 2022). Extensive evidence shows that MNP exposure, particularly in the nanometer range, activates key toxicity pathways, including oxidative stress, lysosomal destabilization, and subsequent cell death mechanisms, consistent with our observations (Feng et al., 2024; Hu & Palić, 2020; Matthews et al., 2021; Stern et al., 2012). Moreover, the aging process of plastics can exacerbate cellular responses by altering protein corona formation and promoting particle uptake, ultimately influencing cellular fate and toxicity outcomes (Chelomin et al., 2024; T. Du et al., 2023). While cellular disturbances were evident particularly at the highest tested concentration, the study also revealed recovery potential during post-exposure periods, highlighting the organism's physiological resilience following exposure.

At the tissue level, histopathological analyses revealed significant structural alterations, most notably in gill tissues, indicating potential disruption of critical physiological functions such as respiration, osmoregulation, and filtration (Hariharan et al., 2021). Similar alterations were observed in gill and digestive gland tissues of mussel *Unio delicatus* exposed to both commercial and environmental MPs, while no changes occurred in other organs, underscoring these tissues as the primary targets of MNP-induced

histopathological changes (Arslan Yüce et al., 2025). Another study reported higher tissue damage indexes for PET than PE in both digestive gland and gill tissues of the oyster *Crassostrea gigas*, an effect attributed to the more angular and rougher edges of PET MPs, which enhance their damage potential (Teng, Zhu, et al., 2021). Despite these histopathological alterations, no significant impacts on organismal survival or growth metrics were observed under the tested conditions, indicating that short-term exposures at environmentally relevant concentrations may not directly translate into acute mortality, but instead manifest as sub-lethal impairments that could potentially compromise fitness and survival under chronic or combined stressors. As indicated, plastic particle exposure rarely induces mortality, which has only been reported at concentrations far exceeding environmental relevance (Galloway et al., 2017).

Building upon the systemic insights gained in the previous chapter, **Chapter 4** provided a more comprehensive mechanistic *in vitro* evaluation of the differential sensitivities of mussel hemocyte subpopulations to aged PET MPs (1.9 µm) and NPs (0.68 µm). This work refined the understanding of how granulocytes and hyalinocytes, two key immune effector cell types in *Mytilus edulis*, respond under environmentally and biologically relevant exposure conditions. The selected particle properties reflect reported concentration ranges and abundant size classes of MNPs in mussel hemolymph (Browne et al., 2008). The findings revealed distinct size- and concentration-dependent effects. Both aged PET MPs and NPs induced lysosomal destabilization, highlighting compromised cellular integrity and impaired immune function. This is particularly critical as lysosomes are essential for maintaining cellular homeostasis and coordinating immune-related processes, such as inter-organelle communication, signal transduction, and plasma membrane repair (Feng et al., 2024). In contrast, aged PET NPs triggered disproportionately stronger oxidative stress responses compared to aged PET MPs, with significantly elevated ROS levels observed in both hemocyte subpopulations at the highest concentration tested. This size-dependent effect underscores the greater hazard potential of nanoscale particles, as their high surface-to-mass ratio alters surface interactions, enhances membrane penetration, and facilitates free radical absorption (Hu & Palić, 2020). Such size-dependent elevations in ROS levels have been reported across various cell lines and with both virgin and aged plastic particles, with nanoscale particles exhibiting an amplified ROS-generating capacity relative to larger counterparts (Annangi et al., 2023; Hu & Palić, 2020; Laganà et al., 2023; Płuciennik et al., 2024; Ruan et al., 2023; L. Wang et al., 2024). Another study reported that aged PP fragments, subjected to UV irradiation, induced nearly twice the ROS generation in mussel hemocytes compared to pristine particles, underscoring the strong influence of particle aging on oxidative stress responses (Chelomin et al., 2024). Adverse outcome pathway (AOP) analyses have identified ROS generation as a common molecular initiating event for MNPs, which propagates through oxidative stress cascades and inflammatory responses to drive higher-level adverse effects (Hu & Palić, 2020). The concentration-dependent increase in hemocyte mortality likely reflects the downstream outcome of earlier subcellular disruptions, lysosomal destabilization and oxidative stress, that escalate to membrane damage and eventual cell death. Mortality within these key immune cell

populations underscores the capacity of plastic particle exposure to compromise immune competence and diminish host defense in mussels (Canesi et al., 2006; Weng et al., 2022). When combined with climate-driven stressors and chemical pollutants, this impairment can further increase susceptibility to pathogen infection, ultimately compromising individual fitness and survival (Gerdol & Pallavicini, 2025).

Taken together, the *in vitro* and *in vivo* findings of this thesis provide complementary evidence that environmentally and biologically relevant concentrations of aged PET MNPs exert biological effects in mussels. *In vitro* exposure of isolated hemocytes revealed early, mechanistically informative cellular-level responses to aged MNP exposure, with granulocytes and hyalinocytes exhibiting distinct sensitivities to particle size and concentration. These cellular perturbations were reflected *in vivo* as pronounced cellular-level alterations, while also indicating a capacity for short-term recovery that may mitigate particle-induced effects. Notably, the absence of acute organism-level mortality despite clear cellular and tissue damage highlights the role of compensatory mechanisms, but also underscores the potential for sublethal effects to accumulate under chronic or multiple-stressor exposure scenarios. Overall, this integrated approach highlights hemocyte-based *in vitro* assays as sensitive tools for detecting early cellular stress, while *in vivo* responses reveal how these perturbations manifest at the organismal level under environmentally relevant exposure scenarios.

6.1.3 Intracellular internalization and localization of aged PET NPs in hemocytes

Chapter 5 contributed to the field of nanoplastic toxicology by addressing a major methodological gap: the lack of reliable approaches to visualize and track the intracellular fate of environmentally relevant nanoplastics in living hemocytes. Using label-free three-dimensional live-cell imaging by holotomography, this study successfully resolved aged PET NPs within hemocytes without the need for artificial labeling or staining, thereby avoiding artifacts commonly associated with fluorescence-based methods (Gottstein et al., 2013). Such advances in imaging have been central to understanding NP trafficking, revealing particle distribution, biointeractions, and downstream subcellular consequences (Behzadi et al., 2017). The findings revealed that aged PET NPs were internalized and localized within cellular compartments and could be clearly distinguished from intrinsic cellular structures through refractive index mapping. Internalized aged PET NPs were mainly localized within dense cytoplasmic granules, a typical form of lysosomes. Similar patterns of lysosomal localization of MNPs in hemocytes have been consistently reported in various studies, primarily using fluorescence microscopy (Chang & Wang, 2024; Katsumiti et al., 2021; Sendra, Saco, et al., 2020). Consistent with the effects observed in the previous chapters, other studies further demonstrate that NP internalization in hemocytes alters immune functions, including ROS production, lysosomal stability, phagocytic capacity, and cell death pathways (Sendra, Saco, et al., 2020).

Evidence of morphological alterations, including extensive cytoplasmic vacuolation, granulation, and membrane disruption, was observed following exposure to aged PET NPs. These hallmarks of cellular stress align with previous reports of nanoplastic-induced organelle damage and altered immune cell morphology in bivalve hemocytes (Balvan et al., 2015; Canesi et al., 2016; Guo et al., 2024; Sendra et al., 2021). With further development and refinement of the image-processing techniques, this work will expand toward quantitative analyses, enabling systematic evaluation of nanoplastic–cell interactions and their implications for cellular integrity. Such advances would facilitate not only the tracking of intracellular localization but also the measurement of dynamic morphological and biophysical alterations at the single-cell level.

6.2 Critical Reflections and Limitations

While this thesis advances the understanding of the biological reactivity of MNPs under environmentally relevant exposure scenarios, several limitations must be acknowledged when interpreting its findings.

6.2.1 Use of a single polymer type

The experimental chapters focused exclusively on aged PET, chosen for its widespread use in consumer products, environmental prevalence, and frequent ingestion by mussels in natural environments (Alaraby et al., 2025; Ashrafy et al., 2023; Pequeno et al., 2021; Qu et al., 2018). While this approach allows mechanistic analyses, it inevitably narrows the scope of generalization to real-world MNP mixtures. Marine ecosystems contain highly heterogeneous mixtures of polymers, including PE, PP, PS, and PVC, often accompanied by additives and sorbed co-contaminants such as persistent organic pollutants and metals. These mixtures may exert additive, synergistic, or antagonistic effects on biological systems (Adeleye et al., 2024; Rani et al., 2015; Rodrigues et al., 2019). For instance, a recent study using polymer mixtures of virgin PE and PS have demonstrated more pronounced biological effects than single-polymer exposures (Ventura et al., 2024).

In addition, the interactions of NPs with cells are primarily governed by their physicochemical properties, including composition, size, shape, surface charge, functionalization, and degree of hydrophobicity or hydrophilicity (Behzadi et al., 2017; Foroozandeh & Aziz, 2018a). The aged PET used in this study represents a test particle with increased hydrophilicity (Seghers et al., 2025). Such aged particles can favor the adsorption of proteins, leading to shifts in corona composition that can enhance cellular recognition and uptake pathways (T. Du et al., 2023). Another study showed that ‘true-to-life’ NPs form a distinct protein corona compared to synthetic nanobeads, offering a more realistic system for investigating cellular interactions and associated effects (Ducoli et al., 2022). However, reliance on a single material is limited in accounting for polymer-specific

differences, such as those demonstrated across pristine PET, PE, PP, and PVC in epithelial cell lines (Stock et al., 2021).

6.2.2 Reliance on a single model species

The mussel *Mytilus edulis* was chosen as a sentinel species because of its ecological relevance, established use in biomonitoring programs, and heightened susceptibility to particle exposure due to filter-feeding behavior (Beyer et al., 2017; Canesi & Procházková, 2014; Weng et al., 2022). Based on the species sensitivity distribution analyses for marine invertebrates presented in Chapter 2, *Mytilus spp*. ranked as the second and third most sensitive species to plastic particle exposure, considering the food dilution and tissue translocation toxicity mechanisms, respectively. This high sensitivity underscores its suitability as model organisms for detecting early, sublethal impact (Canesi et al., 2012; Canesi & Procházková, 2014). However, reliance on a single-species *in vivo* exposure inevitably restricts the taxonomic breadth of inference and cannot capture community-level responses, trophic interactions, or interspecies variability in sensitivity. For instance, pronounced trait-driven differences in NP transfer dynamics were observed in macroinvertebrates (Ockenden et al., 2024), which possess distinct physiological and morphological traits associated with feeding and respiration strategies. As reported, damselfly larvae (*Xanthocnemis zealandica*) accumulated NP from both waterborne and dietary exposure pathways but efficiently eliminated 92% of the burden within five days of depuration, whereas backswimmers (*Anisops wakefieldi*) showed no detectable accumulation from either source. These responses are consistent with growing evidence that particle uptake and retention are strongly species- and trait-dependent. Moreover, responses observed in one taxonomic group, such as bivalves, may not be representative of other marine invertebrates with different physiologies (Doyle et al., 2022; Galloway et al., 2017), such as echinoderms or crustaceans, which Chapter 2 also highlighted as exhibiting distinct sensitivity patterns. Particularly in crustaceans, regurgitation has been described as an efficient adaptation mechanism to remove large or indigestible items from the stomach, which also facilitate expulsion of ingested MPs and thereby reduce their potential adverse effects (Saborowski et al., 2019). These insights highlight the importance of incorporating biological traits and taxon-specific mechanisms when assessing MNP impacts.

6.2.3 Application of mechanically and chemically aged test particles

While the use of aged test particles introduces modifications more representative of naturally aged particles than pristine materials, laboratory aging methods only approximate the complexity of environmental weathering processes. In natural systems, plastics are simultaneously exposed to diverse physical, chemical, and biological processes (Alaraby et al., 2025), such as UV radiation, chemical oxidation, biofouling, and mechanical abrasion, over extended timescales (Baby et al., 2024; W. He et al., 2023). Simulated aging cannot fully replicate the heterogeneous degradation of plastic surface properties, bulk-

phases, chemical signatures or the sorbed contaminant profiles and microbial assemblages that develop under real-world conditions (Bhagwat et al., 2021; Maddison et al., 2023). Weathering processes significantly alter the physicochemical properties of plastic particles, thereby reshaping both their environmental fate and biological interactions. For example, accelerated weathering under UV irradiance over just 10 days increased the dispersibility of PE MPs in the water column and enhanced their surface capacity to adsorb chemical pollutants (Al Harraq et al., 2022). In addition, photodegraded PP fragments markedly enhanced lipid peroxidation in mitochondrial membranes from gill tissues and reduced hemocyte lysosomal membrane stability compared to pristine counterparts (Chelomin et al., 2024). Such weathering-induced alterations directly shape toxicity profiles (Völkl et al., 2022), highlighting the need to account for the combined effects of aged and weathered plastics, their leachates, and degradation products in effect assessments (Arp et al., 2021). In addition, the standardization of aging protocols remains underdeveloped. Different studies apply varying combinations of UV irradiation, heating, oxidation, direct or simulated sunlight, or mechanical shear to mimic weathering, leading to inconsistencies in particle properties and hindering comparability across experiments (L. Wang et al., 2023). This lack of harmonization creates challenges that hinder building cross-study syntheses and integrating mechanistic data into ecologically meaningful risk frameworks (W. He et al., 2023).

6.2.4 Lack of non-plastic particle control

Another limitation of the present work is the absence of non-plastic particle controls, such as mineral or organic particulates. This gap restricts the ability to benchmark plastic-specific effects against those of natural particles, even though evidence suggests that certain plastic types may be inherently more toxic (Arp et al., 2021). For example, unplasticized PVC MPs induced more severe effects than natural particulates such as kaolinite and diatomite of comparable size, potentially due to intrinsic particle properties (Scherer et al., 2020). Similarly, a study comparing aged and virgin PET with kaolin showed that plastics induced stronger effects than the natural particulate, with reduced growth and altered extracellular polymeric substance production in *Rhodomonas salina*. The observed toxicity was further amplified by the aged test plastic particles (Sioen et al., 2024b), which underwent exactly the same aging procedure as that applied in the experimental chapters of this thesis. In practical terms, including non-plastic particulates as controls helps establish whether observed effects are unique to plastic properties (e.g. polymer type, size, additives, surface chemistry) or reflect responses to particle presence and load in general (Arp et al., 2021). Such controls can therefore strengthen causal inference and make comparisons among studies and test parameters more robust.

6.2.5 Scaling and extrapolation challenges

Another practical constraint encountered was the limited longevity of the primary hemocyte cultures used for *in vitro* assessments in Chapters 4 and 5. This limitation restricts

the ability to investigate long-term or chronic effects and hampers assessment on potential recovery dynamics following MNP exposure. Despite several decades of intensive effort in marine invertebrate cell biology, no single permanent cell line from any marine invertebrate species has yet been established. Primary cell cultures typically stop dividing within 24–72 hours of isolation, entering a state of cellular quiescence that hampers extended experimentation (Rinkevich, 2011). Nevertheless, primary cell cultures remain a valuable tool for ecotoxicology, enabling rapid detection of cellular responses under controlled experimental conditions and offering a practical means to evaluate the impacts of diverse MNP types, sizes, and concentrations (Revel et al., 2021). The structure and function of bivalve hemocytes resemble those of vertebrate immune cells, which can be used as basis for the extrapolation of findings to higher biological groups (Weng et al., 2022).

Although sub-organismal alterations were observed, translating these effects to higher levels of biological organization remains challenging, as homeostatic regulatory networks can differ across biological scales (Vitousek et al., 2025). This challenge is particularly evident for MNP exposure, where connecting sub-organismal effects to ecosystem-level consequences is difficult, despite the fact that such broader impacts are of ultimate concern (Galloway et al., 2017).

These limitations, many of which reflect broader challenges in plastic toxicology, shape the interpretation of the findings and highlight avenues for improvement in future studies.

6.3 Future Research Directions

Building on the present work, future research should prioritize several interrelated directions to advance both mechanistic understanding and ecological risk assessment of MNPs (Figure 6.1).

6.3.1 Elucidation of molecular pathways and signaling cascades involved in immune dysregulation

The findings of this thesis highlight immune-cell-specific vulnerabilities to aged MNPs, but the underlying molecular pathways and signaling cascades remain unresolved. In particular, nanoparticle-induced lysosomal damage has been associated with the dysregulation of ion channel proteins such as vacuolar-type ATPase (V-ATPase), transient receptor potential channel M2 (TRPM2), chloride channel 7 (CLC-7), and lysosomal membrane-associated proteins (LAMPs), which play central roles in maintaining lysosomal integrity, ion homeostasis, autophagy, and immune signaling (Feng et al., 2024). MNP exposure can also activate redox sensitive signaling pathways, including the mitogen-activated protein kinase (MAPK). While transient activation of MAPKs may contribute to adaptive stress responses, prolonged or excessive activation has been associated with

negative outcomes, including cell death (Hu & Palić, 2020; Yue & López, 2020). Future research should therefore prioritize elucidating how MNP exposure activates these molecular pathways, with emphasis on downstream signaling cascades that regulate oxidative stress responses. Within the AOP framework, oxidative stress is recognized as a driver of higher-level adverse outcomes, including growth inhibition and behavioral alterations (Hu & Palić, 2020). Linking these mechanisms is essential to establish causal links to organismal and population-level effects, thereby supporting ecologically meaningful risk assessment.

Figure 6.1. *Key future research directions to advance mechanistic understanding and strengthen ecological risk assessment of micro- and nanoplastic particles. Created in BioRender (Hara, J. 2026: https://BioRender.com/oip84nr).*

6.3.2 Examination of multi-stressor interactions

Plastic particles rarely act as isolated stressors in marine environments. Organisms are simultaneously exposed to climate-driven stressors, including ocean warming, acidification, deoxygenation, and heatwaves (Catarino et al., 2022). In parallel, they face chemical contaminants, such as metals and organic compounds, which can bioaccumulate and synergistically disrupt key biological functions (Adeleye et al., 2024; Tang, 2021; T. Wang et al., 2020). MNPs can act as effective vectors for co-occurring contaminants (Mahendran & Ramaswamy, 2024), significantly enhancing the bioaccumulation and toxicity of sorbed chemicals in a size-dependent manner. For instance, NPs have been reported to significantly enhance the bioaccumulation of benzophenone-3 and ciprofloxacin compared with MPs (J. Li et al., 2024), thereby intensifying co-exposure effects and leading to pronounced disruption of antioxidant defense systems in mussels.

Compounding these pressures, MNPs not only exert direct toxicity but also serve as vectors for pathogens such as *Vibrio*, *Pseudomonas*, and *Acinetobacter,* facilitating microbial colonization and transmission (Cholewińska et al., 2025; Zhong et al., 2023). Previous studies on mussels co-exposed to pristine polymethyl methacrylate MPs and pathogenic bacteria (*Vibrio parahaemolyticus)*, either simultaneously (14 days) or sequentially after prolonged MP exposure (30 days), have demonstrated that such combined stressors compromise immune function, elevate energy demands, and increase susceptibility to infection. These observed effects ultimately divert resources away from growth and fitness maintenance (C. Sun, Teng, et al., 2024). Understanding the cumulative and potentially synergistic interactions of environmentally relevant MNPs under multiple stressors is critical for developing predictive risk frameworks that reflect the complexity of marine ecosystems.

6.3.3 Chronic and multigenerational effect assessment

Most available toxicological data on MNPs were derived from acute or short-term laboratory exposures, yet chronic and multigenerational impacts remain poorly understood. Chronic exposures better reflect the persistent conditions organisms face in nature, while transgenerational approaches are critical for determining whether MNP-induced alterations propagate across generations (Cunningham et al., 2023; Gigault & Davranche, 2025). In *Caenorhabditis elegans*, parental exposure to pristine PS NPs reduced reproductive capacity across the F1–F3 generations and impaired gonad development in early generations, underscoring the potential for MNP-induced toxicity to propagate across lineage (L. Sun et al., 2021). The manifestation of transgenerational effects is strongly influenced by multiple factors, including particle characteristics, and degree of aging, as well as the duration and mode of exposure and potential interactions with co-occurring chemicals (Junaid et al., 2023).

To improve ecological realism, controlled microcosm and mesocosm experiments are needed that reflect the complexity of natural systems, including species migration, community-level interactions, and trophic dynamics such as predator–prey relationships (Gigault & Davranche, 2025). Trophic transfer has been shown to be a key pathway of MP exposure, extending to the second and third trophic levels, and with higher ingestion via pre-exposed prey compared to direct waterborne exposure (Kangas et al., 2023). Such approaches will provide critical insights into how individual-level disruptions scale up to influence populations and ecosystems (Auffan et al., 2019).

6.3.4 Methodological standardization

A key priority for advancing MNP research is the methodological standardization of test particle generation, characterization, experimental design, and effect endpoint assessment. While the use of aged and weathered plastics represents significant progress over pristine materials, the absence of standardized protocols for their generation and characterization limits cross-study comparability. To address this, recent guidelines recommend that future studies adopt harmonized approaches, including consistent reporting of polymer type and source, physical and chemical transformations, leachates, as well as weathering pathways and conditions including irradiance, oxidation, temperature, and humidity (Alimi et al., 2022).

Equally critical is the development of robust methods for detecting MNPs in biological tissues to establish clearer links between uptake and toxicological outcomes. Current detection techniques for MPs are far more advanced in environmental media (e.g., water and sediments) than in biological samples, where complex matrices hinder accurate quantification (J. Zhao et al., 2025). This gap is particularly critical for nanosized range plastic particles, which require more advanced methods for detection and quantification across environmental and biological interfaces (Gigault & Davranche, 2025).

The adoption of standardized protocols for testing the effects of MNPs in aquatic systems, as outlined by De Ruijter et al. (2020) is urgently needed to improve reproducibility, comparability, and ecological relevance of experimental findings. Implementing harmonized QA/QC criteria for particle characterization, experimental design, risk assessment applicability and ecological relevance will facilitate the development of robust data and integration of mechanistic insights into risk characterization frameworks. Such high-quality data will also enable the development of models capable of predicting effects across different levels of biological organization (e.g., AOP frameworks from molecular to individual levels, or DEB-IBM (Dynamic Energy Budget with Individual-based modelling) approaches from individual to population levels) (Catarino et al., 2022; Everaert et al., 2022; J. Jeong et al., 2024). This, in turn, allows the scaling of physiological effects at the individual-level to population-level outcomes under both single- and multi-stressor conditions.

6.4 Final Remarks

In closing, this thesis provides a multi-tiered investigation into the biological reactivity of MNPs, with a particular focus on mechanistically assessing cellular, tissue, and organismal responses under environmentally relevant exposure scenarios. Key research questions were addressed in separate chapters, advancing current understanding from community-specific hazard threshold assessments to the intricate cellular mechanisms underlying particle-induced toxicity.

Based on existing studies, primarily with pristine, spherical particles, the first chapter established ecologically relevant hazard benchmarks by systematically comparing species sensitivities and deriving preliminary safe standards for marine invertebrate communities. The subsequent chapters advanced the analysis by employing aged PET MNPs as test particles for multi-level assessments of biological effects. An *in vivo* exposure experiment provided integrative evidence that aged PET MNPs elicit cellular- and tissue-level effects in mussels under environmentally relevant exposure scenarios. Histopathological analyses demonstrated structural damage to key organs, particularly the gills, suggesting potential disruption of critical physiological functions. Complementary *in vitro* assays provided mechanistic insight into the differential sensitivities of the hemocyte subpopulations, particularly granulocytes and hyalinocytes, demonstrating size- and concentration-dependent effects on functional integrity. Through label-free 3D live-cell imaging by holotomography, unlabeled aged PET NPs were successfully resolved within living hemocytes, revealing particle internalization and localization patterns, as well as associated morphological changes. These findings show that, even in the absence of lethal effects at the organismal level, MNP exposure induces measurable sublethal effects across multiple biological levels, potentially compromising individual fitness and survival under chronic or combined stressors**.** While the use of aged test particles advances understanding of effects under environmentally relevant conditions, several methodological limitations were identified and must be considered when interpreting the findings. Future research directions were outlined to further advance the effect assessment of plastic pollution on marine organisms, with the ultimate goal of integrating mechanistic insights into risk characterization frameworks.

The collective insights gained in this thesis reinforces a crucial message: the story of plastics in the marine environment is still unfolding, and understanding their biological reactivity, especially as they age and diminish in size, is key to assessing risks and safeguarding marine ecosystem health in the face of this global challenge.

Bibliography

Bibliography

Abidli, S., Zaidi, S., Ben Younes, R., Lahbib, Y., & Trigui El Menif, N. (2023). Impact of polyethylene microplastics on the clam Ruditapes decussatus (Mollusca: Bivalvia): examination of filtration rate, growth, and immunomodulation. *Ecotoxicology*, *32*(6), 746–755. https://doi.org/10.1007/s10646-023-02683-2

Adeleye, A. T., Bahar, M. M., Megharaj, M., Fang, C., & Rahman, M. M. (2024). The unseen threat of the synergistic effects of microplastics and heavy metals in aquatic environments: A critical review. *Current Pollution Reports*, *10*(3), 478–497. https://doi.org/10.1007/s40726-024-00298-7

Afshar, S. V., Boldrin, A., Astrup, T. F., Daugaard, A. E., & Hartmann, N. B. (2024). Degradation of biodegradable plastics in waste management systems and the open environment: A critical review. *Journal of Cleaner Production*, *434*. https://doi.org/10.1016/j.jclepro.2023.140000

Aguilar-Guzmán, J. C., Bejtka, K., Fontana, M., Valsami-Jones, E., Villezcas, A. M., Vazquez-Duhalt, R., & Rodríguez-Hernández, A. G. (2022). Polyethylene terephthalate nanoparticles effect on RAW 264.7 macrophage cells. *Microplastics and Nanoplastics*, *2*(1). https://doi.org/10.1186/s43591-022-00027-1

Al Harraq, A., Brahana, P. J., Arcemont, O., Zhang, D., Valsaraj, K. T., & Bharti, B. (2022). Effects of weathering on microplastic dispersibility and pollutant uptake capacity. *ACS Environmental Au*, *2*(6), 549–555. https://doi.org/10.1021/acsenvironau.2c00036

Alaraby, M., Abass, D., Velázquez, A., Hernández, A., & Marcos, R. (2025). Occurrence, analysis, and toxicity of polyethylene terephthalate microplastics: a review. *Environmental Chemistry Letters*, *23*(4), 1025–1059. https://doi.org/10.1007/s10311-025-01841-8

Al-Darraji, A., Oluwoye, I., Lagat, C., Tanaka, S., & Barifcani, A. (2024). Erosion of rigid plastics in turbid (sandy) water: quantitative assessment for marine environments and formation of microplastics. *Environmental Science: Processes and Impacts*. https://doi.org/10.1039/d4em00122b

Ali, N., Khan, M. H., Ali, M., Sidra, Ahmad, S., Khan, A., Nabi, G., Ali, F., Bououdina, M., & Kyzas, G. Z. (2024). Insight into microplastics in the aquatic ecosystem: Properties, sources, threats and mitigation strategies. *Science of the Total Environment*, *913*. https://doi.org/10.1016/j.scitotenv.2023.169489

Ali, S. S., Elsamahy, T., Al-Tohamy, R., Zhu, D., Mahmoud, Y. A. G., Koutra, E., Metwally, M. A., Kornaros, M., & Sun, J. (2021). Plastic wastes biodegradation: Mechanisms, challenges and future prospects. *Science of the Total Environment*, *780*. https://doi.org/10.1016/j.scitotenv.2021.146590

Alimi, O. S., Claveau-Mallet, D., Kurusu, R. S., Lapointe, M., Bayen, S., & Tufenkji, N. (2022). Weathering pathways and protocols for environmentally relevant microplastics and nanoplastics: What are we missing? *Journal of Hazardous Materials*, *423*. https://doi.org/10.1016/j.jhazmat.2021.126955

Al-Thawadi, S. (2020). Microplastics and Nanoplastics in Aquatic Environments: Challenges and Threats to Aquatic Organisms. *Arabian Journal for Science and Engineering*, *45*(6), 4419–4440. https://doi.org/10.1007/s13369-020-04402-z

Amran, N. H., Zaid, S. S. M., Mokhtar, M. H., Manaf, L. A., & Othman, S. (2022). Exposure to microplastics during early developmental stage: Review of current evidence. *Toxics*, *10*(10). https://doi.org/10.3390/toxics10100597

Annangi, B., Villacorta, A., López-Mesas, M., Fuentes-Cebrian, V., Marcos, R., & Hernández, A. (2023). Hazard assessment of polystyrene nanoplastics in primary human nasal epithelial cells, focusing on the autophagic effects. *Biomolecules*, *13*(2). https://doi.org/10.3390/biom13020220

Applebaum, S. L., Pan, T. C. F., Hedgecock, D., & Manahan, D. T. (2014). Separating the nature and nurture of the allocation of energy in response to global change. *Integrative and Comparative Biology*, *54*(2), 284–295. https://doi.org/10.1093/icb/icu062

Arp, H. P. H., Kühnel, D., Rummel, C., Macleod, M., Potthoff, A., Reichelt, S., Rojo-Nieto, E., Schmitt-Jansen, M., Sonnenberg, J., Toorman, E., & Jahnke, A. (2021). Weathering plastics as a planetary boundary threat: Exposure, fate, and hazards. *Environmental Science and Technology*, *55*(11), 7246–7255. https://doi.org/10.1021/acs.est.1c01512

Arslan Yüce, P., Günal, A. Ç., Erkmen, B., Yurdakok-Dikmen, B., Çağan, A. S., Çırak, T., Başaran Kankılıç, G., Seyfe, M., Filazi, A., & Tavşanoğlu, Ü. N. (2025). In vitro and in vivo effects of commercial and environmental microplastics on Unio delicatus. *Ecotoxicology*, *34*(1), 22–37. https://doi.org/10.1007/s10646-024-02807-2

Arthur, C., Baker, J., & Bamford S. (2009). *Proceedings of the International Research Workshop on the Occurrence, Effects, and Fate of Microplastic Marine Debris*. www.MarineDebris.noaa.gov

Ashrafy, A., Liza, A. A., Islam, M. N., Billah, M. M., Arafat, S. T., Rahman, M. M., & Rahman, S. M. (2023). Microplastics pollution: A brief review of its source and abundance in different aquatic ecosystems. *Journal of Hazardous Materials Advances*, *9*. https://doi.org/10.1016/j.hazadv.2022.100215

ASTM International. (2012). *Standard Guide for Conducting Static Acute Toxicity Tests Starting with Embryos of Four Species of Saltwater Bivalve Molluscs 1*. https://doi.org/10.1520/E0724-98R12

Au, D. W. T. (2004). The application of histo-cytopathological biomarkers in marine pollution monitoring: A review. *Marine Pollution Bulletin*, *48*(9–10), 817–834. https://doi.org/10.1016/j.marpolbul.2004.02.032

Auffan, M., Masion, A., Mouneyrac, C., de Garidel-Thoron, C., Hendren, C. O., Thiery, A., Santaella, C., Giamberini, L., Bottero, J. Y., Wiesner, M. R., & Rose, J. (2019). Contribution of mesocosm testing to a single-step and exposure-driven environmental risk assessment of engineered nanomaterials. *NanoImpact*, *13*, 66–69. https://doi.org/10.1016/j.impact.2018.12.005

Auguste, M., Balbi, T., Ciacci, C., Canonico, B., Papa, S., Borello, A., Vezzulli, L., & Canesi, L. (2020). Shift in immune parameters after repeated exposure to nanoplastics in the marine bivalve Mytilus. *Frontiers in Immunology*, *11*. https://doi.org/10.3389/fimmu.2020.00426

Avio, C. G., Gorbi, S., Milan, M., Benedetti, M., Fattorini, D., D'Errico, G., Pauletto, M., Bargelloni, L., & Regoli, F. (2015). Pollutants bioavailability and toxicological risk from microplastics to marine mussels. *Environmental Pollution*, *198*, 211–222. https://doi.org/10.1016/j.envpol.2014.12.021

Baby, M. G., Gerritse, J., Beltran-Sanahuja, A., Wolter, H., Rohais, S., & Romero-Sarmiento, M. F. (2024). Aging of plastics and microplastics in the environment: a review on influencing factors, quantification methods, challenges, and future perspectives. *Environmental Science and Pollution Research*. https://doi.org/10.1007/s11356-024-35651-2

Bagaev, A., Khatmullina, L., & Chubarenko, I. (2018). Anthropogenic microlitter in the Baltic Sea water column. *Marine Pollution Bulletin*, *129*(2), 918–923. https://doi.org/10.1016/j.marpolbul.2017.10.049

Bajgelman, M. C. (2019). Principles and applications of flow cytometry. In *Data Processing Handbook for Complex Biological Data Sources* (pp. 119–124). Elsevier. https://doi.org/10.1016/B978-0-12-816548-5.00008-3

Baldwin, K. T., Murai, K. K., & Khakh, B. S. (2024). Astrocyte morphology. *Trends in Cell Biology*, *34*(7), 547–565. https://doi.org/10.1016/j.tcb.2023.09.006

Balvan, J., Krizova, A., Gumulec, J., Raudenska, M., Sladek, Z., Sedlackova, M., Babula, P., Sztalmachova, M., Kizek, R., Chmelik, R., & Masarik, M. (2015). Multimodal holographic microscopy: Distinction between apoptosis and oncosis. *PLoS ONE*, *10*(3). https://doi.org/10.1371/journal.pone.0121674

Barría, C., Balasch, J. C., Brandts, I., Oliva, D., Iriarte, J. L., & Teles, M. (2025). Immunological responses, oxidative stress, and histopathological effects of nanoplastics on commercially relevant mussel

species: A review. *Journal of Hazardous Materials Advances*, *17*. https://doi.org/10.1016/j.hazadv.2024.100540

Barrick, A., Guillet, C., Mouneyrac, C., & Châtel, A. (2018). Investigating the establishment of primary cultures of hemocytes from Mytilus edulis. *Cytotechnology*, *70*(4), 1205–1220. https://doi.org/10.1007/s10616-018-0212-x

Baun, A., Hartmann, N. B., Grieger, K., & Kusk, K. O. (2008). Ecotoxicity of engineered nanoparticles to aquatic invertebrates: A brief review and recommendations for future toxicity testing. *Ecotoxicology*, *17*(5), 387–395. https://doi.org/10.1007/s10646-008-0208-y

Beheshtimaal, A., Alamdari, N., Wang, B., Kamali, M., & Salehi, M. (2024). Understanding the dynamics of microplastics transport in urban stormwater runoff: Implications for pollution control and management. *Environmental Pollution*, *356*. https://doi.org/10.1016/j.envpol.2024.124302

Behzadi, S., Serpooshan, V., Tao, W., Hamaly, M. A., Alkawareek, M. Y., Dreaden, E. C., Brown, D., Alkilany, A. M., Farokhzad, O. C., & Mahmoudi, M. (2017). Cellular uptake of nanoparticles: Journey inside the cell. *Chemical Society Reviews*, *46*(14), 4218–4244. https://doi.org/10.1039/c6cs00636a

Belanger, S., Barron, M., Craig, P., Dyer, S., Galay-Burgos, M., Hamer, M., Marshall, S., Posthuma, L., Raimondo, S., & Whitehouse, P. (2017). Future needs and recommendations in the development of species sensitivity distributions: Estimating toxicity thresholds for aquatic ecological communities and assessing impacts of chemical exposures. *Integrated Environmental Assessment and Management*, *13*(4), 664–674. https://doi.org/10.1002/ieam.1841

Benner, I., & Passow, U. (2024). Why biofouling cannot contribute to the vertical transport of small microplastic. *Microplastics and Nanoplastics*, *4*(1). https://doi.org/10.1186/s43591-024-00098-2

Benson, N. U., Agboola, O. D., Fred-Ahmadu, O. H., De-la-Torre, G. E., Oluwalana, A., & Williams, A. B. (2022). Micro(nano)plastics prevalence, food web interactions, and toxicity assessment in aquatic organisms: A review. *Frontiers in Marine Science*, *9*. https://doi.org/10.3389/fmars.2022.851281

Besseling, E., Redondo-Hasselerharm, P., Foekema, E. M., & Koelmans, A. A. (2019). Quantifying ecological risks of aquatic micro- and nanoplastic. *Critical Reviews in Environmental Science and Technology*, *49*(1), 32–80. https://doi.org/10.1080/10643389.2018.1531688

Beyer, J., Green, N. W., Brooks, S., Allan, I. J., Ruus, A., Gomes, T., Bråte, I. L. N., & Schøyen, M. (2017). Blue mussels (Mytilus edulis spp.) as sentinel organisms in coastal pollution monitoring: A review. *Marine Environmental Research*, *130*, 338–365. https://doi.org/10.1016/j.marenvres.2017.07.024

Bhagwat, G., Carbery, M., Anh Tran, T. K., Grainge, I., O'Connor, W., & Palanisami, T. (2021). Fingerprinting plastic-associated inorganic and organic matter on plastic aged in the marine environment for a decade. *Environmental Science and Technology*, *55*(11), 7407–7417. https://doi.org/10.1021/acs.est.1c00262

Bhat, M. A., Gedik, K., & Gaga, E. O. (2024). A preliminary study on the natural aging behavior of microplastics in indoor and outdoor environments. *International Journal of Environmental Science and Technology*, *21*(2), 1923–1936. https://doi.org/10.1007/s13762-023-05319-4

Bhattacharya, P., Lin, S., Turner, J. P., & Ke, P. C. (2010). Physical adsorption of charged plastic nanoparticles affects algal photosynthesis. *Journal of Physical Chemistry C*, *114*(39), 16556–16561. https://doi.org/10.1021/jp1054759

Bhavika, T., Mayur, T., Tushar, D., Vivek, T., Mitul, T., Nehal, T., Ritika, T., Shriyas, T., Varsha, L., & Bhoomi, P. (2025). Micro- and nanoplastics—Impact on marine vertebrates and invertebrates. In *Sustainable Development Goals Series: Vol. Part F562* (pp. 163–174). Springer. https://doi.org/10.1007/978-981-96-5047-7_14

Biamis, C., Driscoll, K. O., & Hardiman, G. (2021). Microplastic toxicity: A review of the role of marine sentinel species in assessing the environmental and public health impacts. *Case Studies in Chemical and Environmental Engineering*, *3*. https://doi.org/10.1016/j.cscee.2020.100073

Bianco, A., Carena, L., Peitsaro, N., Sordello, F., Vione, D., & Passananti, M. (2023). Rapid detection of nanoplastics and small microplastics by Nile-Red staining and flow cytometry. *Environmental Chemistry Letters*, *21*(2), 647–653. https://doi.org/10.1007/s10311-022-01545-3

Bihannic, I., Gley, R., Gallo, L., Badura, A., Razafitianamaharavo, A., Beuret, M., Billet, D., Bojic, C., Caillet, C., Morlot, P., Zaffino, M., Jouni, F., George, B., Boulet, P., Noûs, C., Danger, M., Felten, V., Pagnout, C., & Duval, J. F. L. (2024). Photodegradation of disposable polypropylene face masks: Physicochemical properties of debris and implications for the toxicity of mask-carried river biofilms. *Journal of Hazardous Materials*, *465*. https://doi.org/10.1016/j.jhazmat.2023.133067

Bodzek, M., Pohl, A., & Rosik-Dulewska, C. (2024). Microplastics in wastewater treatment plants: Characteristics, occurrence and removal technologies. *Water (Switzerland)*, *16*(24). https://doi.org/10.3390/w16243574

Bouallegui, Y., Ben Younes, R., Bellamine, H., & Oueslati, R. (2017). Histopathology and analyses of inflammation intensity in the gills of mussels exposed to silver nanoparticles: role of nanoparticle size, exposure time, and uptake pathways. *Toxicology Mechanisms and Methods*, *27*(8), 582–591. https://doi.org/10.1080/15376516.2017.1337258

Bouallegui, Y., Ben Younes, R., Bellamine, H., & Oueslati, R. (2018). Histopathological indices and inflammatory response in the digestive gland of the mussel Mytilus galloprovincialis as biomarker of immunotoxicity to silver nanoparticles. *Biomarkers*, *23*(3), 277–287. https://doi.org/10.1080/1354750X.2017.1409803

Bouki, E., Dimitriadis, V. K., Kaloyianni, M., & Dailianis, S. (2013). Antioxidant and pro-oxidant challenge of tannic acid in mussel hemocytes exposed to cadmium. *Marine Environmental Research*, *85*, 13–20. https://doi.org/10.1016/j.marenvres.2012.12.005

Bråte, I. L. N., Blázquez, M., Brooks, S. J., & Thomas, K. V. (2018). Weathering impacts the uptake of polyethylene microparticles from toothpaste in Mediterranean mussels (M. galloprovincialis). *Science of the Total Environment*, *626*, 1310–1318. https://doi.org/10.1016/j.scitotenv.2018.01.141

Bricker, S. B., Grizzle, R. E., Trowbridge, P., Rose, J. M., Ferreira, J. G., Wellman, K., Zhu, C., Galimany, E., Wikfors, G. H., Saurel, C., Landeck Miller, R., Wands, J., Rheault, R., Steinberg, J., Jacob, A. P., Davenport, E. D., Ayvazian, S., Chintala, M., & Tedesco, M. A. (2020). Bioextractive removal of nitrogen by oysters in Great Bay Piscataqua River Estuary, New Hampshire, USA. *Estuaries and Coasts*, *43*(1), 23–38. https://doi.org/10.1007/s12237-019-00661-8

Bridson, J. H., Abbel, R., Smith, D. A., Northcott, G. L., & Gaw, S. (2023). Release of additives and non-intentionally added substances from microplastics under environmentally relevant conditions. *Environmental Advances*, *12*. https://doi.org/10.1016/j.envadv.2023.100359

Brown, E., MacDonald, A., Allen, S., & Allen, D. (2023). The potential for a plastic recycling facility to release microplastic pollution and possible filtration remediation effectiveness. *Journal of Hazardous Materials Advances*, *10*. https://doi.org/10.1016/j.hazadv.2023.100309

Browne, M. A., Dissanayake, A., Galloway, T. S., Lowe, D. M., & Thompson, R. C. (2008). Ingested microscopic plastic translocates to the circulatory system of the mussel, Mytilus edulis (L.). *Environmental Science and Technology*, *42*(13), 5026–5031. https://doi.org/10.1021/es800249a

Brunk, U. T., & Terman, A. (2002). Lipofuscin: Mechanism of aged-related accummulation and influence on cell function. *Free Radical Biology and Medicine*. https://doi.org/10.1016/S0891-5849(02)00959-0

Brunk, U. T., Zhang, H., Dalen, H., & Ilinger, K. (1995). Exposure of cells to nonlethal concentrations of hydrogen peroxide induces degeneration-repair mechanisms involving lysosomal destabilization. *Free Radical Biology & Medicine*, *19*(6), 813–822. https://doi.org/10.1016/0891-5849(95)02001-Q

Buzalewicz, I., Mrozowska, M., Kmiecik, A., Kulus, M., Haczkiewicz-Leśniak, K., Dzięgiel, P., Podhorska-Okołów, M., & Zadka, Ł. (2022). Quantitative phase imaging detecting the hypoxia-induced patterns in healthy and neoplastic human colonic epithelial cells. *Cells*, *11*(22), 3599. https://doi.org/10.3390/cells11223599

Cai, H., Chen, M., Du, F., Matthews, S., & Shi, H. (2021). Separation and enrichment of nanoplastics in environmental water samples via ultracentrifugation. *Water Research*, *203*. https://doi.org/10.1016/j.watres.2021.117509

Cai, H., Xu, E. G., Du, F., Li, R., Liu, J., & Shi, H. (2021). Analysis of environmental nanoplastics: Progress and challenges. *Chemical Engineering Journal*, *410*. https://doi.org/10.1016/j.cej.2020.128208

Canesi, L., Ciacci, C., Bergami, E., Monopoli, M. P., Dawson, K. A., Papa, S., Canonico, B., & Corsi, I. (2015). Evidence for immunomodulation and apoptotic processes induced by cationic polystyrene nanoparticles in the hemocytes of the marine bivalve Mytilus. *Marine Environmental Research*, *111*, 34–40. https://doi.org/10.1016/j.marenvres.2015.06.008

Canesi, L., Ciacci, C., Fabbri, R., Balbi, T., Salis, A., Damonte, G., Cortese, K., Caratto, V., Monopoli, M. P., Dawson, K., Bergami, E., & Corsi, I. (2016). Interactions of cationic polystyrene nanoparticles with marine bivalve hemocytes in a physiological environment: Role of soluble hemolymph proteins. *Environmental Research*, *150*, 73–81. https://doi.org/10.1016/j.envres.2016.05.045

Canesi, L., Ciacci, C., Fabbri, R., Marcomini, A., Pojana, G., & Gallo, G. (2012). Bivalve molluscs as a unique target group for nanoparticle toxicity. *Marine Environmental Research*, *76*, 16–21. https://doi.org/10.1016/j.marenvres.2011.06.005

Canesi, L., Ciacci, C., & Pruzzo, C. (2006). Cell signaling in the immune response of mussel hemocytes. *Invertebrate Survival Journal*, *3*(1), 40–49.

Canesi, L., Ciacci, C., Vallotto, D., Gallo, G., Marcomini, A., & Pojana, G. (2010). In vitro effects of suspensions of selected nanoparticles (C60 fullerene, TiO2, SiO2) on Mytilus hemocytes. *Aquatic Toxicology*, *96*(2), 151–158. https://doi.org/10.1016/j.aquatox.2009.10.017

Canesi, L., & Procházková, P. (2014). The Invertebrate Immune System as a Model for Investigating the Environmental Impact of Nanoparticles. In *Nanoparticles and the Immune System* (pp. 91–112). Academic Press. https://doi.org/10.1016/B978-0-12-408085-0.00007-8

Capolupo, M., Sørensen, L., Jayasena, K. D. R., Booth, A. M., & Fabbri, E. (2020). Chemical composition and ecotoxicity of plastic and car tire rubber leachates to aquatic organisms. *Water Research*, *169*, 115270. https://doi.org/10.1016/j.watres.2019.115270

Capolupo, M., Valbonesi, P., & Fabbri, E. (2021). A comparative assessment of the chronic effects of micro- and nano-plastics on the physiology of the mediterranean mussel mytilus galloprovincialis. *Nanomaterials*, *11*(3), 1–17. https://doi.org/10.3390/nano11030649

Caputo, F., Vogel, R., Savage, J., Vella, G., Law, A., Della Camera, G., Hannon, G., Peacock, B., Mehn, D., Ponti, J., Geiss, O., Aubert, D., Prina-Mello, A., & Calzolai, L. (2021). Measuring particle size distribution and mass concentration of nanoplastics and microplastics: addressing some analytical challenges in the sub-micron size range. *Journal of Colloid and Interface Science*, *588*, 401–417. https://doi.org/10.1016/j.jcis.2020.12.039

Carella, F., Feist, S. W., Bignell, J. P., & De Vico, G. (2015). Comparative pathology in bivalves: Aetiological agents and disease processes. *Journal of Invertebrate Pathology*, *131*, 107–120. https://doi.org/10.1016/j.jip.2015.07.012

Carpenter, E. J., & Smith, K. L. (1972). Plastics on the Sargasso sea surface. *Science*, *175*(4027), 1240–1241. https://doi.org/10.1126/science.175.4027.1240

Catarino, A. I., Asselman, J., Niu, Z., & Everaert, G. (2022). Micro- and nanoplastics effects in a multiple stressed marine environment. *Journal of Hazardous Materials Advances*, *7*. https://doi.org/10.1016/j.hazadv.2022.100119

Chaitanya, R. K., Shashank, K., & Sridevi, P. (2016). Oxidative Stress in Invertebrate Systems. In *Free Radicals and Diseases*. InTech. https://doi.org/10.5772/64573

Chan, C. K. M., Fang, J. K. H., Fei, B., & Kan, C. W. (2023). Microfibres release from textile industry wastewater effluents are underestimated: Mitigation actions that need to be prioritised. *Fibers*, *11*(12). https://doi.org/10.3390/fib11120105

Chandramouli Swamy, T. M., Nagarathna, S. V., Reddy, P. V., & Nayak, A. S. (2024). Efficient biodegradation of Polyethylene terephthalate (PET) plastic by Gordonia sp. CN2K isolated from plastic contaminated environment. *Ecotoxicology and Environmental Safety*, *281*. https://doi.org/10.1016/j.ecoenv.2024.116635

Chang, X., & Wang, W. X. (2024). Differential cellular uptake and trafficking of nanoplastics in two hemocyte subpopulations of mussels Perna viridis. *Journal of Hazardous Materials*, *471*. https://doi.org/10.1016/j.jhazmat.2024.134388

Chelomin, V. P., Istomina, A. A., Mazur, A. A., Slobodskova, V. V., Zhukovskaya, A. F., & Dovzhenko, N. V. (2024). New Insights into the Mechanisms of Toxicity of Aging Microplastics. *Toxics*, *12*(10), 726. https://doi.org/10.3390/toxics12100726

Chen, J. H., & Bayne, C. J. (1995). Bivalve mollusc hemocyte behaviors: characterization of hemocyte aggregation and adhesion and their inhibition in the California Mussel (Mytilus californianus). *The Biological Bulletin*, *188*, 255–266. https://doi.org/10.2307/1542303

Chen, Y., Li, W., Xiang, L., Mi, X., Duan, M., & Wu, C. (2022). Fish personality affects their exposure to microplastics. *Ecotoxicology and Environmental Safety*, *233*. https://doi.org/10.1016/j.ecoenv.2022.113301

Choi, G., Ryu, D., Jo, Y., Kim, Y. S., Park, W., Min, H., & Park, Y. (2019). Cycle-consistent deep learning approach to coherent noise reduction in optical diffraction tomography. *Optics Express*, *27*(4), 4927. https://doi.org/10.1364/oe.27.004927

Choi, J. S., Kim, K., Park, K., & Park, J. W. (2022). Long-term exposure of the Mediterranean mussels, Mytilus galloprovincialis to polyethylene terephthalate microfibers: Implication for reproductive and neurotoxic effects. *Chemosphere*, *299*. https://doi.org/10.1016/j.chemosphere.2022.134317

Cholewińska, P., Wojnarowski, K., Moniuszko, H., Pokorny, P., & Palić, D. (2025). An exploratory review of microplastic pollution, associated microbiomes and pathogens in water. *Applied Sciences*, *15*(15), 8128. https://doi.org/10.3390/app15158128

Choy, C. A., Robison, B. H., Gagne, T. O., Erwin, B., Firl, E., Halden, R. U., Hamilton, J. A., Katija, K., Lisin, S. E., Rolsky, C., & S. Van Houtan, K. (2019). The vertical distribution and biological transport of marine microplastics across the epipelagic and mesopelagic water column. *Scientific Reports*, *9*(1). https://doi.org/10.1038/s41598-019-44117-2

Coleman, E. A. (2017). Plastics Additives. In *Applied Plastics Engineering Handbook: Processing, Materials, and Applications: Second Edition* (pp. 489–500). Elsevier Inc. https://doi.org/10.1016/B978-0-323-39040-8.00021-3

Corona, E., Martin, C., Marasco, R., & Duarte, C. M. (2020). Passive and active removal of marine microplastics by a Mushroom Coral (Danafungia scruposa). *Frontiers in Marine Science*, *7*. https://doi.org/10.3389/fmars.2020.00128

Correia, M., & Loeschner, K. (2018). Detection of nanoplastics in food by asymmetric flow field-flow fractionation coupled to multi-angle light scattering: possibilities, challenges and analytical limitations. *Analytical and Bioanalytical Chemistry*, *410*(22), 5603–5615. https://doi.org/10.1007/s00216-018-0919-8

Costa, P. M., Carreira, S., Costa, M. H., & Caeiro, S. (2013). Development of histopathological indices in a commercial marine bivalve (Ruditapes decussatus) to determine environmental quality. *Aquatic Toxicology*, *126*, 442–454. https://doi.org/10.1016/j.aquatox.2012.08.013

Cowger, W., Gray, A., Christiansen, S. H., DeFrond, H., Deshpande, A. D., Hemabessiere, L., Lee, E., Mill, L., Munno, K., Ossmann, B. E., Pittroff, M., Rochman, C., Sarau, G., Tarby, S., & Primpke, S. (2020). Critical Review of Processing and Classification Techniques for Images and Spectra in Microplastic Research. *Applied Spectroscopy*, *74*(9), 989–1010. https://doi.org/10.1177/0003702820929064

Cózar, A., Echevarría, F., González-Gordillo, J. I., Irigoien, X., Úbeda, B., Hernández-León, S., Palma, Á. T., Navarro, S., García-de-Lomas, J., Ruiz, A., Fernández-de-Puelles, M. L., & Duarte, C. M. (2014). Plastic debris in the open ocean. *Proceedings of the National Academy of Sciences of the United States of America*, *111*(28), 10239–10244. https://doi.org/10.1073/pnas.1314705111

Crowley, L. C., Scott, A. P., Marfell, B. J., Boughaba, J. A., Chojnowski, G., & Waterhouse, N. J. (2016). Measuring cell death by propidium iodide uptake and flow cytometry. *Cold Spring Harbor Protocols*, *2016*(7), 647–651. https://doi.org/10.1101/pdb.prot087163

Crusot, M., Gaertner, J. C., Rodriguez, T., Lo, C., & Gaertner-Mazouni, N. (2023). Assessment of plastic waste generated by the aquaculture industry: The case study of pearl farming in French Polynesia. *Journal of Cleaner Production*, *425*. https://doi.org/10.1016/j.jclepro.2023.138902

Cubas, A. L. V., Bianchet, R. T., Reis, I. M. A. S. dos, & Gouveia, I. C. (2022). Plastics and microplastic in the cosmetic industry: Aggregating sustainable actions aimed at alignment and interaction with UN Sustainable Development Goals. *Polymers*, *14*(21). https://doi.org/10.3390/polym14214576

Cuevas, N., Zorita, I., Costa, P. M., Franco, J., & Larreta, J. (2015). Development of histopathological indices in the digestive gland and gonad of mussels: Integration with contamination levels and effects of confounding factors. *Aquatic Toxicology*, *162*, 152–164. https://doi.org/10.1016/j.aquatox.2015.03.011

Cunningham, B. E., Sharpe, E. E., Brander, S. M., Landis, W. G., & Harper, S. L. (2023). Critical gaps in nanoplastics research and their connection to risk assessment. *Frontiers in Toxicology*, *5*. https://doi.org/10.3389/ftox.2023.1154538

da Costa, J. P., Reis, V., Paço, A., Costa, M., Duarte, A. C., & Rocha-Santos, T. (2019). Micro(nano)plastics – Analytical challenges towards risk evaluation. *TrAC - Trends in Analytical Chemistry*, *111*, 173–184. https://doi.org/10.1016/j.trac.2018.12.013

D'Costa, A. H. (2022). Microplastics in decapod crustaceans: Accumulation, toxicity and impacts, a review. *Science of the Total Environment*, *832*. https://doi.org/10.1016/j.scitotenv.2022.154963

de la Ballina, N. R., Maresca, F., Cao, A., & Villalba, A. (2022). Bivalve haemocyte subpopulations: A review. *Frontiers in Immunology*, *13*. https://doi.org/10.3389/fimmu.2022.826255

De Ruijter, V. N., Redondo-Hasselerharm, P. E., Gouin, T., & Koelmans, A. A. (2020). Quality criteria for microplastic effect studies in the context of risk assessment: A critical review. *Environmental Science and Technology*, *54*(19), 11692–11705. https://doi.org/10.1021/acs.est.0c03057

de Souza Teodoro, L., Jablonski, C. A., Pelegrini, K., Pereira, T. C. B., Maraschin, T. G., de Sousa Araujo, A. C., Monserrat, J. M., de Souza Basso, N. R., Kist, L. W., & Bogo, M. R. (2024). Toxic effects of environmental-relevant exposure to polyethylene terephthalate (PET) micro and nanoparticles in zebrafish early development. *NanoImpact*, *33*. https://doi.org/10.1016/j.impact.2024.100497

De-la-Torre, G. E., Bapp, C., Forero-López, A. D., & Dobaradaran, S. (2025). Analytical techniques for quantifying and identifying nanoplastics: recent advances. *Current Opinion in Chemical Engineering*, *48*. https://doi.org/10.1016/j.coche.2025.101134

Delre, A., Goudriaan, M., Morales, V. H., Vaksmaa, A., Ndhlovu, R. T., Baas, M., Keijzer, E., de Groot, T., Zeghal, E., Egger, M., Röckmann, T., & Niemann, H. (2023). Plastic photodegradation under simulated marine conditions. *Marine Pollution Bulletin*, *187*. https://doi.org/10.1016/j.marpolbul.2022.114544

Deng, J., Ibrahim, M. S., Tan, L. Y., Yeo, X. Y., Lee, Y. A., Park, S. J., Wüstefeld, T., Park, J. W., Jung, S., & Cho, N. J. (2022). Microplastics released from food containers can suppress lysosomal activity in mouse macrophages. *Journal of Hazardous Materials*, *435*. https://doi.org/10.1016/j.jhazmat.2022.128980

Desforges, J. P. W., Galbraith, M., Dangerfield, N., & Ross, P. S. (2014). Widespread distribution of microplastics in subsurface seawater in the NE Pacific Ocean. *Marine Pollution Bulletin*, *79*(1–2), 94–99. https://doi.org/10.1016/j.marpolbul.2013.12.035

Détrée, C., & Gallardo-Escárate, C. (2018). Single and repetitive microplastics exposures induce immune system modulation and homeostasis alteration in the edible mussel Mytilus galloprovincialis. *Fish and Shellfish Immunology*, *83*, 52–60. https://doi.org/10.1016/j.fsi.2018.09.018

Di, X., Zhang, H., & Sun, T. (2024). Spatiotemporal response of microplastics to natural and anthropogenic factors in estuarine waters. *Science of the Total Environment*, *955*. https://doi.org/10.1016/j.scitotenv.2024.176822

Do, A. T. N., Ha, Y., & Kwon, J. H. (2022). Leaching of microplastic-associated additives in aquatic environments: A critical review. *Environmental Pollution*, *305*, 119258. https://doi.org/10.1016/j.envpol.2022.119258

Doyle, D., Sundh, H., & Almroth, B. C. (2022). Microplastic exposure in aquatic invertebrates can cause significant negative effects compared to natural particles - A meta-analysis. *Environmental Pollution*, *315*. https://doi.org/10.1016/j.envpol.2022.120434

Du, T., Yu, X., Shao, S., Li, T., Xu, S., & Wu, L. (2023). Aging of nanoplastics significantly affects protein corona composition thus enhancing macrophage uptake. *Environmental Science and Technology*, *57*(8), 3206–3217. https://doi.org/10.1021/acs.est.2c05772

Du, Y., Liu, X., Dong, X., & Yin, Z. (2022). A review on marine plastisphere: biodiversity, formation, and role in degradation. *Computational and Structural Biotechnology Journal*, *20*, 975–988. https://doi.org/10.1016/j.csbj.2022.02.008

Ducoli, S., Federici, S., Nicsanu, R., Zendrini, A., Marchesi, C., Paolini, L., Radeghieri, A., Bergese, P., & Depero, L. E. (2022). A different protein corona cloaks “true-to-life” nanoplastics with respect to synthetic polystyrene nanobeads. *Environmental Science: Nano*, *9*(4), 1414–1426. https://doi.org/10.1039/d1en01016f

Duis, K., & Coors, A. (2016). Microplastics in the aquatic and terrestrial environment: sources (with a specific focus on personal care products), fate and effects. *Environmental Sciences Europe*, *28*(1), 1–25. https://doi.org/10.1186/s12302-015-0069-y

Egebjerg, J. M., Szomek, M., Thaysen, K., Juhl, A. D., Kozakijevic, S., Werner, S., Pratsch, C., Schneider, G., Kapishnikov, S., Ekman, A., Röttger, R., & Wüstner, D. (2024). Automated quantification of vacuole fusion and lipophagy in Saccharomyces cerevisiae from fluorescence and cryo-soft X-ray microscopy data using deep learning. *Autophagy*, *20*(4), 902–922. https://doi.org/10.1080/15548627.2023.2270378

Enders, K., Lenz, R., Stedmon, C. A., & Nielsen, T. G. (2015). Abundance, size and polymer composition of marine microplastics ≥10 μm in the Atlantic Ocean and their modelled vertical distribution. *Marine Pollution Bulletin*, *100*(1), 70–81. https://doi.org/10.1016/j.marpolbul.2015.09.027

Eriksen, M., Lebreton, L. C. M., Carson, H. S., Thiel, M., Moore, C. J., Borerro, J. C., Galgani, F., Ryan, P. G., & Reisser, J. (2014). Plastic pollution in the world's oceans: More than 5 trillion plastic pieces weighing over 250,000 tons afloat at sea. *PLoS ONE*, *9*(12). https://doi.org/10.1371/journal.pone.0111913

Eriksen, M., Maximenko, N., Thiel, M., Cummins, A., Lattin, G., Wilson, S., Hafner, J., Zellers, A., & Rifman, S. (2013). Plastic pollution in the South Pacific subtropical gyre. *Marine Pollution Bulletin*, *68*(1–2), 71–76. https://doi.org/10.1016/j.marpolbul.2012.12.021

Ershova, A., & Frank, Y. (2024). Separation and purification of microplastics from the environmental samples. In *Analysis of Microplastics and Nanoplastics* (pp. 135–154). Elsevier. https://doi.org/10.1016/B978-0-443-15779-0.00019-5

Ertürk Gürkan, S., & Gürkan, M. (2021). Toxicity of gamma aluminium oxide nanoparticles in the Mediterranean mussel (Mytilus galloprovincialis): histopathological alterations and antioxidant responses in the gill and digestive gland. *Biomarkers*, *26*(3), 248–259. https://doi.org/10.1080/1354750X.2021.1878558

Escartin, C., Galea, E., Lakatos, A., O'Callaghan, J. P., Petzold, G. C., Serrano-Pozo, A., Steinhäuser, C., Volterra, A., Carmignoto, G., Agarwal, A., Allen, N. J., Araque, A., Barbeito, L., Barzilai, A., Bergles, D. E., Bonvento, G., Butt, A. M., Chen, W. T., Cohen-Salmon, M., … Verkhratsky, A. (2021). Reactive astrocyte nomenclature, definitions, and future directions. *Nature Neuroscience*, *24*(3), 312–325. https://doi.org/10.1038/s41593-020-00783-4

European Commission. (2018). *Technical Guidance for Deriving Environmental Quality Standards Environment. Common Implementation Strategy for the Water Framework Directive (2000/60/EC) Guidance Document No. 27*.

Evangeliou, N., Grythe, H., Klimont, Z., Heyes, C., Eckhardt, S., Lopez-Aparicio, S., & Stohl, A. (2020). Atmospheric transport is a major pathway of microplastics to remote regions. *Nature Communications*, *11*(1). https://doi.org/10.1038/s41467-020-17201-9

Evariste, L., Auffret, M., Audonnet, S., Geffard, A., David, E., Brousseau, P., Fournier, M., & Betoulle, S. (2016). Functional features of hemocyte subpopulations of the invasive mollusk species Dreissena polymorpha. *Fish and Shellfish Immunology*, *56*, 144–154. https://doi.org/10.1016/j.fsi.2016.06.054

Evariste, L., Rioult, D., Brousseau, P., Geffard, A., David, E., Auffret, M., Fournier, M., & Betoulle, S. (2017). Differential sensitivity to cadmium of immunomarkers measured in hemocyte subpopulations of zebra mussel Dreissena polymorpha. *Ecotoxicology and Environmental Safety*, *137*, 78–85. https://doi.org/10.1016/j.ecoenv.2016.11.027

Everaert, G., Vlaeminck, K., Vandegehuchte, M. B., & Janssen, C. R. (2022). Effects of microplastic on the population dynamics of a marine copepod: Insights from a laboratory experiment and a mechanistic model. *Environmental Toxicology and Chemistry*, *41*(7), 1663–1674. https://doi.org/10.1002/etc.5336

Falcone, C. (2022). Evolution of astrocytes: From invertebrates to vertebrates. *Frontiers in Cell and Developmental Biology*, *10*. https://doi.org/10.3389/fcell.2022.931311

Fazey, F. M. C., & Ryan, P. G. (2016). Biofouling on buoyant marine plastics: An experimental study into the effect of size on surface longevity. *Environmental Pollution*, *210*, 354–360. https://doi.org/10.1016/j.envpol.2016.01.026

Feng, Y., Fu, H., Zhang, X., Liu, S., & Wei, X. (2024). Lysosome toxicities induced by nanoparticle exposure and related mechanisms. *Ecotoxicology and Environmental Safety*, *286*. https://doi.org/10.1016/j.ecoenv.2024.117215

Fernández, B., & Albentosa, M. (2019a). Dynamic of small polyethylene microplastics (≤10 µm) in mussel's tissues. *Marine Pollution Bulletin*, *146*, 493–501. https://doi.org/10.1016/j.marpolbul.2019.06.021

Fernández, B., & Albentosa, M. (2019b). Insights into the uptake, elimination and accumulation of microplastics in mussel. *Environmental Pollution*, *249*, 321–329. https://doi.org/10.1016/j.envpol.2019.03.037

Ferreira, I., Venâncio, C., Lopes, I., & Oliveira, M. (2019). Nanoplastics and marine organisms: What has been studied? *Environmental Toxicology and Pharmacology*, *67*, 1–7. https://doi.org/10.1016/j.etap.2019.01.006

Filipe, V., Hawe, A., & Jiskoot, W. (2010). Critical evaluation of nanoparticle tracking analysis (NTA) by NanoSight for the measurement of nanoparticles and protein aggregates. *Pharmaceutical Research*, *27*(5), 796–810. https://doi.org/10.1007/s11095-010-0073-2

Fischer, R., Lobelle, D., Kooi, M., Koelmans, A., Onink, V., Laufkötter, C., Amaral-Zettler, L., Yool, A., & Van Sebille, E. (2022). Modelling submerged biofouled microplastics and their vertical trajectories. *Biogeosciences*, *19*(8), 2211–2234. https://doi.org/10.5194/bg-19-2211-2022

Foley, C. J., Feiner, Z. S., Malinich, T. D., & Höök, T. O. (2018). A meta-analysis of the effects of exposure to microplastics on fish and aquatic invertebrates. *Science of the Total Environment*, *631–632*, 550–559. https://doi.org/10.1016/j.scitotenv.2018.03.046

Foroozandeh, P., & Aziz, A. A. (2018). Insight into cellular uptake and intracellular trafficking of nanoparticles. *Nanoscale Research Letters*, *13*, 339. https://doi.org/10.1186/s11671-018-2728-6

Fox, D. R., van Dam, R. A., Fisher, R., Batley, G. E., Tillmanns, A. R., Thorley, J., Schwarz, C. J., Spry, D. J., & McTavish, K. (2021). Recent developments in species sensitivity distribution modeling. *Environmental Toxicology and Chemistry*, *40*(2), 293–308. https://doi.org/10.1002/etc.4925

Fraissinet, S., De Benedetto, G. E., Malitesta, C., Holzinger, R., & Materić, D. (2024). Microplastics and nanoplastics size distribution in farmed mussel tissues. *Communications Earth and Environment*, *5*(1). https://doi.org/10.1038/s43247-024-01300-2

Franzellitti, S., Canesi, L., Auguste, M., Wathsala, R. H. G. R., & Fabbri, E. (2019). Microplastic exposure and effects in aquatic organisms: A physiological perspective. *Environmental Toxicology and Pharmacology*, *68*(November 2018), 37–51. https://doi.org/10.1016/j.etap.2019.03.009

Frère, L., Paul-Pont, I., Moreau, J., Soudant, P., Lambert, C., Huvet, A., & Rinnert, E. (2016). A semi-automated Raman micro-spectroscopy method for morphological and chemical characterizations of microplastic litter. *Marine Pollution Bulletin*, *113*(1–2), 461–468. https://doi.org/10.1016/j.marpolbul.2016.10.051

Frias, J. P. G. L., & Nash, R. (2019). Microplastics: Finding a consensus on the definition. *Marine Pollution Bulletin*, *138*(September 2018), 145–147. https://doi.org/10.1016/j.marpolbul.2018.11.022

Fries, E., Dekiff, J. H., Willmeyer, J., Nuelle, M. T., Ebert, M., & Remy, D. (2013). Identification of polymer types and additives in marine microplastic particles using pyrolysis-GC/MS and scanning electron microscopy. *Environmental Sciences: Processes and Impacts*, *15*(10), 1949–1956. https://doi.org/10.1039/c3em00214d

Galloway, T. S., Cole, M., & Lewis, C. (2017). Interactions of microplastic debris throughout the marine ecosystem. *Nature Ecology and Evolution*, *1*(5), 1–8. https://doi.org/10.1038/s41559-017-0116

Galloway, T. S., & Lewisa, C. N. (2016). Marine microplastics spell big problems for future generations. *Proceedings of the National Academy of Sciences of the United States of America*, *113*(9), 2331–2333. https://doi.org/10.1073/pnas.1600715113

Galloway, T. S., & Porter, A. (2024). Microplastics, microfibres and marine snows. *Nature Water*, *2*(6), 507–508. https://doi.org/10.1038/s44221-024-00263-0

Gangadoo, S., Owen, S., Rajapaksha, P., Plaisted, K., Cheeseman, S., Haddara, H., Truong, V. K., Ngo, S. T., Vu, V. V., Cozzolino, D., Elbourne, A., Crawford, R., Latham, K., & Chapman, J. (2020). Nano-plastics

and their analytical characterisation and fate in the marine environment: From source to sea. *Science of the Total Environment*, *732*, 138792. https://doi.org/10.1016/j.scitotenv.2020.138792

Garcés-Ordóñez, O., Espinosa, L. F., Cardoso, R. P., Issa Cardozo, B. B., & Meigikos dos Anjos, R. (2020). Plastic litter pollution along sandy beaches in the Caribbean and Pacific coast of Colombia. *Environmental Pollution*, *267*. https://doi.org/10.1016/j.envpol.2020.115495

Gaudioso, Á., Silva, T. P., & Dolores Ledesma, M. (2022). Models to study basic and applied aspects of lysosomal storage disorders. *Advanced Drug Delivery Reviews*, *190*, 114532. https://doi.org/10.1016/j.addr.2022.114532

Gaylarde, C. C., Neto, J. A. B., & da Fonseca, E. M. (2021). Paint fragments as polluting microplastics: A brief review. *Marine Pollution Bulletin*, *162*. https://doi.org/10.1016/j.marpolbul.2020.111847

Géloën, A., Isaieva, K., Isaiev, M., Levinson, O., Berger, E., & Lysenko, V. (2021). Intracellular detection and localization of nanoparticles by refractive index measurement. *Sensors*, *21*(15). https://doi.org/10.3390/s21155001

Gerdol, M., & Pallavicini, A. (2025). Exploring the immune resilience of Mediterranean mussels: Recent advances and future directions. *Fish and Shellfish Immunology*, *158*. https://doi.org/10.1016/j.fsi.2025.110147

Gewert, B., Ogonowski, M., Barth, A., & MacLeod, M. (2017). Abundance and composition of near surface microplastics and plastic debris in the Stockholm Archipelago, Baltic Sea. *Marine Pollution Bulletin*, *120*(1–2), 292–302. https://doi.org/10.1016/j.marpolbul.2017.04.062

Gewert, B., Plassmann, M. M., & Macleod, M. (2015). Pathways for degradation of plastic polymers floating in the marine environment. In *Environmental Sciences: Processes and Impacts* (Vol. 17, Issue 9, pp. 1513–1521). Royal Society of Chemistry. https://doi.org/10.1039/c5em00207a

Geyer, R., Jambeck, J. R., & Law, K. L. (2017). Production, use, and fate of all plastics ever made. *Science Advances*, *7*. https://doi.org/10.1126/sciadv.1700782

Gigault, J., & Davranche, M. (2025). Nanoplastics in focus: Exploring interdisciplinary approaches and future directions. *NanoImpact*, *37*. https://doi.org/10.1016/j.impact.2025.100544

Gilbert, M. (2016). Plastics Materials: Introduction and Historical Development. In *Brydson's Plastics Materials: Eighth Edition* (pp. 2–18). Elsevier Inc. https://doi.org/10.1016/B978-0-323-35824-8.00001-3

Gonçalves, J. M., & Bebianno, M. J. (2021). Nanoplastics impact on marine biota: A review. *Environmental Pollution*, *273*. https://doi.org/10.1016/j.envpol.2021.116426

González-Soto, N., Hatfield, J., Katsumiti, A., Duroudier, N., Lacave, J. M., Bilbao, E., Orbea, A., Navarro, E., & Cajaraville, M. P. (2019). Impacts of dietary exposure to different sized polystyrene microplastics alone and with sorbed benzo[a]pyrene on biomarkers and whole organism responses in mussels Mytilus galloprovincialis. *Science of the Total Environment*, *684*, 548–566. https://doi.org/10.1016/j.scitotenv.2019.05.161

Gornati, R., Longo, A., Rossi, F., Maisano, M., Sabatino, G., Mauceri, A., Bernardini, G., & Fasulo, S. (2016). Effects of titanium dioxide nanoparticle exposure in Mytilus galloprovincialis gills and digestive gland. *Nanotoxicology*, *10*(6), 807–817. https://doi.org/10.3109/17435390.2015.1132348

Gottstein, C., Wu, G., Wong, B. J., & Zasadzinski, J. A. (2013). Precise quantification of nanoparticle internalization. *ACS Nano*, *7*(6), 4933–4945. https://doi.org/10.1021/nn400243d

Green, D. S., Boots, B., Blockley, D. J., Rocha, C., & Thompson, R. (2015). Impacts of discarded plastic bags on marine assemblages and ecosystem functioning. *Environmental Science and Technology*, *49*(9), 5380–5389. https://doi.org/10.1021/acs.est.5b00277

Green, D. S., Boots, B., O'Connor, N. E., & Thompson, R. (2017). Microplastics affect the ecological functioning of an important biogenic habitat. *Environmental Science and Technology*, *51*(1), 68–77. https://doi.org/10.1021/acs.est.6b04496

Green, D. S., Boots, B., Sigwart, J., Jiang, S., & Rocha, C. (2016). Effects of conventional and biodegradable microplastics on a marine ecosystem engineer (Arenicola marina) and sediment nutrient cycling. *Environmental Pollution*, *208*, 426–434. https://doi.org/10.1016/j.envpol.2015.10.010

Gul, B., Ashraf, S., Khan, S., Nisar, H., & Ahmad, I. (2021). Cell refractive index: Models, insights, applications and future perspectives. *Photodiagnosis and Photodynamic Therapy*, *33*. https://doi.org/10.1016/j.pdpdt.2020.102096

Guo, J., Yang, W. T., Mai, F. Y., Liang, J. R., Luo, J., Zhou, M. C., Yu, D. D., Wang, Y. L., & Li, C. G. (2024). Unravelling oncosis: morphological and molecular insights into a unique cell death pathway. *Frontiers in Immunology*, *15*. https://doi.org/10.3389/fimmu.2024.1450998

Gustafson, H. H., Holt-Casper, D., Grainger, D. W., & Ghandehari, H. (2015). Nanoparticle uptake: The phagocyte problem. *Nano Today*, *10*(4), 487–510. https://doi.org/10.1016/j.nantod.2015.06.006

Habib, T., Muhammad, M., Liu, Y.-H., Fang, B.-Z., & Li, W.-J. (2024). Biodegradation of plastics—An overview. In *Microbiome-Assisted Bioremediation* (pp. 171–197). Elsevier. https://doi.org/10.1016/b978-0-443-21911-5.00011-8

Hampton, L. M. T., Wyler, D. B., Almroth, B. C., Coffin, S., Cowger, W., Doyle, D., Hataley, E. K., Hutton, S. J., Mair, M. M., Miller, E. L., Monclús, L., Sharpe, E. E., Samreen, S., Ahmed, K. T., Allamby, Q. P. V., Vital, A. L. A., Asnicar, D., Bare, J. L., Barrick, A., … Mehinto, A. C. (2025). The Toxicity of Microplastics Explorer (ToMEx) 2.0. *Microplastics and Nanoplastics*, *5*(1), 38. https://doi.org/10.1186/s43591-025-00145-6

Hara, J., Vercauteren, M., Schoenaers, S., Janssen, C. R., Blust, R., Asselman, J., & Town, R. M. (2024). Differential sensitivity of hemocyte subpopulations (Mytilus edulis) to aged polyethylene terephthalate micro- and nanoplastic particles. *Ecotoxicology and Environmental Safety*, *286*. https://doi.org/10.1016/j.ecoenv.2024.117255

Hariharan, G., Purvaja, R., Anandavelu, I., Robin, R. S., & Ramesh, R. (2021). Accumulation and ecotoxicological risk of weathered polyethylene (wPE) microplastics on green mussel (Perna viridis). *Ecotoxicology and Environmental Safety*, *208*. https://doi.org/10.1016/j.ecoenv.2020.111765

Hartmann, N. B., Hüffer, T., Thompson, R. C., Hassellöv, M., Verschoor, A., Daugaard, A. E., Rist, S., Karlsson, T., Brennholt, N., Cole, M., Herrling, M. P., Hess, M. C., Ivleva, N. P., Lusher, A. L., & Wagner, M. (2019). Are we speaking the same language? Recommendations for a definition and categorization framework for plastic debris. *Environmental Science and Technology*, *53*(3), 1039–1047. https://doi.org/10.1021/acs.est.8b05297

Hatzonikolakis, Y., Raitsos, D. E., Sailley, S. F., Digka, N., Theodorou, I., Tsiaras, K., Tsangaris, C., Skia, G., Ntzouvaras, A., & Triantafyllou, G. (2024). Assessing the physiological effects of microplastics on cultured mussels in the Mediterranean Sea. *Environmental Pollution*, *363*. https://doi.org/10.1016/j.envpol.2024.125052

He, T., Qu, Y., Yang, X., Liu, L., Xiong, F., Wang, D., Liu, M., & Sun, R. (2023). Research progress on the cellular toxicity caused by microplastics and nanoplastics. *Journal of Applied Toxicology*, *43*(11), 1576–1593. https://doi.org/10.1002/jat.4449

He, W., Liu, S., Zhang, W., Yi, K., Zhang, C., Pang, H., Huang, D., Huang, J., & Li, X. (2023). Recent advances on microplastic aging: Identification, mechanism, influence factors, and additives release. *Science of the Total Environment*, *889*, 164035. https://doi.org/10.1016/j.scitotenv.2023.164035

Heris, Y. S. (2024). Bacterial biodegradation of synthetic plastics: a review. *Bulletin of the National Research Centre*, *48*(1). https://doi.org/10.1186/s42269-024-01241-y

Hernán, G., Rodríguez, E., & Tomas, F. (2024). Identifying patterns of microplastic accumulation in coastal vegetated habitats: A systematic review and meta-analysis. *Science of The Total Environment*, 175985. https://doi.org/10.1016/j.scitotenv.2024.175985

Hidalgo-Ruz, V., Gutow, L., Thompson, R. C., & Thiel, M. (2012). Microplastics in the marine environment: A review of the methods used for identification and quantification. *Environmental Science and Technology*, *46*(6), 3060–3075. https://doi.org/10.1021/es2031505

Hoang, V. H., Nguyen, M. K., Hoang, T. D., Nguyen, H. L., Lin, C., Yousaf, B., Ha, M. C., Bui, V. K. H., Pham, M. T., Chang, S. W., & Nguyen, D. D. (2025). Global occurrence and environmental fate of microplastics in stormwater runoff: Unlock the in-depth knowledge on nature-based removal strategies. *Reviews of Environmental Contamination and Toxicology*, *263*(1). https://doi.org/10.1007/s44169-025-00078-4

Hu, M., & Palić, D. (2020). Micro- and nano-plastics activation of oxidative and inflammatory adverse outcome pathways. *Redox Biology*, *37*. https://doi.org/10.1016/j.redox.2020.101620

Huang, W., Chen, M., Song, B., Deng, J., Shen, M., Chen, Q., Zeng, G., & Liang, J. (2021). Microplastics in the coral reefs and their potential impacts on corals: A mini-review. *Science of the Total Environment*, *762*. https://doi.org/10.1016/j.scitotenv.2020.143112

Huang, X., Leung, J. Y. S., Hu, M., Xu, E. G., & Wang, Y. (2022). Microplastics can aggravate the impact of ocean acidification on the health of mussels: Insights from physiological performance, immunity and byssus properties. *Environmental Pollution*, *308*. https://doi.org/10.1016/j.envpol.2022.119701

Huang, Y., Liu, Q., Jia, W., Yan, C., & Wang, J. (2020). Agricultural plastic mulching as a source of microplastics in the terrestrial environment. *Environmental Pollution*, *260*. https://doi.org/10.1016/j.envpol.2020.114096

Huang, Z., Pan, M., & Zhou, X. (2023). Distribution and solutions for marine debris: A case study on the Great Pacific Ocean Garbage Patch. *Applied and Computational Engineering*, *3*(1), 253–262. https://doi.org/10.54254/2755-2721/3/20230471

Huntington, T. (2019). *Marine Litter and Aquaculture Gear - White Paper*.

Impellitteri, F., Curpăn, A. S., Plăvan, G., Ciobica, A., & Faggio, C. (2022). Hemocytes: A Useful Tool for Assessing the Toxicity of Microplastics, Heavy Metals, and Pesticides on Aquatic Invertebrates. *International Journal of Environmental Research and Public Health*, *19*(24). https://doi.org/10.3390/ijerph192416830

Ivar do Sul, J. A. (2021). Why it is important to analyze the chemical composition of microplastics in environmental samples. *Marine Pollution Bulletin*, *165*. https://doi.org/10.1016/j.marpolbul.2021.112086

Iwasaki, Y., Takeshita, K. M., Ueda, K., & Naito, W. (2023). Estimating species sensitivity distributions for microplastics by quantitively considering particle characteristics using a recently created ecotoxicity database. *Microplastics and Nanoplastics*, *3*(1). https://doi.org/10.1186/s43591-023-00070-6

Jalón-Rojas, I., Romero-Ramírez, A., Fauquembergue, K., Rossignol, L., Cachot, J., Sous, D., & Morin, B. (2022). Effects of biofilms and particle physical properties on the rising and settling velocities of microplastic fibers and sheets. *Environmental Science and Technology*, *56*(12), 8114–8123. https://doi.org/10.1021/acs.est.2c01302

Jambeck, J. R., Geyer, R., Wilcox, C., Siegler, T. R., Perryman, M., Andrady, A., Narayan, R., & Law, K. L. (2015). Plastic waste inputs from land into the ocean. *Science*, *347*(6223), 768–771. https://doi.org/10.1126/science.1260352

Jeon, S., Lee, D. K., Jeong, J., Yang, S. I., Kim, J. S., Kim, J., & Cho, W. S. (2021). The reactive oxygen species as pathogenic factors of fragmented microplastics to macrophages. *Environmental Pollution*, *281*, 117006. https://doi.org/10.1016/j.envpol.2021.117006

Jeong, C. B., Kang, H. M., Lee, M. C., Kim, D. H., Han, J., Hwang, D. S., Souissi, S., Lee, S. J., Shin, K. H., Park, H. G., & Lee, J. S. (2017). Adverse effects of microplastics and oxidative stress-induced MAPK/Nrf2 pathway-mediated defense mechanisms in the marine copepod Paracyclopina nana. *Scientific Reports*, *7*. https://doi.org/10.1038/srep41323

Jeong, C. B., Won, E. J., Kang, H. M., Lee, M. C., Hwang, D. S., Hwang, U. K., Zhou, B., Souissi, S., Lee, S. J., & Lee, J. S. (2016). Microplastic size-dependent toxicity, oxidative stress induction, and p-JNK and p-p38 activation in the Monogonont Rotifer (Brachionus koreanus). *Environmental Science and Technology*, *50*(16), 8849–8857. https://doi.org/10.1021/acs.est.6b01441

Jeong, J., Im, J., & Choi, J. (2024). Integrating aggregate exposure pathway and adverse outcome pathway for micro/nanoplastics: A review on exposure, toxicokinetics, and toxicity studies. *Ecotoxicology and Environmental Safety*, *272*. https://doi.org/10.1016/j.ecoenv.2024.116022

Jose, S., Lonappan, L., & Cabana, H. (2024). Prevalence of microplastics and fate in wastewater treatment plants: a review. *Environmental Chemistry Letters*, *22*(2), 657–690. https://doi.org/10.1007/s10311-023-01679-y

Junaid, M., Siddiqui, J. A., Liu, S., Lan, R., Abbas, Z., Chen, G., & Wang, J. (2023). Adverse multigeneration combined impacts of micro(nano)plastics and emerging pollutants in the aquatic environment. *Science of the Total Environment*, *882*. https://doi.org/10.1016/j.scitotenv.2023.163679

Jung, J. W., Park, J. W., Eo, S., Choi, J., Song, Y. K., Cho, Y., Hong, S. H., & Shim, W. J. (2021). Ecological risk assessment of microplastics in coastal, shelf, and deep sea waters with a consideration of environmentally relevant size and shape. *Environmental Pollution*, *270*, 116217. https://doi.org/10.1016/j.envpol.2020.116217

Kang, H. M., Byeon, E., Jeong, H., Kim, M. S., Chen, Q., & Lee, J. S. (2021). Different effects of nano- and microplastics on oxidative status and gut microbiota in the marine medaka Oryzias melastigma. *Journal of Hazardous Materials*, *405*. https://doi.org/10.1016/j.jhazmat.2020.124207

Kangas, A., Setälä, O., Kauppi, L., & Lehtiniemi, M. (2023). Trophic transfer increases the exposure to microplastics in littoral predators. *Marine Pollution Bulletin*, *196*. https://doi.org/10.1016/j.marpolbul.2023.115553

Kaposi, K. L., Mos, B., Kelaher, B. P., & Dworjanyn, S. A. (2014). Ingestion of microplastic has limited impact on a marine larva. *Environmental Science and Technology*, *48*(3), 1638–1645. https://doi.org/10.1021/es404295e

Karami, A. (2017). Gaps in aquatic toxicological studies of microplastics. *Chemosphere*, *184*(June), 841–848. https://doi.org/10.1016/j.chemosphere.2017.06.048

Karlsson, T. M., Arneborg, L., Broström, G., Almroth, B. C., Gipperth, L., & Hassellöv, M. (2018). The unaccountability case of plastic pellet pollution. *Marine Pollution Bulletin*, *129*(1), 52–60. https://doi.org/10.1016/j.marpolbul.2018.01.041

Kataoka, C., & Kashiwada, S. (2021). Ecological risks due to immunotoxicological effects on aquatic organisms. *International Journal of Molecular Sciences*, *22*(15). https://doi.org/10.3390/ijms22158305

Kataržytė, M., Balčiūnas, A., Haseler, M., Sabaliauskaitė, V., Lauciūtė, L., Stepanova, K., Nazzari, C., & Schernewski, G. (2020). Cigarette butts on Baltic Sea beaches: Monitoring, pollution and mitigation measures. *Marine Pollution Bulletin*, *156*. https://doi.org/10.1016/j.marpolbul.2020.111248

Katsumiti, A., Losada-Carrillo, M. P., Barros, M., & Cajaraville, M. P. (2021). Polystyrene nanoplastics and microplastics can act as Trojan horse carriers of benzo(a)pyrene to mussel hemocytes in vitro. *Scientific Reports*, *11*(1). https://doi.org/10.1038/s41598-021-01938-4

Katsumiti, A., Tomovska, R., & Cajaraville, M. P. (2017). Intracellular localization and toxicity of graphene oxide and reduced graphene oxide nanoplatelets to mussel hemocytes in vitro. *Aquatic Toxicology*, *188*, 138–147. https://doi.org/10.1016/j.aquatox.2017.04.016

Kaufmann, C. B. (2011). Leo H. Baekeland. In *100+ years of Plastics: Leo Baekeland and beyond* (Vol. 1080, p. 23). American Chemical Society. https://doi.org/10.1021/bk-2011-1080

Khanna, R., Chandra, A., Sen, S., Konyukhov, Y., Fuentes, E., Burmistrov, I., & Kravchenko, M. (2024). Microplastics and nanoplastics as environmental contaminants of emerging concern: Potential hazards for human health. *Sustainability*, *16*(19). https://doi.org/10.3390/su16198704

Khoshtinat, S. (2023). State-of-the-art review of aliphatic polyesters and polyolefins biodeterioration by microorganisms: from mechanism to characterization. *Corrosion and Materials Degradation*, *4*(4), 542–572. https://doi.org/10.3390/cmd4040029

Kim, G., Hugonnet, H., Kim, K., Lee, J. H., Lee, S. S., Ha, J., Lee, C., Park, H., Yoon, K. J., Shin, Y., Csucs, G., Hitchcock, I., Mackinder, L., Kim, J. H., Hwang, T. H., Lee, S., O'Toole, P., Koo, B. K., Guck, J., & Park, Y. K. (2024). Holotomography. *Nature Reviews Methods Primers*, *4*(1). https://doi.org/10.1038/s43586-024-00327-1

Kim, L., Cui, R., Il Kwak, J., & An, Y. J. (2022). Trophic transfer of nanoplastics through a microalgae–crustacean–small yellow croaker food chain: Inhibition of digestive enzyme activity in fish. *Journal of Hazardous Materials*, *440*. https://doi.org/10.1016/j.jhazmat.2022.129715

Kim, S. W., Chae, Y., Kim, D., & An, Y. J. (2019). Zebrafish can recognize microplastics as inedible materials: Quantitative evidence of ingestion behavior. *Science of the Total Environment*, *649*, 156–162. https://doi.org/10.1016/j.scitotenv.2018.08.310

Koelmans, A. A., Redondo-Hasselerharm, P. E., Mohamed Nor, N. H., & Kooi, M. (2020). Solving the nonalignment of methods and approaches used in microplastic research to consistently characterize risk. *Environmental Science and Technology*, *54*(19), 12307–12315. https://doi.org/10.1021/acs.est.0c02982

Kögel, T., Bjorøy, Ø., Toto, B., Bienfait, A. M., & Sanden, M. (2020). Micro- and nanoplastic toxicity on aquatic life: Determining factors. *Science of the Total Environment*, *709*(5817). https://doi.org/10.1016/j.scitotenv.2019.136050

Kooi, M., Primpke, S., Mintenig, S. M., Lorenz, C., Gerdts, G., & Koelmans, A. A. (2021). Characterizing the multidimensionality of microplastics across environmental compartments. *Water Research*, *202*. https://doi.org/10.1016/j.watres.2021.117429

Kooi, M., Van Nes, E. H., Scheffer, M., & Koelmans, A. A. (2017). Ups and downs in the ocean: Effects of biofouling on vertical transport of microplastics. *Environmental Science and Technology*, *51*(14), 7963–7971. https://doi.org/10.1021/acs.est.6b04702

Kooijman, S. A. L. M. (2006). Pseudo-faeces production in bivalves. *Journal of Sea Research*, *56*(2), 103–106. https://doi.org/10.1016/j.seares.2006.03.003

Kukulka, T., Proskurowski, G., Morét-Ferguson, S., Meyer, D. W., & Law, K. L. (2012). The effect of wind mixing on the vertical distribution of buoyant plastic debris. *Geophysical Research Letters*, *39*(7). https://doi.org/10.1029/2012GL051116

Kusch, P. (2022). Challenges in the Analysis of Microand Nanoplastics: The Role of Laboratory Studies. In *Handbook of Microplastics in the Environment* (pp. 477–501). Springer International Publishing. https://doi.org/10.1007/978-3-030-39041-9_41

Kwak, J. Il, & An, Y. J. (2021). Microplastic digestion generates fragmented nanoplastics in soils and damages earthworm spermatogenesis and coelomocyte viability. *Journal of Hazardous Materials*, *402*. https://doi.org/10.1016/j.jhazmat.2020.124034

Lacerda, A. L., Casotti, R., Briand, J.-F., Lenoble, V., Muniategui-Lorenzo, S., Kessler, F., Barre, A., Moscoso-Pérez, C. M., Fernández-González, V., Andrade-Garda, J. M., Murano, C., Donnarumma, V., Oreste, E., Joyce, H., Hannon, C., Nash, R., Orange, F., Frias, J., & Pedrotti, M. L. (2025). The plastisphere: a comprehensive description of geographic and temporal community patterns across the Mediterranean Sea and the Atlantic Ocean. *Environmental Research*, 121929. https://doi.org/10.1016/j.envres.2025.121929

Laganà, A., Visalli, G., Facciolà, A., Celesti, C., Iannazzo, D., & Di Pietro, A. (2023). Uptake of breathable nano- and micro-sized polystyrene particles: Comparison of virgin and oxidised nPS/mPS in human alveolar cells. *Toxics*, *11*(8). https://doi.org/10.3390/toxics11080686

Lambert, S., & Wagner, M. (2016a). Characterisation of nanoplastics during the degradation of polystyrene. *Chemosphere*, *145*, 265–268. https://doi.org/10.1016/j.chemosphere.2015.11.078

Lambert, S., & Wagner, M. (2016b). Formation of microscopic particles during the degradation of different polymers. *Chemosphere*, *161*, 510–517. https://doi.org/10.1016/j.chemosphere.2016.07.042

Lambert, S., & Wagner, M. (2018). Microplastics are contaminants of emerging concern in freshwater environments: An overview. In *Handbook of Environmental Chemistry* (Vol. 58, pp. 1–23). Springer Verlag. https://doi.org/10.1007/978-3-319-61615-5_1

Law, K. L. (2017). Plastics in the Marine Environment. In *Annual Review of Marine Science* (Vol. 9, Issue 1, pp. 205–229). Annual Reviews Inc. https://doi.org/10.1146/annurev-marine-010816-060409

Law, K. L., Morét-Ferguson, S. E., Goodwin, D. S., Zettler, E. R., Deforce, E., Kukulka, T., & Proskurowski, G. (2014). Distribution of surface plastic debris in the eastern pacific ocean from an 11-year data set. *Environmental Science and Technology*, *48*(9), 4732–4738. https://doi.org/10.1021/es4053076

Law, K. L., Morét-Ferguson, S., Maximenko, N. A., Proskurowski, G., Peacock, E. E., Hafner, J., & Reddy, C. M. (2010). Plastic accumulation in the North Atlantic subtropical gyre. *Science*, *329*(5996), 1185–1188. https://doi.org/10.1126/science.1192321

Le Foll, F., Rioult, D., Boussa, S., Pasquier, J., Dagher, Z., & Leboulenger, F. (2010). Characterisation of Mytilus edulis hemocyte subpopulations by single cell time-lapse motility imaging. *Fish and Shellfish Immunology*, *28*(2), 372–386. https://doi.org/10.1016/j.fsi.2009.11.011

Lebreton, L., & Andrady, A. (2019). Future scenarios of global plastic waste generation and disposal. *Palgrave Communications*, *5*(1). https://doi.org/10.1057/s41599-018-0212-7

Lebreton, L. C. M., Van Der Zwet, J., Damsteeg, J. W., Slat, B., Andrady, A., & Reisser, J. (2017). River plastic emissions to the world's oceans. *Nature Communications*, *8*. https://doi.org/10.1038/ncomms15611

Lebreton, L., Slat, B., Ferrari, F., Sainte-Rose, B., Aitken, J., Marthouse, R., Hajbane, S., Cunsolo, S., Schwarz, A., Levivier, A., Noble, K., Debeljak, P., Maral, H., Schoeneich-Argent, R., Brambini, R., & Reisser, J. (2018). Evidence that the Great Pacific Garbage Patch is rapidly accumulating plastic. *Scientific Reports*, *8*(1). https://doi.org/10.1038/s41598-018-22939-w

Lee, H. G., Wheeler, M. A., & Quintana, F. J. (2022). Function and therapeutic value of astrocytes in neurological diseases. In *Nature Reviews Drug Discovery* (Vol. 21, Issue 5, pp. 339–358). Nature Research. https://doi.org/10.1038/s41573-022-00390-x

Lee, Y., Sung, M., Sung, S. E., Choi, J. H., Kang, K. K., Park, J. W., Kim, Y. J., & Lee, S. (2025). The histopathological and functional consequences of microplastic exposure. *Discover Applied Sciences*, *7*(1). https://doi.org/10.1007/s42452-025-06470-y

Legland, D., Arganda-Carreras, I., & Andrey, P. (2016). MorphoLibJ: Integrated library and plugins for mathematical morphology with ImageJ. *Bioinformatics*, *32*(22), 3532–3534. https://doi.org/10.1093/bioinformatics/btw413

Leis, M., Noya Abad, T., Martinez, M. F., Calcagno, J. A., Sabatini, S. E., & Genovese, G. (2024). Histological alterations as a recommended biomarker in the mussel Mytilus platensis (Bivalvia, Mytilidae) to study anthropic impact on seaports. *Regional Studies in Marine Science*, *70*. https://doi.org/10.1016/j.rsma.2024.103373

Leistenschneider, D., Wolinski, A., Cheng, J., ter Halle, A., Duflos, G., Huvet, A., Paul-Pont, I., Lartaud, F., Galgani, F., Lavergne, É., Meistertzheim, A. L., & Ghiglione, J. F. (2023). A critical review on the evaluation of toxicity and ecological risk assessment of plastics in the marine environment. *Science of the Total Environment*, *896*. https://doi.org/10.1016/j.scitotenv.2023.164955

Lenz, R., Enders, K., & Nielsen, T. G. (2016). Microplastic exposure studies should be environmentally realistic. *Proceedings of the National Academy of Sciences of the United States of America*, *113*(29), E4121–E4122. https://doi.org/10.1073/pnas.1606615113

Leslie, H. A., Brandsma, S. H., van Velzen, M. J. M., & Vethaak, A. D. (2017). Microplastics en route: Field measurements in the Dutch river delta and Amsterdam canals, wastewater treatment plants, North Sea sediments and biota. *Environment International*, *101*, 133–142. https://doi.org/10.1016/j.envint.2017.01.018

Levin, R., Grinstein, S., & Canton, J. (2016). The life cycle of phagosomes: formation, maturation, and resolution. *Immunological Reviews*, *273*, 156–179. https://doi.org/10.1111/imr.12439

Li, J., You, L., Xu, Z., Gin, K. Y. H., & He, Y. (2024). Nano-scale and micron-scale plastics amplify the bioaccumulation of benzophenone-3 and ciprofloxacin, as well as their co-exposure effect on disturbing the antioxidant defense system in mussels, Perna viridis. *Environmental Pollution*, *346*. https://doi.org/10.1016/j.envpol.2024.123547

Li, L. L., Amara, R., Souissi, S., Dehaut, A., Duflos, G., & Monchy, S. (2020). Impacts of microplastics exposure on mussel (Mytilus edulis) gut microbiota. *Science of the Total Environment*, *745*. https://doi.org/10.1016/j.scitotenv.2020.141018

Li, X., Tian, Z., Kong, Y., Cao, X., Liu, N., Zhang, T., Xiao, Z., & Wang, Z. (2024). The suspension stability of nanoplastics in aquatic environments revealed using meta-analysis and machine learning. *Journal of Hazardous Materials*, *471*. https://doi.org/10.1016/j.jhazmat.2024.134426

Li, X., Wu, H., Gong, J., Li, Q., Li, Z., & Zhang, J. (2023). Improvement of biodegradation of PET microplastics with whole-cell biocatalyst by interface activation reinforcement. *Environmental Technology (United Kingdom)*, *44*(20), 3121–3130. https://doi.org/10.1080/09593330.2022.2052359

Li, Z., Chang, X., Hu, M., Fang, J. K. H., Sokolova, I. M., Huang, W., Xu, E. G., & Wang, Y. (2022). Is microplastic an oxidative stressor? Evidence from a meta-analysis on bivalves. *Journal of Hazardous Materials*, *423*. https://doi.org/10.1016/j.jhazmat.2021.127211

Lim, K. P., Sun, C., & Lim, P. E. (2024). Observation and visual identification of microplastics. In *Analysis of Microplastics and Nanoplastics* (pp. 155–182). Elsevier. https://doi.org/10.1016/B978-0-443-15779-0.00008-0

Lin, L., Chen, C. C., Zhu, X., Pan, K., & Xu, X. (2022). Risk of aquaculture-derived microplastics in aquaculture areas: An overlooked issue or a non-issue? *Frontiers in Marine Science*, *9*. https://doi.org/10.3389/fmars.2022.923471

Liu, L., Du, R., Niu, L., Li, P., & Li, Z. H. (2024). A latest review on micro- and nanoplastics in the aquatic environment: The comparative impact of size on environmental behavior and toxic effect. *Bulletin of Environmental Contamination and Toxicology*, *112*(2). https://doi.org/10.1007/s00128-024-03865-2

Liu, P. Y., Chin, L. K., Ser, W., Chen, H. F., Hsieh, C. M., Lee, C. H., Sung, K. B., Ayi, T. C., Yap, P. H., Liedberg, B., Wang, K., Bourouina, T., & Leprince-Wang, Y. (2016). Cell refractive index for cell biology and disease diagnosis: Past, present and future. *Lab on a Chip*, *16*(4), 634–644. https://doi.org/10.1039/c5lc01445j

Liu, P., Zhan, X., Wu, X., Li, J., Wang, H., & Gao, S. (2020). Effect of weathering on environmental behavior of microplastics: Properties, sorption and potential risks. *Chemosphere*, *242*. https://doi.org/10.1016/j.chemosphere.2019.125193

Liu, W., Liao, H., Wei, M., Junaid, M., Chen, G., & Wang, J. (2024). Biological uptake, distribution and toxicity of micro(nano)plastics in the aquatic biota: A special emphasis on size-dependent impacts. *TrAC - Trends in Analytical Chemistry*, *170*. https://doi.org/10.1016/j.trac.2023.117477

Liu, X., Lan, R., Liu, L., Zhao, Y., & Zhao, J. (2024). Definition and features of microplastics and nanoplastics. In *Analysis of Microplastics and Nanoplastics* (pp. 19–37). Elsevier. https://doi.org/10.1016/B978-0-443-15779-0.00007-9

Liu, Y., Nie, Z., Meng, Y., Liu, G., Chen, Y., & Chai, G. (2025). Influence of meteorological conditions on atmospheric microplastic transport and deposition. *Environmental Research*, *265*. https://doi.org/10.1016/j.envres.2024.120460

Liu, Z., Huang, Q., Wang, H., & Zhang, S. (2022). An enhanced risk assessment framework for microplastics occurring in the Westerscheldt estuary. *Science of the Total Environment*, *817*. https://doi.org/10.1016/j.scitotenv.2022.153006

Lobo-da-Cunha, A. (2019). Structure and function of the digestive system in molluscs. *Cell and Tissue Research*, *377*(3), 475–503. https://doi.org/10.1007/s00441-019-03085-9

Löder, M. G. J., & Gerdts, G. (2015). Methodology used for the detection and identification of microplastics—a critical appraisal. In *Marine Anthropogenic Litter* (pp. 201–227). Springer International Publishing. https://doi.org/10.1007/978-3-319-16510-3_8

Lorenz, C., Roscher, L., Meyer, M. S., Hildebrandt, L., Prume, J., Löder, M. G. J., Primpke, S., & Gerdts, G. (2019). Spatial distribution of microplastics in sediments and surface waters of the southern North Sea. *Environmental Pollution*, *252*, 1719–1729. https://doi.org/10.1016/j.envpol.2019.06.093

Lu, Q., Zhou, Y., Sui, Q., & Zhou, Y. (2023). Mechanism and characterization of microplastic aging process: A review. *Frontiers of Environmental Science and Engineering*, *17*(8). https://doi.org/10.1007/s11783-023-1700-6

Lu, Y., Zhang, Y., Deng, Y., Jiang, W., Zhao, Y., Geng, J., Ding, L., & Ren, H. (2016). Uptake and accumulation of polystyrene microplastics in Zebrafish (Danio rerio) and toxic effects in liver. *Environmental Science and Technology*, *50*(7), 4054–4060. https://doi.org/10.1021/acs.est.6b00183

Lu, Z., Wu, S., Xiao, Z., Song, J., Wu, H., & Peng, X. (2023). Responses of microRNA in digestive glands of mussel Mytilus galloprovincialis exposed to polystyrene nanoplastics. *Ecotoxicology and Environmental Safety*, *249*. https://doi.org/10.1016/j.ecoenv.2022.114412

Lunov, O., Syrovets, T., Loos, C., Nienhaus, G. U., Mailänder, V., Landfester, K., Rouis, M., & Simmet, T. (2011). Amino-functionalized polystyrene nanoparticles activate the NLRP3 inflammasome in human macrophages. *ACS Nano*, *5*(12), 9648–9657. https://doi.org/10.1021/nn203596e

Luo, Y., Hu, R., Zheng, Y., Ding, L., Qiu, X., Yang, J., Liang, X., & Guo, X. (2025). Sampling, extraction, and analysis of micro- and nano-plastics in environmental and biological compartments: A review. *TrAC - Trends in Analytical Chemistry*, *183*. https://doi.org/10.1016/j.trac.2024.118056

Luo, Y., & Wang, W. X. (2022). Immune responses of oyster hemocyte subpopulations to in vitro and in vivo zinc exposure. *Aquatic Toxicology*, *242*, 106022. https://doi.org/10.1016/j.aquatox.2021.106022

Lusher, A. (2015). Microplastics in the marine environment: Distribution, interactions and effects. In *Marine Anthropogenic Litter* (pp. 245–307). Springer International Publishing. https://doi.org/10.1007/978-3-319-16510-3_10

Ma, M., Huo, M., Coulon, F., Ali, M., Tang, Z., Liu, X., Ying, Z., Wang, B., & Song, X. (2024). Understanding microplastic presence in different wastewater treatment processes: Removal efficiency and source

identification. *Science of the Total Environment*, *929*. https://doi.org/10.1016/j.scitotenv.2024.172680

Macfadyen, G., Huntington, T., & Cappel, R. (2009). *Abandoned, Lost or Otherwise Discarded Fishing Gear : FAO Fisheries and Aquaculture Technical Paper No. 523* (Vol. 523). Food & Agriculture Organization of the United Nations Environment Programme (FAO).

MacIntyre, S., Alldredge, A. L., & Gotschalk, C. C. (1995). Accumulation of marines now at density discontinuities in the water column. *Limnology and Oceanography*, *40*(3), 449–468. https://doi.org/10.4319/lo.1995.40.3.0449

Maddison, C., Sathish, C. I., Lakshmi, D., Wayne, O. C., & Palanisami, T. (2023). An advanced analytical approach to assess the long-term degradation of microplastics in the marine environment. *Npj Materials Degradation*, *7*(1). https://doi.org/10.1038/s41529-023-00377-y

Magrì, D., Sánchez-Moreno, P., Caputo, G., Gatto, F., Veronesi, M., Bardi, G., Catelani, T., Guarnieri, D., Athanassiou, A., Pompa, P. P., & Fragouli, D. (2018). Laser ablation as a versatile tool to mimic polyethylene terephthalate nanoplastic pollutants: Characterization and toxicology assessment. *ACS Nano*, *12*(8), 7690–7700. https://doi.org/10.1021/acsnano.8b01331

Mahendran, R., & Ramaswamy, S. N. (2024). Nanoplastics as Trojan horses: deciphering complex connections and environmental ramifications: A review. *Chemistry Africa*, *7*(5), 2265–2282. https://doi.org/10.1007/s42250-023-00865-3

Majno, G., & Joris, I. (1995). Apoptosis, Oncosis, and Necrosis An Overview of Cell Death. *American Journal of Pathology*, *146*(1).

Manzo, S., & Schiavo, S. (2022). Physical and chemical threats posed by micro(nano)plastic to sea urchins. *Science of the Total Environment*, *808*. https://doi.org/10.1016/j.scitotenv.2021.152105

Mao, F., Wong, N. K., Lin, Y., Zhang, X., Liu, K., Huang, M., Xu, D., Xiang, Z., Li, J., Zhang, Y., & Yu, Z. (2020). Transcriptomic evidence reveals the molecular basis for functional differentiation of hemocytes in a marine invertebrate, Crassostrea gigas. *Frontiers in Immunology*, *11*. https://doi.org/10.3389/fimmu.2020.00911

Martí, E., Martin, C., Galli, M., Echevarría, F., Duarte, C. M., & Cózar, A. (2020). The colors of the ocean plastics. *Environmental Science and Technology*, *54*(11), 6594–6601. https://doi.org/10.1021/acs.est.9b06400

Masseroni, A., Rizzi, C., Urani, C., & Villa, S. (2022). Nanoplastics: Status and knowledge gaps in the finalization of environmental risk assessments. *Toxics*, *10*(5). https://doi.org/10.3390/toxics10050270

Materić, D., Kjær, H. A., Vallelonga, P., Tison, J. L., Röckmann, T., & Holzinger, R. (2022). Nanoplastics measurements in Northern and Southern polar ice. *Environmental Research*, *208*. https://doi.org/10.1016/j.envres.2022.112741

Matthews, S., Mai, L., Jeong, C. B., Lee, J. S., Zeng, E. Y., & Xu, E. G. (2021). Key mechanisms of micro- and nanoplastic (MNP) toxicity across taxonomic groups. *Comparative Biochemistry and Physiology Part - C: Toxicology and Pharmacology*, *247*. https://doi.org/10.1016/j.cbpc.2021.109056

Mattsson, K., Jocic, S., Doverbratt, I., & Hansson, L. (2018). Nanoplastics in the Aquatic Environment. In *Microplastic Contamination in Aquatic Environments*. Elsevier Inc. https://doi.org/10.1016/B978-0-12-813747-5.00013-8

McAfee, D., Leung, J. Y. S., & Connell, S. D. (2023). Improving ecological function of polluted coasts under a tide of plastic waste. *Frontiers in Ecology and the Environment*, *21*(9), 435–442. https://doi.org/10.1002/fee.2667

McKeen, L. W. (2012). Polyvinyls and Acrylics. In *Film Properties of Plastics and Elastomers* (pp. 219–254). Elsevier. https://doi.org/10.1016/b978-1-4557-2551-9.00010-4

Mehinto, A. C., Coffin, S., Koelmans, A. A., Brander, S. M., Wagner, M., Thornton Hampton, L. M., Burton, A. G., Miller, E., Gouin, T., Weisberg, S. B., & Rochman, C. M. (2022). Risk-based management framework for microplastics in aquatic ecosystems. *Microplastics and Nanoplastics*, *2*(1). https://doi.org/10.1186/s43591-022-00033-3

Melchor-Martínez, E. M., Macías-Garbett, R., Alvarado-Ramírez, L., Araújo, R. G., Sosa-Hernández, J. E., Ramírez-Gamboa, D., Parra-Arroyo, L., Alvarez, A. G., Monteverde, R. P. B., Cazares, K. A. S., Reyes-Mayer, A., Lino, M. Y., Iqbal, H. M. N., & Parra-Saldívar, R. (2022). Towards a Circular Economy of Plastics: An Evaluation of the Systematic Transition to a New Generation of Bioplastics. *Polymers*, *14*(6). https://doi.org/10.3390/polym14061203

Meng, L., Sun, X., Li, Q., Zheng, S., Liang, J., & Zhao, C. (2024). Quantification of the vertical transport of microplastics by biodeposition of typical mariculture filter-feeding organisms. *Science of the Total Environment*, *908*. https://doi.org/10.1016/j.scitotenv.2023.168226

Messner, B., Türkcan, A., Ploner, C., Laufer, G., & Bernhard, D. (2016). Cadmium overkill: Autophagy, apoptosis and necrosis signalling in endothelial cells exposed to cadmium. *Cellular and Molecular Life Sciences*, *73*(8), 1699–1713. https://doi.org/10.1007/s00018-015-2094-9

Meyers, N., Everaert, G., Hostens, K., Schmidt, N., Herzke, D., Fuda, J. L., Janssen, C. R., & De Witte, B. (2024). Towards reliable data: Validation of a machine learning-based approach for microplastics analysis in marine organisms using Nile red staining. *Marine Pollution Bulletin*, *207*. https://doi.org/10.1016/j.marpolbul.2024.116804

Mishnaevsky, L., Tempelis, A., Belahurau, Y., & Johansen, N. F. J. (2024). Microplastics emission from eroding wind turbine blades: Preliminary estimations of volume. *Energies*, *17*(24). https://doi.org/10.3390/en17246260

Mishra, S., Rath, C. charan, & Das, A. P. (2019). Marine microfiber pollution: A review on present status and future challenges. *Marine Pollution Bulletin*, *140*, 188–197. https://doi.org/10.1016/j.marpolbul.2019.01.039

Mkuye, R., Gong, S., Zhao, L., Masanja, F., Ndandala, C., Bubelwa, E., Yang, C., & Deng, Y. (2022). Effects of microplastics on physiological performance of marine bivalves, potential impacts, and enlightening the future based on a comparative study. *Science of the Total Environment*, *838*. https://doi.org/10.1016/j.scitotenv.2022.155933

Montazer, Z., Najafi, M. B. H., & Levin, D. B. (2020). Challenges with verifying microbial degradation of polyethylene. *Polymers*, *12*(1). https://doi.org/10.3390/polym12010123

Moore, D., McCarroll-Butler, C., Avanasi, R., Chen, W., White, M., & Brain, R. (2021). How protective to the environment is the pesticide risk assessment and registration process in the United States? *Journal of Regulatory Science*, *9*(2), 1–20. https://doi.org/10.21423/jrs-v09i2moore

Moore, M. N., Allen, J. I., McVeigh, A., & Shaw, J. (2006). Lysosomal and autophagic reactions as predictive indicators of environmental impact in aquatic animals. *Autophagy*, *2*(3), 217–220. https://doi.org/10.4161/auto.2663

Moyo, S. (2022). An enigma: A meta-analysis reveals the effect of ubiquitous microplastics on different taxa in aquatic systems. *Frontiers in Environmental Science*, *10*. https://doi.org/10.3389/fenvs.2022.999349

Mutuku, J., Yanotti, M., Tocock, M., & Hatton MacDonald, D. (2024). The abundance of microplastics in the world's Oceans: A systematic review. *Oceans*, *5*(3), 398–428. https://doi.org/10.3390/oceans5030024

Naidoo, T., & Glassom, D. (2019). Decreased growth and survival in small juvenile fish, after chronic exposure to environmentally relevant concentrations of microplastic. *Marine Pollution Bulletin*, *145*, 254–259. https://doi.org/10.1016/j.marpolbul.2019.02.037

Nandakumar, A., Chuah, J. A., & Sudesh, K. (2021). Bioplastics: A boon or bane? *Renewable and Sustainable Energy Reviews*, *147*. https://doi.org/10.1016/j.rser.2021.111237

Nechifor, M. (2016). Factors influencing the photochemical behavior of multicomponent polymeric materials. In *Advanced Structured Materials* (Vol. 26, pp. 21–65). Springer Verlag. https://doi.org/10.1007/978-3-319-25196-7_2

Nel, A. E., Mädler, L., Velegol, D., Xia, T., Hoek, E. M. V., Somasundaran, P., Klaessig, F., Castranova, V., & Thompson, M. (2009). Understanding biophysicochemical interactions at the nano-bio interface. *Nature Materials*, *8*(7), 543–557. https://doi.org/10.1038/nmat2442

Nel, H. A., & Froneman, P. W. (2015). A quantitative analysis of microplastic pollution along the south-eastern coastline of South Africa. *Marine Pollution Bulletin*, *101*(1), 274–279. https://doi.org/10.1016/j.marpolbul.2015.09.043

Nene, A., Sadeghzade, S., Viaroli, S., Yang, W., Uchenna, U. P., Kandwal, A., Liu, X., Somani, P., & Galluzzi, M. (2025). Recent advances and future technologies in nano-microplastics detection. *Environmental Sciences Europe*, *37*(1). https://doi.org/10.1186/s12302-024-01044-y

Nolte, T. M., Hartmann, N. B., Kleijn, J. M., Garnæs, J., van de Meent, D., Jan Hendriks, A., & Baun, A. (2017). The toxicity of plastic nanoparticles to green algae as influenced by surface modification, medium hardness and cellular adsorption. *Aquatic Toxicology*, *183*, 11–20. https://doi.org/10.1016/j.aquatox.2016.12.005

Nunes, B. Z., Huang, Y., Ribeiro, V. V., Wu, S., Holbech, H., Moreira, L. B., Xu, E. G., & Castro, I. B. (2023). Microplastic contamination in seawater across global marine protected areas boundaries. *Environmental Pollution*, *316*. https://doi.org/10.1016/j.envpol.2022.120692

Oberle, C., Huai, J., Reinheckel, T., Tacke, M., Rassner, M., Ekert, P. G., Buellesbach, J., & Borner, C. (2010). Lysosomal membrane permeabilization and cathepsin release is a Bax/Bak-dependent, amplifying event of apoptosis in fibroblasts and monocytes. *Cell Death and Differentiation*, *17*(7), 1167–1178. https://doi.org/10.1038/cdd.2009.214

Ockenden, A., Mitrano, D. M., Kah, M., Tremblay, L. A., & Simon, K. S. (2024). Predator traits influence uptake and trophic transfer of nanoplastics in aquatic systems–a mechanistic study. *Microplastics and Nanoplastics*, *4*(1). https://doi.org/10.1186/s43591-024-00096-4

OECD. (2022). *Global Plastics Outlook Economic Drivers, Environmental Impacts and Policy Options*. https://doi.org/10.1787/de747aef-en

Olabarrieta, I., L'azou, B., Yuric, S., Cambar, J., Cajaraville, M. P., Zelularra, B., Laborategia, H., Eta, Z., Zelulen, A., Saila, D., & Fakultatea, Z. (2001). In vitro effects of cadmium on two different animal cell models. *Toxicology in Vitro*, *15*, 511–517. https://doi.org/10.1016/S0887-2333(01)00056-X

Osman, A. I., Hosny, M., Eltaweil, A. S., Omar, S., Elgarahy, A. M., Farghali, M., Yap, P. S., Wu, Y. S., Nagandran, S., Batumalaie, K., Gopinath, S. C. B., John, O. D., Sekar, M., Saikia, T., Karunanithi, P., Hatta, M. H. M., & Akinyede, K. A. (2023). Microplastic sources, formation, toxicity and remediation: a review. *Environmental Chemistry Letters*, *21*(4), 2129–2169. https://doi.org/10.1007/s10311-023-01593-3

Paço, A., Duarte, K., da Costa, J. P., Santos, P. S. M., Pereira, R., Pereira, M. E., Freitas, A. C., Duarte, A. C., & Rocha-Santos, T. A. P. (2017). Biodegradation of polyethylene microplastics by the marine fungus Zalerion maritimum. *Science of the Total Environment*, *586*, 10–15. https://doi.org/10.1016/j.scitotenv.2017.02.017

Page, M. J., McKenzie, J. E., Bossuyt, P. M., Boutron, I., Hoffmann, T. C., Mulrow, C. D., Shamseer, L., Tetzlaff, J. M., Akl, E. A., Brennan, S. E., Chou, R., Glanville, J., Grimshaw, J. M., Hróbjartsson, A., Lalu, M. M., Li, T., Loder, E. W., Mayo-Wilson, E., McDonald, S., … Moher, D. (2021). The PRISMA 2020

statement: An updated guideline for reporting systematic reviews. *BMJ*, *372*. https://doi.org/10.1136/bmj.n71

Panariti, A., Miserocchi, G., & Rivolta, I. (2012). The effect of nanoparticle uptake on cellular behavior: Disrupting or enabling functions? *Nanotechnology, Science and Applications*, *5*(1), 87–100. https://doi.org/10.2147/NSA.S25515

Patil, S., Bafana, A., Naoghare, P. K., Krishnamurthi, K., & Sivanesan, S. (2020). Environmental prevalence, fate, impacts, and mitigation of microplastics—a critical review on present understanding and future research scope. *Environmental Science and Pollution Research*, 4951–4974. https://doi.org/10.1007/s11356-020-11700-4

Paul-Pont, I., Lacroix, C., González Fernández, C., Hégaret, H., Lambert, C., Le Goïc, N., Frère, L., Cassone, A. L., Sussarellu, R., Fabioux, C., Guyomarch, J., Albentosa, M., Huvet, A., & Soudant, P. (2016). Exposure of marine mussels Mytilus spp. to polystyrene microplastics: Toxicity and influence on fluoranthene bioaccumulation. *Environmental Pollution*, *216*, 724–737. https://doi.org/10.1016/j.envpol.2016.06.039

Pavičić-Hamer, D., Kovačić, I., Sović, T., Marelja, M., & Lyons, D. M. (2022). Exposure to polymethylmethacrylate microplastics induces a particle size-dependent immune response in Mediterranean Mussel Mytilus galloprovincialis. *Fishes*, *7*(6). https://doi.org/10.3390/fishes7060307

Peng, L., Fu, D., Qi, H., Lan, C. Q., Yu, H., & Ge, C. (2020). Micro- and nano-plastics in marine environment: Source, distribution and threats — A review. *Science of the Total Environment*, *698*. https://doi.org/10.1016/j.scitotenv.2019.134254

Peng, M., Vercauteren, M., Grootaert, C., Rajkovic, A., Boon, N., Janssen, C., & Asselman, J. (2023). Cellular and bioenergetic effects of polystyrene microplastic in function of cell type, differentiation status and post-exposure time. *Environmental Pollution*, *337*. https://doi.org/10.1016/j.envpol.2023.122550

Pequeno, J., Antunes, J., Dhimmer, V., Bessa, F., & Sobral, P. (2021). Microplastics in marine and estuarine species from the Coast of Portugal. *Frontiers in Environmental Science*, *9*. https://doi.org/10.3389/fenvs.2021.579127

Periyasamy, A. P., & Tehrani-Bagha, A. (2022). A review on microplastic emission from textile materials and its reduction techniques. In *Polymer Degradation and Stability* (Vol. 199). Elsevier Ltd. https://doi.org/10.1016/j.polymdegradstab.2022.109901

Phuong, N. N., Zalouk-Vergnoux, A., Poirier, L., Kamari, A., Châtel, A., Mouneyrac, C., & Lagarde, F. (2016). Is there any consistency between the microplastics found in the field and those used in laboratory experiments? *Environmental Pollution*, *211*, 111–123. https://doi.org/10.1016/j.envpol.2015.12.035

Pikula, K., Chaika, V., Zakharenko, A., Savelyeva, A., Kirsanova, I., Anisimova, A., & Golokhvast, K. (2020). Toxicity of carbon, silicon, and metal-based nanoparticles to the hemocytes of three marine bivalves. *Animals*, *10*(5). https://doi.org/10.3390/ani10050827

Pinheiro, L. M., Ivar do Sul, J. A., & Costa, M. F. (2020). Uptake and ingestion are the main pathways for microplastics to enter marine benthos: A review. *Food Webs*, *24*. https://doi.org/10.1016/j.fooweb.2020.e00150

Pinto, J., Costa, M., Leite, C., Borges, C., Coppola, F., Henriques, B., Monteiro, R., Russo, T., Di Cosmo, A., Soares, A. M. V. M., Polese, G., Pereira, E., & Freitas, R. (2019). Ecotoxicological effects of lanthanum in Mytilus galloprovincialis: Biochemical and histopathological impacts. *Aquatic Toxicology*, *211*, 181–192. https://doi.org/10.1016/j.aquatox.2019.03.017

Pipe, R. K. (1990). Hydrolytic enzymes associated with the granular haemocytes of the marine mussel Mytilus edulis. *The Histochemical Journal*. https://doi.org/10.1007/BF01072941

Pires, A., Cuccaro, A., Sole, M., & Freitas, R. (2022). Micro(nano)plastics and plastic additives effects in marine annelids: A literature review. *Environmental Research*, *214*. https://doi.org/10.1016/j.envres.2022.113642

Pittura, L., Gorbi, S., León, V. M., Bellas, J., Campillo González, J. A., Albentosa, M., & Regoli, F. (2023). Microplastics and nanoplastics in the marine environment. In *Contaminants of Emerging Concern in the Marine Environment: Current Challenges in Marine Pollution* (pp. 311–348). Elsevier. https://doi.org/10.1016/B978-0-323-90297-7.00004-4

Plastics Europe. (2024). *The Circular Economy for Plastics A European Analysis*.

Płuciennik, K., Sicińska, P., Misztal, W., & Bukowska, B. (2024). Important factors affecting induction of cell death, oxidative stress and DNA damage by nano- and microplastic particles in vitro. *Cells*, *13*(9). https://doi.org/10.3390/cells13090768

Porter, A., Godbold, J. A., Lewis, C. N., Savage, G., Solan, M., & Galloway, T. S. (2023). Microplastic burden in marine benthic invertebrates depends on species traits and feeding ecology within biogeographical provinces. *Nature Communications*, *14*(1). https://doi.org/10.1038/s41467-023-43788-w

Porter, A., Lyons, B. P., Galloway, T. S., & Lewis, C. (2018). Role of marine snows in microplastic fate and bioavailability. *Environmental Science and Technology*, *52*(12), 7111–7119. https://doi.org/10.1021/acs.est.8b01000

Posthuma, L., van Gils, J., Zijp, M. C., van de Meent, D., & de Zwartd, D. (2019). Species sensitivity distributions for use in environmental protection, assessment, and management of aquatic ecosystems for 12 386 chemicals. *Environmental Toxicology and Chemistry*, *38*(4), 703–711. https://doi.org/10.1002/etc.4373

Potenza, M. A. C., Sanvito, T., Argentiere, S., Cella, C., Paroli, B., Lenardi, C., & Milani, P. (2015). Single particle optical extinction and scattering allows real time quantitative characterization of drug payload and degradation of polymeric nanoparticles. *Scientific Reports*, *5*. https://doi.org/10.1038/srep18228

Potenza, M. A. C., Sanvito, T., & Pullia, A. (2015). Measuring the complex field scattered by single submicron particles. *AIP Advances*, *5*(11). https://doi.org/10.1063/1.4935927

Prata, J. C., da Costa, J. P., Duarte, A. C., & Rocha-Santos, T. (2019). Methods for sampling and detection of microplastics in water and sediment: A critical review. *TrAC - Trends in Analytical Chemistry*, *110*, 150–159. https://doi.org/10.1016/j.trac.2018.10.029

Prinz, N., & Korez, Š. (2020). Understanding how microplastics affect marine biota on the cellular level is important for assessing ecosystem function: A review. In *YOUMARES 9 - The Oceans: Our Research, Our Future* (pp. 101–120). Springer International Publishing. https://doi.org/10.1007/978-3-030-20389-4_6

Qi, P., Qiu, L., Feng, D., Gu, Z., Guo, B., & Yan, X. (2023). Distinguish the toxic differentiations between acute exposure of micro- and nano-plastics on bivalves: An integrated study based on transcriptomic sequencing. *Aquatic Toxicology*, *254*. https://doi.org/10.1016/j.aquatox.2022.106367

Qu, X., Su, L., Li, H., Liang, M., & Shi, H. (2018). Assessing the relationship between the abundance and properties of microplastics in water and in mussels. *Science of the Total Environment*, *621*, 679–686. https://doi.org/10.1016/j.scitotenv.2017.11.284

Rahman, M. H., & Bhoi, P. R. (2021). An overview of non-biodegradable bioplastics. *Journal of Cleaner Production*, *294*. https://doi.org/10.1016/j.jclepro.2021.126218

Raj, P., Paidi, S. K., Conway, L., Chatterjee, A., & Barman, I. (2024). CellSNAP: a fast, accurate algorithm for 3D cell segmentation in quantitative phase imaging. *Journal of Biomedical Optics*, *29*(S2). https://doi.org/10.1117/1.jbo.29.s2.s22706

Ramkumar, M., Balasubramani, K., Santosh, M., & Nagarajan, R. (2022). The plastisphere: A morphometric genetic classification of plastic pollutants in the natural environment. *Gondwana Research*, *108*, 4–12. https://doi.org/10.1016/j.gr.2021.07.004

Rangel-Buitrago, N., Neal, W. J., & Galgani, F. (2023). Plastics in the Anthropocene: A multifaceted approach to marine pollution management. *Marine Pollution Bulletin*, *194*. https://doi.org/10.1016/j.marpolbul.2023.115359

Rani, M., Shim, W. J., Han, G. M., Jang, M., Al-Odaini, N. A., Song, Y. K., & Hong, S. H. (2015). Qualitative analysis of additives in plastic marine debris and its new products. *Archives of Environmental Contamination and Toxicology*, *69*(3), 352–366. https://doi.org/10.1007/s00244-015-0224-x

Ray, M., Bhunia, A. S., Bhunia, N. S., & Ray, S. (2013). Density shift, morphological damage, lysosomal fragility and apoptosis of hemocytes of Indian molluscs exposed to pyrethroid pesticides. *Fish and Shellfish Immunology*, *35*(2), 499–512. https://doi.org/10.1016/j.fsi.2013.05.008

Renner, G., Schmidt, T. C., & Schram, J. (2018). Analytical methodologies for monitoring micro(nano)plastics: Which are fit for purpose? *Current Opinion in Environmental Science and Health*, *1*, 55–61. https://doi.org/10.1016/j.coesh.2017.11.001

Revel, M., Roman, C., & Châtel, A. (2021). Is cell culture a suitable tool for the evaluation of micro- and nanoplastics ecotoxicity? *Ecotoxicology*, *30*(3), 421–430. https://doi.org/10.1007/s10646-021-02355-z

Ribeiro, F., O'Brien, J. W., Galloway, T., & Thomas, K. V. (2019). Accumulation and fate of nano- and micro-plastics and associated contaminants in organisms. *TrAC - Trends in Analytical Chemistry*, *111*, 139–147. https://doi.org/10.1016/j.trac.2018.12.010

Ribeiro, V. V., Nobre, C. R., Moreno, B. B., Semensatto, D., Sanz-Lazaro, C., Moreira, L. B., & Castro, Í. B. (2023). Oysters and mussels as equivalent sentinels of microplastics and natural particles in coastal environments. *Science of the Total Environment*, *874*. https://doi.org/10.1016/j.scitotenv.2023.162468

Richardson, K., Hardesty, B. D., Vince, J., & Wilcox, C. (2022). Global estimates of fishing gear lost to the ocean each year. *Sci. Adv*, *8*, 135. https://doi.org/10.1126/sciadv.abq0135

Riisgard, H. U. (1991). Filtration rate and growth in the blue mussel, Mytilus edulis Linnaeaus, 1758: Dependence on algal concentration. *Journal of Shellfish Research*, *10*(1), 29–35.

Riisgard, H. U., Egede, P. P., & Saavedra, I. B. (2011). Feeding behaviour of the mussel, Mytilus edulis: New observations, with a minireview of current knowledge. *Journal of Marine Sciences*, *2011*. https://doi.org/10.1155/2011/312459

Rinkevich, B. (2011). Cell cultures from marine invertebrates: New insights for capturing endless stemness. *Marine Biotechnology*, *13*(3), 345–354. https://doi.org/10.1007/s10126-010-9354-3

Rist, S., & Hartmann, N. B. (2018). Aquatic Ecotoxicity of Microplastics and Nanoplastics: Lessons Learned from Engineered Nanomaterials. In *Freshwater Microplastics - The Handbook of Environmental Chemistry* (p. 302). https://doi.org/10.1007/978-3-319-61615-5

Ritchie, H., & Roser, M. (2018). *Plastic Pollution*. https://ourworldindata.org/plastic-pollution

Rocha, T. L., Sabóia-Morais, S. M. T., & Bebianno, M. J. (2016). Histopathological assessment and inflammatory response in the digestive gland of marine mussel Mytilus galloprovincialis exposed to cadmium-based quantum dots. *Aquatic Toxicology*, *177*, 306–315. https://doi.org/10.1016/j.aquatox.2016.06.003

Rodrigues, J. P., Duarte, A. C., Santos-Echeandía, J., & Rocha-Santos, T. (2019). Significance of interactions between microplastics and POPs in the marine environment: A critical overview. *TrAC - Trends in Analytical Chemistry*, *111*, 252–260. https://doi.org/10.1016/j.trac.2018.11.038

Roman, C., Mahé, P., Latchere, O., Catrouillet, C., Gigault, J., Métais, I., & Châtel, A. (2023). Effect of size continuum from nanoplastics to microplastics on marine mussel Mytilus edulis: Comparison in vitro/in vivo exposure scenarios. *Comparative Biochemistry and Physiology Part - C: Toxicology and Pharmacology*, *264*. https://doi.org/10.1016/j.cbpc.2022.109512

Rosales, C., & Uribe-Querol, E. (2017). Phagocytosis: A Fundamental Process in Immunity. *BioMed Research International*, *2017*. https://doi.org/10.1155/2017/9042851

Roscher, L., Fehres, A., Reisel, L., Halbach, M., Scholz-Böttcher, B., Gerriets, M., Badewien, T. H., Shiravani, G., Wurpts, A., Primpke, S., & Gerdts, G. (2021). Microplastic pollution in the Weser estuary and the German North Sea. *Environmental Pollution*, *288*. https://doi.org/10.1016/j.envpol.2021.117681

Ruan, Y., Zhong, Z., Liu, X., Li, Z., Li, J., Sun, L., & Sen, H. (2023). Correlation between cellular uptake and cytotoxicity of polystyrene micro/nanoplastics in HeLa cells: A size-dependent matter. *PLoS ONE*, *18*(8 August). https://doi.org/10.1371/journal.pone.0289473

Ryan, P. G. (2019). Ingestion of Plastics by Marine Organisms. In *Handbook of Environmental Chemistry* (Vol. 78, pp. 235–266). Springer Verlag. https://doi.org/10.1007/698_2016_21

Saborowski, R., Paulischkis, E., & Gutow, L. (2019). How to get rid of ingested microplastic fibers? A straightforward approach of the Atlantic ditch shrimp Palaemon varians. *Environmental Pollution*, *254*. https://doi.org/10.1016/j.envpol.2019.113068

Salamat, N., & Zarie, M. (2016). Fish histopathology as a tool for use in marine environment monitoring: a review. *Comparative Clinical Pathology*, *25*(6), 1273–1278. https://doi.org/10.1007/s00580-014-2037-0

Salvati, A., Åberg, C., dos Santos, T., Varela, J., Pinto, P., Lynch, I., & Dawson, K. A. (2011). Experimental and theoretical comparison of intracellular import of polymeric nanoparticles and small molecules: Toward models of uptake kinetics. *Nanomedicine: Nanotechnology, Biology, and Medicine*, *7*(6), 818–826. https://doi.org/10.1016/j.nano.2011.03.005

Sandoz, P. A., Maresca, F., Cao, A., & Villalba, A. (2019). Image-based analysis of living mammalian cells using label-free 3D refractive index maps reveals new organelle dynamics and dry mass flux. *PLoS Biology*, *17*(12). https://doi.org/10.1371/journal.pbio.3000553

Santana, M. F. M., Moreira, F. T., Pereira, C. D. S., Abessa, D. M. S., & Turra, A. (2018). Continuous exposure to microplastics does not cause physiological effects in the cultivated mussel Perna perna. *Archives of Environmental Contamination and Toxicology*, *74*(4), 594–604. https://doi.org/10.1007/s00244-018-0504-3

Santos, R. G., Machovsky-Capuska, G. E., & Andrades, R. (2021). Plastic ingestion as an evolutionary trap: Toward a holistic understanding. *Science*, *373*(6550), 56–60. https://doi.org/10.1126/science.abh0945

Sarkhel, R., Sengupta, S., Das, P., & Bhowal, A. (2020). Comparative biodegradation study of polymer from plastic bottle waste using novel isolated bacteria and fungi from marine source. *Journal of Polymer Research*, *27*(1). https://doi.org/10.1007/s10965-019-1973-4

Satlewal, A., & Zaidi, M. G. H. (2008). Comparative biodegradation of HDPE and LDPE using an indigenously developed microbial consortium Ravindra Soni. *Article in Journal of Microbiology and Biotechnology*. https://www.researchgate.net/publication/5465014

Satterthwaite, K. (2017). Plastics Based on Styrene. In *Brydson's Plastics Materials: Eighth Edition* (pp. 311–328). Elsevier Inc. https://doi.org/10.1016/B978-0-323-35824-8.00012-8

Scherer, C., Wolf, R., Völker, J., Stock, F., Brennhold, N., Reifferscheid, G., & Wagner, M. (2020). Toxicity of microplastics and natural particles in the freshwater dipteran Chironomus riparius: Same same but different? *Science of the Total Environment*, *711*. https://doi.org/10.1016/j.scitotenv.2019.134604

Schmid, B., Schindelin, J., Cardona, A., Longair, M., & Heisenberg, M. (2010). A high-level 3D visualization API for Java and ImageJ. *BMC Bioinformatics*, *11*, 274. http://www.biomedcentral.com/1471-2105/11/274

Schönlau, C., Karlsson, T. M., Rotander, A., Nilsson, H., Engwall, M., van Bavel, B., & Kärrman, A. (2020). Microplastics in sea-surface waters surrounding Sweden sampled by manta trawl and in-situ pump. *Marine Pollution Bulletin*, *153*. https://doi.org/10.1016/j.marpolbul.2020.111019

Schwaferts, C., Niessner, R., Elsner, M., & Ivleva, N. P. (2019). Methods for the analysis of submicrometer- and nanoplastic particles in the environment. *Trends in Analytical Chemistry*, *112*, 52–65. https://doi.org/10.1016/j.trac.2018.12.014

Schwarz, C., Tillmanns, A., Schwarz, C. J., Stat, P., Tillmanns, A. R., & Bio, R. P. (2019). *Improving statistical methods for modeling species sensitivity distributions*. https://a100.gov.bc.ca/pub/acat/public/viewReport.do?reportId=57400

Seghers, J., Cella, C., Pequeur, E., La Spina, R., Roncari, F., Valsesia, A., Mehn, D., Gilliland, D., Trapmann, S., & Emteborg, H. (2025). Approaches for the preparation and evaluation of hydrophilic polyethylene and polyethylene terephthalate microplastic particles suited for toxicological effect studies. *Analytical and Bioanalytical Chemistry*, *417*. https://doi.org/10.1007/s00216-024-05726-7

Sendra, M., Carrasco-Braganza, M. I., Yeste, P. M., Vila, M., & Blasco, J. (2020). Immunotoxicity of polystyrene nanoplastics in different hemocyte subpopulations of Mytilus galloprovincialis. *Scientific Reports*, *10*(1), 1–14. https://doi.org/10.1038/s41598-020-65596-8

Sendra, M., Saco, A., Yeste, M. P., Romero, A., Novoa, B., & Figueras, A. (2020). Nanoplastics: From tissue accumulation to cell translocation into Mytilus galloprovincialis hemocytes. resilience of immune cells exposed to nanoplastics and nanoplastics plus Vibrio splendidus combination. *Journal of Hazardous Materials*, *388*(October 2019), 121788. https://doi.org/10.1016/j.jhazmat.2019.121788

Sendra, M., Sparaventi, E., Novoa, B., & Figueras, A. (2021). An overview of the internalization and effects of microplastics and nanoplastics as pollutants of emerging concern in bivalves. *Science of the Total Environment*, *753*. https://doi.org/10.1016/j.scitotenv.2020.142024

Şener, İ., & Yabanlı, M. (2023). Macro- and microplastic abundance from recreational beaches along the South Aegean Sea (Türkiye). *Marine Pollution Bulletin*, *194*. https://doi.org/10.1016/j.marpolbul.2023.115329

Setälä, O., Norkko, J., & Lehtiniemi, M. (2016). Feeding type affects microplastic ingestion in a coastal invertebrate community. *Marine Pollution Bulletin*, *102*(1), 95–101. https://doi.org/10.1016/j.marpolbul.2015.11.053

Shafi, M., Lodh, A., Khajuria, M., Ranjan, V. P., Gani, K. M., Chowdhury, S., & Goel, S. (2024). Are we underestimating stormwater? Stormwater as a significant source of microplastics in surface waters. *Journal of Hazardous Materials*, *465*. https://doi.org/10.1016/j.jhazmat.2024.133445

Sharifinia, M., Bahmanbeigloo, Z. A., Keshavarzifard, M., Khanjani, M. H., & Lyons, B. P. (2020). Microplastic pollution as a grand challenge in marine research: A closer look at their adverse impacts on the immune and reproductive systems. *Ecotoxicology and Environmental Safety*, *204*. https://doi.org/10.1016/j.ecoenv.2020.111109

Shashoua, Y. (2008). Conservation of Plastics: Materials Science, Degradation and Preservation. In *Journal of Chemical Information and Modeling* (Vol. 53, Issue 9). Elsevier/Butterworth-Heinemann.

Sheavly, S. B., & Register, K. M. (2007). Marine debris & plastics: Environmental concerns, sources, impacts and solutions. *Journal of Polymers and the Environment*, *15*(4), 301–305. https://doi.org/10.1007/s10924-007-0074-3

Shim, W. J., Hong, S. H., & Eo, S. (2018). Marine microplastics: Abundance, distribution, and composition. In *Microplastic Contamination in Aquatic Environments: An Emerging Matter of Environmental Urgency* (pp. 1–26). Elsevier. https://doi.org/10.1016/B978-0-12-813747-5.00001-1

Shubin, A. V, Demidyuk, I. V, Komissarov, A. A., Rafieva, L. M., & Kostrov, S. V. (2016). Cytoplasmic vacuolization in cell death and survival. *Oncotarget*, *7*(34). https://doi.org/10.18632/oncotarget.10150

Simmons, S. O., Fan, C. Y., & Ramabhadran, R. (2009). Cellular stress response pathway system as a sentinel ensemble in toxicological screening. *Toxicological Sciences*, *111*(2), 202–225. https://doi.org/10.1093/toxsci/kfp140

Singh, A., & Mishra, B. K. (2023). Microbeads in personal care products: An overlooked environmental concern. *Journal of Cleaner Production*, *427*. https://doi.org/10.1016/j.jclepro.2023.139082

Singh, S., S, S., Sachdev, S., Sahoo, K. S., Ambade, B., & Bauddh, K. (2025). Microplastic pollution in agricultural environments: Origins, impacts, and mitigation strategies. *Physics and Chemistry of the Earth*, *138*. https://doi.org/10.1016/j.pce.2025.103866

Sioen, M., Vercauteren, M., Blust, R., Town, R. M., Janssen, C., & Asselman, J. (2024a). Impact of weathered and virgin polyethylene terephthalate (PET) micro- and nanoplastics on growth dynamics and the production of extracellular polymeric substances (EPS) of microalgae. *Science of the Total Environment*, *953*. https://doi.org/10.1016/j.scitotenv.2024.176074

Sioen, M., Vercauteren, M., Blust, R., Town, R. M., Janssen, C., & Asselman, J. (2024b). Impact of weathered and virgin polyethylene terephthalate (PET) micro- and nanoplastics on growth dynamics and the production of extracellular polymeric substances (EPS) of microalgae. *Science of the Total Environment*, *953*. https://doi.org/10.1016/j.scitotenv.2024.176074

Skirtun, M., Sandra, M., Strietman, W. J., van den Burg, S. W. K., De Raedemaecker, F., & Devriese, L. I. (2022). Plastic pollution pathways from marine aquaculture practices and potential solutions for the North-East Atlantic region. *Marine Pollution Bulletin*, *174*. https://doi.org/10.1016/j.marpolbul.2021.113178

Smith, M. (2020). Maintaining homeostasis and mitigating effects of harmful factors in the intrinsic or extrinsic environment. In *Gene Environment Interactions* (pp. 139–175). Elsevier. https://doi.org/10.1016/b978-0-12-819613-7.00006-2

Song, Y. K., Hong, S. H., Jang, M., Han, G. M., Jung, S. W., & Shim, W. J. (2017). Combined effects of UV exposure duration and mechanical abrasion on microplastic fragmentation by polymer type. *Environmental Science and Technology*, *51*(8), 4368–4376. https://doi.org/10.1021/acs.est.6b06155

Soni, R., Kapri, A., Zaidi, M. G. H., & Goel, R. (2009). Comparative biodegradation studies of non-poronized and poronized LDPE using indigenous microbial consortium. *Journal of Polymers and the Environment*, *17*(4), 233–239. https://doi.org/10.1007/s10924-009-0143-x

Soon, Z. Y., Tamburri, M. N., Kim, T., & Kim, M. (2024). Estimating total microplastic loads to the marine environment as a result of ship biofouling in-water cleaning. *Frontiers in Marine Science*, *11*. https://doi.org/10.3389/fmars.2024.1502000

Stanley, J., Culliton, D., Jovani-Sancho, A. J., & Neves, A. C. (2025). The journey of plastics: Historical development, environmental challenges, and the emergence of bioplastics for single-use products. *Eng*, *6*(1). https://doi.org/10.3390/eng6010017

Stern, S. T., Adiseshaiah, P. P., & Crist, R. M. (2012). Autophagy and lysosomal dysfunction as emerging mechanisms of nanomaterial toxicity. *Particle and Fibre Toxicology*, *9*. https://doi.org/10.1186/1743-8977-9-20

Stock, V., Laurisch, C., Franke, J., Dönmez, M. H., Voss, L., Böhmert, L., Braeuning, A., & Sieg, H. (2021). Uptake and cellular effects of PE, PP, PET and PVC microplastic particles. *Toxicology in Vitro*, *70*. https://doi.org/10.1016/j.tiv.2020.105021

Suman, K. H., Haque, M. N., Uddin, M. J., Begum, M. S., & Sikder, M. H. (2021). Toxicity and biomarkers of micro-plastic in aquatic environment: a review. *Biomarkers*, *26*(1), 13–25. https://doi.org/10.1080/1354750X.2020.1863470

Sun, C., Gao, F., Ding, J., & Cao, W. (2024). Sample collection and pre-treatment. In *Analysis of Microplastics and Nanoplastics* (pp. 115–133). Elsevier. https://doi.org/10.1016/B978-0-443-15779-0.00010-9

Sun, C., Teng, J., Wang, D., Li, J., Wang, X., Zhao, J., Shan, E., Chen, H., & Wang, Q. (2024). Potential threats of microplastics and pathogenic bacteria to the immune system of the mussels Mytilus galloprovincialis. *Aquatic Toxicology*, *272*. https://doi.org/10.1016/j.aquatox.2024.106959

Sun, L., Liao, K., & Wang, D. (2021). Comparison of transgenerational reproductive toxicity induced by pristine and amino modified nanoplastics in Caenorhabditis elegans. *Science of the Total Environment*, *768*. https://doi.org/10.1016/j.scitotenv.2020.144362

Sussarellu, R., Suquet, M., Thomas, Y., Lambert, C., Fabioux, C., Pernet, M. E. J., Goïc, N. Le, Quillien, V., Mingant, C., Epelboin, Y., Corporeau, C., Guyomarch, J., Robbens, J., Paul-Pont, I., Soudant, P., & Huvet, A. (2016). Oyster reproduction is affected by exposure to polystyrene microplastics. *Proceedings of the National Academy of Sciences of the United States of America*, *113*(9), 2430–2435. https://doi.org/10.1073/pnas.1519019113

Sutton, R., Mason, S. A., Stanek, S. K., Willis-Norton, E., Wren, I. F., & Box, C. (2016). Microplastic contamination in the San Francisco Bay, California, USA. *Marine Pollution Bulletin*, *109*(1), 230–235. https://doi.org/10.1016/j.marpolbul.2016.05.077

Swinnerton, S., Su, J., & Tsai, C. S. J. (2024). The emission and physicochemical properties of airborne microplastics and nanoplastics generated during the mechanical recycling of plastic via shredding. *Scientific Reports*, *14*(1), 24755. https://doi.org/10.1038/s41598-024-73775-0

Talvitie, J., Mikola, A., Koistinen, A., & Setälä, O. (2017). Solutions to microplastic pollution – Removal of microplastics from wastewater effluent with advanced wastewater treatment technologies. *Water Research*, *123*, 401–407. https://doi.org/10.1016/j.watres.2017.07.005

Tamminga, M., Hengstmann, E., & Fischer, E. K. (2018). Microplastic analysis in the South Funen Archipelago, Baltic Sea, implementing manta trawling and bulk sampling. *Marine Pollution Bulletin*, *128*, 601–608. https://doi.org/10.1016/j.marpolbul.2018.01.066

Tang, K. H. D. (2021). Interactions of microplastics with persistent organic pollutants and the ecotoxicological effects: A review. *Tropical Aquatic and Soil Pollution*, *1*(1), 24–34. https://doi.org/10.53623/tasp.v1i1.11

Tanguy, M., Gauthier-Clerc, S., Pellerin, J., Danger, J. M., & Siah, A. (2018). The immune response of Mytilus edulis hemocytes exposed to Vibrio splendidus LGP32 strain: A transcriptomic attempt at identifying molecular actors. *Fish and Shellfish Immunology*, *74*, 268–280. https://doi.org/10.1016/j.fsi.2017.12.038

Teng, J., Zhao, J., Zhu, X., Shan, E., & Wang, Q. (2021). Oxidative stress biomarkers, physiological responses and proteomic profiling in oyster (Crassostrea gigas) exposed to microplastics with irregular-shaped PE and PET microplastic. *Science of the Total Environment*, *786*. https://doi.org/10.1016/j.scitotenv.2021.147425

Teng, J., Zhu, X., Shan, E., Zhang, C., Zhang, W., & Wang, Q. (2021). Toxic effects of exposure to microplastics with environmentally relevant shapes and concentrations: Accumulation, energy

metabolism and tissue damage in oyster Crassostrea gigas. *Environmental Pollution*, *269*, 116169. https://doi.org/10.1016/j.envpol.2020.116169

Ter Halle, A., Jeanneau, L., Martignac, M., Jardé, E., Pedrono, B., Brach, L., & Gigault, J. (2017). Nanoplastic in the North Atlantic Subtropical Gyre. *Environmental Science and Technology*, *51*(23), 13689–13697. https://doi.org/10.1021/acs.est.7b03667

Thakur, S., Chaudhary, J., Sharma, B., Verma, A., Tamulevicius, S., & Thakur, V. K. (2018). Sustainability of bioplastics: Opportunities and challenges. *Current Opinion in Green and Sustainable Chemistry*, *13*, 68–75. https://doi.org/10.1016/j.cogsc.2018.04.013

Thibodeau, M. S., Giardina, C., Knecht, D. A., Helble, J., & Hubbard, A. K. (2004). Silica-induced apoptosis in mouse alveolar macrophages is initiated by lysosomal enzyme activity. *Toxicological Sciences*, *80*(1), 34–48. https://doi.org/10.1093/toxsci/kfh121

Thiyagarajan, D. B., Stette, M. H. S., Afzal, B. M., Ahluwalia, B. S., Agarwal, K., Dalmo, R. A., & Wolfson, D. L. (2024). 3D imaging shows nano- and microparticles are internalized by salmon skin and corneal epithelial cells. *Frontiers in Marine Science*, *11*. https://doi.org/10.3389/fmars.2024.1422748

Thompson, R. C., Courtene-Jones, W., Boucher, J., Pahl, S., Raubenheimer, K., & Koelmans, A. A. (2024). Twenty years of microplastic pollution research-what have we learned? *Science*, *386*(6720). https://doi.org/10.1126/science.adl2746

Thompson, R. C., Olson, Y., Mitchell, R. P., Davis, A., Rowland, S. J., John, A. W. G., McGonigle, D., & Russell, A. E. (2004). Lost at sea: Where is all the plastic? *Science*, *304*(5672), 838. https://doi.org/10.1126/science.1094559

Thornton Hampton, L. M., Lowman, H., Coffin, S., Darin, E., De Frond, H., Hermabessiere, L., Miller, E., de Ruijter, V. N., Faltynkova, A., Kotar, S., Monclús, L., Siddiqui, S., Völker, J., Brander, S., Koelmans, A. A., Rochman, C. M., Wagner, M., & Mehinto, A. C. (2022). A living tool for the continued exploration of microplastic toxicity. *Microplastics and Nanoplastics*, *2*(1). https://doi.org/10.1186/s43591-022-00032-4

Tian, L., Jinjin, C., Ji, R., Ma, Y., & Yu, X. (2022). Microplastics in agricultural soils: sources, effects, and their fate. *Current Opinion in Environmental Science and Health*, *25*. https://doi.org/10.1016/j.coesh.2021.100311

Town, R. M., van Leeuwen, H. P., & Duval, J. F. L. (2023). Effect of polymer aging on uptake/release kinetics of metal ions and organic molecules by micro- and nanoplastics: Implications for the bioavailability of the associated compounds. *Environmental Science and Technology*, *57*(43), 16552–16563. https://doi.org/10.1021/acs.est.3c05148

Town, R. M., van Leeuwen, H. P., & Duval, J. F. L. (2025). Sorption kinetics of metallic and organic contaminants on micro- and nanoplastics: remarkable dependence of the intraparticulate contaminant diffusion coefficient on the particle size and potential role of polymer crystallinity. *Environmental Science: Processes and Impacts*, *27*(3), 634–648. https://doi.org/10.1039/d4em00744a

Trestrail, C., Nugegoda, D., & Shimeta, J. (2020). Invertebrate responses to microplastic ingestion: Reviewing the role of the antioxidant system. *Science of the Total Environment*, *734*. https://doi.org/10.1016/j.scitotenv.2020.138559

Udhayakumar, M., Udhayakumar, S., Pitchaimuthu, S. B., Alagarsamy, S., Thirumalaisamy, K., Azeem, M., Govindarajan, R., Damodharan, K., Madhubala Parameswaran, A. Das, & Arockiam Jeyasundar, P. G. S. (2025). Addressing the microplastic pollution: A societal challenge. *Water, Air, and Soil Pollution*, *236*(1). https://doi.org/10.1007/s11270-024-07667-4

UNEP. (2016). *Marine Plastic Debris and Microplastics: Global Lessons and Research to Inspire Action and Guide Policy Change*. https://www.unep.org/resources/publication/marine-plastic-debris-and-microplastics-global-lessons-and-research-inspire

Urbanek, A. K., Rymowicz, W., & Mirończuk, A. M. (2018). Degradation of plastics and plastic-degrading bacteria in cold marine habitats. *Applied Microbiology and Biotechnology*, *102*(18), 7669–7678. https://doi.org/10.1007/s00253-018-9195-y

Uribe-Querol, E., & Rosales, C. (2020). Phagocytosis: Our current understanding of a universal biological process. *Frontiers in Immunology*, *11*(June), 1–13. https://doi.org/10.3389/fimmu.2020.01066

Van Sebille, E., Aliani, S., Law, K. L., Maximenko, N., Alsina, J. M., Bagaev, A., Bergmann, M., Chapron, B., Chubarenko, I., Cózar, A., Delandmeter, P., Egger, M., Fox-Kemper, B., Garaba, S. P., Goddijn-Murphy, L., Hardesty, B. D., Hoffman, M. J., Isobe, A., Jongedijk, C. E., … Wichmann, D. (2020). The physical oceanography of the transport of floating marine debris. *Environmental Research Letters*, *15*(2). https://doi.org/10.1088/1748-9326/ab6d7d

Van Sebille, E., Wilcox, C., Lebreton, L., Maximenko, N., Hardesty, B. D., Van Franeker, J. A., Eriksen, M., Siegel, D., Galgani, F., & Law, K. L. (2015). A global inventory of small floating plastic debris. *Environmental Research Letters*, *10*(12). https://doi.org/10.1088/1748-9326/10/12/124006

Veneral, C., Camargo, A. F., Klein, G. H., Veneral, J., & Treichel, H. (2023). From macro to micro: Plastic as an environmental problem. *Environmental Nanotechnology, Monitoring and Management*, *20*. https://doi.org/10.1016/j.enmm.2023.100906

Ventura, E., Gonçalves, J. M., Vilke, J. M., d'Errico, G., Benedetti, M., Regoli, F., & Bebianno, M. J. (2024). Are mixtures of micro/nanoplastics more toxic than individual micro or nanoplastic contamination in the clam Ruditapes decussatus? *Marine Pollution Bulletin*, *206*. https://doi.org/10.1016/j.marpolbul.2024.116697

Vitousek, M. N., Taff, C. C., & Williamson, J. L. (2025). Resilience and robustness: from sub-organismal responses to communities. *Trends in Ecology and Evolution*, *40*(5), 468–478. https://doi.org/10.1016/j.tree.2025.03.001

Völkl, M., Jérôme, V., Weig, A., Jasinski, J., Meides, N., Strohriegl, P., Scheibel, T., & Freitag, R. (2022). Pristine and artificially-aged polystyrene microplastic particles differ in regard to cellular response. *Journal of Hazardous Materials*, *435*. https://doi.org/10.1016/j.jhazmat.2022.128955

von der Esch, E., Lanzinger, M., Kohles, A. J., Schwaferts, C., Weisser, J., Hofmann, T., Glas, K., Elsner, M., & Ivleva, N. P. (2020). Simple generation of suspensible secondary microplastic reference particles via ultrasound treatment. *Frontiers in Chemistry*, *8*. https://doi.org/10.3389/fchem.2020.00169

Von Moos, N., Burkhardt-Holm, P., & Köhler, A. (2012). Uptake and effects of microplastics on cells and tissue of the blue mussel Mytilus edulis L. after an experimental exposure. *Environmental Science and Technology*, *46*(20), 11327–11335. https://doi.org/10.1021/es302332w

Wagner, S., Hüffer, T., Klöckner, P., Wehrhahn, M., Hofmann, T., & Reemtsma, T. (2018). Tire wear particles in the aquatic environment - A review on generation, analysis, occurrence, fate and effects. *Water Research*, *139*, 83–100. https://doi.org/10.1016/j.watres.2018.03.051

Wan, X., Zhang, X., Pan, W., Liu, B., Yu, L., Wang, H., Li, N., & Tang, B. (2019). Ratiometric fluorescent quantification of the size-dependent cellular toxicity of silica nanoparticles. *Analytical Chemistry*, *91*(9), 6088–6096. https://doi.org/10.1021/acs.analchem.9b00633

Wang, F., Bexiga, M. G., Anguissola, S., Boya, P., Simpson, J. C., Salvati, A., & Dawson, K. A. (2013). Time resolved study of cell death mechanisms induced by amine-modified polystyrene nanoparticles. *Nanoscale*, *5*(22), 10868–10876. https://doi.org/10.1039/c3nr03249c

Wang, F., Salvati, A., & Boya, P. (2018). Lysosome-dependent cell death and deregulated autophagy induced by amine-modified polystyrene nanoparticles. *Open Biology*, *8*(8). https://doi.org/10.1098/rsob.170271

Wang, J., Zhao, X., Wu, F., Niu, L., Tang, Z., Liang, W., Zhao, T., Fang, M., Wang, H., & Wang, X. (2021). Characterization, occurrence, environmental behaviors, and risks of nanoplastics in the aquatic environment: Current status and future perspectives. *Fundamental Research*, *1*(3), 317–328. https://doi.org/10.1016/j.fmre.2021.05.001

Wang, L., Pei, W., Li, J., Feng, Y., Gao, X., Jiang, P., Wu, Q., & Li, L. (2024). Microplastics induced apoptosis in macrophages by promoting ROS generation and altering metabolic profiles. *Ecotoxicology and Environmental Safety*, *271*. https://doi.org/10.1016/j.ecoenv.2024.115970

Wang, L., Zhang, J., Huang, W., & He, Y. (2023). Laboratory simulated aging methods, mechanisms and characteristic changes of microplastics: A review. *Chemosphere*, *315*. https://doi.org/10.1016/j.chemosphere.2023.137744

Wang, S., Hu, M., Zheng, J., Huang, W., Shang, Y., Kar-Hei Fang, J., Shi, H., & Wang, Y. (2021). Ingestion of nano/micro plastic particles by the mussel Mytilus coruscus is size dependent. *Chemosphere*, *263*. https://doi.org/10.1016/j.chemosphere.2020.127957

Wang, T., Huang, X., Jiang, X., Hu, M., Huang, W., & Wang, Y. (2019a). Differential in vivo hemocyte responses to nano titanium dioxide in mussels: Effects of particle size. *Aquatic Toxicology*, *212*, 28–36. https://doi.org/10.1016/j.aquatox.2019.04.012

Wang, T., Huang, X., Jiang, X., Hu, M., Huang, W., & Wang, Y. (2019b). Differential in vivo hemocyte responses to nano titanium dioxide in mussels: Effects of particle size. *Aquatic Toxicology*, *212*, 28–36. https://doi.org/10.1016/j.aquatox.2019.04.012

Wang, T., Wang, L., Chen, Q., Kalogerakis, N., Ji, R., & Ma, Y. (2020). Interactions between microplastics and organic pollutants: Effects on toxicity, bioaccumulation, degradation, and transport. *Science of the Total Environment*, *748*. https://doi.org/10.1016/j.scitotenv.2020.142427

Wang, Y., Liu, X., Han, W., Jiao, J., Ren, W., Jia, G., Huang, C., & Yang, Q. (2024). Migration and transformation modes of microplastics in reclaimed wastewater treatment plant and sludge treatment center with thermal hydrolysis and anaerobic digestion. *Bioresource Technology*, *400*. https://doi.org/10.1016/j.biortech.2024.130649

Wen, X., & Ma, H. (2025). Cytoplasmic Vacuolization: A Fascinating Morphological Alteration From Cellular Stress to Cell Death. *Cancer Science*, *116*(5), 1181–1192. https://doi.org/10.1111/cas.70013

Weng, N., Meng, J., Huo, S., Wu, F., & Wang, W. X. (2022). Hemocytes of bivalve mollusks as cellular models in toxicological studies of metals and metal-based nanomaterials. *Environmental Pollution*, *312*. https://doi.org/10.1016/j.envpol.2022.120082

Wigger, H., Kawecki, D., Nowack, B., & Adam, V. (2020). Systematic consideration of parameter uncertainty and variability in probabilistic species sensitivity distributions. *Integrated Environmental Assessment and Management*, *16*(2), 211–222. https://doi.org/10.1002/ieam.4214

Wright, S. L., Thompson, R. C., & Galloway, T. S. (2013). The physical impacts of microplastics on marine organisms: a review. *Environmental Pollution*, *178*, 483–492. https://doi.org/10.1016/j.envpol.2013.02.031

Xia, T., Kovochich, M., Liong, M., Zink, J. I., & Nel, A. E. (2008). Cationic polystyrene nanosphere toxicity depends on cell-specific endocytic and mitochondrial injury pathways. *ACS Nano*, *2*(1), 85–96. https://doi.org/10.1021/nn700256c

Xu, R. (2015). Light scattering: A review of particle characterization applications. *Particuology*, *18*, 11–21. https://doi.org/10.1016/j.partic.2014.05.002

Yakimovich, A., Witte, R., Andriasyan, V., Georgi, F., & Greber, U. F. (2018). Label-free digital holo-tomographic microscopy reveals virus-induced cytopathic effects in live cells. *MSphere*, *3*(6). https://doi.org/10.1128/mspheredirect.00599-18

Yamazaki, T., Hirayama, K., Matsukawa, Y., Takemura, M., & Umemura, K. (2022). Digital holographic microscopy of living Hela cells before and after enzyme treatments. *ACM International Conference Proceeding Series*, 127–129. https://doi.org/10.1145/3543081.3543100

Yanagihara, M., Hiki, K., & Iwasaki, Y. (2024). Which distribution to choose for deriving a species sensitivity distribution? Implications from analysis of acute and chronic ecotoxicity data. *Ecotoxicology and Environmental Safety*, *278*. https://doi.org/10.1016/j.ecoenv.2024.116379

Yang, M., & Wang, W. X. (2022). Differential cascading cellular and subcellular toxicity induced by two sizes of nanoplastics. *Science of the Total Environment*, *829*. https://doi.org/10.1016/j.scitotenv.2022.154593

Yang, Z., DeLoid, G. M., Zarbl, H., Baw, J., & Demokritou, P. (2023). Micro- and nanoplastics (MNPs) and their potential toxicological outcomes: State of science, knowledge gaps and research needs. *NanoImpact*, *32*. https://doi.org/10.1016/j.impact.2023.100481

Yeo, B. G., Mizukawa, K., & Takada, H. (2023). Microplastics in global marine waters and biota: Effectiveness of potential bioindicators in mirroring local pollution levels. *Environmental Monitoring and Contaminants Research*, *3*(0), 43–68. https://doi.org/10.5985/emcr.20230005

Yi, J., Ma, Y., Ruan, J., You, S., Ma, J., Yu, H., Zhao, J., Zhang, K., Yang, Q., Jin, L., Zeng, G., & Sun, D. (2024). The invisible threat: Assessing the reproductive and transgenerational impacts of micro- and nanoplastics on fish. In *Environment International* (Vol. 183). Elsevier Ltd. https://doi.org/10.1016/j.envint.2024.108432

Yoon, J., Kim, K., Park, H., Choi, C., Jang, S., & Park, Y. (2015). Label-free characterization of white blood cells by measuring 3D refractive index maps. *Biomedical Optics Express*, *6*(10), 3865–3875. https://doi.org/10.1364/boe.6.003865

Yoshida, S., Hiraga, K., Takehana, T., Taniguchi, I., Yamaji, H., Maeda, Y., Toyohara, K., Miyamoto, K., Kimura, Y., & Oda, K. (2016). *A bacterium that degrades and assimilates poly(ethylene terephthalate)*. https://doi.org/10.1126/science.aad6359

Yue, J., & López, J. M. (2020). Understanding MAPK signaling pathways in apoptosis. *International Journal of Molecular Sciences*, *21*(7). https://doi.org/10.3390/ijms21072346

Zadka, Ł., Buzalewicz, I., Ulatowska-Jarża, A., Rusak, A., Kochel, M., Ceremuga, I., & Dzięgiel, P. (2021). Label-free quantitative phase imaging reveals spatial heterogeneity of extracellular vesicles in select colon disorders. *American Journal of Pathology*, *191*(12), 2147–2171. https://doi.org/10.1016/j.ajpath.2021.08.005

Zaki, M. R. M., & Aris, A. Z. (2022). An overview of the effects of nanoplastics on marine organisms. *Science of the Total Environment*, *831*. https://doi.org/10.1016/j.scitotenv.2022.154757

Zhang, L., Zhu, J., Wilke, K. L., Xu, Z., Zhao, L., Lu, Z., Goddard, L. L., & Wang, E. N. (2019). Enhanced environmental scanning electron microscopy using phase reconstruction and its application in condensation. *ACS Nano*, *13*(2), 1953–1960. https://doi.org/10.1021/acsnano.8b08389

Zhang, Z., Zou, S., & Li, P. (2024). Aging of plastics in aquatic environments: Pathways, environmental behavior, ecological impacts, analyses and quantifications. *Environmental Pollution*, *341*. https://doi.org/10.1016/j.envpol.2023.122926

Zhao, F., Zhao, Y., Liu, Y., Chang, X., Chen, C., & Zhao, Y. (2011). Cellular uptake, intracellular trafficking, and cytotoxicity of nanomaterials. *Small*, *7*(10), 1322–1337. https://doi.org/10.1002/smll.201100001

Zhao, J., Lan, R., Tan, H., Wang, J., Ma, Y., Chen, Q., Jiang, F., Wang, Z., & Xing, B. (2025). Detection and characterization of microplastics and nanoplastics in biological samples. *Nature Reviews Bioengineering*. https://doi.org/10.1038/s44222-025-00335-0

Zhao, S., Kvale, K. F., Zhu, L., Zettler, E. R., Egger, M., Mincer, T. J., Amaral-Zettler, L. A., Lebreton, L., Niemann, H., Nakajima, R., Thiel, M., Bos, R. P., Galgani, L., & Stubbins, A. (2025). The distribution of subsurface microplastics in the ocean. *Nature*, *641*(8061), 51–61. https://doi.org/10.1038/s41586-025-08818-1

Zhao, S., Zhu, L., Wang, T., & Li, D. (2014). Suspended microplastics in the surface water of the Yangtze Estuary System, China: First observations on occurrence, distribution. *Marine Pollution Bulletin*, *86*(1–2), 562–568. https://doi.org/10.1016/j.marpolbul.2014.06.032

Zheng, K., Wang, P., Lou, X., Zhou, Z., Zhou, L., Hu, Y., Luan, Y., Quan, C., Fang, J., Zou, H., & Gao, X. (2024). A review of airborne micro- and nano-plastics: Sampling methods, analytical techniques, and exposure risks. *Environmental Pollution*, *363*. https://doi.org/10.1016/j.envpol.2024.125074

Zhong, H., Wu, M., Sonne, C., Lam, S. S., Kwong, R. W. M., Jiang, Y., Zhao, X., Sun, X., Zhang, X., Li, C., Li, Y., Qu, G., Jiang, F., Shi, H., Ji, R., & Ren, H. (2023). The hidden risk of microplastic-associated pathogens in aquatic environments. *Eco-Environment and Health*, *2*(3), 142–151. https://doi.org/10.1016/j.eehl.2023.07.004

Zhou, Q., Tu, C., Yang, J., Fu, C., Li, Y., & Waniek, J. J. (2021). Trapping of microplastics in halocline and turbidity layers of the semi-enclosed Baltic Sea. *Frontiers in Marine Science*, *8*. https://doi.org/10.3389/fmars.2021.761566

Zhou, X. X., Hao, L. T., Wang, H. Y. Z., Li, Y. J., & Liu, J. F. (2019). Cloud-point extraction combined with thermal degradation for nanoplastic analysis using Pyrolysis Gas Chromatography-Mass Spectrometry. *Analytical Chemistry*, *91*(3), 1785–1790. https://doi.org/10.1021/acs.analchem.8b04729

Zobkov, M. B., Esiukova, E. E., Zyubin, A. Y., & Samusev, I. G. (2019). Microplastic content variation in water column: The observations employing a novel sampling tool in stratified Baltic Sea. *Marine Pollution Bulletin*, *138*, 193–205. https://doi.org/10.1016/j.marpolbul.2018.11.047

Supplementary Information

Supplementary Information: Chapter 2

Selection process for the systematic review

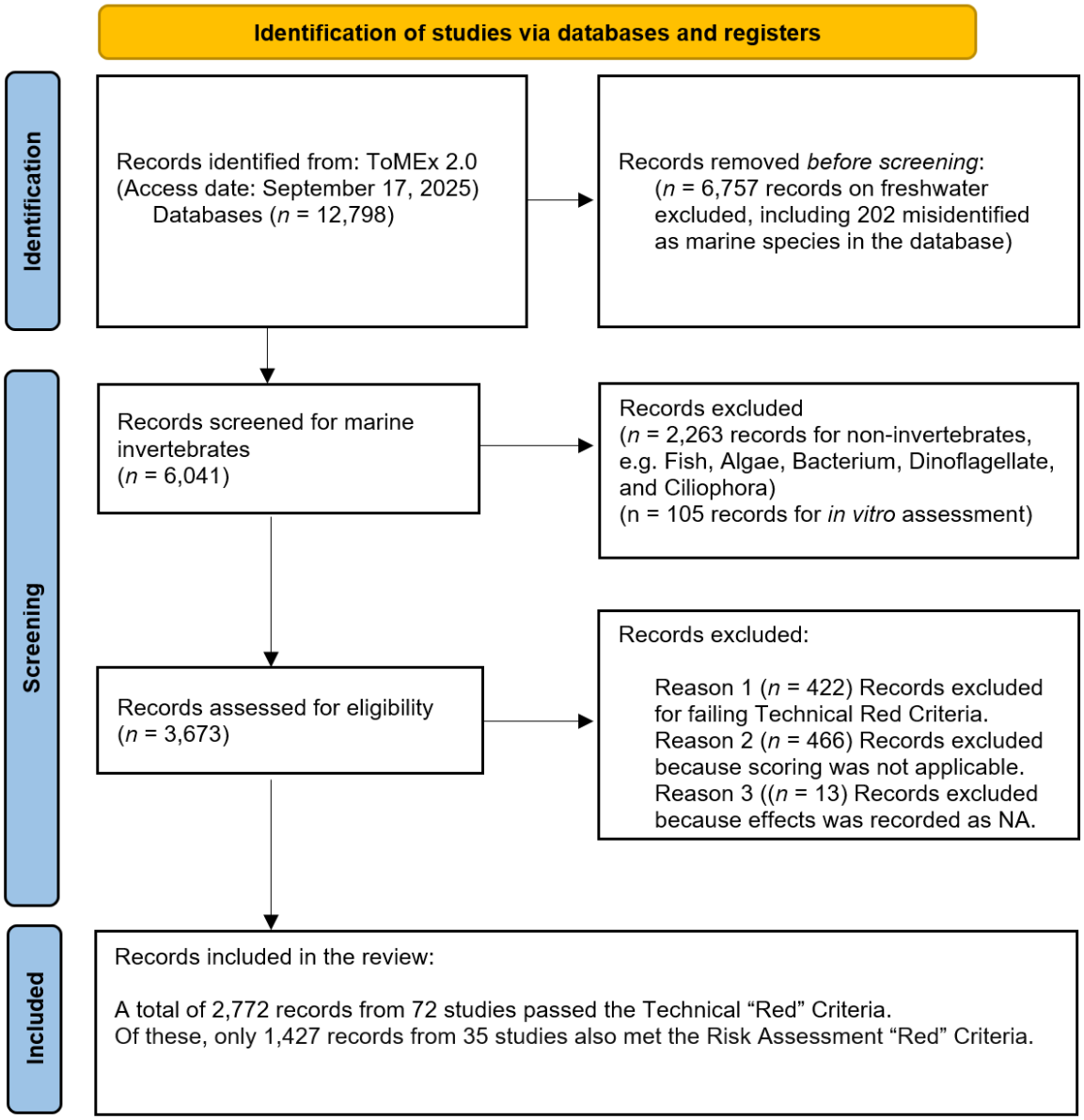

Figure A2.1. *Flowchart of the selection process following the Preferred Reporting Items for Systematic Reviews and Meta-Analyses (PRISMA) guidelines.*

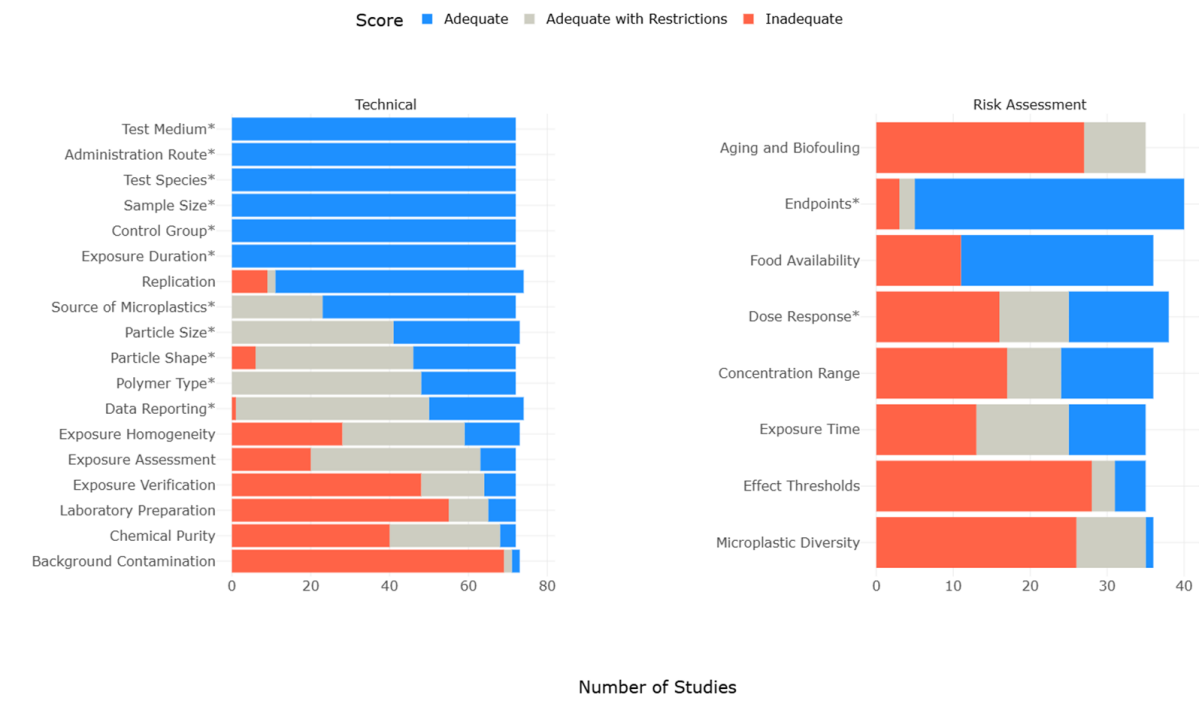

Figure A2.2. *Quality scores of MNP toxicity studies in ToMEx 2.0 that met the Technical (n = 72) and Risk Assessment (subset, n = 35) Red Criteria. Bar plot depicting the number of studies rated as Adequate (blue, score 2), Adequate with Restrictions (gray, score 1), or Inadequate (red, score 0) across assessed criteria. 'Red Criteria', indicated by an asterisk (*), denote the minimum requirements for technical and risk assessment, as defined by Mehinto et al. (2022).*

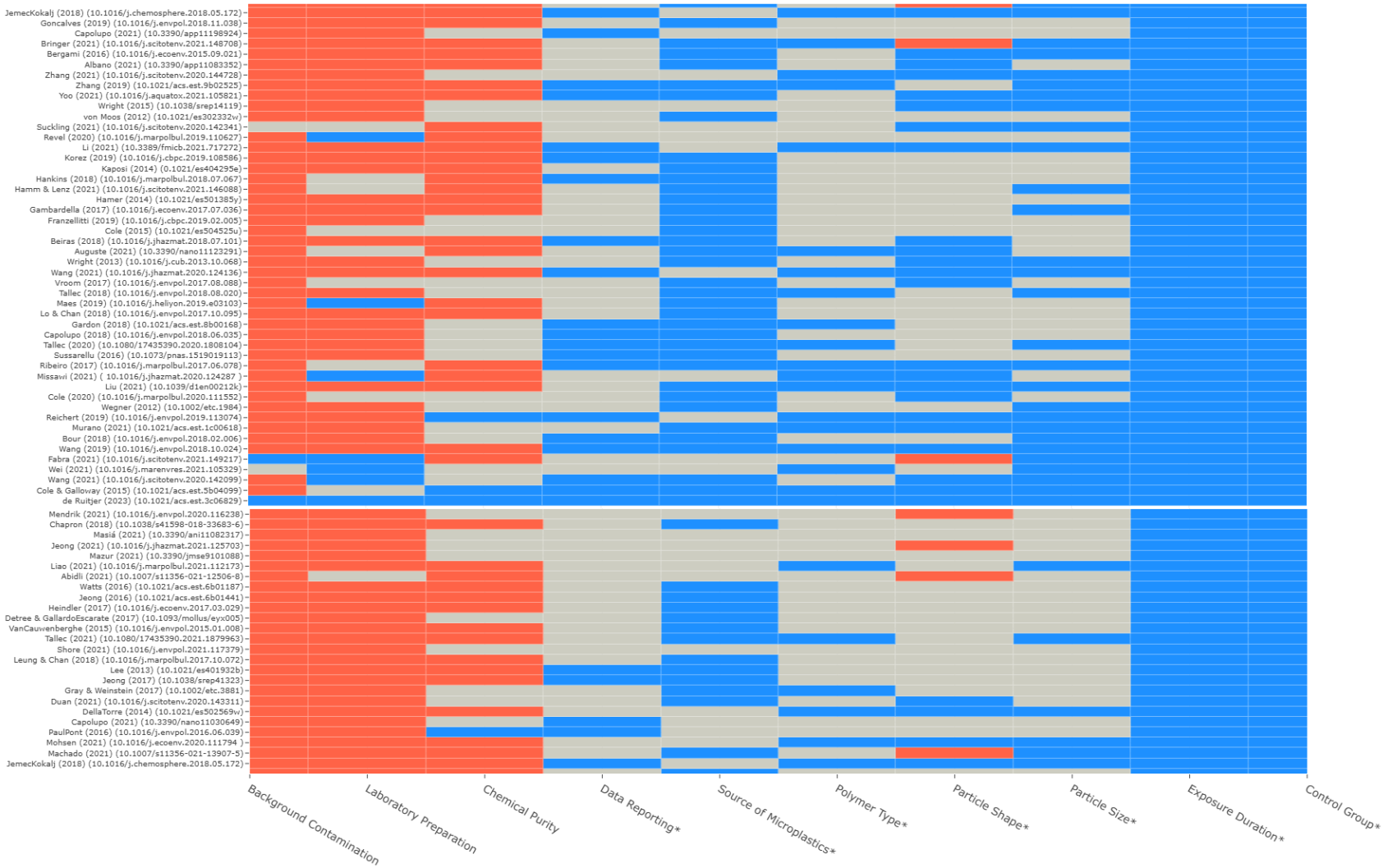

***Figure A2.3**. Heatmap showing the scoring of individual MNP toxicity studies (n = 72) across technical criteria. Colors represent scores: Adequate (blue, score = 2), Adequate*

with Restrictions (gray, score = 1), and Inadequate (red, score = 0). Asterisks (*) denote 'Red Criteria', representing minimum requirements for risk assessment as defined by Mehinto et al. (2022).

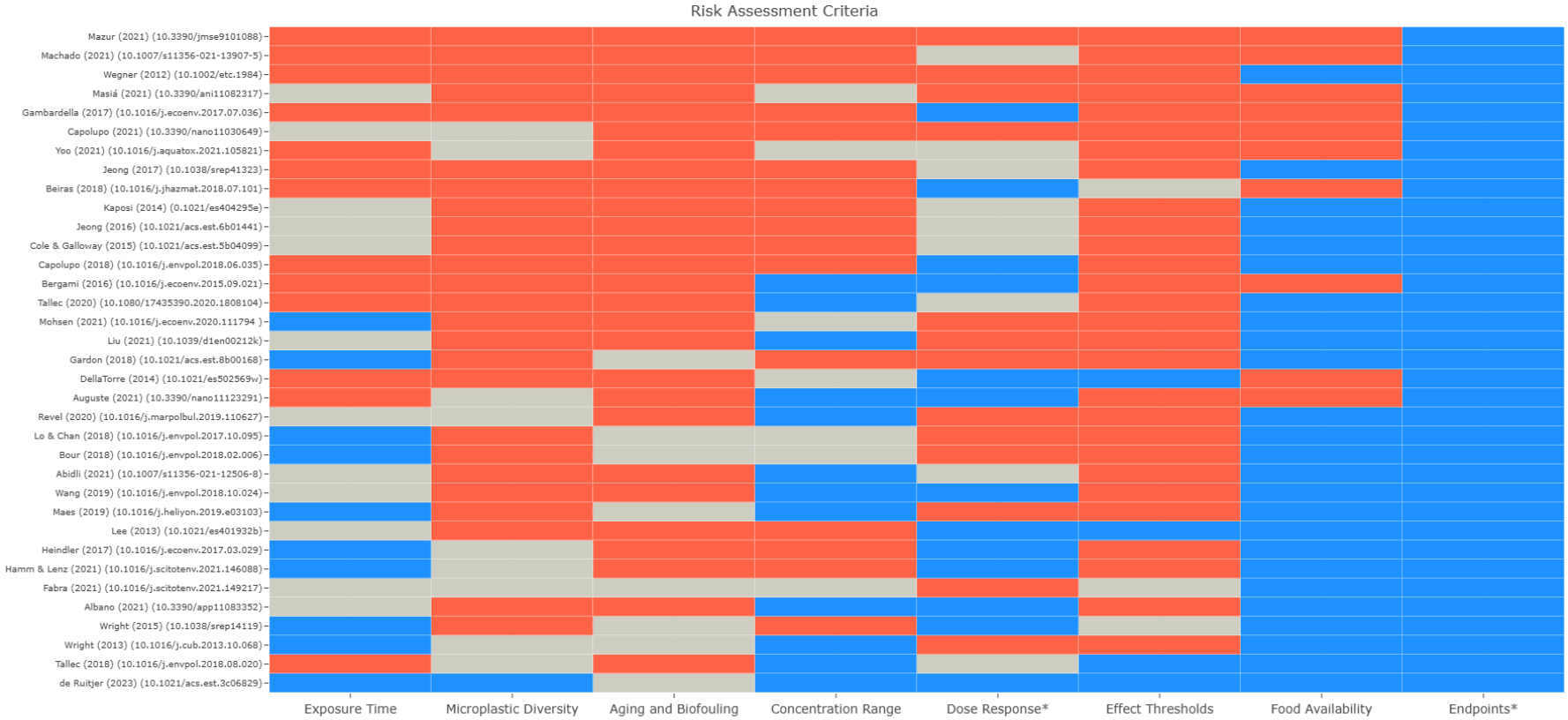

Figure A2.4. *Heatmap showing the scoring of individual MNP toxicity studies (n = 35) across risk assessment criteria. Colors represent scores: Adequate (blue, score = 2), Adequate with Restrictions (gray, score = 1), and Inadequate (red, score = 0). Asterisks (*) denote 'Red Criteria', representing minimum requirements for risk assessment as defined by Mehinto et al. (2022).*

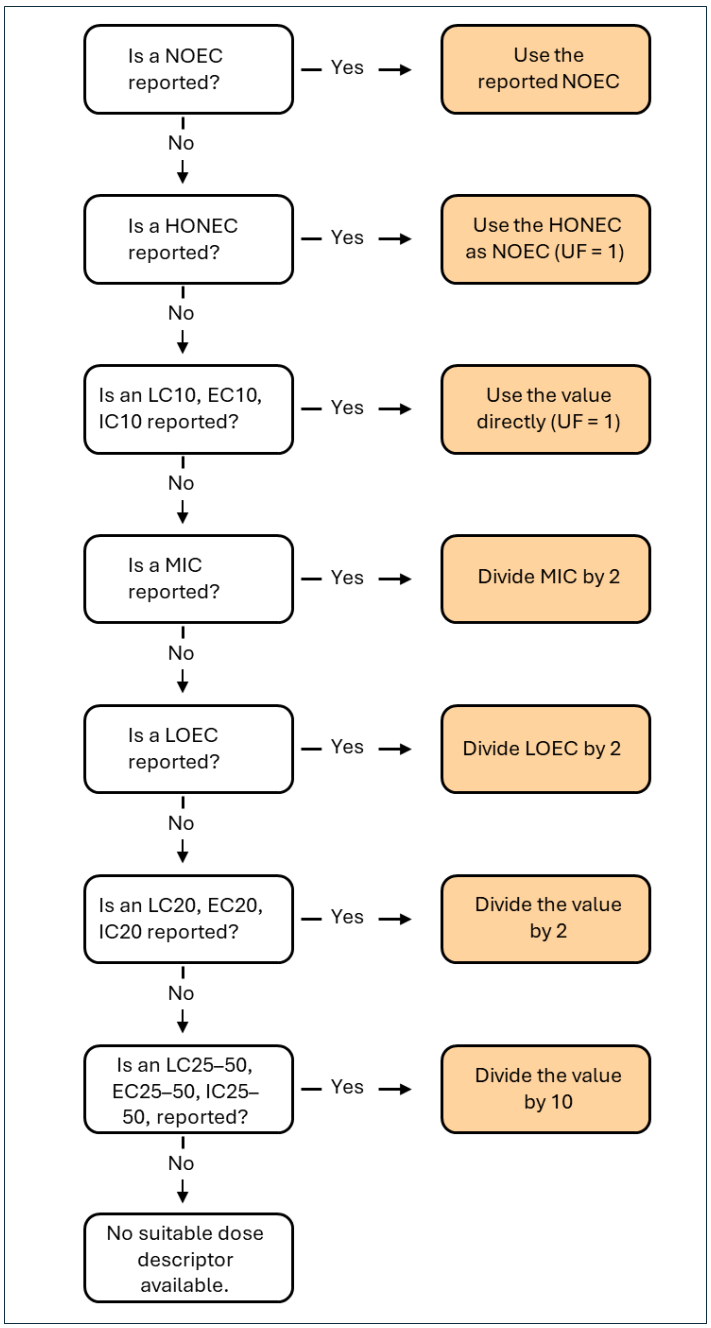

Figure A2.5. *Decision tree used for standardizing effect concentrations to no-observed-effect concentrations (NOECs) in MNP toxicity studies. The figure illustrates the hierarchical approach and associated uncertainty factors (UFs) applied to convert various reported dose descriptors to NOECs, based on established reference (Wigger et al., 2020). Abbreviations: HONEC, highest observed no-effect concentration; MIC, minimum inhibitory concentration; LOEC, lowest observed effect concentration; LC, lethal concentration; EC, effective concentration; IC, inhibitory concentration; UF, uncertainty factor.*

Table A2.1. *Default power-law scaling parameters used for microplastic toxicity data alignment in ToMEx 2.0 from Kooi et al. (2021).*

Parameter	Value
Length Alpha Value	2.07
Surface Area Alpha Value	1.5
Volume Alpha Value	1.48
Mass Alpha Value	1.32
Specific Surface Area Alpha Value	1.98
Average Particle Width to Length Ratio	0.77
Average Particle Density (g/cm^3)	1.1
Average Particle Height to Width Ratio	0.77
Lower Length (µm)	1
Upper Length (µm)	5000

Trends in experimental studies

Table A2.2. *Relative species contribution (%) by taxonomic group in the in vivo toxicity assessment of micro- and nanoplastic particles in marine invertebrates.*

Species	Contribution (%) of species per Taxonomic Group
Annelida	
Alitta virens	2.9
Arenicola marina	5.4
Hediste diversicolor	89.7
Perinereis aibuhitensis	2.0
Cnidaria	
Acropora muricata	10.3
Acropora sp.	10.3
Heliopora coerulea	10.3
Lophelia pertusa	2.6
Montastraea cavernosa	0.9
Orbicella faveolata	0.9
Pocillopora verrucosa	10.3
Porites lutea	10.3
Seriatopora hystrix	10.3
Tubastrea aurea	34.2
Crustacea	
Acartia clausi	0.60
Acartia tonsa	1.05
Amphibalanus amphitrite	3.31
Artemia franciscana	10.09
Artemia parthenogenetica	3.31

Artemia salina	3.01
Calanus finmarchicus	0.30
Calanus helgolandicus	0.75
Carcinus maenas	4.22
Charybdis japonica	2.26
Corophium volutator	1.81
Diaphanosoma celebensis	23.49
Idotea emarginata	3.92
Litopenaeus vannamei	2.26
Palaemonetes pugio	1.66
Paracyclopina nana	8.13
Parvocalanus crassirostris	1.05
Porcellana platycheles	1.81
Tigriopus fulvus	1.81
Tigriopus japonicus	25.15
Echinoderm	
Apostichopus japonicus	41.3
Paracentrotus lividus	42.9
Psammechinus miliaris	5.3
Scaphechinus mirabilis	6.3
Tripneustes gratilla	4.2
Mollusca	
Abra nitida	4.8
Crassostrea gigas	34.3
Crepidula onyx	0.7
Ennucula tenuis	4.8
Limecola balthica	1.4
Mactra veneriformis	0.5
Meretrix meretrix	6.3
Mytilus coruscus	3.9
Mytilus edulis	1.7
Mytilus galloprovincialis	28.1
Mytilus species	10.3
Ostrea edulis	0.8
Pinctada margaritifera	1.6
Scrobicularia plana	1.1
Rotifera	
Brachionus koreanus	84.2
Brachionus plicatilis	15.8

Distributions of toxicity data

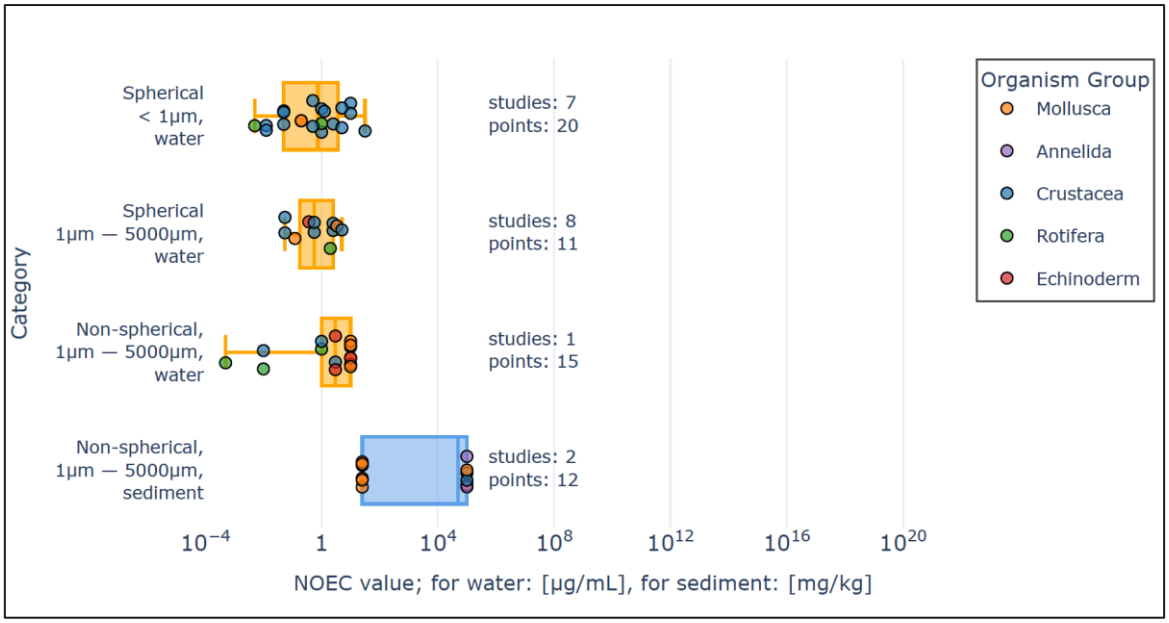

Figure A2.6. *Distribution of chronic NOEC values (particle mass concentrations) for mortality across particle characteristics. Data were categorized according to size class (<1 µm and 1–5000 µm), shape (spherical vs. non-spherical), and exposure route (water vs. sediment), with individual data points color-coded by organism group. An interactive version of this plot, developed using Plotly, is available at this link: https://jphara.github.io/EES2026PaperChronicToxicityData/MassConc/1Mortality_MassConc.html. Users can open the link and hover over individual points to view detailed data, including species, specific endpoint, polymer type, original and converted effect metrics, and study reference.*

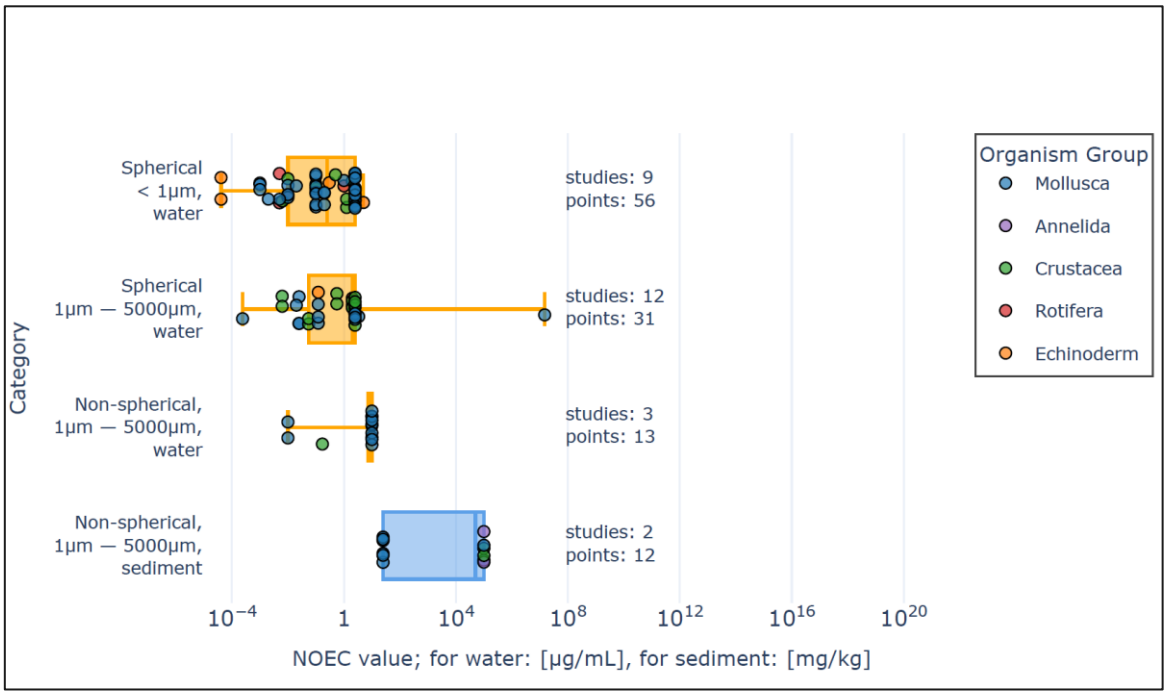

Figure A2.7. *Distribution of chronic NOEC values (particle mass concentrations) for fitness-related endpoints, including reproduction, growth, development, and body condition, across particle characteristics. Data were categorized according to size class (<1 µm and 1–5000 µm), shape (spherical vs. non-spherical), and exposure*

route (water vs. sediment), with individual data points color-coded by organism group. An interactive version of this plot, developed using Plotly, is available at this link: https://jphara.github.io/EES2026PaperChronicToxicityData/MassConc/2Fitness_MassConc.html. Users can open the link and hover over individual points to view detailed data, including species, specific endpoint, polymer type, original and converted effect metrics, and study reference.

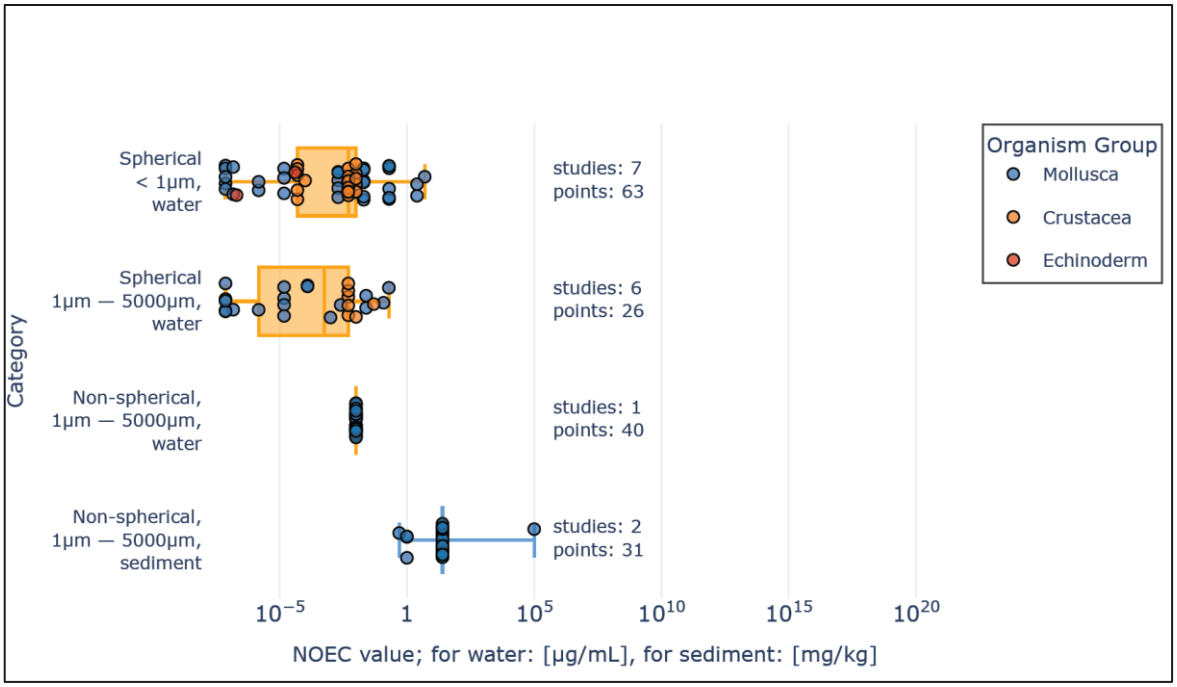

Figure A2.8. *Distribution of chronic NOEC values (particle mass concentrations) for functional endpoints across particle characteristics. Endpoints include metabolism, immune system responses, alimentary and excretory functions, circulatory and respiratory functions, as well as behavioral, sensory, and neurological processes. Data were categorized according to size class (<1 µm and 1–5000 µm), shape (spherical vs. non-spherical), and exposure route (water vs. sediment), with individual data points color-coded by organism group. An interactive version of this plot, developed using Plotly, is available at this link: https://jphara.github.io/EES2026PaperChronicToxicityData/MassConc/3FunctionalEndpoints_MassConc.html. Users can open the link and hover over individual points to view detailed data, including species, specific endpoint, polymer type, original and converted effect metrics, and study reference.*

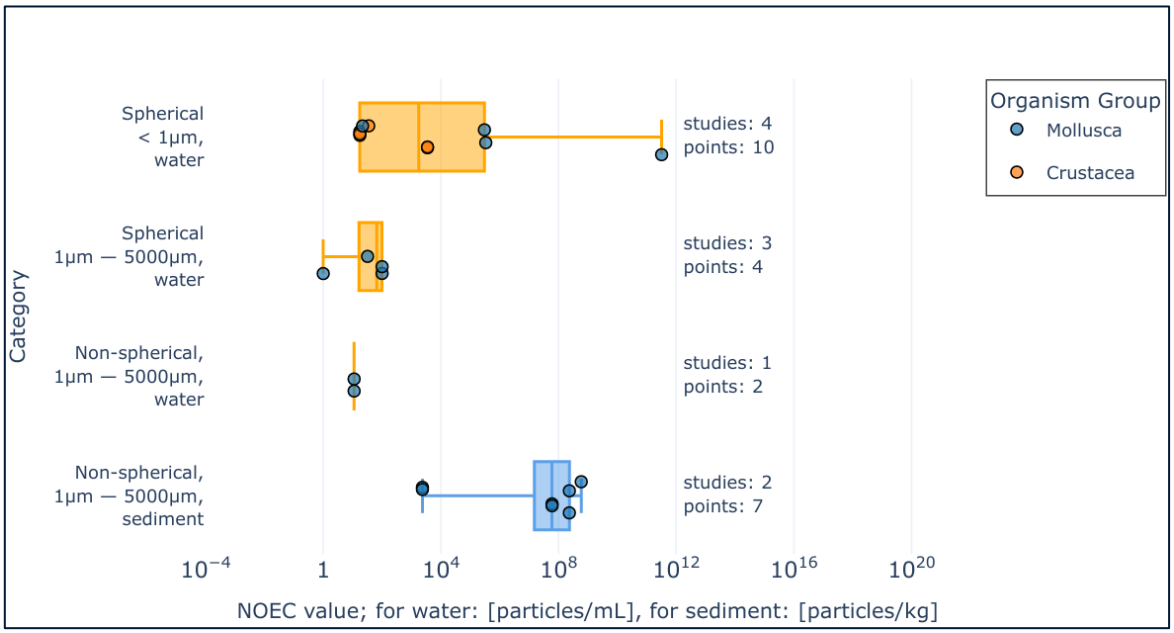

Figure A2.9. *Distribution of chronic NOEC values for behavioral, sensory, and neurological endpoints. Data were categorized according to size class (<1 µm and 1–5000 µm), shape (spherical vs. non-spherical), and exposure route (water vs. sediment), with individual data points color-coded by organism group.*

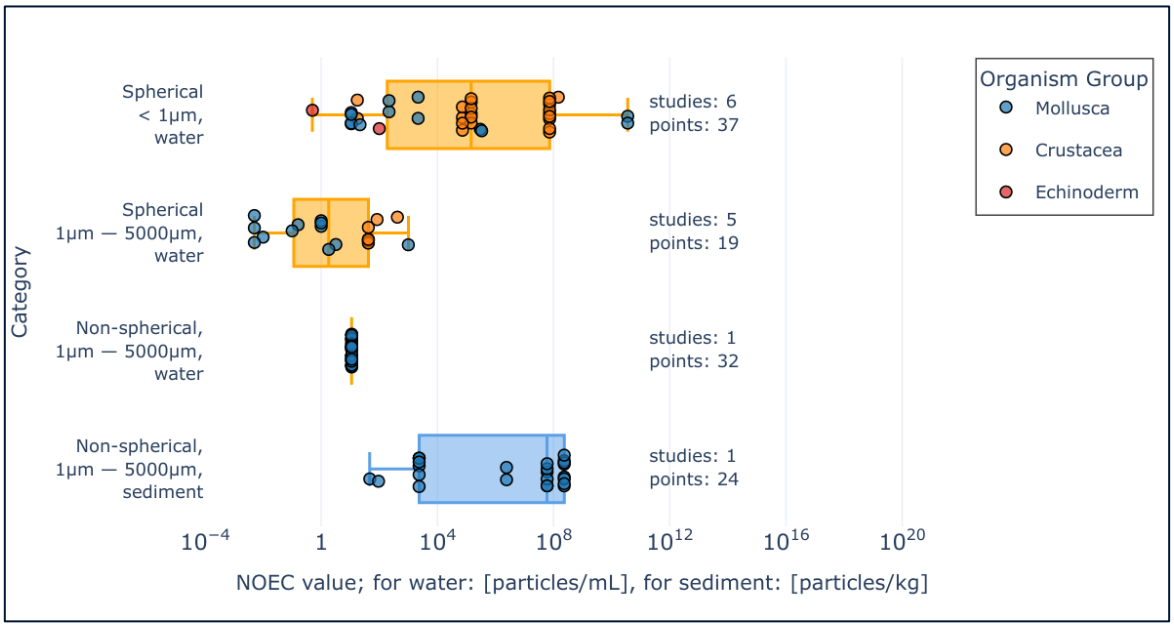

Figure A2.10. *Distribution of chronic NOEC values for metabolism endpoints. Data were categorized according to size class (<1 µm and 1–5000 µm), shape (spherical vs. non-spherical), and exposure route (water vs. sediment), with individual data points color-coded by organism group.*

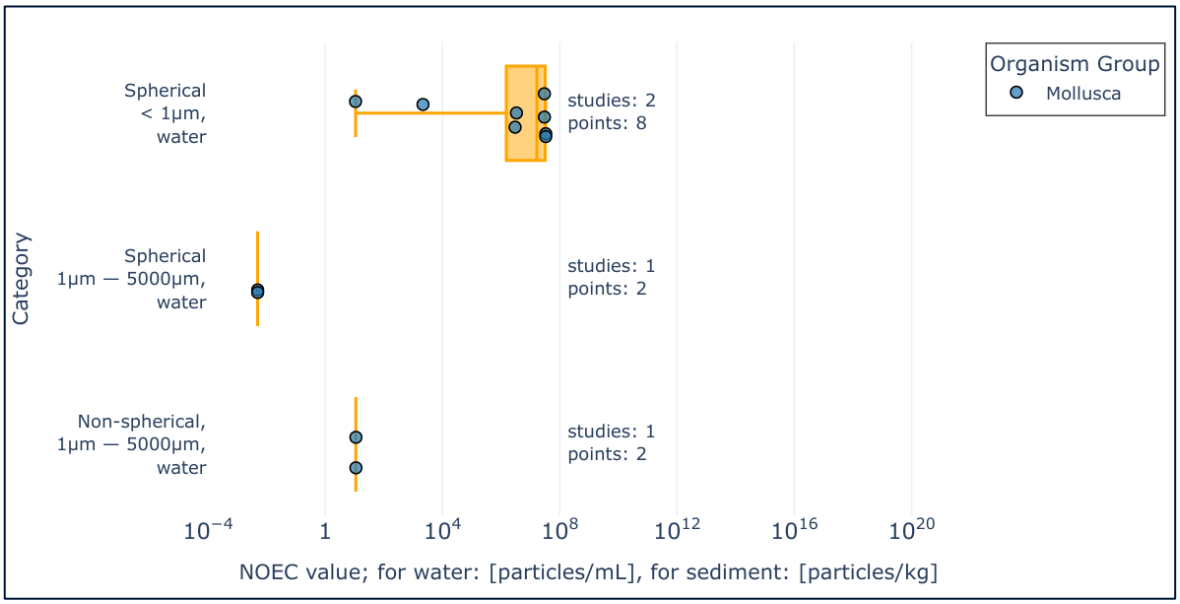

Figure A2.11. *Distribution of chronic NOEC values for immune system endpoints. Data were categorized according to size class (<1 µm and 1–5000 µm), shape (spherical vs. non-spherical), and exposure route (water vs. sediment), with individual data points color-coded by organism group.*

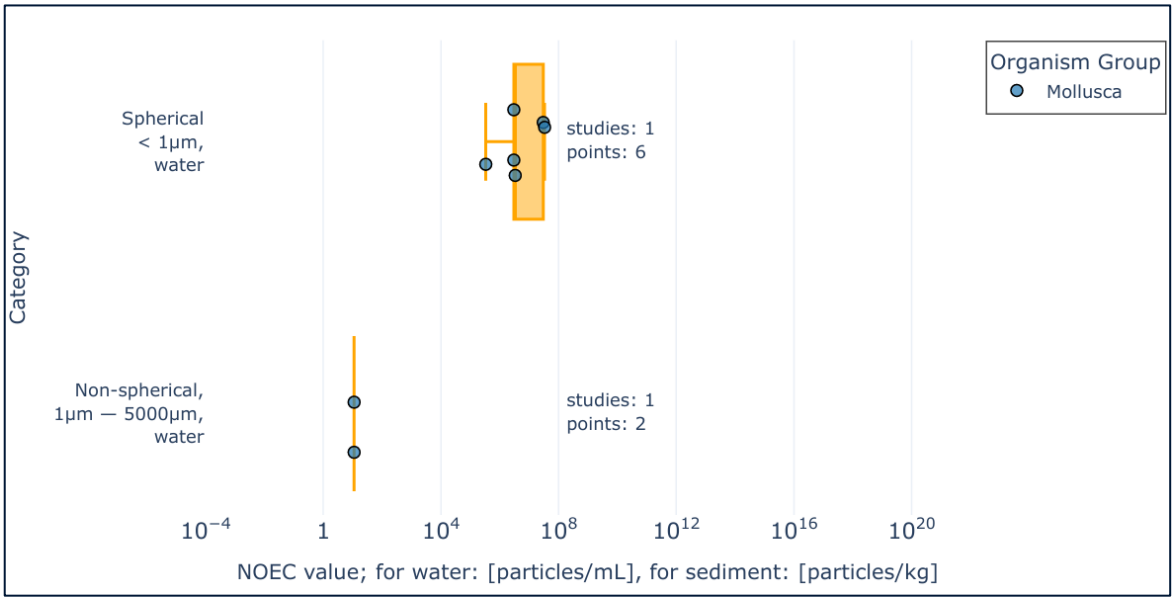

Figure A2.12. *Distribution of chronic NOEC values for alimentary and excretory endpoints. Data were categorized according to size class (<1 µm and 1–5000 µm), shape (spherical vs. non-spherical), and exposure route (water vs. sediment), with individual data points color-coded by organism group.*

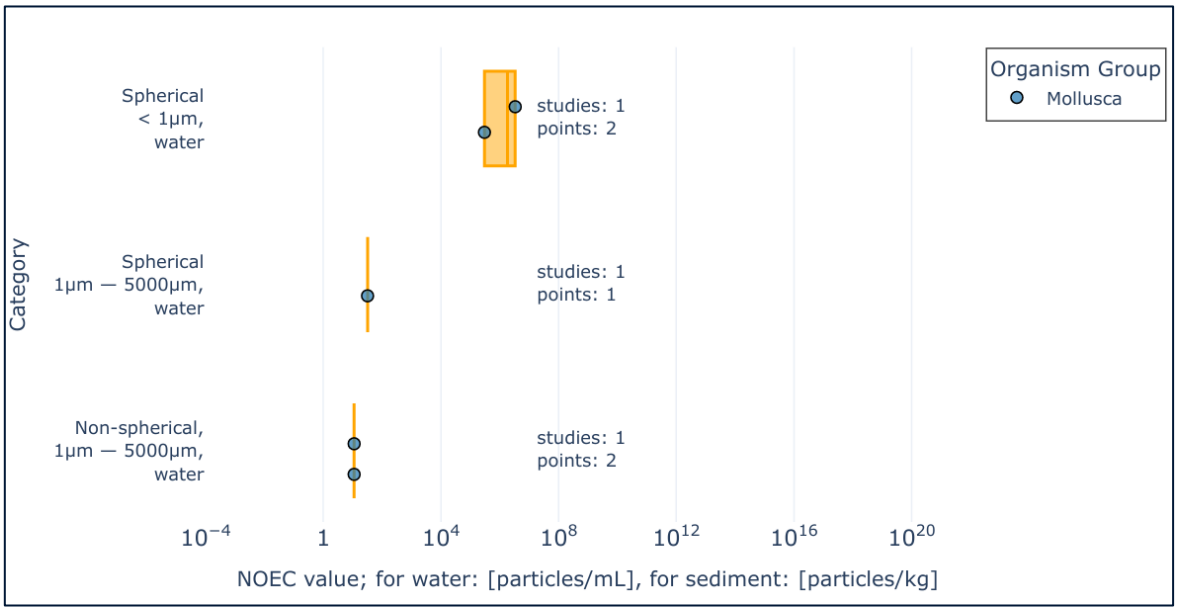

Figure A2.13. *Distribution of chronic NOEC values for circulatory and respiratory endpoints. Data were categorized according to size class (<1 µm and 1–5000 µm), shape (spherical vs. non-spherical), and exposure route (water vs. sediment), with individual data points color-coded by organism group.*

Species sensitivity distributions

Table A2.3. *Raw data used to generate the SSD curves for food dilution mechanism of toxicity (volume-based ERM), expressed in particle number concentrations.*

Group	Species	Most Sensitive Conc. (particles/mL)	Min Conc. Broad Endpoint	Min Conc. Specific Endpoint	Min Environment	DOI	Minimum Effect Conc.	95% Lower Effect Conc.	1st Quartile Effect Conc.	Average Effect Conc.	Median Effect Conc.	3rd Quartile Effect Conc.	95% Upper Effect Conc.	Max. Observed Effect Conc.	Std Dev Effect Conc.	Number of doses with Effects	Min Conc. Tested (with or without effects)	Max Conc. Tested (with or without effects)	Total Studies	Total PODs
Rotifera	*Brachionus plicatilis*	39.6	Fitness	Mortality	Marine	10.1016/j.jhazmat.2018.07.101	3.77	-72.1	39.6	152	75.4	226	376	377	198	3	3.77	377	1	3
Mollusca	*Crepidula onyx*	0.685	Fitness	Growth	Marine	10.1016/j.envpol.2017.10.095	0.000913	-1.31	0.685	1.37	1.37	2.05	4.05	2.74	1.94	2	0.000913	2.74	1	2
Mollusca	*Mytilus galloprovincialis*	0.117	Fitness	Body Condition	Marine	10.3390/ani11082317	0.0587	-0.054	0.117	0.176	0.176	0.235	0.406	0.293	0.166	2	0.0587	0.293	1	2
Echinoderm	*Paracentrotus lividus*	810000	Fitness	Mortality	Marine	10.1016/j.jhazmat.2018.07.101	694000	472000	810000	926000	926000	1040000	1380000	1160000	327000	2	694000	1160000	1	2
Crustacea	*Parvocalanus crassirostris*	1860	Fitness	Reproduction	Marine	10.1016/j.ecoenv.2017.03.029	1860	1860	1860	1860	1860	1860	1860	1860	0	2	1860	1860	1	2
Crustacea	*Tigriopus fulvus*	54.5	Fitness	Mortality	Marine	10.1016/j.jhazmat.2018.07.101	27.3	-25.1	54.5	81.8	81.8	109	189	136	77.1	2	27.3	136	1	2
Crustacea	*Tigriopus japonicus*	5.16	Fitness	Reproduction	Marine	10.1021/es401932b	5.16	5.16	5.16	5.16	5.16	5.16	5.16	5.16	0	2	5.16	5.16	1	1
Echinoderm	*Tripneustes gratilla*	0.411	Fitness	Growth	Marine	0.1021/es404295e	0.366	0.278	0.411	0.457	0.457	0.503	0.636	0.548	0.129	2	0.366	0.548	1	2
Echinoderm	*Pseudocentrotus huttoni*	0.000266	Fitness	Body Condition	Marine	10.1016/j.marpolbul.2021.112369	0.000133	-0.000122	0.000266	0.000399	0.000399	0.000532	0.00092	0.000665	0.000376	2	0.000133	0.000665	1	2

Table A2.4. *Raw data used to generate the SSD curves for food dilution mechanism of toxicity (volume-based ERM), expressed in particle mass concentrations.*

Group	Species	Most Sensitive Conc. (µg/mL)	Min Conc. Broad Endpoint	Min Conc. Specfic Endpoint	Min Environment	DOI	Minimum Effect Conc.	95% Lower CI Effect Conc.	1st Quartile Effect Conc.	Average Effect Conc.	Median Effect Conc.	3rd Quartile Effect Conc.	95% Upper CI Conc.	Max. Observed Effect Conc.	Std Dev Effect Conc.	Number of doses with Effects	Min Conc. Tested (with or without effects)	Max Conc. Tested (with or without effects)	Total Studies	Total PODs
Rotifera	*Brachionus plicatilis*	6510	Fitness	Mortality	Marine	10.1016/j.jhazmat.2018.07.101	620	-11900	6510	25000	12400	37200	61800	62000	32600	3	620	62000	1	3
Mollusca	*Crepidula onyx*	113	Fitness	Growth	Marine	10.1016/j.envpol.2017.10.095	0.15	-216	113	225	225	338	667	450	318	2	0.15	450	1	2
Mollusca	*Mytilus galloprovincialis*	19.3	Fitness	Body Condition	Marine	10.3390/ani11082317	9.65	-8.87	19.3	28.9	28.9	38.6	66.7	48.2	27.3	2	9.65	48.2	1	2
Echinoderm	*Paracentrotus lividus*	133000000	Fitness	Mortality	Marine	10.1016/j.jhazmat.2018.07.101	114000000	77700000	133000000	152000000	152000000	171000000	227000000	190000000	53800000	2	114000000	190000000	1	2
Crustacea	*Parvocalanus crassirostris*	307000	Fitness	Reproduction	Marine	10.1016/j.ecoenv.2017.03.029	307000	307000	307000	307000	307000	307000	307000	307000	0	2	307000	307000	1	2
Crustacea	*Tigriopus fulvus*	8960	Fitness	Mortality	Marine	10.1016/j.jhazmat.2018.07.101	4480	-4120	8960	13400	13400	17900	31000	22400	12700	2	4480	22400	1	2
Crustacea	*Tigriopus japonicus*	849	Fitness	Reproduction	Marine	10.1021/es401932b	849	849	849	849	849	849	849	849	0	2	849	849	1	1
Echinoderm	*Tripneustes gratilla*	67.6	Fitness	Growth	Marine	0.1021/es404295e	60.1	45.7	67.6	75.1	75.1	82.7	105	90.2	21.3	2	60.1	90.2	1	2
Echinoderm	*Pseudechinus huttoni*	0.0437	Fitness	Body Condition	Marine	10.1016/j.marpolbul.2021.112369	0.0219	-0.0201	0.0437	0.0656	0.0656	0.0875	0.151	0.109	0.0619	2	0.0219	0.109	1	2

Table A2.5. *Raw data used to generate the SSD curves for tissue translocation mechanism of toxicity (surface area-based ERM), expressed in particle number concentrations.*

Group	Species	Most Sensitive Conc. (particles/mL)	Min Conc. Broad Endpoint	Min Conc. Specfic Endpoint	Min Environment	DOI	Minimum Effect Conc.	95% Lower CI Effect Conc.	1st Quartile Effect Conc.	Average Effect Conc.	Median Effect Conc.	3rd Quartile Effect Conc.	95% Upper CI Conc.	Max Observed Effect Conc.	Std Dev Effect Conc.	Number of doses with Effects	Min Conc. Tested (with or without effects)	Max Conc. Tested (with or without effects)	Total Studies	Total PODs
Rotifera	*Brachionus plicatilis*	222	Fitness	Mortality	Marine	10.1016/j.jhazmat.2018.07.101	21.1	-404	222	852	422	1270	2110	2110	1110	3	21.1	2110	1	3
Mollusca	*Crepidula onyx*	842	Fitness	Growth	Marine	10.1016/j.envpol.2017.10.095	1.12	-1610	842	1680	1680	2520	4980	3360	2380	2	1.12	3360	1	2
Mollusca	*Mytilus galloprovincialis*	81.5	Fitness	Body Condition	Marine	10.3390/ani11082317	40.8	-37.5	81.5	122	122	163	282	204	115	2	40.8	204	1	2
Echinoderm	*Paracentrotus lividus*	712000	Fitness	Mortality	Marine	10.1016/j.jhazmat.2018.07.101	610000	415000	712000	814000	814000	915000	1210000	1020000	288000	2	610000	1020000	1	2
Crustacea	*Parvocalanus crassirostris*	2880	Fitness	Reproduction	Marine	10.1016/j.ecoenv.2017.03.029	2880	2880	2880	2880	2880	2880	2880	2880	0	2	2880	2880	1	2
Crustacea	*Tigriopus fulvus*	476	Fitness	Mortality	Marine	10.1016/j.jhazmat.2018.07.101	238	-219	476	713	713	951	1650	1190	673	2	238	1190	1	2
Crustacea	*Tigriopus japonicus*	22.6	Fitness	Reproduction	Marine	10.1021/es401932b	22.6	22.6	22.6	22.6	22.6	22.6	22.6	22.6	0	2	22.6	22.6	1	1
Echinoderm	*Tripneustes gratilla*	101	Fitness	Growth	Marine	0.1021/es404295e	89.7	68.2	101	112	112	123	156	135	31.7	2	89.7	135	1	2
Echinoderm	*Pseudechinus huttoni*	0.897	Fitness	Body Condition	Marine	10.1016/j.marpolbul.2021.112369	0.448	-0.413	0.897	1.35	1.35	1.79	3.1	2.24	1.27	2	0.448	2.24	1	2

Table A2.6. *Raw data used to generate the SSD curves for tissue translocation mechanism of toxicity (surface area-based ERM), expressed in particle mass concentrations.*

Group	Species	Most Sensitive Conc. (µg/mL)	Min Conc. Broad Endpoint	Min Conc. Specfic Endpoint	Min Environment	DOI	Minimum Effect Conc.	95% Lower CI Effect Conc.	1st Quartile Effect Conc.	Average Effect Conc.	Median Effect Conc.	3rd Quartile Effect Conc.	95% Upper CI Conc.	Maximum Observed Effect Conc.	Std Dev Effect Conc.	Number of doses with Effects	Min Conc. Tested (with or without effects)	Max Conc. Tested (with or without effects)	Total Studies	Total PODs
Rotifera	*Brachionus plicatilis*	36500	Fitness	Mortality	Marine	10.1016/j.jhazmat.2018.07.101	3470	-66400	36500	140000	69500	208000	347000	347000	182000	3	3470	347000	1	3
Mollusca	*Crepidula onyx*	138000	Fitness	Growth	Marine	10.1016/j.envpol.2017.10.095	184	-265000	138000	277000	277000	415000	818000	553000	391000	2	184	553000	1	2
Mollusca	*Mytilus galloprovincialis*	13400	Fitness	Body Condition	Marine	10.3390/ani11082317	6700	-6170	13400	20100	20100	26800	46400	33500	19000	2	6700	33500	1	2
Echinoderm	*Paracentrotus lividus*	117000000	Fitness	Mortality	Marine	10.1016/j.jhazmat.2018.07.101	100000000	68300000	117000000	134000000	134000000	151000000	199000000	167000000	47300000	2	100000000	167000000	1	2
Crustacea	*Parvocalanus crassirostris*	474000	Fitness	Reproduction	Marine	10.1016/j.ecoenv.2017.03.029	474000	474000	474000	474000	474000	474000	474000	474000	0	2	474000	474000	1	2
Crustacea	*Tigriopus fulvus*	78200	Fitness	Mortality	Marine	10.1016/j.jhazmat.2018.07.101	39100	-36000	78200	117000	117000	156000	271000	196000	111000	2	39100	196000	1	2
Crustacea	*Tigriopus japonicus*	3720	Fitness	Reproduction	Marine	10.1021/es401932b	3720	3720	3720	3720	3720	3720	3720	3720	0	2	3720	3720	1	1
Echinoderm	*Tripneustes gratilla*	16600	Fitness	Growth	Marine	0.1021/es404295e	14700	11200	16600	18400	18400	20300	25700	22100	5210	2	14700	22100	1	2
Echinoderm	*Pseudechinus huttoni*	147	Fitness	Body Condition	Marine	10.1016/j.marpolbul.2021.112369	73.7	-67.8	147	221	221	295	510	369	209	2	73.7	369	1	2

Table A2.7. *Predicted species sensitivity distributions (SSDs) with associated uncertainties for food dilution-based toxicity (ERM: volume), expressed as particle number concentrations.*

Hazard Concentration (%)	Estimated Mean Concentration Particles/mL	Standard Error Particles/mL	Lower 95% Confidence Limit	Upper 95% Confidence Limit	Distribution	Proportion of Data Sets Successfully Fitted
1	0.0000369	0.00521	0.00000214	0.0132	average	1
2	0.000103	0.0153	0.00000531	0.0392	average	1
3	0.000217	0.0334	0.0000101	0.0861	average	1
4	0.000399	0.0609	0.0000172	0.157	average	1
5	0.000674	0.0997	0.0000276	0.255	average	1
6	0.00107	0.151	0.0000422	0.387	average	1
7	0.00163	0.218	0.0000625	0.557	average	1
8	0.00239	0.303	0.0000902	0.771	average	1
9	0.0034	0.408	0.000128	1.04	average	1
10	0.00471	0.537	0.000177	1.36	average	1
11	0.0064	0.692	0.000242	1.76	average	1
12	0.00852	0.879	0.000327	2.23	average	1
13	0.0112	1.1	0.000436	2.79	average	1
14	0.0145	1.36	0.000576	3.45	average	1
15	0.0185	1.67	0.000754	4.24	average	1
16	0.0234	2.04	0.000979	5.15	average	1
17	0.0294	2.46	0.00126	6.22	average	1
18	0.0365	2.95	0.00162	7.46	average	1
19	0.0451	3.52	0.00206	8.9	average	1
20	0.0553	4.17	0.00261	10.6	average	1
21	0.0674	4.93	0.00329	12.5	average	1
22	0.0818	5.81	0.00413	14.7	average	1
23	0.0987	6.81	0.00516	17.2	average	1
24	0.119	7.96	0.0063	20.1	average	1
25	0.142	9.28	0.00764	23.5	average	1
26	0.17	10.8	0.00925	27.3	average	1
27	0.202	12.5	0.0112	31.6	average	1
28	0.241	14.5	0.0135	36.6	average	1
29	0.286	16.8	0.0163	42.4	average	1
30	0.339	19.4	0.0195	48.9	average	1
31	0.401	22.4	0.0232	56.4	average	1
32	0.475	25.8	0.0275	65	average	1
33	0.562	29.8	0.0327	74.8	average	1
34	0.665	34.3	0.0388	86.1	average	1
35	0.787	39.5	0.0461	99	average	1
36	0.932	45.4	0.0547	114	average	1
37	1.1	52.3	0.0648	131	average	1
38	1.31	60.3	0.0767	150	average	1
39	1.56	69.5	0.091	173	average	1
40	1.85	80.2	0.108	199	average	1
41	2.2	92.5	0.126	229	average	1
42	2.62	107	0.147	264	average	1
43	3.12	124	0.171	306	average	1
44	3.73	143	0.199	354	average	1
45	4.45	166	0.23	410	average	1
46	5.31	193	0.266	477	average	1
47	6.35	225	0.309	555	average	1
48	7.6	262	0.359	646	average	1
49	9.08	306	0.417	755	average	1
50	10.9	358	0.482	884	average	1
51	13	420	0.556	1040	average	1
52	15.5	495	0.641	1220	average	1
53	18.6	584	0.744	1440	average	1
54	22.2	690	0.866	1700	average	1
55	26.5	819	0.999	2020	average	1
56	31.6	975	1.16	2400	average	1
57	37.7	1160	1.35	2870	average	1
58	44.9	1390	1.59	3440	average	1
59	53.5	1680	1.88	4140	average	1
60	63.6	2020	2.23	5000	average	1
61	75.7	2450	2.66	6060	average	1
62	89.9	2980	3.18	7380	average	1
63	107	3650	3.83	9020	average	1
64	126	4470	4.64	11100	average	1
65	150	5520	5.64	13700	average	1
66	177	6840	6.88	17000	average	1
67	210	8530	8.43	21200	average	1
68	249	10700	10.3	26600	average	1
69	294	13500	12.7	33600	average	1
70	348	17100	15.6	42800	average	1
71	412	21900	19.2	54800	average	1
72	488	28200	23.7	70700	average	1
73	578	36500	29.2	91900	average	1
74	687	47800	36	120000	average	1
75	816	63100	44.3	159000	average	1
76	973	84100	54.5	213000	average	1
77	1160	113000	67	287000	average	1
78	1400	154000	82.4	392000	average	1
79	1680	213000	101	543000	average	1
80	2040	298000	124	761000	average	1
81	2500	424000	153	1080000	average	1
82	3090	612000	187	1570000	average	1
83	3870	901000	230	2320000	average	1
84	4910	1350000	282	3500000	average	1
85	6350	2090000	347	5410000	average	1
86	8410	3300000	429	8590000	average	1
87	11500	5400000	532	14100000	average	1
88	16200	9180000	664	24000000	average	1
89	23800	16400000	838	42500000	average	1
90	36900	31000000	1070	79500000	average	1
91	61100	63600000	1390	158000000	average	1
92	109000	147000000	1820	355000000	average	1
93	216000	408000000	2550	986000000	average	1
94	484000	1460000000	3980	3820000000	average	1
95	1280000	7230000000	7390	19300000000	average	1
96	4250000	54600000000	17900	1.43E+11	average	1
97	20300000	7.51E+11	64300	1.9E+12	average	1
98	184000000	2.98E+13	437000	7.38E+13	average	1
99	7990000000	1.54E+16	8670000	3.79E+16	average	1

Table A2.8 *Predicted species sensitivity distributions (SSDs) with associated uncertainties for food dilution-based toxicity (ERM: volume), expressed as particle mass concentrations.*

Hazard Concentration (%)	Estimated Mean Concentration Particles/mL	Standard Error µg/mL	Lower 95% Confidence Limit	Upper 95% Confidence Limit	Distribution	Proportion of Data Sets Successfully Fitted
1	0.00607	0.858	0.000351	2.16	average	1
2	0.017	2.52	0.000873	6.45	average	1
3	0.0357	5.49	0.00166	14.2	average	1
4	0.0657	10	0.00284	25.8	average	1
5	0.111	16.4	0.00454	42	average	1
6	0.177	24.9	0.00694	63.6	average	1
7	0.269	35.9	0.0103	91.5	average	1
8	0.394	49.8	0.0149	127	average	1
9	0.56	67.1	0.021	170	average	1
10	0.776	88.2	0.0292	224	average	1
11	1.05	114	0.0399	289	average	1
12	1.4	144	0.0538	366	average	1
13	1.84	181	0.0718	458	average	1
14	2.39	224	0.0949	568	average	1
15	3.05	275	0.124	696	average	1
16	3.86	334	0.161	846	average	1
17	4.84	404	0.208	1020	average	1
18	6.02	484	0.267	1230	average	1
19	7.43	578	0.34	1460	average	1
20	9.11	686	0.43	1730	average	1
21	11.1	810	0.542	2050	average	1
22	13.5	953	0.68	2410	average	1
23	16.3	1120	0.851	2830	average	1
24	19.5	1310	1.04	3310	average	1
25	23.4	1520	1.26	3850	average	1
26	28	1770	1.52	4480	average	1
27	33.3	2060	1.84	5200	average	1
28	39.6	2380	2.23	6020	average	1
29	47	2760	2.69	6960	average	1
30	55.8	3190	3.21	8040	average	1
31	66	3680	3.82	9270	average	1
32	78.2	4240	4.54	10700	average	1
33	92.5	4890	5.39	12300	average	1
34	109	5630	6.4	14100	average	1
35	130	6480	7.59	16300	average	1
36	153	7470	9.01	18700	average	1
37	182	8600	10.7	21500	average	1
38	216	9910	12.6	24700	average	1
39	256	11400	15	28400	average	1
40	304	13200	17.8	32700	average	1
41	362	15200	20.8	37700	average	1
42	431	17600	24.2	43500	average	1
43	514	20300	28.2	50300	average	1
44	613	23500	32.7	58200	average	1
45	732	27300	37.9	67500	average	1
46	875	31700	43.9	78400	average	1
47	1050	36900	50.9	91200	average	1
48	1250	43000	59.2	106000	average	1
49	1490	50300	68.7	124000	average	1
50	1790	58900	79.5	145000	average	1
51	2140	69100	91.5	170000	average	1
52	2560	81300	106	201000	average	1
53	3060	96000	122	237000	average	1
54	3650	114000	143	280000	average	1
55	4360	135000	164	332000	average	1
56	5200	160000	190	395000	average	1
57	6200	191000	222	472000	average	1
58	7390	229000	261	566000	average	1
59	8800	276000	309	680000	average	1
60	10500	333000	367	822000	average	1
61	12400	403000	437	996000	average	1
62	14800	490000	524	1210000	average	1
63	17500	599000	631	1480000	average	1
64	20800	736000	764	1820000	average	1
65	24700	908000	929	2250000	average	1
66	29200	1130000	1130	2790000	average	1
67	34600	1400000	1390	3490000	average	1
68	40900	1760000	1700	4380000	average	1
69	48400	2220000	2090	5530000	average	1
70	57300	2820000	2570	7030000	average	1
71	67800	3600000	3170	9010000	average	1
72	80300	4630000	3900	11600000	average	1
73	95100	6010000	4810	15100000	average	1
74	113000	7860000	5920	19800000	average	1
75	134000	10400000	7290	26200000	average	1
76	160000	13800000	8970	35000000	average	1
77	191000	18600000	11000	47200000	average	1
78	230000	25400000	13600	64500000	average	1
79	277000	35100000	16700	89300000	average	1
80	336000	49000000	20500	125000000	average	1
81	411000	69700000	25100	178000000	average	1
82	508000	101000000	30800	258000000	average	1
83	636000	148000000	37800	382000000	average	1
84	807000	223000000	46500	576000000	average	1
85	1040000	343000000	57200	889000000	average	1
86	1380000	544000000	70600	1410000000	average	1
87	1880000	889000000	87500	2320000000	average	1
88	2660000	1510000000	109000	3940000000	average	1
89	3910000	2690000000	138000	6990000000	average	1
90	6070000	5090000000	176000	13100000000	average	1
91	10100000	10500000000	228000	26000000000	average	1
92	18000000	24200000000	299000	58400000000	average	1
93	35600000	66800000000	419000	1.61E+11	average	1
94	79500000	2.38E+11	655000	6.23E+11	average	1
95	210000000	1.18E+12	1220000	3.14E+12	average	1
96	699000000	8.88E+12	2940000	2.32E+13	average	1
97	3330000000	1.22E+14	10600000	3.1E+14	average	1
98	30300000000	4.83E+15	71900000	1.2E+16	average	1
99	1.31E+12	2.5E+18	1420000000	6.13E+18	average	1

Table A2.9 *Predicted species sensitivity distributions (SSDs) with associated uncertainties for translocation-based toxicity (ERM: surface area), expressed as particle number concentrations.*

Hazard Concentration (%)	Estimated Mean Concentration Particles/mL	Standard Error Particles/mL	Lower 95% Confidence Limit	Upper 95% Confidence Limit	Distribution	Proportion of Data Sets Successfully Fitted
1	0.229	3.16	0.0233	8.65	average	1
2	0.44	5.36	0.0462	14.7	average	1
3	0.698	7.7	0.0752	21.1	average	1
4	1.01	10.2	0.111	28	average	1
5	1.37	12.9	0.155	35.4	average	1
6	1.8	15.9	0.207	43.3	average	1
7	2.28	19	0.269	51.8	average	1
8	2.83	22.3	0.342	60.9	average	1
9	3.46	25.8	0.427	70.6	average	1
10	4.16	29.6	0.524	81	average	1
11	4.93	33.6	0.636	92	average	1
12	5.8	37.8	0.764	104	average	1
13	6.75	42.3	0.908	116	average	1
14	7.81	47.1	1.07	129	average	1
15	8.96	52.2	1.26	143	average	1
16	10.2	57.6	1.46	158	average	1
17	11.6	63.3	1.7	173	average	1
18	13.1	69.4	1.96	189	average	1
19	14.8	75.9	2.25	207	average	1
20	16.6	82.8	2.58	225	average	1
21	18.5	90.2	2.94	244	average	1
22	20.7	98	3.34	266	average	1
23	23	106	3.79	289	average	1
24	25.5	115	4.28	314	average	1
25	28.2	125	4.84	340	average	1
26	31.2	135	5.45	368	average	1
27	34.4	145	6.13	398	average	1
28	37.8	157	6.89	430	average	1
29	41.6	169	7.73	465	average	1
30	45.6	182	8.66	503	average	1
31	50.1	197	9.69	543	average	1
32	54.8	212	10.8	586	average	1
33	60	228	12.1	631	average	1
34	65.7	246	13.5	681	average	1
35	71.8	264	15.1	733	average	1
36	78.4	285	16.9	790	average	1
37	85.6	307	18.8	851	average	1
38	93.4	330	21	917	average	1
39	102	356	23.4	988	average	1
40	111	384	26	1060	average	1
41	121	414	28.9	1150	average	1
42	132	447	31.7	1240	average	1
43	144	482	34.7	1330	average	1
44	157	521	38	1440	average	1
45	171	564	41.4	1550	average	1
46	186	610	45	1680	average	1
47	203	661	48.9	1820	average	1
48	221	717	53.3	1970	average	1
49	241	779	58	2130	average	1
50	263	847	63.2	2310	average	1
51	287	922	68.6	2510	average	1
52	313	1010	74.6	2730	average	1
53	341	1100	81.1	2970	average	1
54	373	1200	88.1	3240	average	1
55	407	1320	95	3540	average	1
56	445	1450	102	3870	average	1
57	487	1590	111	4240	average	1
58	532	1750	119	4650	average	1
59	583	1940	129	5120	average	1
60	639	2150	140	5650	average	1
61	700	2390	151	6250	average	1
62	768	2660	164	6930	average	1
63	844	2970	178	7710	average	1
64	928	3330	194	8600	average	1
65	1020	3750	212	9620	average	1
66	1130	4230	232	10800	average	1
67	1240	4790	254	12200	average	1
68	1370	5450	278	13900	average	1
69	1520	6220	306	15900	average	1
70	1690	7140	337	18200	average	1
71	1870	8230	373	21000	average	1
72	2080	9540	413	24300	average	1
73	2320	11100	460	28300	average	1
74	2600	13000	513	33100	average	1
75	2920	15400	574	39100	average	1
76	3280	18300	645	46400	average	1
77	3710	21800	727	55500	average	1
78	4200	26300	822	67000	average	1
79	4780	32000	936	81600	average	1
80	5470	39400	1070	100000	average	1
81	6300	48900	1230	125000	average	1
82	7290	61300	1420	157000	average	1
83	8500	78000	1640	200000	average	1
84	9990	101000	1920	258000	average	1
85	11900	132000	2270	339000	average	1
86	14200	176000	2720	454000	average	1
87	17300	240000	3300	621000	average	1
88	21400	336000	4060	870000	average	1
89	27000	483000	5100	1260000	average	1
90	34700	717000	6550	1870000	average	1
91	46000	1110000	8610	2910000	average	1
92	63200	1810000	11500	4760000	average	1
93	90800	3140000	15800	8280000	average	1
94	139000	5920000	23000	15700000	average	1
95	231000	12500000	35200	33300000	average	1
96	436000	31300000	56000	83200000	average	1
97	1010000	102000000	103000	270000000	average	1
98	3340000	538000000	248000	1410000000	average	1
99	27000000	9550000000	1200000	24900000000	average	1

Table A2.10. *Predicted species sensitivity distributions (SSDs) with associated uncertainties for translocation-based toxicity (ERM: surface area), expressed as particle mass concentrations.*

Hazard Concentration (%)	Estimated Mean Concentration µg/mL	Standard Error µg/mL	Lower 95% Confidence Limit	Upper 95% Confidence Limit	Distribution	Proportion of Data Sets Successfully Fitted
1	37.6	519	3.82	1420	average	1
2	72.3	880	7.58	2410	average	1
3	115	1270	12.3	3470	average	1
4	166	1680	18.2	4600	average	1
5	225	2130	25.4	5810	average	1
6	295	2610	34	7110	average	1
7	375	3120	44.2	8510	average	1
8	466	3660	56.2	10000	average	1
9	568	4240	70.1	11600	average	1
10	683	4860	86.1	13300	average	1
11	811	5520	104	15100	average	1
12	953	6220	125	17000	average	1
13	1110	6960	149	19100	average	1
14	1280	7750	176	21200	average	1
15	1470	8580	207	23500	average	1
16	1680	9470	241	25900	average	1
17	1910	10400	279	28400	average	1
18	2160	11400	322	31100	average	1
19	2430	12500	370	34000	average	1
20	2730	13600	423	36900	average	1
21	3050	14800	483	40100	average	1
22	3400	16100	549	43700	average	1
23	3780	17500	622	47500	average	1
24	4190	18900	704	51600	average	1
25	4640	20500	795	55900	average	1
26	5120	22200	896	60500	average	1
27	5650	23900	1010	65400	average	1
28	6220	25800	1130	70800	average	1
29	6830	27900	1270	76600	average	1
30	7500	30000	1420	82700	average	1
31	8230	32400	1590	89300	average	1
32	9020	34900	1780	96400	average	1
33	9870	37500	1990	104000	average	1
34	10800	40400	2230	112000	average	1
35	11800	43500	2490	121000	average	1
36	12900	46900	2780	130000	average	1
37	14100	50500	3090	140000	average	1
38	15300	54400	3450	151000	average	1
39	16700	58600	3840	163000	average	1
40	18300	63200	4280	175000	average	1
41	19900	68100	4750	189000	average	1
42	21700	73500	5210	204000	average	1
43	23600	79400	5710	220000	average	1
44	25800	85800	6260	237000	average	1
45	28100	92800	6800	256000	average	1
46	30600	100000	7400	277000	average	1
47	33300	109000	8050	299000	average	1
48	36300	118000	8760	324000	average	1
49	39600	128000	9540	351000	average	1
50	43200	139000	10400	381000	average	1
51	47100	152000	11300	413000	average	1
52	51400	166000	12300	449000	average	1
53	56100	181000	13300	489000	average	1
54	61300	198000	14500	534000	average	1
55	66900	217000	15600	583000	average	1
56	73200	238000	16800	638000	average	1
57	80000	262000	18200	699000	average	1
58	87500	289000	19600	767000	average	1
59	95800	320000	21200	845000	average	1
60	105000	354000	23000	932000	average	1
61	115000	394000	24900	1030000	average	1
62	126000	438000	27000	1140000	average	1
63	139000	490000	29400	1270000	average	1
64	153000	549000	32000	1420000	average	1
65	168000	618000	34900	1590000	average	1
66	185000	697000	38100	1780000	average	1
67	204000	790000	41700	2010000	average	1
68	226000	899000	45800	2290000	average	1
69	250000	1030000	50400	2610000	average	1
70	277000	1180000	55500	3000000	average	1
71	308000	1360000	61400	3450000	average	1
72	343000	1570000	68100	4000000	average	1
73	382000	1830000	75700	4660000	average	1
74	428000	2150000	84400	5460000	average	1
75	480000	2540000	94500	6440000	average	1
76	540000	3010000	106000	7650000	average	1
77	610000	3600000	120000	9150000	average	1
78	691000	4350000	135000	11000000	average	1
79	787000	5290000	154000	13400000	average	1
80	900000	6500000	176000	16500000	average	1
81	1040000	8070000	203000	20500000	average	1
82	1200000	10100000	233000	25800000	average	1
83	1400000	12900000	271000	32900000	average	1
84	1650000	16600000	317000	42600000	average	1
85	1950000	21800000	375000	55900000	average	1
86	2350000	29100000	449000	74900000	average	1
87	2850000	39700000	544000	102000000	average	1
88	3530000	55500000	671000	144000000	average	1
89	4440000	79700000	842000	207000000	average	1
90	5720000	119000000	1080000	309000000	average	1
91	7580000	184000000	1420000	480000000	average	1
92	10400000	299000000	1890000	785000000	average	1
93	15000000	519000000	2610000	1370000000	average	1
94	22900000	979000000	3800000	2590000000	average	1
95	38200000	2070000000	5810000	5500000000	average	1
96	72000000	5180000000	9220000	13800000000	average	1
97	166000000	16800000000	17000000	44700000000	average	1
98	552000000	89000000000	41000000	2.33E+11	average	1
99	4470000000	1.58E+12	199000000	4.12E+12	average	1

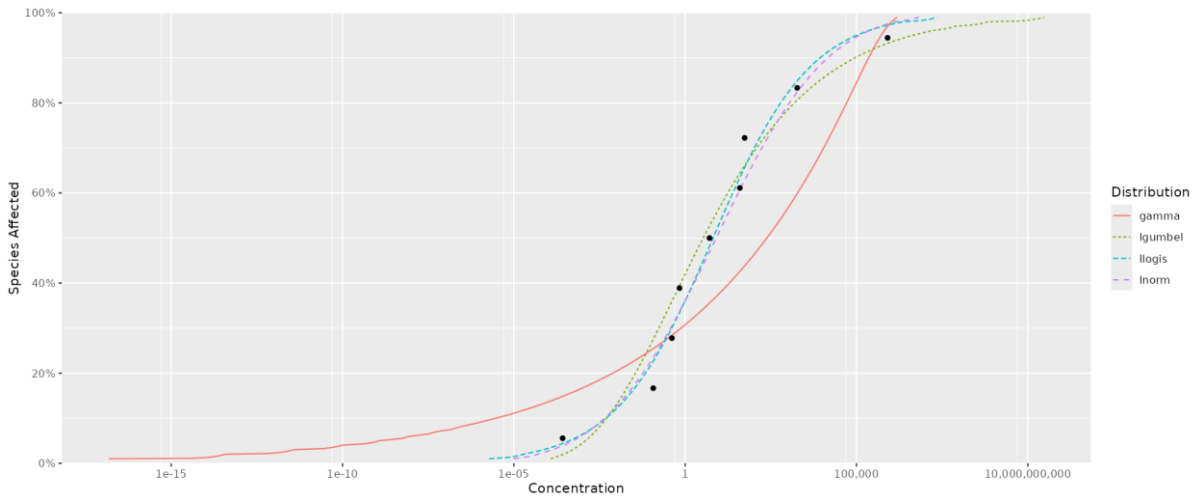

Toxicity of Microplastics Explorer 2.0									
Distributions and their according fit paramaters are displayed									
	Distribution	Anderson-Darlin	Kolmogorv Smirno	Cramer-Von Mises	Akaike's Information Criteria	Akaike's Information Criteria (Corrected for sample size)	Bayesian Information Criteria	delta	weight
1	lnorm	0.2073	0.1499	0.02855	98.96	101	99.35	0	0.358
2	llogis	0.1728	0.1212	0.02271	98.99	101	99.39	0.032	0.352
3	lgumbel	0.26	0.1642	0.03563	99.52	101.5	99.91	0.555	0.271
4	gamma	1.085	0.3397	0.2256	104.8	106.8	105.2	5.803	0.02

Figure A2.14. *SSDs fitted to minimum observed effect concentrations for food dilution-based MNP toxicity (ERM: volume, expressed as particle number concentrations, particles/mL), comparing log-normal, log-logistic, log-Gumbel, and gamma models along with their corresponding fit parameters.*

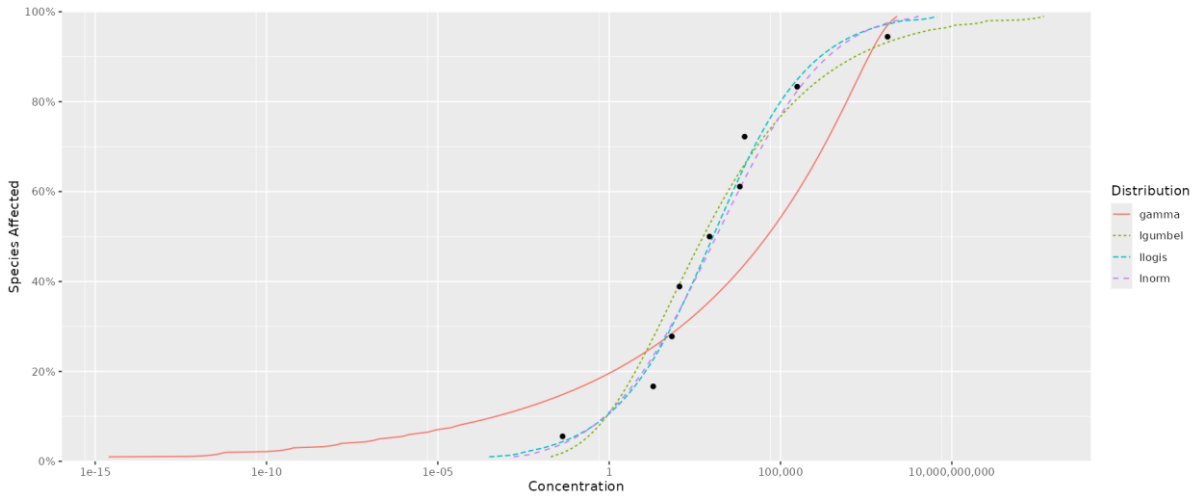

Toxicity of Microplastics Explorer 2.0									
Distributions and their according fit paramaters are displayed									
	Distribution	Anderson-Darlin	Kolmogorv Smirno	Cramer-Von Mises	Akaike's Information Criteria	Akaike's Information Criteria (Corrected for sample size)	Bayesian Information Criteria	delta	weight
1	lnorm	0.2073	0.1499	0.02857	190.8	192.8	191.2	0	0.358
2	llogis	0.1729	0.1211	0.0227	190.8	192.8	191.2	0.032	0.352
3	lgumbel	0.26	0.1642	0.03563	191.4	193.4	191.8	0.555	0.271
4	gamma	1.085	0.3397	0.2256	196.6	198.6	197	5.803	0.02

Figure A2.15. *SSDs fitted to minimum observed effect concentrations for food dilution-based MNP toxicity (ERM: volume, expressed as particle mass concentrations, µg/mL), comparing log-normal, log-logistic, log-Gumbel, and gamma models along with their corresponding fit parameters.*

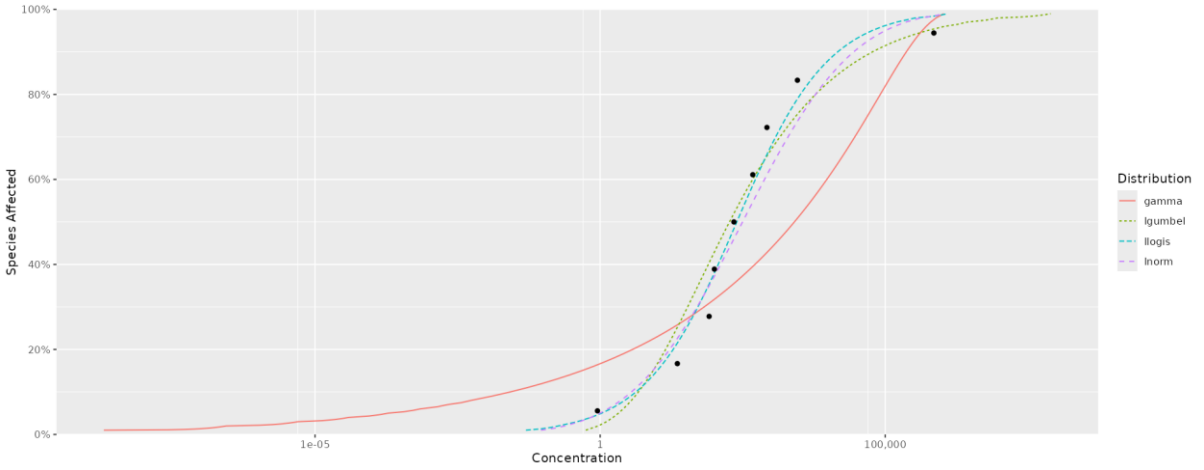

Toxicity of Microplastics Explorer 2.0									
Distributions and their according fit paramaters are displayed									
	Distribution	Anderson-Darling	Kolmogorv Smirnov	Cramer-Von Mises	Akaike's Information Criteria	Akaike's Information Criteria (Corrected for sample size)	Bayesian Information Criteria	delta	weight
1	llogis	0.236	0.1315	0.02615	155.1	157.1	155.5	0	0.374
2	lgumbel	0.3103	0.1818	0.04696	155.4	157.4	155.8	0.26	0.328
3	lnorm	0.3359	0.1671	0.04754	155.6	157.6	156	0.5	0.291
4	gamma	1.393	0.3803	0.2958	163.2	165.2	163.6	8.04	0.007

Figure A2.16. *SSDs fitted to minimum observed effect concentrations for translocation-based MNP toxicity (ERM: surface area, expressed as particle number concentrations, particles/mL), comparing log-normal, log-logistic, log-Gumbel, and gamma models along with their corresponding fit parameters.*

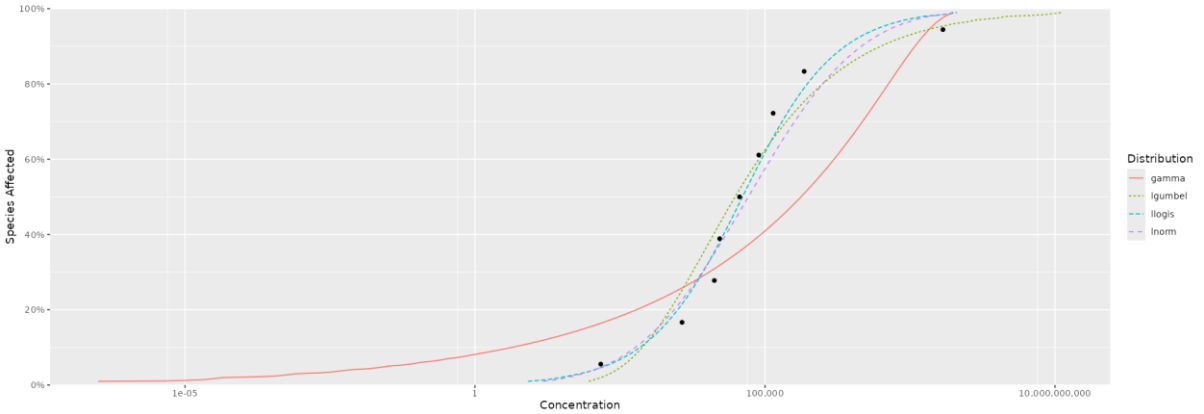

Toxicity of Microplastics Explorer 2.0									
Distributions and their according fit paramaters are displayed									
	Distribution	Anderson-Darling	Kolmogorv Smirnov	Cramer-Von Mises	Akaike's Information Criteria	Akaike's Information Criteria (Corrected for sample size)	Bayesian Information Criteria	delta	weight
1	llogis	0.236	0.1316	0.02616	247	249	247.4	0	0.374
2	lgumbel	0.3102	0.1817	0.04698	247.2	249.2	247.6	0.26	0.328
3	lnorm	0.3358	0.167	0.04752	247.5	249.5	247.9	0.5	0.291
4	gamma	1.392	0.3801	0.2955	255	257	255.4	8.04	0.007

Figure A2.17. *SSDs fitted to minimum observed effect concentrations for translocation-based MNP toxicity (ERM: surface area, expressed as particle mass concentrations, µg/mL), comparing log-normal, log-logistic, log-Gumbel, and gamma models along with their corresponding fit parameters.*

MNP abundance and characteristics in marine environmental matrices

Table A2.11. *Micro- and nanoplastic abundance, characteristics, and polymer composition in different marine environmental matrices.*

Sample Types/Location	Reported Concentrations	Particle Size	Particle Type	References
Seawater				
Seawater (North Atlantic)	500000–7000000 pieces/km^2	20–999 µm	PE (73%), PP (13%), PVC (8%), PS (2%, and PET (1%)	(Ter Halle et al., 2017)
Seawater (North Atlantic)	10000–250000 pieces/km^2	1000–5000 µm	PE (90%), PP (10%)	(Ter Halle et al., 2017)
Seawater (North Sea)	0.1–254.4 particles/m^3	<100 µm (86% of particles)	PP (26.7%), PE (14%), PA (11%), Polyester/PET (9%), acrylates/PUR/varnish (17.5%), PVC (5%), PS (1.3), PE chlorinated (6%), Rubber type 3 (9%) Other polymer types contributed less than 1% (in descending order): CMC, poly-caprolactone, EVA, rubber type 1, POM, PE oxidized, PC, nitrile rubber, rubber type 2, and polychloroprene	(Lorenz et al., 2019)
Seawater (Northeast Pacific Ocean)	8–9200 particles/m^3	<100 µm (30.8% of particles)	Not available	(Desforges et al., 2014)
Seawater (German North Sea)	23–9700 particles/m^3	11–500 µm	Acrylates/PUR/varnish (66.7%), rubber type 3 (9.8%), PP (6%)	(Roscher et al., 2021)
Seawater (German North Sea)	0.01–0.98 particles/m^3	500–5000 µm	PE (63.1%), PP (24.6%), PS (5.8%),	(Roscher et al., 2021)
Surface water (Western Scheldt)	0–113 particles/m^3	<1000 µm (approx. 80% of particles)	PP, PET, PS, PA and PVC	(Z. Liu et al., 2022)
Surface water (South Funen Archipelago, Baltic Sea)	0.045 particles/m^3	300 µm–630 µm	Not available	(Tamminga et al., 2018)
Surface water (South Funen Archipelago, Baltic Sea)	0.006 particles/m^3	630 µm–1000 µm	Not available	(Tamminga et al., 2018)
Surface water (Yangtze Estuary, China)	500–10,200 particles/m^3	>500 µm–1000 µm (67% of particles)	Not available	(S. Zhao et al., 2014)
Surface water (East China Sea)	0.030–0.455 particles/m^3	>500–1000 µm (35.4% of particles)	Not available	(S. Zhao et al., 2014)
Surface water (San Francisco Bay, USA)	15,000–2,000,000 particle/km^2	355–1000 µm (94% of particles)	Not available	(Sutton et al., 2016)
Seawater (Coast of South Africa)	258–1215 particles/m^3	80–5000 µm	Not available	(H. A. Nel & Froneman, 2015)

Seawater (Sweden)	0–70.3 particles/m^3	50 µm	PE (65%) and PP (21%)	(Schönlau et al., 2020)
Seawater (Sweden)	0–10.5 particles/m^3	≥300 µm		(Schönlau et al., 2020)
Stratified seawater (Baltic Sea)	11–79 particles/m^3	≥ 174 µm	PET (25%), PA (9.1%), PE (9.1), PP (9.1), PS (4.5) PVC (2.3), PMMA (2.3%), PTR (2.3%), etc.	(Zobkov et al., 2019)
Surface water (Sweden)	15600–618000 particles/km^2 or 0.19 – 7.73 particles/m^3	≥335 µm	PP (23%) and PE (24%)	(Gewert et al., 2017)
Sea water column (Baltic Sea)	0.09±0.19–0.93± 0.84 particles/L	500–5000 µm	Not available	(Bagaev et al., 2018)
Sea water (Atlantic Ocean)	13–501 particles/m^3	<40 µm (64% of particles)	PE (42%), PP (6%), PS (4%), PA (11%), PU (3%), PVC (1.8%), PES (6%)	(Enders et al., 2015)
Sediment				
Sediment (North Sea)	2.8–1188.8 particles/kg	<100 µm (98% of particles)	Acrylates/PUR/varnish (21%), PE (4%), PE chlorinated (5%), PP (11%), PS (1.5%) PA (9.5%), PVC (9.5%), CMC (2.5%), Polyester/PET (11%), polychloroprene (11%), Rubber type 3 (9%), Nitrile rubber (1.3%) Other polymer types contributed less than 1% (in descending order): EVA, poly-caprolactone, rubber type 1, PE oxidized, polyisoprene, chlorinated, acrylonitrile butadiene, PC, and PSU	(Lorenz et al., 2019)
Sediment (Dutch North Sea Coast)	100–3600 particles/kg	10–300 µm (55% of particles)	Not available	(Leslie et al., 2017)
Sediment (Western Scheldt)	15–413 particles/kg	<1000 µm (approx. 80% of particles)	PP, PET, PS, PA and PVC	(Z. Liu et al., 2022)
Seawater (Coast of South Africa)	689–3,308 particles/m^2	65–5000 µm	Not available	(H. A. Nel & Froneman, 2015)

Supplementary Information: Chapter 3

Characterization of the aged micro-and-nanoplastic particles (MNPs)

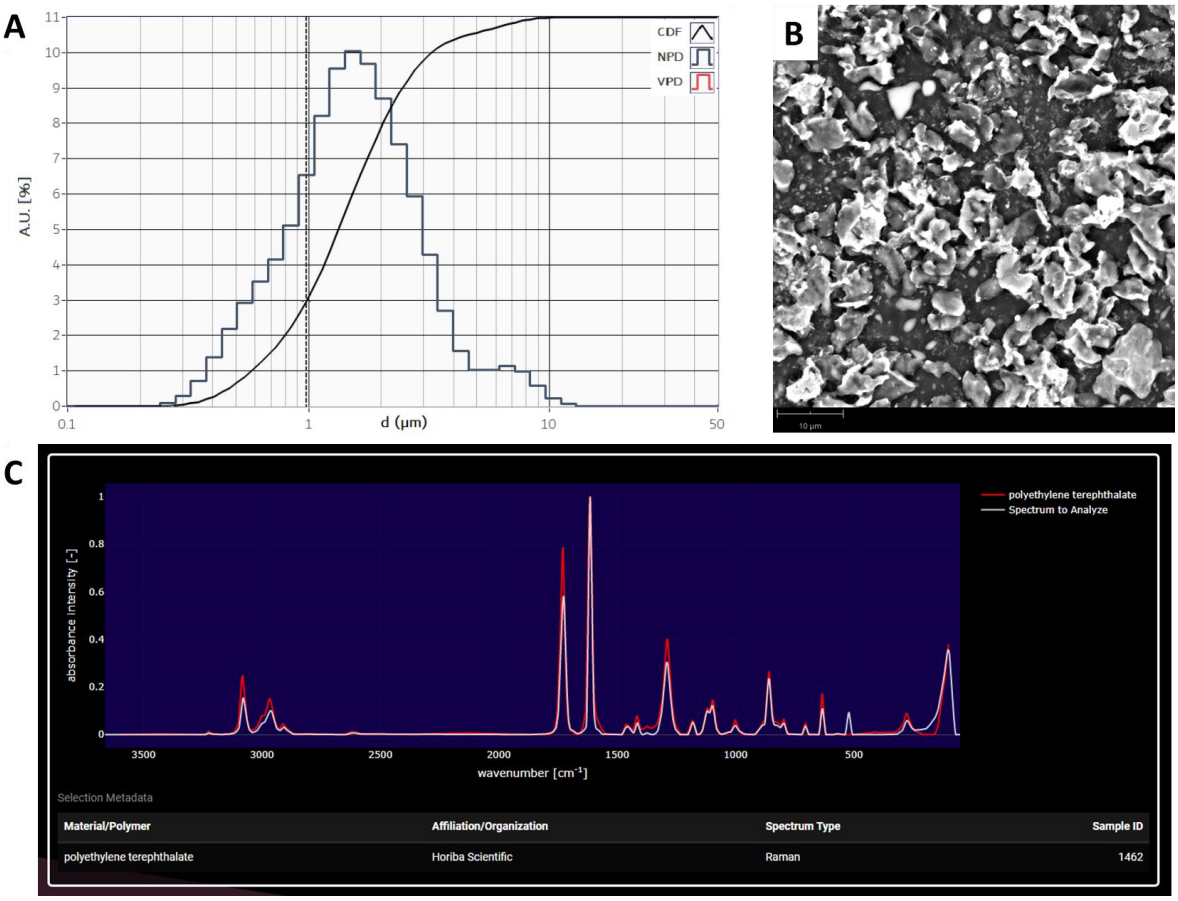

Figure A3.1. *Particle size distribution (A), shape (B), and polymer type (C) of aged PET MNPs analyzed using Single Particle Extinction and Scattering (SPES) technique (ClassizerONE, S1.4.34, EOS), scanning electron microscopy (SEM, Phenom™ ProX) and Raman spectroscopy with Open Specy reference library.* ***Panel A*** *displays the particle size distribution of the aged PET MNPs measured by SPES. The number-based particle size distribution is shown together with the corresponding cumulative distribution function (CDF) as a function of particle diameter (d).* ***Panel B*** *SEM images of the particles captured using a Phenom™ ProX Desktop SEM system. The image, taken at magnifications of 4400x, reveals the weathered and irregular shapes of the particles with evident heterogeneous sizes.* ***Panel C*** *shows the Raman spectrum of the aged PET MNP sample acquired using an inVia™ Qontor® confocal Raman microscope (Renishaw, Wotton-under-Edge, UK) equipped with a 785 nm excitation laser and a 20× objective. PET suspensions were diluted in ethanol (1:3, v/v), deposited onto a silicon wafer, and measured in the dry state after solvent evaporation. The instrument was operated at 10% laser power, with an accumulation time of 1 s, averaging 5 accumulations. The spectrum was compared against the Open Specy reference library, confirming the material as PET with a 0.97 match score relative to the reference spectrum.*

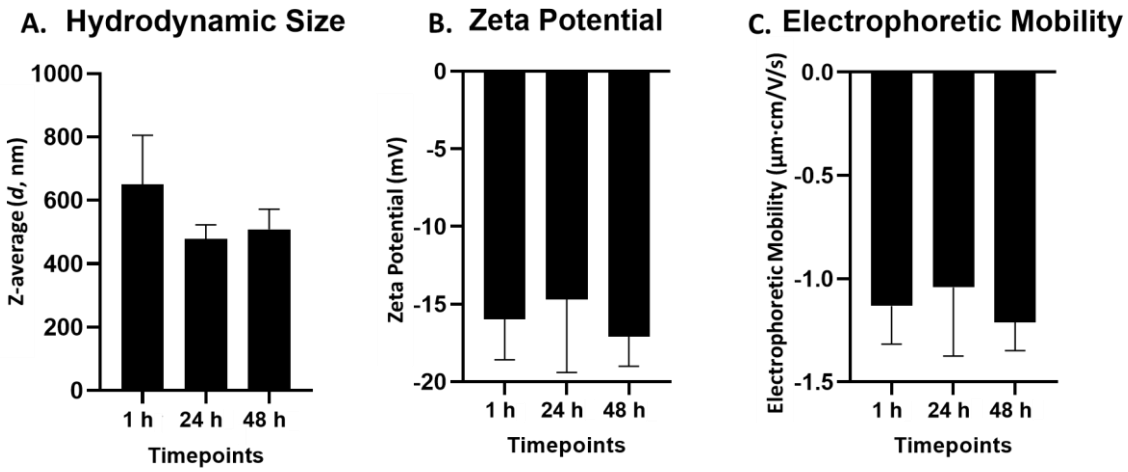

Figure A3.2. *Hydrodynamic size (A), zeta potential (B), and electrophoretic mobility (C) of aged PET MNPs in artificial seawater (pH 8.1) measured over time (1 h, 24 h, and 48 h) using Dynamic Light Scattering. Data are expressed as mean ± standard deviation (n = 3) for each time point.*

Experimental set-up and handling procedure

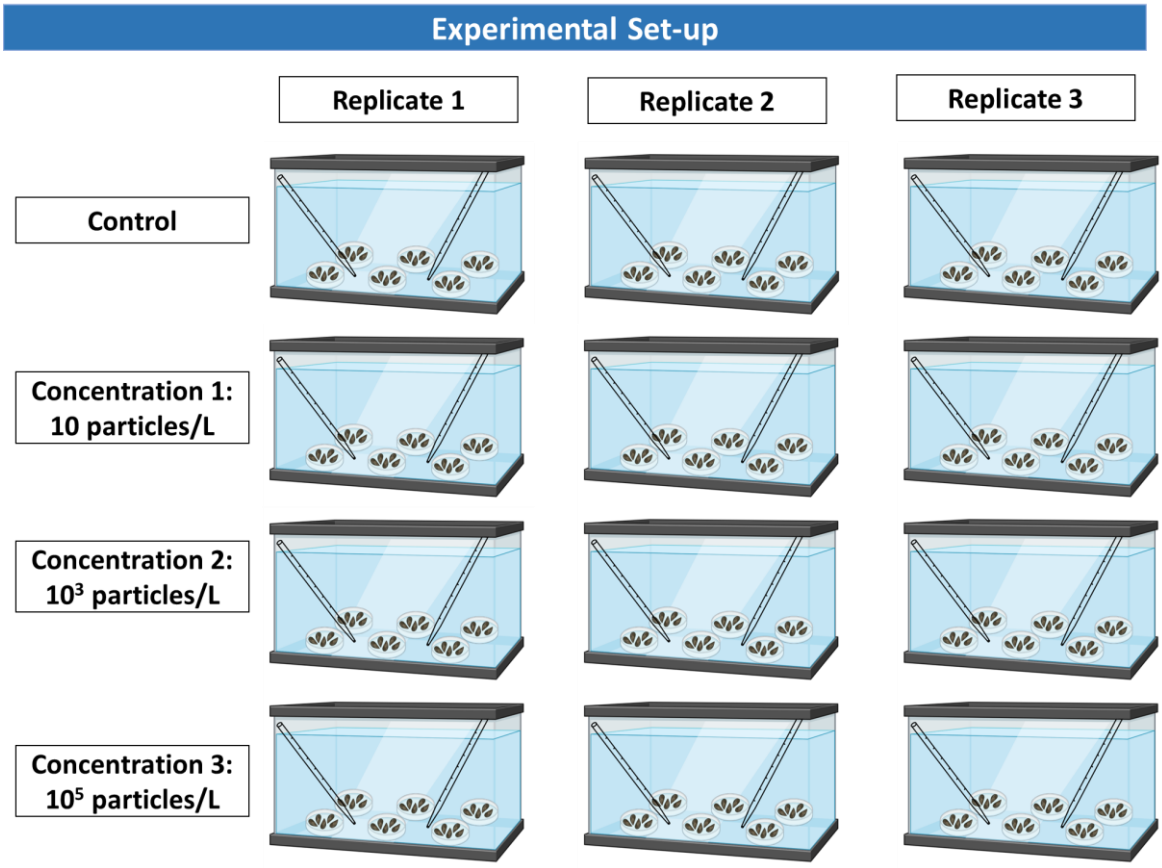

Figure A3.3. *Experimental setup of in vivo exposure of mussels (Mytilus edulis) to aged PET MNPs, including the control and treatment groups with different particle concentrations (10, 10^3, and 10^5 particles/L). The graphical illustration was created using Biorender.com.*

Table A3.1. *Detailed handling procedure for mussel exposure to aged PET MNPs: sampling time points during both exposure and depuration period, number of mussels, water volume, and the volume of aged PET MNP suspension administered at different concentrations.*

Handling Procedure						
	Exposure Period				**Depuration Period**	
Days	1	3	7	14	17	24
Number of mussels per replicate tank	30	25	20	15	10	5
Total volume of ASW added per replicate tank	30 L	25 L	20 L	15 L	15 L	15 L
Treatment	**Volume of aged PET MNP suspension added from the working suspension per replicate tank (10^6 particles/mL)**					
Negative Control	0	0	0	0	0	0
Concentration 1: 10 particles/L	0.3 µL	0.25 µL	0.2 µL	0.15 µL	0	0
Concentration 2: 10^3 particles/L	30 µL	25 µL	20 µL	15 µL	0	0
Concentration 3: 10^5 particles/L	3 mL	2.5 mL	2 mL	1.5 mL	0	0

Quality assurance and control

Table A3.2. *Quality assurance and quality control criteria proposed by De Ruijter et al. (2020).*

Criterion	Score	Explanation
Particle Characterization		
1. Particle size	2	Particle size distribution was measured using a SPES (ClassizerONE S1.4.34, EOS), with data reported in the Supplementary Figure S.1.A.
2. Particle shape	2	Scanning electron microscopy (SEM, Phenom™ ProX) images confirmed the fragmented shapes of the particle (Supplementary Figure S.1.B).
3. Polymer type	2	The polymer type was confirmed using Raman spectroscopy and Open Specy reference library (Supplementary Figure S.1.C).
4. Source of MP	2	Details on the source of the aged PET test particles are provided in the materials and methods section (2.1).
5. Data reporting	2	Age PET MNP concentrations in mass concentration were calculated based on the average diameter of the reported size distribution (1.9 µm) and polymer density (1.38 g/cm³). The corresponding mass concentration ranges are as follows: • C1: 10 particles/L or 0.0495 µg/L • C2 : 10^3 particles/L or 4.956 µg/L • C3: 10^5 particles/L or 495.6 µg/L
Experimental Design		
6. Chemical purity	2	The aged PET particles were suspended in milli-Q water without surfactants.
7. Laboratory preparation	2	All materials used were thoroughly washed with high-quality water (e.g. Milli-Q water). Working solutions (e.g. anesthetic: $MgCl_2$) were filtered (100 nm, Millipore) and sterilized. Exposure experiment was conducted in glass tanks covered with aluminium foil to prevent contamination from the air and was set up in a climate chamber. Sample collection of mussel hemolymph and tissues was conducted within a laminar flow cabinet (only assigned for plastic research). Cotton lab coats were used to avoid microfiber contamination.
8. Verification of background contamination	0	Due to the lack of adequate MNP measurement techniques in complex samples, the background contamination could not be verified.
9. Verification of exposure	0	Due to the lack of adequate MNP measurement techniques in complex samples, the actual exposure concentration could not be verified.
10. Homogeneity of exposure	1	Each exposure tank was equipped with two aeration systems using glass pipettes to ensure constant aeration and to promote uniform particle dispersion.
11. Exposure assessment	0	Due to the lack of adequate MNP measurement techniques in complex samples, the exposure of the organism could not be verified.
12. Replication	2	The experiment was conducted with three replicates.
Applicable to Risk Assessment		
13. Endpoints	1	Immunological and histopathological parameters were measured as endpoints, with a demonstrated causal relationship to the individual-level endpoints (e.g., survival, mortality, growth, and development).

14. Presence of natural (food) particles	2	Test organisms were fed during the experiment with microalgae suspension (*Tetraselmis suecica*).
15. Reporting of effect thresholds	0	Effect thresholds were not reported due to the limited range of test concentrations.
16. Quality of dose–response relationship	0	Only 4 treatment groups, including the negative control treatment.
Ecological Relevance		
17. Concentration range tested	1	Given the lack of measured environmental concentrations (MECs) for micro- and nanoplastics (MNPs), the tested concentration range is primarily based on the modeled scenarios for marine environments (Besseling et al., 2019; Lenz et al., 2016) and reflect the estimated exposure concentrations, assuming the complete degradation of spherical PET particles (Sioen et al., 2024a).
18. Aging and biofouling	1	Aged PET particles were used in this experiment.
19. Diversity of MP tested	2	Aged PET MNPs, with a wide particle size distribution and irregular shape, was used.
20. Exposure time	1	An exposure period of 14 days and a subsequent recovery period of 10 days was used.
Final Score		This experiment achieved a score of **62.5% (25/40)** on the proposed quality assurance and control (QA/QC) criteria, surpassing the reported average score of 44.6% (De Ruijter et al., 2020). Although using MNPs posed analytical challenges that hindered compliance with quality criteria 8, 9, and 11 for background contamination, exposure concentration, and organism exposure, the overall score demonstrates strong quality performance.

Growth parameters

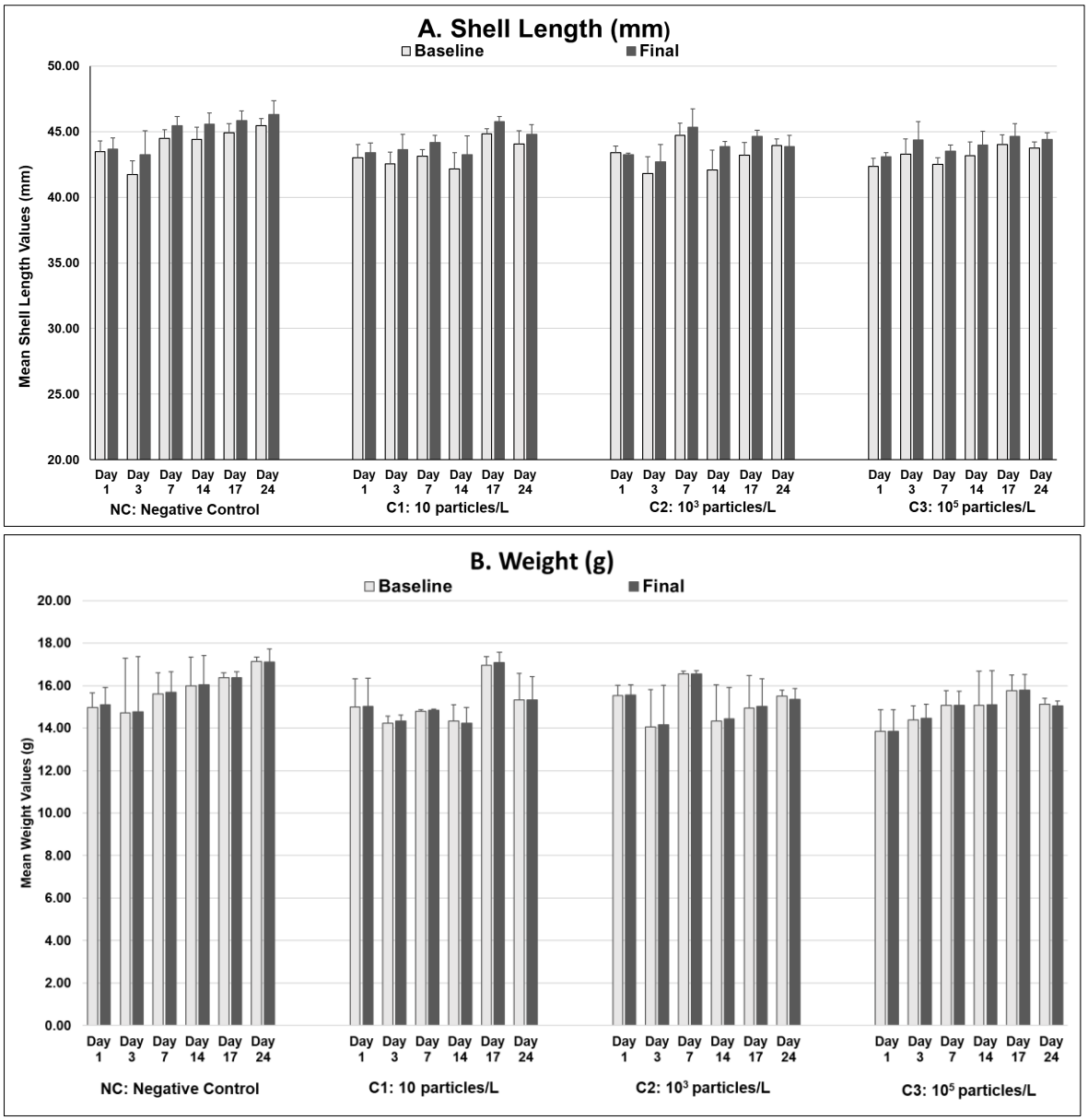

Figure A3.4. *Comparison of mean (A) length (mm) and (B) wet weight (g) between baseline and final values M. edulis exposed to different aged PET MNP concentrations. Measurements were taken at baseline (Day 0), after each exposure period (Day 1, 3, 7, and 14), and depuration (Day 17, 3 days post-exposure and (Day 24, 10 days post-exposure). Data are presented as mean ± standard deviation of three replicates per timepoint (n = 5 mussels per replicate).*

Summary of recently published *in vivo* studies on MNP toxicity

Table A3.3. *Summary of recently published papers evaluating the uptake and effects of pristine and aged micro-and nanoplastic particles.*[1]

Particle type	Particle size	Reported Concentration	Converted Concentration (particles/L)	Test organisms	Max Exposure Time	References
PS	50 nm	1.5 ng/L	2.17×10^{5}	Mussels (*Mytilus galloprovincialis*)	*In vivo* exposure: 21 days	(Capolupo et al., 2021)
		15 ng/L	2.17×10^{6}			
		150 ng/L	2.17×10^{7}			
	3 µm	1.5 ng/L	100			
		15 ng/L	1000			
		150 ng/L	10, 000			
PS-NH_2	50 nm	10 µg/L	1.46×10^{11}	Mussels (*Mytilus galloprovincialis*)	Repeated *in vivo* exposure: 1 day (1st exposure 3 days (depuration) 1 day (2nd exposure)	(Auguste et al., 2020)
PS	2 µm and 6 µm (mixed)	32 µg/L or 2000 microbeads/mL	2.0×10^{6}	Mussels (*Mytilus spp.*)	*In vivo* exposure: 7 days	(Paul-Pont et al., 2016)
Aged PET	1.9 µm	10 particles/mL	10,000	Mussels (*Mytilus edulis*)	*In vitro* exposure: 2 days	(Hara et al., 2024)
		1.0×10^{3} particles/mL	1.0×10^{6}			
		1.0×10^{5} particles/mL	1.0×10^{8}			
	680 nm	10 particles/mL	10,000			
		1.0×10^{3} particles/mL	1.0×10^{6}			
		1.0×10^{5} particles/mL	1.0×10^{8}			

[1] Particle number concentrations per volume are reported in the reference paper. Calculation as applied by (M. Peng et al., 2023): The density (ρ) values of PS, PE, PET, PMMA, and HDPE are 1.05 g/cm³, 0.92 g/cm³, 1.38 g/cm³, 1.18 g/cm³ and 0.94 g/cm³, respectively. The volume of each spherical plastic particle is $V = \frac{4}{3} \cdot \pi \cdot R^3$, and *R* is the radius. The particle number $n = m/(\rho \cdot V)$, and *m* is the mass of particles. PS, PE, HDPE, PET, and PMMA correspond to full names of polystyrene, polyethylene, high-density polyethylene, polyethylene terephthalate, and polymethyl methacrylate, respectively.

Weathered PE	1–1200 nm	0.08 µg/L	1.66×10^{14}–9.61×10^{4}	Mussels (*Mytilus edulis*)	*In vitro* and *in vivo* exposure: 1 day	(Roman et al., 2023)
		10 µg/L	2.08×10^{16}–1.20×10^{7}			
		100 µg/L	2.08×10^{17}–1.20×10^{8}			
	1.2–300 µm	0.08 µg/L	9.61×10^{4}–6.15×10^{-3}			
		10 µg/L	1.20×10^{7}–7.69×10^{-1}			
		100 µg/L	1.20×10^{8}–7.69×10^{0}			
PS	2 µm	0.51 g/L	1.16×10^{8}	Mussels (*Mytilus edulis*)	*In vivo* exposure: 12 h	(Browne et al., 2008)
	4–16 µm		1.45×10^{7}–2.26×10^{5}			
	3 µm	15, 000 particles per treatment (with 1 mussel, 350 mL seawater)			*In vivo* exposure: 3 h	
	9.6 µm					
HDPE	4–6 µm	3 mg/L	9.52×10^{7}–2.82×10^{7}	Mussels (*Mytilus galloprovincialis*)	*In vivo* exposure: 4 h	(Fernández & Albentosa, 2019)
PMMA	10 µm	0.1 mg/L	1.62×10^{5}	Mussels (*Mytilus galloprovincialis*)	*In vivo* exposure: 3 days	(Pavičić-Hamer et al., 2022)
		1 mg/L	1.62×10^{6}			
		10 mg/L	1.62×10^{7}			
	50 µm	0.1 mg/L	1.29×10^{3}			
		1 mg/L	1.29×10^{4}			
		10 mg/L	1.29×10^{5}			
PE	36.72±24 µm (10.7–93.9 µm)	10 µg/L	4.19×10^{2}	Oysters (*Crassostrea gigas*)	*In vivo* exposure: 21 days	(Teng, Zhao, et al., 2021; Teng, Zhu, et al., 2021)
		1000 µg/L	4.19×10^{4}			
PET	31.11±14.36 µm (9.0–56 µm)	10 µg/L	4.60×10^{2}			
		1000 µg/L	4.60×10^{4}			
Virgin PE	247.7 ± 95.1 µm (50–590 µm)	0.01 mg/mL or 1.18 particles/mL	1,180	Mussels (*Mytilus galloprovincialis*)	*In vivo* exposure: 21 days	(Bråte et al., 2018)
Weathered PE	241.2 ± 103.7 µm (50–590 µm)	0.01 mg/mL or 1.86 particles/mL	1,186			
PET microfibers	106.5 ±74.8 µm (20–140 µm)	0.0005 mg/L	30.5 particles/L	Mussels (*Mytilus galloprovincialis*)	*In vivo* exposure: 32 days	(J. S. Choi et al., 2022)
		0.1 mg/L	6.1×10^{3} particles/L			
		1 mg/L	6.1×10^{4} particles/L			
		10 mg/L	6.1×10^{5} particles/L			

		100 mg/L	6.1×10^{6} particles/L			
PS	200 nm	20 µg/L	4.55×10^{9} particles/L	Mussels (*Mytilus galloprovincialis*)	*In vivo* exposure: 7 days	(Z. Lu et al., 2023)
		200 µg/L	4.55×10^{10} particles/L			
		2000 µg/L	4.55×10^{11} particles/L			
Weathered PE	<43 µm (32–43 µm)	1 µg/L or 1150±150 MPs/m^3	1.15	Mussels (*Perna viridis*)	*In vivo* exposure: 30 days	(Hariharan et al., 2021)
		2 µg/L or 2087±338 MPs/m^3	2.09			
		3 µg/L or 3360±543 MPs/m^3	3.36			
PS	100 nm	20 mg/L	6.34×10^{13}	Mussels (*Mytilus coruscus*)	*In vivo* exposure: 2 days	(Qi et al., 2023)
	1 µm	20 mg/L	6.34×10^{10}			
PE	40–48 µm	10 µg/L	3.24×10^{2}–1.88×10^{2}	Clam (*Ruditapes decussatus*)	*In vivo* exposure: 14 days	(Abidli et al., 2023)
		100 µg/L	3.24×10^{3}–1.88×10^{3}			
		1000 µg/L	3.24×10^{4}–1.88×10^{4}			
HDPE	1–50 µm	0.03 mg/L	4.6×10^{5} particles/L	Mussels (*Mytilus galloprovincialis*)	Repeated *in vivo* exposure: 18 days (1st exposure 28 days (depuration) 18 days (2nd exposure)	(Détrée & Gallardo-Escárate, 2018)

Supplementary Information: Chapter 4

Characterization of the aged micro-and-nanoplastic particles (MNPs)

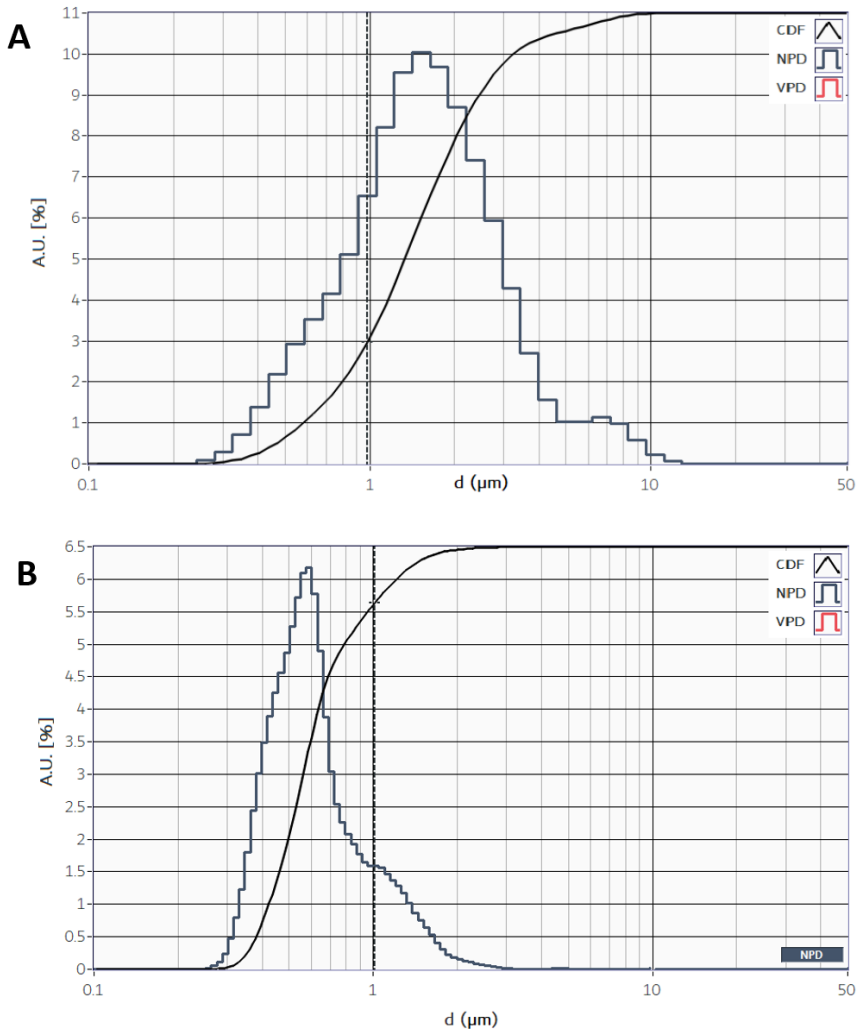

Figure A4.1. *Particle size distribution analysis of aged PET MPs (**Panel A**) and NPs (**Panel B**) using Single Particle Extinction and Scattering (SPES). The number-based particle size distribution is shown together with the corresponding cumulative distribution function (CDF) as a function of particle diameter (d).*

Table A4.1. *Summary of particle size distribution (d) for aged PET microplastics (MPs) and nanoplastics (NPs). Dimensional averages (Dim. Avg) along with the 10th percentile (D10), median diameter (D50), and 90th percentile (D90) were provided for each size range.*

Test Particle	Particle Size Distribution			
	Dim. Avg.	D_{10}	D_{50}	D_{90}
Aged PET MPs	1.9 µm	0.6 µm	1.4 µm	3.1 µm
Aged PET NPs	0.68 µm	0.39 µm	0.57 µm	1.1 µm

Figure A4.2. *Raman spectroscopy characterization of aged polyethylene terephthalate microplastics (MPs, top) and nanoplastic particles (NPs, bottom) with reference spectra from Open Specy reference library. The displayed white spectra correspond to the Raman signals of chemically aged PET particles, while the red spectrum represents the reference material of PET as indexed in the database. The table on the left lists the top spectral matches with a similarity index, indicating a high spectral match score of 0.97 and 0.94 between the aged PET MPs and NPs samples and the reference PET spectrum, respectively. Spectral data are measured in wavenumbers (cm^{-1}), highlighting the unique vibrational fingerprints indicative of PET's molecular structure.*

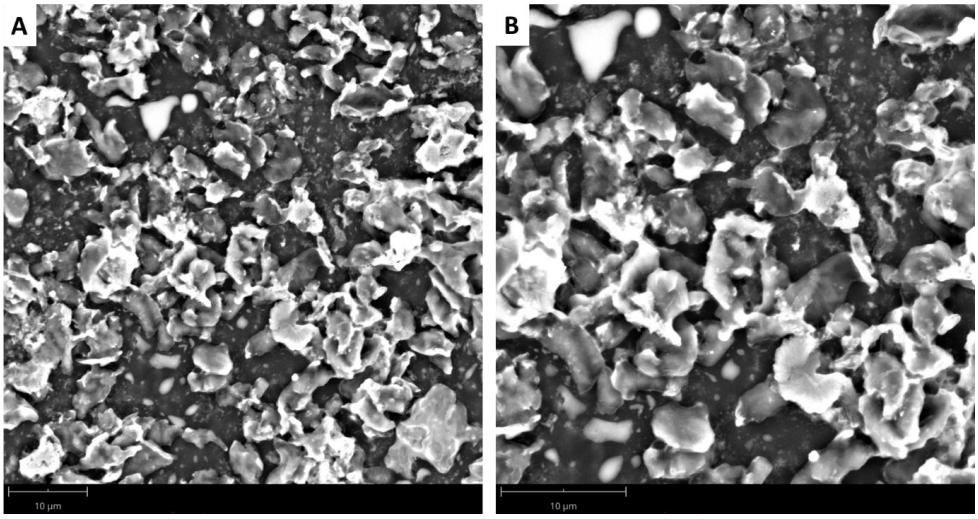

Figure A4.3. *Scanning electron microscopy (SEM) images of the aged PET micro-and nanoplastic particles (MNPs) captured using a Phenom™ ProX Desktop SEM system. The images, taken at magnifications of (Panel A) 4400x and (Panel B) 7000x, reveal the weathered and irregular shapes of the particles with evident heterogeneous sizes.*

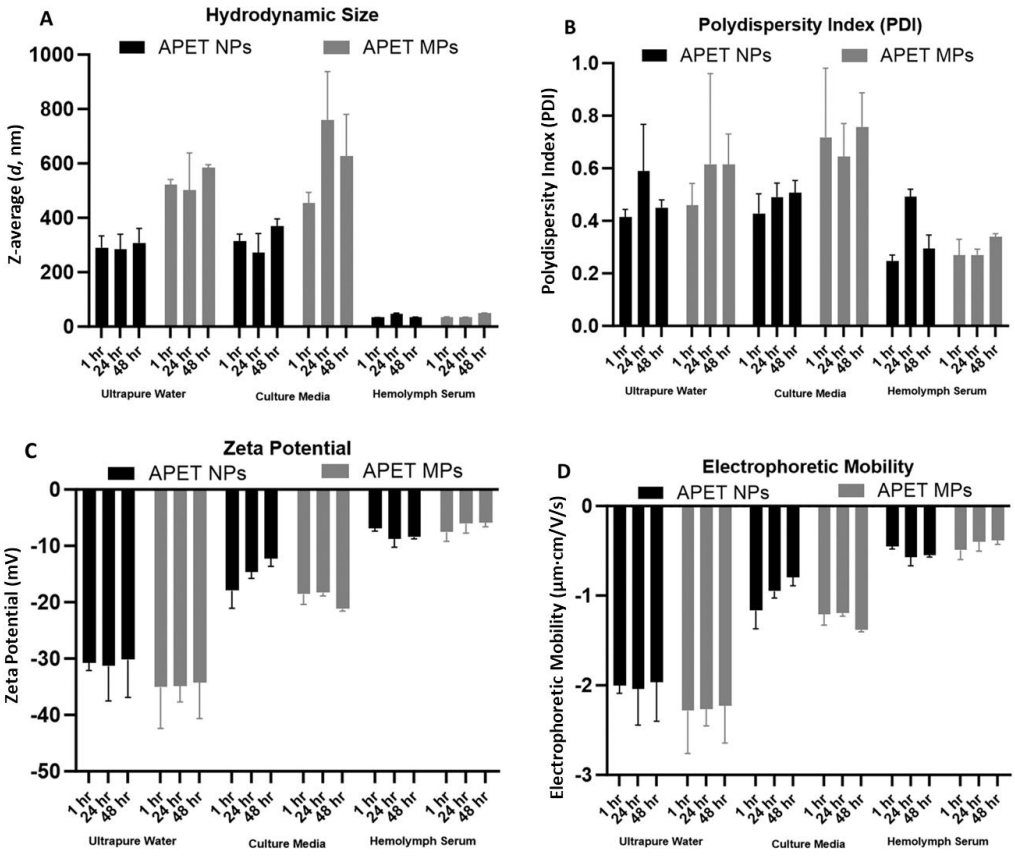

Figure A4.4. *Secondary characterization of aged PET MPs and NPs analyzed using DLS: (A) hydrodynamic size; (B) polydispersity index (PDI); (C) zeta potential (ζ); and (D) electrophoretic mobility in ultrapure water, culture media, and hemolymph serum (1:2, serum of hemolymph: culture media) at various time points (1 h, 24 h, and 48 h).*

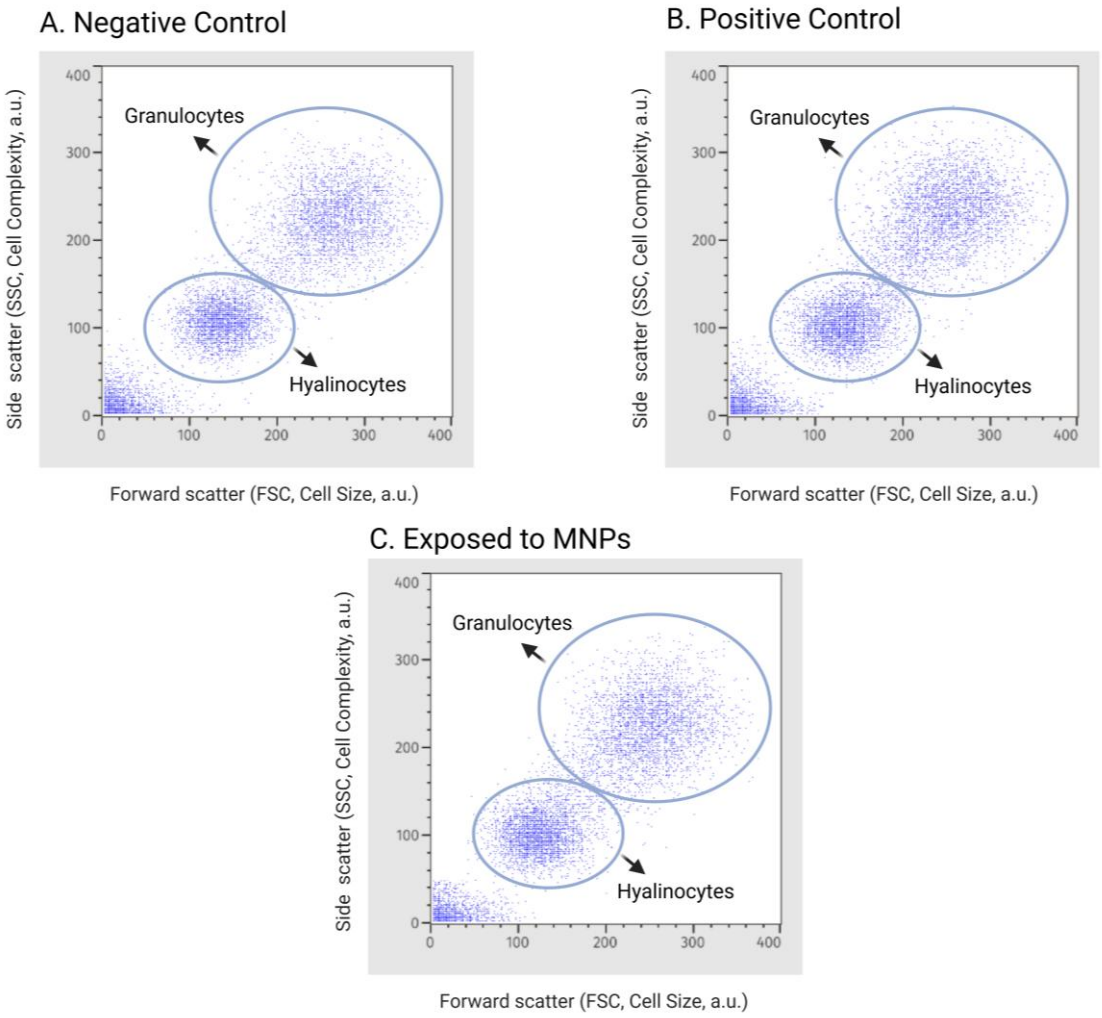

Figure A4.5. *Flow cytometric characterization of hemocyte subpopulations based on forward scatter (FSC, cell size) and side scatter (SSC, cell complexity or granularity) profiles. Representative FSC vs SSC profiles showing the distribution of hemocyte populations under (A) negative control, (B) positive control (Cadmium chloride, $CdCl_2$, 800 µM), and (C) exposed to micro- and nanoplastic particles (MNPs, 10^5 particles/mL) after 48 h. Two hemocyte subpopulations were distinguished based on cell size and internal complexity: hyalinocytes, characterized by lower FSC and SSC signals, and granulocytes, exhibiting higher FSC and SSC values. A low FSC/SSC region corresponding to cellular debris was excluded from analysis. Flow cytometry analysis was performed on a BD LSR II and data were analyzed using FlowJo.*

Validation of the cellular assays

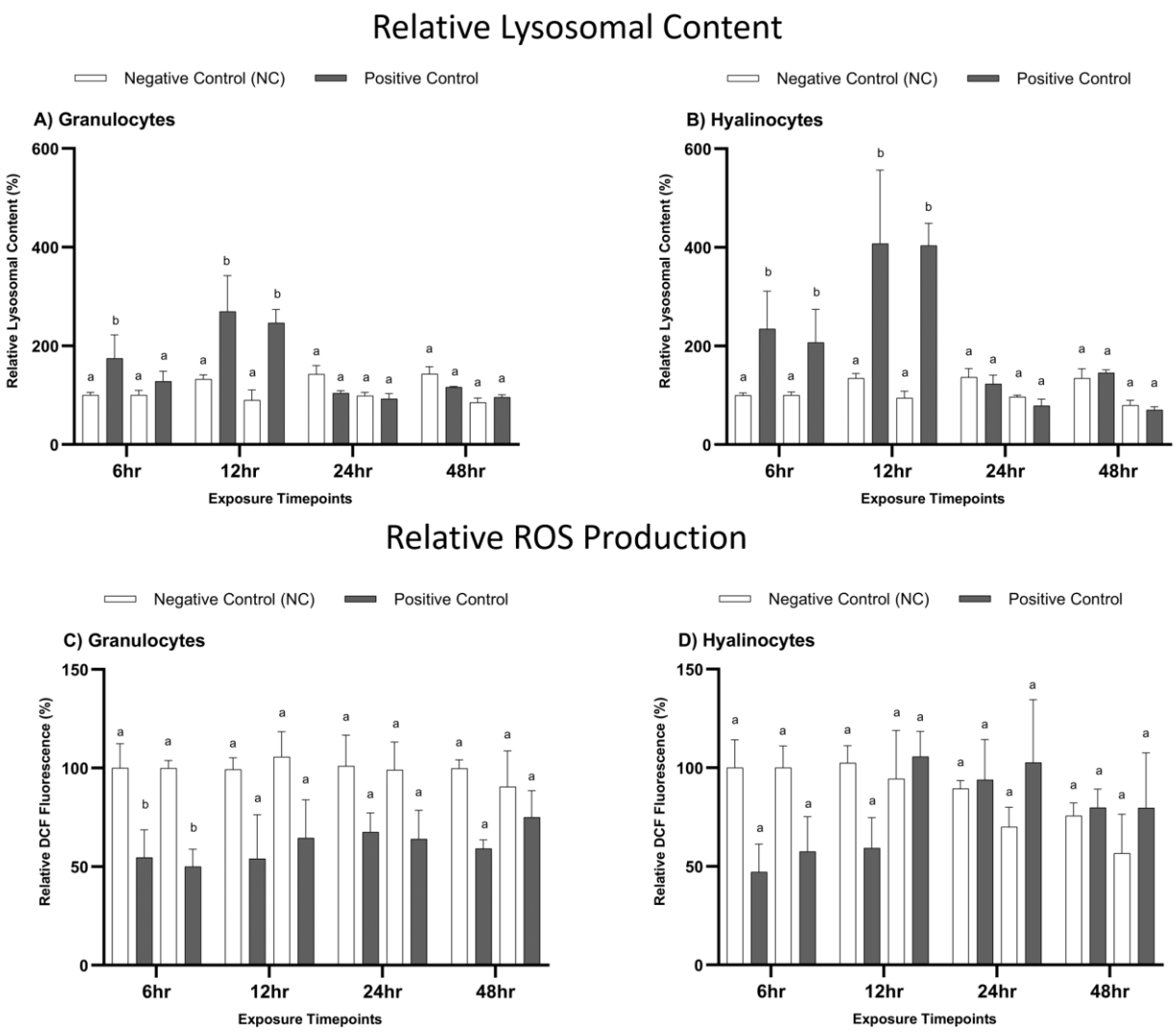

Figure A4.6. *Relative lysosomal content (Panels A–B) and reactive oxygen species (ROS) production (Panels C–D) in granulocytes and hyalinocytes exposed to positive control treatment (H_2O_2, 100 µM) over 6, 12, 24, and 48 h. Data are expressed as a mean ± SD (n=3), with two sets of control samples analyzed in parallel with the plastic treatment groups, corresponding to the nanoparticle (NP) and microplastic (MP) treatments at each time point. Different letters indicate significant differences between negative and positive control groups at each time point.*

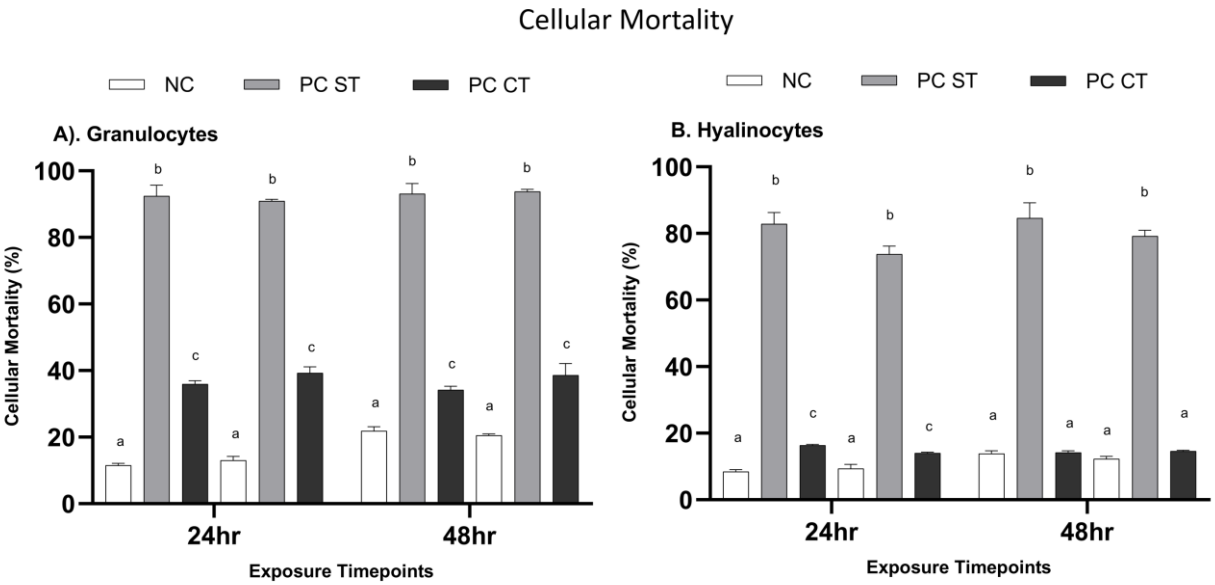

Figure A4.7. *Cellular mortality in granulocytes (A) and hyalinocytes (B) exposed to different treatments (NC: negative control; PC ST: sonication treatment and PC CT: chemical treatment with 800 µM $CdCl_2$) over 24, and 48 h. Data are expressed as a mean ± SD (n=3), with two sets of control samples analyzed in parallel with the plastic treatment groups, corresponding to the nanoparticle (NP) and microplastic (MP) treatments at each time point. Different letters indicate significant differences between negative and positive control groups at each time point (P < 0.05).*

Overview of cellular responses to aged PET micro- and nanoplastic exposure

Table A4.2. *Overview of cellular effects of aged PET MPs and NPs on hemocyte subpopulations across multiple effect endpoints at various time points. Note: Gran, Granulocytes; Hyal, Hyalinocytes. Differences were considered significant at $p < 0.05$. Percentage increases were calculated for effect endpoints that showed significant changes (highlighted in red) compared with the control. For more detailed and time-resolved quantitative measures of each cellular endpoint, please refer to the corresponding graphs.*

Particle	Concentrations	Cell Type	Values	Cell Size (FSC)				Cell Complexity (SSC)				Lysosomal Content				ROS Production				Cellular Mortality	
				6h	12h	24h	48h	6h	12h	24h	48h	6h	12h	24h	48h	6h	12h	24h	48h	24h	48h
Aged PET MPs	C1: 10 P/mL	Gran	%										75.9								
			p	>0.999	>0.999	>0.999	>0.999	>0.999	>0.999	>0.999	0.996	0.992	0.009	>0.999	>0.999	0.999	>0.999	>0.999	>0.999	0.604	>0.999
		Hyal	%																		
			p	>0.999	>0.999	>0.999	>0.999	>0.999	>0.999	>0.999	>0.999	0.999	0.397	>0.999	0.995	>0.999	0.939	>0.999	>0.999	0.786	>0.999
	C2: 10^3 P/mL	Gran	%										87.6		43.2					37.8	
			p	>0.999	>0.999	>0.999	>0.999	>0.999	>0.999	0.999	0.765	0.636	0.002	0.999	0.045	0.583	>0.999	>0.999	>0.999	0.021	0.259
		Hyal	%												54.3						
			p	>0.999	>0.999	>0.999	>0.999	>0.999	>0.999	>0.999	>0.999	0.999	0.215	>0.999	0.015	0.993	0.735	>0.999	>0.999	0.150	0.334
	C3: 10^5 P/mL	Gran	%										100		45.5					42.9	
			p	>0.999	>0.999	>0.999	>0.999	>0.999	>0.999	0.143	0.279	0.594	<0.001	0.999	0.030	0.845	>0.999	0.999	>0.999	0.007	0.988
		Hyal	%												50.9					54.5	
			p	>0.999	>0.999	>0.999	>0.999	>0.999	>0.999	>0.999	>0.999	0.993	0.155	>0.999	0.026	0.999	0.998	0.997	>0.999	0.039	0.790
Aged PET NPs	C1: 10 P/mL	Gran	%																		
			p	>0.999	>0.999	>0.999	>0.999	>0.999	>0.999	0.957	>0.999	0.995	>0.999	>0.999	0.983	0.999	>0.999	0.999	>0.999	>0.999	>0.999
		Hyal	%																		
			p	>0.999	>0.999	>0.999	>0.999	>0.999	>0.999	>0.999	>0.999	0.998	>0.999	>0.999	0.999	0.829	0.998	0.259	>0.999	>0.999	>0.999
	C2: 10^3 P/mL	Gran	%																		
			p	>0.999	>0.999	>0.999	>0.999	>0.999	>0.999	0.957	>0.999	0.998	>0.999	0.47	0.857	0.996	>0.999	0.978	>0.999	0.895	>0.999
		Hyal	%																		
			p	>0.999	>0.999	>0.999	>0.999	>0.999	>0.999	>0.999	>0.999	0.971	>0.999	>0.999	0.889	0.999	0.683	0.218	>0.999	0.928	0.999
	C3: 10^5 P/mL	Gran	%											78.7				45.5		35.0	
			p	>0.999	>0.999	>0.999	>0.999	>0.999	>0.999	0.910	0.996	>0.999	>0.999	0.020	0.473	0.076	>0.999	0.047	>0.999	0.016	0.747
		Hyal	%															184			
			p	>0.999	>0.999	>0.999	>0.999	>0.999	>0.999	>0.999	>0.999	>0.999	>0.999	0.157	0.496	0.573	0.792	0.009	>0.999	0.899	0.955

Summary of recently published studies on MNP toxicity

Table A4.3. *Summary of published papers evaluating the toxicity of micro and nanoparticles in various cell types.*[2]

Particle type	Particle size	Reported concentration	Converted Concentration (P/mL)	Cell Type	Max Exposure Time	Reference
PS	50 nm	1 – 10 mg/L	1.46×10^{10} - 1.46×10^{11}	*Hemocytes,* Mussels *(Mytilus galloprovincialis)*	24 h (*In vitro*)	(Sendra, Carrasco-Braganza, et al., 2020)
	100 nm	1 – 10 mg/L	1.82×10^{9} - 1.82×10^{10}			
	1000 nm	1 – 10 mg/L	1.82×10^{6} - 1.82×10^{7}			
PS	50 nm	50 µg/mL	7.28×10^{11}	Human brain astrocytoma 1321N1	24 h (*In vitro*)	(Wang et al., 2013)
PS- NH_2	100 nm	20 µg/mL	3.64×10^{10}	Fibroblast (ZF4), Zebrafish (*Danio rerio*)	9 h (*In vitro*)	(M. Yang & Wang, 2022)
	1000 nm	20 µg/mL	3.64×10^{7}			
PS	0.05 µm	10^2, 10^3, 10^5, 10^6, 10^8, 10^9 and 10^{12} P/mL		*Hemocytes,* Mussels *(Mytilus galloprovincialis)*	24 h (*In vitro*)	(Katsumiti et al., 2021)
	0.5 µm	10^2, 10^3, 10^5, 10^6, 10^8, 10^9 P/mL				
	4.5 µm	10^2, 10^3, 10^5, 10^6, 10^8 P/mL				
PET	191.6 nm	4 µg/mL	7.87×10^{8}	Macrophage RAW264.7 cell line, Mouse	3 h (*In vitro*)	(Deng et al., 2022)
	1.85 µm	4 µg/mL	8.74×10^{5}			
PS	1.62 µm	4 µg/mL	1.71×10^{6}			
LDPE	160.5 nm	4 µg/mL	1.99×10^{9}			
	1.30 µm	4 µg/mL	3.74×10^{6}			
PS	2 µm	15 µg/mL	3.41×10^{6}	Macrophage ImKC cell line, Mouse	24 h (*In vitro*)	(Völkl et al., 2022)
		150 µg/mL	3.41×10^{7}			
PP & PS	90 µm	20,000 P/mL		THP-1 macrophages	24 h (*In vitro*)	(Jeon et al., 2021)
PS- NH_2	50 nm	1 µg/mL	1.46×10^{10} P/mL	*Hemocytes,* Mussels *(Mytilus galloprovincialis)*	45 min	(Canesi et al., 2015)
		5 µg/mL	7.28×10^{10} P/mL			
		50 µg/mL	7.28×10^{11} P/mL			

[2] As applied by (M. Peng et al., 2023): The density (ρ) values of PS, PE, LDPE, and PET are 1.05 g/cm³, 0.92 g/cm³, 0.93 g/cm³, and 1.38 g/cm³, respectively. The volume of each spherical plastic particle is $V = \frac{4}{3} \cdot \pi \cdot R^3$, and R is the radius. The particle number $n = m/(\rho \cdot V)$, and m is the mass of particles. PS, PE, LDPE, and PET correspond to full names of polystyrene, polyethylene, low-density polyethylene, and polyethylene terephthalate, respectively.

PE	1 – 1200 nm	0.08 µg/L	1.66×10^{11} – 9.61×10^{1}	*Hemocytes,* Mussels *(Mytilus edulis)*	24 h (*In vitro* & *In vivo*)	(Roman et al., 2023)
		10 µg/L	2.08×10^{13} – 1.20×10^{4}			
		100 µg/L	2.08×10^{14} – 1.20×10^{5}			
	1.2 – 300 µm	0.08 µg/L	9.61×10^{1} – 6.15×10^{6}			
		10 µg/L	1.20×10^{4} – 7.69×10^{4}			
		100 µg/L	1.20×10^{5} - 7.69×10^{3}			
PET	50 – 250 nm	7.5 µg/mL	8.30×10^{10} – 6.64×10^{8}	Macrophage RAW264.7 cell line, Mouse	72 h (*In vitro*)	(Aguilar-Guzmán et al., 2022)
		15 µg/mL	1.66×10^{10} – 1.33×10^{8}			
		30 µg/mL	3.32×10^{11} – 2.66×10^{9}			
		60 µg/mL	6.64×10^{11} – 5.31×10^{9}			

Supplementary Information: Chapter 5

Characterization of the aged PET NPs

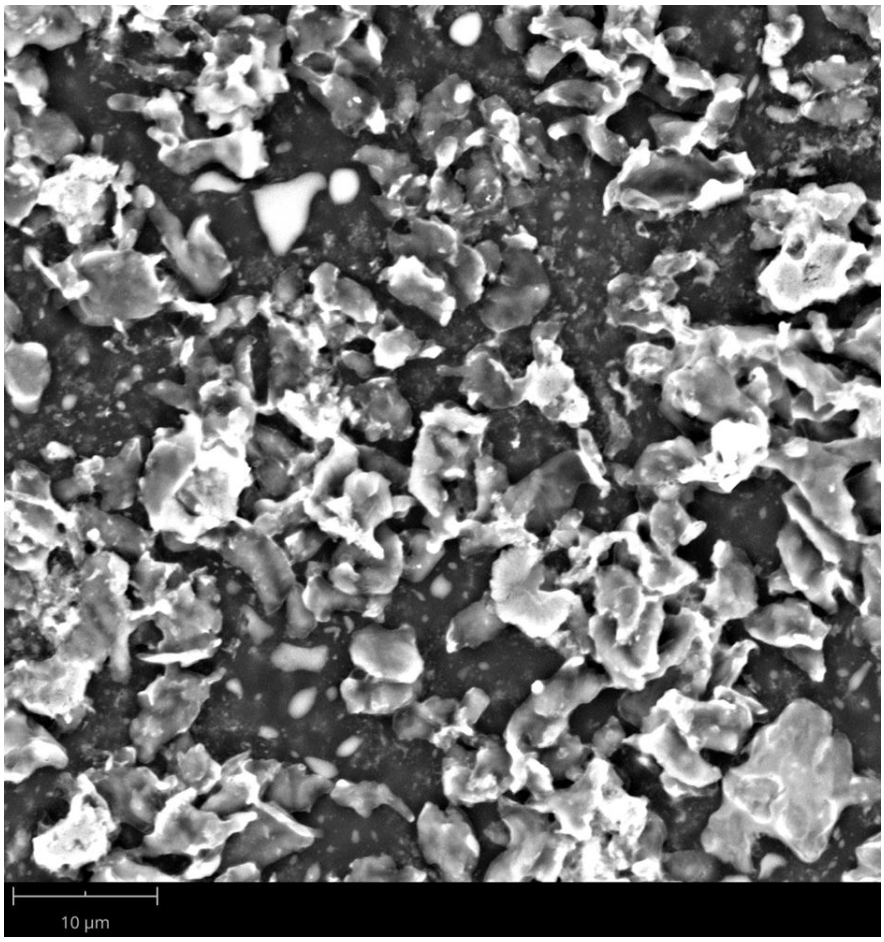

Figure A5.1. *Scanning electron microscopy (SEM, Phenom™ ProX) micrograph confirming the particle morphology of the primary stock suspension provided by the JRC, containing aged micro- and nanoplastic particles <5 µm, from which the NP fraction used in this study was obtained by filtration.*

A. SPES optical fingerprint of the sample: Forward scattering amplitude S(0)

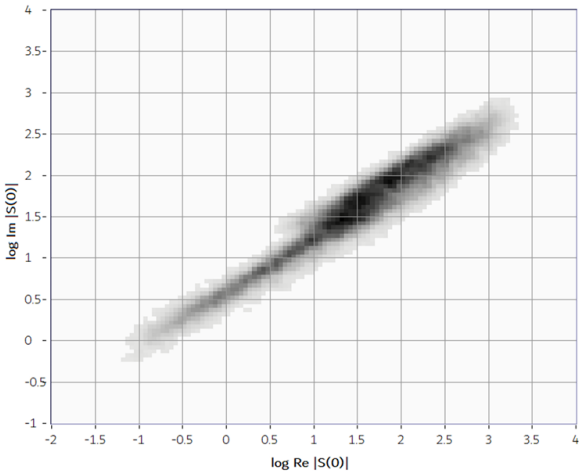

B. Particle Size Distribution

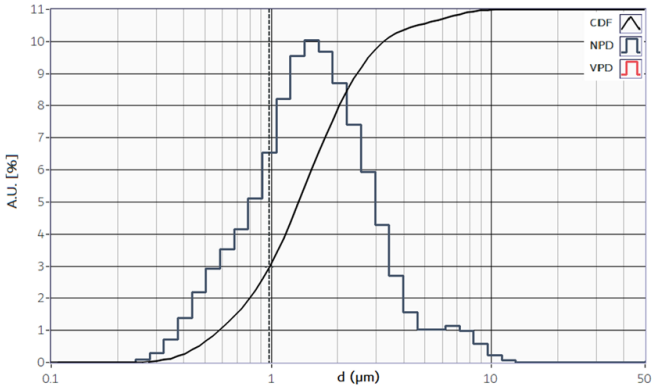

C. SPES analytical output

Conc. PTCs/mL	4.0E+7	RI	1.45 + i 0.00
Dilution	41	RI CV	0.03
Selection %	100.0	RI Std. Dev.	0.05
LUT superpos.	1.00	RI Skewness	0.41
PTCs validated	21012	Dim. Avg	1.9 µm
Avg Log[Re S]	1.46	Dim. Peak	1.5 µm
Avg Log[Im S]	1.57	Dim. CV	0.77
Sigma Log[Re S]	0.89	D10	0.60 µm
Sigma Log[Im S]	0.61	D50	1.4 µm
Mode Log[Re S]	1.30	D90	3.1 µm
Mode Log[Im S]	1.45	D[4,3]	6.5 µm
Comment	17.05.2022 F6/JRC-GEEL 500uL + 20 mL MilliQ aggregates were visible, 30' US applied		

Oversize Detection

Dimensional Class	Meas Num Conc [ptc/mL]	Std.Dev. MNC [ptc/mL]	Scaled Num Conc [ptc/mL]	Std.Dev. SNC [ptc/mL]
Overall	9.66E+5	6.66E+3	3.96E+7	2.73E+5
> 0.5 µm	9.31E+5	6.54E+3	3.82E+7	2.68E+5
> 0.7 µm	8.60E+5	6.29E+3	3.53E+7	2.58E+5
> 1.0 µm	7.52E+5	5.88E+3	3.08E+7	2.41E+5
> 2.0 µm	3.07E+5	3.76E+3	1.26E+7	1.54E+5
> 5.0 µm	5.17E+4	1.54E+3	2.12E+6	6.32E+4
> 10.0 µm	2.53E+2	Poor Statistics!	1.04E+4	Poor Statistics!

Figure A5.2. *Single-Particle Extinction and Scattering (SPES) analysis of the primary stock suspension of aged polyethylene terephthalate micro- and nanoplastic particles (aged PET MNPs, <5 µm) provided by the Joint Research Centre (JRC, Geel, Belgium).* ***Panel A*** *shows the two-dimensional histogram of the forward scattering amplitude S(0) of the measured particles. Darker greys indicate a higher number of particles in a*

given bin. $\mathcal{S}(0)$ is the complex optical signal used in SPES to characterize the particle's scattering behavior and to retrieve the effective refractive index (Potenza, Sanvito, & Pullia, 2015). ***Panel B*** *displays the particle size distribution in number representation and* ***panel C*** *summarizes the analytical outputs, with the relevant values highlighted using colored boxes: effective refractive index (RI) and its dispersion statistics (blue), particle size distribution descriptors (green) in number representation, and particle number concentration. The particle number concentration was 4.0×10^7 particles/mL (Panel C, red box). The derived RI was 1.45+i0.00 (Panel C, blue box), with a standard deviation (0.05), coefficient of variation (CV = 0.03), and skewness (0.41), describing the dispersion and asymmetry of the RI distribution. The particle size distribution descriptors (Panel C, green box) include the average equivalent diameter (1.9 µm), D_{10} (0.60 µm), D_{50} (1.4 µm), and D_{90} (3.1 µm). Aged PET MNPs were suspended and measured in Milli-Q water with no added surfactants.*

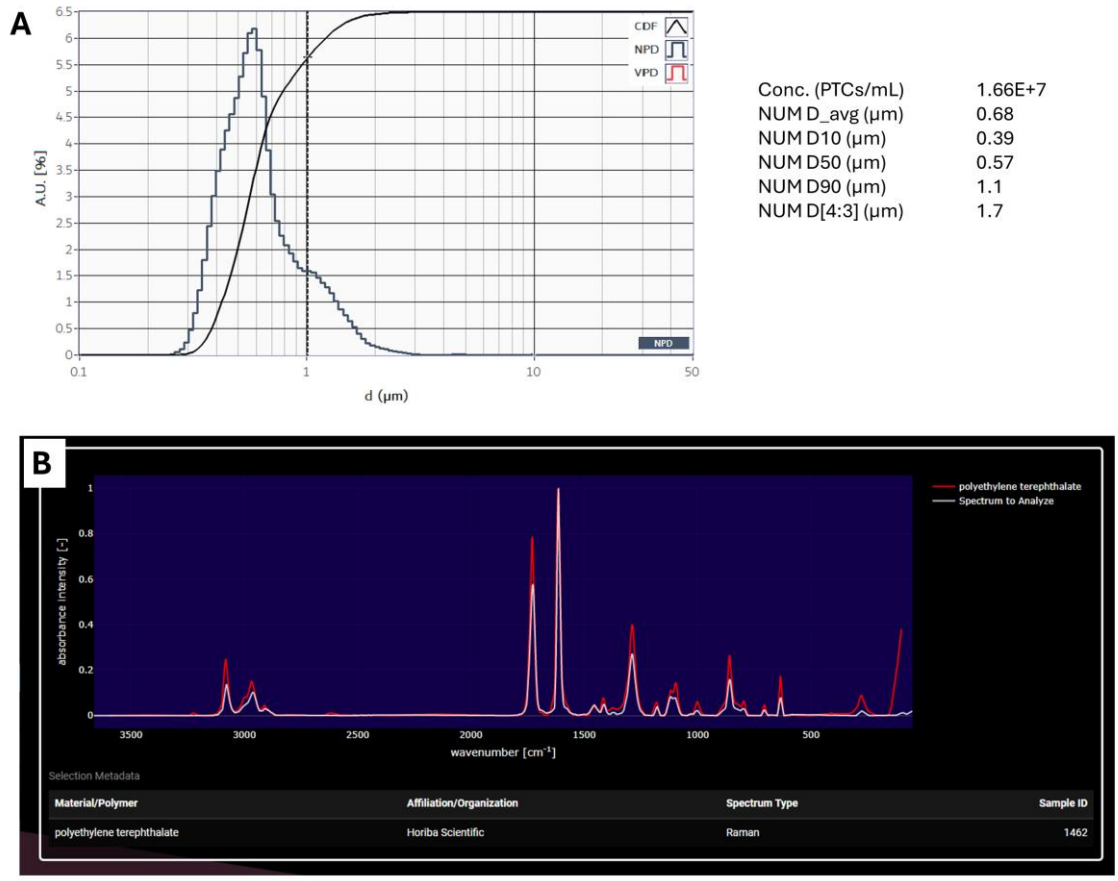

Figure A5.3. *Polymer type (A) and particle size distribution (B) of aged PET NPs analyzed using Raman spectroscopy with Open Specy reference library, and Single Particle Extinction and Scattering (SPES) technique (ClassizerONE (S1.4.34, EOS), respectively.* ***Panel A*** *displays the particle size distribution of the aged PET NPs measured by SPES. The number-based particle size distribution is shown together with the corresponding cumulative distribution function (CDF) as a function of particle diameter (d). The aged PET NP suspension exhibited a particle concentration of 1.66×10^7 particles/mL, with a number-based average equivalent diameter of 0.68 µm and percentile values of D_{10} = 0.39 µm, D_{50} = 0.57 µm, and D_{90} = 1.1 µm.* ***Panel B*** *shows the Raman spectrum of the aged PET nanoplastic (NP) sample acquired using an inVia™ Qontor® confocal Raman microscope (Renishaw, Wotton-under-Edge, UK) equipped with a 785 nm excitation laser and a 20× objective. PET suspensions were diluted in ethanol (1:3, v/v), deposited onto a silicon wafer, and measured in the dry state after solvent evaporation. The instrument was operated at 10% laser power, with an accumulation time of 1 s, averaging 5 accumulations. The spectrum was compared against the Open Specy reference library, confirming the material as polyethylene terephthalate with a 0.94 match score relative to the reference spectrum.*

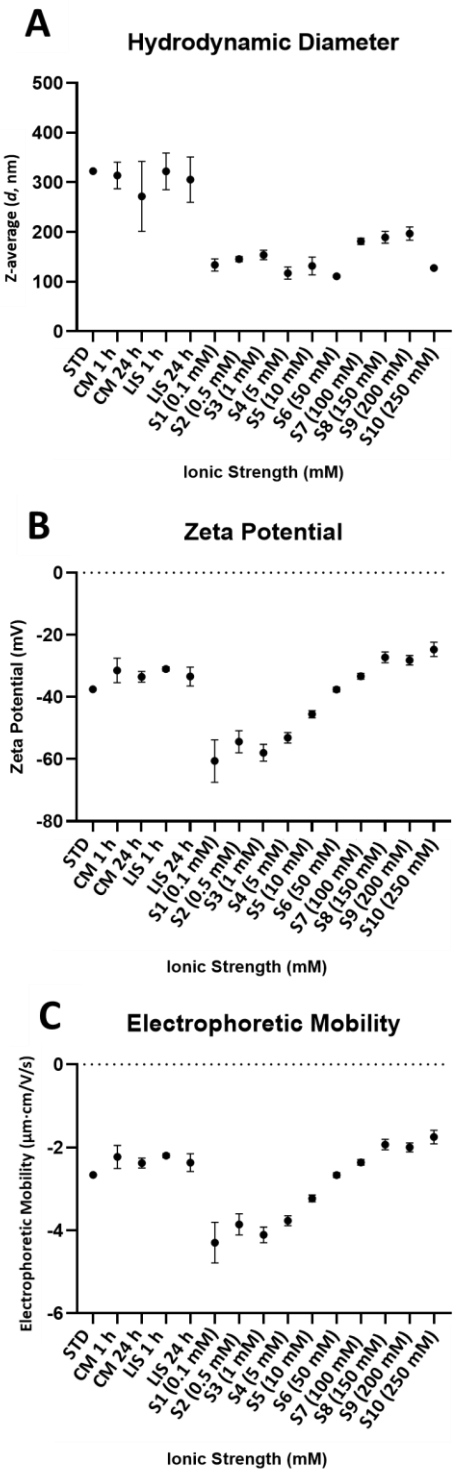

Figure A5.4. *Hydrodynamic size (**Panel A**; d, nm), zeta potential (**Panel B**; mV), and electrophoretic mobility (**Panel C**; µm·cm/V/s) of aged PET NPs measured in culture medium (CM, 1 h and 24 h), live-cell imaging solution (LIS, 1 h and 24 h), and in sodium chloride (NaCl) solutions of increasing ionic strength after 24 h incubation (S1–S10: 0.1–250 mM NaCl, pH 7). Reference standards (STD; ZTS1240, Malvern Panalytical) were included in the analytical process for quality control. Measurements were performed in triplicate, with 10 runs per replicate, by Dynamic Light Scattering (DLS, Zetasizer Nanoseries, Malvern Instruments).*

Annotation of the cellular structures

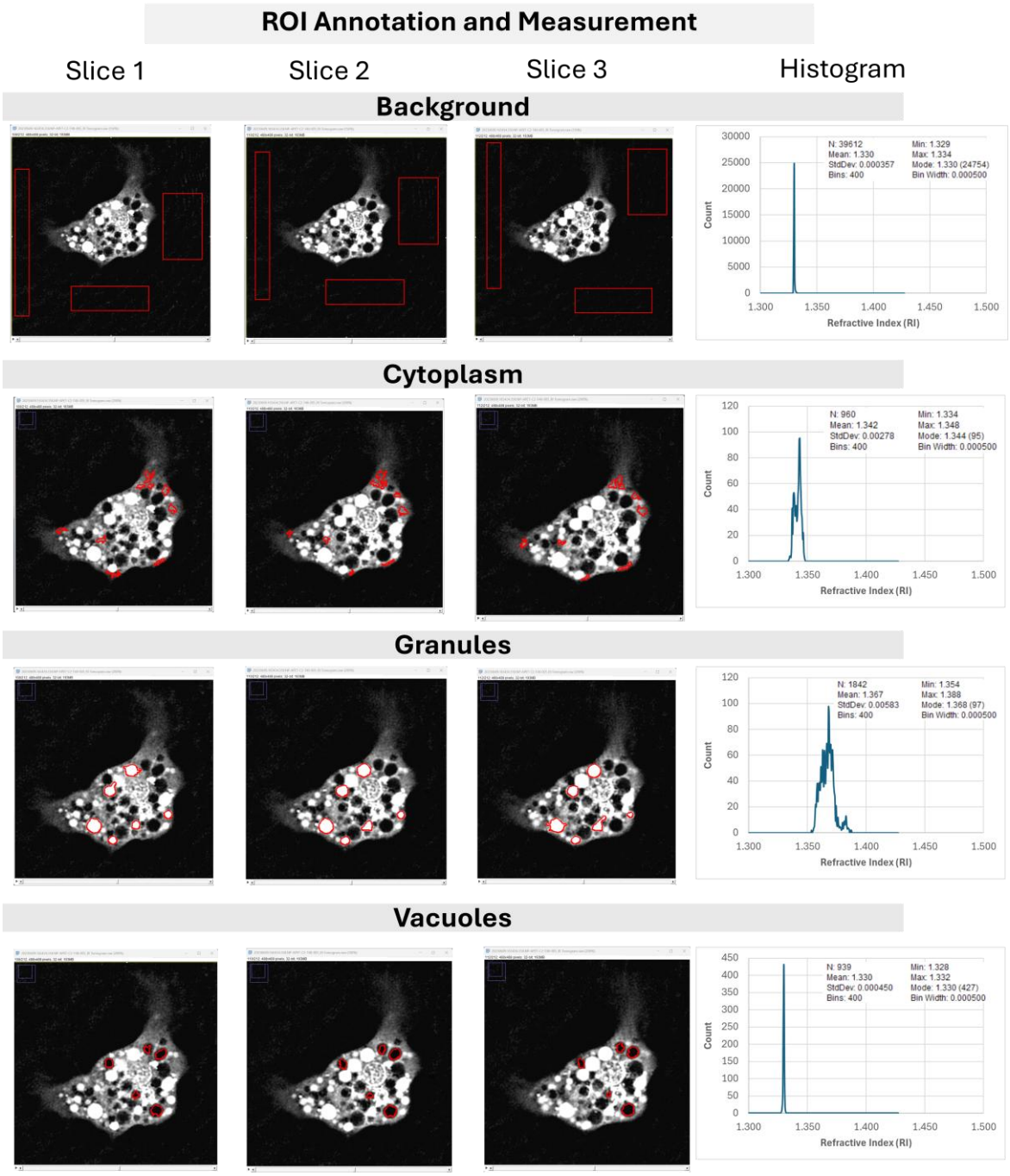

Figure A5.5. *Annotation and refractive index profiling of the target regions of interest (ROI), including the cytoplasm, granules, vacuoles, and the background. For each representative hemocyte image (n = 50) across all experimental conditions and time points. The annotations of the target structures were performed on three slices per tomogram (total number = 150 slices) to capture variability along the z-axis and measurement reproducibility. For each ROI in every slice, quantitative morphological metrics (number, area, slice number, and stack position), and refractive index (RI) distributions were extracted. The ROIs are drawn in red color for each targeted cell compartment and the background.*

Refractive index distributions of the cellular structures

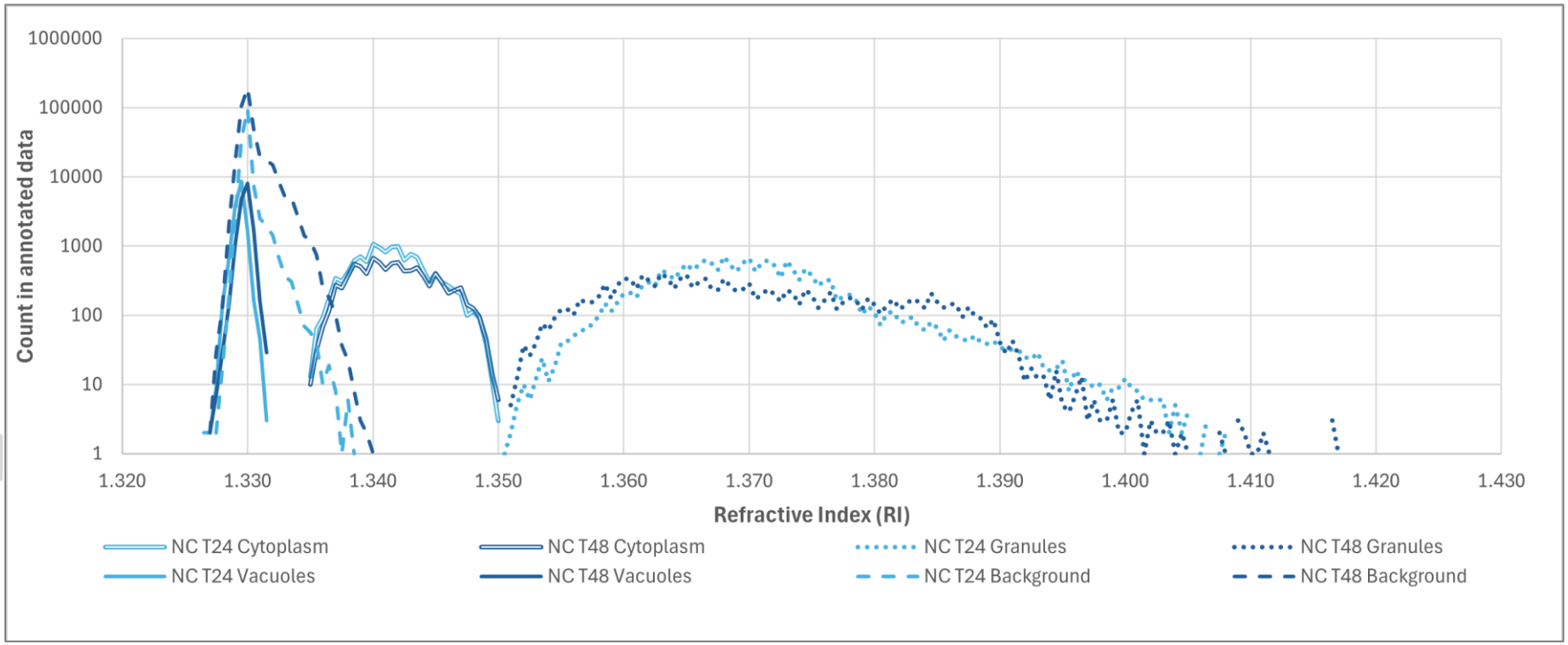

Figure A5.6. *Distribution of refractive index (RI) values across manually annotated structures, including cytoplasm (double lines), granules (dotted lines), vacuoles (solid lines), and the background (dashed lines). RI histograms were generated from manually annotated regions in representative images corresponding to the negative control (NC) for 24 h and 48 h incubation period. For each condition tested, the same color shade was used for both time points, with the 48 h lines shown in a darker tone. These distributions served as the empirical basis for RI-based thresholding in the image analysis pipeline. Note that the counts shown reflect the number of annotated voxels. As annotating was limited to a few representative samples, they do not reflect the total count of voxels of the given class in the whole 3D volume. Thus, the lines allow the assessment of the shape of the probability distributions from which descriptive characteristics like the spread and modality can be deducted, but the actual number of overlapping voxels between classes in the full image representatives is not possible to assess.*

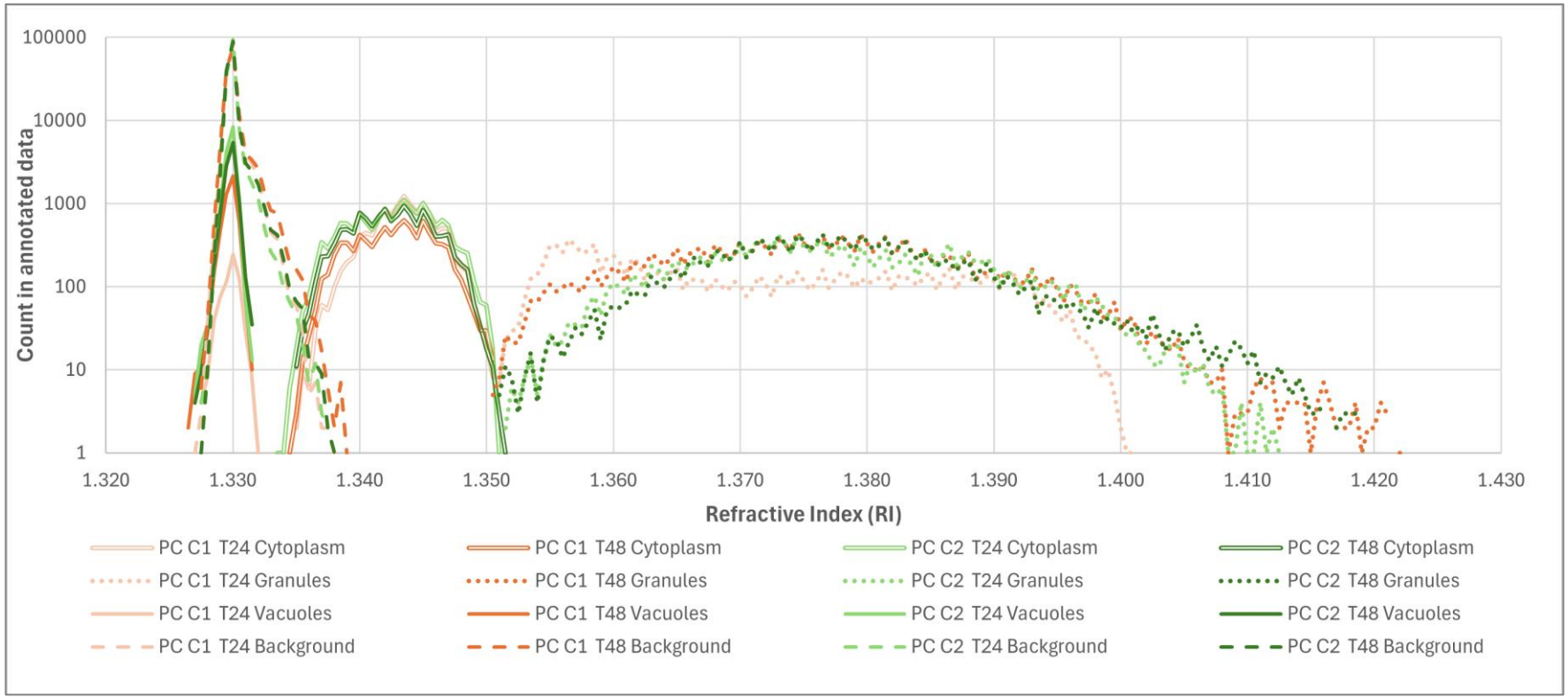

Figure A5.7. *Distribution of refractive index (RI) values across manually annotated structures, including cytoplasm (double lines), granules (dotted lines), vacuoles (solid lines), and the background (dashed lines). RI histograms were generated from manually annotated regions in representative images corresponding to the positive controls (PC C1 and C2) for 24 h and 48 h incubation period. For each condition tested, the same color shade was used for both time points, with the 48 h lines shown in a darker tone. These distributions served as the empirical basis for RI-based thresholding in the image analysis pipeline. Note that the counts shown reflect the number of annotated voxels. As annotating was limited to a few representative samples, they do not reflect the total count of voxels of the given class in the whole 3D volume. Thus, the lines allow the assessment of the shape of the probability distributions from which descriptive characteristics like the spread and modality can be deducted, but the actual number of overlapping voxels between classes in the full image representatives is not possible to assess.*

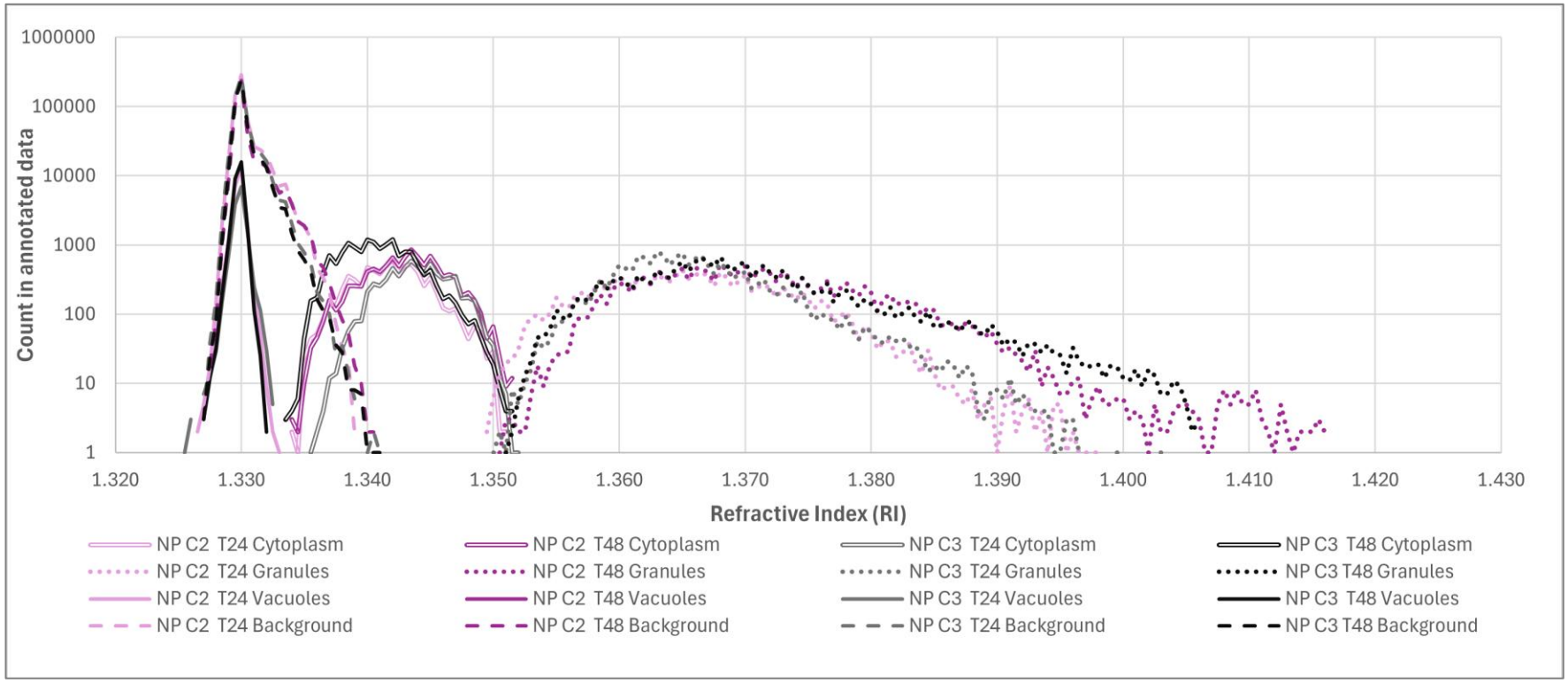

Figure A5.8. *Distribution of refractive index (RI) values across manually annotated structures, including cytoplasm (double lines), granules (dotted lines), vacuoles (solid lines), and the background (dashed lines). RI histograms were generated from manually annotated regions in representative images corresponding to hemocytes exposed to aged PET nanoparticles (NP C2 and C3) for 24 h and 48 h incubation period. For each condition tested, the same color shade was used for both time points, with the 48 h lines shown in a darker tone. These distributions served as the empirical basis for RI-based thresholding in the image analysis pipeline. Note that the counts shown reflect the number of annotated voxels. As annotating was limited to a few representative samples, they do not reflect the total count of voxels of the given class in the whole 3D volume. Thus, the lines allow the assessment of the shape of the probability distributions from which descriptive characteristics like the spread and modality can be deducted, but the actual number of overlapping voxels between classes in the full image representatives is not possible to assess.*

Image processing workflow

Figure A5.9. *Hemocyte with internalized aged PET NPs: details of the processing workflow.*

Part I. *Development of a preliminary mask for the hemocyte (without background and vacuoles).*

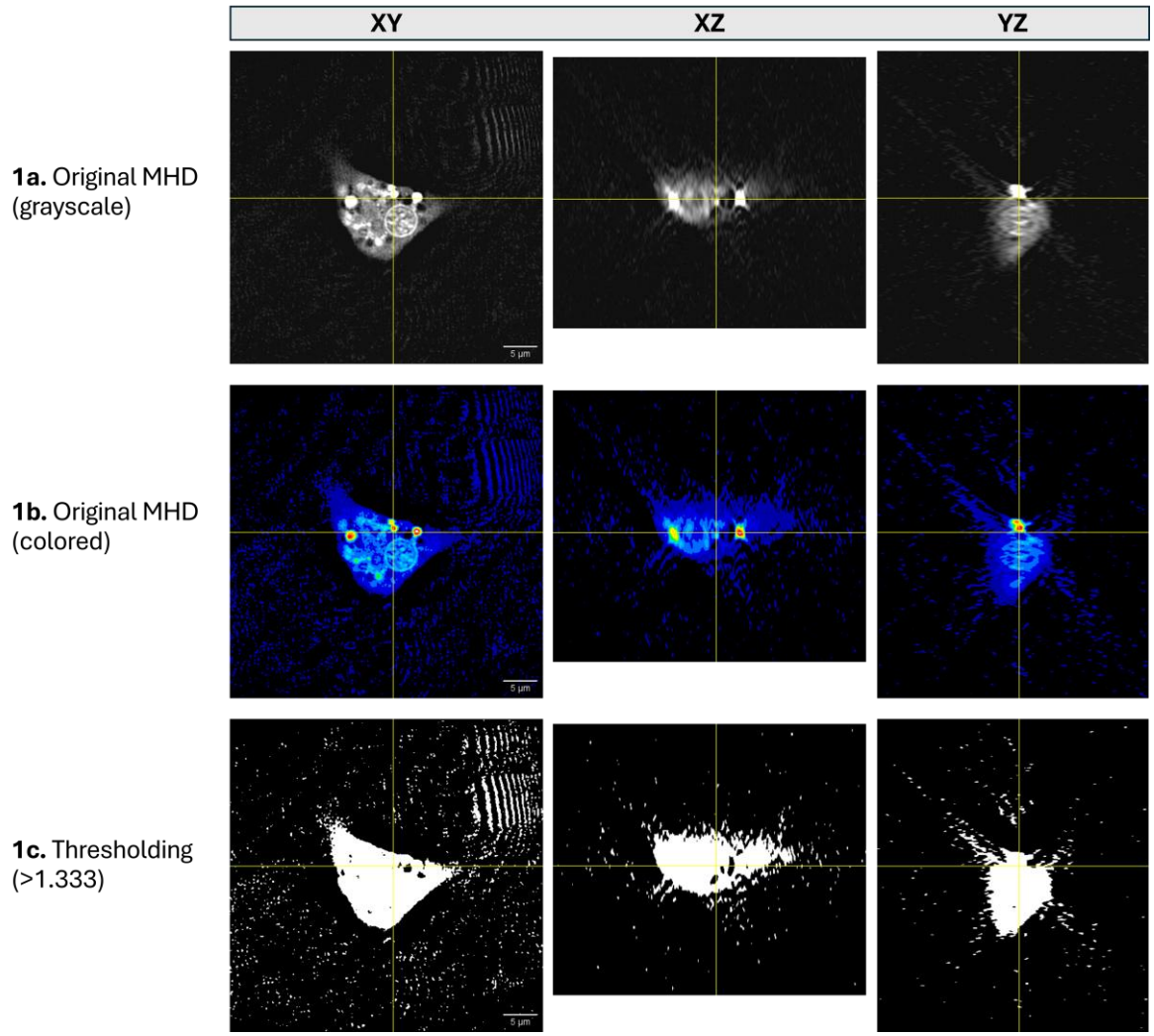

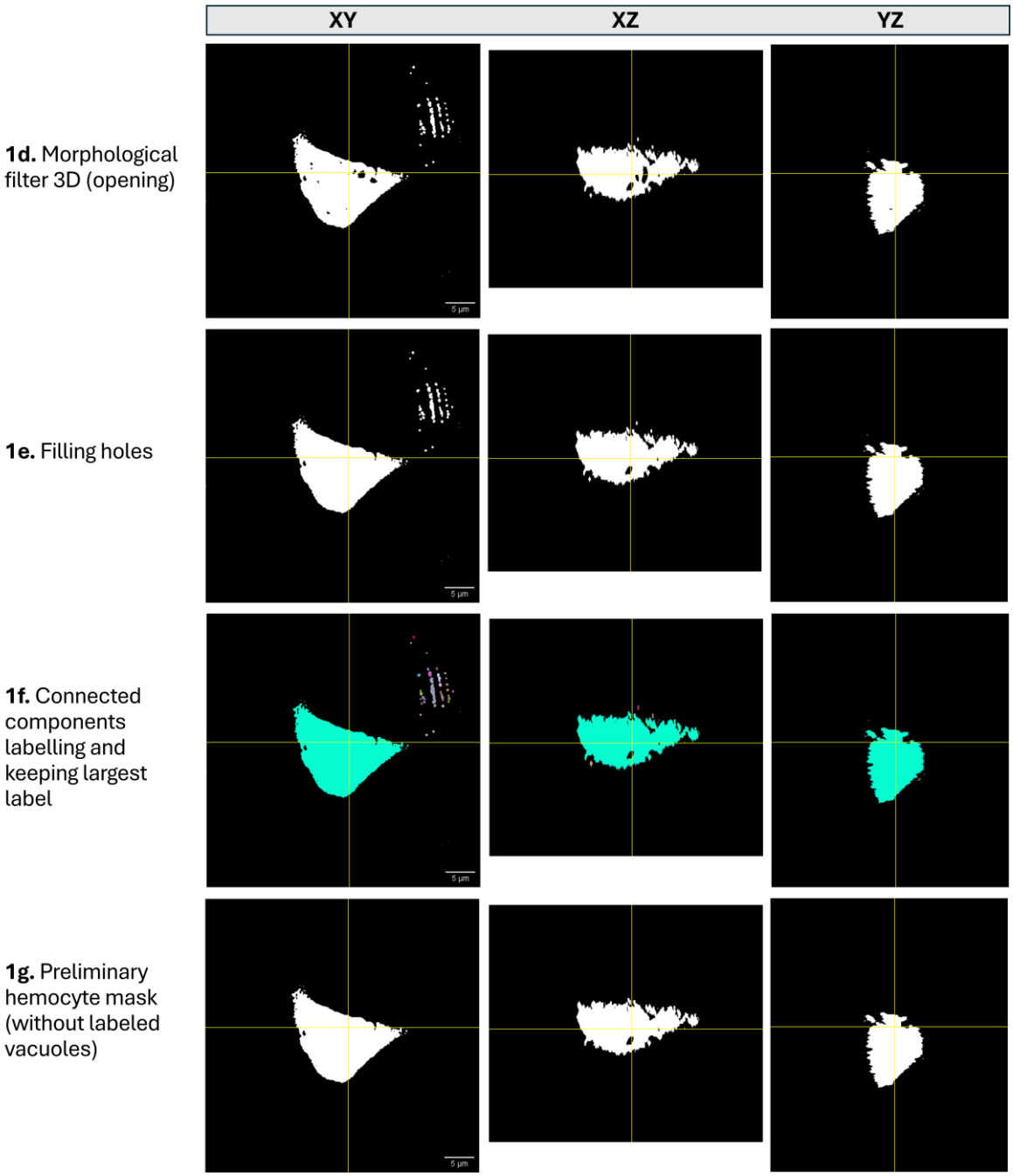
XY
XZ
YZ
1d. Morphological filter 3D (opening)
1e. Filling holes
1f. Connected components labelling and keeping largest label
1g. Preliminary hemocyte mask (without labeled vacuoles)

Part II. *Segmentation and development of a mask for vacuoles.*

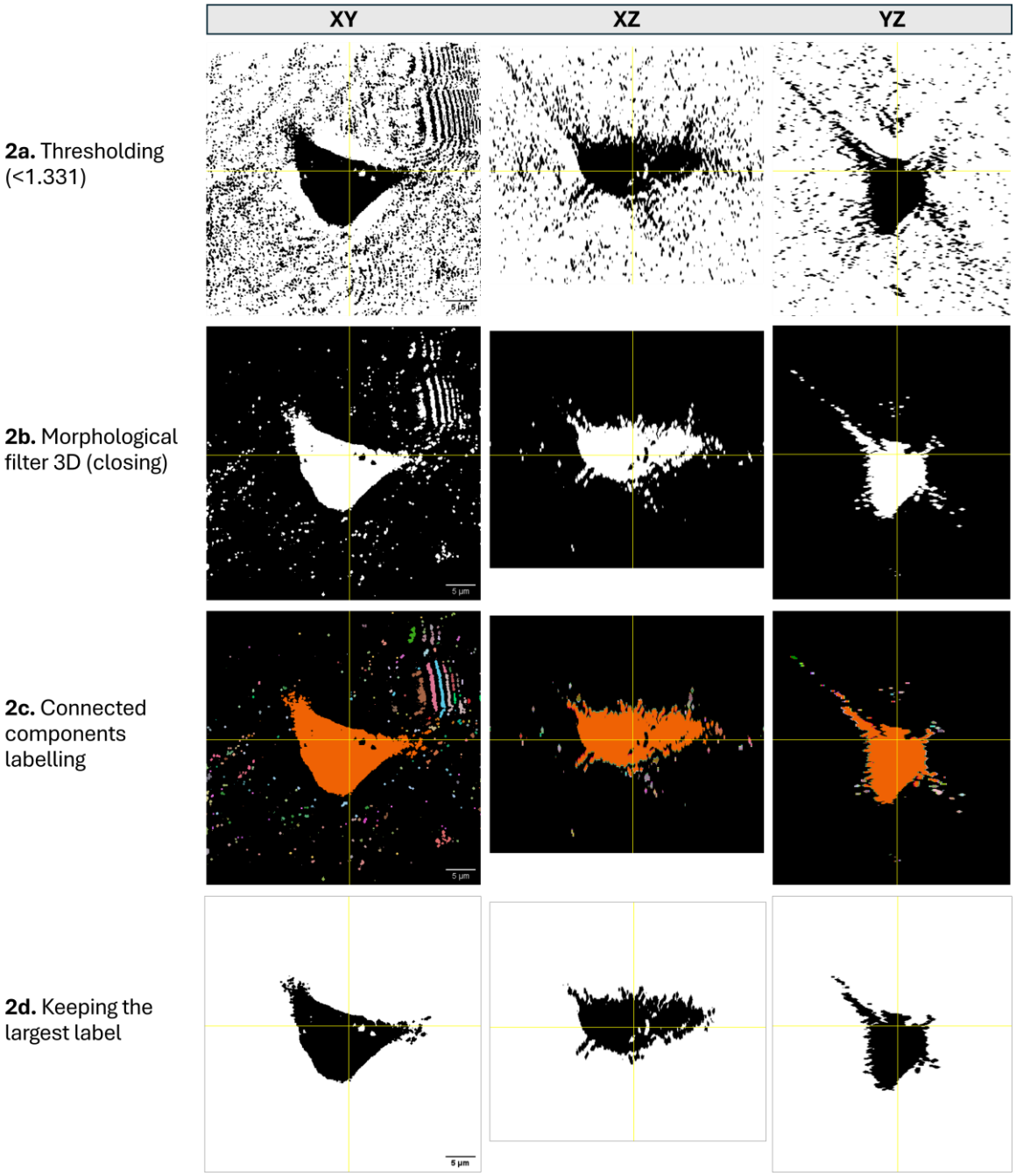

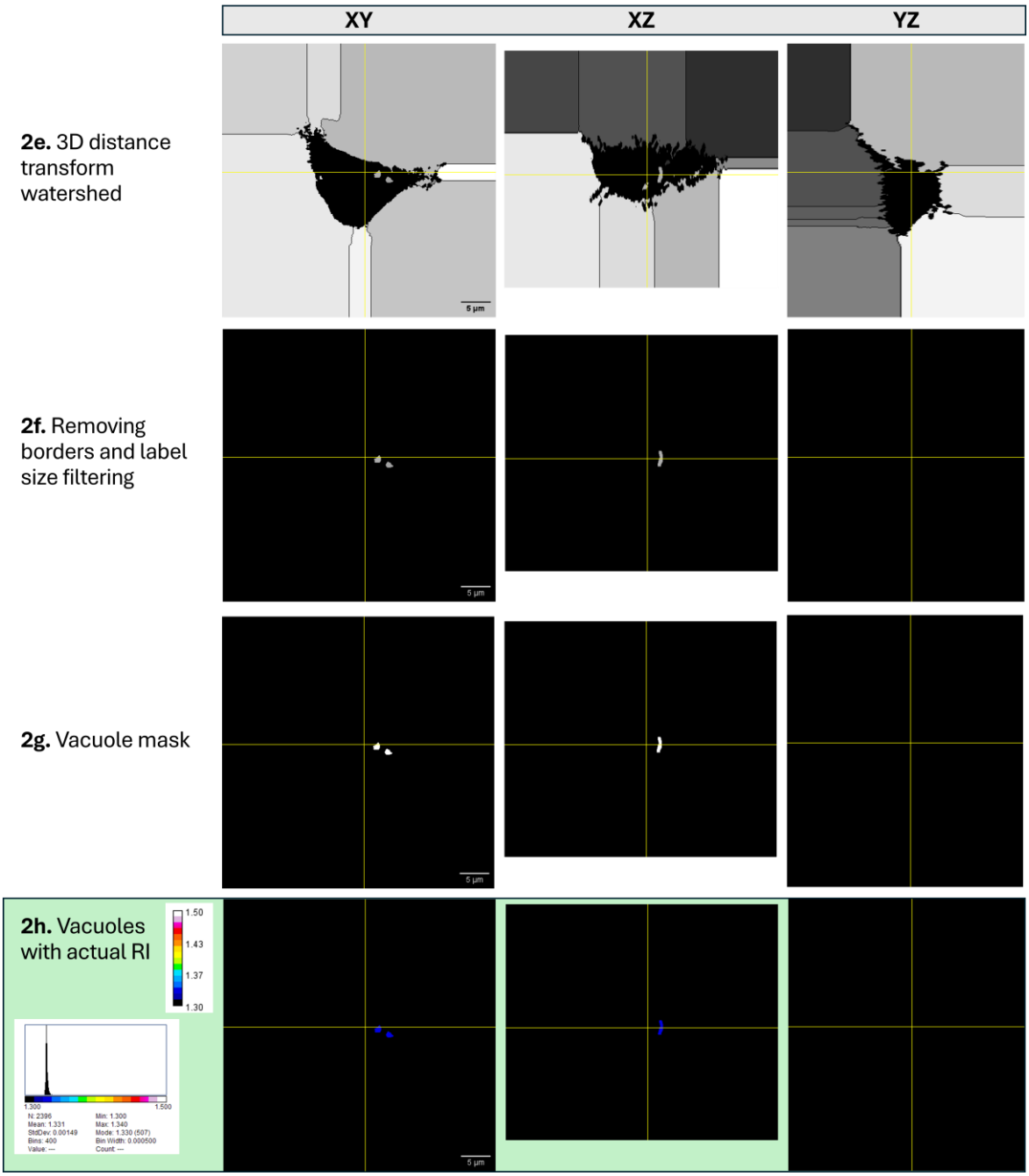
XY
XZ
YZ
2e. 3D distance transform watershed
2f. Removing borders and label size filtering
2g. Vacuole mask
2h. Vacuoles with actual RI
1.50
1.43
1.37
1.30
5 µm

Part III. *Combination of vacuoles and hemocyte masks.*

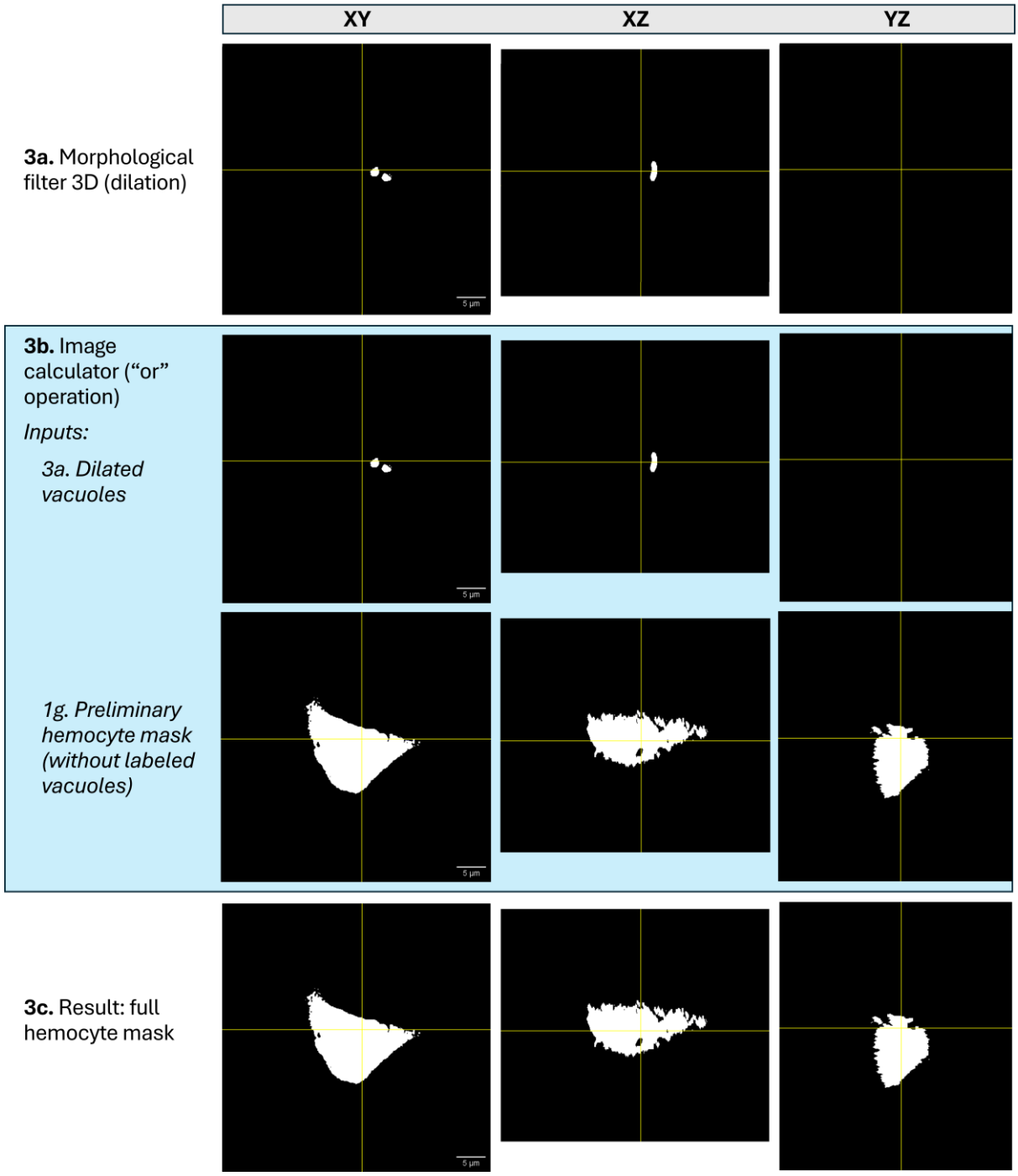

Part IV. *Segmentation of the cytoplasm.*

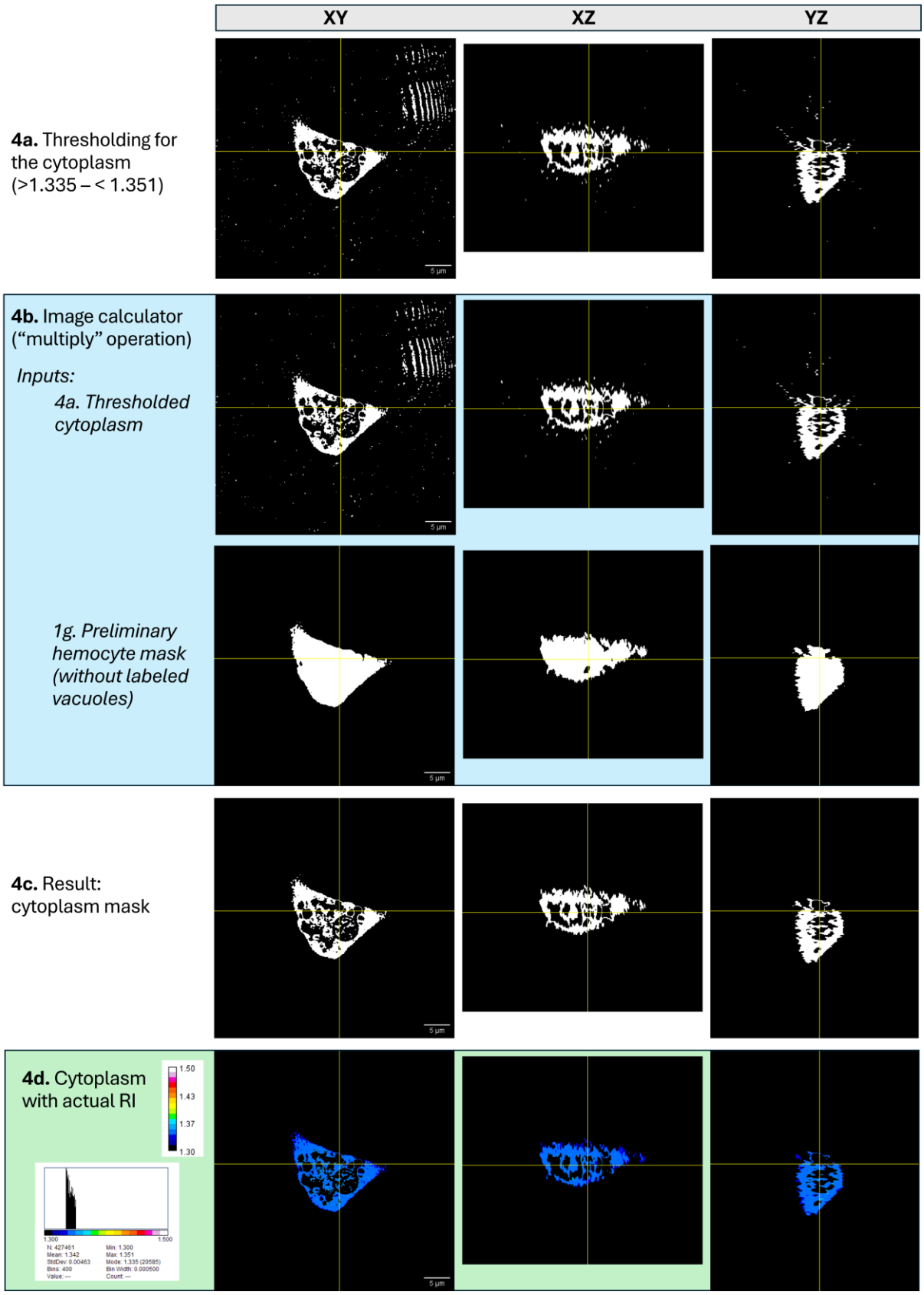

Part V. *Segmentation of granules.*

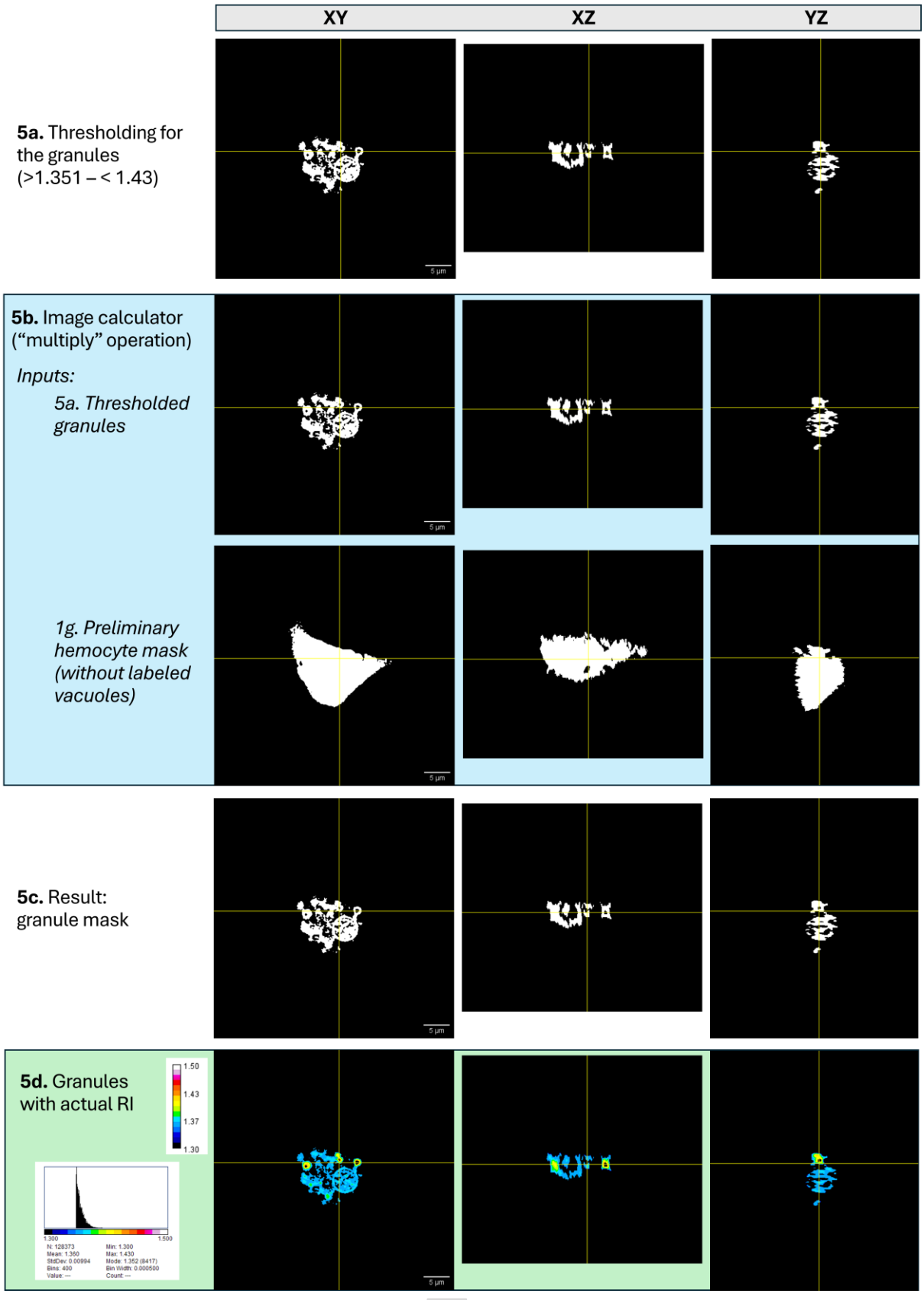

Part VI. *Segmentation of aged PET nanoplastics.*

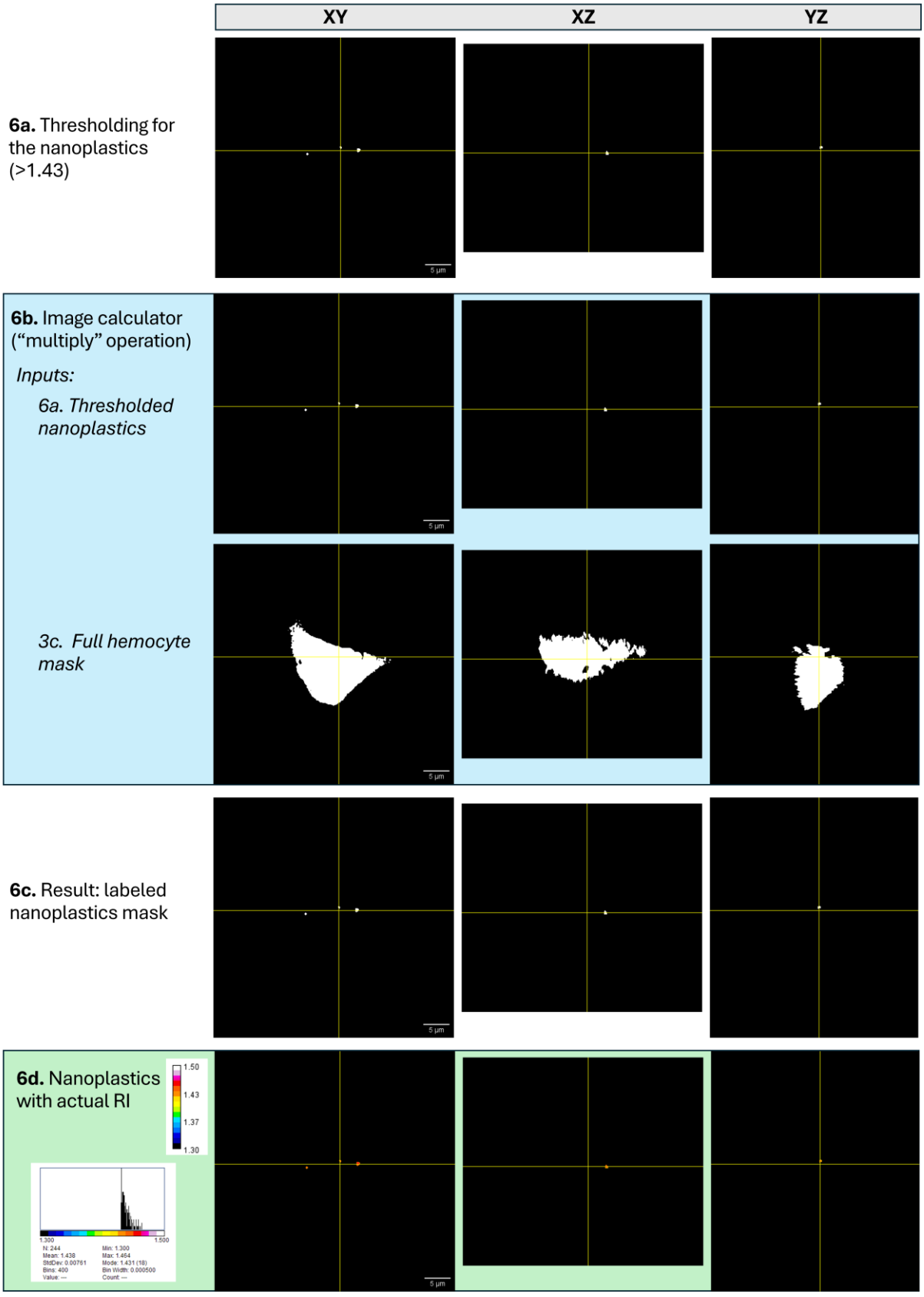

Part VII. *3D Visualization*

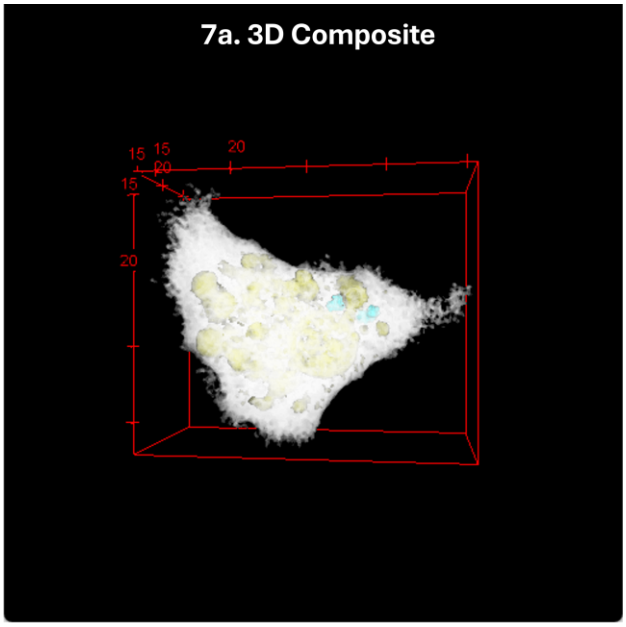

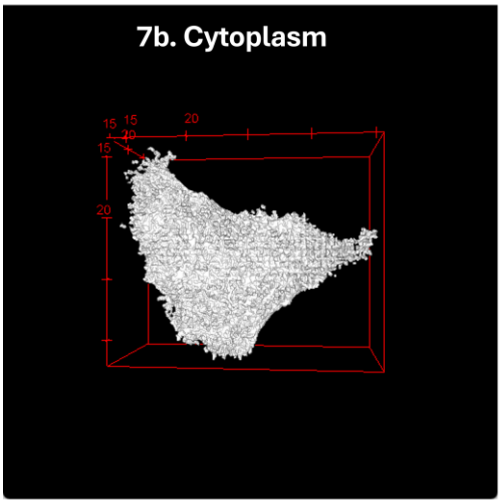

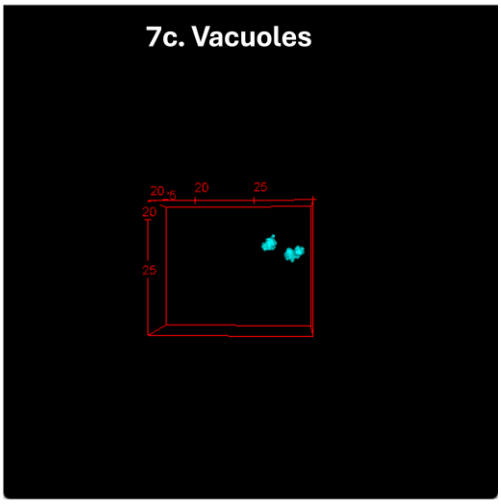

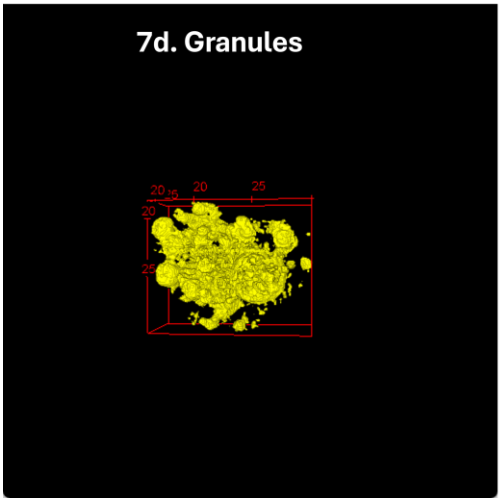

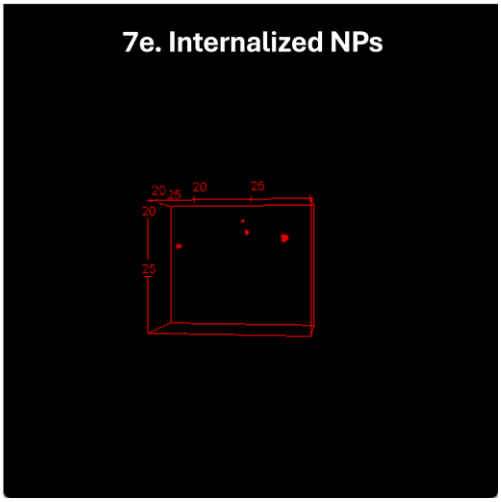

Figure A5.10. *Hemocyte without internalized aged PET NPs.*

Part I. *Development of a preliminary mask for hemocyte (without background and vacuoles).*

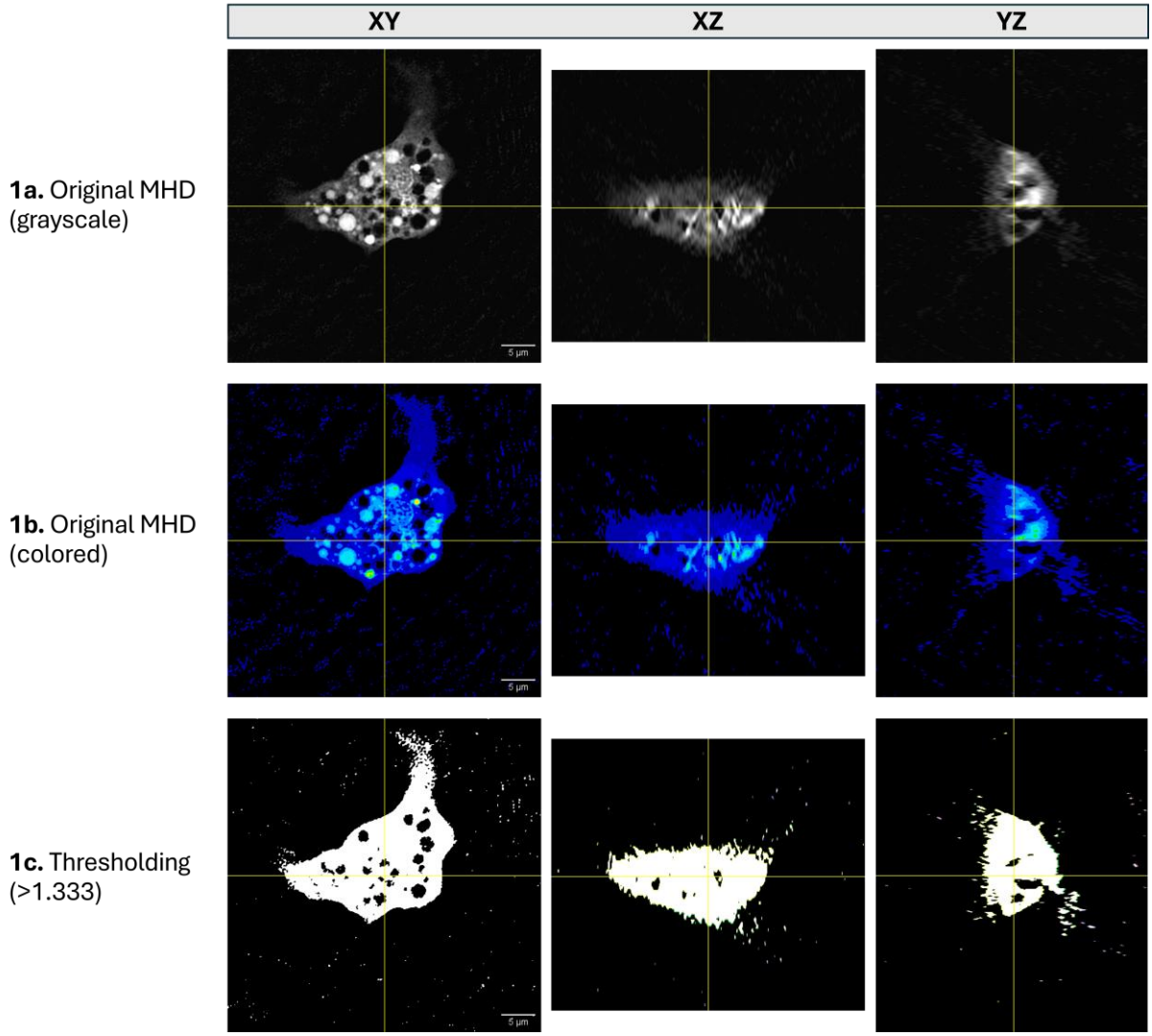

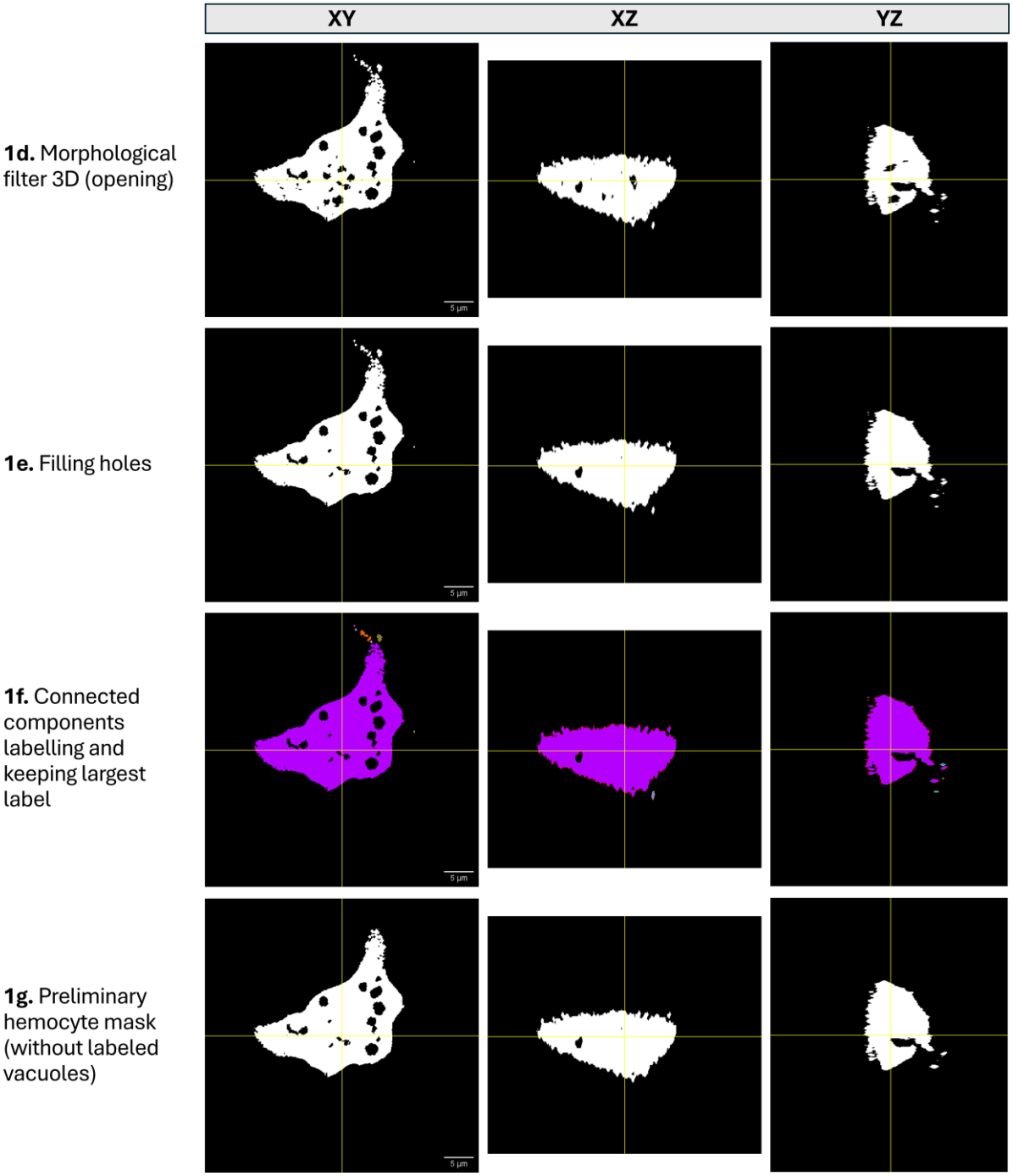
XY
XZ
YZ
1d. Morphological filter 3D (opening)
1e. Filling holes
1f. Connected components labelling and keeping largest label
1g. Preliminary hemocyte mask (without labeled vacuoles)

Part II. *Development of a mask for vacuoles.*

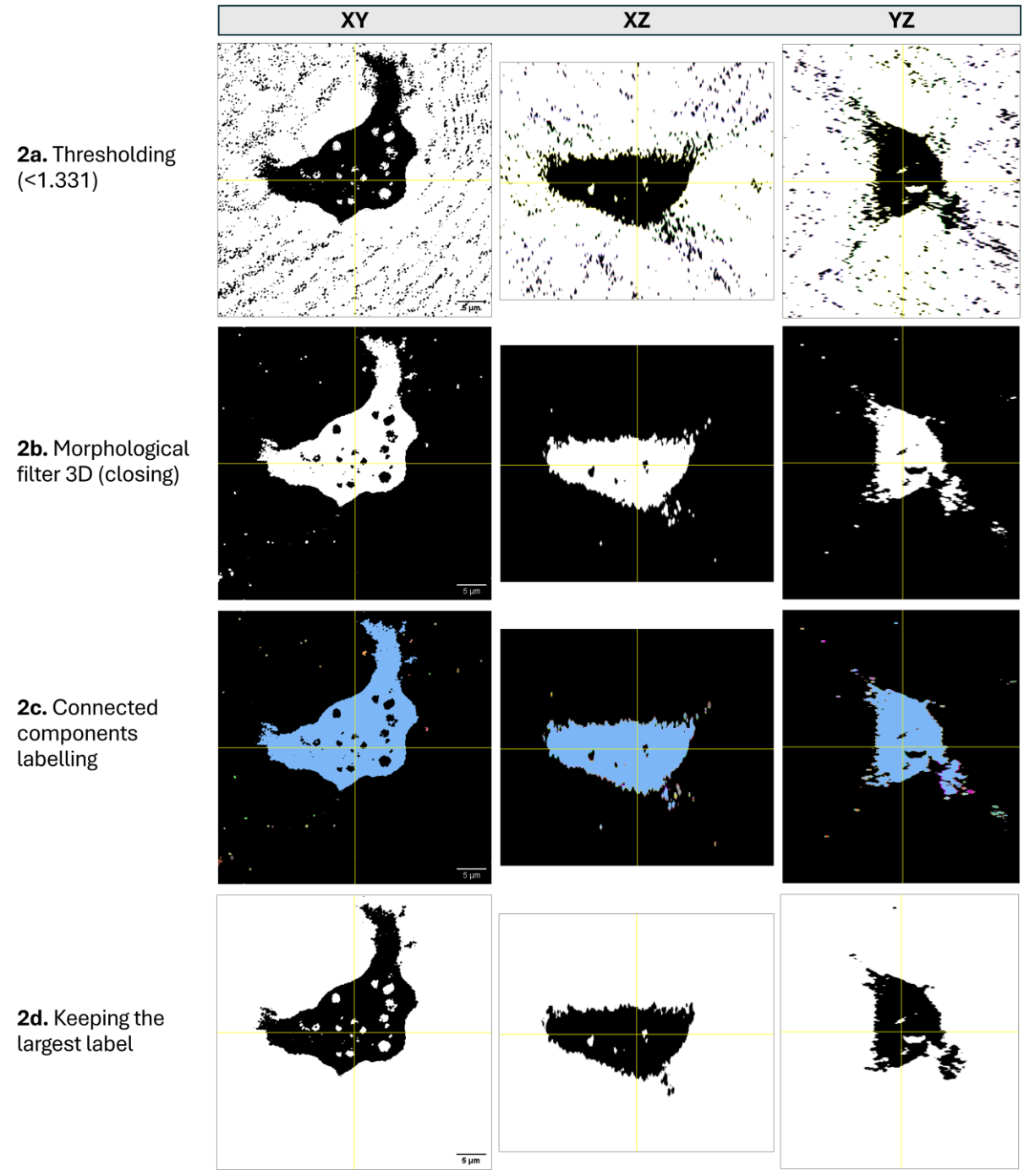

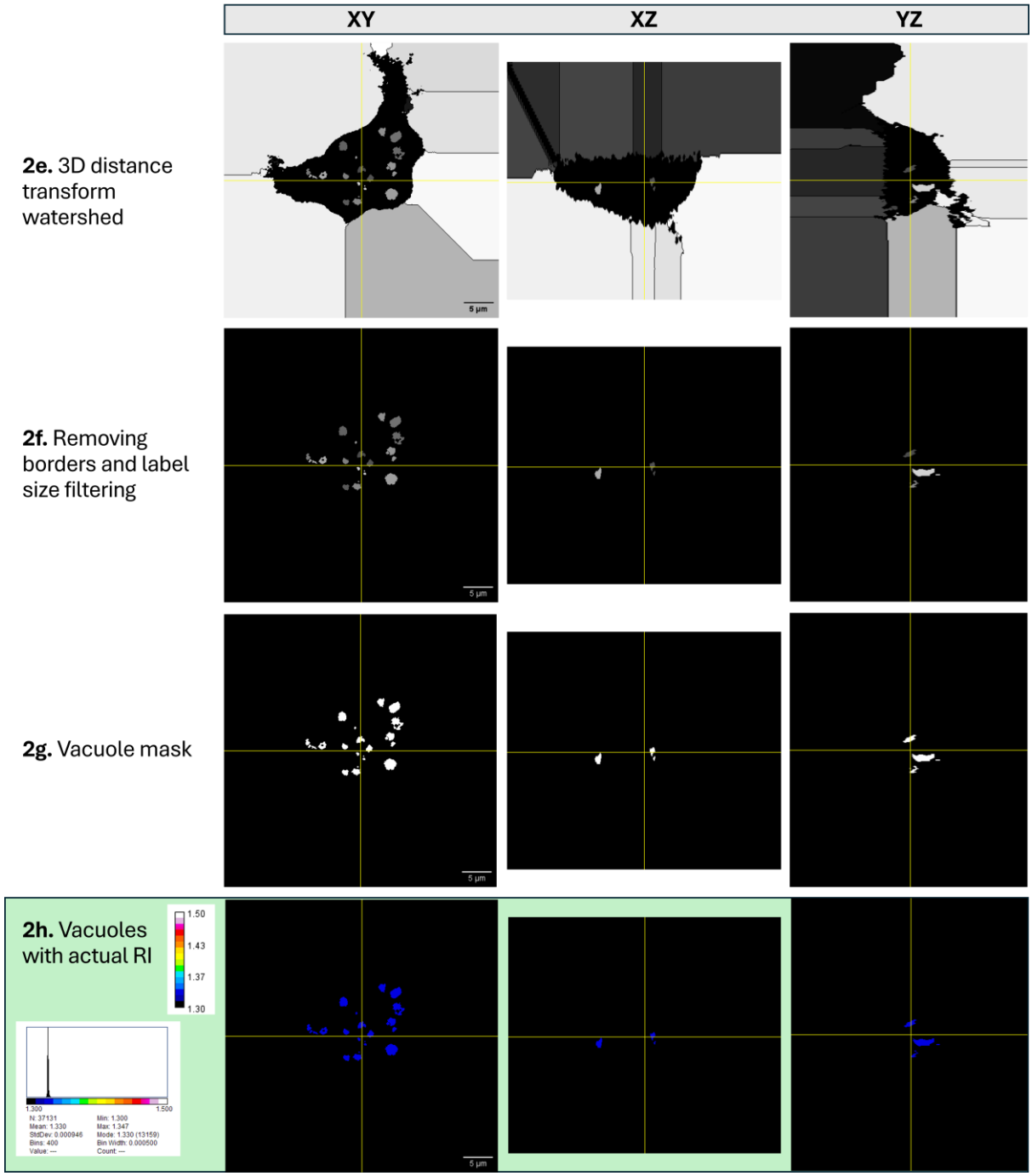
XY
XZ
YZ
2e. 3D distance transform watershed
2f. Removing borders and label size filtering
2g. Vacuole mask
2h. Vacuoles with actual RI
1.50
1.43
1.37
1.30
5 µm

Part III. *Combination of vacuoles and hemocyte masks.*

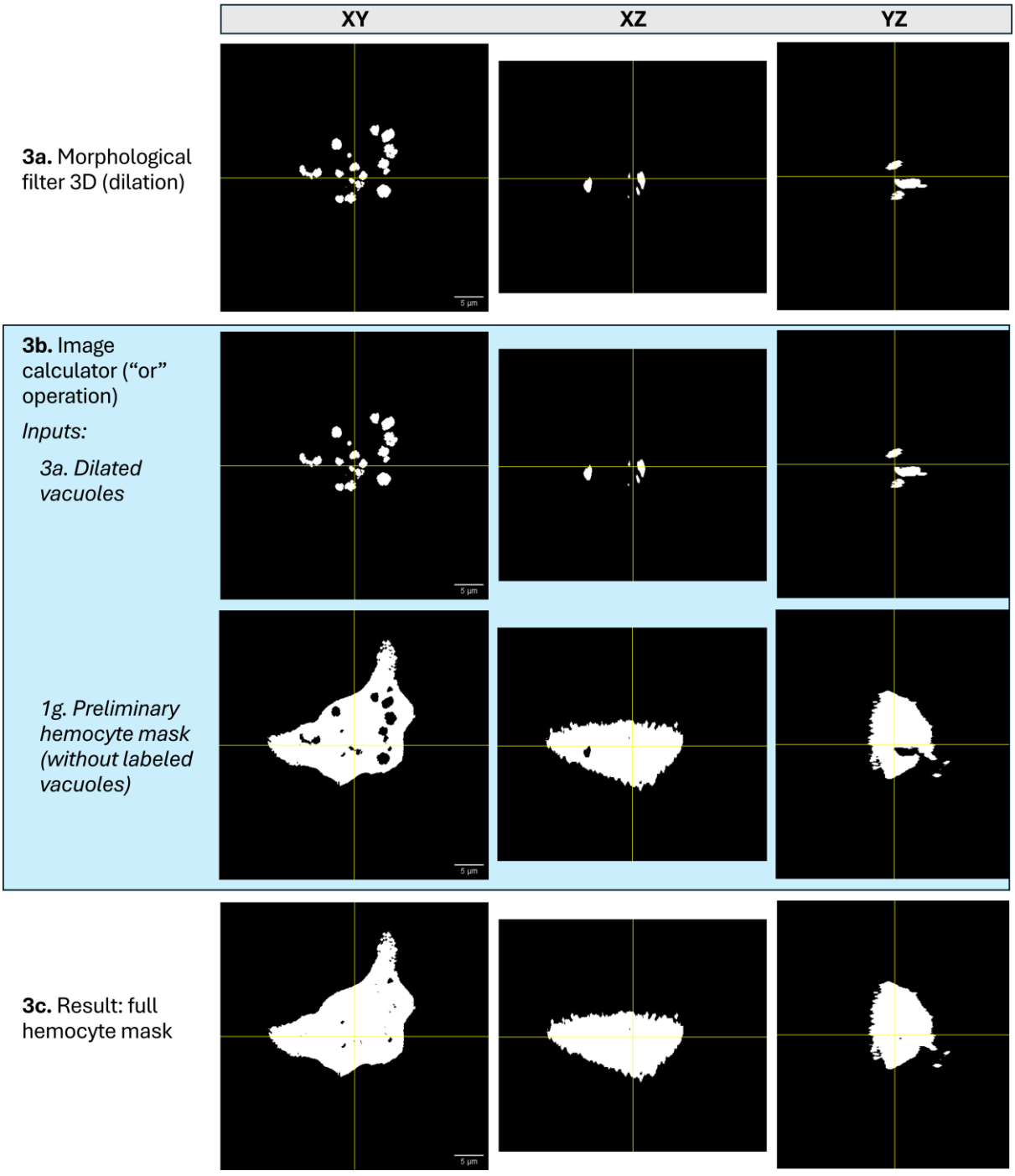

Part IV. *Segmentation of the cytoplasm.*

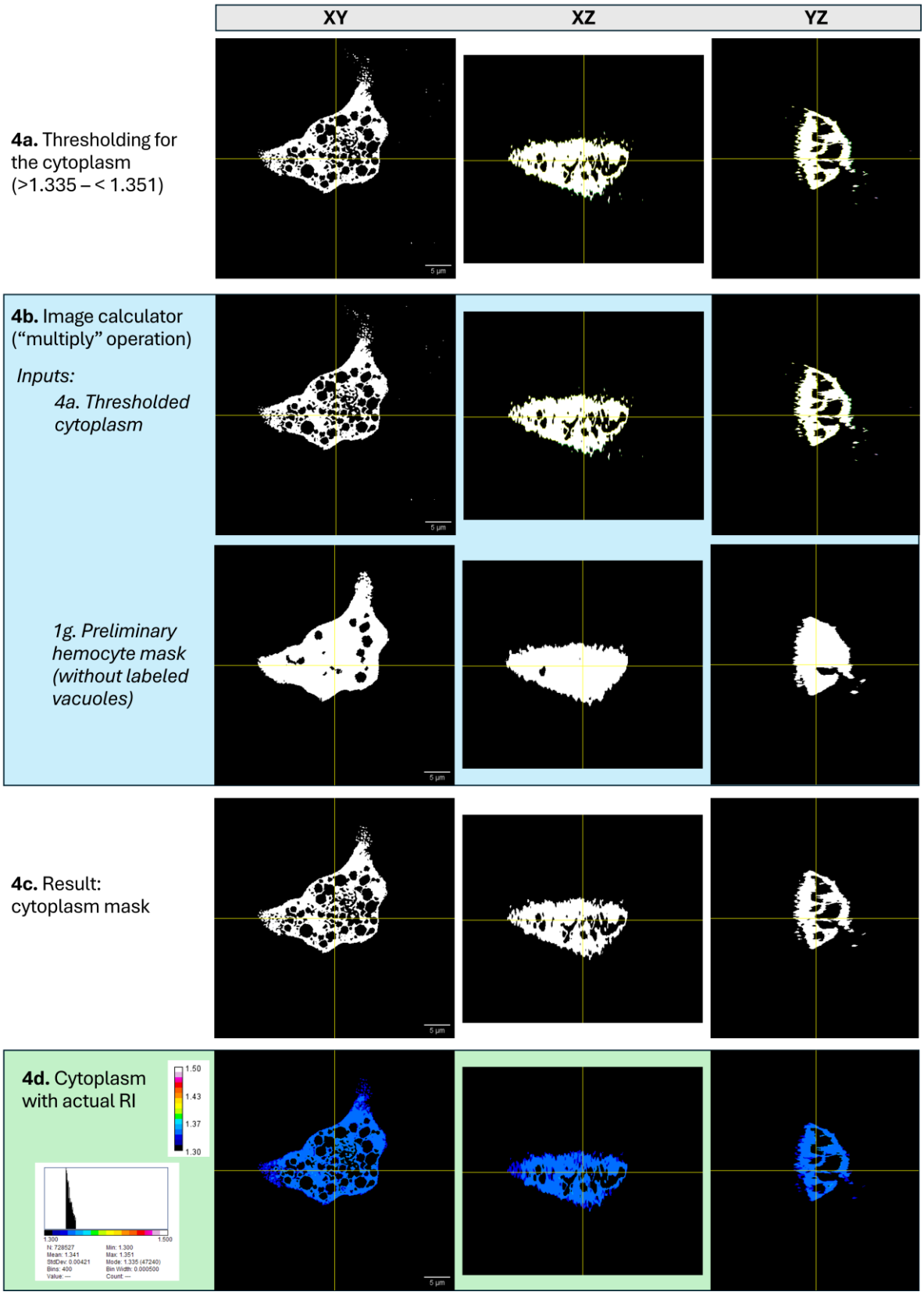

Part V. *Segmentation of granules.*

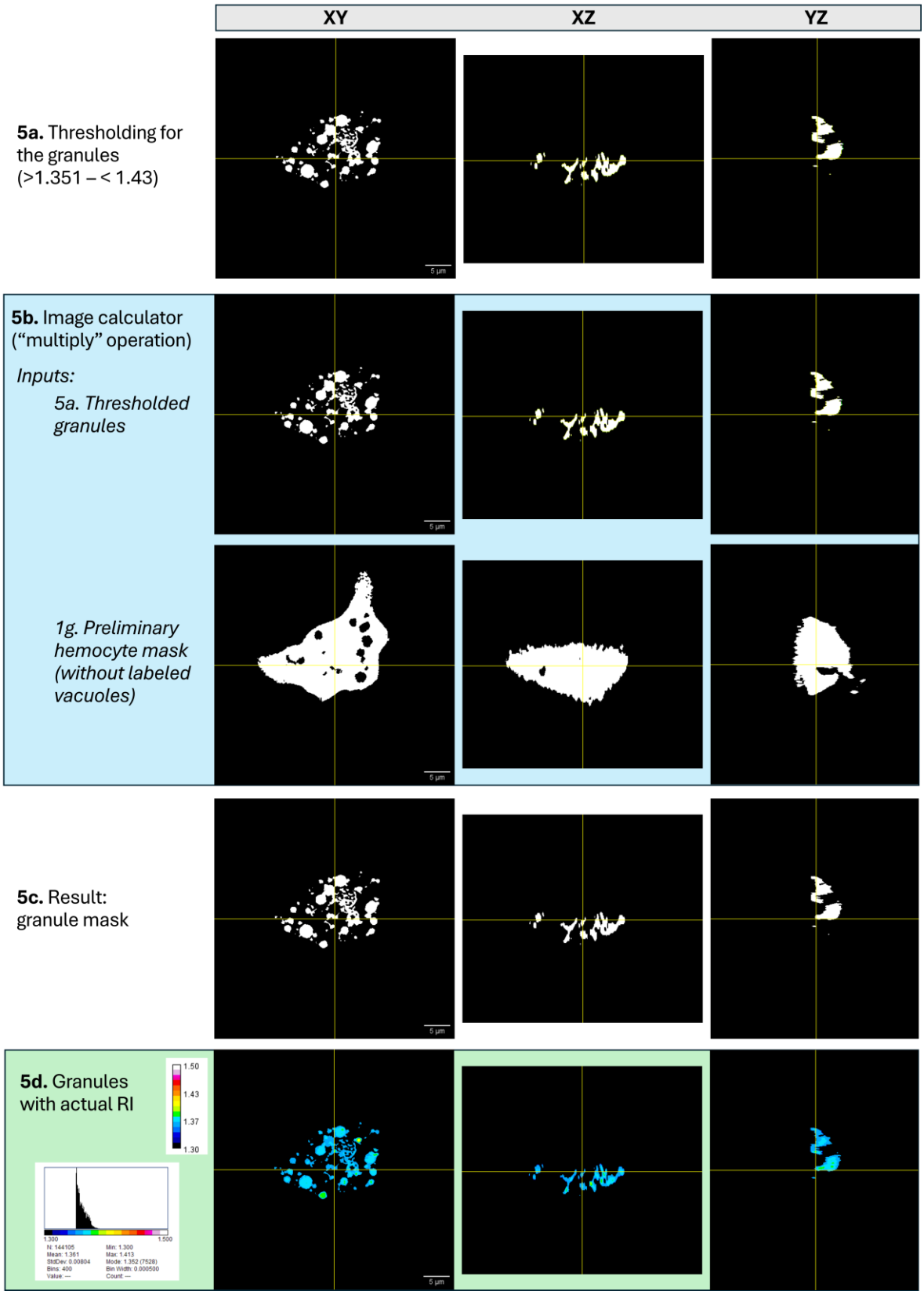

Part VII. *3D visualization*

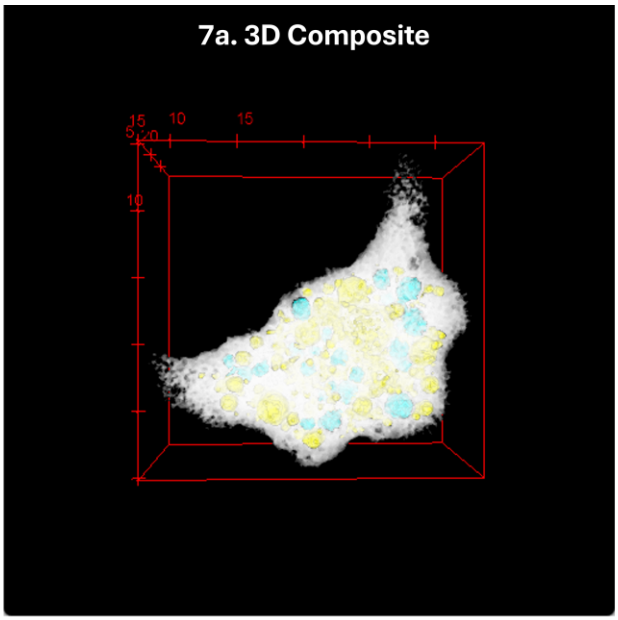

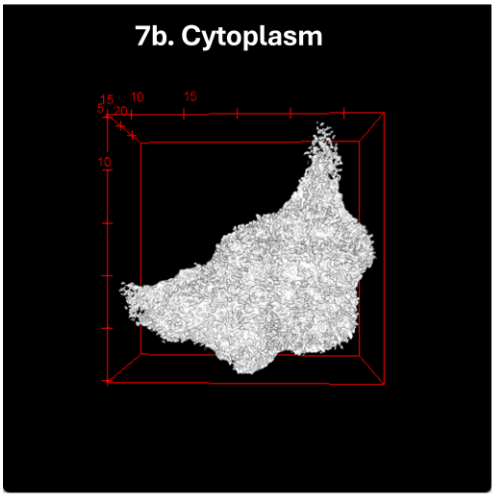

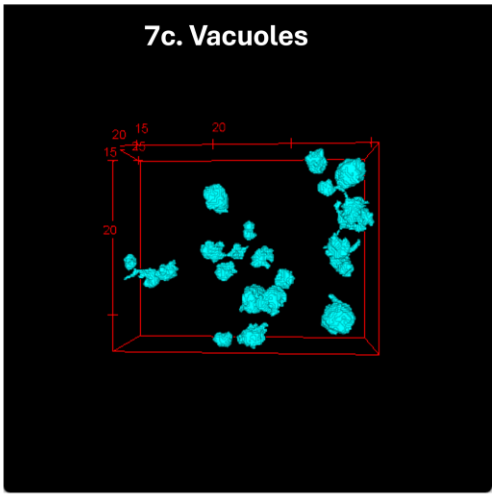

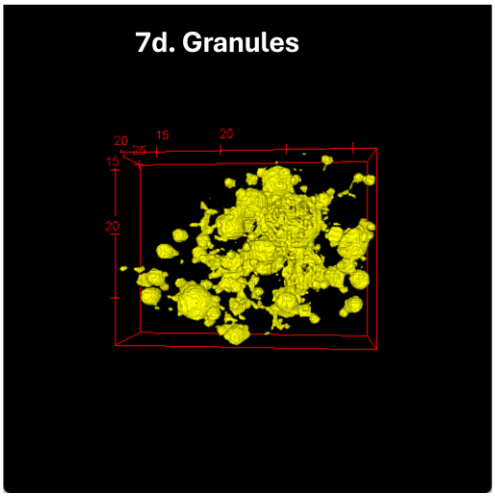

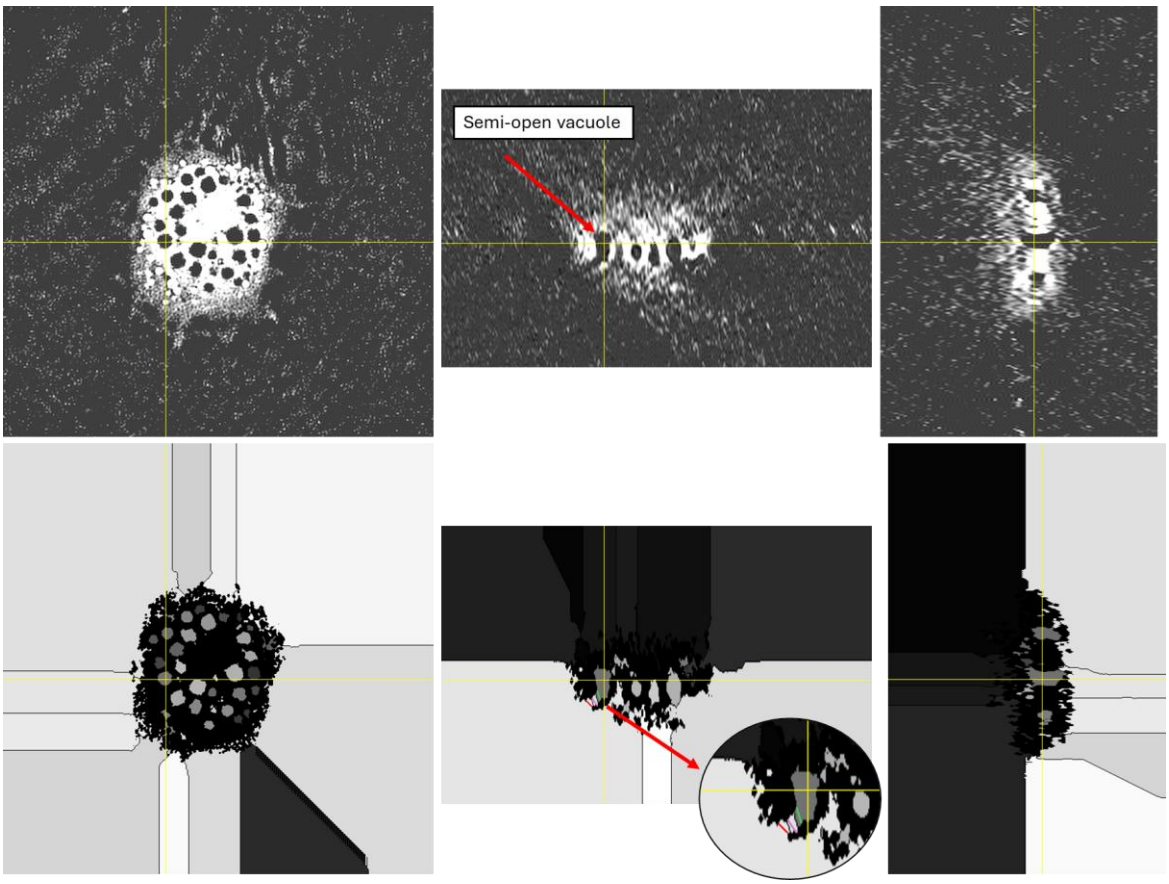

Figure A5.11. *Defining semi-closed vacuole boundaries using the 3D distance-transform watershed algorithm. In the magnified sample, several visually plausible border options (highlighted in different colors, with the black border line determined by the watershed algorithm) can be identified. This illustrates the need for an automated distance-transform watershed approach to obtain consistent and reproducible vacuole boundary definitions across images.*

Image processing validation

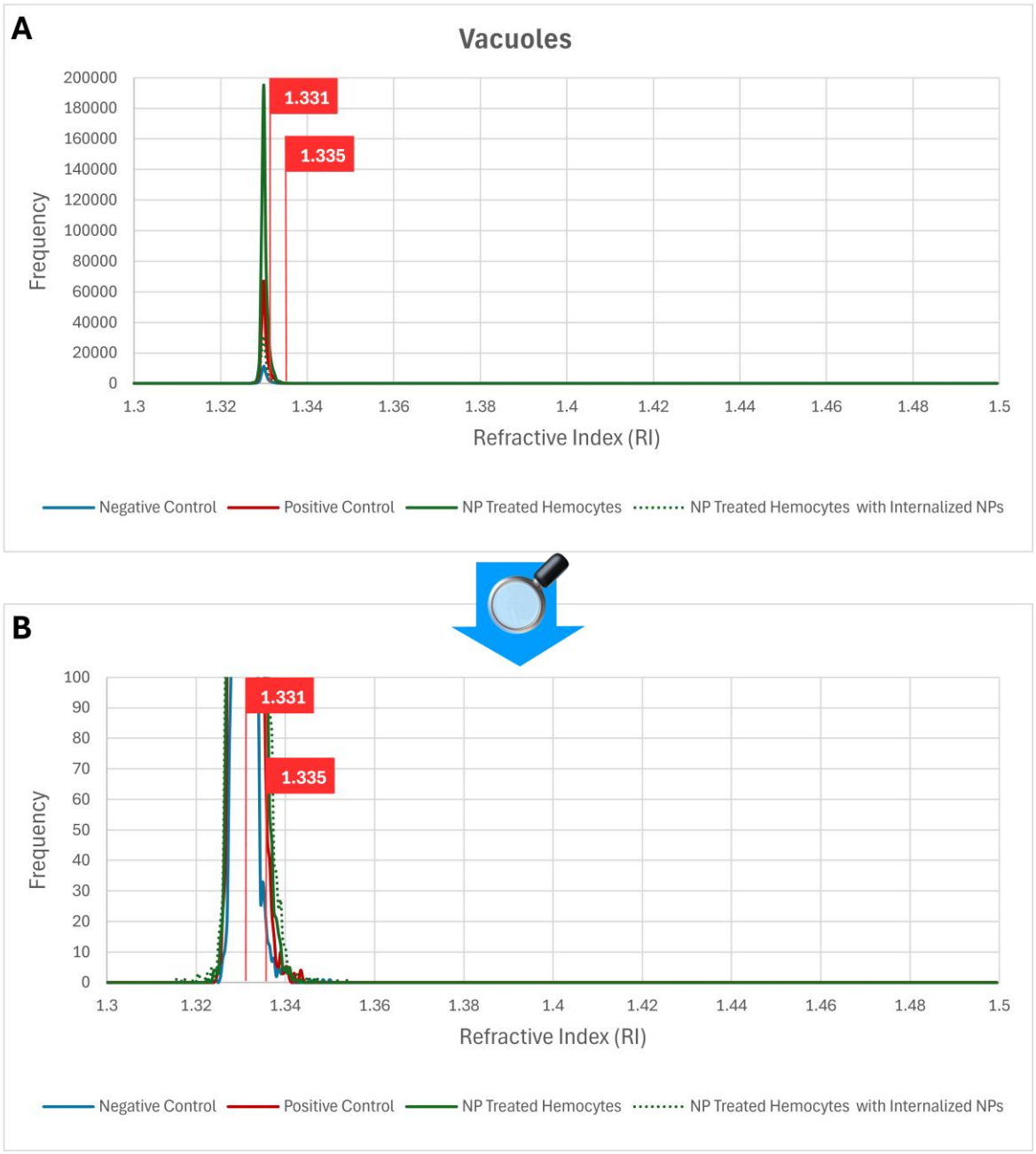

Figure A5.12. *Stacked RI distributions of the segmented vacuoles from representative 3D images (total n = 28) of hemocyte subpopulations across all experimental conditions (negative control (n = 5), positive control (n = 6), NP-treated hemocytes (n = 12), and NP-treated hemocytes with internalized NPs (n = 5)). The upper panel* ***(A)*** *displays the full voxel-frequency distribution, while the lower panel* ***(B)*** *magnifies the lower-frequency range for improved visualization. Vertical red lines indicate the applied RI threshold for vacuoles (1.331), and the lower threshold applied for cytoplasm (1.335).*

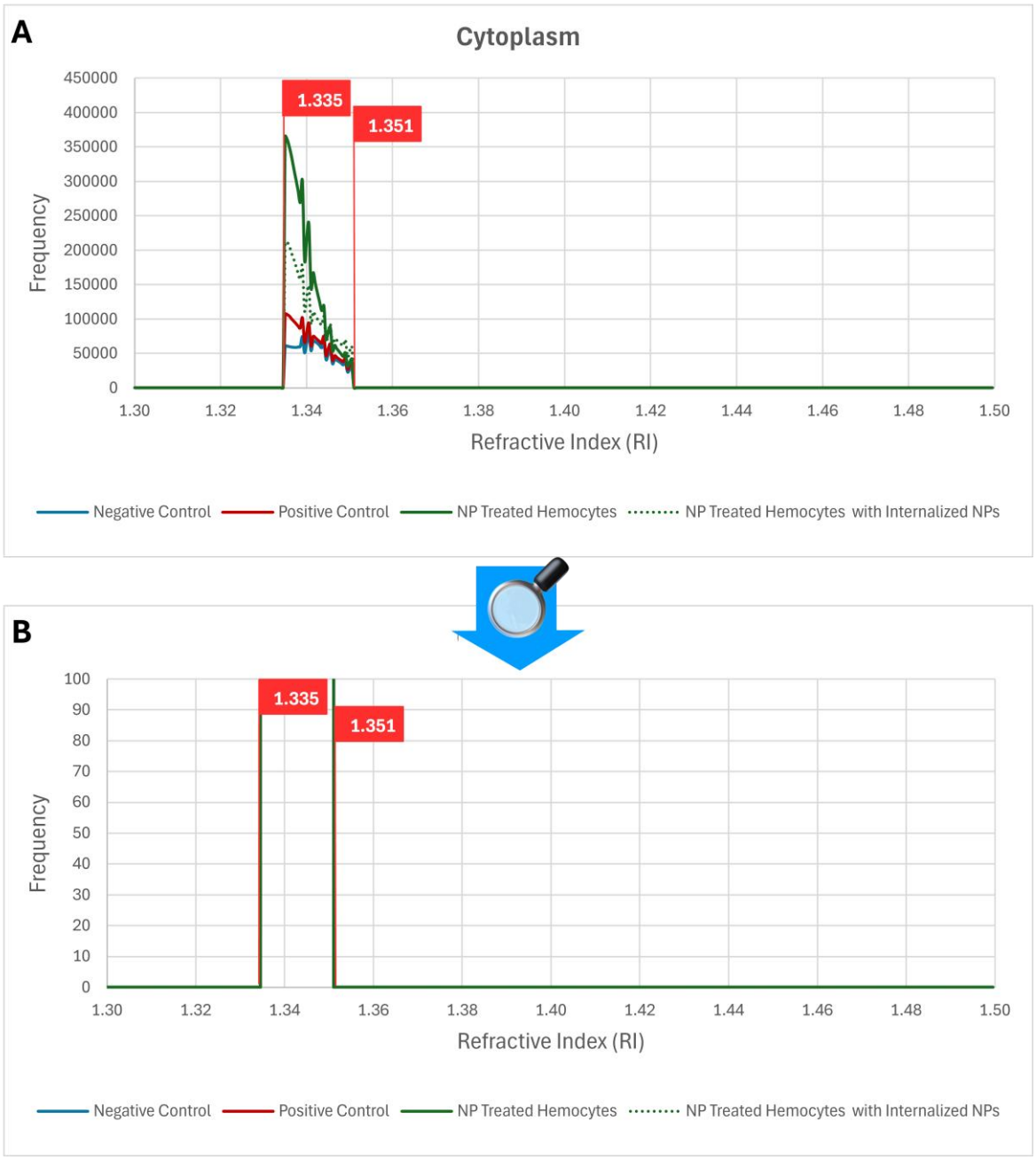

Figure A5.13. *Stacked RI distributions of the segmented cytoplasm from representative 3D images (total n = 28) of hemocyte subpopulations across all experimental conditions tested (negative control (n = 5), positive control (n = 6), NP-treated hemocytes (n = 12), and NP-treated hemocytes with internalized NPs (n = 5)). The upper panel* ***(A)*** *displays the full voxel-frequency distribution, while the lower panel* ***(B)*** *magnifies the lower-frequency range for improved visualization. Vertical red lines indicate the applied RI thresholds (1.335–1.351). No voxels were detected outside the threshold boundaries, confirming the robustness and consistency of the segmentation approach across conditions.*

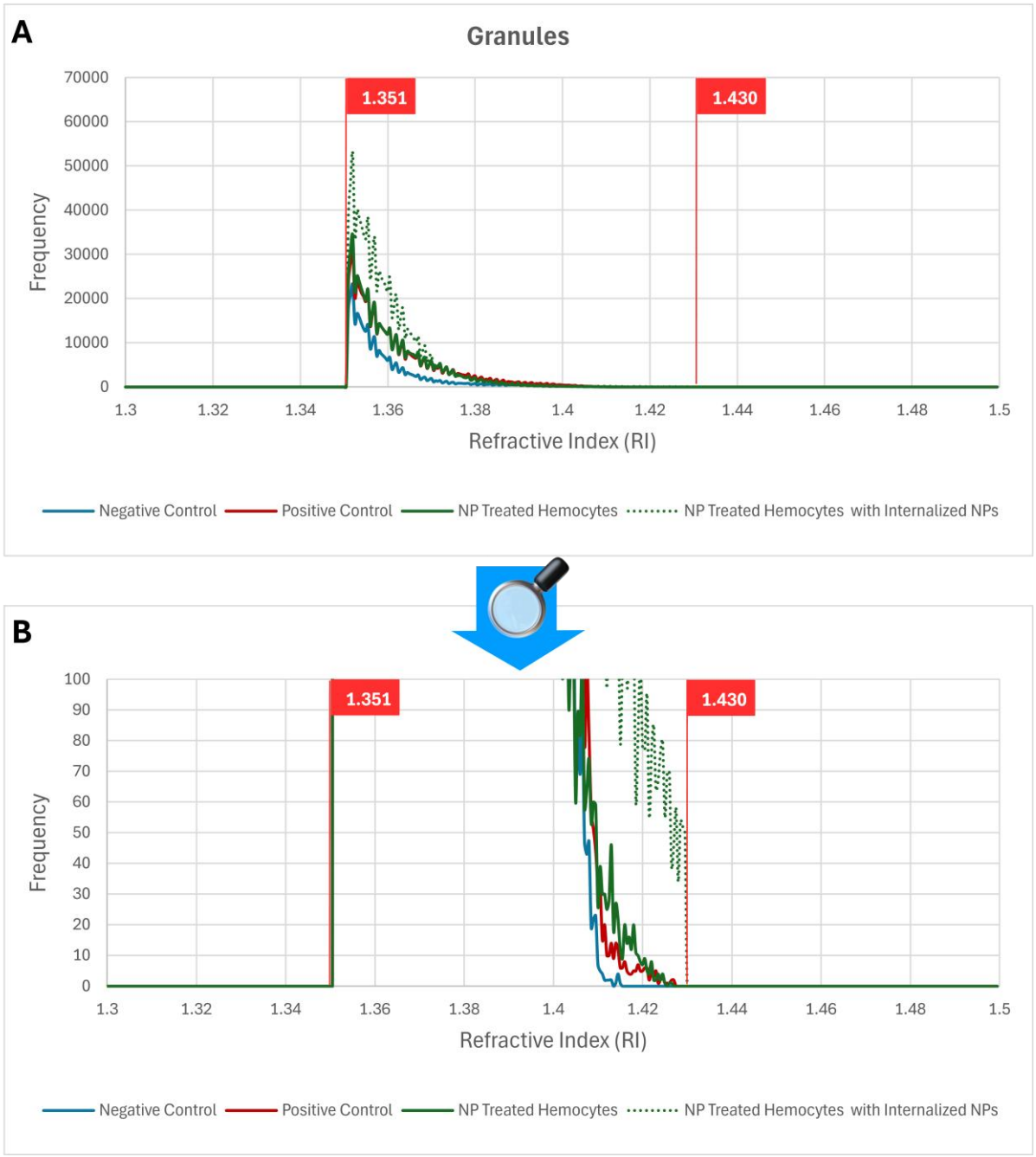

Figure A5.14. *Stacked RI distributions of the segmented granules from representative 3D images (total n = 28) of hemocyte subpopulations across all experimental conditions tested (negative control (n = 5), positive control (n = 6), NP-treated hemocytes (n = 12), and NP-treated hemocytes with internalized NPs (n = 5)). The upper panel* ***(A)*** *displays the full voxel-frequency distribution, while the lower panel* ***(B)*** *magnifies the lower-frequency range for improved visualization. Vertical red lines indicate the applied RI thresholds (1.351–1.430). No voxels were detected outside the threshold boundaries, confirming the robustness and consistency of the segmentation approach across conditions.*

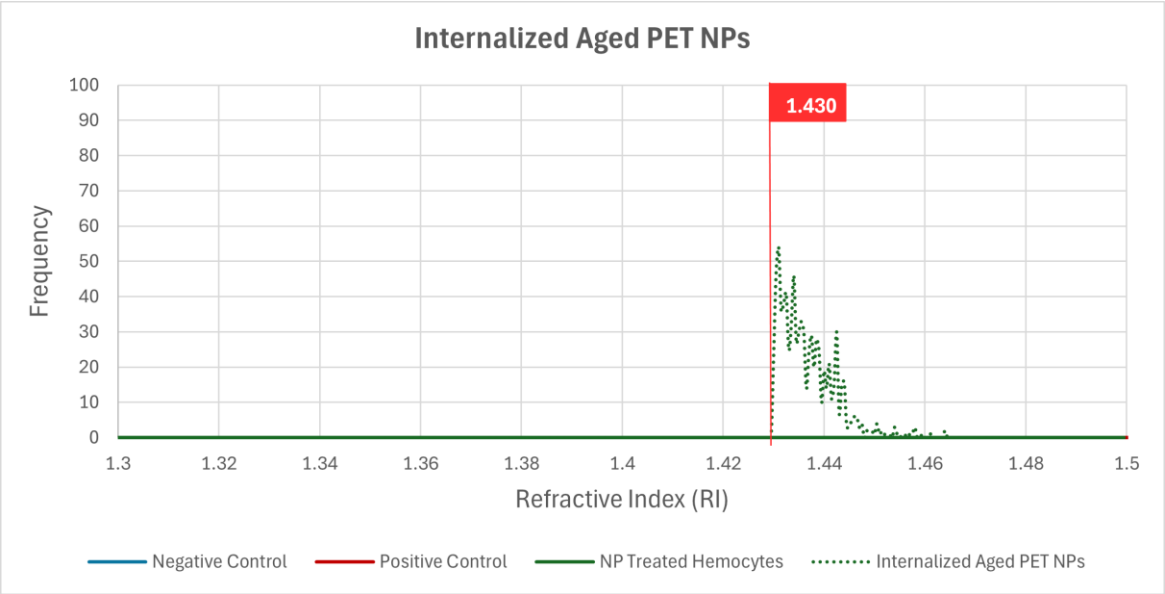

Figure A5.15. *Stacked RI distributions of the detected internalized aged PET NPs from representative 3D images (total n = 28) of hemocyte subpopulations across all experimental conditions tested (negative control (n = 5), positive control (n = 6), NP-treated hemocytes (n = 12), and NP-treated hemocytes with internalized NPs (n = 5)). Vertical red lines indicate the applied RI thresholds (> 1.430). No voxels were detected below the threshold boundary, confirming the robustness and consistency of the segmentation approach across conditions.*

Reference hemocyte images

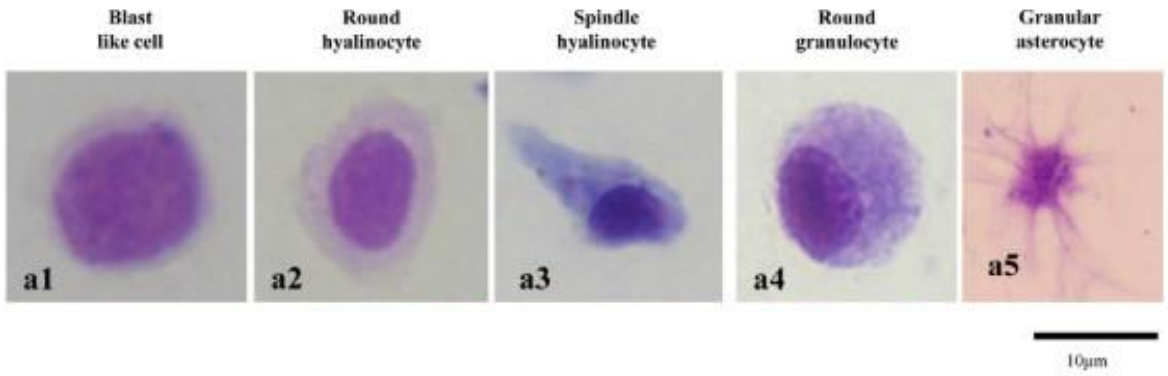

Figure A5.16. *Morphological reference images used for the identification of hemocyte subpopulations: blast-like cells (a1), round hyalinocytes (a2), spindle hyalinocytes (a3), round granulocytes (a4), and granular asterocytes (a5). Scale bar: 10 µm. Adapted from Ray et al., 2013.*

Curriculum Vitae

PERSONAL INFORMATION

Name: **Jenevieve Hara**

Email Address: **harajenevieve@gmail.com**

EDUCATION AND TRAINING

1 Oct 2020 – 21 April 2026	**Joint PhD (Doctor of Science: Biology and Doctor of Bioscience Engineering)** ECOSPHERE, University of Antwerp (Belgium) GhenTox/BGRL Lab, Ghent University (Belgium) Scholarship: Fund for Scientific Research – Flanders (FWO) and RESPONSE Project (JPI Oceans)
20 Sep 2017–4 Jul 2019	**International Master of Science in Marine Biological Resources (IMBRSea)** Ghent University, Ghent (Belgium) Scholarship: Erasmus Mundus Scholarship (Partner Country) funded by the European Commission Award: Cum Laude Thesis: "Quantification of Microplastic Ingestion by the Decapod Crustacean *Nephrops norvegicus* from Irish Waters".
24 Jun 2015–17 Nov 2017	**Master of Science in Marine Biology** Western Philippines University (Philippines) Scholarship: Malampaya Sustainable Development Scholarship Program funded by the Malampaya Foundation Incorporated Thesis: "Characterization of Actinomycetes with Antibiotic-producing Potential from the Rhizosphere of Mangrove Plant *Camptostemon philippinensis*".
11 May 2009–23 Apr 2013	**Bachelor of Science in Environmental Management** Western Philippines University (Philippines) Scholarship: Department of Agriculture – Agricultural Comprehensive Enhancement Fund Award: Cum Laude Thesis: "Status of Two River Systems in Puerto Princesa City, Palawan, Philippines".

JOURNAL PUBLICATIONS

- **Hara, J**., Vercauteren, M., Janssen, C. R., Blust, R., Asselman, J., & Town, R. M. (2026). Systematic assessment of the mechanisms and risks of micro- and nanoplastic particle exposure in marine invertebrates. *Ecotoxicology and Environmental Safety*, 311, 119877.
- **Hara, J**., Oraño, G. B., Vercauteren, M., Mubiana, K. V., Janssen, C. R., Blust, R., Asselman, J., & Town, R. M. (2025). Cellular and Tissue-Level Responses of Mussels (*Mytilus edulis*) to Aged Polyethylene Terephthalate (PET) Micro-and Nanoplastic Particles. *Aquatic Toxicology*, 107369.
- **Hara, J**., Vercauteren, M., Schoenaers, S., Janssen, C. R., Blust, R., Asselman, J., & Town, R. M. (2024). Differential Sensitivity of Hemocyte Subpopulations (*Mytilus edulis*) to Aged Polyethylene Terephthalate Micro- and Nanoplastic Particles. *Ecotoxicology and Environmental Safety*, 286.
- **Hara, J.,** Frias, J., Nash, R. (2020). Quantification of Microplastic Ingestion by the Decapod Crustacean *Nephrops norvegicus* from Irish Waters. *Marine Pollution Bulletin*,152.
- Joyce, H., **Hara J**., Nash, R., and Mychkova, A. (2021) EU Aquaculture. In Aquaculture: With focus on Vietnam and Thailand (pp. 56 - 67*). Ostfalia Hochschule für angewandte Wissenschaften*.
- Martinico-Perez, M.F.G., **Hara J**., Cabrestante, M.P. (2016). Water Quality Index as Evaluation Tool of River Water Quality in Palawan. *Palawan Journal*.

CONFERENCES

- Elucidating the Cellular and Tissue-level Responses of Mussels (*Mytilus edulis*) to Aged Polyethylene Terephthalate (PET) Micro- and Nanoplastic Particles. [Oral Presenter, BelTox – BEMS 2025: Unmasking Microplastics: Impacts, Challenges and Implications for Eco(Toxicology), Brussels, Belgium, 4 December 2025].
- Differential Sensitivity of Hemocyte Subpopulations (*Mytilus edulis*) to Aged Polyethylene Terephthalate Micro- and Nanoplastic Particles. [Oral Presenter, MICRO 2024: From Macro to Nano, Lanzarote, Spain, 23–27 September 2024].
- Mechanistic Assessment of Cellular Responses to Aged Polyethylene Terephthalate Micro- and Nanoplastic Particles in Bivalve Hemocytes (*Mytilus edulis*). [Poster Presenter, SETAC Europe 34th Annual Meeting, Sevilla, Spain, 5–9 May 2024].
- Automated Quantification of Fluorescence Signals for Apoptosis and Necrosis in Bivalve Hemocytes (*Mytilus edulis*) using Fiji/ImageJ as a Proxy for *In Vitro* Toxicity Assessment. [Poster Presenter, SETAC Europe 33rd Annual Meeting, Dublin, Ireland, 30 April–4 May 2023].
- Automated Quantification of Apoptosis Signals in Bivalve Hemocytes as a Proxy for Micro- and nanoplastic Risk Assessment [Poster Presenter, Interfaces Against Pollution: Chemical and Biological Perspectives (IAP2022), Antwerp, Belgium, 18–21 September 2022].
- *In vitro* Assessment of the Sensitivity of Bivalve Hemocytes to Nanoplastic Exposure. [Poster Presenter, SETAC Europe 32nd Annual Meeting, Copenhagen, Denmark 15–19 May 2022].
- Snapshot of Palawan's River Water Quality: A Call for Sustainable Water Resources Management [Poster Presenter, International Biodiversity Conference, Mati City, Davao Oriental, 11–14 November 2019].
- Quantification of Microplastic Ingestion by the Decapod Crustacean *Nephrops norvegicus* from Irish Waters [Oral Presenter, Diving into Marine Minds-IMBRSea Annual Symposium, Brest, France, 24–28 June 2019].

- Characterization of Actinomycetes with Antibiotic-producing Potential from the Rhizosphere of Mangrove Plant *Camptostemon philippinensis* [Poster Presenter, YOUMARES Conference for Young Marine Researchers, Oldenburg, Germany, 11–14 September 2018].
- Enumeration, Isolation and Characterization of Actinomycetes with Antibiotic-producing Potential from the Rhizosphere of Mangrove Plant *Camptostemon philippinensis* [Oral Presenter, ASEAN Mangrove Congress, Manila, Philippines, 4–8 September 2017].
- Actinomycetes and Fungi Enumerated from Sediments Associated with Three Mangrove Species in Puerto Princesa City, Philippines [Oral Presenter, International Conference on Food, Environment, and Culture, Baguio, Philippines, 15–18 May 2017].
- Evaluation of Water Quality of Major Rivers in Palawan, Philippines Using Physico-chemical Parameters and Water Quality Index [Oral Presenter, 13th National Convention on Statistics, Mandaluyong, Philippines, 3–4 October 2016].
- Are The Coastal Marine Waters of North Mainland Palawan's Major Tourism Sites Fit for Recreation Purposes? [Poster Presenter, 2nd Palawan Research Symposium on Palawan's Sustainable Development, Puerto Princesa, Philippines, 9–10 December 2015].
- Water Quality Index as Evaluation Tool of River Water Quality in Palawan [Oral Presenter, 2nd Palawan Research Symposium on Palawan's Sustainable Development, Puerto Princesa, Philippines, 9–10 December 2015].
- Status of Two River Systems in Puerto Princesa City, Palawan, Philippines [Oral Presenter, 6th International Conference of the Philippines Network of Educator's on Environment, Butuan, Philippines, 20–22 March 2013].

CERTIFICATIONS

- Career Service Eligibility (Professional, Civil Service Commission of the Philippines)
- Proficiency in Personal Sea Survival Techniques (Marine Survey Centre of Ireland)
- Open Water Scuba Diving (Professional Association of Diving Instructor)

AWARDS

• Best Oral Presentation, Belgian Society of Toxicology and Ecotoxicology and Belgian Environmental Mutagen Society (BelTox-BEMS) Annual Meeting: Unmasking Microplastics: Impacts, Challenges and Implications for Eco(Toxicology), 2025, Brussels, Belgium.

• Best Poster Presentation, Interfaces Against Pollution: Chemical and Biological Perspectives Conference, 2022, Antwerp, Belgium.

• Best Student Researcher of the Year, Western Philippines University, 2013, Puerto Princesa City, Philippines

OTHER GRANTS

• Society of Environmental Toxicology and Chemistry (SETAC) Grant (2022) for attending the SETAC Europe 32nd Annual Meeting in Copenhagen, Denmark.